Design of Catalytic Systems based on Halogen Bonding Interactions: Synthesis and Application in Catalytic Reactions

Alba Martínez Bascuñana

Design of Catalytic Systems based on Halogen Bonding Interactions:

Synthesis and Application in Catalytic Reactions

UNIVERSITAT DE BARCELONA

Alba Martínez Bascuñana

Design of Catalytic Systems based on Halogen Bonding Interactions: Synthesis and Application in Catalytic Reactions

Alba Martínez Bascuñana

Doctoral Thesis

Doctoral program: Química Orgánica

Supervised by Prof. Dr. Anton Vidal i Ferran and
Dr. José Luis Núñez Rico

Facultad de Química
Departamento de Química Inorgánica y Orgánica
Universidad de Barcelona

UNIVERSITAT DE BARCELONA

Doctoral thesis presented by Alba Martínez Bascuñana to obtain the Ph.D. degree in chemistry from the University of Barcelona.

Alba Martínez Bascuñana

Prof. Dr. Anton Vidal i Ferran, Research Professor of the Catalan Institution for Research and Advance Studies (ICREA), and Dr. José Luis Núñez Rico, Adjunct Professor of the Inorganic and Organic Department of the University of Barcelona,

CERTIFIES that the present Doctoral Thesis entitled: "Design of Catalytic Systems based on Halogen Bonding Interactions: Synthesis and Application in Catalytic Reactions" that Alba Martínez Bascuñana presents to obtain the Ph.D. degree in chemistry has been carried out under our supervision in the corresponding research group at the University of Barcelona.

Prof. Dr. Anton Vidal i Ferran

Dr. José Luis Núñez Rico

Barcelona, June 2023

The research work developed in the present Ph.D. thesis has been possible thanks to the MICINN for a FPI predoctoral fellowship (PRE2018-084131), and the financial support by the MICINN (CTQ2017-89814-P and PID2020-115658GB-I00).

ACKNOWLEDGMENTS

En primer lugar, me gustaría agradecer a mis directores de tesis, el **Prof. Dr. Anton Vidal** y el **Dr. José Luis Núñez**, por darme la oportunidad de realizar la tesis doctoral en su grupo de investigación tanto en el ICIQ como en la Universidad de Barcelona. Gracias por dejarme desarrollar mi potencial y creatividad, por vuestra supervisión y, por supuesto, por la dedicación durante estos cinco años.

Cinco años es mucho tiempo, aunque se diga pronto. Cuando ese tiempo lo compartes con una buena compañía todo se hace más llevadero. Durante estos años me he encontrado con gente buena y dedicada. De ellos he aprendido muchas cosas tanto a nivel profesional como personal. En primer lugar, me gustaría agradecer a aquellos que me acompañaron en mis primeras etapas: **Héctor**, **José Luis**, **Lucas**, **Alicia**, **Nuria**, **Ester** y **Andrés**. En especial me gustaría agradecer a **José Luis** por ver siempre en mi algo que ni yo veía, por su apoyo incondicional y buenos consejos. También me gustaría hacer una mención especial a **Lucas,** de quien he aprendido infinidad de cosas y con quien he disfrutado muchísimo. Gracias por inculcarme buenos valores, por los consejos y las charlas aquellas tardes de *glovebox*, por hacerme reír y por estar ahí, aunque sigan pasando los años. Y a **Andrés**, con quien he andado en paralelo todo este camino. Los cambios son difíciles, pero como he dicho, todo es más llevadero con buena compañía a tu lado, especialmente con personas tan buenas y bondadosas como él. Recuerda que vales mucho.

Por otro lado, también me gustaría agradecer al **Prof. Arnald Grabulosa** y el **Prof. Daniel Sainz** por darnos la bienvenida con los brazos abiertos y ayudarnos a gestionar y organizar todo en tan poco tiempo. Durante mis últimos años de doctorado he tenido la suerte de compartir batallas con nuevos compañeros con los que he pasado buenos momentos y de los que me llevo grandes recuerdos: **Javier**, **Edgar**, **Hannah**, **Yuzelfy**, **Dana**, **Ignasi** y **Adriana**. Me gustaría agradecer

especialmente a **Edgar** y a **Javier** por todos los momentos juntos: comidas, cotilleos, charlas, etc., y por hacer más llevaderos los momentos más difíciles. I would also like to thank **Hannah** for her constant interest and for learning so much from each other.

I would like to express my gratitude to **Dr. Josep Cornellà** for giving me the opportunity to join his research group at the Max Plank Institute für Kohlenforschung for three months. I would like to thank as well all the members of his group for making me feel comfortable during the stay, especially those with whom I shared the most special moments: **Jenny**, **Rakan**, **Ana**, **Uri**, **Marc**, **Mauro** and **Sergio**. During these months I had the pleasure to work with a human encyclopedia, **Rakan**, from whom I have learned many things, and to share my secrets and experiences with my favorite German girl, **Jenny**. I have really found a true friend. Thank you so much for all that you have given me these last few years and for always being with me.

También me gustaría agradecer a todas aquellas personas que han sido partícipes de este proyecto y que me han aportado tanto durante estos años. Por un lado, me gustaría dar las gracias a mis Pavipollos, a todos y cada uno de ellos, por todos los buenos momentos, las risas y todas las experiencias que hemos vividos juntos. **Andreu**, **Jesús**, **Miguel**, **Raúl**, **Alicia M**, **Chuchi** y **Kike**, sois de las mejores personas que he conocido, siempre dispuestos a ayudarme y a darme buenos consejos. Gracias por todo lo que me habéis aportado estos años. Por otro lado, mil gracias a mis chicas: **Alicia**, **Ester**, **Nuria** y **Cris**, porque desde el principio me acogisteis bajo vuestra ala (aunque allí me encontrara con la lima de grano gordo…) y me enseñasteis todo lo que sé. Todo lo que soy y el hecho de que hoy esté aquí, en este punto, es en gran parte gracias a vosotras. Solo me queda daros las gracias por ello y por seguir a mi lado, siempre. A todos mis Pavipollos, os quiero mucho.

Durante mi primer año en Tarragona tuve la suerte de conocer gente increíble, los cuales me han acompañado durante estos años. Me gustaría agradecer a mis turbos: **Pol**, **Luis** y **Dani**, quienes han estado siempre ahí, a pie de cañón. En especial me gustaría agradecer a mi **Policho**, con quien lo he compartido todo: lo bueno, lo malo y sobre todo el sushi, y de quien he aprendido muchísimo. Gracias por aguantarme todos estos años.

El primer día que aterricé en Tarragona, recién llegada del pueblo, allí estaba mi **Albi**. Quien me iba a decir a mi aquel día que en ti encontraría una de las amistades más verdaderas que he tenido y tendré. Por haber sido mi apoyo incondicional, por habernos enseñado tantas cosas la una a la otra, por ser familia, por estar siempre conmigo y por mil cosas más, muchas gracias. Eres increíble y no sé qué habría hecho sin ti. Te quiero. Un tiempo después llegaría **Ana**. Desde el primer día que te conocí supe que te convertirías en alguien importante en mi vida. Y no me equivocaba. En ti he encontrado mi otra mitad y la persona que mejor me complementa en todos los sentidos. Por ser la persona que más me entiende y por todas las risas y momentos únicos juntas (y los que quedan), muchas gracias por estar a mi lado. Te quiero. Me gustaría hacer una pequeña mención a **David**, con quien también he compartido muchas cosas, especialmente la buena música, y a las chicas del Echavarren's Lab y a **Ali**, con quienes he compartido gran parte del tiempo de este último año y con quienes me llevo muy buenos recuerdos.

Por último, me gustaría agradecer a mis padres **Javier** y **Ana** y a mi hermana **Natalia**. Sin vosotros nada de esto hubiera sido posible. Estoy y estaré infinitamente agradecida por todo el apoyo y amor que me habéis dado siempre y por todos los valores que me habéis inculcado. Sin vosotros no estaría aquí y no sería quien soy ahora. Gracias por estar a mi lado incluso en la distancia y por creer en mi de manera incondicional. Os quiero mucho y esto es en gran parte vuestro.

A mi familia y amigos

“Yet it is in our idleness, in our dreams,
that the submerged truth sometimes
comes to the top.”

Virginia Woolf

“Science is competitive, aggressive,
demanding. It is also imaginative,
inspiring, uplifting.”

Vera Rubin

TABLE OF CONTENTS

LIST OF ACRONYMS AND ABBREVIATIONS

The acronyms and abbreviations used in this manuscript have been used following the recommendations given by the American Chemical Society in the ACS guidelines for authors. Abbreviations and acronyms used in this manuscript are referenced in the list below.

º	angle
Å	angstrom(s)
Ac	acetyl
acac	acetylacetonate (ligand)
AcO	acetate
aq.	aqueous
Ar	aryl
atm	atmosphere(s)
BArF	tetrakis[3,5-bis(trifluoromethyl)phenylborate]
Bcat	derived from catecholborane
BCP	bond critical points
Bdan	derived from 1,8-diaminonaphthalatoborane
Bpin	derived from pinacolborane
br	broad (spectral), branched (isomer)
br/*l*	branched-linear ratio
n-Bu	normal butyl
t-Bu	*tert*-butyl
°C	degrees, Celsius
ca.	*circa* (about)
calcd.	calculated
cat.	catalyst
cm^{-1}	wavenumber(s)
cod	1,5-cyclooctadiene

Conv.	conversion
Cy	cyclohexyl (group), cyclohexane (solvent)
δ	chemical shift in ppm
d	doublet (spectral)
DBU	1,8-diazabicyclo[5.4.0]undec-7-ene
DCE	1,2-dichloroethane
DCM	dichloromethane (solvent)
DFT	density-functional theory
DIPEA	*N,N*-diisopropylethylamine
ee	enantiomeric excess
e.g.	*exempli gratia* (for example)
equiv.	equivalent(s)
ESI	electrospray ionization
et al.	*et alii* (and coworkers)
Et	ethyl
FID	flame ionization detector
g	gram(s)
GC	gas chromatography
h	hour(s)
HB	hydroboration
HMBC	heteronuclear multiple-bond correlation spectroscopy
HPLC	high-performance liquid chromatography
HRMS	high resolution mass spectrometry
Hz	hertz
i.e.	*id est* (in other words)
IGD	inverse gated decoupling
IS	internal standard
IR	infrared

J	coupling constant
LDA	lithium diisopropylamide
μ	micro- (prefix)
m	multiplet (spectral); milli- (prefix)
M	molar (moles per liter)
M^+	parent molecular ion
Me	methyl
MeCN	acetonitrile
MHz	megahertz
min	minute(s)
mM	millimolar
mol	mole(s), molecular
MS	mass spectrometry or molecular sieves
μW	microwave
m/z	mass-to-charge ratio
NCIPlot	non-covalent interaction plot
n.d.	not detected
NMR	nuclear magnetic resonance
NTf_2	bis(trifluoromethanesulfonyl)imide
OMs	methanesulfonate or mesylate
ORTEP	oak ridge thermal ellipsoid plot program
OTf	trifluoromethanesulfonate or triflate
Ph	phenyl
PTSA	*p*-toluenesulfonic acid
ppm	part(s) per million
i-Pr	isopropyl
q	quartet (spectral)
QTAIM	quantum theory of atoms in molecules

rac	racemic
RDG	reduced density gradient
ref.	reference
s	singlet (spectral); second(s)
select.	selectivity
t	triplet (spectral); time
T	temperature
TEA	trimethylamine
THF	tetrahydrofuran
TLC	thin layer chromatography
TMS	tetramethylsilyl; tetramethylsilane
TOF	turnover frequency
TON	turnover number
t_R	retention time
Ts	*p*-toluenesulfonyl or tosyl
vs.	versus (opposed to)
XB	halogen bond (X = halogen, B = bond)

CHAPTER I:

GENERAL INTRODUCTION AND OBJECTIVES

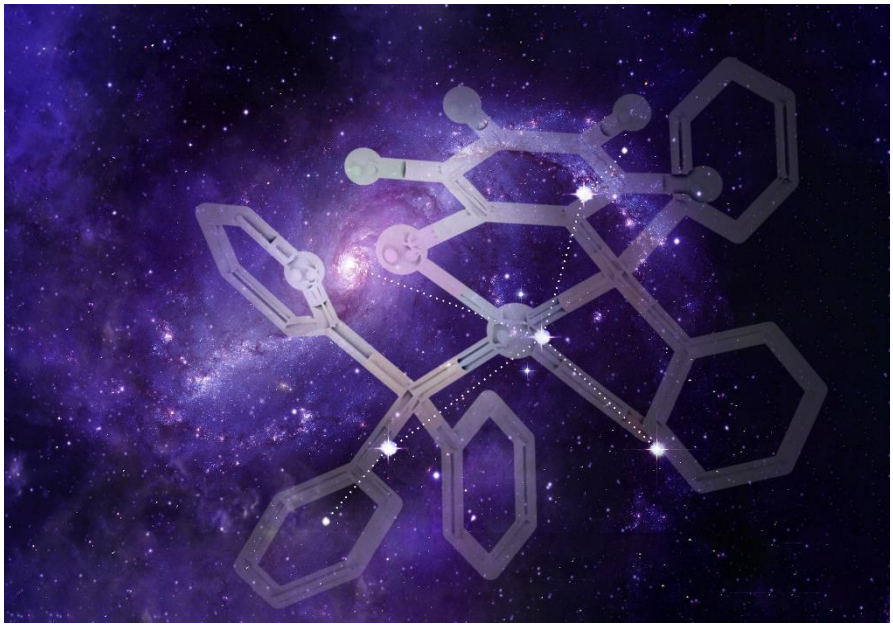

1.1 GENERAL INTRODUCTION

It was in 1987 when Jean-Marie Lehn (together with D. J. Cram and C. J. Pedersen) won the Nobel Prize for his extensive contributions to supramolecular chemistry. 'Chemistry beyond the molecule' was literally the definition that Lehn proposed for this field.[1] According to Lehn, the term supramolecular chemistry comprises the formation of functional chemical systems by assembling molecular components *via* reversible interactions.[2] Relevant examples of these reversible interactions[3] include metal-ligand, dipole, ionic, hydrogen bonding interactions along with aromatic stacking and other more recently studied non-covalent forces such as halogen and chalcogen bonding (see Figure 1.1).

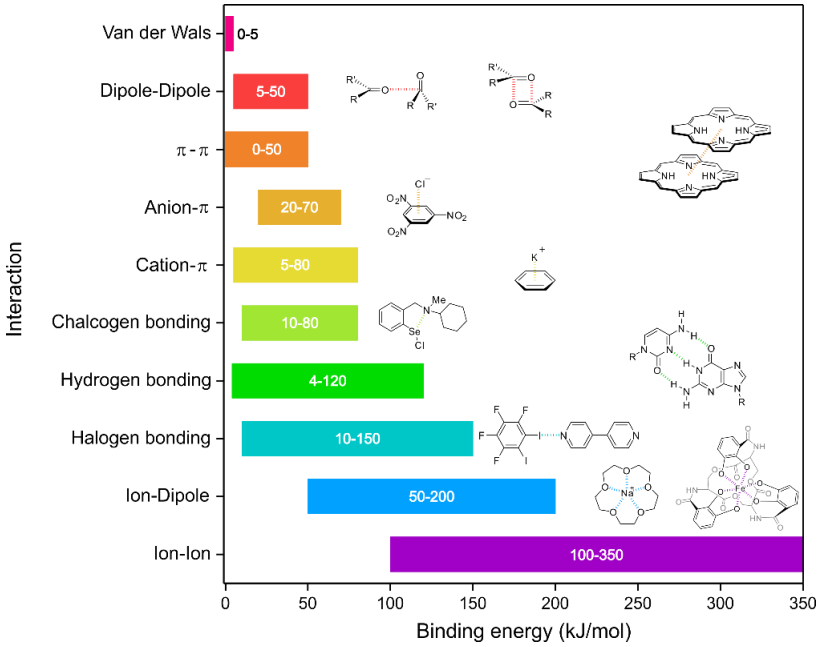

Figure 1.1. Summary of relevant non-covalent interactions.

[1] Lehn, J.-M. *Supramolecular Chemistry*: Concepts and Perspectives. VCH, 1995.
[2] For more information, see: (a) Kubik, S. *Supramolecular Chemistry*. De Gruyter, 2021; (b) Raynal, M.; van Leeuwen, P. W. *Supramolecular Catalysis: New Directions and Developments*. John Wiley & Sons, 2021; (c) Steed, J. W.; Atwood, J. L. *Supramolecular Chemistry*. John Wiley & Sons, 2022; and refences herein.
[3] Schneider, H.-J. *J. Phys. Org. Chem.* **2022**, *35*, e4340.

Originally, only chemistries related to the study of reversible intermolecular forces between a host (*e.g.*, crown ethers, cryptands or spherands) and a guest (*e.g.*, alkali metal cations) molecule (the so-called host-guest chemistry) were included in the definition of supramolecular chemistry. However, supramolecular chemistry has been a rapidly expanding field of research over the past 35 years. Nowadays, modern supramolecular chemistry includes a wide range of areas such as: molecular recognition, crystal engineering, molecular devices and machines, self-assembly or supramolecular materials.[2] In the present, supramolecular chemistry can be used together with molecular and material chemistry as an important toolbox, playing a relevant role in medicine, data storage, material science, molecular recognition and catalysis, amongst other topics.[2,4]

In parallel, major advances have been achieved in the field of homogeneous transition metal catalysis, becoming one of the most efficient and powerful strategies to perform chemical transformations with excellent selectivities and high levels of efficiency.[5] Spectacular progress has also been made in using supramolecular interactions to accelerate

[4] Maharramov, A. M.; Mahmudov, K. T.; Kopylovich, M. N.; Pombeiro, A. J. L. *Non-Covalent Interactions in the Synthesis and Design of New Compounds*. John Wiley & Sons, Inc., 2016.

[5] (a) Masters, C. *Homogeneous Transition-Metal Catalysis*. Mir, 1983; (b) Bates, R. *Organic Synthesis Using Transition Metals, Second Edition*. Wiley, 2012; (c) Karan, R.; Bhatia, R.; Rawal, R. K. Applications of Homogeneous Catalysis in Organic Synthesis. In *Green Sustainable Process for Chemical and Environmental Engineering and Science*, 2021; pp 159-188.

and/or control the selectivity in transition metal based-catalyzed transformations.[6,7]

For all these reasons, supramolecular catalysis has undergone an exponential growth in the last two decades due to the attention that has been devoted to both supramolecular and catalytic processes. Within this field of research, several approaches have been exploited depending on the interacting species and the reversible interactions involved (Figure 1.2):[8]

i. Ligand-ligand additive interactions:[2b,9] In this case, the addition of a molecule or ion, which is neither the catalyst nor the substrate, influences the performance of a catalytic system, in a parallel manner to allosteric modulation in enzymes.

ii. Inter or intra ligand-ligand interactions: [2b,9c,10] One of the most successful approaches consists of the assembly of two complementary building blocks *via* reversible interactions to construct more complex architectures.

---

[6] (a) van Leeuwen, P. W. N. M. *Supramolecular Catalysis*. Wiley-VCH, 2008; (b) Olivo, G.; Capocasa, G.; Del Giudice, D.; Lanzalunga, O.; Di Stefano, S. *Chem. Soc. Rev.* **2021**, *50*, 7681-7724; (c) Vidal-Ferran, A. Supramolecularly Regulated Enantioselective Catalysts. In *Supramolecular Catalysis*, 2022; pp 591-603.

[7] Catalysis by itself can be described as a supramolecular phenomenon, as the catalyst "recognizes" substrates, "organizes" the substrates in a certain way, and "assembles" a new molecule. To avoid this confusion, the name supramolecular catalysis is reserved in this thesis to processes that involve supramolecular interactions that do not form part of the basic catalytic reaction. The concept supramolecular catalysis does not refer in this thesis either to systems that aim to mimic enzymes by stabilizing the transition state of a chemical transformation.

[8] Raynal, M.; Ballester, P.; Vidal-Ferran, A.; van Leeuwen, P. W. N. M. *Chem. Soc. Rev.* **2014**, *43*, 1660-1733.

[9] For general information, see: (a) Wiester, M. J.; Ulmann, P. A.; Mirkin, C. A. *Angew. Chem. Int. Ed.* **2011**, *50*, 114-137; (b) Llorente, N.; Fernández-Pérez, H.; Núñez-Rico, J. L.; Carreras, L.; Martínez-Carrión, A.; Iniesta, E.; Romero-Navarro, A.; Martínez-Bascuñana, A.; Vidal-Ferran, A. *Pure Appl. Chem.* **2019**, *91*, 3-15; (c) Trouvé, J.; Gramage-Doria, R. *Chem. Soc. Rev.* **2021**, *50*, 3565-3584. For a selected example, see: Mon, I.; Jose, D. A.; Vidal-Ferran, A. *Chem. – Eur. J.* **2013**, *19*, 2720-2725.

[10] For general information, see: (a) Ohmatsu, K.; Ooi, T. *Tetrahedron Lett.* **2015**, *56*, 2043-2048; (b) Pignataro, L.; Gennari, C. *Chem. Rec.* **2016**, *16*, 2544-2560; (c) Mote, N. R.; Chikkali, S. H. *Chem. – Asian J.* **2018**, *13*, 3623-3646. For a seminal work using this approach, see: (d) Breit, B.; Seiche, W. *J. Am. Chem. Soc.* **2003**, *125*, 6608-6609.

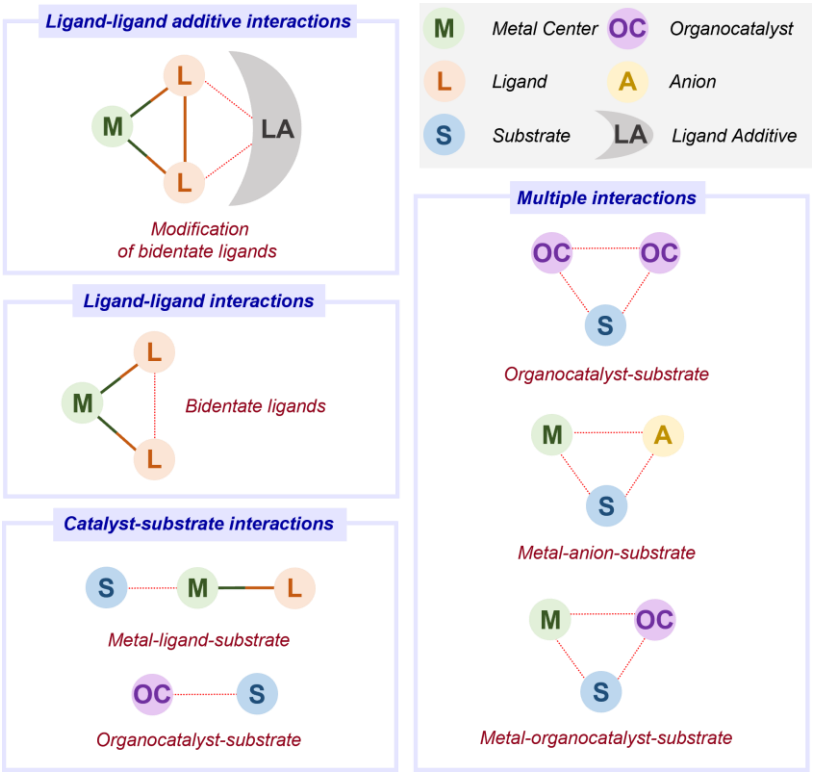

Figure 1.2. Supramolecular catalysis approaches.

iii. Catalyst-substrate interactions: [2b,9c,11] This approach is based on the generation of assemblies involving interactions between the catalyst and the substrate.

iv. Multiple interactions:[2b,9c,12] Additionally, a number of reversible interactions can be simultaneously operating in supramolecular catalysts (see Figure 1.2).

[11] For example, see: (a) Anebouselvy, K.; Shruthi, K. S.; Ramachary, D. B. *Eur. J. Org. Chem.* **2017**, *2017*, 5460-5483; (b) Fanourakis, A.; Docherty, P. J.; Chuentragool, P.; Phipps, R. J. *ACS Catal.* **2020**, *10*, 10672-10714; (c) Kuninobu, Y.; Torigoe, T. *Org. Biomol. Chem.* **2020**, *18*, 4126-4134. For an example of catalyst-substrate interaction, see: (d) Hart-Cooper, W. M.; Clary, K. N.; Toste, F. D.; Bergman, R. G.; Raymond, K. N. *J. Am. Chem. Soc.* **2012**, *134*, 17873-17876.

[12] For example, see: (a) Brière, J.-F.; Oudeyer, S.; Dalla, V.; Levacher, V. *Chem. Soc. Rev.* **2012**, *41*, 1696-1707; (b) Zurakowski, J. A.; Austen, B. J. H.; Drover, M. W. *Trends in Chemistry* **2022**, *4*, 331-346; (d) Chen, D.-F.; Gong, L.-Z. *J. Am. Chem. Soc.* **2022**, *144*, 2415-2437. For a selected example, see: Hamilton, G. L.; Kang, E. J.; Mba, M.; Toste, F. D. *Science* **2007**, *317*, 496-499.

Trivalent phosphorus compounds (Figure 1.3) have played and still play a crucial role in homogeneous catalysis.[13] The importance of these compounds arises from their special ligating properties that generate stable complexes with diverse metal precursors that are active in many catalytic transformations. The possibility to easily functionalize P(III) derivatives has also helped in widespreading their use, together with their simple analysis by ^{31}P NMR spectroscopy.[13] Among trivalent phosphorus derivatives, phosphanes are a valuable class of ligands that have been widely used as a crucial component of the catalytic system in many different transformations.

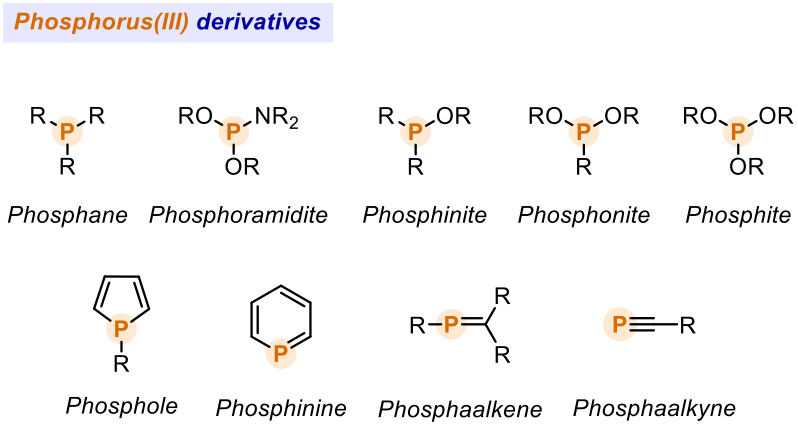

Figure 1.3. Phosphorus(III) derivatives.

A seminal example of the importance of phosphane ligands was studied in the sixties by Wilkinson and co-workers after the discovery of $[RhCl(PPh_3)_3]$ as catalyst for the homogeneous hydrogenation of alkenes.[14] Furthermore, the same authors found that rhodium(I) carbonyl complexes, which incorporated alkyl and arylphosphanes as ligands, were effective for the hydroformylation of alkenes.[15] Starting from these studies,

[13] Kamer, P. C. J.; van Leeuwen, P. W. N. M. *Phosphorus(III) Ligands in Homogeneous Catalysis: Design and Synthesis*. John Wiley & Sons Ltd., 2012.
[14] Young, J. F.; Osborn, J. A.; Jardine, F. H.; Wilkinson, G. *Chem. Commun.* **1965**, 131-132.
[15] (a) Jardine, F. H.; Osborn, J. A.; Wilkinson, G.; Young, J. F. *Chem. Ind.* **1965**, 560; (b) Evans, D.; Osborn, J. A.; Wilkinson, G. *J. Chem. Soc. A* **1968**, 3133-3142.

a large library of phosphorus ligands with different stereoelectronic features has been developed and studied in catalysis.[13]

Although monodentate ligands have gained increasing importance in catalysis,[16] both at the academic and industrial levels, bidentate ligands have also been developed and used in numerous catalytic reactions. Bidentate ligands present some interesting structural features (*i.e.*, enhanced stability of the metal complexes incorporating bidentate ligands, control of the coordination mode, prevention of the free rotation of the metal-ligand bond, formation of an organized three-dimensional structure around the metal center, etc.) which often translate into higher regio- or stereo-chemical discrimination in the outcome of the chemical transformation.[17]

The use of bidentate ligands was crucial in asymmetric hydrogenation, in which the discovery and study of bisphosphanes such as (*S*,S)-DIPAMP ligand[18] (Figure 1.4) were decisive for the application of enantioselective catalysis in industrial processes, especially in the production of L-DOPA using an asymmetric rhodium catalyst. Moreover, many more relevant bisphosphanes have been applied in the area of asymmetric hydrogenation,[19] for example Noyori's (R_a)-BINAP ligand,[20] or asymmetric

[16] For the application of monodentate phosphanes, see for example: (a) Teichert, J. F.; Feringa, B. L. *Angew. Chem., Int. Ed.* **2010**, *49*, 2486-2528; (b) Ager, D. J.; de Vries, A. H. M.; de Vries, J. G. *Chem. Soc. Rev.* **2012**, *41*, 3340-3380.

[17] Goudriaan, P. E.; van Leeuwen, P. W. N. M.; Birkholz, M.-N.; Reek, J. N. H. *Eur. J. Inorg. Chem.* **2008**, 2939-2958.

[18] (a) Kagan, H. B.; Dang Tuan, P. *J. Am. Chem. Soc.* **1972**, *94*, 6429-6433; (b) Poulin, J. C.; Dang, T. P.; Kagan, H. B. *J. Organomet. Chem.* **1975**, *84*, 87-92.

[19] For selected reviews and books of asymmetric hydrogenation, see: (a) Knowles, W. S. *Acc. Chem. Res.* **1983**, *16*, 106-112; (b) Knowles, W. S. *Adv. Synth. Catal.* **2003**, *345*, 3-13; (c) Blaser, H.-U.; Pugin, B.; Spindler, F. Asymmetric Hydrogenation. In *Organometallics as Catalysts in the Fine Chemical Industry*, 2012; pp 65-102; (d) Ratovelomanana-Vidal, V.; Phansavath, P. *Asymmetric Hydrogenation and Transfer Hydrogenation*. John Wiley & Sons, 2021; (e) Vidal-Ferran, A.; Grabulosa, A.; Verdaguer, X.; Riera, A. Asymmetric Hydrogenation. In *Catalytic Asymmetric Synthesis*, 2022; pp 559-616.

[20] Miyashita, A.; Yasuda, A.; Takaya, H.; Toriumi, K.; Ito, T.; Souchi, T.; Noyori, R. *J. Am. Chem. Soc.* **1980**, *102*, 7932-7934.

hydroformylation, for instance Takaya's (R_a,S_a)-BINAPHOS ligand[21] (Figure 1.4).

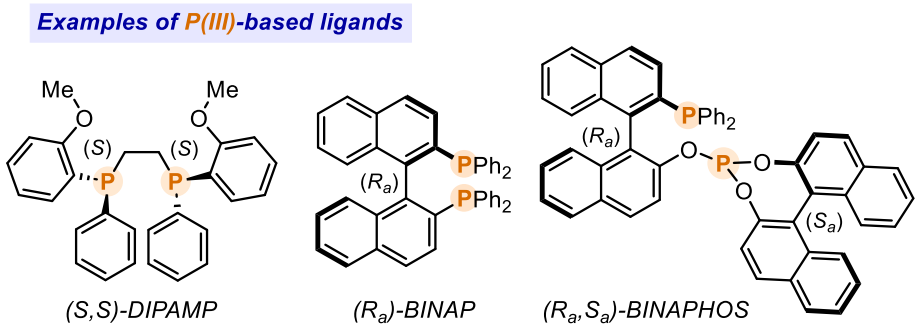

Figure 1.4. Relevant examples of bidentate P(III)-containing ligands.

However, the main drawback to the use of (enantiopure) bidentate ligands is their synthesis: construction of libraries of structurally diverse bidentate ligands may be associated in some cases to huge synthetic efforts, as the preparation of these ligands often imply multiple steps involving non-trivial synthetic operations.

As a solution to this problem, and as an interesting alternative to the classical synthesis of bidentate ligands, supramolecular chemistry has allowed for the preparation of the latter type of ligands with unprecedented ease relative to standard covalent chemistry.[22,23] The supramolecular strategy to synthesize bidentate ligands relies on the modular attachment of building blocks by supramolecular interactions (*e.g.*, hydrogen bonding or metal-ligand interactions).[24] The building blocks employed in this strategy contain the donor groups required for the coordination to the metal center as well as the motifs necessary for the supramolecular assembly.[22] This synthetic strategy is shown in a simplified manner in Figure 1.5. It is interesting to note at this point that the supramolecular

[21] Sakai, N.; Mano, S.; Nozaki, K.; Takaya, H. *J. Am. Chem. Soc.* **1993**, *115*, 7033-7034.
[22] Breit, B. *Angew. Chem. Int. Ed.* **2005**, *44*, 6816-6825.
[23] Carboni, S.; Gennari, C.; Pignataro, L.; Piarulli, U. *Dalton Trans.* **2011**, *40*, 4355-4373.
[24] For example, see: Breit, B. *Pure Appl. Chem.* **2008**, *80*, 855-860.

complexes obtained with this strategy resemble traditional non-symmetric bidentate ligands.

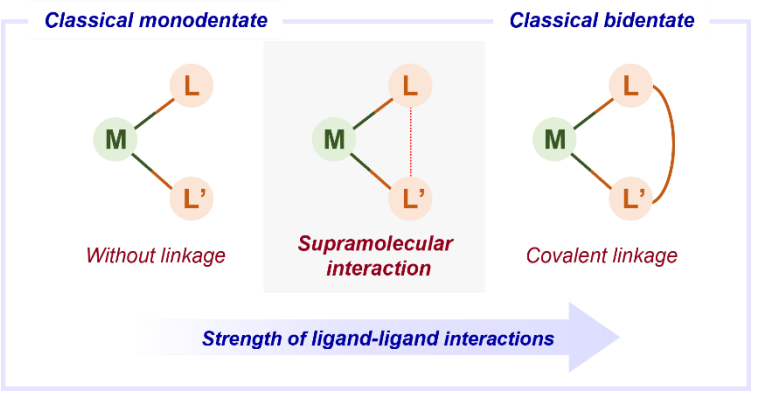

Figure 1.5. Ligand-ligand interactions in an MLL' complex.

By mixing the desired metal precursor together with the two building blocks, which contain the functional groups required for catalysis and the complementary moieties needed for the supramolecular assembly, two homodimeric and one heterodimeric metal complexes can be formed and, therefore, three possible metal-based systems may be present in solution. The composition of the mixture of supramolecular complexes after the assembly process is shifted to the formation of heterodimeric species (see Figure 1.6) if complementary supramolecular binding motifs are present in the starting building blocks.[22]

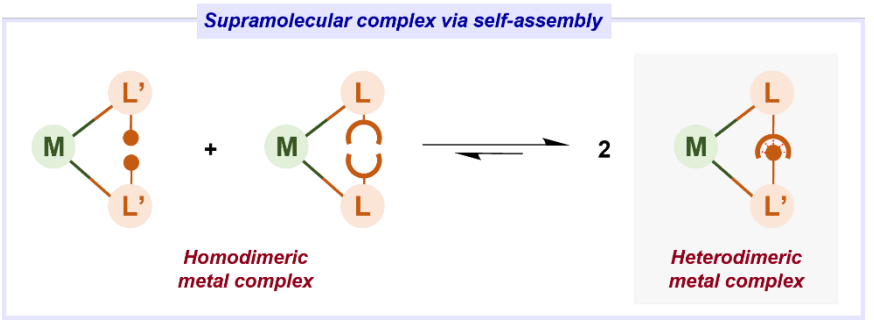

Figure 1.6. Homodimeric and heterodimeric species formation *via* self-assembly of monodentate ligands.

Numerous examples on the preparation of supramolecular catalytic systems by this strategy employing different supramolecular interactions have been already published.[2,9c] Remarkably, the use of metal-ligand and hydrogen bonding interactions have been widely explored.[25] For example, Reek and co-workers[26] reported the self-assembly of a dimeric zinc(II) porphyrin template and 4-(diphenylphosphaneyl)pyridine *via* metal-ligand interactions[27] in the presence of a rhodium(I) precursor to obtain supramolecular complex **3** (Scheme 1.1).

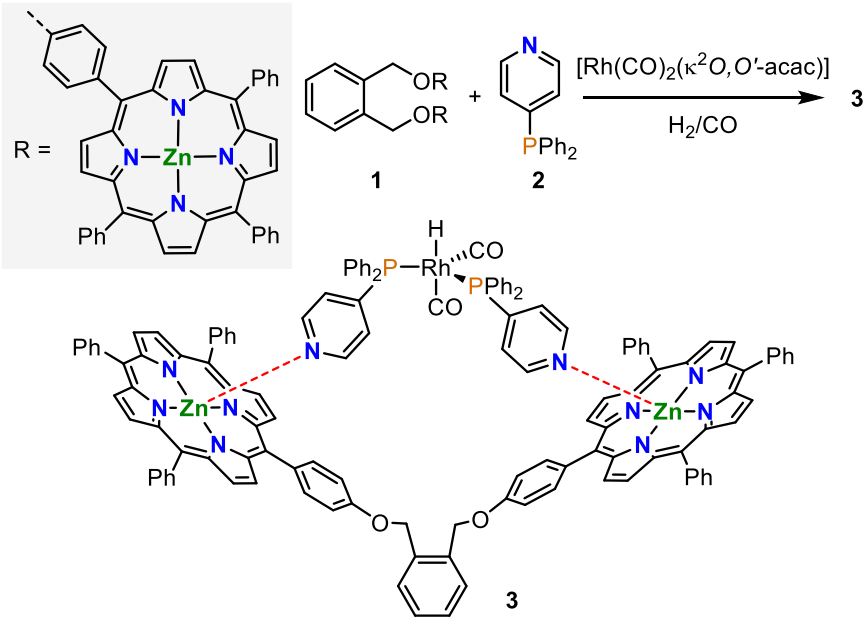

Scheme 1.1. Self-assembled rhodium(I) catalyst for hydroformylation.

Besides, complex **3** showed an enhanced selectivity toward the linear aldehyde in case of the hydroformylation of oct-1-yne and toward the

[25] For recent reviews, see: (a) Nurttila, S. S.; Linnebank, P. R.; Krachko, T.; Reek, J. N. H. *ACS Catal.* **2018**, *8*, 3469-3488. For more recent examples, see: (b) Reek, J. N. H.; de Bruin, B.; Pullen, S.; Mooibroek, T. J.; Kluwer, A. M.; Caumes, X. *Chem. Rev.* **2022**, *122*, 12308-12369.

[26] Slagt, V. F.; van Leeuwen, P. W. N. M.; Reek, J. N. H. *Chem. Commun.* **2003**, 2474-2475.

[27] In this section, except halogen bonds (green dashes to highlight the non-covalent force), the rest of non-covalent interactions mentioned (*e.g.*, metal-ligand interactions and hydrogen bonding interactions) are represented by red dashes.

branched isomer in case of the hydroformylation of styrene compared to the results with monodentate ligands.

Another supramolecular interaction, which has been explored as an assembly strategy for the preparation of supramolecular bidentate ligands, is hydrogen bonding.[24,28] This type of interaction can be easily combined to form an arrangement of several hydrogen bonds. In addition, the directionality of this interaction allows for the prediction of the geometry of the final assembly. The first example of self-assembled bidentate ligands *via* hydrogen bonding was reported in 2003 by Breit and co-workers.[10] In this case, the 2-pyridone/2-hydroxypyridine (6-DPPon) tautomeric system (structures **4a** and **4b** in Scheme 1.2) was employed. The tautomeric equilibrium was shifted in the presence of a metal center to a mixture of the two possible tautomers (*P*-containing pyridone and hydroxypyridine derivatives). The final bidentate complex Rh(I)/6-DPPon **5** (Scheme 1.2) was stabilized by coordination of the donor groups to the metal center and the chelation effect created by the intermolecular hydrogen bonds. Interestingly, the supramolecular catalytic system **5** was successfully tested in the hydroformylation of terminal alkenes. The authors also demonstrated that hydrogen bonding is maintained throughout the catalytic cycle.[10]

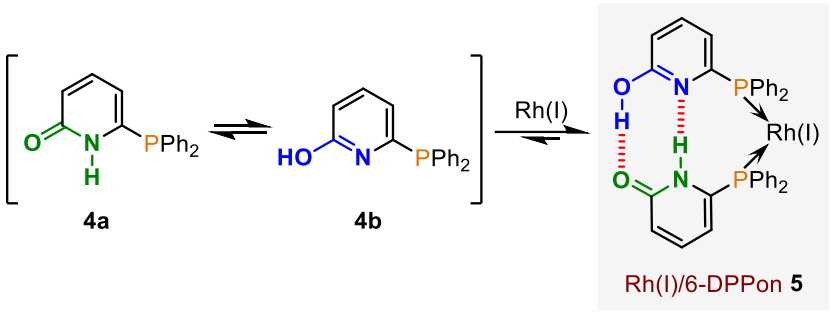

Scheme 1.2. Rh(I)/6-DPPon **5** catalyst formation *via* self-assembly.

[28] Bellini, R.; van der Vlugt, J. I.; Reek, J. N. H. *Isr. J. Chem.* **2012**, *52*, 613-629.

The applicability of the above-mentioned catalytic system was also reported. Thanks to the efficiency of catalyst **5** in hydroformylations under mild conditions (room temperature and ambient pressure), several tandem processes such as a highly selective domino hydroformylation/ hydrogenation[29] or a tandem hydroformylation/enantioselective organocatalytic cross-aldol reactions[30] were developed. Apart from the latter examples, an organocatalytic anti-selective Mannich reaction[31] or a Wittig olefination[32] could also be combined with the hydroformylation reaction catalyzed by Rh(I)/6-DPPon **5.**

More recently, in 2011, the same group carried out an exhaustive investigation on the above-mentioned assembled ligand (Scheme 1.2), alone and coordinated to a late transition metal such as platinum(II).[33] The authors were able to prove the existence of the ligand-ligand supramolecular assembly and the presence of the hydrogen bonding interaction after in-depth spectroscopic studies (UV-vis, IR, NMR, X-Ray). Also, computational studies were performed in order to analyze the energetic barriers of the tautomeric species formed.

In 2008, Reek *et al.*[34] described METAMORPhos ligand, which consists of the self-assembly of sulfonamidophosphane ligand **6** and can exist as a mixture of tautomers, giving the corresponding complex **7** after addition of [$Rh(CO)_2(\kappa^2$*O,O'*-acac)] (Scheme 1.3a). In this assembly, a *trans* arrangement of the two phosphorus ligands was established by ^{31}P NMR studies. When the enantiomerically pure phosphoramidite ligand **8** was used, heterocomplex **9** was exclusively formed instead of complex **7**

[29] Fuchs, D.; Rousseau, G.; Diab, L.; Gellrich, U.; Breit, B. *Angew. Chem. Int. Ed.* **2012**, *51*, 2178-2182.
[30] Abillard, O.; Breit, B. *Adv. Synth. Catal.* **2007**, *349*, 1891-1895.
[31] Diezel, S.; Breit, B. *Synthesis* **2014**, *46*, 1311-1320.
[32] Ruan, Q.; Zhou, L.; Breit, B. *Catal. Commun.* **2014**, *53*, 87-90.
[33] Gellrich, U.; Huang, J.; Seiche, W.; Keller, M.; Meuwly, M.; Breit, B. *J. Am. Chem. Soc.* **2011**, *133*, 964-975.
[34] Patureau, F. W.; Kuil, M.; Sandee, A. J.; Reek, J. N. H. *Angew. Chem. Int. Ed.* **2008**, *47*, 3180-3183.

(Scheme 1.3b). Additionally, heterocomplex **9** was successfully tested in the enantioselective hydrogenation of α-(acylamino)acrylate derivatives giving rise to excellent enantioselectivities of the hydrogenated products.

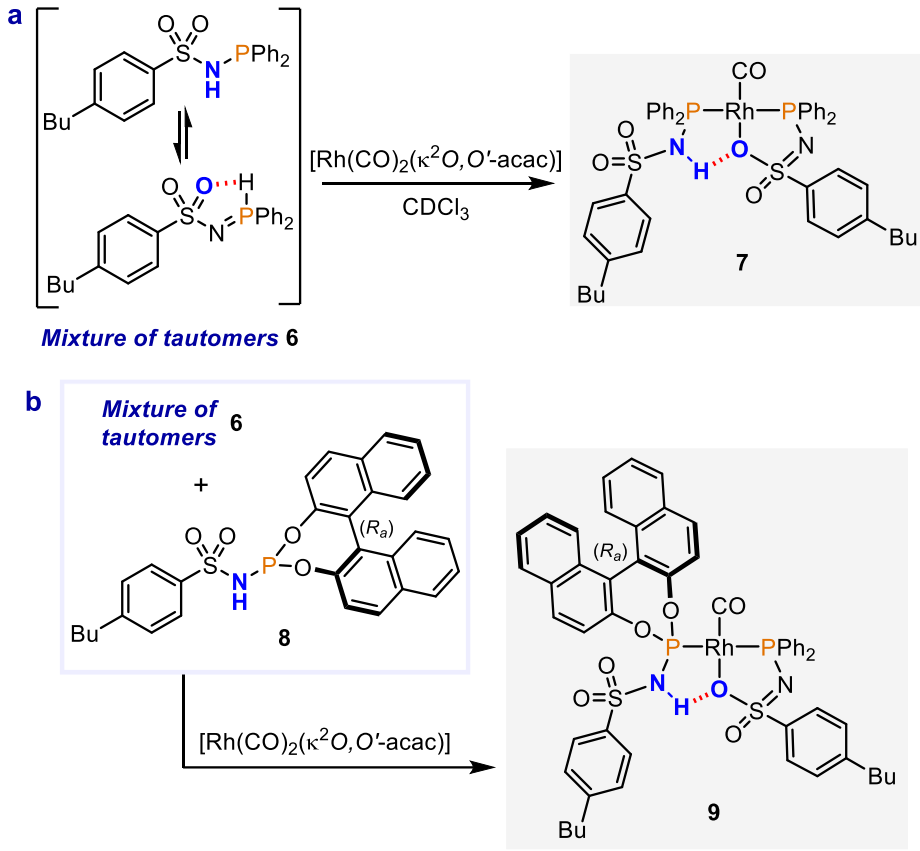

Scheme 1.3. (a) Tautomeric equilibrium of METAMORPhos ligand **6** and its coordination with rhodium; (b) Formation of heterocomplex **9**.

This approach (*i.e.*, ligand-ligand interactions to form a MLL' complex) has been widely studied in the last years and a vast number of new supramolecular ligand libraries based on hydrogen bonding interactions have been well established in the literature.[9c,10c,25b] This approach allows for the simple evaluation of a larger number of ligand libraries using a combinatorial strategy, leading to the identification of the highest-performing catalyst in a more straightforward manner.

Following this idea, apart from the examples previously mentioned, other types of building blocks (mainly based on heterocyclic scaffolds) have been developed. Another good example is the use of complementary building blocks akin to A-T base pairs in DNA as donor/acceptor units that selectively bind to each other (Scheme 1.4).[35] Bidentate ligands based on peptidic structures[36] and phosphinourea motifs[37] have also been developed in the last decades.

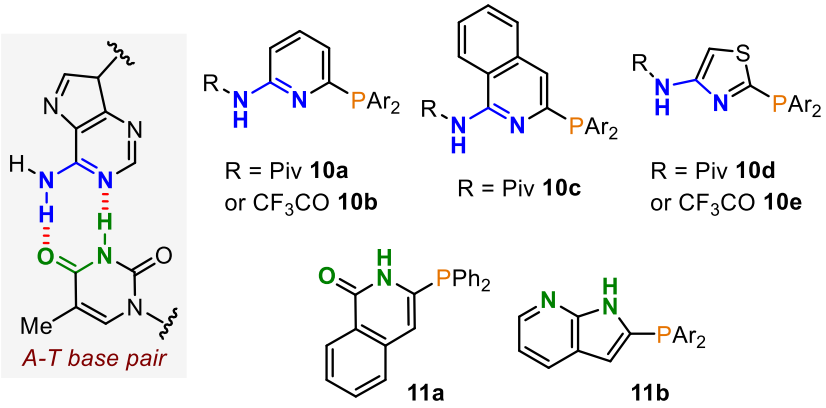

Scheme 1.4. Representative examples of complementary hydrogen bonding building blocks reported by Breit *et al.* Ref. 35.

Other non-covalent interactions have also gained the attention from the scientific community for constructing the framework of diverse catalytic systems. In 2007, van Leeuwen *et al.*[38] described the first example of heterobidentate phosphane ligands assembled *via* ionic interactions. In this case, the monodentate phosphorus ligands **12** and **13** contained complementary cationic and anionic moieties that formed a strong ion pair in several solvents, including polar and protic media (Scheme 1.5). The

[35] (a) Breit, B.; Seiche, W. *Angew. Chem. Int. Ed.* **2005**, *44*, 1640-1643; (b) Breit, B.; Seiche, W. *Pure Appl. Chem.* **2006**, *78*, 249-256; (c) Waloch, C.; Wieland, J.; Keller, M.; Breit, B. *Angew. Chem.* **2007**, *119*, 3097-3099.

[36] Laungani, A. C.; Slattery, J. M.; Krossing, I.; Breit, B. *Chem. – Eur. J.* **2008**, *14*, 4488-4502.

[37] Meeuwissen, J.; Sandee, A. J.; de Bruin, B.; Siegler, M. A.; Spek, A. L.; Reek, J. N. H. *Organometallics* **2010**, *29*, 2413-2421.

[38] Gulyás, H.; Benet-Buchholz, J.; Escudero-Adan, E. C.; Freixa, Z.; van Leeuwen, P. W. N. M. *Chem. – Eur. J.* **2007**, *13*, 3424-3430.

authors discovered that, depending on the position of the ionic motifs, *cis*- or *trans*-coordination arrangements were observed in the final square planar metal complexes. Some years later, this area of research was further explored by the group of Gennari,[39] who described a small library of enantiopure BINOL-based phosphites containing complementary carboxylic acid and tertiary amine functional groups. The ligands obtained by self-assembly were successfully applied in the rhodium-catalyzed hydrogenation of functionalized alkenes.

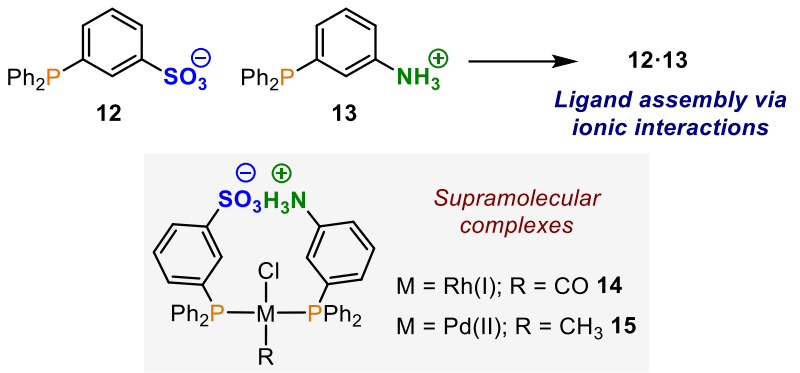

Scheme 1.5. Supramolecular metal-based complexes assembled *via* ionic interactions.

More recently, the evaluation of π-π interactions as a suitable driving force for the formation of supramolecular bidentate ligands has been reported by Lebœuf and co-workers.[40] The authors took advantage of the ability to strongly self-assemble *via* π-π staking that naphthalene diimides (NDIs) present to prepare the supramolecular bidentate enantiopure ligand NDIPhos **16**. The formation of the expected rhodium complex **17** (*i.e.*, [Rh(κ²*P*,*P*-**16·16**)]⁺) was demonstrated by ^{31}P NMR spectroscopy and computational studies, which pointed to the formation of π-π interactions as well as to a coordination to the rhodium center in a *cis*-fashion (Scheme 1.6). Finally, the combination of the enantiopure

[39] Pignataro, L.; Lynikaite, B.; Cvengroš, J.; Marchini, M.; Piarulli, U.; Gennari, C. Eur. *J. Org. Chem.* **2009**, *2009*, 2539-2547.
[40] Force, G.; Mayer, R. J.; Vayer, M.; Lebœuf, D. *Chem. Commun.* **2023**, *59*, 6231-6234.

ligand NDIPhos **16** with different rhodium(I) precursors was assessed in the hydrogenation of functionalized alkenes, demonstrating to be a highly active and selective catalytic system.

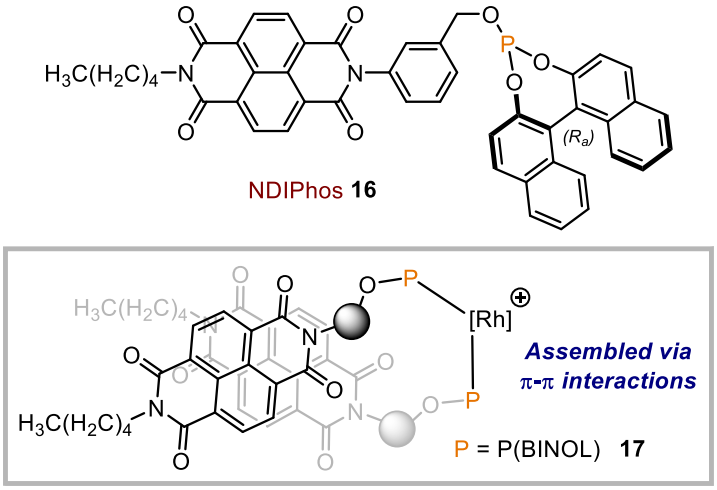

Scheme 1.6. Preparation of supramolecular complexes by using π-π interaction.

Halogen bond (XB, X refers to halogen and B to bonding) is an interesting supramolecular interaction that presents some similarities with hydrogen bonding. Since its serendipitous discovery in 1814 by Colin when mixing ammonia with iodine,[41] halogen bond has attracted lots of attention. The halogen bonding interaction takes place by an attractive interaction between an electrophilic region in a halogen atom in a molecule and a nucleophilic region in another molecule (Figure 1.7).[42] The formation of a halogen bonding interaction is driven by an enthalpy gain but penalized by an entropic unfavorable contribution arising from the geometry constraints for effective bonding. The enthalpic gain arises mainly from the transfer of electron density of the halogen bond acceptor

[41] Colin, M. *Ann. Chim* **1814**, *91*, 252-272.
[42] Desiraju, G. R.; Ho, P. S.; Kloo, L.; Legon, A. C.; Marquardt, R.; Metrangolo, P.; Politzer, P.; Resnati, G.; Rissanen, K. *Pure Appl. Chem.* **2013**, *85*, 1711-1713.

to the region of positive electrostatic potential of an electron poor halogen atom (*i.e.*, halogen bond donor).[43]

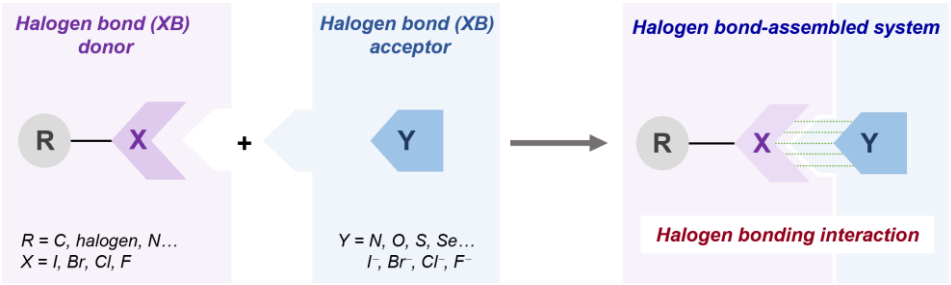

Figure 1.7. Supramolecular system *via* halogen bonding interaction.

This region of positive electrostatic potential is known as the σ-hole and is located on the outermost portion of the halogen's electrostatic potential surface and centered on the C–X axis. Although Kollman had computationally established in 1977 a positive electrostatic potential at one end of diatomic halogen-based molecules (*e.g.*, Cl_2 and F_2),[44] it was in 1992 when Brinck *et al.*[45] described that this positive region in the halogen atoms allowed them to interact with negative regions in other molecules (attractive interactions), therefore, leading to the formation of halogen bond interactions. As a representative example, the σ-hole (or region of positive electrostatic potential) in 1,2,3,4,5-pentafluoroiodobenzene is indicated in Figure 1.8a.[43]

[43] (a) Politzer, P.; Lane, P.; Concha, M. C.; Ma, Y.; Murray, J. S. *J. Mol. Model.* **2007**, *13*, 305-311; (b) Clark, T.; Hennemann, M.; Murray, J. S.; Politzer, P. *J. Mol. Model.* **2007**, *13*, 291-296; (c) Metrangolo, P.; Resnati, G. *Halogen Bonding: Fundamentals and Applications*. Vol. 126; Springer, 2008; (d) Metrangolo, P.; Meyer, F.; Pilati, T.; Resnati, G.; Terraneo, G. *Angew. Chem. Int. Ed.* **2008**, *47*, 6114-6127; (e) Erdélyi, M. *Chem. Soc. Rev.* **2012**, *41*, 3547-3557; (f) Gilday, L. C.; Robinson, S. W.; Barendt, T. A.; Langton, M. J.; Mullaney, B. R.; Beer, P. D. *Chem. Rev.* **2015**, *115*, 7118-7195; (g) Cavallo, G.; Metrangolo, P.; Milani, R.; Pilati, T.; Priimagi, A.; Resnati, G.; Terraneo, G. *Chem. Rev.* **2016**, *116*, 2478-2601.

[44] Kollman, P. *J. Am. Chem. Soc.* **1977**, *99*, 4875-4894.

[45] Brinck, T.; Murray, J. S.; Politzer, P. *Int. J. Quantum Chem* **1992**, *44*, 57-64.

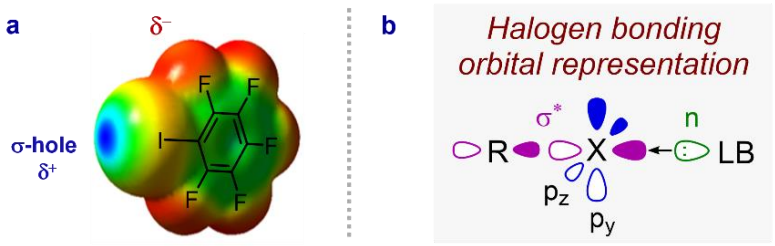

Figure 1.8. (a) σ-Hole in 1,2,3,4,5-pentafluoroiodobenzene; (b) orbital representation of the halogen bond interaction.

The exact nature of the halogen bond interaction is still in discussion, with the bonding factors of this supramolecular interaction, such as electrostatic or polarization effects, often depending on the individual interacting species.[43f,g] In the last few years, it has been well established *via* computational studies that both electrostatic and orbital interactions are involved in this non-covalent interaction. Cremer and co-workers[46] reported an exhaustive work, in which they calculated several bonding parameters at high computational level (*e.g.*, binding energies, geometries, Natural Bond Orbital (NBO) analysis, electrostatic potentials, electron and energy density distributions, interaction energy decomposition or relative bond strength orders, among others) for the purpose of establishing a clear halogen bond trend by comparing several halogen bond donor/acceptor pairs. The nature of the halogen bonding interaction was also analyzed by using the above-mentioned computational studies and the authors concluded that halogen bond arises from both electrostatic and strong covalent contributions. These covalent contributions come from orbital interactions that exist between the lone pair of electrons of the halogen bond acceptor and a σ* molecular orbital of the halogen bond donor (Figure 1.8b). The relative electrostatic and covalent contributions depend on the nature of both halogen bond donor and acceptor components.[46]

[46] Oliveira, V.; Kraka, E.; Cremer, D. *Phys. Chem. Chem. Phys.* **2016**, *18*, 33031-33046.

More recently, Berlinguette et al[47] demonstrated in an experimental and computational manner that, apart from the already described σ-symmetric orbital overlap (as shown in Figure 1.8b), a π-symmetric overlap influencing the properties of halogen bond molecules is also possible. This discovery may have an impact on the future designs of halogen bond donors and acceptors.

As it was previously mentioned, halogen bonding interactions present some similarities with hydrogen bonds. Comparable trends in geometric and energetic properties have been found for halogen and hydrogen bonding. However, halogen atoms are bigger than hydrogen atoms and, therefore, are more prone to be readily affected by external interactions. Moreover, the strength of the halogen bond can be easily fine-tuned by modifying the halogen atom and substitution pattern of the molecule containing it.[43] Regarding the strength of the halogen bond interaction, the σ-hole becomes larger and more positive as the size of the halogen atoms increases (F<<Cl<Br<I). In the case of fluorine, the smallest halogen, the σ-hole formation has been found only in special cases (*e.g.*, F_2 molecule).[48]

The strength of this non-covalent interaction can also be influenced by modifying the nature of the moiety directly bonded to the halogen atom. In this way, better electron-withdrawing motifs lead to an increase in the halogen bond strength. Haloalkynes (*i.e.*, highly electronegative *sp*-carbon atoms) are particularly good halogen bond donors (observed trend: Csp–X > Csp^2–X > Csp^3–X, being X the same halogen atom in all cases).[43g] Moreover, larger σ-holes can be reached by changing the chemical environment around the halogen atom with electron-withdrawing groups.

[47] Kellett, C. W.; Kennepohl, P.; Berlinguette, C. P. *Nat. Commun.* **2020**, *11*, 1-8.

[48] For some relevant examples, see: (a) Metrangolo, P.; Murray, J. S.; Pilati, T.; Politzer, P.; Resnati, G.; Terraneo, G. *CrystEngComm* **2011**, *13*, 6593-6596; (b) Metrangolo, P.; Murray, J. S.; Pilati, T.; Politzer, P.; Resnati, G.; Terraneo, G. *Cryst. Growth Des.* **2011**, *11*, 4238-4246; (c) Eskandari, K.; Lesani, M. *Chem. – Eur. J.* **2015**, *21*, 4739-4746; (d) Sirohiwal, A.; Hathwar, V. R.; Dey, D.; Regunathan, R.; Chopra, D. *Acta Crystallogr. Sect. B: Struct. Sci.* **2017**, *73*, 140-152.

Thus, an overall increase of the halogen bond strength (*i.e.*, larger and more positive σ-holes) can be obtained by increasing the electron-withdrawing character of the environment of the halogen group.

For the geometric characterization of the halogen bonding interaction, there are three common features that must be considered:[43g,46]

i. The distance between the halogen atom and the nucleophile; the X···LB bond distance must be shorter than the sum of the van der Waals radii of the individual components.

ii. Elongation of the Y–X covalent distance.

iii. Linearity of the Y–X···LB bond angle.

Due to the unique features of the halogen bond and the possibility to create 1D-, 2D- and 3D-arquitectures,[43d] this non-covalent interaction has become a widely used tool in some important areas such as crystal engineering,[49] polymer science[50] and medicinal chemistry[51] among others. Moreover, thanks to the directionality of this type of supramolecular interaction, together with its tolerance to changes in the solvent polarity,[52] halogen bond has been recently utilized in applications in solution,[53] such as organocatalysts in interesting chemical transformations.[54] Concretely, representative examples of halogen bonding interactions in catalysis consist of the activation of reactants containing halogen bond moieties that can be recognized by a catalyst containing complementary halogen bond

[49] For more information, see: (a) Metrangolo, P.; Resnati, G.; Pilati, T.; Biella, S. Halogen Bonding in Crystal Engineering. In *Halogen Bonding: Fundamentals and Applications*, 2008; pp 105-136; (b) Teyssandier, J.; Mali, K. S.; De Feyter, S. *ChemistryOpen* **2020**, *9*, 225-241; and references herein.

[50] Berger, G.; Soubhye, J.; Meyer, F. *Polym. Chem.* **2015**, *6*, 3559-3580.

[51] (a) Méndez, L.; Henriquez, G.; Sirimulla, S.; Narayan, M. *Molecules* **2017**, *22*, 1397-1412; (b) Berger, G.; Frangville, P.; Meyer, F. *Chem. Commun.* **2020**, *56*, 4970-4981.

[52] Sarwar, M. G.; Dragisic, B.; Salsberg, L. J.; Gouliaras, C.; Taylor, M. S. *J. Am. Chem. Soc.* **2010**, *132*, 1646-1653.

[53] Peluso, P.; Mamane, V. *Molecules* **2022**, *27*, 4625-4648.

[54] (a) Heinen, F.; Engelage, E.; Dreger, A.; Weiss, R.; Huber, S. M. *Angew. Chem. Int. Ed.* **2018**, *57*, 3830-3833; (b) Sutar, R. L.; Huber, S. M. *ACS Catal.* **2019**, *9*, 9622-9639; (c) Bamberger, J.; Ostler, F.; Mancheño, O. G. *ChemCatChem* **2019**, *11*, 5198-5211; (d) Breugst, M.; Koenig, J. J. *Eur. J. Org. Chem.* **2020**, *2020*, 5473-5487.

motifs. Selected examples related to the use of halogen bonding interactions in organic synthesis and catalysis are shown in the discussion that follows.

The first example of halogen bonding interactions in catalysis was reported by Bolm and co-workers in 2008.[55] In this study, the use of haloperfluoroalkane **20** as catalyst for the reduction of quinolines **18** to its corresponding hydrogenated derivatives **21** by using a Hantzsch ester **19** as reductant was described (Scheme 1.7). The authors proved a hydrogen transfer to the C=N bond of the quinoline *via* halogen bond-induced activation of the quinolinic substrate. Moreover, ^{13}C and ^{19}F NMR experiments were carried out in order to demonstrate the proposed N···I interaction between the quinoline and the halogen containing catalyst.

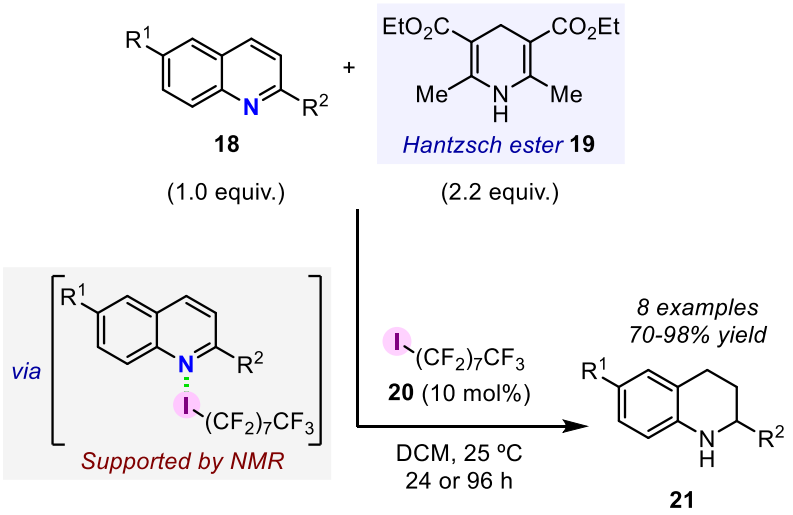

Scheme 1.7. Reduction of quinolines with Hantzsch ester *via* halogen bond.

Another good example was reported by Yeung and Chan,[56] in which the bromo-carbocyclization reaction of *N*-cinnamyl sulfonamides or *O*-cinnamyl phenyl ethers **23** with 1,3-dibromo-5,5-dimethylimidazolidine-2,4-dione **DBDMH** and *N*-methyl

[55] Bruckmann, A.; Pena, M. A.; Bolm, C. *Synlett* **2008**, *2008*, 900-902.
[56] Chan, Y.-C.; Yeung, Y.-Y. *Angew. Chem. Int. Ed.* **2018**, *57*, 3483-3487.

4-iodopyridinium triflate **22** as organocatalyst has been studied (Scheme 1.8). In this case, the reaction proceeds with excellent chemo- and diastereo-selectivities under mild conditions. The authors describe that halogen bonding interactions between the organocatalyst and the brominating agent enhance the brominating ability of the latter compound and facilitate the cyclization reaction.

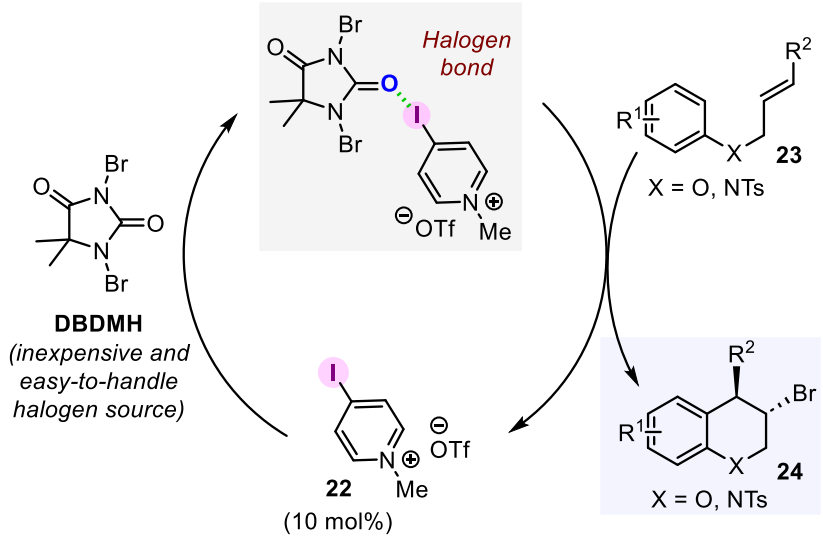

Scheme 1.8. Halogen bond-catalyzed bromo-carbocyclization.

At this point, not only monodentate halogen bond catalysts have been reported. Numerous examples including multidentate halogen bond donors have appeared in the last years. It is worthy to mention the contribution of Huber and co-workers in this area (Scheme 1.9). Huber's research group has pioneered on the application of (neutral and cationic) multidentate halogen bond donors as catalysts in a wide range of relevant transformations such as tandem halide abstraction/C–C bond formation,[57] Diels-Alder reactions (in this case the authors proved that activation of

[57] (a) Kniep, F.; Jungbauer, S. H.; Zhang, Q.; Walter, S. M.; Schindler, S.; Schnapperelle, I.; Herdtweck, E.; Huber, S. M. *Angew. Chem. Int. Ed.* **2013**, *52*, 7028-7032; (b) Jungbauer, S. H.; Huber, S. M. *J. Am. Chem. Soc.* **2015**, *137*, 12110-12120.

carbonyl moieties can be promoted by halogen bonding interactions),[58] Michael addition reactions[59] or Nazarov cyclizations[60] among other transformations (Scheme 1.9).

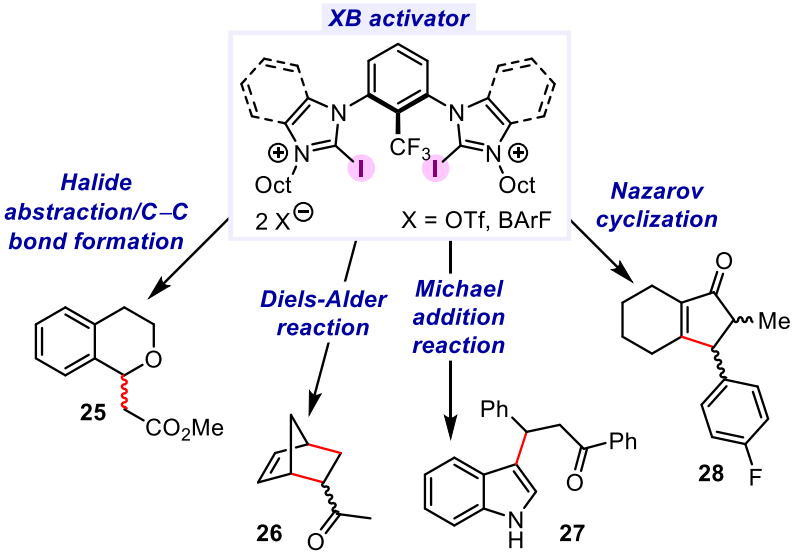

Scheme 1.9. Application of multidentate halogen bond catalysts in organic transformations reported by Huber *et al.*

Although examples in the literature are still scarce, "hypervalent" iodine(III) derivatives have been also found to be excellent halogen bond donors and have been recently applied as active catalysts.[54]

For example, in 2015, Han and Liu reported the use of diaryliodonium salts (Figure 1.9a) in a solventless three-component Mannich reaction.[61] Moreover, Huber *et al.*[62] described structurally diverse cyclic iodolium compounds (Figure 1.9b) as catalyst for halide abstraction and Diels-Alder reactions. These latter iodo(III)-based compounds were found to be even

[58] Jungbauer, S. H.; Walter, S. M.; Schindler, S.; Rout, L.; Kniep, F.; Huber, S. M. *Chem. Commun.* **2014**, *50*, 6281-6284.
[59] Gliese, J.-P.; Jungbauer, S. H.; Huber, S. M. *Chem. Commun.* **2017**, *53*, 12052-12055.
[60] Dreger, A.; Wonner, P.; Engelage, E.; Walter, S. M.; Stoll, R.; Huber, S. M. *Chem. Commun.* **2019**, *55*, 8262-8265.
[61] Zhang, Y.; Han, J.; Liu, Z.-J. *RSC Adv.* **2015**, *5*, 25485-25488.
[62] Heinen, F.; Engelage, E.; Dreger, A.; Weiss, R.; Huber, S. M. *Angew. Chem. Int. Ed.* **2018**, *57*, 3830-3833.

more active than the previously reported bidentate dicationic organoiodine(I) donors. More recently, the group of Huber also published the first example of bidentate bis(iodolium) salts (Figure 1.9c) as organocatalysts in Michael and Diels-Alder reactions.[63]

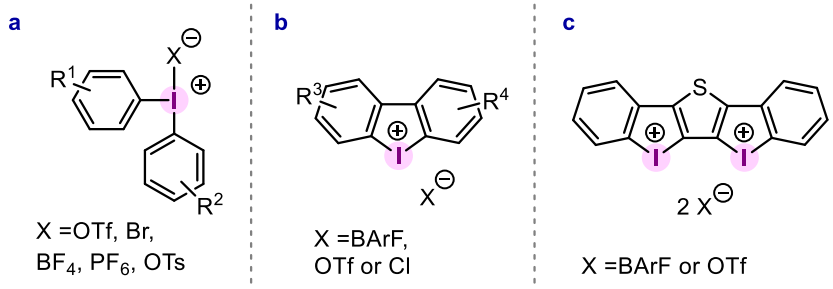

Figure 1.9. Examples of iodine(III) derivatives as halogen bond donors in catalysis.

Regarding enantioselective transformations, researchers have also directed their efforts to the design of enantioenriched halogen bond donors for enantioselective transformations.[64] Although a very limited scope of chiral structures was reported, some interesting examples that described the use of halogen bonding interactions in enantioselective catalysis appeared in the literature in the last few years.

One of the most relevant examples was reported by Arai and co-workers.[65] In this work, *Cinchona* alkaloid-derived enantiopure catalyst **32** was successfully applied in the asymmetric Mannich-type reaction of *N*-Boc α-ketiminoesters **29** with malononitrile **30**. The target products **31** were obtained in excellent yields and high enantiomeric excesses (*ee's*) (Scheme 1.10). This latter enantiopure halogen bond donor was also found to be effective in the enantio-and diastereo-selective double Mannich reaction of *N*-Boc imines with malononitrile **30**.[66]

[63] Heinen, F.; Reinhard, D. L.; Engelage, E.; Huber, S. M. *Angew. Chem. Int. Ed.* **2021**, *60*, 5069-5073.
[64] See, for example: Kaasik, M.; Kanger, T. *Front. Chem.* **2020**, *8*, 599064; and references herein.
[65] Kuwano, S.; Nishida, Y.; Suzuki, T.; Arai, T. *Adv. Synth. Catal.* **2020**, *362*, 1674-1678.
[66] Kuwano, S.; Ogino, E.; Arai, T. *Org. Biomol. Chem.* **2021**, *19*, 6969-6973.

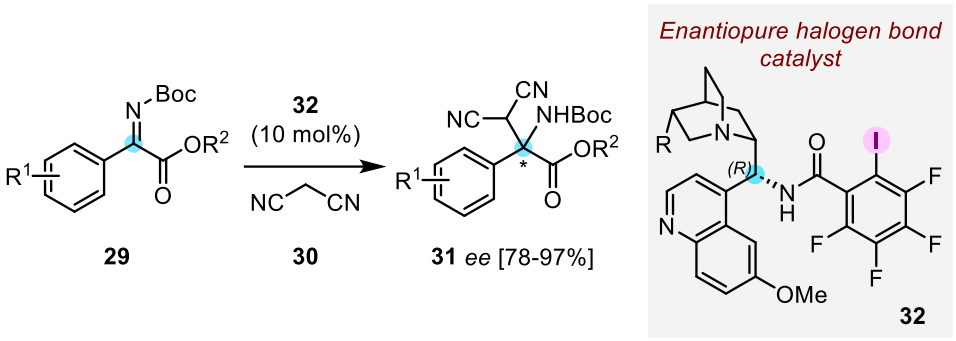

Scheme 1.10. Asymmetric Mannich-type reaction catalyzed by enantiopure halogen bond donor **32.**

In 2022, Yoshida *et al.*[67] developed an enantioselective catalytic method based on enantiomerically pure iodonium salt **36**. Asymmetric addition of bulky thiols **34** to ketimines **33** was achieved by using a halogen and hydrogen bond-based bifunctional system **36** obtaining *N,S*-acetal products **35** in high yields and good *ee's* (Scheme 1.11). Besides, the applicability of **36** was also demonstrated since a wide range of thiols and ketimines were tolerated under the reported conditions. Together with the experimental data, DFT calculations also supported the halogen bond-mediated activation of the ketimine substrate and provided a reasonable structure for the reaction outcome.

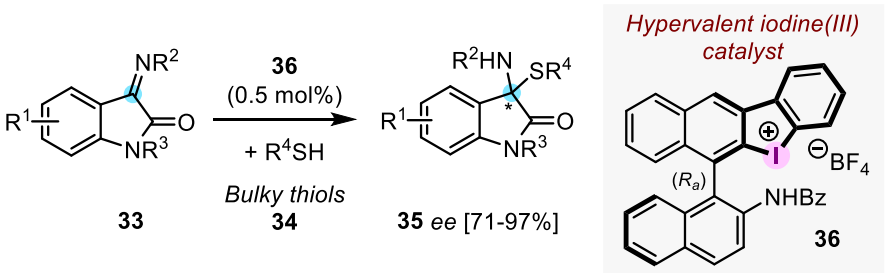

Scheme 1.11. Representative example of enantiopure halogen bond catalysis based on iodine(III) systems.

[67] Yoshida, Y.; Fujimura, T.; Mino, T.; Sakamoto, M. *Adv. Synth. Catal.* **2022**, *364*, 1091-1098. For other example based on enantiopure hypervalent bromine(III) halogen bond donor, see: Yoshida, Y.; Mino, T.; Sakamoto, M. *ACS Catal.* **2021**, *11*, 13028-13033.

As it has been shown in the previous discussion, halogen bonding interactions have found increasing applications in organocatalysis during the last decade. However, the use of halogen bond interactions within transition metal-based catalysis is still underdeveloped, and only a few examples with elemental iodine have been reported.[68] It was in 2020 when Huber *et al.*[69] presented the first example of metal-halogen bond activation by different halogen bond donors and the use of this approach in homogeneous gold catalysis (Scheme 1.12).

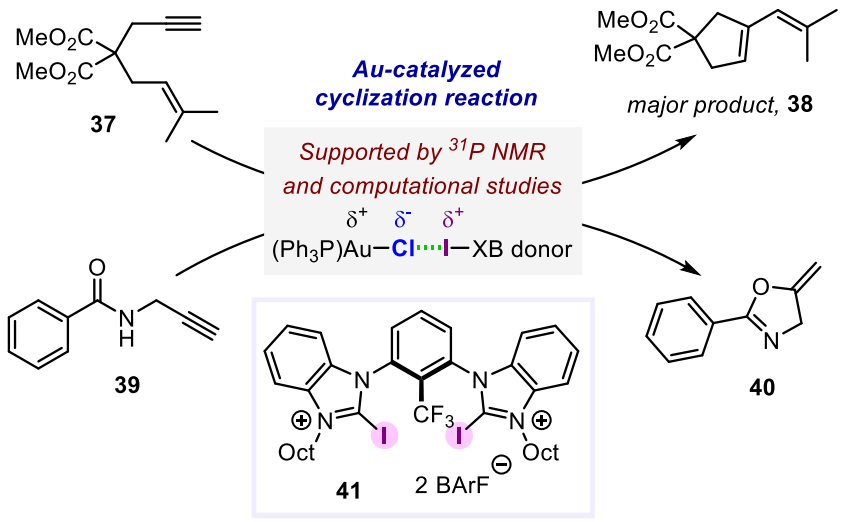

Scheme 1.12. Metal-halogen bond activation *via* halogen bonding interactions.

Cyclic diaryl iodonium motifs resulted to be effective activators in both cyclization reactions. However, it was found that bis(benzimidazolium)-based halogen bond donor **41** provided more rapid conversions becoming the most active halogen bond activator. ^{31}P NMR experiments, together with computational studies, suggested that the

[68] For some examples, see: (a) Mosquera, M. E. G.; Gómez-Sal, P.; Díaz, I.; Aguirre, L. M.; Ienco, A.; Manca, G.; Mealli, C. *Inorg. Chem.* **2016**, *55*, 283-291; (b) Mosquera, M. E. G.; Egido, I.; Hortelano, C.; López-López, M.; Gómez-Sal, P. *Faraday Discuss.* **2017**, *203*, 257-283; (c) Bezzubov, S. I.; Kalle, P.; Bilyalova, A. A.; Tatarin, S. V.; Dolzhenko, V. D. *Chem. – Eur. J.* **2018**, *24*, 12779-12783.

[69] Wolf, J.; Huber, F.; Erochok, N.; Heinen, F.; Guérin, V.; Legault, C. Y.; Kirsch, S. F.; Huber, S. M. *Angew. Chem. Int. Ed.* **2020**, *59*, 16496-16500.

halogen bond is crucial to the activation of the metal-halogen Au(I)–Cl bond.

It deserves special mention at this point that the use of halogen bonding interactions for constructing the backbone of a catalyst remained unexplored until our research group[70] reported the first example on the use of this supramolecular interaction to assemble suitably designed building blocks (*i.e.*, pyridyl- (**L1**) and iodotetrafluoroaryl-substituted (**L2**) phosphanes) in the presence of a rhodium(I) metal precursor. Halogen bonded-complex XBphos-Rh **C1** was efficiently prepared with the synthetic strategy indicated in Scheme 1.13.

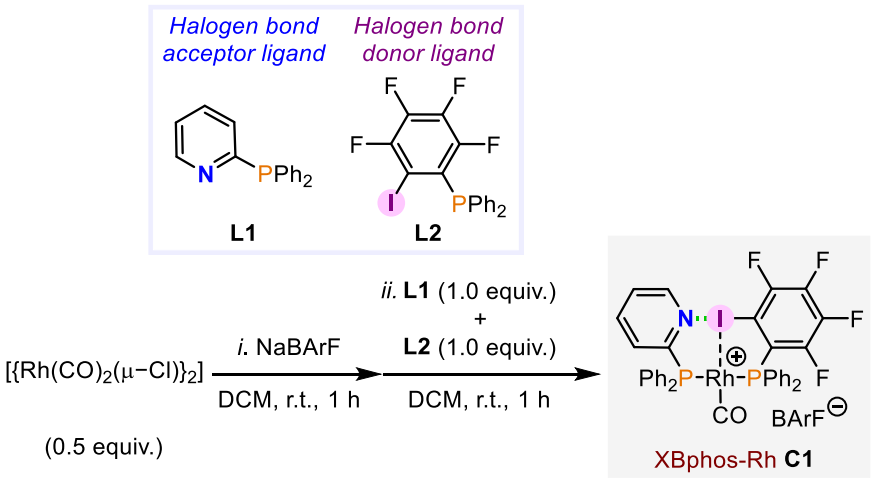

Scheme 1.13. Synthesis of XBphos-Rh **C1**.

The authors envisaged that the use of [{Rh(CO)$_2$(μ−Cl)}$_2$] along with NaBArF as a halide scavenger would render a putative [Rh(CO)$_2$]BArF intermediate that should react with phosphanes **L1** and **L2** to afford complex **C1**. The structure of the complex was established by spectroscopic studies and X-Ray analysis. These structural studies revealed that the nitrogen and iodine atoms are aligned in complex **C1** and that the iodine

[70] Carreras, L.; Serrano-Torné, M.; van Leeuwen, P. W. N. M.; Vidal-Ferran, A. *Chem. Sci.* **2018**, *9*, 3644-3648.

atom appears to be coordinated to the rhodium center. Besides, this supramolecular complex was successfully tested in the hydroboration of oct-1-yne and aryl substituted acetylenes as benchmark substrates.

After having developed a straightforward and selective synthesis of this halogen bond-assembled rhodium-based complex **C1**, our research group also studied the use of halogen bond interactions for modifying and tuning the coordination sphere at the metal center.[71] The authors discovered that, apart from the selection of the rhodium precursor, the geometry of both halogen bond donor and acceptor ligands controls the final Rh–P complexation event and the final structure of the metal complex (Scheme 1.14).

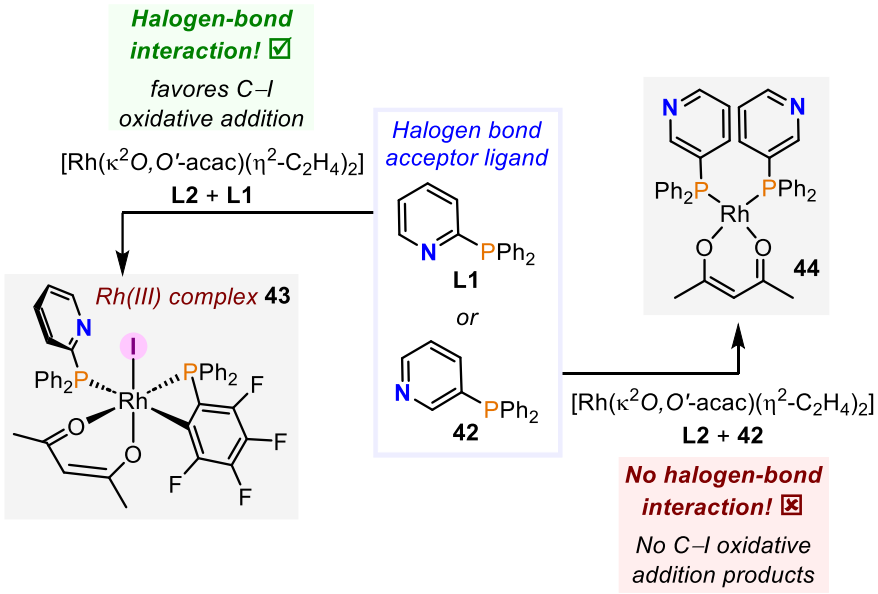

Scheme 1.14. Halogen bond effects on rhodium complexes.

The formation of a P–I–P pincer-type halogen bond-assembled Rh(I) compound (XBphos-Rh **C1**), or the formation of a new Rh(III) complex

[71] Carreras, L.; Benet-Buchholz, J.; Franconetti, A.; Frontera, A.; van Leeuwen, P. W. N. M.; Vidal-Ferran, A. *Chem. Commun.* **2019**, *55*, 2380-2383.

that comes from the unpredicted halogen bond-induced C_{Ar}–I oxidative addition to the Rh(I) center, can be controlled by using **L1** or ligand **42**. Experimental and computational studies revealed that both N···I halogen bond between ligands and the electron density at the rhodium center were crucial aspects for the control of the ligand-metal assembly and oxidative addition processes.

Taking the above-mentioned results as background, it was planned that this thesis would focus on the expansion of the structural diversity of the XBphos complexes and the study of the structure of the new halogen bond-assembled complexes as well as their reactivity as catalysts in transformations of interest.

1.2 OBJECTIVES

As summarized in the previous section, the use of supramolecular interactions in catalysis has been widely studied and exploited for the easy preparation of the backbones of an array of structurally diverse stereoselective catalysts. The large number of supramolecular complexes assembled *via* reversible interactions (*e.g.*, metal-ligand or hydrogen bonding interactions) that have already been published reflect the interest of the scientific community in this field of research. Moreover, it has been also summarized the current interest in halogen bonding interactions as an activation strategy in catalysis.

In addition to the broad application of halogen bond donors as organocatalysts for many organic transformations, the use of this non-covalent interaction has been also employed for the preparation of catalytically active complexes. Our group pioneered the use of halogen bonding interactions for the construction of bidentate phosphorus ligands by assembly of suitably designed phosphorus(III)-based complementary starting materials (XBphos-Rh **C1**).

Therefore, the main objectives of the present thesis are as follows:

i. Experimental study of the electronic and structural features of halogen bond-assembled rhodium(I) complexes.

ii. Assessment of the performance of XBphos-Rh **C1** as catalytic system in chemical transformations of interest, such as the hydroboration of alkynes and [4+2] cyclization reactions.

iii Expansion of the structural diversity of the XBphos-metal complexes from iridium(I) precursors. Study of the new iridium(I)-based halogen-bonded complexes in catalysis.

CHAPTER II:

EXPANDING THE STRUCTURAL DIVERSITY OF HALOGEN BOND DONORS AND ACCEPTORS AS BUILDING BLOCKS TOWARDS HALOGEN BOND-ASSEMBLED RHODIUM(I) COMPLEXES

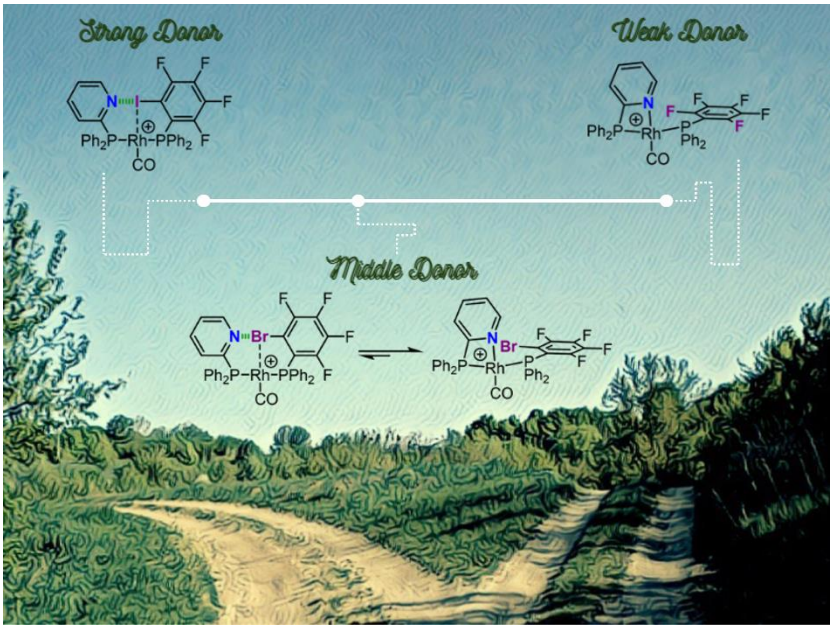

2.1 INTRODUCTION

Since the serendipitous discovery of the halogen bond, this non-covalent interaction has rapidly emerged as an interesting and useful component of the supramolecular toolbox. The vast number of research areas, in which halogen bonding interactions have proven to play an important role in the last decades (*e.g.*, crystal engineering,[49] polymer science,[50] medicinal chemistry[51] and its emergent role in catalysis), demonstrates the great utility and evident importance of this non-covalent interaction.

A deep understanding of the mechanism of halogen bond formation, as well as of the nature of this supramolecular force, is essential to expand the applicability of halogen bonding interactions. The understanding of halogen bond has mostly lied on computational predictions[43a,43b,45,72] and crystallographic analysis.[43d,73] Since Hassel *et al.*[74] described pioneering crystallographic studies that revealed short O–Br intermolecular distances in the adducts formed between bromine and 1,4-dioxane in the solid state, an extensive number of X-Ray crystallographic studies have been widely reported in the literature.[43,49] In these reports, the existence of the halogen bonding interaction and the study of their binding features and characteristic geometric parameters (*e.g.*, halogen bond distance and halogen bond angle) have been studied.

On the other hand, the utilization of halogen bond in solution has gained importance during the last decades. A vast number of applications

[72] (a) Lommerse, J. P. M.; Stone, A. J.; Taylor, R.; Allen, F. H. *J. Am. Chem. Soc.* **1996**, *118*, 3108-3116; (b) Wang, C.; Danovich, D.; Mo, Y.; Shaik, S. *J. Chem. Theory Comput.* **2014**, *10*, 3726-3737; (c) Wolters, L. P.; Schyman, P.; Pavan, M. J.; Jorgensen, W. L.; Bickelhaupt, F. M.; Kozuch, S. *WIREs Comput. Mol. Sci.* **2014**, *4*, 523-540.

[73] (a) Ramasubbu, N.; Parthasarathy, R.; Murray-Rust, P. *J. Am. Chem. Soc.* **1986**, *108*, 4308-4314; (b) Desiraju, G. R.; Parthasarathy, R. *J. Am. Chem. Soc.* **1989**, *111*, 8725-8726; (c) Metrangolo, P.; Neukirch, H.; Pilati, T.; Resnati, G. *Acc. Chem. Res.* **2005**, *38*, 386-395.

[74] (a) Hassel, O.; Hvoslef, J. *Acta Chem. Scand.* **1954**, *8*, 873-873; (b) Hassel, O. *Science* **1970**, *170*, 497-502.

of this non-covalent interaction in solution has been recently reported (*e.g.*, research on biomolecules relevant in medicinal chemistry[51] or catalysis,[53,54] which has been detailed in Chapter I). This fact has led to an increasing development and improvement of suitable techniques and methods for the study of halogen bonding interactions. In this sense, a variety of spectroscopic techniques (*e.g.*, UV-vis[75] or IR[76]) have gained importance in the analysis of this weak interaction, being NMR spectroscopy the most utilized one for studies in solution.[43e]

Several binding parameters (*e.g.*, energetics, binding constants, etc.) of a wide range of donor/acceptor halogen bond pairs were studied by using the aforementioned techniques. Among these halogen bond pairs, systems involving organic complementary acceptor and donor partners have been predominantly explored during the last years. Assembled systems *via* halogen bond between haloarenes,[77] haloalkynes[78] or haloalkanes[79] and neutral organic bases as halogen bond acceptors have been thoroughly studied in solution by using some of the spectroscopic techniques described above.

In 2010, Taylor *et al.*[80] reported a detailed study analyzing the thermodynamics of the halogen bonding interaction formed between a wide range of organic bases and fluorinated iodoalkanes and iodoarenes in

[75] For some examples, see: (a) Wash, P. L.; Ma, S.; Obst, U.; Rebek, J. *J. Am. Chem. Soc.* **1999**, *121*, 7973-7974; (b) Chudzinski, M. G.; McClary, C. A.; Taylor, M. S. *J. Am. Chem. Soc.* **2011**, *133*, 10559-10567.

[76] For example, see: Vasylyeva, V.; Catalano, L.; Nervi, C.; Gobetto, R.; Metrangolo, P.; Resnati, G. *CrystEngComm* **2016**, *18*, 2247-2250.

[77] For example, see reference 75a and Widner, D. L.; Knauf, Q. R.; Merucci, M. T.; Fritz, T. R.; Sauer, J. S.; Speetzen, E. D.; Bosch, E.; Bowling, N. P. *J. Org. Chem.* **2014**, *79*, 6269-6278.

[78] For example, see: (a) Laurence, C.; Queignec-Cabanetos, M.; Wojtkowiak, B. *J. Chem. Soc., Perkin Trans. 2* **1982**, 1605-1610; (b) Dumele, O.; Wu, D.; Trapp, N.; Goroff, N.; Diederich, F. *Org. Lett.* **2014**, *16*, 4722-4725.

[79] For example, see: (a) Metrangolo, P.; Panzeri, W.; Recupero, F.; Resnati, G. *J. Fluorine Chem.* **2002**, *114*, 27-33; (b) Cabot, R.; Hunter, C. A. *Chem. Commun.* **2009**, 2005-2007; (c) Hawthorne, B.; Fan-Hagenstein, H.; Wood, E.; Smith, J.; Hanks, T. *Int. J. Spectro.* **2013**, *2013*, 1-10.

[80] Sarwar, M. G.; Dragisic, B.; Salsberg, L. J.; Gouliaras, C.; Taylor, M. S. *J. Am. Chem. Soc.* **2010**, *132*, 1646-1653.

solution. The use of ^{19}F NMR spectroscopy allowed for the determination of the corresponding association constants, which resulted to be larger for all the halogen bond donor/acceptor pairs with the perfluoroalkane containing moiety than those for perfluoroarene compounds (*e.g.*, 1.3 ± 0.2 M^{-1} for iodopentafluorobenzene **45**/triethylamine $C_6F_5I\cdots NEt_3$ halogen-bonded system in comparison to 2.8 ± 0.6 M^{-1} for iodoperfluorooctane **46**/triethylamine $C_8F_{17}I\cdots NEt_3$ halogen bond pair).[80]

It is interesting to note that, due to the higher polarizability of the iodine atom and its stronger bonding ability, halogen bond donor structures based on iodine have been explored in a broader manner than bromine- and chlorine-based structures (for some examples related to iodine-based halogen bond donors, see Chapter I), which have been only considered for the sake of completeness. Most of the publications found in the literature concerning the study of bromo-based halogen bond donors have been generally done by X-Ray diffraction analysis, demonstrating that fluorinated bromoarenes form temperature-dependent halogen bonds in the solid state.[81] Moreover, a vast variety of aggregates have been found for the halogen bond assemblies of bromo-substituted polyfluoroarenes.[82]

Few examples describing a detailed comparison of halogen bonding interactions in solution by varying the halogen atoms have been reported in the last years.[83] For example, Bowling and co-workers[84] investigated the intramolecular halogen bond formation in solution by using 1,2-aryldiyne-linked donor and acceptor structures **47**-**49** by ^{19}F, ^{15}N and

[81] Forni, A.; Metrangolo, P.; Pilati, T.; Resnati, G. *Cryst. Growth Des.* **2004**, *4*, 291-295.
[82] For some examples, see: (a) De Santis, A.; Forni, A.; Liantonio, R.; Metrangolo, P.; Pilati, T.; Resnati, G. *Chem. – Eur. J.* **2003**, *9*, 3974-3983; (b) Oh, S. Y.; Nickels, C. W.; Garcia, F.; Jones, W.; Friščić, T. *CrystEngComm* **2012**, *14*, 6110-6114; (c) Ravat, P.; SeethaLekshmi, S.; Biswas, S. N.; Nandy, P.; Varughese, S. *Cryst. Growth Des.* **2015**, *15*, 2389-2401.
[83] For a more recent example, see: Stoesser, J.; Engelage, E.; Belmonte, D.; Huber, S. M. *CrystEngComm* **2023**, *25*, 1501–1506.
[84] Thorson, R. A.; Woller, G. R.; Driscoll, Z. L.; Geiger, B. E.; Moss, C. A.; Schlapper, A. L.; Speetzen, E. D.; Bosch, E.; Erdélyi, M.; Bowling, N. P. *Eur. J. Org. Chem.* **2015**, *2015*, 1685-1695.

^{13}C NMR spectroscopy (Figure 2.1). Spectroscopic data were collected at different temperatures and in several solvents with the aim of studying the solvent dependence of the halogen bond (strength order: cyclohexane > toluene > benzene > dichloromethane > acetone > pyridine, as indicated by ^{19}F NMR chemical shifts). Besides, the formation of iodine- and bromine-centered halogen bonding interactions were demonstrated by a decrease in the ^{15}N NMR chemical shift, pointing to the weakness of the halogen bond with a bromo donor (–63.83 ppm for halogen bond donor **47** (X = I) and –58.88 ppm for **48** (X = Br), compared to –57.96 ppm for **49** (X = F), Figure 2.1). This fact was also demonstrated computationally and experimentally by the group of Ciancaleoni,[85] who studied the influence of the halogen group in the formation of halogen-bonded complexes between perfluoro aryl donors and pyridyl-based acceptors *via* NOE NMR studies, in particular ^{19}F, ^{1}H HOESY NMR experiments.

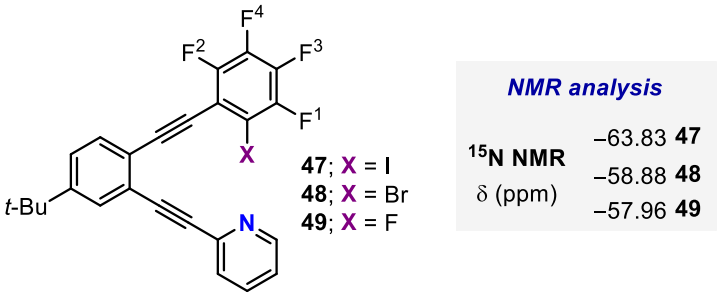

Figure 2.1. Spectroscopic data obtained for 1,2-aryldiyne-linked donor and acceptor structures in benzene at 25 ºC. Ref. 84.

On the other hand, regarding transition metal-based entities, a few research groups have also reported some examples, in which crystallographic and spectroscopic analysis revealed the existence of halogen bonding interactions in the ligand domain[86] of organometallic

[85] Ciancaleoni, G.; Bertani, R.; Rocchigiani, L.; Sgarbossa, P.; Zuccaccia, C.; Macchioni, A. *Chem. – Eur. J.* **2015**, *21*, 440-447.

[86] Ligand domain refers to the region surrounding the metal center and generally consists of those ligands directly bound to the metal center. Brammer, L. *Dalton Trans.* **2003**, 3145-3157.

species.[87] Brammer and co-workers[88] demonstrated the formation of 1:1 halogen bond adducts between Group 10 transition metal fluoride complexes, such as *trans*-[M(F)(κ*P*-PR_3)$_2$(κ*C*-pyr^F)] (where M = Ni, Pd or Pt), and iodoperfluorobenzene **45** as halogen bond donor. Authors took advantage of the dramatic changes observed in ^{19}F NMR due to the modification of the chemical environment of the metal-based complex (*e.g.*, substitution pattern of the fluorinated pyridyl-based ligand or the substituents of the phosphane ligands) for the determination of the binding strength. More recently, the same group also established the significance of changes in the halogen bonding interaction from iodo- to bromo-containing halogen bond donors by using a variety of nickel fluoride-based halogen bond acceptors **51**-**54** (Figure 2.2).[89]

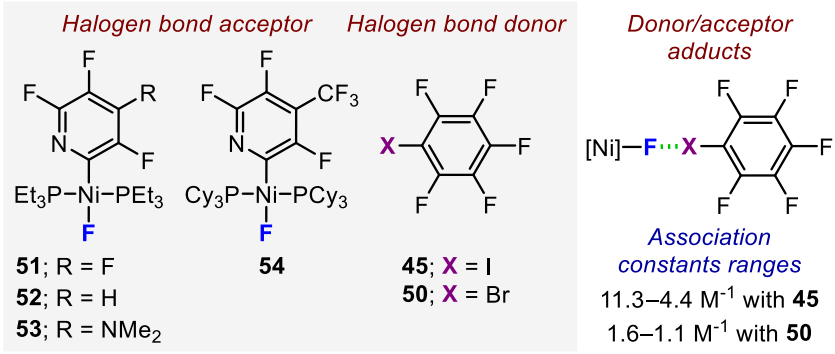

Figure 2.2. Halogen bond donor and acceptor structures and comparison of their observed association constants. Ref. 89.

[87] For some examples, see: (a) Derossi, S.; Brammer, L.; Hunter, C. A.; Ward, M. D. *Inorg. Chem.* **2009**, *48*, 1666-1677; (b) Ormond-Prout, J. E.; Smart, P.; Brammer, L. *Cryst. Growth Des.* **2012**, *12*, 205-216; (c) Sattler, W.; Ruccolo, S.; Parkin, G. *J. Am. Chem. Soc.* **2013**, *135*, 18714-18717; (d) Rauch, M.; Ruccolo, S.; Mester, J. P.; Rong, Y.; Parkin, G. *Chem. Sci.* **2016**, *7*, 142-149; (e) Luconi, L.; Garino, C.; Cerreia Vioglio, P.; Gobetto, R.; Chierotti, M. R.; Yakhvarov, D.; Gafurov, Z. N.; Morozov, V.; Sakhapov, I. y.; Rossin, A.; Giambastiani, G. *ACS Omega* **2019**, *4*, 1118-1129.

[88] Beweries, T.; Brammer, L.; Jasim, N. A.; McGrady, J. E.; Perutz, R. N.; Whitwood, A. C. *J. Am. Chem. Soc.* **2011**, *133*, 14338-14348.

[89] Pike, S. J.; Hunter, C. A.; Brammer, L.; Perutz, R. N. *Chem. – Eur. J.* **2019**, *25*, 9237-9241.

The association constants obtained for the donor/acceptor systems based on the brominated analogue **50** appeared to be significantly lower than the ones measured when iodopentafluorobenzene **45** was used as halogen bond donor.

To the best of our knowledge, no examples regarding intramolecular halogen bonding interactions in transition metal-based complexes have been reported in the literature. As depicted in the previous section (*i.e.*, General Introduction), our group pioneered the design and preparation of halogen bond-assembled metal-based complexes, in which the formation of an intramolecular halogen bond between two inequivalent and complementary phosphane ligands led to the stable rhodium(I) complex XBphos-Rh **C1** (see Scheme 1.13).[70]

The wide repertoire of spectroscopic techniques for the characterization and study of the halogen bonding interaction in solution, together with the breakthrough in the utilization of halogen bond for the selective preparation of the halogen bond-assembled XBphos-Rh **C1** complex, prompted us to continue with the study of structural and bonding properties in XBphos-Rh analogues. By modifying the structure and electronics of our halogen bond donor and acceptor ligands, we aimed to gain new insights into the halogen bond formation process and into the final structural and electronic features of XBphos-Rh analogues. A comparative study based on the modification of the halogen bond donor and acceptor moieties is summarized in the discussion that follows.

2.2 RESULTS AND DISCUSSION

As previously mentioned, we aimed to gain new insights into the halogen bond formation event and into relevant structural and electronic features of XBphos-Rh analogues. To do that, we expanded the structural diversity of the XBphos building blocks by varying the stereo electronics of both halogen bond donor and acceptor ligands. Besides, we envisaged that these studies would allow us to generate larger supramolecular ligand libraries based on the halogen bonding interaction.

Regarding the halogen bond acceptor ligand, we envisaged that secondary ketimine-based ligands could constitute perfect candidates for our halogen bond acceptor analogues. Secondary ketimine compounds incorporate an imine moiety (C=N) that contains a sp^2-hybridized nitrogen atom with the lone pair located in a sp^2-orbital. Conjugated imines (*i.e.*, compounds with multiple bonds, -COOR groups or aryl groups bonded to the C=N moiety) are planar molecules that present very similar C_{sp^2}=N_{sp^2} distances (1.35 Å) compared to those in pyridine (Figure 2.3).[90]

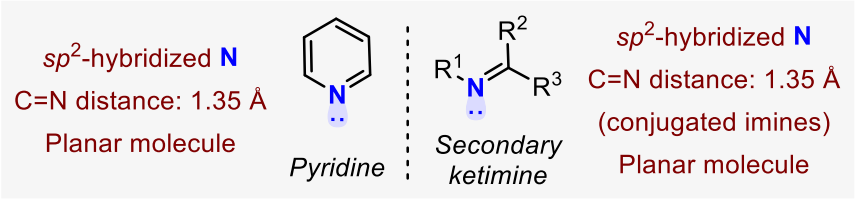

Figure 2.3. Structural and bonding parameters of pyridine and secondary ketimine compounds.

Due to the above-mentioned reasons, we considered that phosphaamidine compounds (structures **L3** and **L4,** Figure 2.4a) would behave as suitable halogen bond acceptor ligands. Besides, we hypothesized that phosphaamidine ligands **L3** and **L4** would be available

[90] (a) Sandorfy, C. General and Theoretical Aspects. In *Carbon–Nitrogen Double Bonds*, 1970; pp 1-60; (b) Mootz, D.; Wussow, H. G. *J. Chem. Phys.* **1981**, *75*, 1517-1522.

by using a two-step synthetic pathway from affordable, simple and commercially available starting materials **55a** and **55b** (Figure 2.4b).

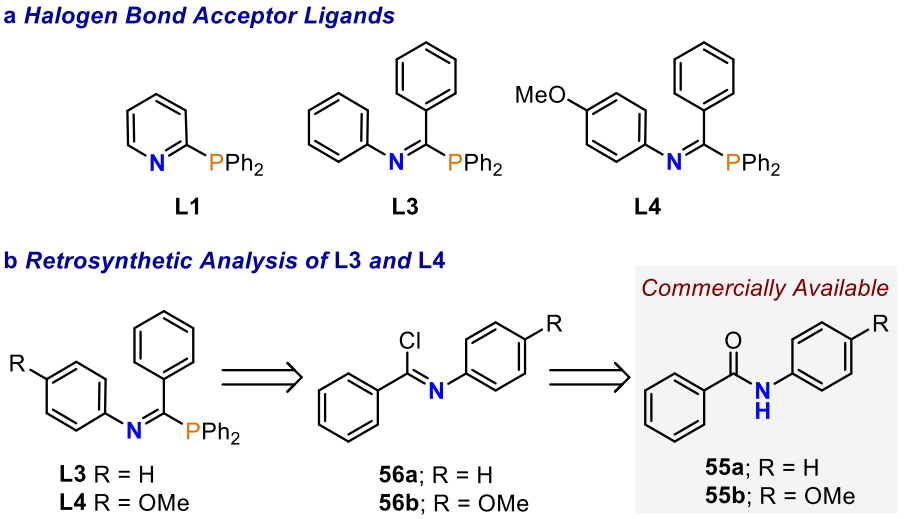

Figure 2.4. (a) Halogen bond acceptor ligands; (b) Retrosynthetic analysis of phosphaamidine ligands **L3** and **L4**.

For the preparation of ligands **L3** and **L4** (see Section 2.4 for more experimental details), the corresponding imidoyl chlorides **56a** and **56b** were initially synthesized by reacting the commercially available aryl amides **55a** and **55b** with thionyl chloride as halogenating agent since its by-products (*i.e.*, HCl and SO_2) can be easily removed after the reaction. Both **56a** and **56b** were isolated in quantitative yields. Then, based on the methodology reported by Jessop and co-workers,[91] the reaction of lithium diphenylphosphide with both imidoyl chloride derivatives **56a** and **56b** allowed us to isolate the desired phosphaamidine ligands **L3** and **L4** in moderate yields (48% yield for **L3** and an 42% yield for **L4**, Scheme 2.1).

[91] Kandel, R.; Huynh, K.; Dalgliesh, L.; Wang, R.; Jessop, P. G. *Inorg. Chim. Acta* **2016**, *445*, 117-123.

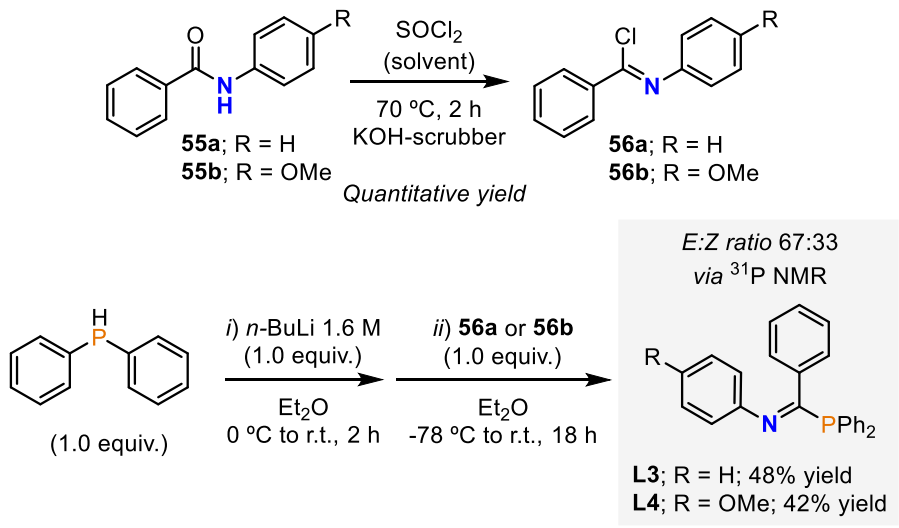

Scheme 2.1. Synthesis of halogen bond acceptor ligands **L3** and **L4**.

Considering that **L1** and **L3** might present similar electronic and structural features towards the formation of halogen bond-assembled rhodium(I) complexes, we decided to increase the acceptor ability of **L3** towards halogen bond by synthesizing ligand **L4**, which contains an electron donating *para*-methoxy substituent. We reasoned that the electron density on the nitrogen atom would thus be increased, making **L4** more basic and, therefore, a better halogen bond acceptor.

With ligands **L3** and **L4** in hand, we moved to the synthesis of the corresponding halogen bond-assembled complexes. Thus, following the methodology previously reported by our group for the XBphos-Rh **C1** complex,[70] supramolecular rhodium(I) complexes **C2** and **C3** were obtained. The synthetic strategy involved the *in situ* preparation of the putative rhodium(I) intermediate $[Rh(CO)_2]BArF$ by using NaBArF as halide scavenger, which, after reacting with an equimolar mixture of the corresponding halogen bond donor and acceptor ligands, gave rise to both complexes **C2** and **C3** in good yields (86% yield for **C2** and 81% yield for **C3**, Scheme 2.2).

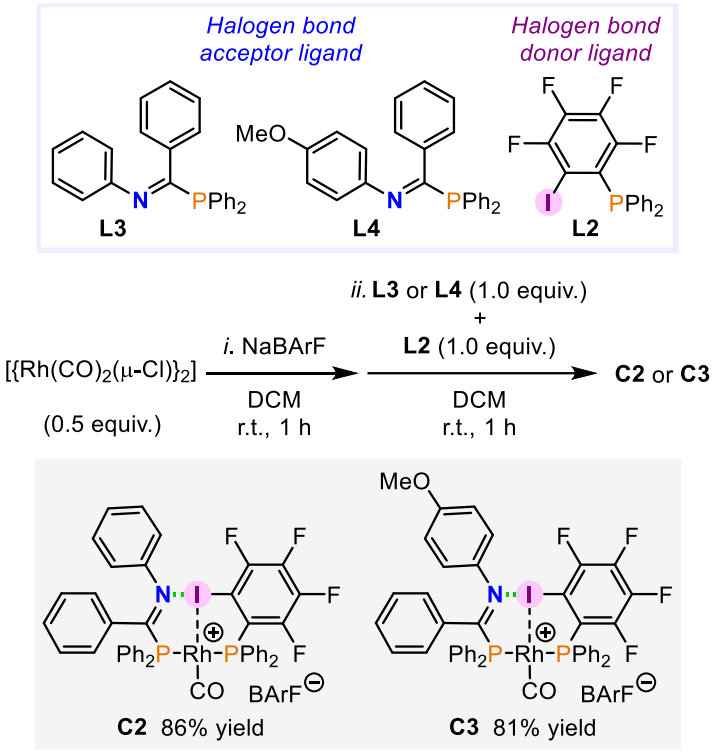

Scheme 2.2. Synthesis of complexes **C2** and **C3.**

Complexes **C2** and **C3** were fully characterized by using spectroscopic techniques. Unfortunately, no crystals of **C2** and **C3** suitable for X-Ray diffraction analysis could be grown. However, NMR spectroscopic data allowed us to unequivocally establish the structure of our new halogen bond-assembled complexes **C2** and **C3** and to compare their structural features with those for halogen bond-assembled complex XBphos-Rh **C1**.

We envisaged that **C2** should present similar NMR spectral data (*i.e.*, chemical shifts and coupling patterns) than those for complex XBphos-Rh **C1** since **L3** is electronically and structurally analogous to pyridine-containing **L1** (Figure 2.3). The most characteristic and diagnostic spectroscopic data are shown in Figure 2.5.

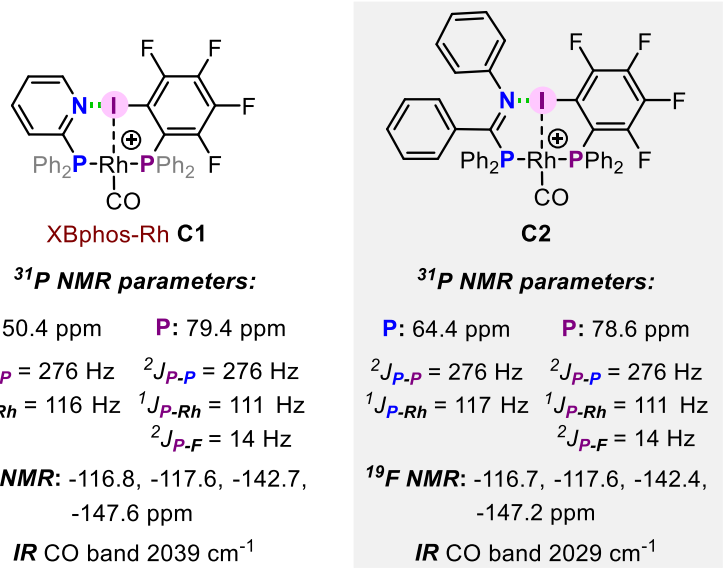

Figure 2.5. Selected spectroscopic data of complex **C2**. XBphos-Rh **C1** data included to aid comparison.

As expected, the analysis of the ^{31}P NMR spectral data obtained for complex **C2** pointed to a halogen-bonded *trans*-spanning bisphosphane coordination to the rhodium(I) center. Even though the signal corresponding to **L3** was slightly shifted downfield in ^{31}P NMR, the chemical shifts observed for **C2** were in accordance with those obtained for XBphos-Rh **C1** (compare **C2** with **C1**, Figure 2.5).

A large phosphorus-phosphorus coupling constant was observed for complex **C2**, which was in agreement with that observed for XBphos-Rh **C1** ($^2J_{P\text{-}P}$ = 276 Hz both for **C2** and XBphos-Rh **C1**, see Figure 2.5). The ^{31}P NMR signals of both phosphanes experienced an additional splitting by virtue of their coupling through one bond with the magnetically active Rh nucleus ($^1J_{P\text{-}Rh}$ = 117 Hz and 111 Hz, Figure 2.5). Moreover, the signal of the phosphino group in the fluorine-substituted derivative **L2** was further split due to its coupling with the ^{19}F nucleus placed three bonds away ($^3J_{P\text{-}F}$ = 14 Hz for complex **C2**, see Figure 2.5). Analogously, the chemical shifts

and multiplicities of the fluorine nuclei were in agreement with those previously described by our group for XBphos-Rh **C1**.

Only one band attributable to the carbonyl ligand was detected by using solid state IR spectroscopy, which was quite close to the one observed in the case of XBphos-Rh **C1**, indicating that the electronic environments of the cationic rhodium(I) center in both **C1** and **C2** are quite similar (compare 2039 cm^{-1} for XBphos-Rh **C1** to 2029 cm^{-1} for **C2**, Figure 2.5).

Therefore, although single crystals suitable for X-Ray analysis were not obtained, we concluded that halogen bond-assembled rhodium(I) complex **C2**, which constitutes a similar and comparable analogue of XBphos-Rh complex **C1**, was formed.

In an analogous manner to **C2**, complex **C3** was fully characterized by using spectroscopic techniques in solution. Spectroscopic data corresponding to **C3** are shown in Figure 2.6.

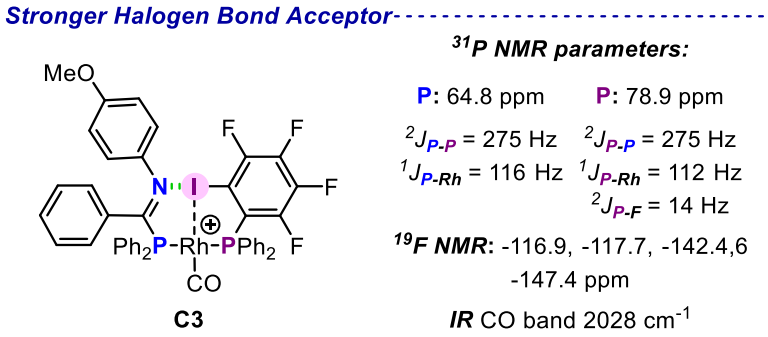

Figure 2.6. Spectroscopic data obtained for complex **C3**.

As it can be observed, NMR spectroscopic data (*i.e.*, chemical shifts and multiplicity patterns) were almost identical to those observed for the XBphos-Rh analogue **C2** (compare Figure 2.5 and Figure 2.6). In addition, the wavenumber attributable to the CO ligand for complex **C3** in IR spectroscopy (2028 cm^{-1}, Figure 2.6) was quite close to the one observed in complex **C2** (2029 cm^{-1}, Figure 2.5) indicating that the structures of **C3** and **C2** are similar.

Besides, with the aim of proving the presence of the expected halogen bonding interaction between both complementary ligands, we took advantage of the presence of the methoxy substituent placed in *para*-position to the nitrogen atom, whose chemical shift should experience a change when the N···I interaction takes place due to the electronic substituent effect. In complex **C3**, it was found that the signal corresponding to the methoxy substituent was shifted downfield in ^{1}H NMR with respect to the free ligand (from 3.68 ppm in **L4** to 3.75 ppm in **C3**).[92] This observation points to an electron donation from the nitrogen atom to the iodine, which translates into a loss of electron density in the methoxy group due to π-conjugation effects between the N atom and the MeO group. Considering all the spectroscopic evidence, we assumed that the halogen bonding interaction between ligands **L2** and **L4**, as well as between **L2** and **L3**, was taking place with formation of the halogen-bonded rhodium(I) complexes **C2** and **C3** depicted in Figure 2.6 and Figure 2.5.

Thus, we could conclude that electronic changes in the halogen bond acceptor ligand (*i.e.*, increase of the Lewis basicity of the halogen bond acceptor group by π-conjugation effects) did not influence the formation of the halogen bond-assembled rhodium(I) complexes, which presented similar structural and electronic features.

Thereupon, we describe our efforts in the study of the influence of the halogen atom in the donor moiety on the formation of halogen bond-assembled complexes. Even though it is well-established that larger and more positive σ-holes lead to stronger halogen bonding interactions, being the iodine atom the most efficient halogen bond within Group 17 in the periodic table,[43] also bromo-, chloro- and fluoro-derivatives have been found to be capable of forming halogen-bonded structures under special conditions (section 2.1). Taking this into consideration, we focused our

[92] Deuterated dichloromethane was used in both cases (**L4** and complex **C3**).

research efforts on the modification of the halogen bond donor ligand **L2**, in which the iodo group was exchanged by a fluoro and bromo substituent (Figure 2.7).

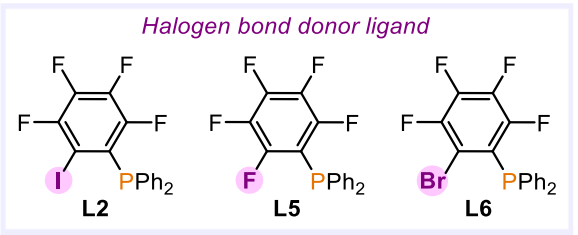

Figure 2.7. Halogen bond donor ligands.

Initially, we turned our attention to the phosphane ligand **L5** that contains a perfluorinated aryl moiety and corresponds to the formal substitution product of the iodo group in **L2** by a fluoro substituent. Fluorine represents the smallest and the least polarizable halogen atom of the Group 17 and the most electronegative atom of the periodic table. Although halogen bonding interactions involving organofluorine derivatives R–F seem implausible since no σ-holes are expected in these latter compounds, it has been recently demonstrated (at the theoretical level and in the solid state) that fluorine-based moieties are able to form non-covalent interactions if the R group bonded to the fluorine atom (in R-F) is electron withdrawing enough.[48]

In the case of complex XBphos-Rh **C1**, apart from the N···I halogen bond, the iodo group was also found to be coordinated to the rhodium(I) metal center (Rh–I distance = 2.5535(7) Å).[70] This interaction was supposed to enhance the magnitude of the σ-hole on the iodo group of the halogen bond donor, and therefore to strengthen the halogen bonding interaction.[70] In view of this fact, we envisaged that the electron density located around the fluorine atom could be perturbated *via* metal-halogen coordination, increasing this way the polarizability of the fluoro group and

enhancing (or creating) the required σ-hole for the formation of the desired halogen bond.

With this idea in mind, we moved to the preparation of the supramolecular complex derived from pyridine containing ligand **L1** and the commercially available ligand **L5**. The complex **C4** was synthesized following the above-mentioned methodology (Scheme 2.2) in excellent yield (94% of isolated yield, see Section 2.4 for more details). Subsequently, full characterization studies of complex **C4** were performed. Very broad signals centered at 13.7 and −26.7 ppm were observed in ^{31}P NMR (Figure 2.8) at room temperature. The broadness of the signals suggested that dynamic processes were taking place in solution. This behavior pointed to a quite different structure compared to XBphos-Rh **C1** (Figure 2.5). Low temperature NMR experiments allowed us to observe the expected ^{31}P NMR splitting pattern of the resulting rhodium(I) complex and measure the phosphorus-phosphorus ($^{2}J_{P\text{-}P}$ = 291 Hz) and phosphorus-rhodium ($^{1}J_{P\text{-}Rh}$ = 129 Hz and 103 Hz) coupling constants (Figure 2.8).

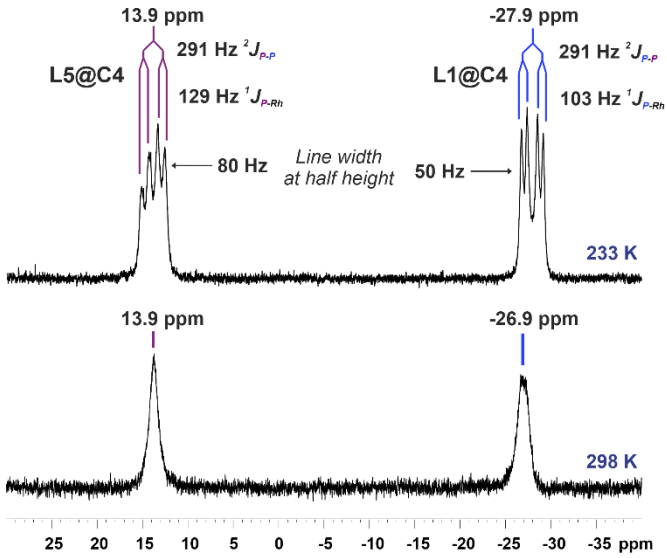

Figure 2.8. Low temperature ^{31}P NMR experiment of complex **C4** (Peak width at half height was measured with respect to the most intense signal).

The large phosphorus-phosphorus coupling constant observed for **C4** indicated a *trans*-coordination of the *P*-ligating groups of **L1** and **L5** to the rhodium(I) center. Unfortunately, the sharpening of the signals at low temperature was not enough for observing the phosphorus-fluorine coupling constants.

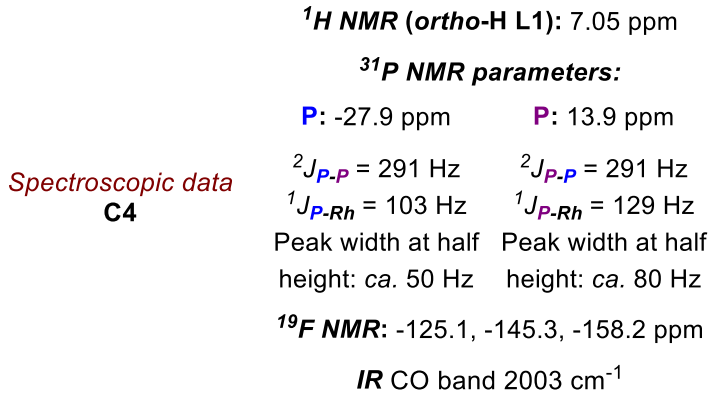

Figure 2.9. Spectroscopic data obtained for **C4** at 233 K.

Moreover, we assigned the doublet of doublets observed at 13.9 ppm in ^{31}P NMR to the phosphino group in the perfluorinated ligand **L5**, given the smaller width at half height of its signal with respect to that observed for the *P*-group in ligand **L5** (*ca*. 50 Hz vs. *ca*. 80 Hz, Figure 2.8), in which the ^{31}P NMR signal was expected to be broader due to couplings with the ^{19}F nucleus. In addition, The phosphorus chemical shift and $^{1}J_{P\text{-}Rh}$ coupling constant corresponding to coordinated **L5** were in agreement with the values reported in the literature for the Vaska-type complex [Rh(CO)(Cl)(κ*P*-**L5**)$_2$] **57** (δ = 24.0 ppm, $^{1}J_{P\text{-}Rh}$ = 133.0 Hz).[93]

In addition to that, only three signals were observed in ^{19}F NMR (Figure 2.10) that were attributed to a symmetric perfluorinated aryl moiety in the halogen bond donor ligand **L5**.

[93] Atherton, M. J.; Coleman, K. S.; Fawcett, J.; Holloway, J. H.; Hope, E. G.; Karaçar, A.; Peck, L. A.; Saunders, G. C. *J. Chem. Soc., Dalton Trans.* **1995**, 4029-4037.

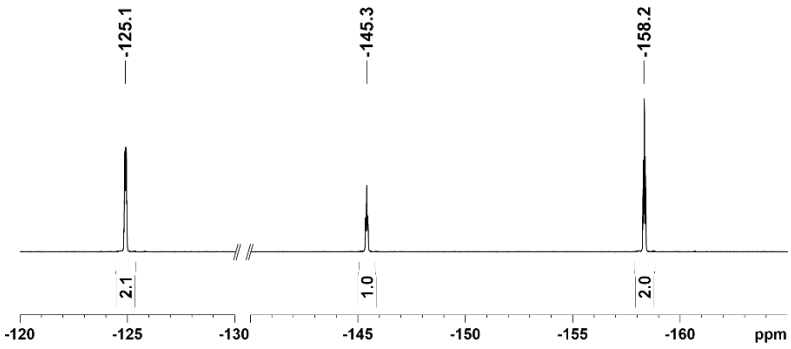

Figure 2.10. ^{19}F NMR spectrum of complex **C4** at room temperature.

The proton *ortho*-positioned to the nitrogen atom of the pyridine moiety in **L1** appeared to be more shielded in complex **C4** (7.05 ppm, see Figure 2.9) than in the XBphos-Rh **C1** complex (8.88 ppm, reference 70) and the free ligand **L1** (8.68 ppm). This observation suggested a distinct coordination environment of the nitrogen atom in **C4** than in the XBphos-Rh **C1** complex. It should be noted at this point that the ^{31}P NMR chemical shifts for the *P*-group of **L1** coordinated to rhodium were very close to those reported in the literature[94] for ligand **L1** coordinated to rhodium in a κ^2*P,N*-coordination fashion such as in structure **59** (Figure 2.11). Overall, the spectroscopic evidence gathered point to the fact that the expected N···F halogen bond interaction is not present in complex **C4**.

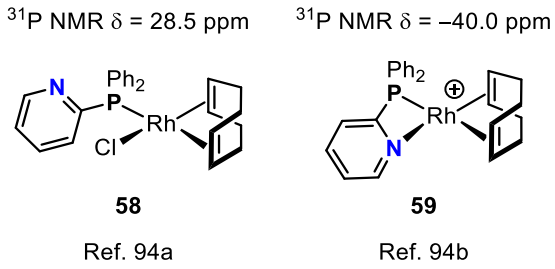

Figure 2.11. Ligand **L1** coordination modes to the rhodium(I) center.

[94] (a) Brück, A.; Ruhland, K. *Organometallics* **2009**, *28*, 6383-6401; (b) Angoy, M.; Jiménez, M. V.; Modrego, F. J.; Oro, L. A.; Passarelli, V.; Pérez-Torrente, J. J. *Organometallics* **2018**, *37*, 2778-2794.

Fortunately, crystals suitable for X-Ray diffraction analysis were grown and allowed us to unequivocally elucidate the structure of **C4**, which is shown in Figure 2.12.

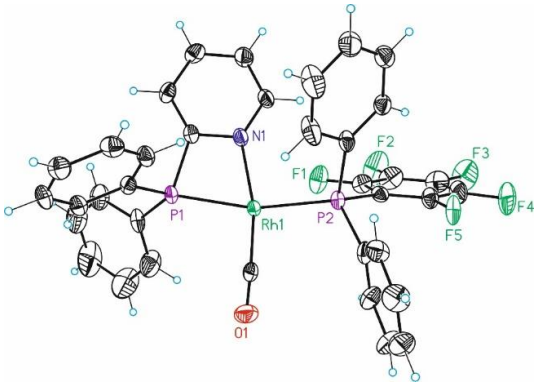

Figure 2.12. ORTEP drawing (thermal ellipsoids drawn at a 50% probability level) showing the structure of **C4**. BArF counterion have been omitted for clarity. Color scheme: C: black, O: red, N: dark blue, F: green, P: purple, Rh: green.

It can be seen in the ORTEP drawing above that the two phosphino groups are coordinated in a *trans*-fashion to the rhodium(I) center (P–Rh–P angle = 162.93(3)º). However, no halogen bonding interaction between the nitrogen and fluorine groups was observed. Instead, the nitrogen atom was found to be coordinated to the rhodium center (Rh–N distance = 2.112(3) Å) leading to the formation of a κ^2*P,N*-ligand (P–Rh–N angle = 69.70(7)º). This κ^2*P,N*-coordination mode of **L1** to the rhodium center accounts for the dramatic changes in the NMR chemical shifts observed for the ligand **L1** in complex **C4** (both in ^{1}H and ^{31}P NMR, Figure 2.9). As the nitrogen lone pair in **L1** is involved in the Rh–N bond, there is no possibility for it to form any N···F halogen bond. Probably, the C_{Ar}–F bond is not long enough to allow effective coordination of one of the *ortho*-to-phosphorus fluorine groups in **L5** to the rhodium center. Without this coordination, the magnitude of the σ-hole in the fluorine atoms is not large enough for an energetically favored halogen bond between the nitrogen and fluorine atoms.

Once we demonstrated that rhodium complexes derived from **L1** and **L5** do not involve halogen bonding interactions, we decided to investigate other halogen bond donor atoms belonging to the Group 17. Bromine is located one row above iodine in Group 17 and, even though bromine is smaller than iodine, it is well-known that bromine also presents an anisotropic distribution of charge leaving the outermost region of the bromo substituent positively charged and forming a positive σ-hole. Besides, a vast number of reports in the literature established the applicability of bromo-containing compounds in halogen bonding interactions.[53,64,67,81-85,95]

Although the magnitude of the σ-hole in bromo derivatives must be smaller than that in iodo groups, we envisaged that bromine could be a good candidate for the study of halogen bond donor effects on the formation of our halogen bond-assembled rhodium(I) analogues. In this sense, we decided to synthesize ligand **L6**. A slight modification of the already reported synthetic methodology[96] allowed us to obtain the bromine-based derivative **L6**. This compound was prepared *via* selective lithiation of the commercially available starting material **60**, giving rise to the desired ligand in excellent yields (Scheme 2.3).

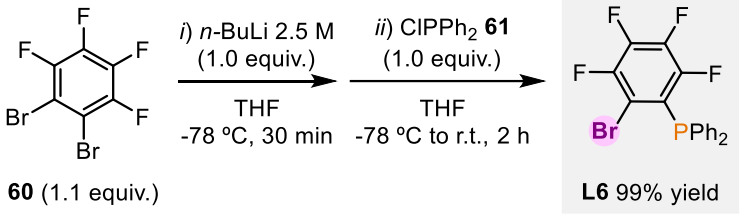

Scheme 2.3. Synthesis of ligand **L6**.

With the ligand **L6** in hand, we set about synthesizing the expected halogen-bonded rhodium(I) complex **C5** from **L1** and **L6** by following the

[95] Rosokha, S. V.; Stern, C. L.; Ritzert, J. T. *Chem. – Eur. J.* **2013**, *19*, 8774-8788.
[96] Eller, P. G.; Meek, D. W. *J. Organomet. Chem.* **1970**, *22*, 631-636.

previously used synthetic pathway. After full characterization of the resulted rhodium(I) complex, solid state spectroscopic methods confirmed the formation of the desired halogen bond-assembled rhodium(I) complex **C5** (Scheme 2.4).

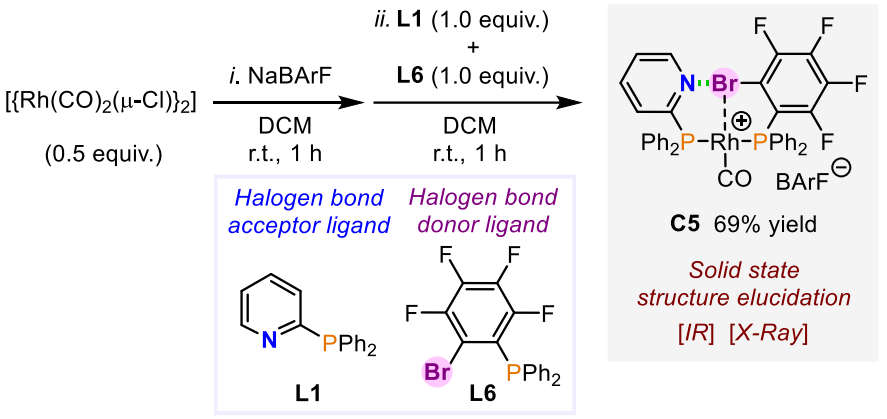

Scheme 2.4. Synthesis of **C5**.

Solid state IR spectroscopic analysis showed a CO stretching band at 2037 cm^{-1}, which was almost identical to the CO stretching band observed in the case of XBphos-Rh **C1** (CO band = 2039 cm^{-1}, Figure 2.5). On the other hand, single crystals were analyzed by X-Ray diffraction and the structure of complex **C5** was unequivocally elucidated. Complex **C5** presented the desired halogen bond-assembled structure that is shown in Figure 2.13. Moreover, relevant distances and angles related to the structure of the rhodium(I) complex and to the halogen bonding interaction are summarized in Table 2.1.

The X-Ray structure obtained for **C5** confirmed the expected square planar geometry for the rhodium(I) center as well as the presence of the halogen bond between the nitrogen and bromo groups that were found to be aligned with a N···Br distance of 2.801(5) Å and arranged with a N···X–C angle of 163.5(1)º.

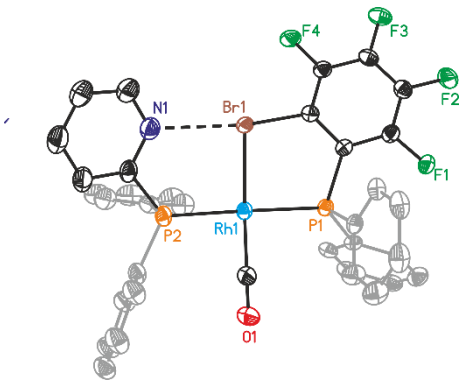

Figure 2.13. ORTEP drawing (thermal ellipsoids drawn at a 50% probability level) showing the structure of **C5**. Hydrogen atoms and BArF anion have been omitted for clarity. Color scheme: C: black or grey, O: red, N: dark blue, F: green, P: orange, Rh: blue, Br: brown.

Table 2.1. Relevant crystallographic data.[a]

	C5	XBphos-Rh **C1**
N···X (Å)	2.801(5)	2.757(8)
X–C (Å)	1.908(3)	2.16(1)
N···X–C (º)	163.5(1)	169.4(5)
Rh–X (Å)	2.4640(4)	2.5535(7)

[a] X refers to the halogen atom present on the complex; X = I or Br. Selected distances and angles were obtained from X-Ray structure of complex **C5**. XBphos-Rh **C1** values were obtained from X-Ray structure reported by our group.[70]

The halogen bond distance in **C5** was found to be smaller than the sum of the Van der Waals radii for Br and N atoms (3.40 Å).[97] This observation was in agreement with the results reported for similar halogen-bonded assemblies between pyridine and bromoaryl derivatives.[76] The N···Br distance in complex **C5** resulted to be longer than the N···I distance in

[97] Bondi, A. *J. Phys. Chem.* **1964**, *68*, 441-451.

XBphos-Rh **C1** complex pointing to a weaker halogen bonding interaction between the nitrogen and bromo groups in complex **C5** (Table 2.1).[84,98]

The bromo substituent appeared to be coordinated to the rhodium(I) center with an overall tridentate coordination (Figure 2.13). Complex **C5** presented a shorter rhodium(I)-bromo distance (2.4640(4) Å, Table 2.1) compared to the analogous distance in XBphos-Rh **C1** complex (d_{Rh-I} = 2.5535(7) Å). This observation is in agreement with reported data, with the metal-ligand distances decreasing in the order I > Br > Cl).[99]

Characterization of complex **C5** in solution by ^{31}P NMR spectroscopy at room temperature revealed two signals: one doublet of doublets at 40.0 ppm ($^{2}J_{P-P}$ = 298 Hz and $^{1}J_{P-Rh}$ = 137 Hz) and a very broad doublet of doublets at −12.4 ppm respectively ($^{2}J_{P-P}$ = 302 Hz and $^{1}J_{P-Rh}$ = 101 Hz). It is interesting to note that the ^{31}P NMR chemical shifts in complex **C5** are very different to those observed for **C1** (Figure 2.5). Variable temperature NMR studies were also carried out and the relevant NMR spectral data are summarized in Figure 2.14.

	^{1}***H NMR*** **(*ortho*-H L1):** 6.85 ppm (213 K)	
	^{31}***P NMR parameters*** (253 K)**:**	
	P: -15.5 ppm	**P:** 38.1 ppm
Spectroscopic data **C5**	$^{2}J_{P-P}$ = 295 Hz $^{1}J_{P-Rh}$ = 106 Hz Peak width at half height: *ca.* 33 Hz	$^{2}J_{P-P}$ = 295 Hz $^{1}J_{P-Rh}$ = 137 Hz Peak width at half height: *ca.* 27 Hz
	^{19}***F NMR*** (298 K)**:** -117.8, -122.8, -143.6, -150.1 ppm	

Figure 2.14. NMR chemical shifts and coupling constants for **C5**.

[98] Other reports also established halogen bond donor atom effects on halogen bonding interactions, especially between perfluorinated iodo or bromo aryl/alkyl compounds and pyridine-based molecules. For some examples see Section 2.1. For additional examples, see: Messina, M. T.; Metrangolo, P.; Panzeri, W.; Ragg, E.; Resnati, G. *Tetrahedron Lett.* **1998**, *39*, 9069-9072.

[99] Kuppuraj, G.; Dudev, M.; Lim, C. *J. Phys. Chem. B* **2009**, *113*, 2952-2960.

As it can be observed in Figure 2.14, ^{31}P NMR chemical shift values found for complex **C5** lied between those previously observed for our halogen bond-assembled complex XBphos-Rh **C1** (Figure 2.5) and those corresponding to the **C4** complex (Figure 2.8), in which no halogen bond is involved and the pyridine group is bound to the rhodium center. Thus, we hypothesized that complex **C5** might exist in solution as an equilibrium between the halogen-bonded complex **C5** and complex **C6**, which contains ligand **L1** bound in a κ^2*P,N*-coordination fashion (Scheme 2.5). As the ^{31}P NMR chemical shift of the mixture of **C5** and **C6** is closer to that for **C1** than to **C4**, we hypothesized that this equilibrium is shifted towards complex **C6**.

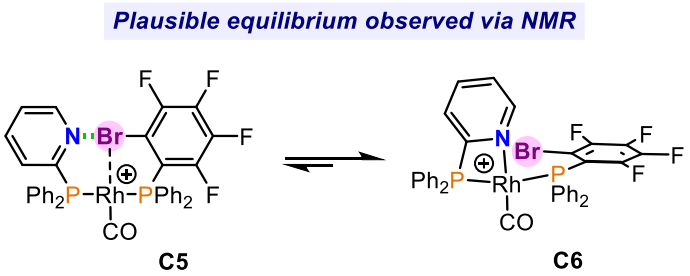

Scheme 2.5. Plausible equilibrium between **C5** and **C6** in solution.

As in previous cases, a large phosphorus-phosphorus coupling constant ($^2J_{P\text{-}P}$ = 295 Hz, 253 K, Figure 2.15) was observed for the mixture of **C5** and **C6** indicating a *trans*-coordination mode of both phosphorus ligands to the rhodium(I) center. The width of the two signals at half height in the ^{31}P NMR spectrum at 253 K was found to be almost identical and we tentatively assigned the downfield signal (38.1 ppm, Figure 2.15) to the phosphino group of the halogen bond donor ligand **L6**. Its chemical shift and coupling constant with rhodium (38.1 ppm,$^1J_{P\text{-}Rh}$ = 137 Hz, Figure 2.15) were also in agreement with those reported for the Vaska-type complex [Rh(CO)Cl(κ*P*-**L5**)$_2$] **57** (δ = 24.0 ppm, $^1J_{P\text{-}Rh}$ = 133.0 Hz).[93]

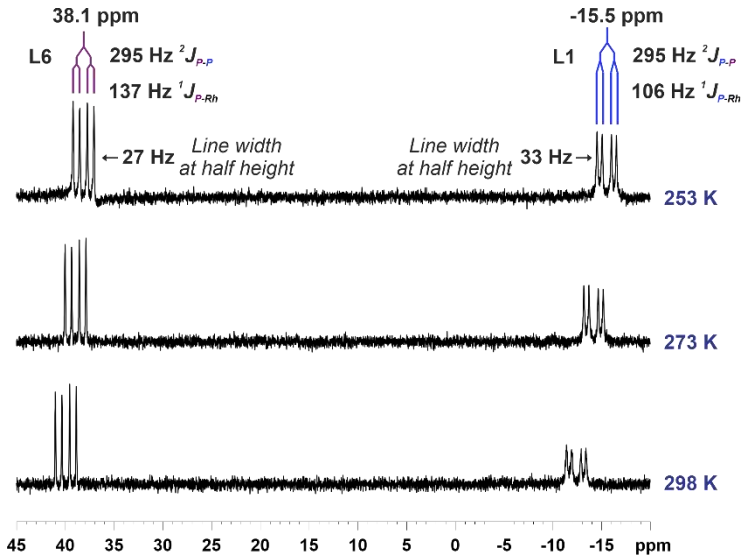

Figure 2.15. Variable temperature ^{31}P NMR analysis of **C5** and **C6** mixture.

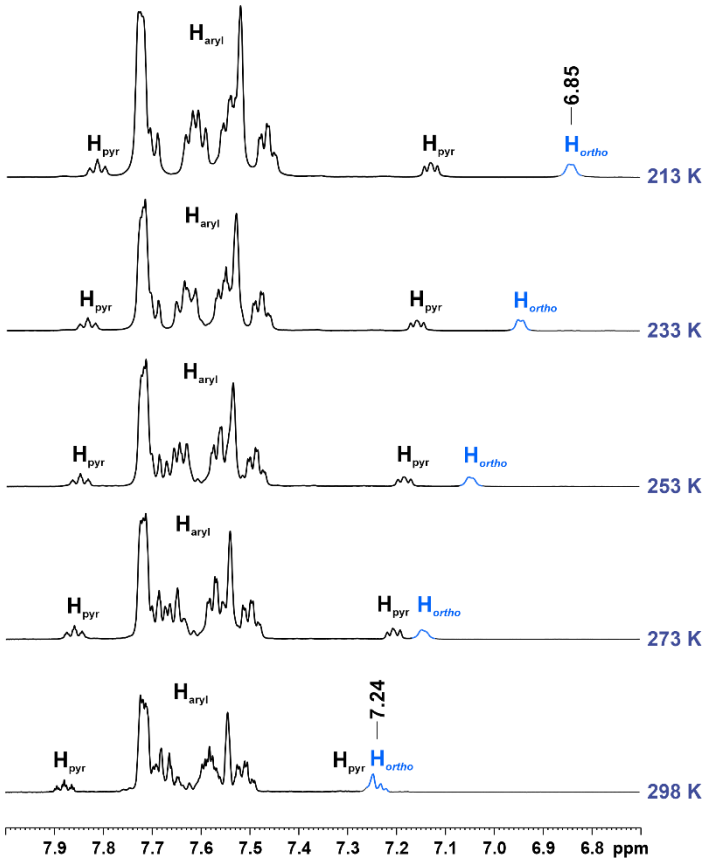

Figure 2.16. Variable temperature ^1H NMR analysis of **C5** and **C6** mixture.

Variable temperature ^{1}H NMR experiments also evidenced this equilibrium in solution between **C5** and **C6**. This technique revealed a remarkable change in the chemical shift of the proton located in *ortho*-position to the nitrogen atom of the pyridine moiety (from 7.24 ppm to 6.85 ppm; $\Delta\delta = 0.39$) when the temperature at which the spectrum was recorded decreased (Figure 2.16). This observation confirmed that complexes **C5** and **C6** were in a dynamic equilibrium in solution.

IR spectra of all the complexes were recorded in solution (DCM). IR data corresponding to the CO stretching band of complexes XBphos-Rh **C1**, complex **C4** and the mixture of complexes **C5**-**C6** are described in Table 2.2. It is interesting to note that when the halogen bond-assembled complex **C5** was dissolved in DCM, the CO stretching band experienced a dramatic change from 2037 cm^{-1} in solid state to 2017 cm^{-1} in a DCM solution. The position of the IR band of **C5** in solution is very close to the value observed for complex **C4** under the same conditions (Table 2.2). This fact confirms that the complex [Rh(CO)(κ^2*N*,*P*-**L1**)(κ*P*-**L6**)]BArF **C6** is being formed in solution from **C5**.

Table 2.2. Selected IR data in solution.

	CO band (cm^{-1})[a]
XBphos-Rh **C1**	2036
	2039[b]
C4	2014
	2003[b]
C5-**C6** mixture	2017
C5	2037[b]

[a] Samples were measured in DCM (10 mM) concentration in all cases. [b] Solid state IR.

Finally, once we confirmed that the bromo-substituted ligand **L6** behaved as a weak halogen bond donor, we wondered whether XBphos-type rhodium complex **C7** could be obtained by using the halogen bond acceptor ligand **L4**, which has the highest acceptor ability from the whole series of molecules prepared within this PhD thesis. The preparation of rhodium(I) complex **C7** was attempted by following the standard methodology. The outcome of the reaction was directly analyzed by NMR spectroscopy at room temperature (Scheme 2.6).

NMR analysis of the reaction mixture revealed that the obtained rhodium complex also consisted of a mixture of complexes. NMR spectral data were similar to those observed for the mixture of complexes **C5** and **C6**. Two phosphorus signals were observed in the ^{31}P NMR spectrum: a doublet of doublet at 35.7 ppm ($^{2}J_{P\text{-}P}$ = 302 Hz and $^{1}J_{P\text{-}Rh}$ = 139 Hz) and a very broad signal at −13.4 ppm (see Section 2.4 for more details), which indicated that complex **C7** was also undergoing a dynamic process due to the transformation of **C7** into **C8**.

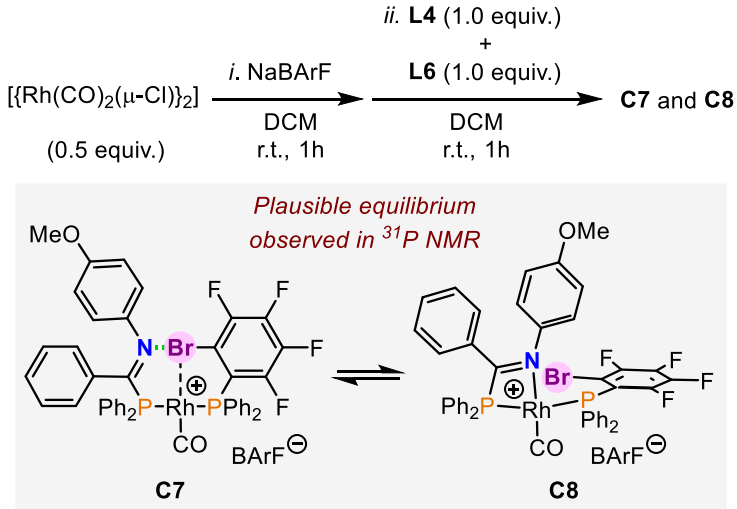

Scheme 2.6. Preparation of rhodium(I) complex **C7** and **C8**.

Broad fluorine signals were also observed in the ^{19}F NMR spectrum. This observation demonstrated that the basicity of the nitrogen in the

halogen bond acceptor did not influence the formation of the halogen bonding interaction and did not cause any effect on the electronic and structural features of the final rhodium(I) complexes.

2.3 CONCLUSIONS

To conclude, the results explained in the previous section illustrate the effects that modifications on the halogen bond acceptor and donor ligands cause on the structure of the final rhodium(I) complexes. Structurally diverse halogen bond acceptor and donor ligands have been designed, synthesized, and subsequently tested in the preparation of halogen bond-assembled rhodium(I) complexes. The final complexes have been fully characterized by spectroscopic techniques in solution and in the solid state. An extensive study of the NMR spectral data obtained for rhodium(I) complexes has allowed for the rationalization of the outcome of the complexation processes and halogen bond formation.

First, it has been demonstrated that halogen bond acceptors containing a phosphaamidine moiety efficiently led to halogen bond-assembled complexes in combination with (2-iodo-3,4,5,6-tetrafluorobenzene)-phosphane-based halogen bond donor **L2**. Two new complexes have been synthesized and fully characterized (**C2** and **C3**), being structurally and electronically analogous to the seminal halogen-bonded rhodium complex prepared by the group (*i.e.* XBphos-Rh **C1**).

Second and last, substitution of the iodo group in (2-iodo-3,4,5,6-tetrafluorobenzene)phosphane-based halogen bond donor **L2** led to changes in the Rh−P complexation processes. For instance, a κ^2*P,N*-type coordination mode of the pyridine containing ligand **L1** was observed in the final complexes when fluorine was chosen as the halogen bond donor group (complexes derived from **L5**). The substitution of the iodo group in the halogen bond donor by a bromo substituent (**L6**) led to the new complex **C5**, whose structure in the solid state incorporated the expected halogen bond-assembled bisphosphane moiety. However, ^{31}P NMR analysis in solution showed the formation of the new complex [Rh(CO)(κ^2*N,P*-**L1**)(κ*P*-**L6**)]BArF **C6** by destruction of the halogen bond and coordination of the halogen bond acceptor **L1** to the rhodium center

in a κ^2*P,N*-fashion. The use of an alternative halogen bond acceptor with enhanced basicity at the nitrogen atom did not revert this behavior and the final complex **C8** did not involve halogen bonding interaction.

2.4 EXPERIMENTAL SECTION

2.4.1 General considerations

All syntheses were carried out using chemicals as purchased from commercial sources unless otherwise stated. Air- and moisture-sensitive manipulations or reactions were performed under inert atmosphere, either in a glove box or with standard Schlenk techniques. Glassware was dried *in vacuo* before use with a hot air gun. All solvents were dried by using a Solvent Purification System (SPS). Silica gel 60 (230–400 mesh) was used for column chromatography. NMR spectra were recorded in 400 MHz or 500 MHz spectrometers in $CDCl_3$ or CD_2Cl_2 unless otherwise cited. ^{1}H and $^{13}C\{^{1}H\}$ NMR chemical shifts are quoted in ppm relative to residual solvent peaks. $^{19}F\{^{1}H\}$ NMR chemical shifts are quoted in ppm relative to $CFCl_3$ in $CDCl_3$. $^{31}P\{^{1}H\}$ NMR chemical shifts are quoted in ppm relative to 85% phosphoric acid in water. HRMS spectra were recorded using ESI ionization method in positive mode. IR spectra were recorded using Attenuated Total Reflection (ATR) technique unless otherwise cited. Ligands **L1** and **L5** are commercially available and were used as received. (2-iodo-3,4,5,6-tetrafluorobenzene)diphenylphosphane ligand **L2** and XBphos-Rh **C1** were prepared according to previous literature reports.[70]

2.4.2 General structural comments on X-Ray crystals

Crystals suitable for X-Ray measurement for complex **C4** and complex **C5** were obtained by slow diffusion of *n*-pentane into concentrated solutions of dichloromethane at −25 ºC under inert atmosphere. The measured crystals were prepared under inert conditions immersed in perfluoropolyether as protecting oil for manipulation.

Crystal structure determination of **C4** and **C5** were carried out using an Apex DUO Kappa 4-axis goniometer equipped with an APPEX 2 4 K CCD area detector, a Microfocus Source E025 IuS using MoK_α radiation (0.71073 Å), Quazar MX multilayer Optics as monochromator and a Oxford Cryosystems low temperature device Cryostream 700 plus (T = -173 ºC). Full-sphere data collection was used with ω and φ scans. *Programs used:* Data collection APEX-2,[100] data reduction Bruker Saint[101] V/.60A and absorption correction SADABS.[102]

Structure Solution and Refinement: Crystal structure solution was achieved using the computer program SHELXT.[103] Visualization was performed with the program SHELXle.[104] Missing atoms were subsequently located from difference Fourier synthesis and added to the atom list. Least-squares refinement on F^2 using all measured intensities was carried out using the program SHELXL 2015.[105] All non-hydrogen atoms were refined including anisotropic displacement parameters.

Comments to the structure **C4**: The asymmetric units contain one molecule of the cationic rhodium metal complex, one BArF anion and a

[100] Data collection with APEX II v2014.9-0. Bruker (2014). Bruker AXS Inc., Madison, Wisconsin, USA.
[101] Data reduction with Bruker SAINT+ version V8.35A. Bruker (2013). Bruker AXS Inc., Madison, Wisconsin, USA.
[102] SADABS: V2014/5 Bruker (2001). Bruker AXS Inc., Madison, Wisconsin, USA. Blessing, Acta Cryst. (1995) A51 33-38.
[103] SHELXT; Sheldrick, G. M. *Acta Cryst*. **2015**, *A71*, 3-8.
[104] SHELXle; Huebschle C. D., Sheldrick G. M., Dittrich B. *J. Appl. Cryst*. **2011**, *44*, 1281-1284.
[105] SHELXL; Sheldrick, G. M. *Acta Cryst*. **2015**, *C71*, 3-8.

highly disordered solvent molecule (probably dichloromethane). In the metal complex, the penta-fluorinated aromatic ring is disordered in two positions with a ratio of 67:33. In the BArF anion all the CF_3 groups show rotational disorder. Since the solvent molecule could not be properly modelled, the program SQUEEZE was applied to remove the solvent molecules from the electron density.[106] The structure is of good quality (no A- or B-alerts) and publishable with a R1 value of 4.81%.

Comments to **C5**: The asymmetric unit contains one molecule of the rhodium metal complex, a BArF anion and 1.25 molecules of dichloromethane (disordered in three positions, occupancy 0.5:0.5:0.25). The main molecule is disordered in two orientations with a ratio of 90:10. If the carbonyl ligand is considered, these two orientations correspond to two different isomers with a different relative position of this carbonyl ligand with respect to the bromine atom. In the BArF anion, a major part of the CF_3 groups show rotational disorder. The structure is of good quality (no A-alerts and one commented B-alert) and publishable with a R1 value of 5.47%.

[106] SQUEEZE implemented in Platon. (a) Platon: Spek, A.L. *J. Appl. Cryst.* **2003**, *36*, 7-13; (b) SQUEEZE: Spek. A. L. *Acta Cryst.* **2015**, *C71* 9-18.

Table 2.3. Crystal data and structural parameters for complex **C4.**

Compound	**C4**
Formula	$C_{68}H_{36}BF_{29}NOP_2Rh$
Formula weight (total)	1609.64
Crystal size (mm^3)	0.30 x 0.07 x 0.02
Temp (K)	100(2)
Crystal system	triclinic
Space group	$P\text{-}_1$
A (Å)	12.742(4)
B (Å)	14.322(5)
C (Å)	20.421(6)
α (deg)	78.610(7)
β (deg)	88.913(6)
γ (deg)	72.347(7)
V ($Å^3$)	3477.9(19)
Z	2
ρ (Mg/m^3)	1.537
μ (mm^{-1})	0.412
θ range (°)	1.018 to 26.861
Reflec. collected	91931
Independent reflections	14839[R(int) = 0.0817]
Absorpt. correct.	multi-scan
Trans. min/max	0.68/0.78
Data/restraints/parameters	14839/ 624/ 1198
R1/wR2 [I>2σ(I)]	0.0481/0.0917
R1/wR2 [all data]	0.0723/0.0999
Goodness-of-fit (F^2)	1.062
Peak/hole ($e/Å^3$)	0.788/-0.947

Table 2.4. Crystal data and structural parameters for complex **C5.**

Compound	**C5**
Formula	$C_{69.25}H_{38.50}BBrCl_{2.50}F_{28}NOP_2Rh$
Formula weight (total)	1776.70
Crystal size (mm^3)	0.50 x 0.50 x 0.40
Temp (K)	100(2)
Crystal system	triclinic
Space group	$P\text{-}_1$
A (Å)	13.0041(5)
B (Å)	15.8549(7)
C (Å)	18.3023(7)
α (deg)	77.9579(11)
β (deg)	73.6817(10)
γ (deg)	87.9528(11)
V ($Å^3$)	3540.8(2)
Z	2
ρ (Mg/m^3)	1.666
μ (mm^{-1})	1.063
θ_{max} (°)	31.649
Reflec. collected	72168
Independent reflections	25133[R(int) = 0.0431]
Absorpt. correct.	multi-scan
Trans. min/max	0.45/0.74
Data/restraints/parameters	25133/ 1829/ 1321
R1/wR2 [I>2σ(I)]	0.0547/0.1430
R1/wR2 [all data]	0.0737/0.1549
Goodness-of-fit (F^2)	1.010
Peak/hole ($e/Å^3$)	3.253/-1.170

2.4.3 Synthesis of ligands L3, L4 and L6

Synthesis of phosphaamidine ligands L3 and L4

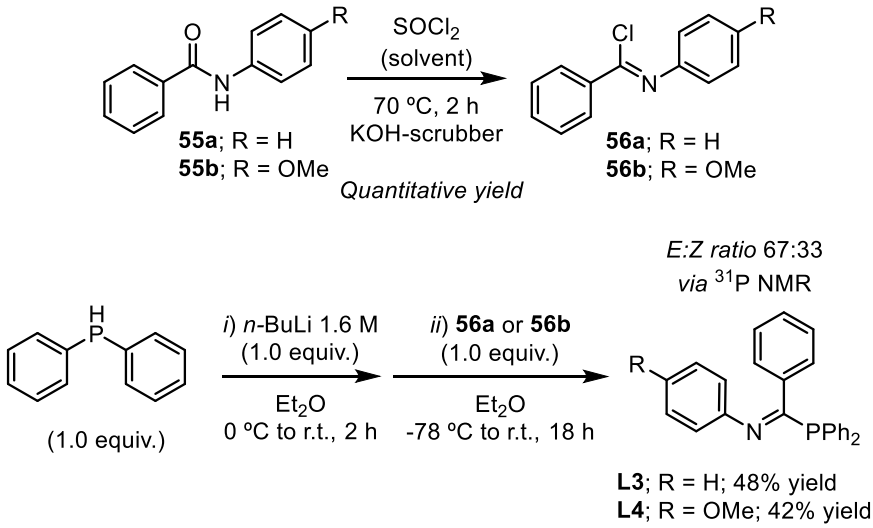

General procedure for **56a** and **56b**: These compounds were synthesized following the methodology reported in the literature.[107] **55a** or **55b** (1.0 equiv, 10.0 mmol) was dissolved in 3.2 mL of thionyl chloride (4.3 equiv.) and the resulting reaction mixture was heated at 70 ºC for 2 hours. The HCl and SO_2 generated were neutralized using an aqueous KOH-scrubber. The reaction mixture was cooled to room temperature and the remaining thionyl chloride was removed under vacuum to afford the final product **56a** or **56b** in quantitative yield. Spectroscopic data were in agreement with those previously reported in the literature.[107,108]

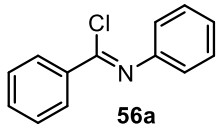
56a

^{1}H NMR (400 MHz, $CDCl_3$) δ: 8.18 (d, *J* = 7.4 Hz, 2 H), 7.58 – 7.38 (m, 5 H), 7.21 (t, *J* = 7.4 Hz, 1 H), 7.02 (d, *J* = 7.6 Hz, 2 H) ppm. **^{13}C{^{1}H} NMR** (126 MHz,

[107] van Dijk, T.; Burck, S.; Rong, M. K.; Rosenthal, A. J.; Nieger, M.; Slootweg, J. C.; Lammertsma, K. *Angew. Chem. Int. Ed.* **2014**, *53*, 9068-9071.

[108] For the full characterization of **56a** and **56b**, see: van den Nieuwendijk, A. M. C. H.; Pietra, D.; Heitman, L.; Göblyös, A.; Ijzerman, A. P. *J. Med. Chem.* **2004**, *47*, 663-672.

$CDCl_3$) δ: 147.8, 143.4, 135.6, 132.2, 129.6, 129.0, 128.6, 125.2, 120.6 ppm.

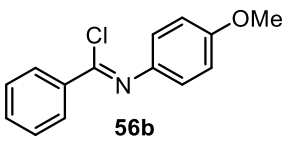

56b

^{1}H NMR (400 MHz, $CDCl_3$) δ: 8.18 – 8.13 (m, 2 H), 7.56 – 7.43 (m, 3 H), 7.10 – 7.04 (m, 2 H), 6.99 – 6.93 (m, 2 H), 3.84 (s, 3 H) ppm. **^{13}C{^{1}H} NMR** (126 MHz, $CDCl_3$) δ: 142.2, 140.3, 135.9, 132.0, 129.5, 128.6, 122.6, 114.2, 55.6 ppm.

General procedure for the synthesis of **L3** and **L4**: phosphaamidine ligands **L3** and **L4** were prepared adapting already reported methods.[91] A fresh Et_2O solution of Ph_2PLi was prepared by the addition of 5.2 mL of a 1.6 M hexanes solution of *n*-BuLi (1.0 equiv., 7.9 mmol) to a colorless Et_2O (90.0 mL) solution of Ph_2PH (1.0 equiv., 7.9 mmol) at 0 ºC. The resulting yellow solution was stirred for 1 h at 0 ºC, then warmed to ambient temperature and stirred for an additional 1 h. To this yellow solution, an Et_2O (23.0 mL) solution of **56a** or **56b** (1.0 equiv., 7.9 mmol) was slowly added at −78 ºC. The yellow mixture was allowed to slowly warm to ambient temperature and stirred for an additional 18 h. The resulting yellow reaction mixture was reduced to dryness *in vacuo* and the residue was refluxed for 2 h in pentane. After filtration of the yellow solution, the filtrate was concentrated under vacuum and kept in the freezer (−20 ºC) for 2 days. **L3** precipitated as a yellow powder, which was filtered and dried to finally obtain **L3** (48% isolated yield) as yellow powder in a 67:33 *E:Z* ratio. On the other hand, **L4** (42% isolated yield) was isolated as a sticky yellow oil, which, after scratching with spatula at −20 ºC, solidified as a yellow powder in a 67:33 *E:Z* ratio.

E:Z ratio 67:33

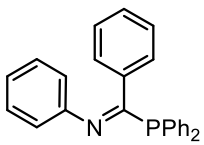

L3

Spectroscopic data were in agreement with those previously reported in the literature.[109] **^{1}H NMR** (500 MHz, $CDCl_3$) δ:[110] 7.60 – 6.62 (m, 20 H) ppm. **^{13}C NMR** (126 MHz, $CDCl_3$) δ: 178.4 (br. s), 151.5 (br .s), 137.7 (br. s), 134.8 (d, J = 20 Hz), 134.2 (br. s), 129.1 (s), 128.8 (br. s), 128.6 – 128.1 (m), 127.8 (br. s), 123.7 (br. s), 123.3 (s), 120.7 (s), 119.2 (br. s) ppm. **^{31}P{^{1}H} NMR** (202 MHz, $CDCl_3$) δ: 8.0 (s, *E*-isomer), −1.5 (s, *Z*-isomer) ppm.

E:Z ratio 67:33

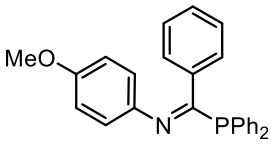

L4

^{1}H NMR (400 MHz, $CDCl_3$) δ:[110] 7.57 – 7.50 (m, 2 H), 7.37 – 7.07 (m, 13 H), 6.77 – 6.60 (m, 4 H), 3.74 (s), 3.70 (s) ppm. **^{13}C{^{1}H} NMR** (126 MHz, $CDCl_3$) δ: 177.7 (s), 177.6 (s), 176.9 (s), 176.4 (s), 156.5 (s), 156.2 (s), 144.9 (d, J = 12.0 Hz), 144.6 (d, J = 8.0 Hz), 140.8 (d, J = 7.5 Hz), 138.1 (d, J = 25 Hz), 135.0 (d, J = 19.6 Hz), 134.5 (d, J = 8.0 Hz), 134.2 (d, J = 20.1 Hz), 129.2 (s), 128.9 (s), 128.8 (s), 128.4-128.2 (m), 128.0 (s), 127.7 (s), 122.6 (s), 120.9 (s), 113.8 (s), 55.5 (s), 55.4 (s) ppm. **^{31}P NMR** (162 MHz, $CDCl_3$) δ: 8.4 (m, *E*-isomer), −1.7 (m, *Z*-isomer) ppm. **HRMS** (ESI): *m/z* calcd. for $C_{26}H_{23}NOP^+$ $[M+H]^+$ 396.1517, found: 396.1512.

Synthesis of ligand L6

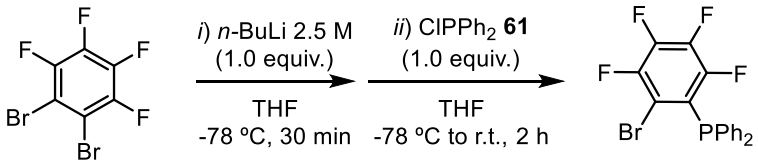

60
(1.1 equiv.)

99% yield

L6

[109] van Dijk, T.; Burck, S.; Rosenthal, A. J.; Nieger, M.; Ehlers, A. W.; Slootweg, J. C.; Lammertsma, K. *Chem. – Eur. J.* **2015**, *21*, 9328-9331.

[110] *E*- and *Z*-isomers can not be distinguished in ^{1}H and ^{13}C{^{1}H} NMR. One set of signals for both isomers is reported in this manuscript.

L6 was prepared following the procedure reported by Meek *et al.*[96] A solution of 0.5 mL (3.2 mmol, 1.1 equiv.) of 1,2-dibromotetrafluorobenzene **60** in 15.0 mL of anhydrous THF was cooled to -78 ºC h. To the cold stirred solution, 1.2 mL of a 2.5 M solution of *n*-butyllithium in hexanes (2.9 mmol, 1.0 equiv.) was added dropwise. After the reaction mixture was stirred for 30 min, 0.6 mL (2.9 mmol, 1.0 equiv.) of chlorodiphenylphosphane **61** was added dropwise. The resulting amber slurry was stirred for an additional 45 min, removed from the low temperature bath and allowed to warm to room temperature, whereupon a white solid separated. After 30 min at room temperature, no further change in the reaction mixture was observed. The reaction mixture was quenched with water (10.0 mL) and the pale amber organic layer that separated was extracted with Et_2O (2 x 15.0 mL). The organic phase was dried by using Na_2SO_4 and the volatiles were removed yielding a yellowish solid. The product was purified *via* column chromatography over SiO_2 using a Cy:EtOAc 80:20 mixture as eluent obtaining 1.2 g of pure compound **L6** (99% yield). Spectroscopic data were in agreement with the reported compounds.[96]

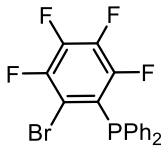

L6

^{1}H NMR (400 MHz, $CDCl_3$) δ: 7.42 – 7.35 (m, 10 H) ppm. **^{13}C{^{1}H} NMR** (126 MHz, $CDCl_3$) δ: 133.7 (dd, J = 11.9, 3.5 Hz), 132.9 (dd, J = 21.2, 1.1 Hz), 129.3 (s), 128.7 (d, J = 6.8 Hz) ppm. **^{19}F{^{1}H} NMR** (376 MHz, $CDCl_3$) δ: –120.9 (m, 1 F), –125.8 (m, 1 F), –149.5 (td, $^{3}J_{F–F}$ = 21.0 Hz, $^{4}J_{F–F}$ = 5.8 Hz, 1 F), –153.4 (t, $^{3}J_{F–F}$ = 21.0 Hz, 1 F) ppm. **^{31}P{^{1}H} NMR** (162 MHz, $CDCl_3$) δ: 0.3 (ddd, $J_{P–F}$ = 19.8, 9.9, 3.9 Hz) ppm.

2.4.4 Synthesis of rhodium(I) complexes C2, C3, C4 and C5

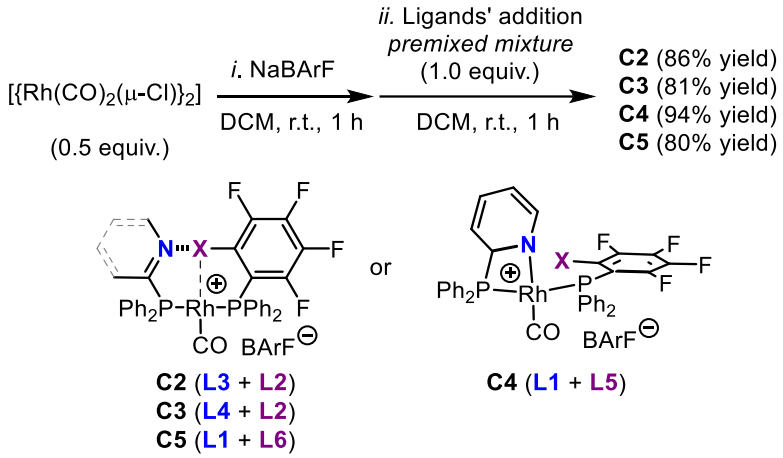

General procedure for rhodium(I) complexes **C2**, **C3**, **C4** and **C5**: In a glovebox filled with N_2, [{Rh(CO)$_2$(μ-Cl)}$_2$] (0.5 equiv.) and NaBArF (1.0 equiv.) were added to an amberized glass vial provided with a magnetic stirrer and dissolved in DCM (0.06 M). The mixture was stirred for 1 hour at room temperature. In parallel, a solution of the corresponding halogen bond acceptor ligand (**L1**, **L3** or **L4**, 1.0 equiv.) and halogen bond donor ligand (**L2**, **L5** or **L6**, 1.0 equiv.) in DCM (0.12 M) was prepared in a vial provided with a magnetic stirrer. The mixture was stirred for 1 hour at room temperature. At due time, the latter solution was added dropwise to the rhodium solution, observing some bubbling (CO release). This mixture was stirred for 1 hour at room temperature, and then filtered by using a HPLC nylon filter to remove the NaCl precipitate. The resulting orange solution was partially evaporated (to *ca.* 1 mL volume) and mixed with 5 mL of *n*-pentane. The resulting solid was washed with *n*-pentane (3 x 2 mL). and dried under vacuum to afford the desired rhodium(I) complexes **C2**, **C3**, **C4** or **C5**.

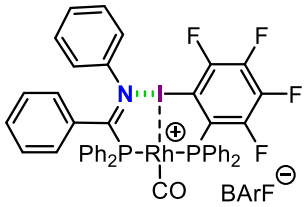

C2

For the preparation of complex **C2**: 24.0 mg (0.05 mmol, 0.5 equiv.) of [{Rh(CO)$_2$(μ-Cl)}$_2$] dimer, 106.0 mg (0.1 mmol, 1.0 equiv.) of NaBArF, 45.1 mg (0.1 mmol, 1.0 equiv.) of **L3** and 56.9 mg (0.1 mmol, 1.0 equiv.) of **L2**. 189.0 mg (86% yield) of complex **C2** was obtained as an orange sticky oil. Spectroscopic data were in agreement with those previously reported.[111] **^{1}H NMR** (400 MHz, CD_2Cl_2) δ: 7.73 – 7.71 (m, 9 H), 7.67 – 7.44 (m, 23 H), 7.33 – 7.29 (m, 2 H), 7.21 – 7.13 (m, 2 H), 6.99 (t, *J* = 7.9 Hz, 2 H), 6.92 (d, *J* = 8.0 Hz, 2 H), 6.48 (d, *J* = 6.9 Hz, 2 H) ppm. **^{13}C{^{1}H} NMR** (101 MHz, CD_2Cl_2) δ:[112] 162.1 (q, *J* = 49.9 Hz, C_{BArF}), 146.7 (d, *J* = 24.0 Hz), 135.2 (C_{BArF}), 133.7 (d, *J* = 12.3 Hz, C_{Ph}), 133.2 – 132.9 (m, C_{Ph}), 130.2 (C_{Ph}), 130.1 (C_{Ph}), 130.0 (C_{Ph}), 129.8 (C_{Ph}), 129.8 (C_{Ph}), 129.2 (qm, *J* = 32.0 Hz, C_{BArF}), 128.8 (C_{Ph}), 128.1 (C_{Ph}), 127.7 (C_{Ph}), 127.6 (C_{Ph}), 127.1 (C_{Ph}), 125.0 (q, *J* = 271.9 Hz, C_{BArF}), 121.7 (C_{Ph}), 120.9 (C_{Ph}) 118.0 – 117.7 (m, C_{BArF}) ppm. **^{19}F{^{1}H} NMR** (471 MHz, CD_2Cl_2) δ: –62.9 (s, 24 F), –116.7 (m, 1 F), –117.6 (m, 1 F), –142.4 (m, 1 F), –147.2 (m, 1 F) ppm. **^{31}P{^{1}H} NMR** (202 MHz, CD_2Cl_2) δ: 78.6 (ddd, $^2J_{P-P}$ = 276.3 Hz, $^1J_{P-Rh}$ = 111.2 Hz, $^3J_{P-F}$ = 13.8 Hz), 64.4 (dd, $^2J_{P-P}$ = 276.3 Hz, $^1J_{P-Rh}$ = 116.6 Hz). **IR** (neat): 2029, 1499, 1440, 1353, 1273, 1117, 886, 839, 744, 722, 712, 690, 681, 669 cm^{-1}. **HRMS** (ESI$^+$): *m*/*z* calcd. for $C_{44}H_{30}F_4INOP_2Rh^+$ [M–BArF]$^+$ 955.9791, found 955.9833.

[111] Llorente, N. Transition Metal-Catalyzed Cycloaddition Reactions for the Formation of Eight- and Six-membered Rings. Ph.D. Thesis, University of Rovira i Virgili, Tarragona, Spain, 2021.

[112] A heavily overlapped ^{13}C{^{1}H} NMR spectrum was observed due to multiple couplings of the carbons with other NMR active heteronuclei present in the molecule. Whenever possible, the carbons where assigned as it follows: C_{CO} (carbonyl carbon), C_{BArF} (from the counterion), C_{Ph} (phenyl ring carbons), C_{Py} (pyridyl ring carbons), C_F (fluorine-containing ring carbons).

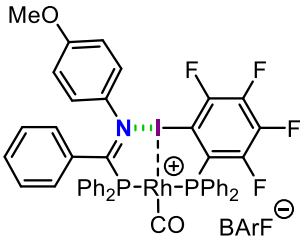

C3

For the preparation of complex **C3**: 7.2 mg (0.02 mmol, 0.5 equiv.) of [{Rh(CO)$_2$(μ-Cl)}$_2$], 33 mg (0.04 mmol, 1.0 equiv.) of NaBArF, 14.3 mg (0.04 mmol, 1.0 equiv.) of **L4** and 17.0 mg (0.04 mmol, 1.0 equiv.) of **L2**. 54.0 mg (81% yield) of complex **C3** was obtained as an orange sticky oil). **^{1}H NMR** (400 MHz, CD_2Cl_2) δ: 7.76 – 7.72 (m, 9 H), 7.68 – 7.43 (m, 23 H), 7.18 (t, *J* = 7.6 Hz, 1 H), 7.01 (t, *J* = 7.9 Hz, 2 H), 6.96 – 6.91 (m, 2 H), 6.84 – 6.79 (m, 2 H), 6.51 (d, *J* = 8.2 Hz, 2 H), 3.75 (m, 3 H) ppm. **^{13}C{^{1}H} NMR** (126 MHz, CD_2Cl_2) δ:[112] 162.1 (q, *J* = 49.9 Hz, C_{BArF}), 159.5 (C_{Ph}), 135.2 (C_{BArF}), 133.7 (d, *J* = 12.3 Hz, C_{Ph}), 133.2 – 132.8 (m, C_{Ph}), 130.9 (d, *J* = 12.6 Hz, C_{Ph}), 130.3 (C_{Ph}), 130.3 (C_{Ph}), 130.1 (C_{Ph}), 130.0 (C_{Ph}), 130.0 (d, *J* = 2.5 Hz, C_{Ph}), 129.3 (qm, *J* = 32.0 Hz, C_{BArF}), 129.0 (C_{Ph}), 128.6 (C_{Ph}), 128.2 (C_{Ph}), 127.8 (C_{Ph}), 127.4 (C_{Ph}), 125.0 (q, *J* = 272.3 Hz, C_{BArF}), 124.2 (C_{Ph}), 118.0 – 117.7 (m, C_{BArF}), 120.9 (C_{Ph}), 115.6 (C_{Ph}), 114.9 (C_{Ph}), 55.9 (C_{OMe}) ppm. **^{19}F{^{1}H} NMR** (471 MHz, CD_2Cl_2) δ: –62.9 (s, 24 F), –116.8 (m, 1 F), –117.7 (m, 1 F), –142.6 (m, 1 F), –147.4 (m, 1 F) ppm. **^{31}P{^{1}H} NMR** (162 MHz, CD_2Cl_2) δ: 78.9 (ddd, $^2J_{P-P}$ = 275.5 Hz, $^1J_{P-Rh}$ = 111.3 Hz, $^3J_{P-F}$ = 13.9 Hz), 64.7 (dd, $^2J_{P-P}$ = 275.4 Hz, $^1J_{P-Rh}$ = 116.2 Hz). **IR** (neat): 2028, 1502, 1440, 1353, 1272, 1113, 1029, 885, 839, 744, 712, 681, 669 cm^{-1}. **HRMS** (ESI$^+$): *m*/*z* calcd. for $C_{44}H_{32}F_4INOP_2Rh^+$ [M–CO–BArF]$^+$ 957.9989, found 957.9976.

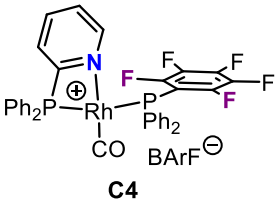

C4

For the preparation of complex **C4**: 27.7 mg (0.07 mmol, 0.5 equiv.) of [{Rh(CO)$_2$(μ-Cl)}$_2$], 123.0 mg (0.1 mmol, 1.0 equiv.) of NaBArF, 36.4 mg (0.1 mmol, 1.0 equiv.) of **L1** and 52.4 mg (0.1 mmol, 1.0 equiv.) of **L5**. 207.0 mg (94% yield) of complex **C4** was obtained as a fine yellow powder. **^{1}H NMR** (400 MHz, CD_2Cl_2, 233 K) δ: 7.89 (tt, *J* = 8.0, 1.7 Hz, 1 H), 7.80 – 7.46 (m, 33 H), 7.18 (br t, *J* = 6.2 Hz, 1 H), 7.05 (d, *J* = 5.1 Hz, 1 H) ppm. **^{13}C{^{1}H} NMR** (101 MHz,

CD_2Cl_2, 233 K) δ:[112] 188.6 (C_{CO}, J = 72.0, 12.3 Hz), 170.4 (dd, J = 51.6, 5.7 Hz, C_{Py}), 161.7 (q, J = 49.7 Hz, C_{BArF}), 149.3 (d, J = 13.8 Hz, C_{Py}), 147.1 (dm, J = 251.8 Hz, C_F), 143.8 (dm, J = 247.4 Hz, C_F), 140.5 (d, J = 3.3 Hz, C_{Py}), 138.1 (dm, J = 258.5 Hz, C_F), 134.6 (C_{BArF}), 133.7 (d, J = 13.8 Hz, C_{Ph}), 133.2 (C_{Ph}), 133.1 (C_{Ph}), 132.4 (C_{Ph}), 130.3 (C_{Py}), 129.9 (d, J = 12.0 Hz), 129.6 (d, J = 11.4 Hz), 129.1-128.1 (m, C_{BArF}), 128.1, 127.7, 124.6 (d, J = 51.3 Hz), 124.4 (q, J = 272.5 Hz, C_{BArF}), 117.4 (C_{BArF}) ppm. **^{19}F{^{1}H} NMR** (376 MHz, CD_2Cl_2) δ: –62.9 (s, 24 F), –124.9 (m, 2 F), –145.4 (t, J_{F-F} = 20.6 Hz, 1 F), –158.3 (m, 2 F) ppm. **^{31}P{^{1}H} NMR** (162 MHz, CD_2Cl_2, 253 K) δ: 13.9 (dd, $^2J_{P-P}$ = 291.0 Hz, $^1J_{P-Rh}$ = 129.0 Hz), –27.9 (dd, $^2J_{P-P}$ = 291.0 Hz, $^1J_{P-Rh}$ = 103.0 Hz) ppm. **IR** (neat): 2003, 1479, 1354, 1273, 1158, 1115, 1094, 983, 886, 838, 682 cm^{-1}. **HRMS** (ESI) *m/z*: calcd. for $C_{36}H_{24}F_5NOP_2Rh^+$ [M–BArF]$^+$ 746.0297, found: 746.0290.

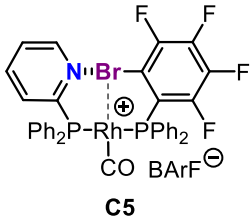

C5

For the preparation of complex **C5**: 9.5 mg (0.02 mmol, 0.5 equiv.) of [{Rh(CO)$_2$(μ-Cl)}$_2$] dimer, 42.0 mg (0.05 mmol, 1.0 equiv.) of NaBArF, 12.5 mg (0.05 mmol, 1.0 equiv.) of **L1** and 19.6 mg (0.05 mmol, 1.0 equiv.) of **L6**. 63.0 mg (80% yield) of complex **C5** was obtained as a brown foamy solid. **^{1}H NMR** (500 MHz, CD_2Cl_2) δ: 7.88 (tt, J = 7.8, 2.2 Hz, 1 H), 7.76 – 7.48 (m, 33 H), 7.27 – 7.21 (br m, 2 H) ppm. **^{13}C{^{1}H} NMR** (126 MHz, CD_2Cl_2) δ:[112] 162.2 (q, J = 49.7 Hz, C_{BArF}), 149.4 (d, J = 14.9 Hz, C_{Py}), 140.3 (d, J = 3.8 Hz, C_{Py}), 135.2 (C_{BArF}), 133.8 (d, J = 13.8 Hz, C_{Ph}), 133.4 (C_{Ph}), 133.1 (C_{Ph}), 133.2 (C_{Ph}) 133.1 (C_{Ph}), 130.4 (d, J = 12.1 Hz, C_{Ph}),130.1 – 129.8 (br m, C_{Ph}), 129.3 (qm, J = 32.2 Hz, C_{BArF}), 128.1 (C_{Pyr}), 127.2 (C_{Ph}), 126.5(br s, C_{Ph}), 124.9 (q, J = 272.5 Hz, C_{BArF}), 117.9 (C_{BArF}) ppm. **^{19}F{^{1}H} NMR** (471 MHz, CD_2Cl_2) δ: –62.9 (s, 24 F), –117.8 (br s, 1 F), –122.8 (br s, 1 F), –143.6 (br s, 1 F), –150.1 (br s, 1 F) ppm. **^{31}P{^{1}H} NMR** (202 MHz, CD_2Cl_2) δ: 40.0 (dd, $^2J_{P-P}$ = 298.9 Hz, $^1J_{P-Rh}$ = 137.2 Hz), –12.3 (dd, $^2J_{P-P}$ = 297.0 Hz, $^1J_{P-Rh}$ = 111.0 Hz) ppm. **IR** (neat): 2037, 1507, 1453, 1353, 1272, 1118, 886,

715, 690, 682, 668 cm^{-1}. **HRMS** (ESI) *m/z*: calcd. for $C_{35}H_{24}BrF_4NP_2Rh^+$ $[M-CO-BArF]^+$ 777.9553, found: 777.9552.

2.4.5 Variable temperature NMR experiments for complex C4 and C5

Variable temperature NMR spectra for C4

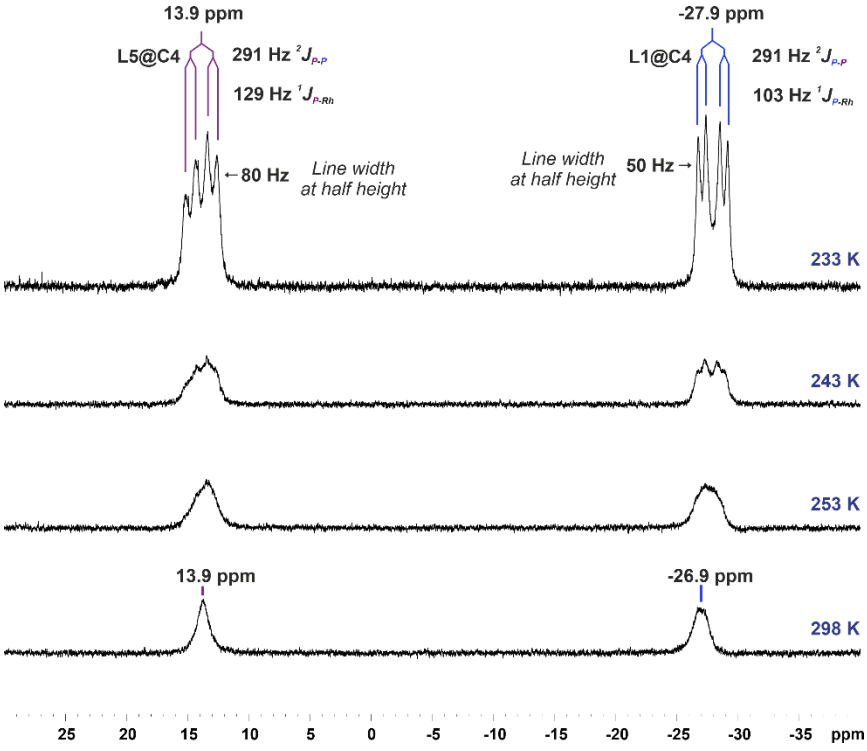

Figure 2.17. Variable temperature ^{31}P NMR experiments for **C4**.

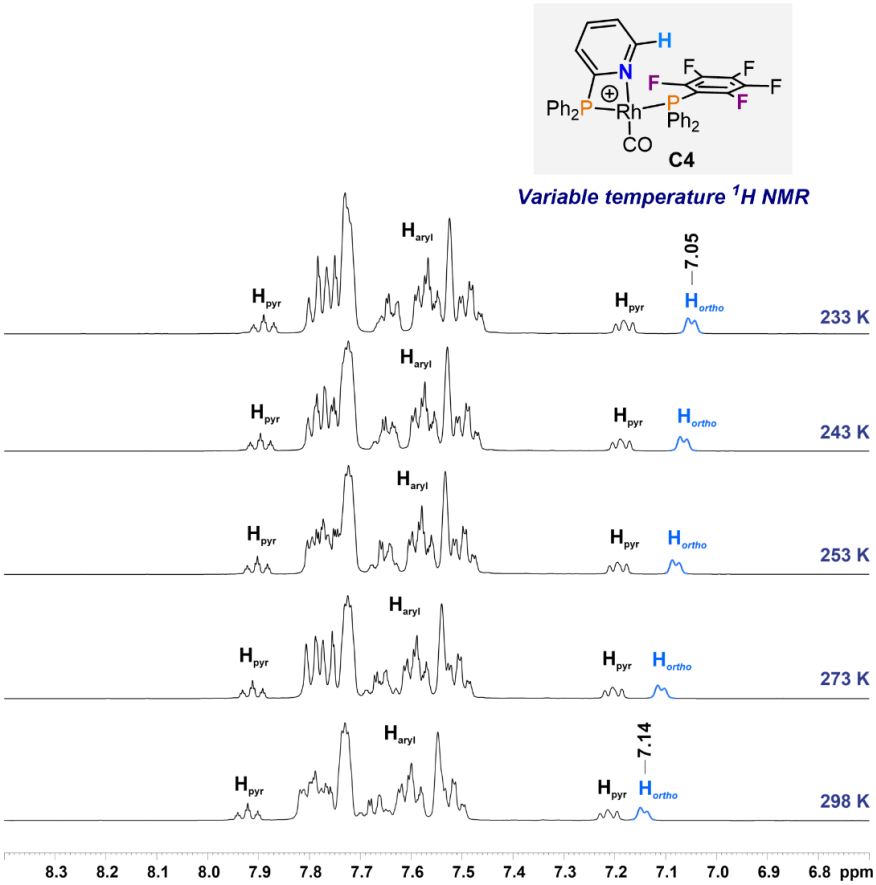

Figure 2.18. Variable temperature ^{1}H NMR experiments for **C4**.

2.4.6 Collection of NMR spectra

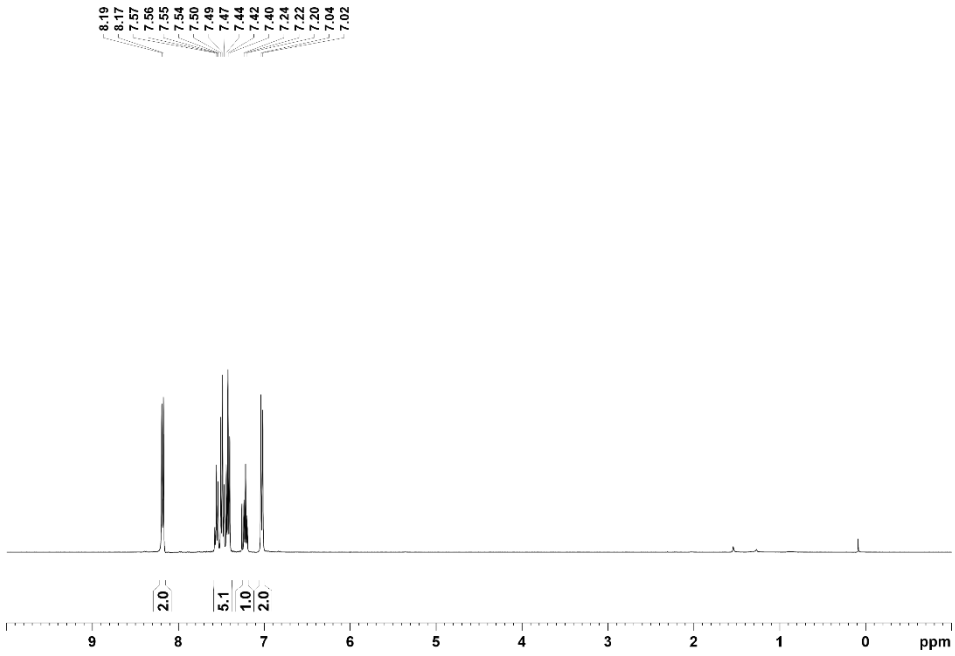

Figure 2.19. ^{1}H NMR (400 MHz, $CDCl_3$) for compound **56a**.

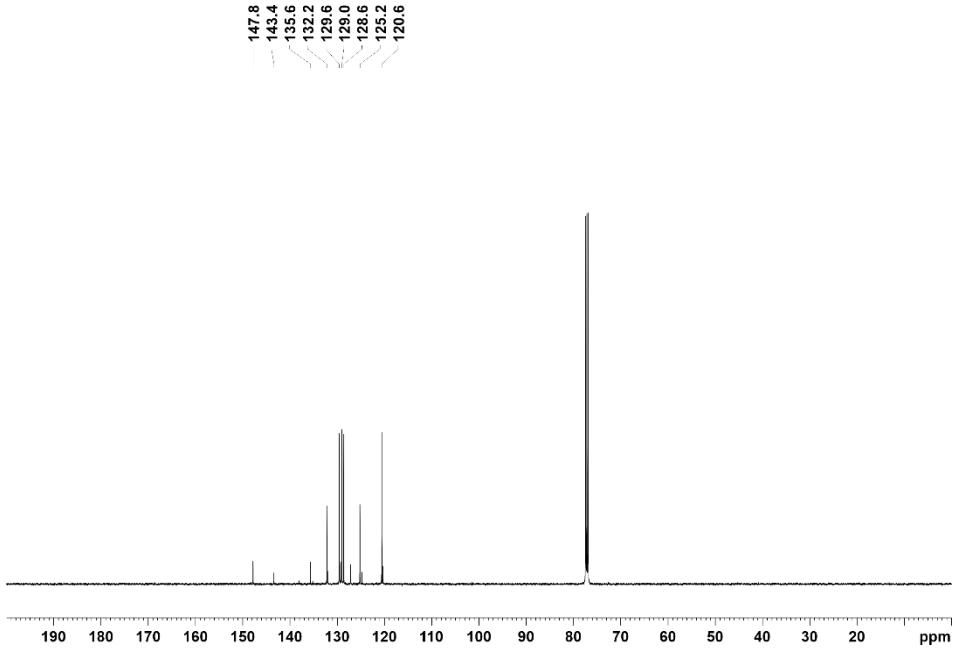

Figure 2.20. $^{13}C\{^{1}H\}$ NMR (126 MHz, $CDCl_3$) for compound **56a**.

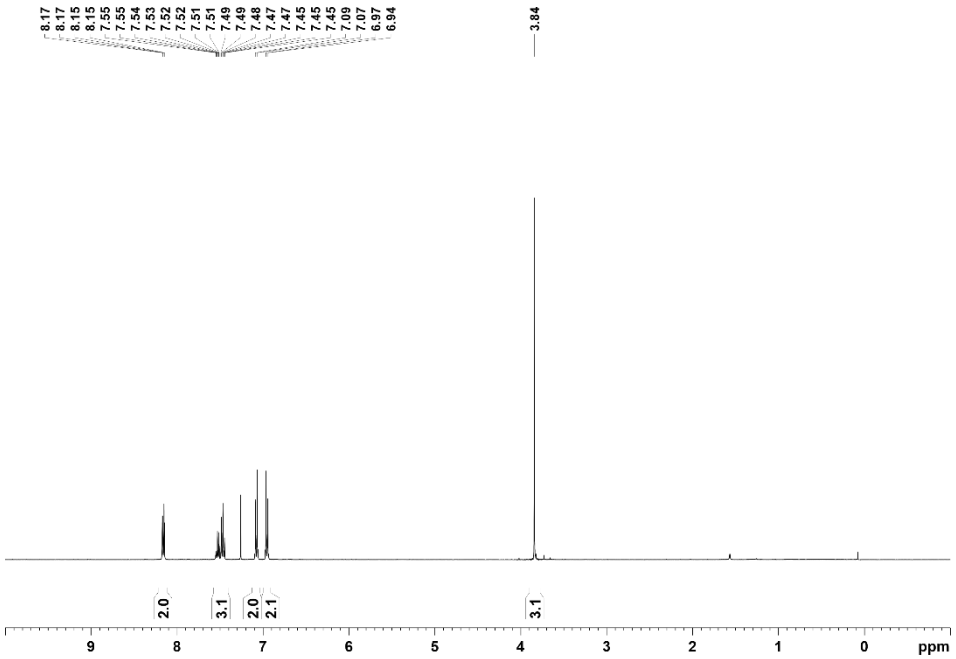

Figure 2.21. ^{1}H NMR (400 MHz, $CDCl_3$) for compound **56b**.

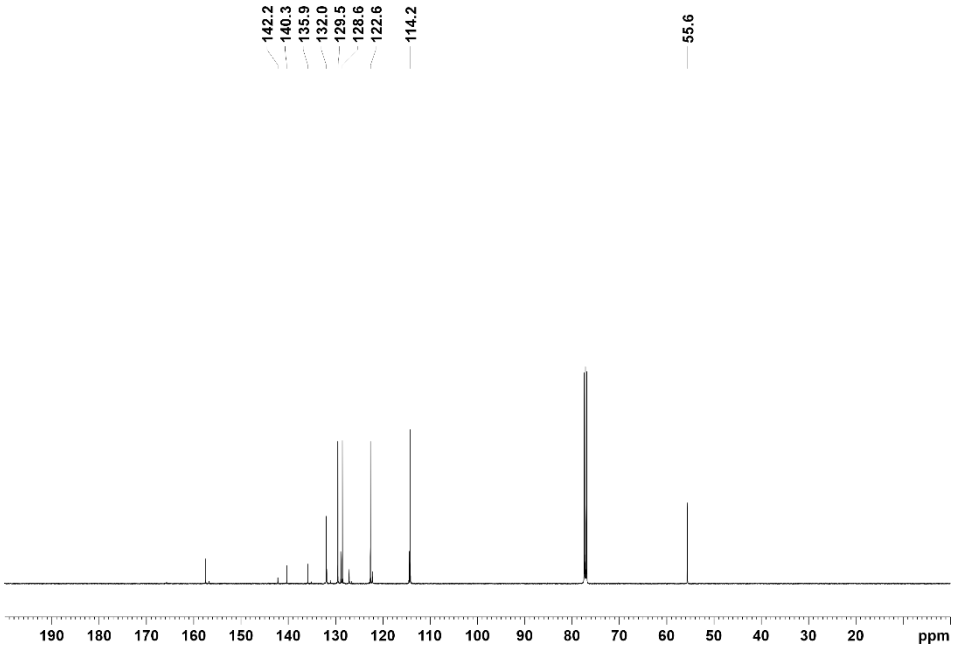

Figure 2.22. $^{13}C\{^{1}H\}$ NMR (126 MHz, $CDCl_3$) for compound **56b**.

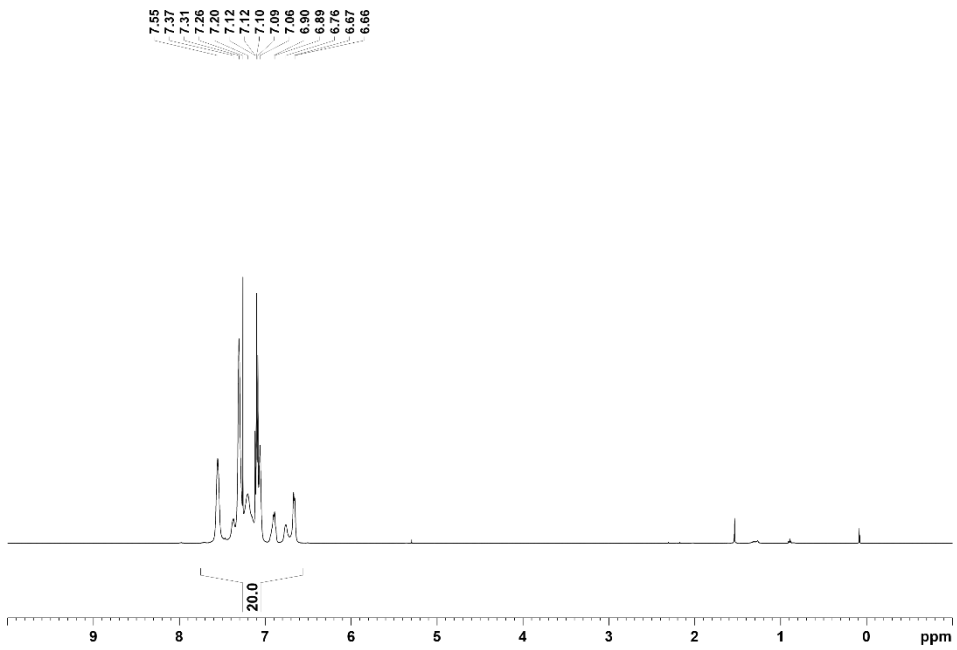

Figure 2.23. ^{1}H NMR (500 MHz, $CDCl_3$) for **L3**.

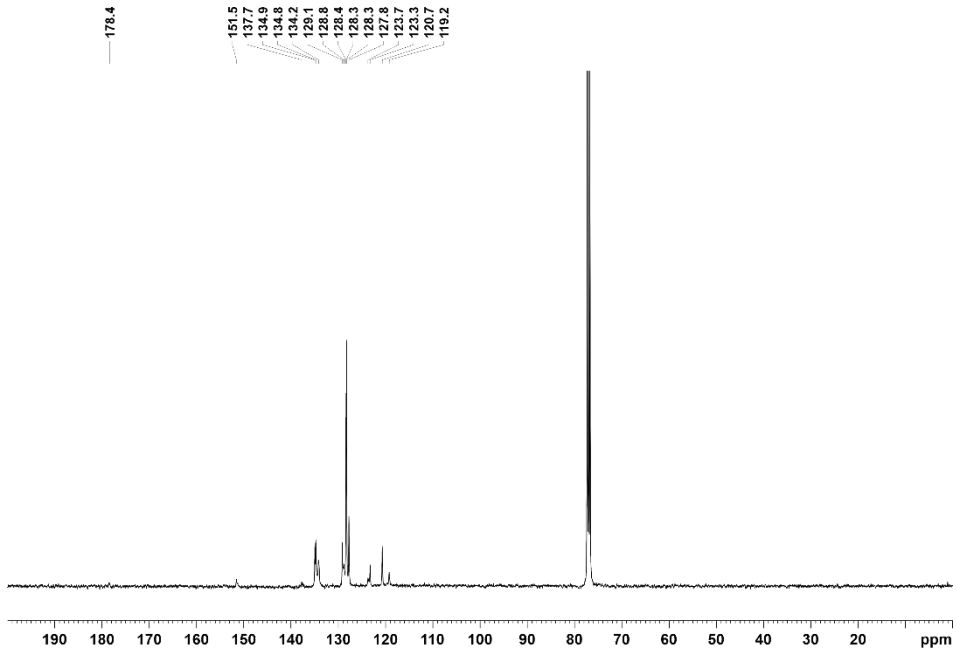

Figure 2.24. $^{13}C\{^{1}H\}$ NMR (126 MHz, $CDCl_3$) for **L3**.

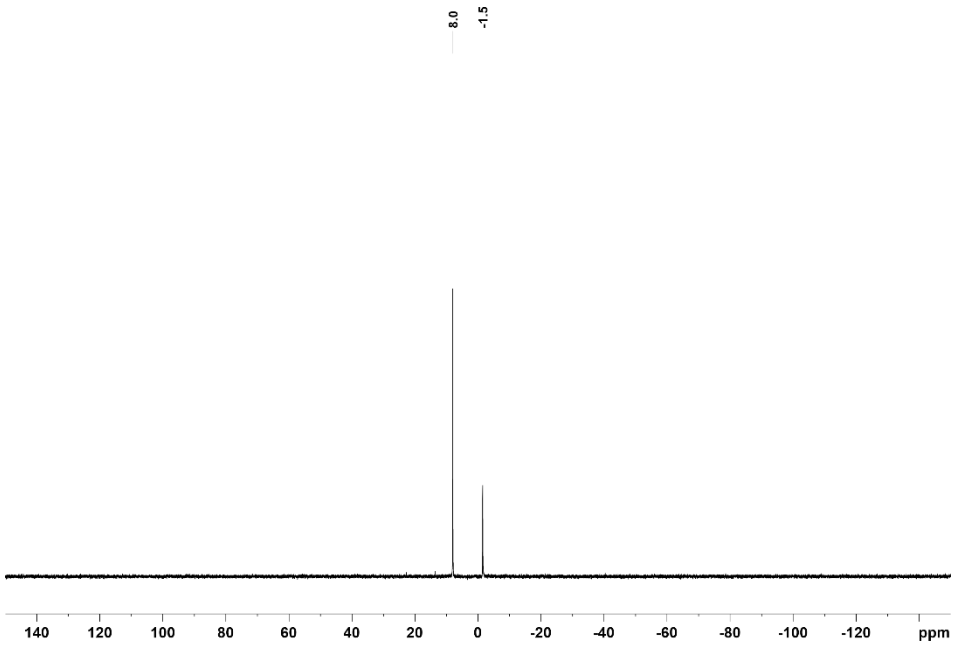

Figure 2.25. $^{31}P\{^{1}H\}$ NMR (202 MHz, $CDCl_3$) for **L3**.

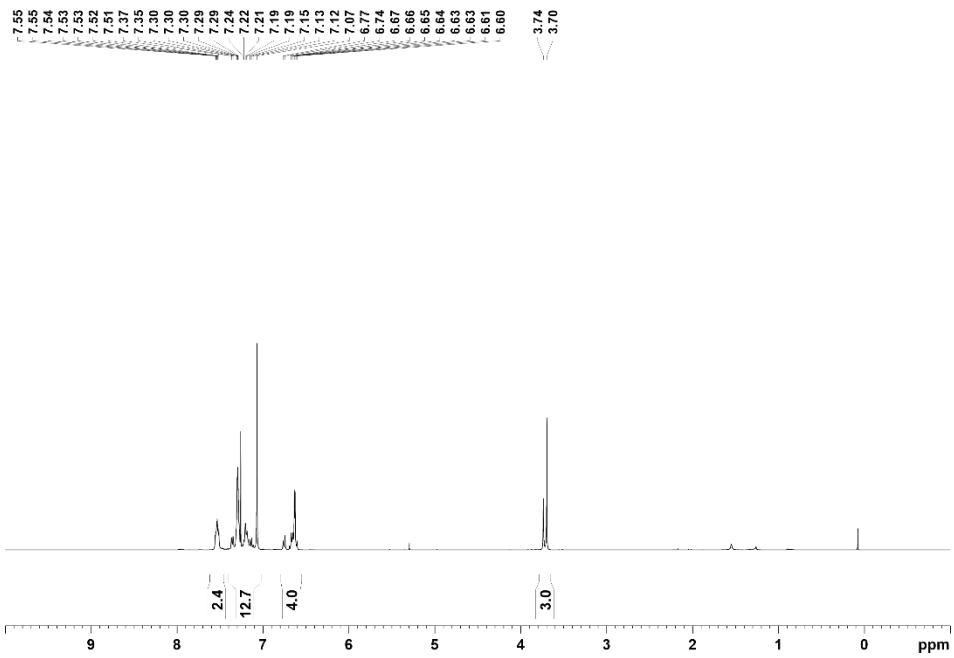

Figure 2.26. ^{1}H NMR (500 MHz, $CDCl_3$) for **L4**.

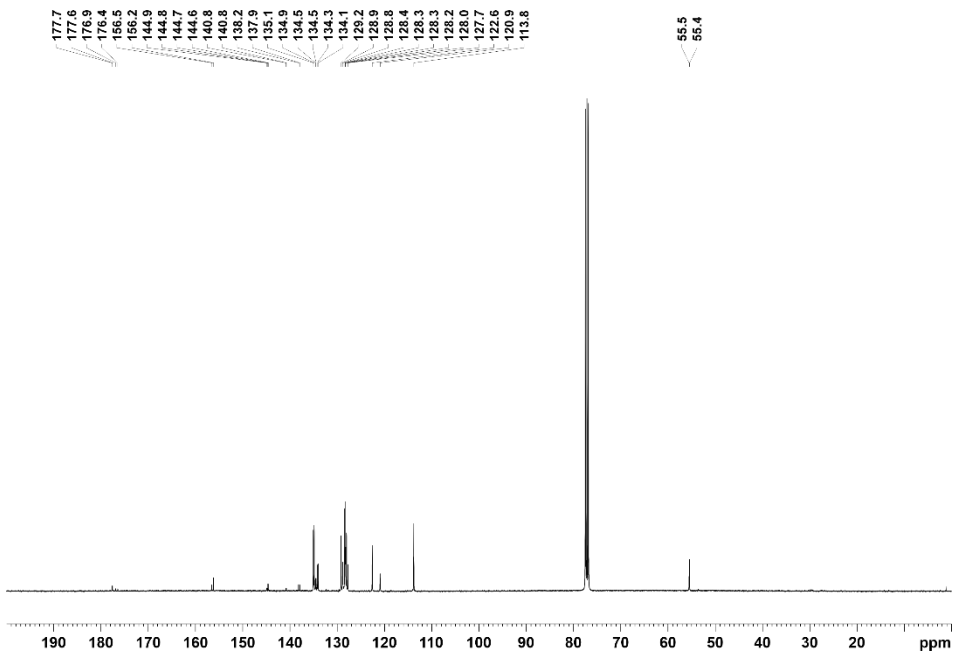

Figure 2.27. $^{13}C\{^{1}H\}$ NMR (126 MHz, $CDCl_3$) for **L4**.

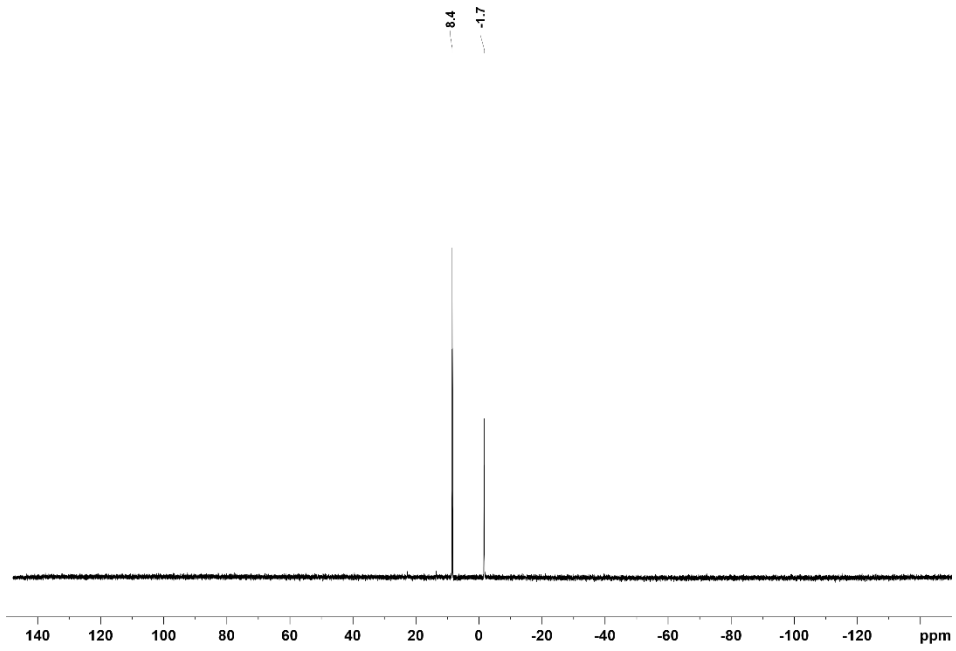

Figure 2.28. $^{31}P\{^{1}H\}$ NMR (202 MHz, $CDCl_3$) for **L4**.

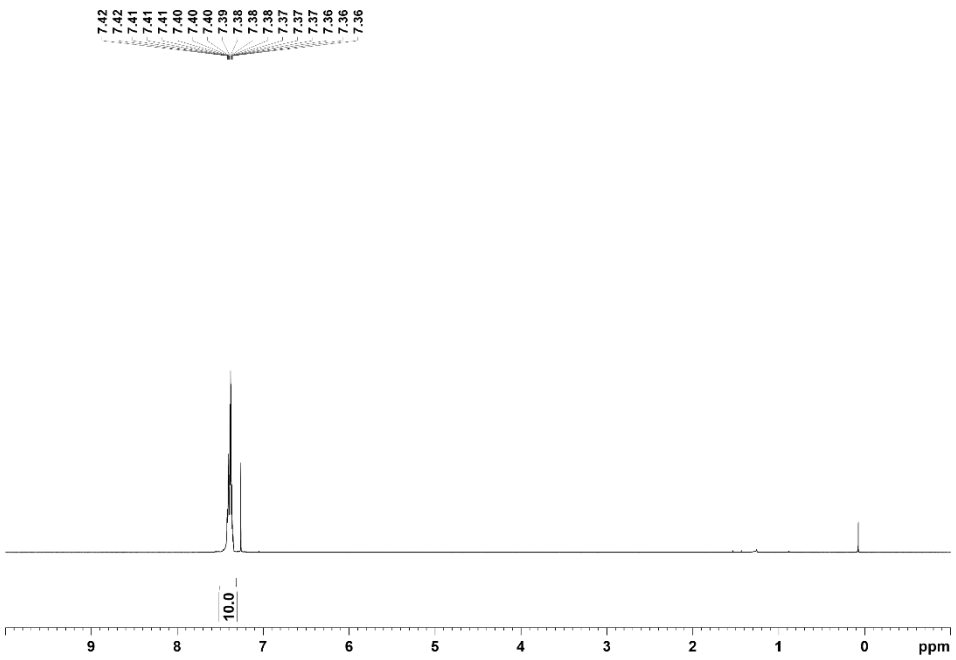

Figure 2.29. ^{1}H NMR (400 MHz, $CDCl_3$) for **L6**.

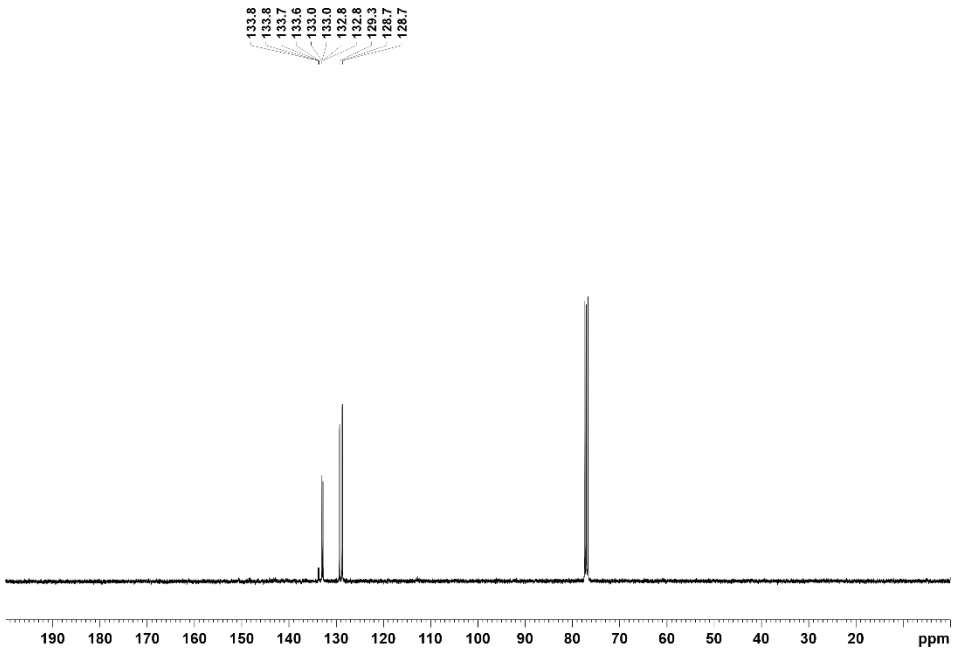

Figure 2.30. $^{13}C\{^{1}H\}$ NMR (126 MHz, $CDCl_3$) for **L6**.

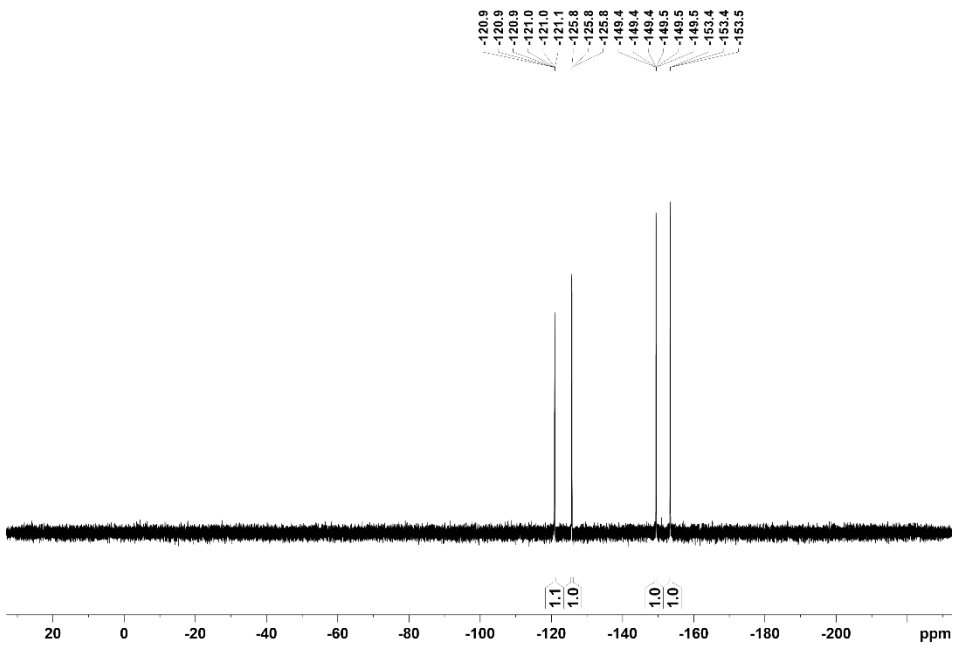

Figure 2.31. $^{19}F\{^{1}H\}$ NMR (376 MHz, $CDCl_3$) for **L6**.

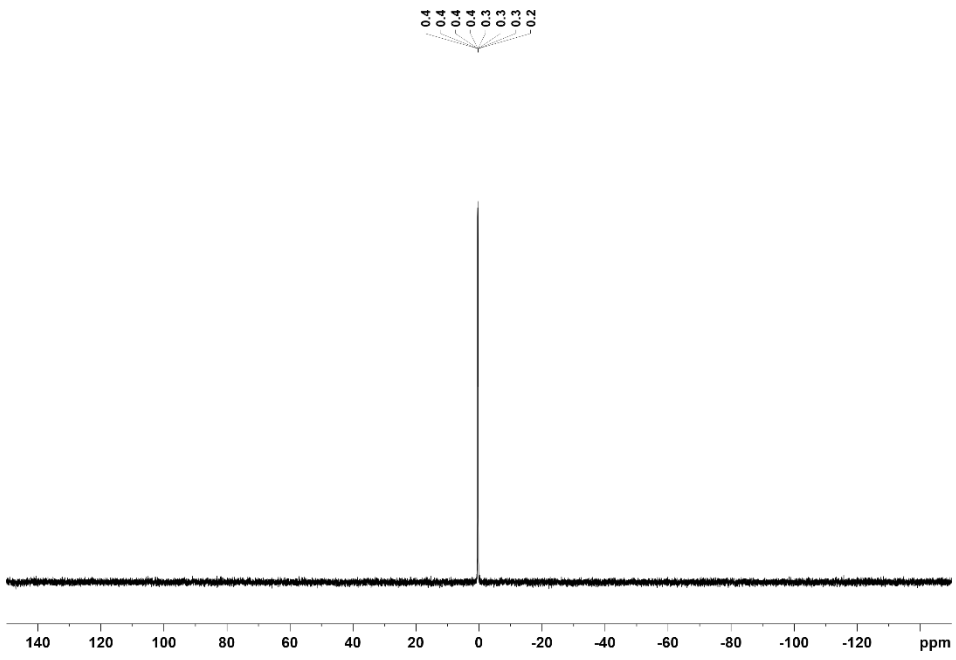

Figure 2. 32. $^{31}P\{^{1}H\}$ NMR (162 MHz, $CDCl_3$) for **L6**.

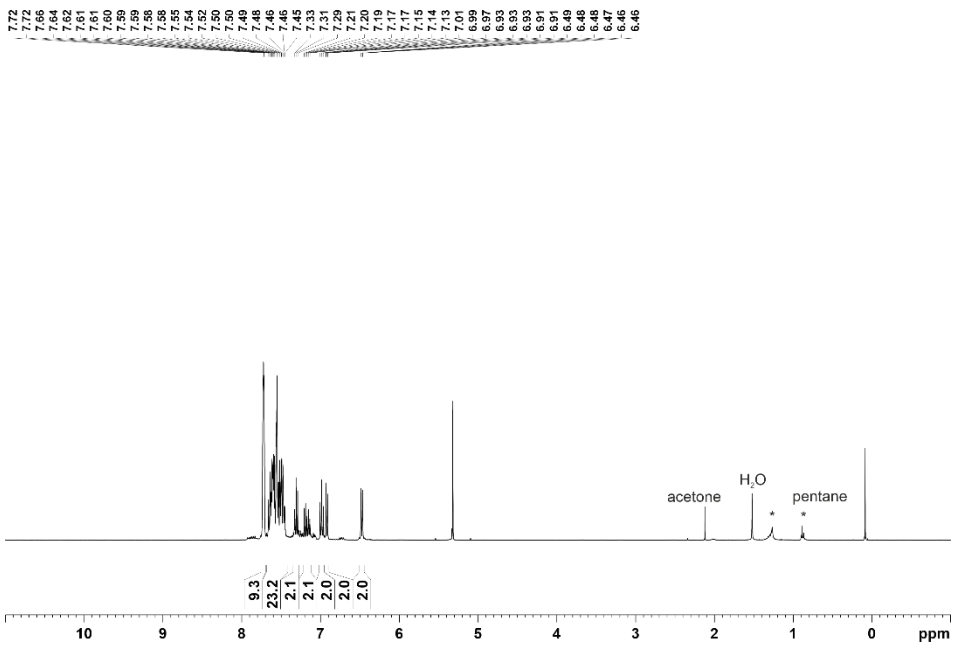

Figure 2.33. ^{1}H NMR (400 MHz, CD_2Cl_2) for complex **C2**.

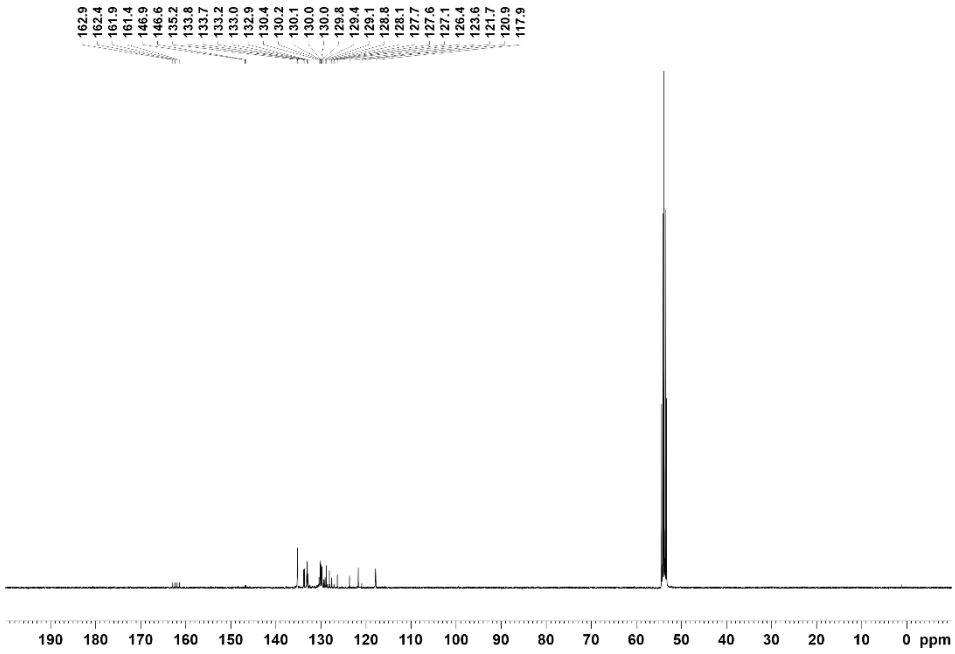

Figure 2.34. $^{13}C\{^{1}H\}$ NMR (101 MHz, CD_2Cl_2) for complex **C2**.

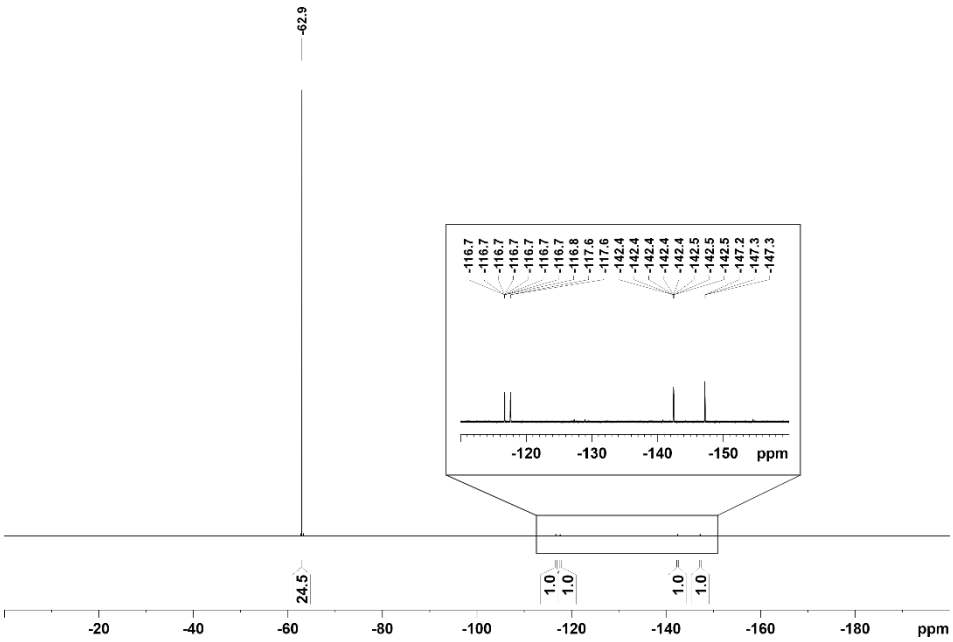

Figure 2.35. $^{19}F\{^{1}H\}$ NMR (471 MHz, CD_2Cl_2) for complex **C2**.

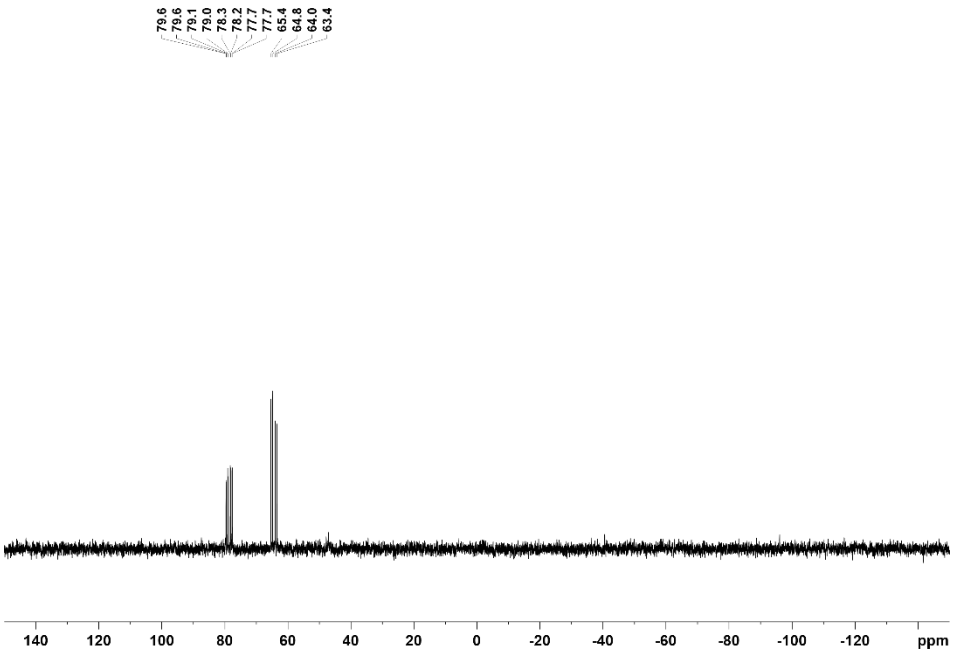

Figure 2.36. $^{31}P\{^{1}H\}$ NMR (202 MHz, CD_2Cl_2) for complex **C2**.

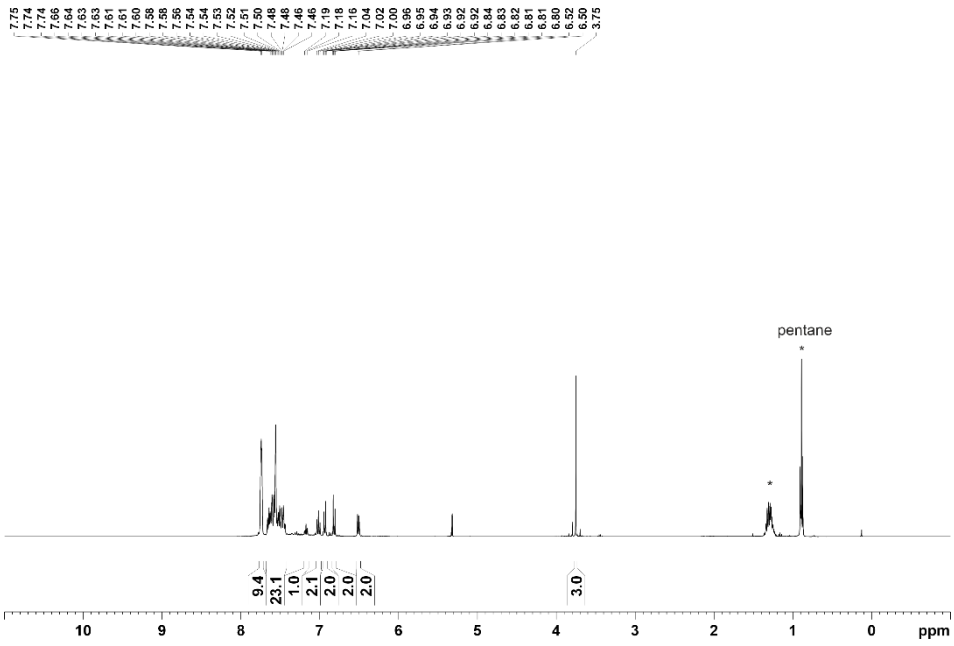

Figure 2.37. ^{1}H NMR (400 MHz, CD_2Cl_2) for complex **C3**.

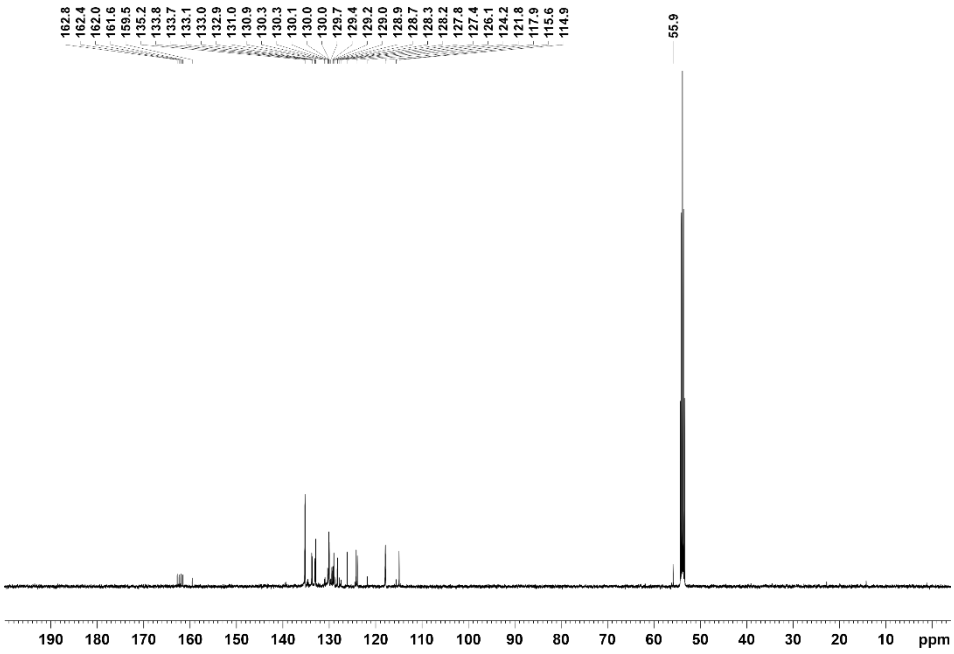

Figure 2.38. $^{13}C\{^{1}H\}$ NMR (126 MHz, CD_2Cl_2) for complex **C3**.

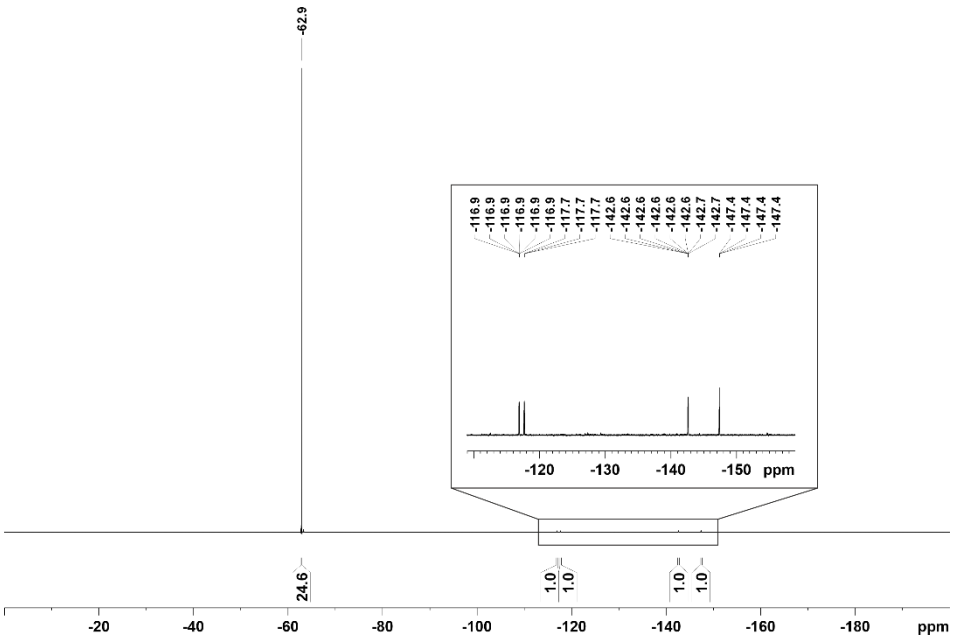

Figure 2.39. $^{19}F\{^{1}H\}$ NMR (471 MHz, CD_2Cl_2) for complex **C3**.

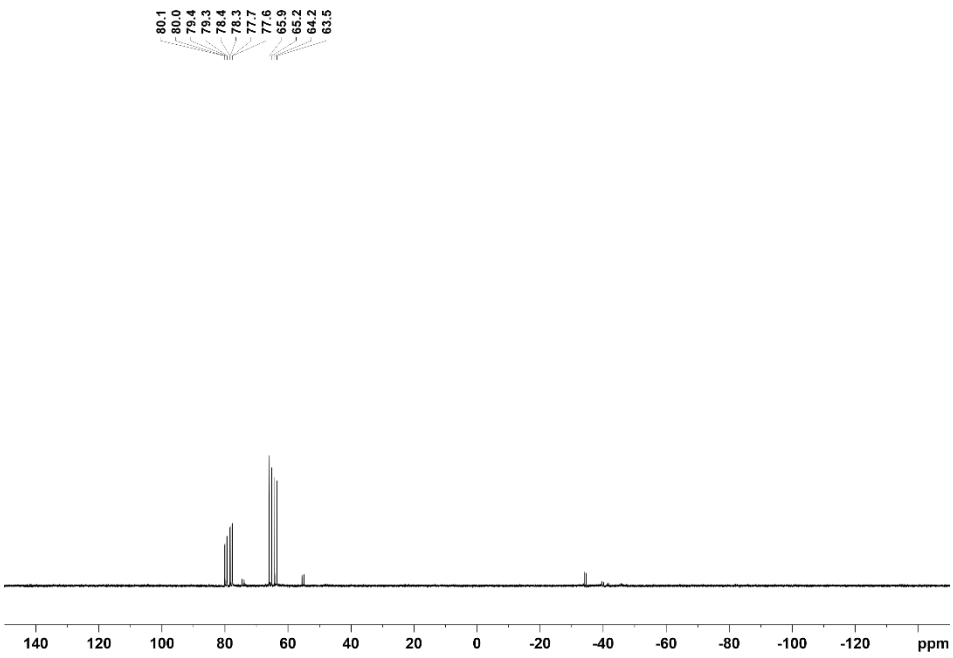

Figure 2.40. $^{31}P\{^{1}H\}$ NMR (162 MHz, CD_2Cl_2) for complex **C3**.

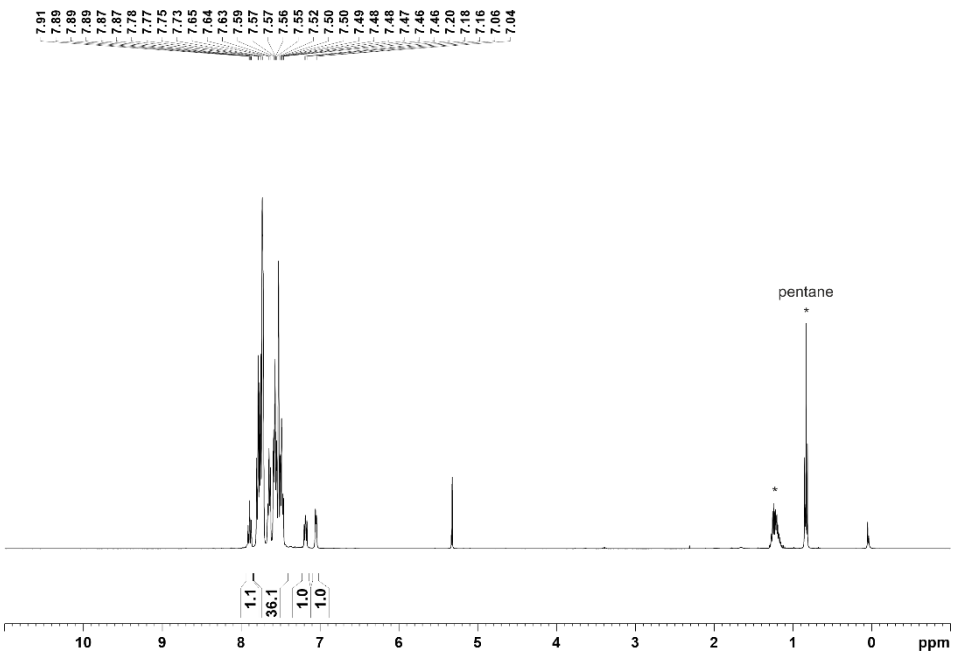

Figure 2.41. ^{1}H NMR (400 MHz, CD_2Cl_2) for complex **C4**.

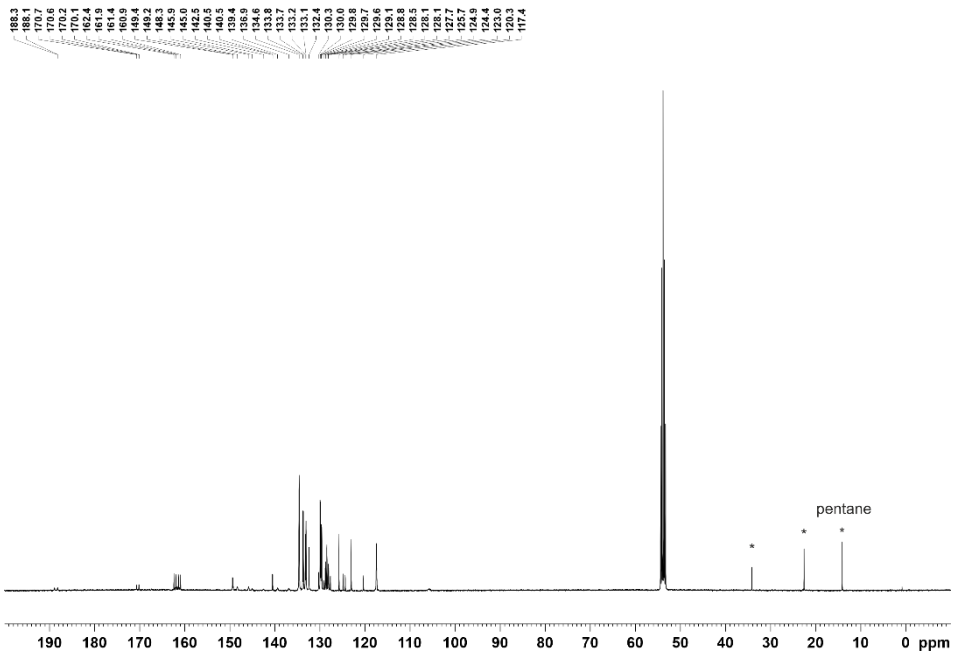

Figure 2.42. $^{13}C\{^{1}H\}$ NMR (101 MHz, CD_2Cl_2) for complex **C4**.

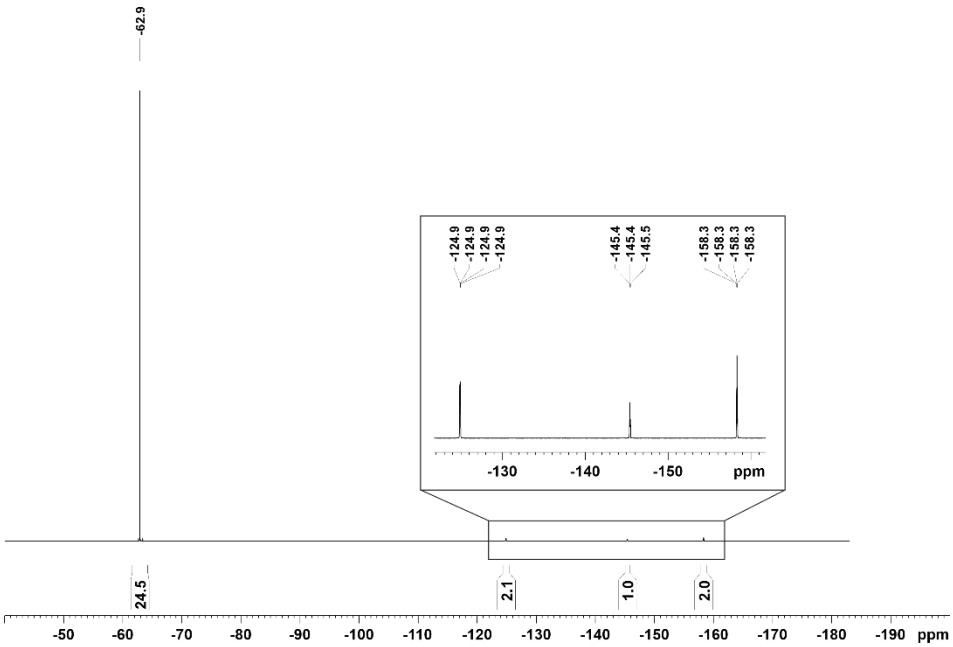

Figure 2.43. $^{19}F\{^{1}H\}$ NMR (376 MHz, CD_2Cl_2) for complex **C4**.

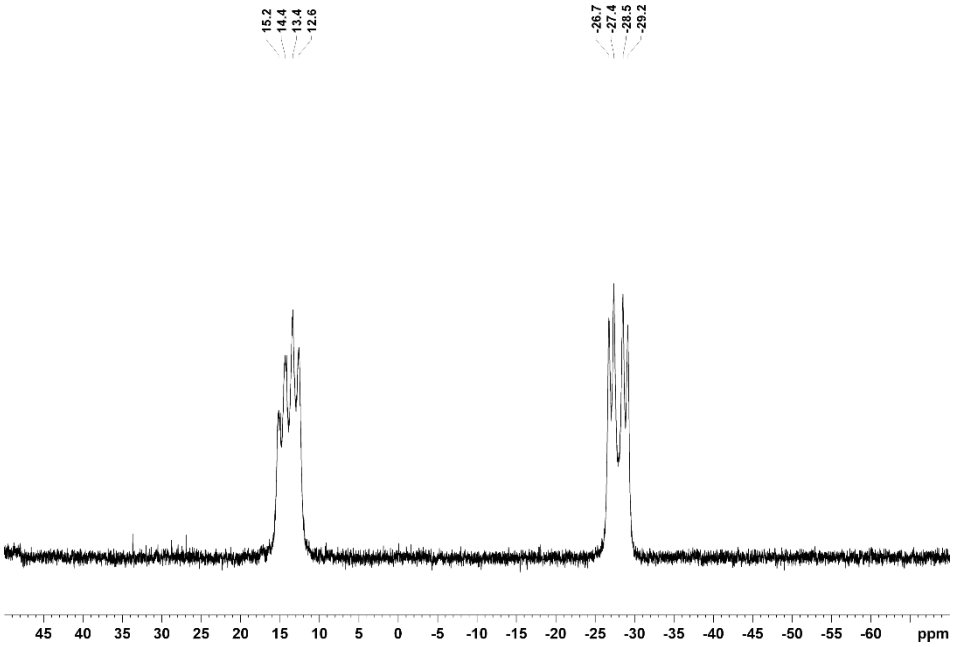

Figure 2.44. $^{31}P\{^{1}H\}$ NMR (162 MHz, CD_2Cl_2) for complex **C4**.

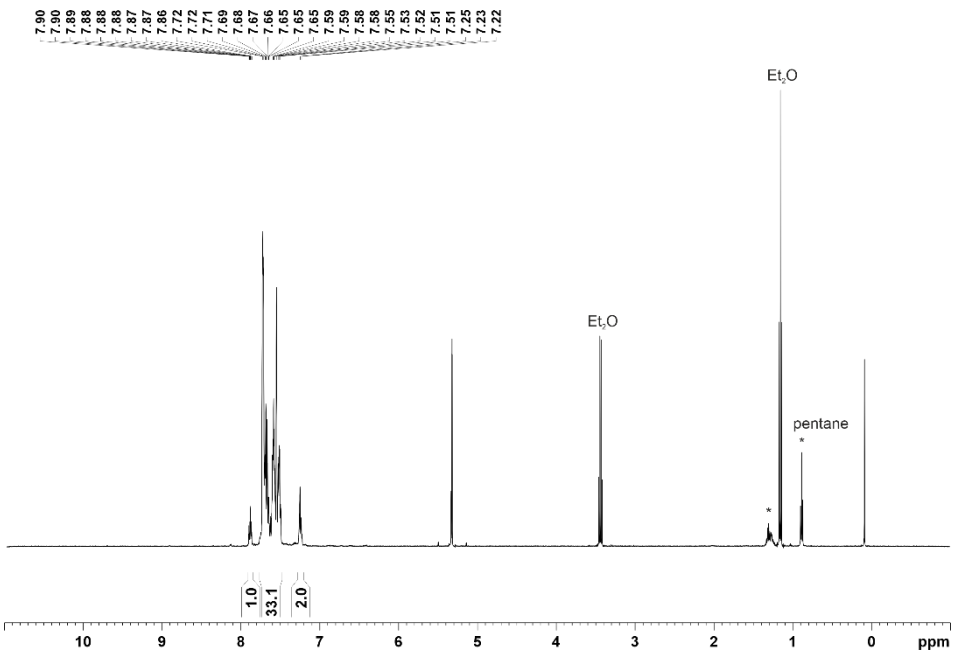

Figure 2.45. ^{1}H NMR (500 MHz, CD_2Cl_2) for complex **C5**.

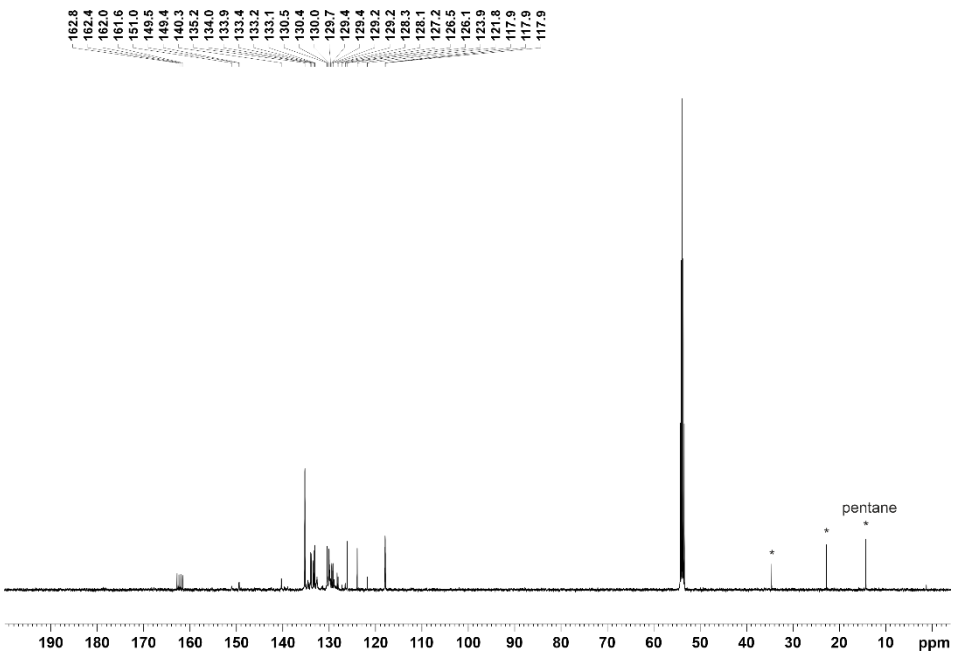

Figure 2.46. $^{13}C\{^{1}H\}$ NMR (126 MHz, CD_2Cl_2) for complex **C5**.

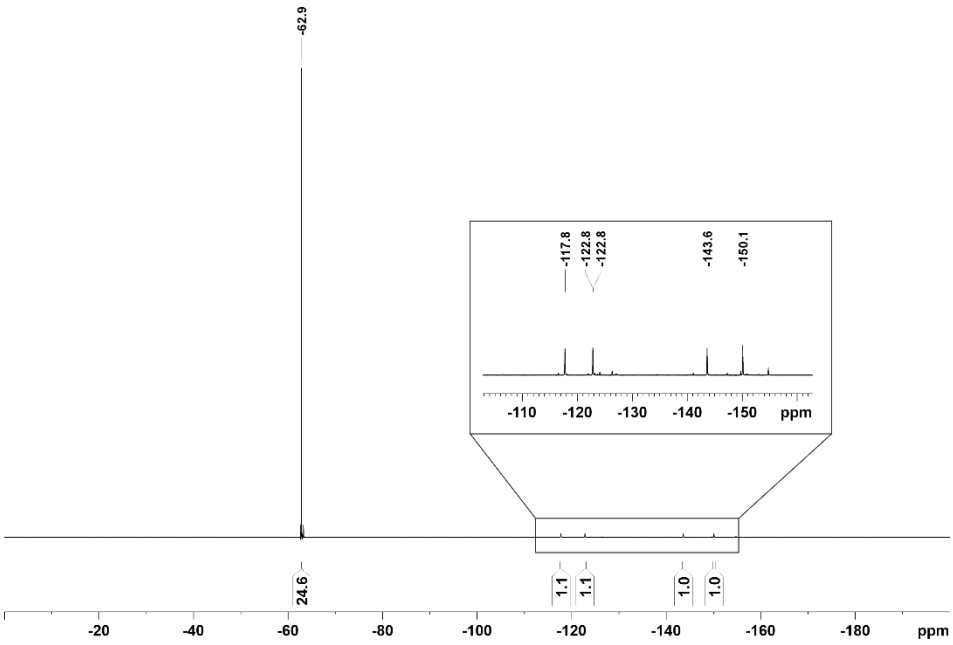

Figure 2.47. $^{19}F\{^{1}H\}$ NMR (471 MHz, CD_2Cl_2) for complex **C5**.

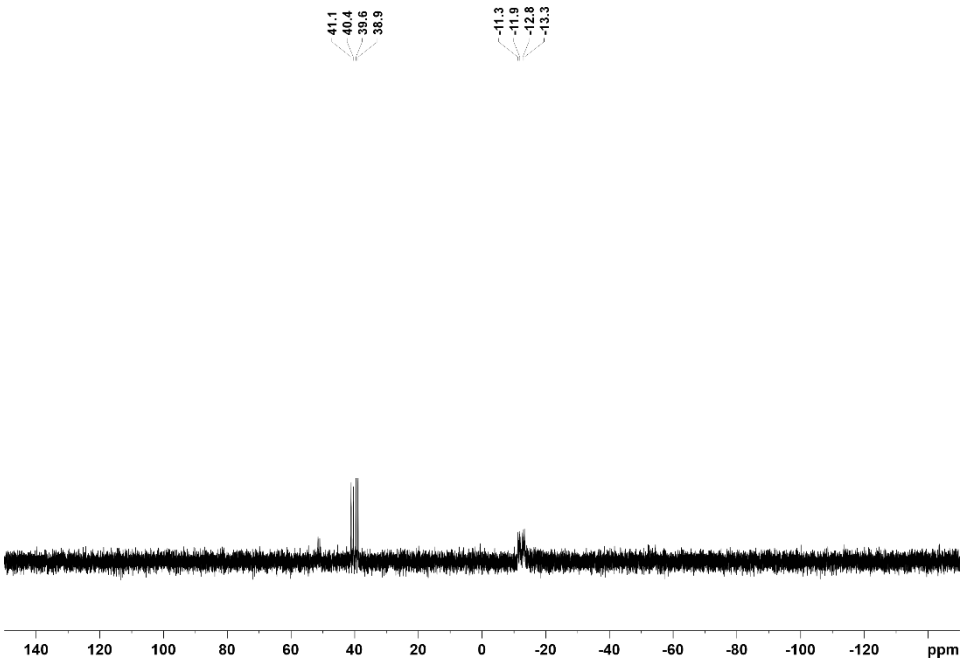

Figure 2.48. $^{31}P\{^{1}H\}$ NMR (162 MHz, CD_2Cl_2) for complex **C5**.

CHAPTER III:

COUNTERION VARIATION: A USEFUL LEVER FOR MAXIMIZING THE REGIOSELECTIVITY IN THE HYDROBORATION OF TERMINAL ALKYNES

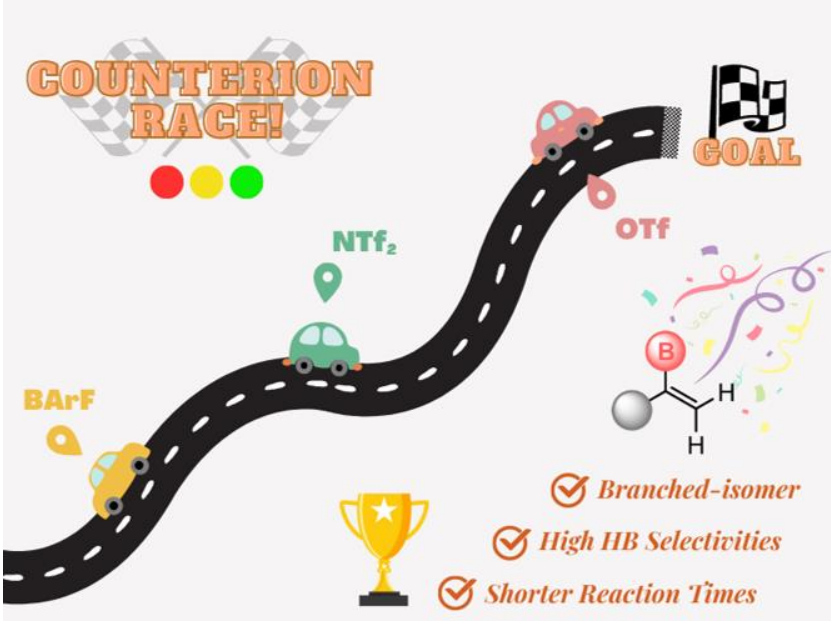

3.1 INTRODUCTION

Transition-metal catalysis is an important and efficient approach for the synthesis of functional molecules.[5,113] The critical step in most transition metal-based catalysts is the assembly of a supramolecular system around the metal center. This supramolecular system involves the substrate(s), the metal center, molecules and/or ions that are attached directly to the metal (*i.e.,* the first coordination sphere) and other chemical entities that are generally attached to the first coordination sphere through non-covalent interactions (*i.e.,* the commonly named second coordination sphere). The second coordination sphere consists of neutral molecules and/or also ions for compensating charges and achieving a neutral supramolecular system.

In this supramolecular system, the metal center provides a low-energy reaction pathway that enables catalysis, whereas the first and second coordination spheres may play different roles, such as the stabilization of the supramolecular complex or electronic state of the metal, the orientation of the substrate(s) to enhance the reactivity and/or selectivity, etc.

The most common approach for the modification and/or optimization of the performance of a catalyst relies on ligand design and structural variation, mainly in the first coordination sphere.[114] Ligand design generally incorporates several independent modules (or molecular fragments) orchestrated around a skeleton. These modules are designed such that they can influence the catalytic site by modifying the steric and electronic properties of the metal center. Thus, the discovery of catalysts

[113] For example, see: (a) Tsuji, J. *Transition Metal Reagents and Catalysts: Innovations in Organic Synthesis*. Wiley, 2000; (b) Crawley, M. L.; Trost, B. M. *Applications of Transition Metal Catalysis in Drug Discovery and Development: An Industrial Perspective*. John Wiley & Sons, Inc., 2012.

[114] For example, see: (a) van Leeuwen, P. W. N. M. *Homogeneous Catalysis: Understanding the Art*. Springer, 2004; (b) Lundgren, R. J.; Stradiotto, M. *Key Concepts in Ligand Design: An Introduction*. Wiley: West Sussex, England, 2016; (c) Buchwald, S. L.; Milstein, D. *Ligand Design in Metal Chemistry: Reactivity and Catalysis*. John Wiley & Sons, 2016.

with improved efficiency is achieved by structural variation of the ligand. Alternatively, catalyst discovery for a variety of organic transformations has been achieved through supramolecular regulation strategies,[6,8,9,,115] *e.g.*, by using cationic species[9,115b,116] or other external molecules functioning as regulation agents,[117] which are placed in the second coordination sphere.[118]

An alternative way to influence the activity of catalysts based on positively charged metal centers consists of the electronic and structural modification of the counterion. Even though important progress has been made during the last years in gold(I) chemistry,[119] this strategy remains underexplored in terms of other metals or other chemical transformations that are not catalyzed by gold.[120] It should be noted that the maximization

[115] For some reviews, see: (a) Raynal, M.; Ballester, P.; Vidal-Ferran, A.; van Leeuwen, P. W. N. M. *Chem. Soc. Rev.* **2014**, *43*, 1734-1787; (b) Vaquero, M.; Rovira, L.; Vidal-Ferran, A. *Chem. Commun.* **2016**, *52*, 11038-11051.

[116] For some selected examples, see: (a) Ouyang, G.-H.; He, Y.-M.; Li, Y.; Xiang, J.-F.; Fan, Q.-H. *Angew. Chem. Int. Ed.* **2015**, *54*, 4334-4337; (b) Rovira, L.; Vaquero, M.; Vidal-Ferran, A. *J. Org. Chem.* **2015**, *80*, 10397-10403; (c) Martínez-Carrión, A.; Howlett, M. G.; Alamillo-Ferrer, C.; Clayton, A. D.; Bourne, R. A.; Codina, A.; Vidal-Ferran, A.; Adams, R. W.; Burés, J. *Angew. Chem.* **2019**, *131*, 10295-10299; (d) Iniesta, E.; Vidal-Ferran, A. *Chem. Commun.* **2020**, *56*, 6364-6367; (e) Carreras, L.; Franconetti, A.; Grabulosa, A.; Frontera, A.; Vidal-Ferran, A. *Org. Chem. Front.* **2020**, *7*, 1626-1634; (f) Luo, Y.; Ouyang, G.; Tang, Y.; He, Y.-M.; Fan, Q.-H. *J. Org. Chem.* **2020**, *85*, 8176-8184.

[117] For example, see: (a) Dydio, P.; Rubay, C.; Gadzikwa, T.; Lutz, M.; Reek, J. N. H. *J. Am. Chem. Soc.* **2011**, *133*, 17176-17179; (b) van Leeuwen, P. W. N. M.; Rivillo, D.; Raynal, M.; Freixa, Z. *J. Am. Chem. Soc.* **2011**, *133*, 18562-18565.

[118] Other strategies to modify the second coordination sphere of a catalytic metal center encompass the introduction of specific motifs (*e.g.*, redox groups, Brønsted or Lewis acidic or basic substituents, crown ether groups or negatively- or positively-charged substituents) in the ligand periphery. For selected references, see: (a) Zak, I. L.; Gadekar, S. C.; Milo, A. *Synlett* **2020**, *32*, 329-336; (b) Drover, M. W. *Chem. Soc. Rev.* **2022**, *51*, 1861-1880; (c) Zurakowski, J. A.; Austen, B. J. H.; Drover, M. W. *Trends in Chemistry* **2022**, *4*, 331-346.

[119] For recent reviews, see: (a) Jia, M.; Bandini, M. *ACS Catal.* **2015**, *5*, 1638-1652; (b) Lu, Z.; Li, T.; Mudshinge, S. R.; Xu, B.; Hammond, G. B. *Chem. Rev.* **2021**, *121*, 8452-8477. For recent examples on specific transformations, see: (c) Bandini, M.; Bottoni, A.; Chiarucci, M.; Cera, G.; Miscione, G. P. *J. Am. Chem. Soc.* **2012**, *134*, 20690-20700; (d) Ciancaleoni, G.; Belpassi, L.; Zuccaccia, D.; Tarantelli, F.; Belanzoni, P. *ACS Catal.* **2015**, *5*, 803-814; (e) Franchino, A.; Martí, À.; Echavarren, A. M. *J. Am. Chem. Soc.* **2022**, *144*, 3497-3509.

[120] For selected recent reviews on the influence of counterions in catalysis, see: (a) Li, Y.; Cokoja, M.; Kühn, F. E. *Coord. Chem. Rev.* **2011**, *255*, 1541-1557; (b) Wang, Y.-M.; Lackner, A. D.; Toste, F. D. *Acc. Chem. Res.* **2014**, *47*, 889-901; (c) Riddlestone, I. M.; Kraft, A.; Schaefer, J.; Krossing, I. *Angew. Chem. Int. Ed.* **2018**, *57*, 13982-14024; (d) Alvarez, S. *Chem. – Eur. J.* **2020**, *26*, 4350-4377; (e) Uraguchi, D.; Kimura, Y.; Ueoka, F.; Ooi, T. *J. Am. Chem. Soc.* **2020**, *142*, 19462-19467.

of the regioselectivity in hydroboration chemistry by structural variation of the counterion has not yet been studied.

In 2019, Dong and coworkers[121] reported the rhodium(I)-catalyzed hydrothiolation of 1,3-dienes **62** to afford allylic **64** or homoallylic sulfides **65** with high regioselectivities, which were successfully controlled by the choice of the counterion associated with the cationic rhodium(I) center (Scheme 3.1). Mechanistic studies supported that non-coordinating counterions (*i.e.*, SbF_6^-) favored the η^4-diene coordination of the 1,3-diene substrates **62** to the rhodium center, giving rise to allylic sulfides **64** as products. On the other hand, coordinating counterions (*i.e.*, Cl^-) led to the formation of neutral rhodium intermediates with a η^2-diene coordination mode, which led to homoallylic sulfides **65**.

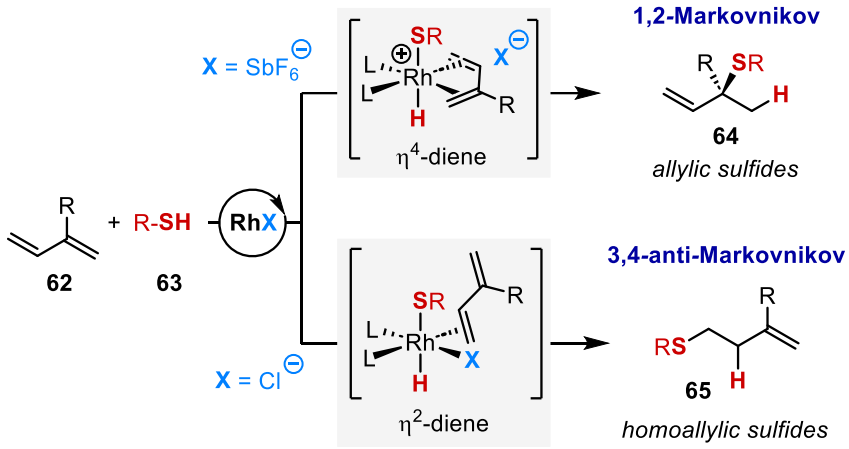

Scheme 3.1. Counterion controlled regiodivergent hydrothiolations.

Rh-catalyzed hydroboration reactions provide a versatile synthetic pathway for the formation of structurally diverse organoboron compounds.[122] These boron derivatives are useful synthetic intermediates for a large number of processes, with the Rh-mediated hydroboration of

[121] Yang, X.-H.; Davison, R. T.; Nie, S.-Z.; Cruz, F. A.; McGinnis, T. M.; Dong, V. M. *J. Am. Chem. Soc.* **2019**, *141*, 3006-3013.
[122] Brown, J. M. Rhodium-Catalyzed Hydroborations and Related Reactions. In *Modern Rhodium-Catalyzed Organic Reactions* 2005; pp 33-53.

terminal alkynes[123] providing straightforward access to the (*E*)-alkenylboronates through an anti-Markovnikov addition.[124] Some Rh-based methods have been developed to selectively form the (*Z*)-isomer.[125] Interestingly, examples of the catalytic non-conventional Markovnikov addition of boranes to alkynes leading to the branched isomers (abbreviated as (*br*)-isomers in the following discussion) are scarce and mainly involve copper[126] or palladium[127] catalysts. Interestingly, non-terminal boron-substituted unsaturated derivatives can be regarded as highly valuable synthetic intermediates as they are prochiral and can be used to broaden the structural diversity of molecules.[123]

An interesting example in which cobalt-catalyzed non-conventional Markovnikov hydroboration of terminal aryl alkynes **66** has been recently published by Lu *et al.*[128] In this work, branched alkenyl boronates **67** were efficiently afforded with good atom economy and functional group tolerance *via* Markovnikov-type alkyne insertion into cobalt-hydride intermediates (Scheme 3.2). The authors observed that unsymmetrical κ^3*N,N,N*-OPQC tridentate ligand **68** favored the non-conventional Markovnikov reaction pathway, giving rise to excellent branched/linear *br*/*l* ratios (up to 94/6 *br*/*l*).

[123] For application of organoboron compounds in synthesis, see: (a) Miyaura, N.; Yamamoto, Y. Boron. In *Comprehensive Organometallic Chemistry III*, 2007; pp 145-244; (b) Fernández, E.; Whiting, A. *Synthesis and Application of Organoboron Compounds*. Vol. 49; Springer, 2015; (c) Fyfe, J. W. B.; Watson, A. J. B. *Chem* **2017**, *3*, 31-55; (d) Carreras, J.; Caballero, A.; Perez, P. J. *Chem. – Asian J.* **2019**, *14*, 329-343.

[124] For example, see: (a) Evans, D. A.; Fu, G. C.; Anderson, B. A. *J. Am. Chem. Soc.* **1992**, *114*, 6679-6685; (b) Trost, B. M.; Ball, Z. T. *Synthesis* **2005**, 853-887; (c) Barbeyron, R.; Benedetti, E.; Cossy, J.; Vasseur, J.-J.; Arseniyadis, S.; Smietana, M. *Tetrahedron* **2014**, *70*, 8431-8452; (d) Wang, K.; Bates, R. W. *Synthesis* **2017**, *49*, 2749-2752.

[125] (a) Ohmura, T.; Yamamoto, Y.; Miyaura, N. *J. Am. Chem. Soc.* **2000**, *122*, 4990-4991; (b) Cid, J.; Carbó, J. J.; Fernández, E. *Chem. – Eur. J.* **2012**, *18*, 1512-1521.

[126] For some selected examples, see: (a) Takahashi, K.; Ishiyama, T.; Miyaura, N. *J. Organomet. Chem.* **2001**, *625*, 47-53; (b) Jang, H.; Zhugralin, A. R.; Lee, Y.; Hoveyda, A. H. *J. Am. Chem. Soc.* **2011**, *133*, 7859-7871; (c) Yoshida, H.; Takemoto, Y.; Takaki, K. *Chem. Commun.* **2014**, *50*, 8299-8302; (d) Tsushima, T.; Tanaka, H.; Nakanishi, K.; Nakamoto, M.; Yoshida, H. *ACS Catal.* **2021**, *11*, 14381-14387.

[127] Ojha, D. P.; Prabhu, K. R. *Org. Lett.* **2016**, *18*, 432-435.

[128] Chen, J.; Shen, X.; Lu, Z. *Angew. Chem. Int. Ed.* **2021**, *60*, 690-694.

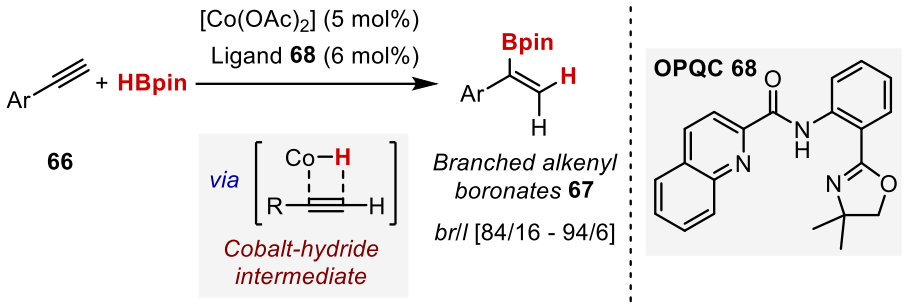

Scheme 3.2. Cobalt-catalyzed non-conventional Markovnikov hydroboration of terminal alkynes.

With the aim of complementing the existing catalytic tools, our group recently reported a rhodium(I)-based catalyst derived from halogen bond-assembled diphosphanes for the hydroboration of terminal alkynes (Scheme 3.3).[70]

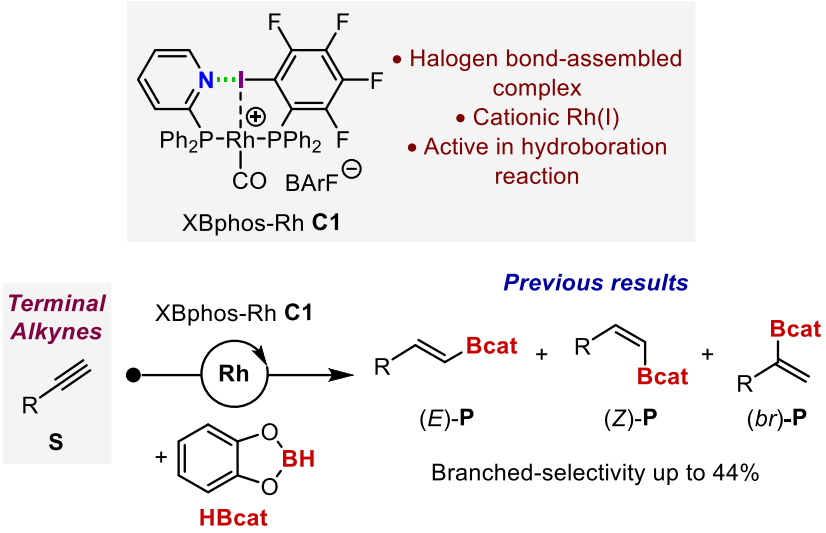

Scheme 3.3. Halogen bond-assembled rhodium(I) complex as active catalyst in hydroboration reaction.

XBphos-Rh **C1** complex gave enhanced ratios of the branched alkenyl boronic acid derivatives (up to 44% of branched selectivity) and provided the highest reported selectivity for the Markovnikov-type products in terms of rhodium-catalyzed hydroboration of terminal alkyl alkynes.

Aiming to maximize the regioselectivity towards the branched hydroboration products of terminal alkynes, we directed our efforts towards: (*i*) synthesizing an array of halogen-bonded analogues of XBphos-Rh **C1** incorporating electron and structurally diverse counterions with different coordination abilities, (*ii*) exploring the potential of structural variation of the counterion as a tool to optimize the activity and selectivity towards the branched products, and (*iii*) demonstrating the synthetic utility of our approach.

3.2 RESULTS AND DISSCUSION

Synthesis and characterization of the XBphos-Rh-X C1·X *complexes*

The initial design reported by our group for XBphos-Rh **C1** only considered the tetrakis[3,5-bis(trifluoromethyl)phenyl]borate anion (*i.e.* [B(3,5-$(CF_3)_2C_6H_3)_4$]; hereinafter referred to as BArF).[70] We envisaged that a change in the coordination properties of the counterion in XBphos-Rh complexes could lead to a maximization of the selectivity of the reaction.[120] We thus prepared XBphos-Rh **C1** analogues incorporating trifluoromethanesulfonate (*i.e.,* OTf), bis(trifluoromethane)sulfonimide (*i.e.,* NTf_2), tetrafluoroborate (*i.e.,* BF_4) and hexafluorophosphate (*i.e.,* PF_6) as counterion following a synthetic procedure adapted from that reported by our group for XBphos-Rh **C1** (Scheme 3.4).

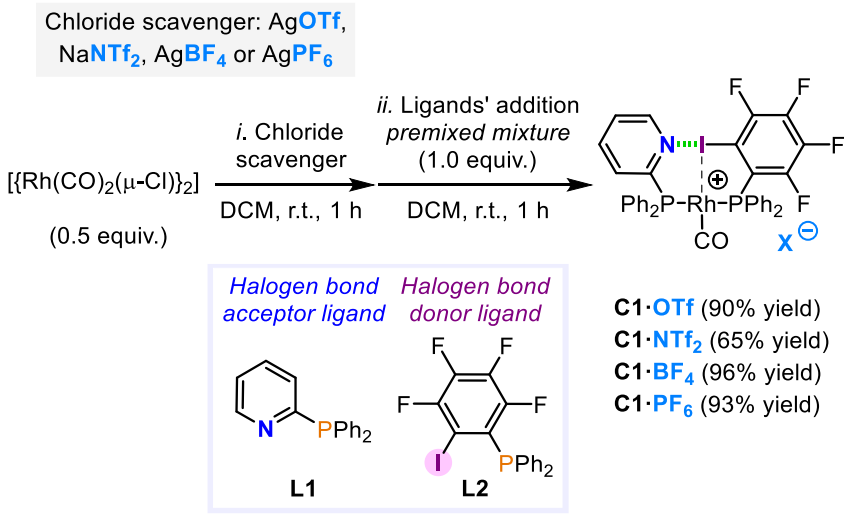

Scheme 3.4. Synthesis of complexes **C1·X**.

We hypothesized that the use of [{$Rh(CO)_2(\mu\text{-}Cl)\}_2$] precursor together with a silver or sodium-based chloride scavenger incorporating the desired counterion X would render putative [$Rh(CO)_2$]X rhodium intermediates, whose isolation was not attempted. We then envisioned that rhodium

intermediates $[Rh(CO)_2]X$ would be transformed into the desired **C1·X** complexes by reaction with an equimolar mixture of complementary phosphane ligands **L1** and **L2**. The target complexes were isolated in good yields using this strategy. The chloride scavenger that was used in each case, as well as the isolated yield for each halogen-bonded complex, are indicated in Scheme 3.4.

NMR spectroscopic and MS spectrometry data were consistent with the proposed structures for the halogen bond-assembled **C1·X** complexes. Interestingly, $^{31}P\{^1H\}$ NMR spectroscopy showed phosphorus-phosphorus coupling constants through two bonds of *ca*. 275.8 Hz (standard deviation $\sigma = 0.5$), which were only consistent with a *trans*-coordination mode of the halogen-bonded diphosphane to the rhodium center. This structural feature was also observed in the already reported XBphos-Rh **C1·BArF** complex.[70]

Crystals suitable for X-Ray analysis were obtained for **C1·NTf₂** and **C1·OTf** and this technique unequivocally established the proposed structure of the halogen-bonded complexes. X-Ray analysis revealed that the nitrogen and iodine atoms are aligned with N···I–C bond angles close to 180 degrees. X-ray analysis also demonstrated a tridentate κ^3*I,P,P'*-tridentate coordination of the halogen-bonded ligands in the square planar XBphos-Rh analogues (Figure 3.1; the already published structure of XBphos-Rh **C1·BArF** is also included in this figure to aid comparison).

Selected crystallographic data for **C1·NTf₂**, **C1·OTf** and **C1·BArF** are summarized in Table 3.1. It is interesting to note that the N···I distances and N···I–C bond angles were consistent with those reported in the literature (see Table 3.1),[70,76] with no significant changes in these parameters being observed as a function of the coordination ability of the counterion fragment (expected coordination ability:[120c] OTf > NTf_2 > BArF).

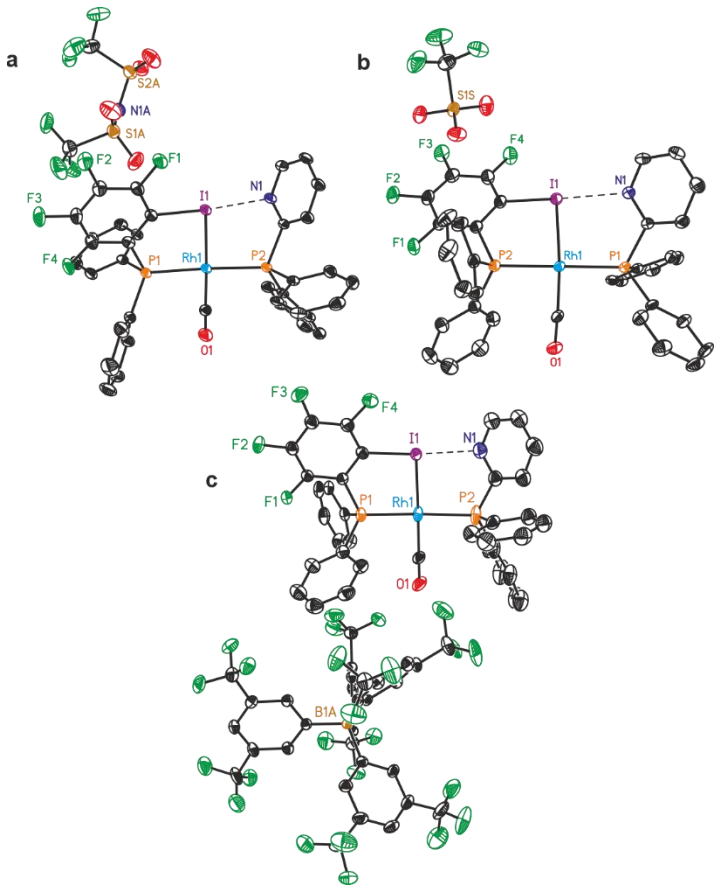

Figure 3.1. Crystal structures of **C1·NTf$_2$** (a), **C1·OTf** (b) and **C1·BArF** (c). Hydrogen atoms have been omitted for the sake of clarity. Color scheme: C: black, O: red, N: dark blue, F: green, S: light brown, P: orange, Rh: blue, I: purple, B: light brown. Atomic displacement ellipsoids are drawn at a 50% probability.

The relative coordination ability of the counterions is nicely demonstrated by the X-Ray data shown in Table 3.1, with decreasing distances between the nominally charged atom of the counterion and the rhodium center as the coordination ability of X increases (OTf > NTf_2 > BArF). A trend in the Rh–I distance was observed depending on the coordination ability, with the longest distance for the strongest coordinating counterion having been measured (Table 3.1). The observed changes in the Rh–I distances as a function of the coordination ability of the counterion seem to point towards counterion effects between the

positively charged rhodium(I) center and its negatively charged counterpart, although the counterion is placed in all cases in the second coordination sphere of the metal.

Table 3.1. Selected X-Ray parameters for **C1·X** complexes.

	C1·BArF[a]	**C1·NTf$_2$**	**C1·OTf**
N···I (Å)	2.757(8)	2.807(2)	2.756(3)
N···X–C (º)	169.4(5)	171.50(9)	172.0(1)
Rh–Y (Å)[b]	8.899(7)	7.184(3)	5.936(3)
Rh–I (Å)	2.5535(7)	2.6046(3)	2.6216(5)

[a] **C1·BArF** values were obtained from X-Ray structure reported by our group. Reference 70. [b] In the case of **C1·BArF**, Y corresponds to the B atom, for **C1·NTf$_2$**, Y corresponds to the N atom; and for **C1·OTf**, Y corresponds to the O atom.

A similar effect was observed in the position of the CO stretching band in IR spectroscopy (Table 3.2), whose wavenumber decreased as the coordination ability of the counterion increased (OTf > NTf_2 > BF_4, PF_6, BArF). A decrease in the wavenumber of the CO band suggests a weakening of the C–O triple bond and points to a higher electron density in the metal center (Table 3.2) due to a stronger interaction between the cationic rhodium-containing moiety and the OTf counterion than those between rhodium and the other counterions.

Table 3.2. IR spectroscopic data for halogen-bonded complexes **C1·X**. [a]

X	**OTf**	**NTf$_2$**	**BF$_4$**	**PF$_6$**	**BArF**
$\bar{\upsilon}_{CO}$ (cm^{-1})	1977	2003	2028	2029	2036

[a] DCM solution (ranging from 6 to 10 mM).

It is well known that attractive interactions can be formed between anions and electron deficient arenes (*i.e.*, anion-π interactions).[129] In these aryl derivatives, the electron-withdrawing substituents induce a positive potential in the center of the aromatic ring, which brings the anion perpendicularly close to the plane of the electron deficient ring. As observed in Figure 3.1, the OTf and NTf_2 anions are located closer to the electron deficient perfluorinated aryl substituent of ligand **L2** (shortest O···C(C_6F_5) distances of 2.944(5) Å for OTf and 3.130(5) Å for NTf_2) than the BArF anion. This structural feature is an agreement with reported data in the literature.[129] Thus, the formation of these stable anion-π complexes may transform the phosphino group **L2** into a stronger σ-donating ligand with an increase in the electron density in the rhodium center when this anion-π interaction is present.[130]

Moreover, the existence of anion-π interactions has been analyzed by using a combination of the Quantum Theory of Atoms in Molecules (*i.e.*, QTAIM)[131] and Non-covalent Interaction Plot (*i.e.*, NCIPlot),[132] which constitute useful methods to describe interactions in real space and to disclose their attractive/repulsive nature (studies performed in collaboration with Prof. Frontera, *Universitat de les Illes Balears*). It can be observed that in the case of OTf (Figure 3.2a), three Bond Critical Points (*i.e.*, BCPs, represented as red spheres)[133] and bond paths (orange lines) connect the three oxygen atoms of the OTf anion to the phosphane ligand.

[129] (a) Quiñonero, D.; Garau, C.; Rotger, C.; Frontera, A.; Ballester, P.; Costa, A.; Deyà, P. M. *Angew. Chem.* **2002**, *114*, 3539-3542; (b) Schottel, B. L.; Chifotides, H. T.; Dunbar, K. R. *Chem. Soc. Rev.* **2008**, *37*, 68-83; (c) Kan, X.; Liu, H.; Pan, Q.; Li, Z.; Zhao, Y. *Chin. Chem. Lett.* **2018**, *29*, 261-266; (d) Rather, I. A.; Wagay, S. A.; Ali, R. *Coord. Chem. Rev.* **2020**, *415*, 213327.

[130] Even though no X-Ray structures could be measured for the BF4- and PF6-containing complexes, we assumed that anion-π interac-tions should be disfavored in them taking into account the close wavenumbers for the CO vibration in both complexes with that for the BArF analogue.

[131] Matta, C. F.; Boyd, R. J. An Introduction to the Quantum Theory of Atoms in Molecules. In *The Quantum Theory of Atoms in Molecules*, 2007; pp 1-34.

[132] Contreras-García, J.; Johnson, E. R.; Keinan, S.; Chaudret, R.; Piquemal, J.-P.; Beratan, D. N.; Yang, W. *J. Chem. Theory Comput.* **2011**, *7*, 625-632.

[133] Wick, C. R.; Clark, T. *J. Mol. Model.* **2018**, *24*, 1-9.

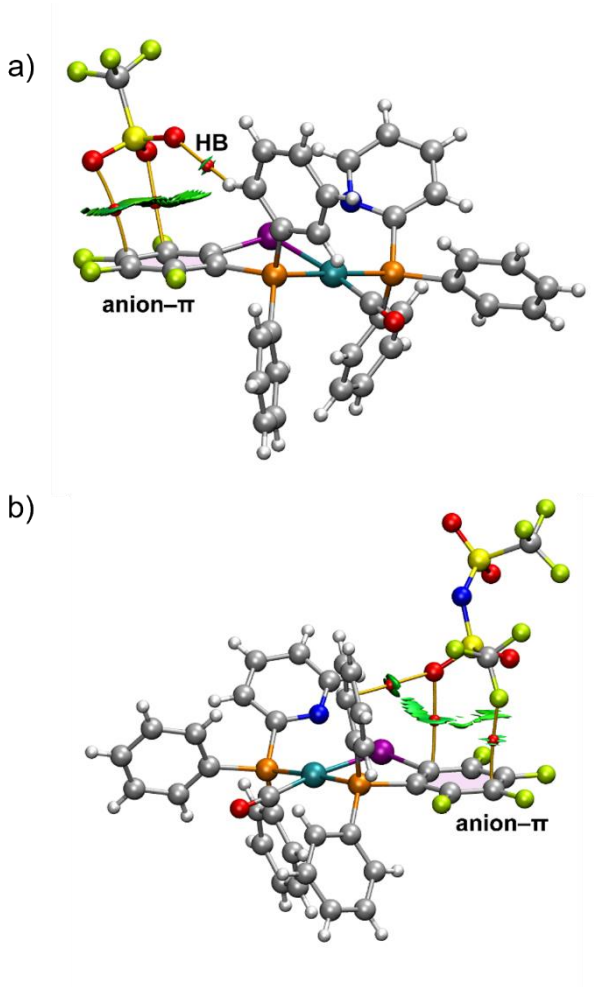

Figure 3.2. QTAIM and NCIplot analysis of **C1·OTf** (a) and **C1·NTf$_2$** (b) compounds. Only BCPs and intermolecular interactions are represented at the RI-PBE0-D4/def2-TZVP level of theory.

Two BCPs connect the OTf anion to two carbon atoms of the fluorinated ring and one BCP connects the oxygen atom to one hydrogen atom of the phenyl ring, thus confirming the existence of the anion–π interactions and revealing the formation of an ancillary C–H···O hydrogen bond. The anion–π interaction is also characterized by an extended green Reduced Density Gradient (*i.e.,* RDG) isosurface[134] (*i.e.*, that embraces most of the

[134] Johnson, E. R.; Keinan, S.; Mori-Sánchez, P.; Contreras-García, J.; Cohen, A. J.; Yang, W. *J. Am. Chem. Soc.* **2010**, *132*, 6498-6506.

aromatic ring and the sulfate group. In the case of the NTf_2 counterion (Figure 3.2b), one oxygen atom and one fluorine atom of the NTf_2 anion are connected to the aromatic ring by two BCPs and bond paths. Moreover, an extra BCP connects the oxygen atom to one carbon atom of the phenyl ring. A RDG isosurface is also located between the NTf_2 anion and the fluorinated ring that is less extended than that observed for the OTf counterion, pointing to a weaker anion–π interaction in the case of NTf_2. This fact was also confirmed by the calculated interaction energies, which are also indicated in Figure 3.2. Interestingly, the interaction with the OTf anion was found to be 7.0 kcal/mol more favorable than with the NTf_2 counterpart, confirming that the anion–π interaction with OTf anion is stronger.

Catalytic hydroboration of terminal alkynes

With our halogen bond-assembled complexes **C1·X** in hand, we set about evaluating their activity and selectivity in the hydroboration (HB) of oct-1-yne (**S1**), employing catecholborane (**HBcat**) as the hydroboration reagent (Table 3.3).

Complexes containing OTf, NTf_2 and BArF as counterions led to the highest conversions and hydroboration selectivities (HB sel. > 80%; entries 1-3, Table 3.3). It is interesting to note that, despite the bonding characteristics in the BArF complex being similar to those in the BF_4- and PF_6-derivatives (as indicated by the wavenumber of the CO bands, see Table 3.2), the BArF-containing complex led to much better results in terms of conversion and HB selectivity (entry 3, Table 3.3) than the BF_4 and PF_6 derivatives did. We reasoned that the robustness of the BArF

counterion and the ability to form highly stable ion-pairs[120c,135] could stay at the origin of these results.

Table 3.3. Hydroboration of oct-1-yne **S1** using catecholborane **HBcat**.[a]

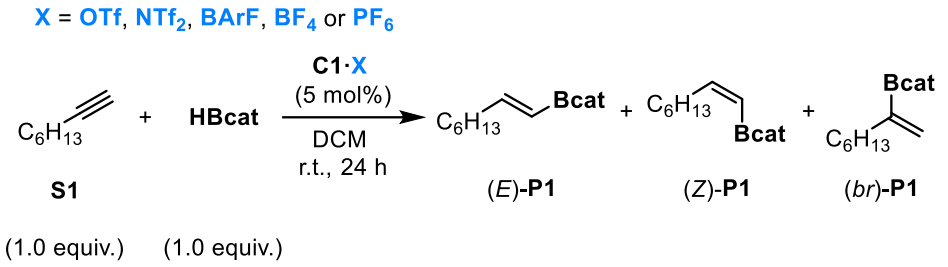

Entry	X	Conv. (%)	HB select. (%)[b]	Ratio *E:Z:br*
1	OTf	93	>99	22:3:75
2	NTf_2	95	90	22:5:73
3	BArF	90	85	24:4:72
4	BF_4	81	45	57:14:29
5	PF_6	53	37	65:13:22

[a] Reactions were performed at least twice in deuterated dichloromethane (0.3 M) under a N_2 atmosphere. Conversion and selectivity were determined by ^1H NMR using 1,2,4,5-tetramethylbenzene as the internal standard. [b] HB selectivity calculated as the molar amount of hydroboration products divided by the reacted molar amount of alkyne.

The ratio between (*E*)-**P1**, (*Z*)-**P1** and (*br*)-**P1** for these three catalysts remained constant within experimental error (compare entries 1-3, Table 3.3). The use of the OTf-containing catalysts led to the best results towards the unconventional branched hydroboration product (entry 1, Table 3.3), with a perfect hydroboration selectivity being observed. The NTf_2- and BArF-containing complexes behaved in a similar manner to **C1·OTf**, although they led to slightly worst results (entries 2 and 3, Table 3.3). As

[135] (a) Krossing, I.; Raabe, I. *Angew. Chem. Int. Ed.* **2004**, *43*, 2066-2090; (b) Carreras, L.; Rovira, L.; Vaquero, M.; Mon, I.; Martin, E.; Benet-Buchholz, J.; Vidal-Ferran, A. *RSC Adv.* **2017**, *7*, 32833-32841; (c) Aldrich, K. E.; Billow, B. S.; Holmes, D.; Bemowski, R. D.; Odom, A. L. *Organometallics* **2017**, *36*, 1227-1237.

for the BF_4-and PF_6-containing complexes, low hydroboration selectivities were observed,[136] with the (*E*)-isomer being the preferred hydroboration product (entries 4 and 5, Table 3.3). Considering that an increase in the steric congestion around the metal center (*e.g.*, ligand bulkiness)[126d,137] translates into increased amounts of the branched-isomer in alkyne hydroborations,[124b] the trend in the regioselectivity towards branched isomers described in Table 3.3 is in agreement with this premise. As X-Ray studies revealed, the anion-π interactions observed in case of the OTf- and NTf_2-derivatives might increase the steric congestion around the rhodium center, favoring the formation of the branched product.

With these results in hand, we studied the effects of other variables in the hydroboration reaction of oct-1-yne **S1** using the highest performing catalyst **C1·OTf** (Table 3.4).

Table 3.4. Effects of the relative amounts of borane and reaction time on the hydroboration of **S1**.[c]

Entry	**HBcat** (equiv.)	t (h)	Conv. (%)[c]	HB select. (%)[b]	Ratio *E:Z:br*
1	2.0[d]	24	>99	96	35:8:57
2	1.2[d]	24	>99	95	27:7:66
3	1.0	24	93	>99	22:3:75
4	0.9	24	>99	>99	19:4:77
5	0.9	6	97	>99	17:5:78

[a] and [b], see footnotes to Table 3.3. [c] Alkyne conversion except for entry 4 and 5, which corresponds to **HBcat** conversion. [d] GC-MS analysis revealed that the sample contained oct-1-ene and alkyl boronates, respectively.

[136] Conversion values refer to the amounts of consumed reagent (*i.e.*, alkyne or catecholborane) with respect to the initial molar amount. Selectivity refers to the overall amounts of vinyl boronic acid derivatives with respect to reacted catecholborane.

[137] Rej, S.; Das, A.; Panda, T. K. *Adv. Synth. Catal.* **2021**, *363*, 4818-4840.

It was observed that the use of substoichiometric amounts of catecholborane **HBcat** enhanced the regioselectivity of the reaction towards the branched product (*br*)-**P1** (from 57% with 2.0 equiv. of **HBcat** to 77% with 0.9 equiv., entries 1 and 4, Table 3.4). We hypothesized that the excess of **HBcat** in the reaction medium is responsible for the transformation of (*Z*)-**P1** and (*br*)-**P1** into the thermodynamically more stable product (*E*)-**P1** *via* H-B addition-elimination processes taking place.[124b] Moreover, an excess of **HBcat** in the reaction medium can also translate into the formation of dihydrido rhodium species capable of reducing the starting alkyne or hydroboration products.[138] It is interesting to note that the reduced analogues of products **S1** or **P1** (*i.e.*, oct-1-ene **69** and alkyl boronate derivatives **70**) were detected by GC-MS in the crude hydroboration reaction mixtures employing an excess of **HBcat** (entries 1 and 2, Table 3.4, see also section 3.4 for more information).

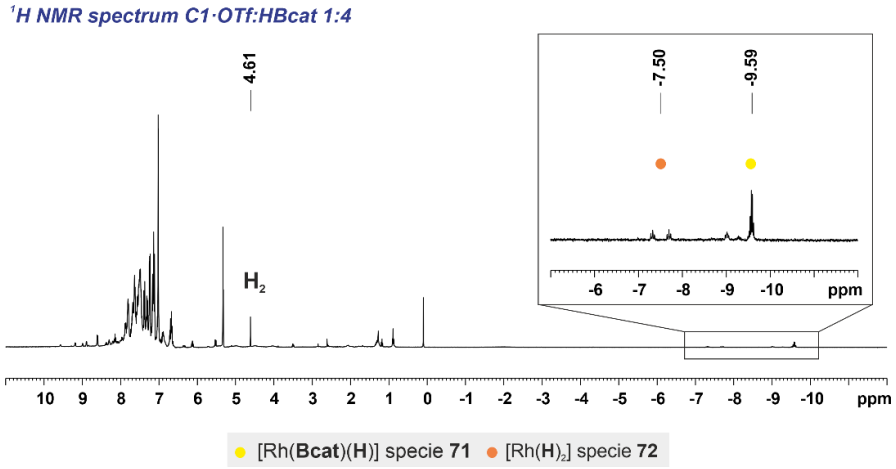

Figure 3.3. ^{1}H NMR analysis of the reaction mixture of 1:4 molar ratio of **C1·OTf**:**HBcat**.

To gain further insights into the formation of these byproducts, **HBcat** and **C1·OTf** were allowed to react in a 4:1 ratio in the absence of alkyne

[138] Burgess, K.; Van der Donk, W. A.; Westcott, S. A.; Marder, T. B.; Baker, R. T.; Calabrese, J. C. *J. Am. Chem. Soc.* **1992**, *114*, 9350-9359.

(Figure 3.3). A weak hydrido signal attributable to dihydrido rhodium complexes **72**[139] was observed at *ca.* –7.5 ppm, together with the characteristic H_2 signal at 4.6 ppm (Figure 3.3). We believe that these rhodium dihydrido species **72** may be responsible for the reduction of **S1** or **P1**. Interestingly, it should be mentioned that these reductions were not observed when **HBcat** was used (sub)stoichiometrically.

We then studied the effects of the reaction time in the outcome of the reaction (compare entries 4 and 5, Table 3.4). The hydroboration reaction proved to be a fast process when using **C1·OTf** as catalyst, with almost complete conversion being achieved after *ca.* 6h (for a graphic with the conversion and HB yield as a function of time, see Figure 3.4).

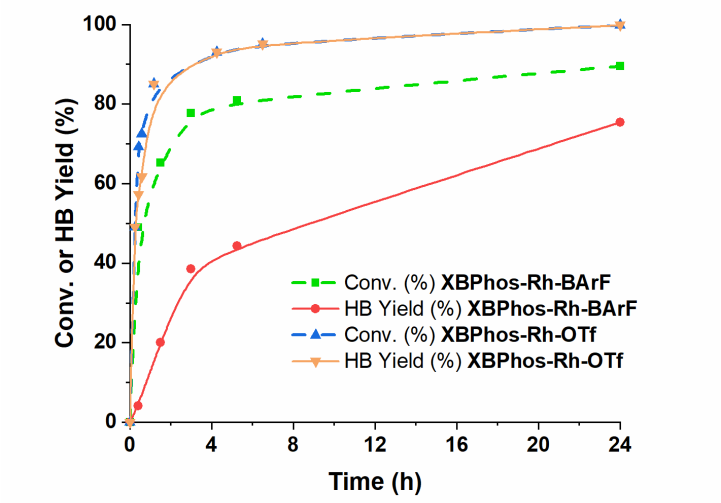

Figure 3.4. Conversion curves for the hydroboration oct-1-yne **S1**. Lines correspond to eye guidelines.

To aid comparison, a conversion curve of the hydroboration of oct-1-yne **S1** employing **C1·BArF** complex under the same reaction conditions is also included in Figure 3.4. This comparative study of the activity of the two catalysts revealed that **C1·OTf** has higher activity than its BArF

[139] Thaler, E. G.; Caulton, K. G. *Organometallics* **1990**, *9*, 1871-1876.

analogue (the $TOF_{1/2}$ value for **C1·OTf** was found to be *ca.* 20-fold higher than that for **C1·BArF**).[140]

Removal of the minor isomers (*i.e.*, (*E*)-**P1** and (*Z*)-**P1**) derived from the hydroboration of **S1** and **HBcat** and isolation of (*br*)-**P1** proved to be challenging. Handling of alkenyl esters derived from catecholborane is difficult, as these products are highly sensitive towards moisture.[141] To overcome this limitation, hydroboration reaction mixtures were treated with an excess of 1,8-diaminonaphtalene **73** (referred to as **dan**) and triethylamine (TEA) to afford the corresponding **Bdan**-containing products **P1·Bdan** (Scheme 3.5).

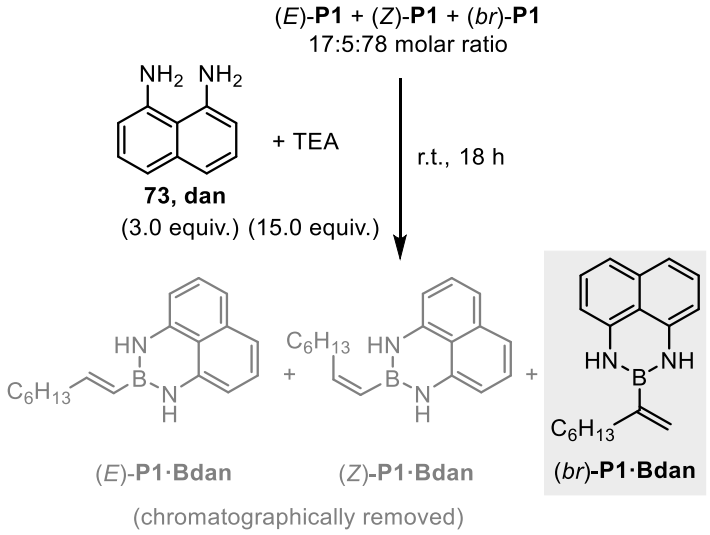

Scheme 3.5. Derivatization of catechol derivatives **P1** with 1,8-diaminonaphtalene **73**. For more details, see Section 3.4.

Interestingly, (*br*)-**P1·Bdan** could be isolated by standard chromatography due to its high stability towards hydrolysis, with the

[140] $TOF_{1/2}$ (turnover frequency at 50% conversion) was measured to be 36 h^{-1} for **C1·OTf**, whilst for **C1·BArF** was 2 h^{-1}.

[141] Brown, H. C.; Gupta, S. K. *J. Am. Chem. Soc.* **1975**, *97*, 5249-5255.

reported method constituting a new synthetic pathway to these interesting boron-based reagents in C_{sp^2}–C_{sp^2} iterative cross-coupling reactions.[142]

The practicality of the developed rhodium-catalyzed hydroboration method was also demonstrated by directly using the hydroboration reaction mixture as the boron-reagent in palladium-catalyzed C_{sp^2}–C_{sp^2} coupling reactions. Interestingly, the corresponding coupling products derived from (*br*)-**P1** or (*E*)-**P1** with 2-iodoaniline **74** were prepared with the herein developed one-pot coupling process (Scheme 3.6), furnishing the corresponding coupling products **75** and **76** in 59% and 12% isolated yields, respectively. The ratio between the isolated yields of **75** and **76** was consistent with that calculated for the (*br*)-**P1** and (*E*)-**P1** hydroboration products.

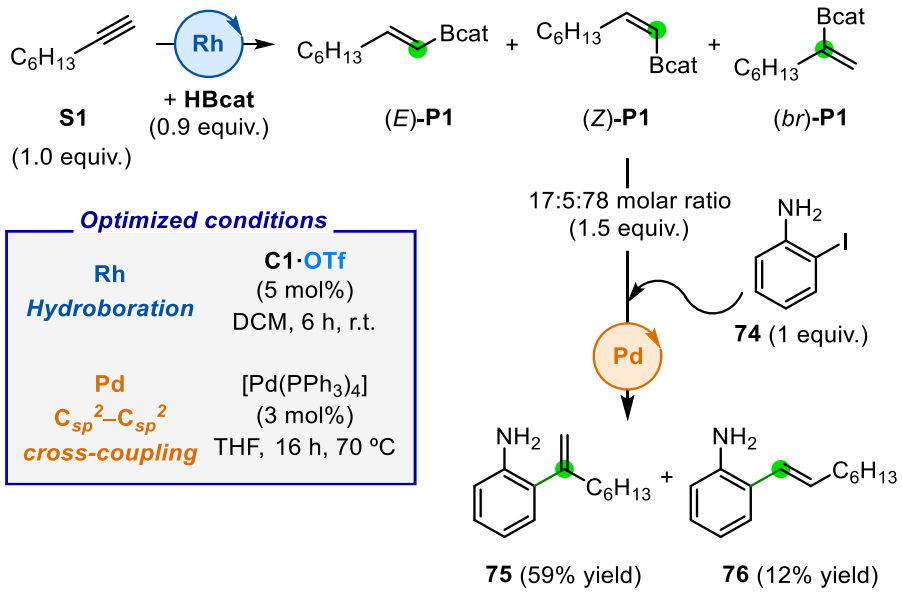

Scheme 3.6. One-pot hydroboration- C_{sp^2}–C_{sp^2}coupling process developed. For more details, see the Experimental Section 3.4.

[142] (a) Colacot, T. J. *New Trends in Cross-Coupling: Theory and Applications*. Royal Society of Chemistry, 2014; (b) Lennox, A. J. J.; Lloyd-Jones, G. C. *Chem. Soc. Rev.* **2014**, *43*, 412-443.

Having demonstrated that **C1·OTf** was an active and efficient catalyst in the hydroboration of oct-1-yne **S1** with **HBcat**, we decided to explore the substrate scope of the reaction with an array of structurally diverse alkynes (Figure 3.5).

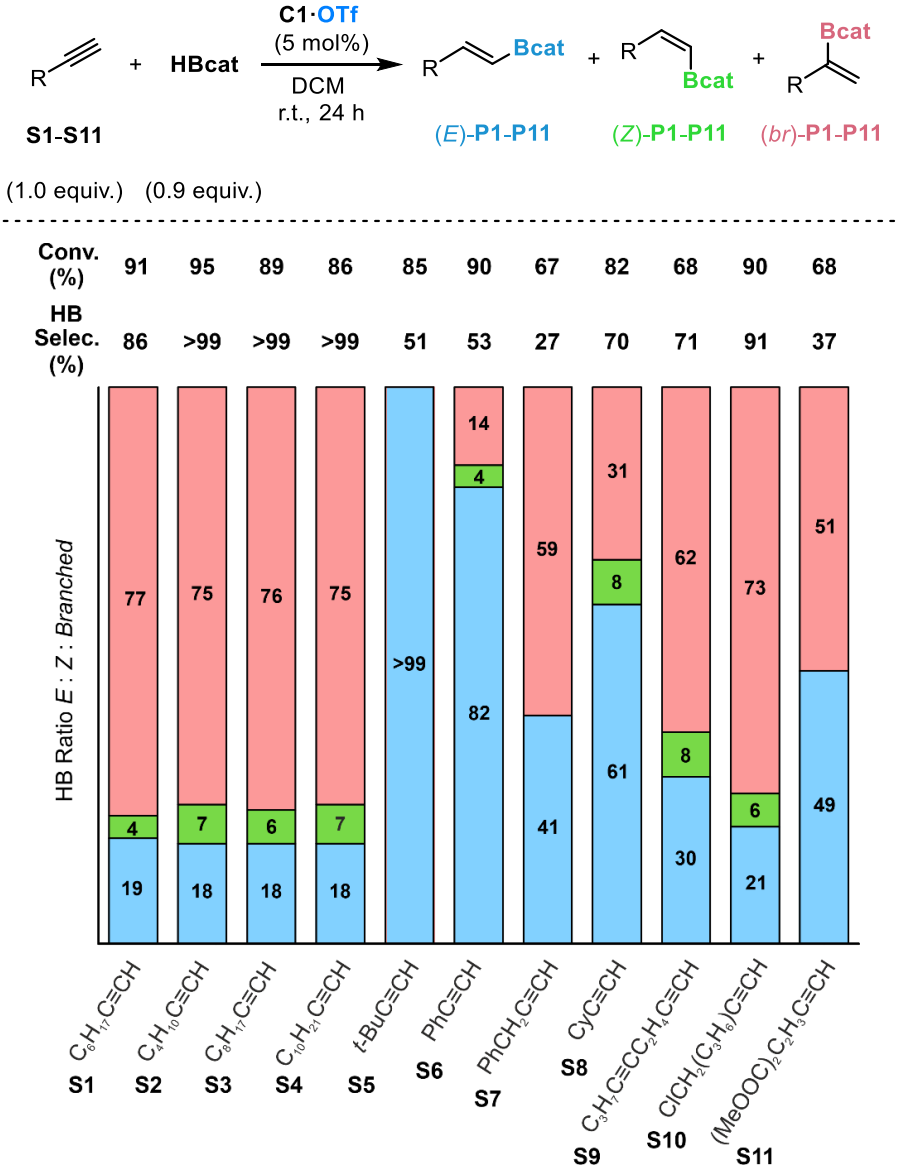

Figure 3.5. Rhodium-catalyzed hydroboration of terminal alkynes. Reactions were performed in deuterated dichloromethane (*ca.* 0.3 M) under N_2 under optimized

conditions. Yields were determined by ^{1}H NMR using 1,2,4,5-tetramethylbenzene as internal standard. The results with **S1** have already been discussed in Table 3.4**.**

Hydroboration of alkynes with a saturated linear four-, eight- and ten-carbon substituent (substrates **S2**-**S4**, Figure 3.5) proceeded with similar hydroboration selectivities and regioselectivities to those obtained for the model substrate **P1**. Substrate **S5** was hydroborated with poor reactivity and surprisingly led to the (*E*)-isomer as the only hydroboration product.

Phenylacetylene **S6** led mostly to (*E*)-**P6.** It is described in literature that in alkyne substrates containing conjugated aryl substituents, the linear isomer predominates.[138,143] The presence of a -CH_2- methylene group adjacent to the alkyne functionality was deemed crucial for selectivity towards the branched product. For instance, prop-2-yn-1-ylbenzene **S7**, which contains unconjugated aryl and alkyne groups, behaves in a different manner with the branched vinyl boronic acid derivative (*br*)-**P7** being the predominant product.

Cyclohexyl acetylene **S8** displayed an activity comparable to **S6**, although in this case selectivity towards the (*br*)-isomer was higher (compare substrates **S6** and **S8**, Figure 3.5). Selective hydroboration of the terminal alkyne in the diyne substrate **S9** proceeded with comparable activity and selectivity to those for non-functionalized linear alkynes (**S1**-**S4**, Figure 3.5). In terms of electronic effects, hydroboration of alkynes containing sigma accepting groups (*i.e.*, chloro or methoxycarbonyl groups) were tolerated but resulted in slightly reduced activity and selectivity (**S10** and **S11**, Figure 3.5).

Mechanistic rationale

The activity of the catalysts in terms of the conversion observed for the different halogen-bonded rhodium complexes (OTf > NTf_2 > BArF > BF_4 >

[143] (a) Pereira, S.; Srebnik, M. *Tetrahedron Lett.* **1996**, *37*, 3283-3286;(b) Beletskaya, I.; Pelter, A. *Tetrahedron* **1997**, *53*, 4957-5026.

PF_6) can mainly be rationalized in terms of the electronic influence exerted by the counterion on the cationic rhodium center. The position of the CO stretching band in IR varies with the coordination ability of the counterion ($\bar{\upsilon}_{CO}$ (OTf) < $\bar{\upsilon}_{CO}$ (NTf_2) < $\bar{\upsilon}_{CO}$ (BF_4) ≅ $\bar{\upsilon}_{CO}$ (PF_6) < $\bar{\upsilon}_{CO}$ (BArF), Table 3.2). Lower vibrational CO wavenumbers are attributable to an increase in π-backbonding from the metal to the CO ligand, and thus, a major electronic donation from the counterion to the cationic rhodium center. The ease of oxidative addition processes (such as those for B–H bonds in hydroboration reactions) increases with the electron density of the metal center.[144] This line of reasoning would be consistent with the high activity of the OTf counterion, as experimentally observed.

Mechanistic studies have mainly focused on metal-catalyzed hydroboration reactions of alkenes with **HBcat** (and other boranes), with the metal-catalyzed reactions generally yielding linear alkyl boronates[124] through a *syn*-addition of borane to the C=C bond in an anti-Markovnikov manner.[124d] Regarding the mechanism for alkynes, several reports have been published using copper, palladium and cobalt,[126-128] but studies using rhodium catalysts are scarce.[124c] Interestingly, our halogen bond-assembled complex **C1·OTf** is one of the very few rhodium-based catalysts that lead mostly to the branched instead of the (*E*)-configured hydroboration products.

We considered that the hydroboration process proceeds through the initial oxidative addition of **HBcat** to the rhodium(I) center of **C1·OTf** complex leading to the formation of a hydrido boryl rhodium(III) intermediate **71** (Scheme 3.7). This observation is supported by ^{1}H NMR studies over short reaction times, which showed a diagnostic ^{1}H NMR signal in the hydride region at *ca.* –9.6 ppm (Figure 3.6). The formation of

[144] Crabtree, R. H. *The Organometallic Chemistry of the Transition Metals*. John Wiley & Sons, 2009.

rhodium(III) hydrido boryl complexes is well established in the literature.[138,145]

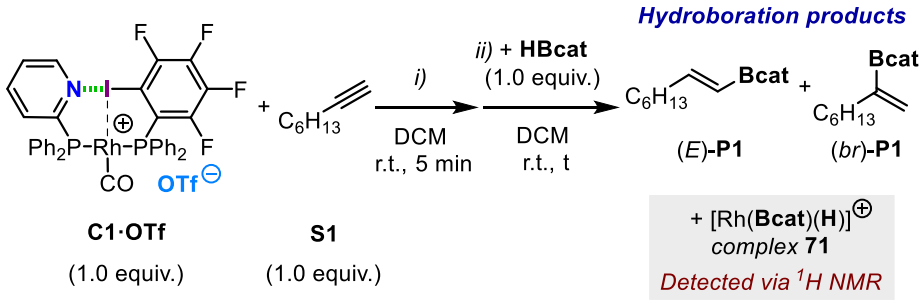

Scheme 3.7. Study of the hydroboration reaction using **C1·OTf** (1.0 equiv.), oct-1-yne **S1** (1.0 equiv.) and **HBcat** (1.0 equiv.).

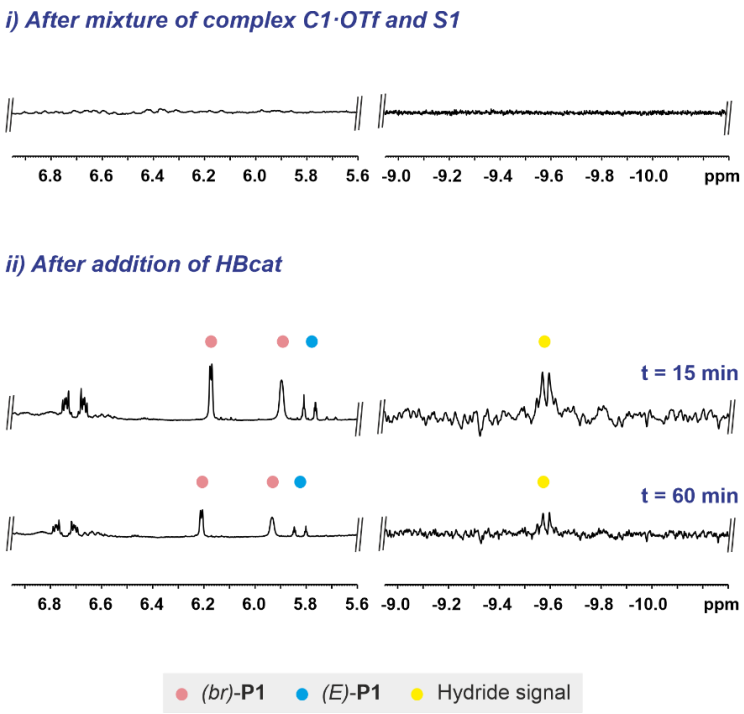

Figure 3.6. ^{1}H NMR study of the hydroboration reaction using **C1·OTf** (1.0 equiv.), oct-1-yne **S1** (1.0 equiv.) and **HBcat** (1.0 equiv.).

[145] For example, see: (a) Lam, W. H.; Shimada, S.; Batsanov, A. S.; Lin, Z.; Marder, T. B.; Cowan, J. A.; Howard, J. A. K.; Mason, S. A.; McIntyre, G. J. *Organometallics* **2003**, *22*, 4557-4568; (b) Esteruelas, M. A.; Oliván, M.; Vélez, A. *J. Am. Chem. Soc.* **2015**, *137*, 12321-12329.

It is interesting to highlight that alkyne **S1** does not react with the rhodium catalyst in the absence of **HBcat** to a measurable extent,[146] which indicates that hydroborations employing **C1·OTf** start with the oxidative addition of the **HBcat** to the rhodium center, as proposed in the literature in other examples.[122,124a,124b,138,141]

Thus, the formation of hydroboration products from terminal alkynes using **C1·OTf** as catalyst could be rationalized as depicted in Scheme 3.8. As demonstrated before, the initial oxidative addition of the borane **HBcat** to the rhodium(I) center constitutes the first step of the catalytic cycle forming hydrido boryl rhodium(III) complex **71**, which would interact with the alkyne **S** through π-coordination of the triple bond.

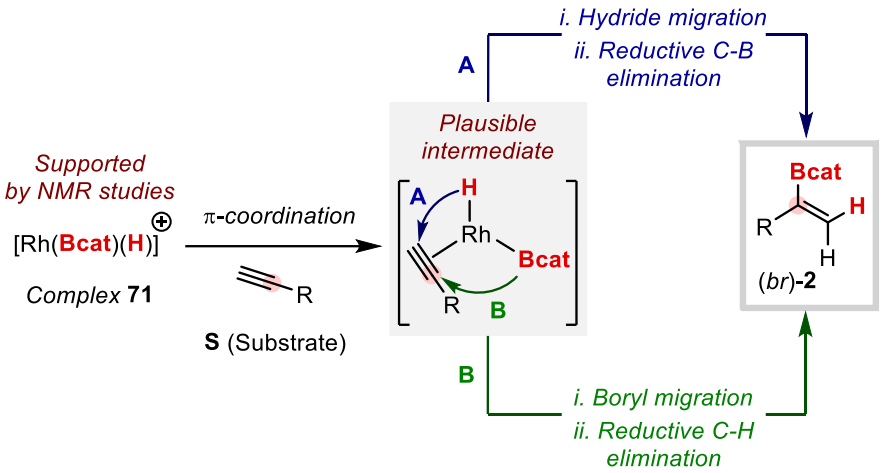

Scheme 3.8. Reaction pathways towards branched alkenyl boronic acid derivatives.

Then, the reaction could proceed through two different reaction manifolds: **A** or **B** depending on the order in which the different steps of the catalytic cycle take place. After alkyne coordination, the hydroboration cycle might continue with hydride migration followed by C–B reductive elimination (path **A**) or boryl migration and subsequent C–H reductive elimination (path **B**), giving rise to the branched product (*br*)-**P**. Generally,

[146] Only starting material **S1** was detected by GC-MS after reacting **S1** with our rhodium complex **C1·OTf** in absent of **HBcat** under optimized conditions.

the reaction manifolds involving first either boryl or hydride migration steps are often indistinguishable by observation of the selectivities.[124b]

3.3 CONCLUSIONS

A series of XBphos-Rh **C1** analogues incorporating diverse counterions were successfully synthesized and characterized. With the aim of maximizing the regioselectivity of the hydroboration of alkynes towards the branched alkenyl boronates by variation of the counterion, octy-1-ne **S1** was used as the benchmark substrate and catecholborane **HBcat** as the borane source. We demonstrated that the stronger the coordination ability of the counterion, the higher the activity and selectivity towards hydroboration products were. The use of (sub)stoichiometric amounts of catecholborane **HBcat** was proven to be beneficial for the preparation of the branched hydroboration products with the highest yields being obtained under these conditions. An array of structurally diverse alkynes was subjected to hydroboration conditions employing XBphos-Rh-OTf **C1·OTf** as the catalyst. Our study concluded that linear and inactivated alkyl-substituted alkynes led to the highest levels of chemo- and regio-selectivity in the hydroboration reaction.

The practicality of our synthetic method was demonstrated by developing a one-pot hydroboration/Csp^2–Csp^2 coupling process. We demonstrated that the coordination ability of the counterion can be correlated with the electronic richness of the metal center and the activity of the XBphos-Rh-X **C1·X** catalyst in hydroborations: OTf > NTf_2 > BArF > BF_4 ≈ PF_6. As for the mechanistic rationale of the reaction, NMR studies demonstrated that the hydroboration process starts with the oxidative addition of **HBcat** to the rhodium(I) center. The reaction further proceeds with the coordination of the alkyne followed by a hydride migration/C–B reductive elimination reaction pathway **A**, or boryl migration/C–H reductive elimination reaction pathway **B**, to give product (*br*)-**P** after a reductive elimination step.

3.4 EXPERIMENTAL SECTION

3.4.1 General considerations

All syntheses were carried out using chemicals as purchased from commercial sources unless otherwise stated. Air- and moisture-sensitive manipulations or reactions were performed under inert atmosphere, either in a glove box or with standard Schlenk techniques. Glassware was dried *in vacuo* before use with a hot air gun. All solvents were dried by using a solvent purification system (SPS). Silica gel 60 (230–400 mesh) was used for column chromatography. NMR spectra were recorded in 400 MHz or 500 MHz spectrometers in $CDCl_3$ or CD_2Cl_2 unless otherwise cited. ^{1}H and $^{13}C\{^{1}H\}$ NMR chemical shifts are quoted in ppm relative to residual solvent peaks. $^{19}F\{^{1}H\}$ NMR chemical shifts are quoted in ppm relative to $CFCl_3$ in $CDCl_3$. $^{31}P\{^{1}H\}$ NMR chemical shifts are quoted in ppm relative to 85% phosphoric acid in water. HRMS spectra were recorded using ESI ionization method in positive mode. GC-MS analyses were performed using EI as ionization method. GC analyses were performed with a flame ionization detector. IR spectra were recorded using Attenuated Total Reflection (ATR) technique unless otherwise cited. Ligands **L1** is commercially available and was used as received. (2-iodo-3,4,5,6-tetrafluorobenzene)diphenylphosphine ligand **L2** and XBphos-Rh **C1**·**BArF** were prepared according to previous literature reports.[70]

3.4.2 General structural comments on X-Ray crystals

Crystals suitable for X-ray measurement for complexes **C1·OTf** and **C1·NTf$_2$** were obtained by slow diffusion of *n*-pentane into concentrated solutions of dichloromethane at −25 ºC under inert atmosphere. The measured crystals were prepared under inert conditions immersed in perfluoropolyether as protecting oil for manipulation.

Crystal structure determination of **C1·OTf** was carried out using an Appex DUO Kappa 4-axis goniometer equipped with an Appex 2 4K CCD area detector, a Microfocus Source E025 IuS using MoK$_\alpha$ radiation (0.71073 Å), Quazar MX multilayer Optics as monochromator and an Oxford Cryosystems low temperature device Cryostream 700 plus (T = −173 ˚C). Full-sphere data collection was used with ω and φ scans. *Programs used:* Data collection APPEX-2,[100] data reduction Bruker Saint[101] V/60A and absorption correction SADABS.[102]

Crystal structure determination of **C1·NTf$_2$** was carried out using a Rigaku diffractometer equipped with a Pilatus 200K area detector, a Rigaku MicroMax-007HF microfocus rotating anode with MoK$_\alpha$ radiation, confocal Max Flux optics and an Oxford Cryosystems low temperature device Cryostream 700 plus (T = -173 ˚C). Full-sphere data collection was used with ω and φ scans. *Programs used:* Data collection and reduction with CrysAlisPro[147] V/.60A and absorption correction with Scale3 Abspack scaling algorithm.[148]

Structure solution and refinement: Crystal structure solution was achieved using the computer program SHELXT.[103] Visualization was performed with the program SHELXle.[104] Missing atoms were subsequently located from difference Fourier synthesis and added to the atom list. Least-squares refinement on F^2 using all measured intensities

[147] Data collection and reduction with CrysAlisPro 1.171.39.12b (Rigaku OD, 2015).
[148] Empirical absorption correction using spherical harmonics implemented in Scale3 Abspack scaling algorithm, CrysAlisPro 1.171.39.12b (Rigaku OD, 2015).

was carried out using the program SHELXL 2015.[105] All non-hydrogen atoms were refined including anisotropic displacement parameters.

Comments to the structure **C1·OTf**: The asymmetric unit contains one molecule of the metal complex, one triflate anion and one dichloromethane molecule. The triflate anion and the dichloromethane molecule are disordered respectively in two and three orientations. Some large residual electron densities observed in the structure were assumed to be the result of the presence of the iodine atom which has a large atomic weight.

Comments to **C1·NTf$_2$**: The asymmetric unit contains one molecule of the metal complex coordinated to a carbon monoxide and a bistrifluoromethanesulfonimidate motif. The carbon monoxide ligand is disordered in two orientations (ratio: 53:47).

Table 3.5. Crystal data and structural parameters for complex **C1·OTf.**

Compound	**C1·OTf**
Formula	$C_{38}H_{26}Cl_2F_7NO_4P_2RhS$
Formula weight (total)	1088.31
Crystal size (mm^3)	0.04 x 0.04 x 0.02
Temp (K)	100(2)
Crystal system	Monoclinic
Space group	P2(1)/n
A (Å)	13.6040(10)
B (Å)	20.2732(15)
C (Å)	14.4401(11)
α (deg)	90
β (deg)	99.787(2)
γ (deg)	90
V ($Å^3$)	3924.6(5)
Z	4
ρ (Mg/m^3)	1.842
μ (mm^{-1})	1.569
θ range (°)	1.748 to 31.676
Reflec. collected	55620
Independent reflections	12738[R(int) = 0.0487]
Absorpt. correct.	Multi-scan
Trans. min/max	0.85/0.969
Data/restraints/parameters	12738/ 520/ 619
R1/wR2 [I>2σ(I)]	0.0402/0.0897
R1/wR2 [all data]	0.0627/0.0990
Goodness-of-fit (F^2)	1.036
Peak/hole ($e/Å^3$)	2.866/-1.120

Table 3.6. Crystal data and structural parameters for complex **C1·NTf₂.**

Compound	**C1·NTf₂**
Formula	$C_{38}H_{24}F_{10}IN_2O_5P_2RhS_2$
Formula weight (total)	1134.48
Temp (K)	100(2)
Crystal system	Triclinic
Space group	P-$_1$
A (Å)	11.1361(5)
B (Å)	11.3846(4)
C (Å)	17.9640(8)
α (deg)	91.239(3)
β (deg)	105.517(4)
γ (deg)	110.910(4)
V (Å^3)	2032.53(16)
Z	2
ρ (Mg/m^3)	1.854
μ (mm^{-1})	1.454
θ range (°)	2.395 to 30.406
Reflec. collected	35499
Independent reflections	11035[R(int) = 0.0432]
Absorpt. correct.	Multi-scan
Trans. min/max	0.726/0.944
Data/restraints/parameters	11035/ 64/ 569
R1/wR2 [I>2σ(I)]	0.0331/0.0749
R1/wR2 [all data]	0.0485/0.0802
Goodness-of-fit (F^2)	1.032
Peak/hole (e/Å^3)	1.071/-0.908

3.4.3 Synthesis of rhodium(I) complexes C1·X

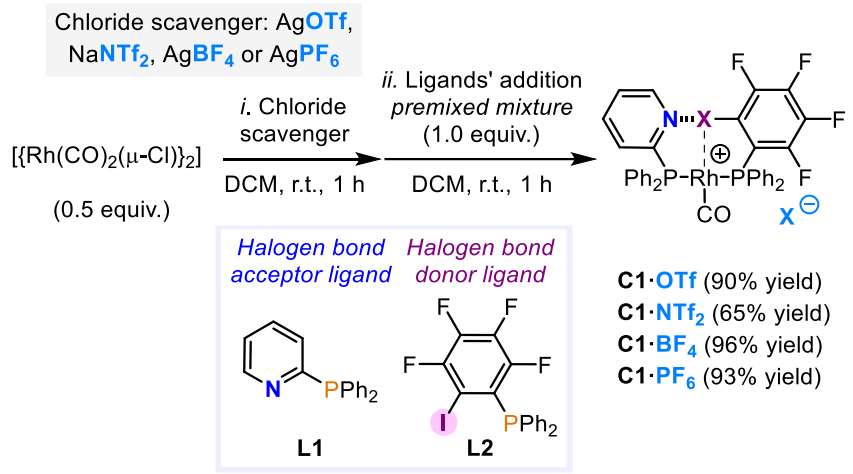

General procedure for rhodium(I) complexes **C1·X** (**X** = OTf, NTf_2, BF_4 or PF_6): In a glovebox filled with N_2, [{Rh(CO)$_2$(μ-Cl)}$_2$] dimer (0.5 equiv.) and the corresponding chloride scavenger (1.0 equiv.) were added to an amberized glass vial provided with a magnetic stirrer and were dissolved in DCM (0.06 M). The mixture was stirred for 1 hour at room temperature. In parallel, a solution of the corresponding halogen bond acceptor ligand **L1** (1.0 equiv.) and halogen bond donor ligand **L2** (1.0 equiv.) in DCM (0.12 M) was prepared in a vial provided with a magnetic stirrer and was stirred for 1 hour at room temperature. At due time, the premixed ligands' solution was added dropwise to the rhodium solution, observing some bubbling (CO release). This mixture was stirred for 1 or 2 hours at room temperature, and then filtered by using a HPLC nylon filter to remove the NaCl precipitate. The resulting orange solution was partially evaporated (to *ca*. 1.0 mL volume) and mixed with 5.0 mL of *n*-pentane. The residue obtained was washed with *n*-pentane (3 x 2.0 mL). and dried under vacuum to afford the desired rhodium(I) complexes **C1·X** (**X** = OTf, NTf_2, BF_4 or PF_6).

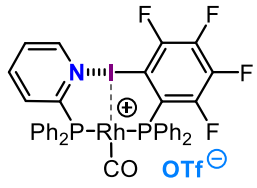

C1·OTf

For the preparation of complex **C1·OTf**: 31.3 mg (0.08 mmol, 0.5 equiv.) of [{Rh(CO)$_2$(μ-Cl)}$_2$] dimer, 40.1 mg (0.2 mmol, 1.0 equiv.) of AgOTf, 42.4 mg (0.2 mmol, 1.0 equiv.) of **L1** and 74.9 mg (0.2 mmol, 1.0 equiv.) of **L2**. 141.0 mg (90% yield) of complex **C1·OTf** was obtained as an orange powder in high purity (*via* NMR). **^{1}H NMR** (500 MHz, CD_2Cl_2) δ: 8.92 (d, J = 5.0 Hz, 1 H), 7.97 (tm, J = 7.7 Hz, 1 H), 7.73 – 7.45 (m, 21 H), 7.35 (dd, J = 7.7, 3.0 Hz, 1 H) ppm. **^{13}C{^{1}H} NMR** (126 MHz, CD_2Cl_2) δ:[149] 185.2 (C_{CO}), 151.7 (dd, J = 67.6 Hz, J = 4.5 Hz, C_{Py}), 149.6 (d, J = 19.2 Hz, C_{Py}), 147.7 (dm, J = 247.8 Hz, C_F), 143.3 (dm, J = 268.3 Hz, C_F), 142.4 (dm, J = 259.8 Hz, C_F), 139.1 (d, J = 4.9 Hz, C_{Py}), 134.0 (d, J = 12.3 Hz, C_{Ph}), 133.0-132.8 (m, C_{Ph}), 130.0 (dd, J = 10.9 Hz, J = 1.9 Hz, C_{Ph}), 129.7 – 129.6 (m), 129.2 (C_{Py}), 128.8, 128.4, 127.5 (C_{Py}), 121.5 (q, J = 321.4 Hz, C_{CF3}) ppm. **^{19}F{^{1}H} NMR** (471 MHz, CD_2Cl_2) δ: –78.9 (s, 3 F), –116.9 (m, 1 F), –118.2 (m, 1 F), –143.0 (m, 1 F), –148.1 (m, 1 F) ppm. **^{31}P{^{1}H} NMR** (161 MHz, CD_2Cl_2) δ: 79.1 (ddd, $^2J_{P-P}$ = 275.1 Hz, $^1J_{P-Rh}$ = 110.8 Hz, $^3J_{P-F}$ = 13.3 Hz), 50.4 (dd, $^2J_{P-P}$ = 275.1 Hz, $^1J_{P-Rh}$ = 116.3 Hz) ppm. **IR** (neat): 3054, 2011, 1498, 1437, 1262, 1028 cm^{-1}. **HRMS** (ESI$^+$): m/z calcd. for $C_{35}H_{24}F_4INP_2Rh^+$ [M–CO–OTf]$^+$ 825.9414, found: 825.9422.

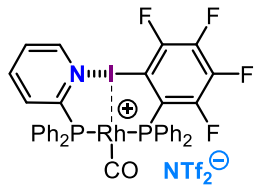

C1·NTf$_2$

For the preparation of complex **C1·NTf$_2$**: 35.3 mg (0.09 mmol, 0.5 equiv.) of [{Rh(CO)$_2$(μ-Cl)}$_2$] dimer, 70.5 mg (0.2 mmol, 1.0 equiv.) of $NaNTf_2$, 46.4 mg (0.2 mmol, 1.0 equiv.) of **L1** and 81.1 mg (0.2 mmol, 1.0 equiv.) of **L2**. 170.0 mg (65% yield) of complex **C1·NTf$_2$** was obtained as a brown powder in high purity (*via*

[149] A heavily overlapped 13C{1H} NMR spectrum was observed due to multiple couplings of the carbons with other NMR active heteronuclei present in the molecule. Whenever possible, the carbons where assigned as it follows: C_{CO} (carbonyl carbon), C_{CF3} (from the counterion), C_{Ph} (phenyl ring carbons), C_{Py} (pyridyl ring carbons), C_F (fluorine-containing ring carbons).

NMR). **^{1}H NMR** (500 MHz, CD_2Cl_2) δ: 8.90 (dd, *J* = 5.0, 0.6 Hz, 1 H), 7.94 (tm, *J* = 7.8 Hz, 1 H), 7.72 – 7.43 (m, 21 H), 7.35 (dm, *J* = 7.8 Hz, 1 H) ppm. **^{13}C{^{1}H} NMR** (126 MHz, CD_2Cl_2) δ:[112] 185.2 (C_{CO}), 151.7 (dd, *J* = 67.8 Hz, *J* = 4.4 Hz, C_{Py}), 149.6 (d, *J* = 19.2 Hz, C_{Py}), 147.8 (dm, *J* = 247.9 Hz, C_F), 143.2 (dm, *J* = 268.2 Hz, C_F), 142.4 (dm, *J* = 260 Hz, C_F), 139.1 (d, *J* = 4.7 Hz, C_{Py}), 134.0 (d, *J* = 12.6 Hz, C_{Ph}), 133.0-132.7 (m, C_{Ph}), 130.0 (dd, *J* = 11.1 Hz, *J* = 1.84 Hz, C_{Ph}), 129.7 – 129.5 (m), 129.2 (C_{Py}), 128.8, 128.4, 127.4 (C_{Py}), 120.3 (q, *J* = 321.6 Hz, C_{CF3}) ppm. **^{19}F{^{1}H} NMR** (363 MHz, CD_2Cl_2) δ: –79.5 (s, 6 F), –116.8 (m, 1 F), –118.3 (m, 1 F), –143.1 (m, 1 F), –148.2 (m, 1 F) ppm. **^{31}P{^{1}H} NMR** (202 MHz, CD_2Cl_2) δ: 79.5 (ddd, $^{2}J_{P-P}$ = 275.8 Hz, $^{1}J_{P-Rh}$ = 110.7 Hz, $^{3}J_{P-F}$ = 13.7 Hz), 50.5 (dd, $^{2}J_{P-P}$ = 275.8 Hz, $^{1}J_{P-Rh}$ = 116.1 Hz) ppm. **IR** (neat): 3061, 2028, 1502, 1436, 1343, 1328, 1179 cm^{-1}. **HRMS** (ESI^{+}): *m*/*z* calcd. for $C_{36}H_{24}F_4INOP_2Rh^{+}$ $[M–NTf_2]^{+}$ 853.936, found: 853.934.

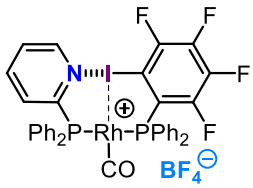

C1·BF$_4$

For the preparation of complex **C1·BF$_4$**: 23.3 mg (0.06 mmol, 0.5 equiv.) of $[\{Rh(CO)_2(\mu\text{-}Cl)\}_2]$ dimer, 23.1 mg (0.1 mmol, 1.0 equiv.) of $AgBF_4$, 31.6 mg (0.1 mmol, 1.0 equiv.) of **L1** and 55.7 mg (0.1 mmol, 1.0 equiv.) of **L2**. 105.0 mg (96% yield) of complex **C1·BF$_4$** was obtained as a fine orange powder in high purity (*via* NMR). **^{1}H NMR** (500 MHz, CD_2Cl_2) δ: 8.91 (dm, *J* = 5.0 Hz, 1 H), 7.96 (tm, *J* = 7.9 Hz, 1 H), 7.73 – 7.45 (m, 21 H), 7.36 (dm, *J* = 7.8 Hz, 1 H) ppm. **^{13}C{^{1}H} NMR** (126 MHz, CD_2Cl_2) δ:[112] 185.2 (C_{CO}), 151.7 (dd, *J* = 67.8 Hz, *J* = 4.4 Hz, C_{Py}), 150.7 (dm, *J* = 254.0 Hz, *J* = 11.1 Hz, C_F) 149.6 (d, *J* = 19.2 Hz, C_{Py}), 147.7 (dm, *J* = 249.2 Hz, C_F), 143.2 (dm, *J* = 273.4 Hz, C_F), 142.4 (dm, *J* = 259.6 Hz, C_F), 139.1 (d, *J* = 4.7 Hz, C_{Py}), 134.0 (d, *J* = 12.7 Hz, C_{Ph}), 133.0 – 132.8 (m, C_{Ph}), 130.0 (dd, *J* = 10.8 Hz, *J* = 1.7 Hz, C_{Ph}), 129.7 – 129.5 (m), 129.2 (C_{Py}), 128.8, 128.4, 127.5 (C_{Py}) ppm. **^{19}F{^{1}H} NMR** (376 MHz, CD_2Cl_2) δ: –116.9 (m, 1 F), –118.2 (m, 1 F), –143.0 (m, 1 F), –148.0 (m, 1 F), –153.3 (*br* s) ppm. **^{31}P{^{1}H} NMR** (162

MHz, CD_2Cl_2) δ: 79.2 (ddd, $^2J_{P-P}$ = 275.9 Hz, $^1J_{P-Rh}$ = 110.7 Hz, $^3J_{P-F}$ = 13.8 Hz), 50.4 (dd, $^2J_{P-P}$ = 275.9 Hz, $^1J_{P-Rh}$ = 116.4 Hz) ppm. **IR** (neat): 3058, 2014, 1498, 1436, 1048 cm^{-1}. **HRMS** (ESI) *m/z*: calcd. for $C_{35}H_{24}F_4INP_2Rh^+$ $[M-CO-BF_4]^+$ 825.9414, found: 825.9404.

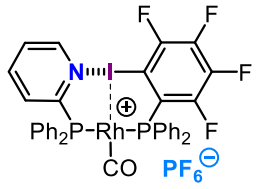

C1·PF$_6$

For the preparation of complex **C1·PF$_6$**: 28.8 mg (0.07 mmol, 0.5 equiv.) of $[\{Rh(CO)_2(\mu\text{-}Cl)\}_2]$ dimer, 35.6 mg (0.1 mmol, 1.0 equiv.) of $AgPF_6$, 39.0 mg (0.1 mmol, 1.0 equiv.) of **L1** and 67.5 mg (0.1 mmol, 1.0 equiv.) of **L2**. 132.0 mg (93% yield) of complex **C1·PF$_6$** was obtained as an orange powder in high purity (*via* NMR). **^{1}H NMR** (500 MHz, CD_2Cl_2) δ: 8.90 (dd, *J* = 5.0, 0.6 Hz, 1 H), 7.94 (tm, *J* = 7.8 Hz, 1 H), 7.72 – 7.43 (m, 21 H), 7.35 (dm, *J* = 7.8 Hz, 1 H) ppm. **^{13}C{^{1}H} NMR** (126 MHz, CD_2Cl_2) δ:[112] 185.2 (C_{CO}), 151.7 (dd, *J* = 67.8 Hz, *J* = 4.4 Hz, C_{Py}), 150.7 (dm, *J* = 254.0 Hz, *J* = 11.1 Hz, C_F), 149.6 (d, *J* = 19.2 Hz, C_{Py}), 147.7 (dm, *J* = 249.2 Hz, C_F), 143.2 (dm, *J* = 273.4 Hz, C_F), 142.4 (dm, *J* = 259.6 Hz, C_F), 139.1 (d, *J* = 4.7 Hz, C_{Py}), 134.0 (d, *J* = 12.7 Hz, C_{Ph}), 133.0 – 132.8 (m, C_{Ph}), 130.0 (dd, *J* = 10.8 Hz, *J* = 1.7 Hz, C_{Ph}), 129.7 – 129.5 (m), 129.2 (C_{Py}), 128.8, 128.4, 127.5 (C_{Py}) ppm. **^{19}F{^{1}H} NMR** (376 MHz, CD_2Cl_2) δ: –73.7 (d, J_{F-P} = 710.3 Hz, 6 F), –116.8 (m, 1 F), –118.2 (m, 1 F), –142.9 (m, 1 F), –147.9 (m, 1 F) ppm. **^{31}P{^{1}H} NMR** (202 MHz, CD_2Cl_2) δ: 79.2 (ddd, $^2J_{P-P}$ = 276.5 Hz, $^1J_{P-Rh}$ = 111.8 Hz, $^3J_{P-F}$ = 11.5 Hz), 50.4 (dd, $^2J_{P-P}$ = 276.5 Hz, $^1J_{P-Rh}$ = 116.0 Hz), –141.4 (sept, J_{P-F} = 710.3 Hz) ppm. **IR** (neat): 2013, 1498, 1436, 832 cm^{-1}. **HRMS** (ESI) *m/z*: calcd. for $C_{35}H_{24}F_4INP_2Rh^+$ $[M-CO-PF_6]^+$ 825.9414, found: 825.9406.

3.4.4 General procedure for the Rh-catalyzed hydroboration reaction

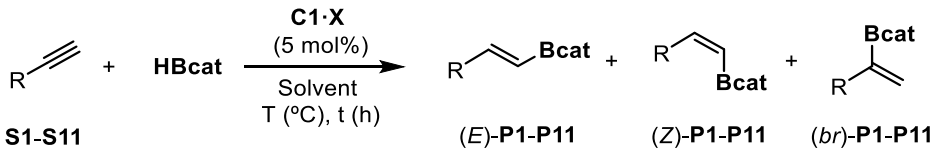

General procedure for hydroboration reaction: Under N_2 atmosphere, the rhodium(I) catalyst (5 mol%) along with 600 μL of solvent were added to a 10 mL screw cap vial provided with a stirrer. Then, 1.0 equiv. of the alkyne **S1-S11** (0.3 M) and the corresponding equivalents of catecholborane **HBcat** were subsequently added. The mixture was stirred at different temperatures for the required reaction time. Finally, a known amount of 1,2,4,5-tetramethylbenzene (Sigma-Aldrich TraceCERT®) as internal standard was added. Reaction mixtures were analyzed using quantitative ^{1}H NMR. Vinyl boronic acid derivatives (*E*)-**P1-P11**, (*Z*)-**P1-P11** and (*br*)-**P1-P11** were not isolated[150] and directly characterized from the reaction mixture based on previous reports in the literature or analogous compounds.

[150] Catecholborane and catecholborane-derived vinyl boronic acid derivatives are sensitive to air, moisture as well as to the presence of methanol or other nucleophiles such as phosphanes. See reference 141.

Hydroboration of* S1 *using* HBcat *and* XBphos-Rh-X *as catalysts

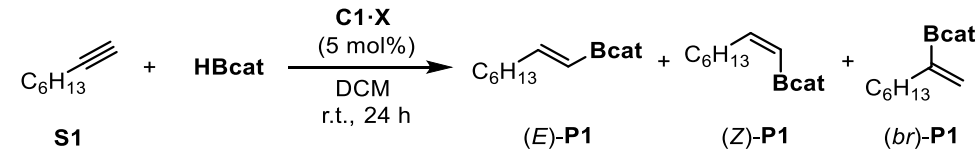

Table 3.7. Hydroboration of oct-1-yne **S1** (1.0 equiv.) with **HBcat** (1.0 equiv.) using complexes **C1·X**.[a]

Entry	**X**	Conv. (%)	HB select. (%)[b]	Ratio *E:Z:br*
1	BArF	90	85	24:4:72
2	OTf	93	>99	22:3:75
3	NTf_2	95	90	22:5:73
4	BF_4	81	45	57:14:29
5	PF_6	53	37	65:13:22

[a] Reactions were performed in deuterated dichloromethane (*ca*. 0.3 M) under N_2 atmosphere for 24h at room temperature. Yields were determined by ^1H NMR using 1,2,4,5-tetramethylbenzene as the internal standard. HBcat = catecholborane. [b] HB = Hydroboration.

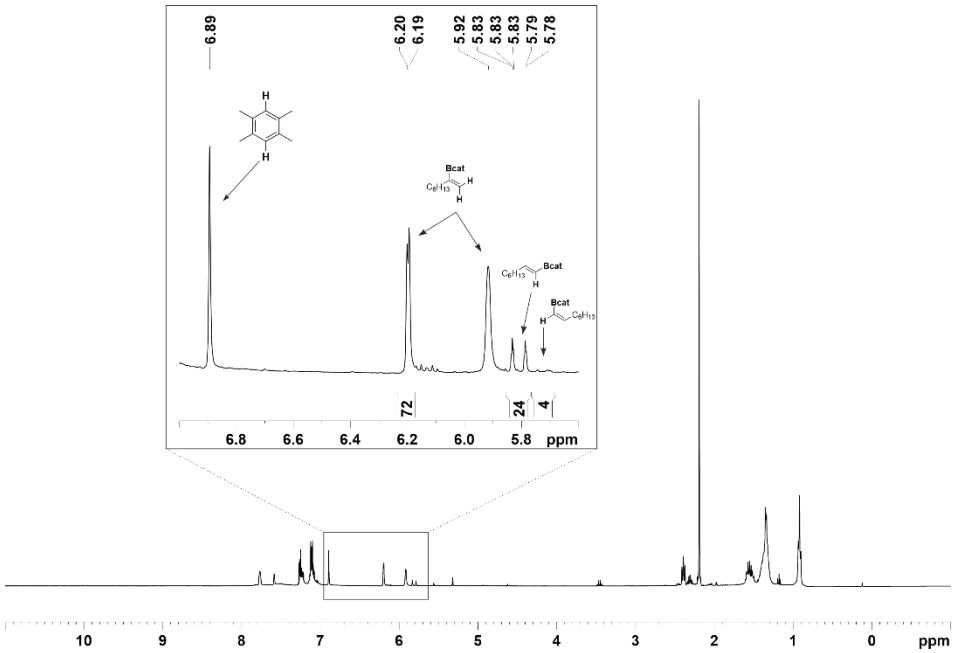

Figure 3.7. Catalytic hydroboration of **S1** (1.0 equiv.) with **HBcat** (1.0 equiv.) using complex **C1·BArF**.

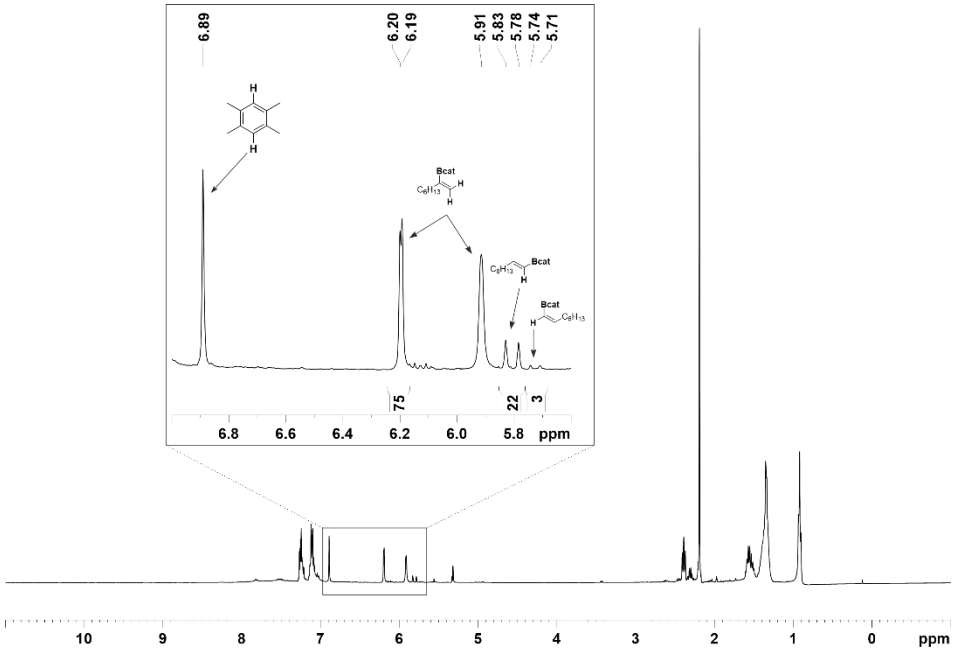

Figure 3.8. Catalytic hydroboration of **S1** (1.0 equiv.) with **HBcat** (1.0 equiv.) using complex **C1·OTf**.

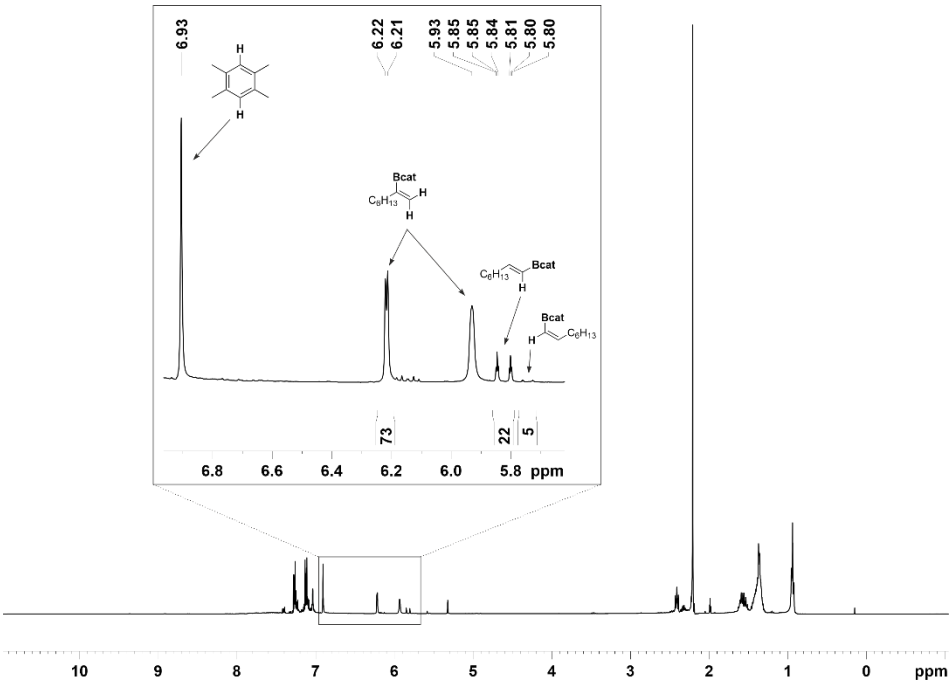

Figure 3.9. Catalytic hydroboration of **S1** (1.0 equiv.) with **HBcat** (1.0 equiv.) using complex **C1·NTf$_2$**.

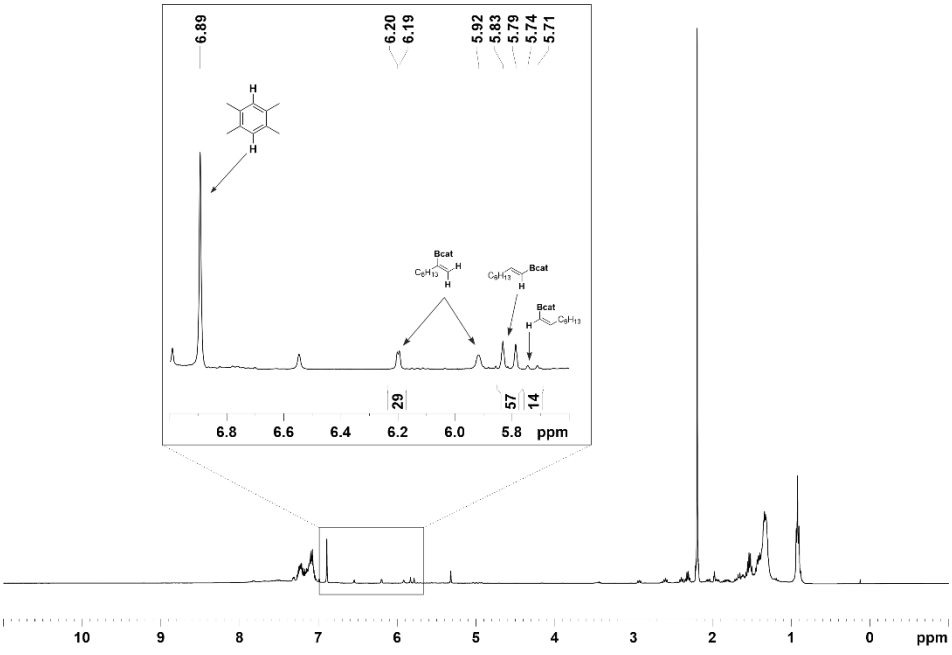

Figure 3.10. Catalytic hydroboration of **S1** (1.0 equiv.) with **HBcat** (1.0 equiv.) using complex **C1·BF$_4$**.

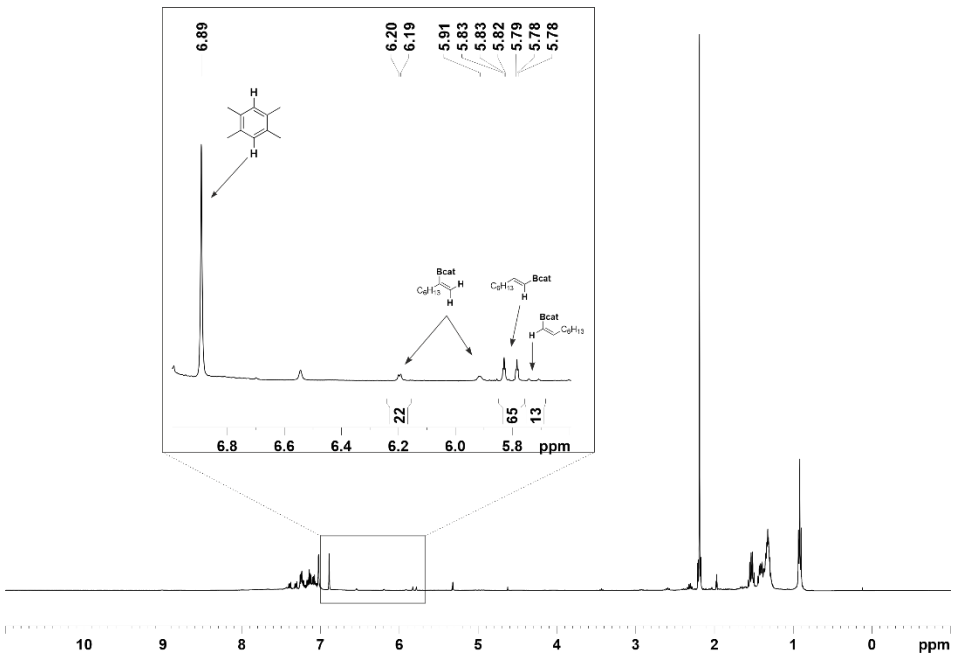

Figure 3.11. Catalytic hydroboration of **S1** (1.0 equiv.) with **HBcat** (1.0 equiv.) using complex **C1**·$\mathbf{PF_6}$.

Effects of the relative amounts of the borane and reaction time

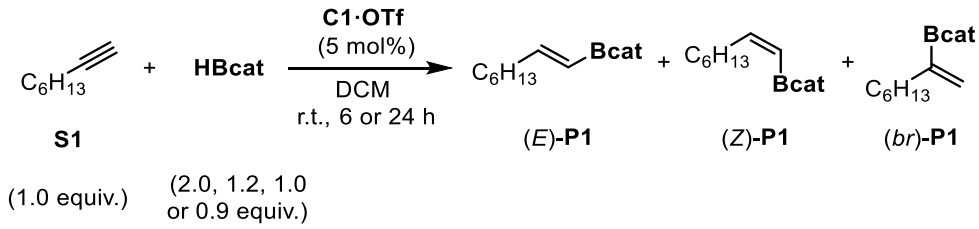

Table 3.8. Hydroboration of oct-1-yne **S1** (1.0 equiv.) with several amounts of **HBcat** using complexe **C1·OTf**. [a]

Entry	**HBcat** (equiv.)	Conv. (%)[c]	HB select. (%)[b]	Ratio *E:Z:br*
1	2.0	>99	96	35:8:57
2	1.2	>99	95	27:7:66
3	1.0	93	>99	22:3:75
4	0.9	>99	>99	19:4:77
5[d]	0.9	97	>99	17:5:78

[a] Reactions were performed in deuterated dichloromethane (*ca*. 0.3 M) under N_2 atmosphere for 24h at room temperature. Yields were determined by ^1H NMR using 1,2,4,5-tetramethylbenzene as the internal standard. HBcat = catecholborane. [b] HB = Hydroboration. [c] Alkyne conversion except for entry 4 and 5, which corresponds to **HBcat** conversion. [d] 6 hours of reaction time.

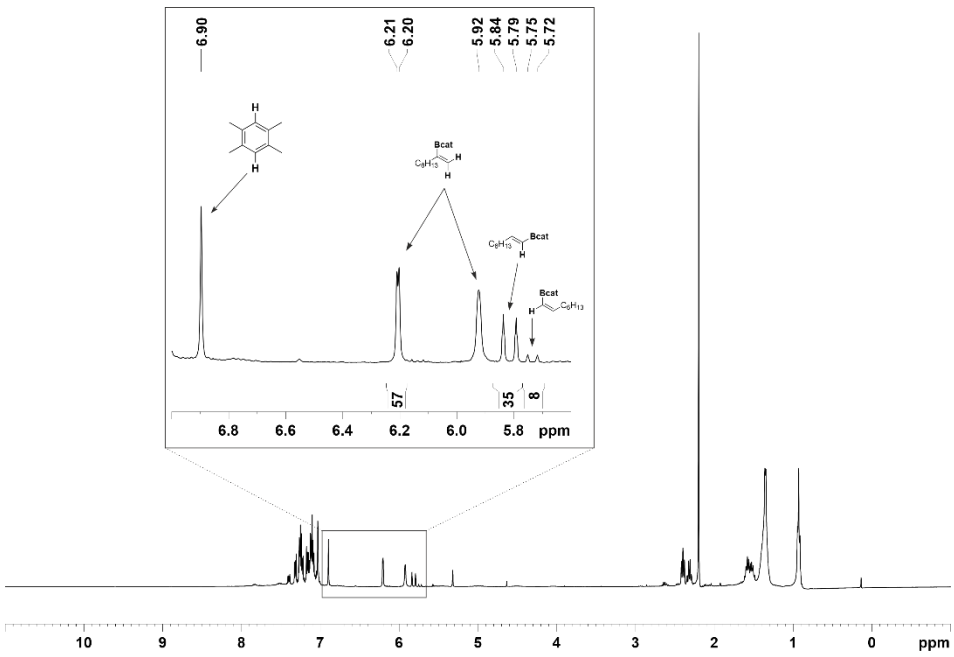

Figure 3.12. Catalytic hydroboration of **S1** (1.0 equiv.) with **HBcat** (2.0 equiv.) using complex **C1·OTf**.

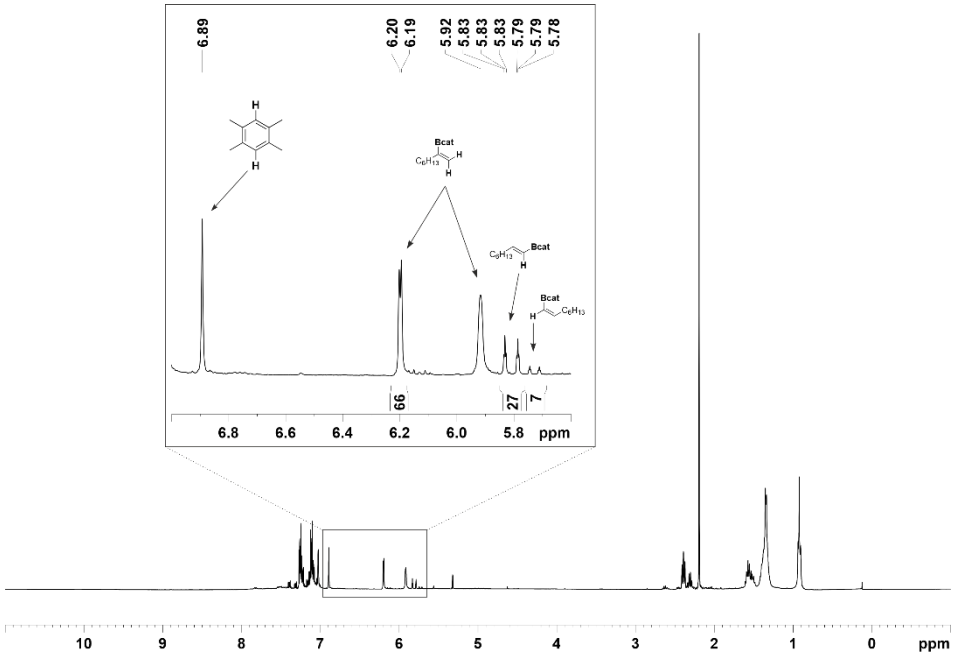

Figure 3.13. Catalytic hydroboration of **S1** (1.0 equiv.) with **HBcat** (1.2 equiv.) using complex **C1·OTf**.

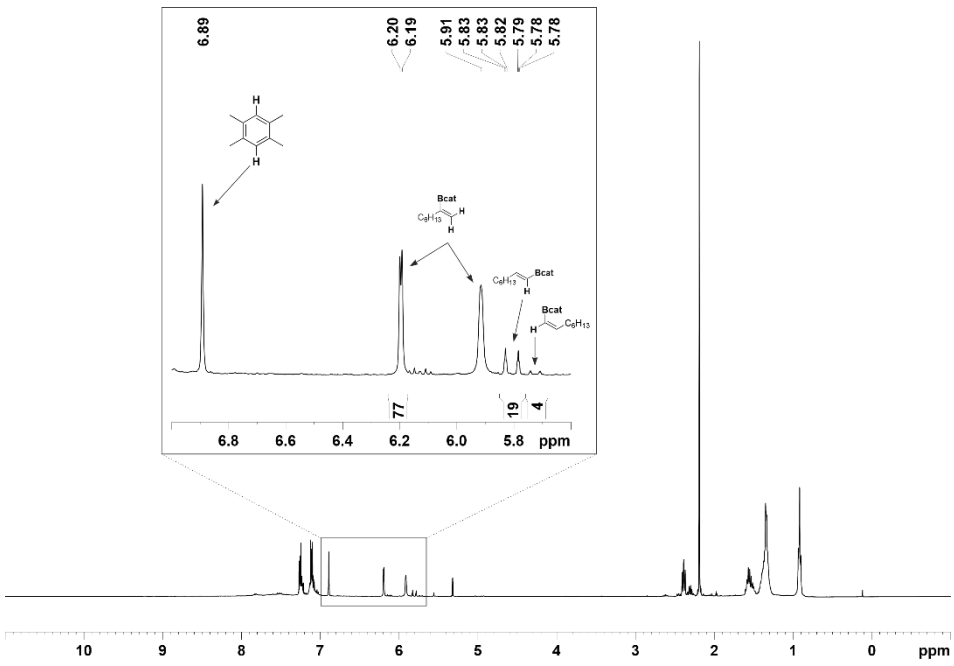

Figure 3.14. Catalytic hydroboration of **S1** (1.0 equiv.) with **HBcat** (0.9 equiv.) using complex **C1·OTf**.

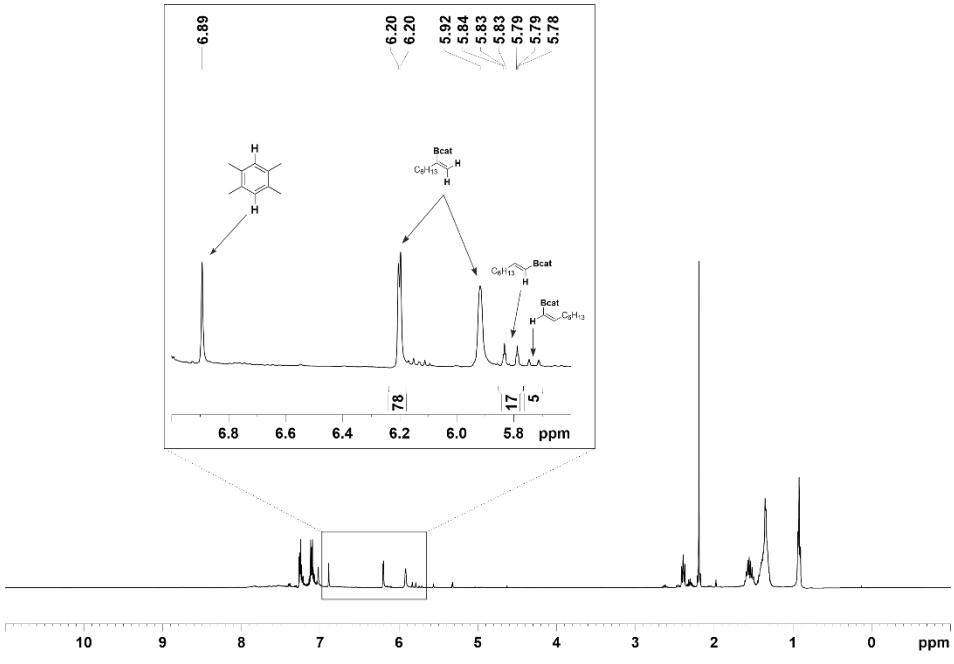

Figure 3.15. Catalytic hydroboration of **S1** (1.0 equiv.) with **HBcat** (0.9 equiv.) using complex **C1·OTf** at 6 hours.

Temperature screening of the hydroboration reaction

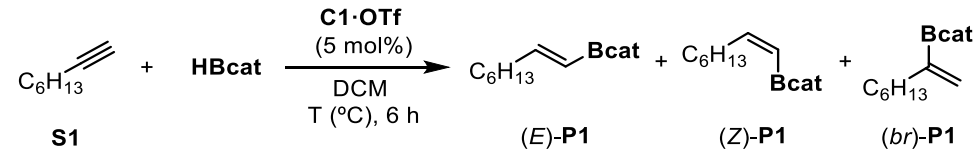

Table 3.9. Hydroboration of oct-1-yne **S1** (1.0 equiv.) with **HBcat** (0.9 equiv.) at several temperatures using complexe **C1·OTf**. [a]

Entry	T (ºC)	Conv. (%)	HB select. (%)[b]	Ratio *E:Z:br*
1	r.t.	97	>99	17:5:78
2	40	91	67	26:7:67
3	0	78	46	14:6:80

[a] Reactions were performed in deuterated dichloromethane (*ca.* 0.3 M) under N_2 atmosphere for 24h at room temperature. Yields were determined by ^1H NMR using 1,2,4,5-tetramethylbenzene as the internal standard. HBcat = catecholborane. [b] HB = Hydroboration.

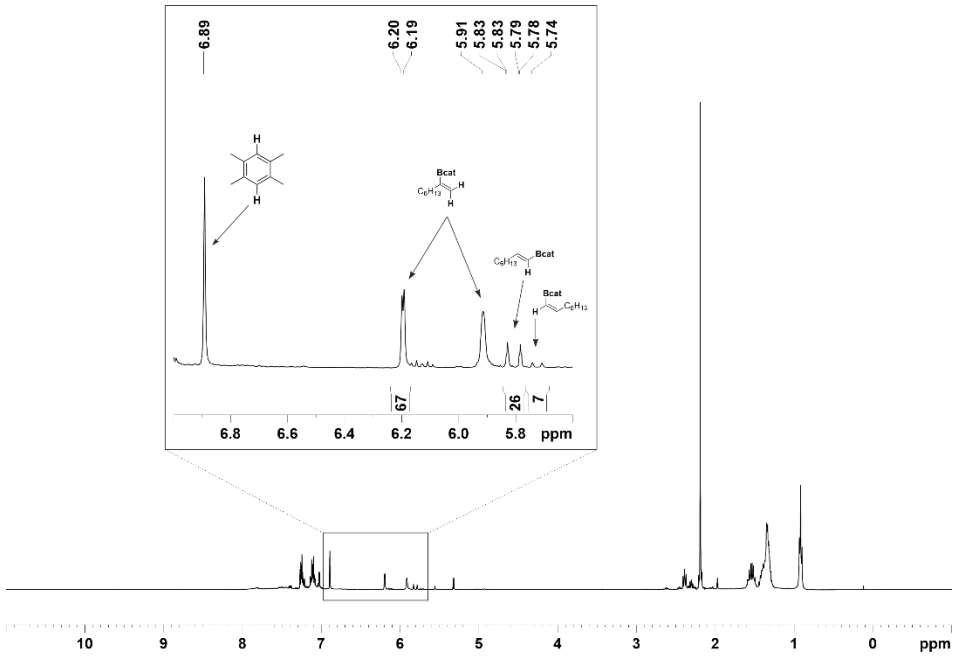

Figure 3.16. Catalytic hydroboration of **S1** (1.0 equiv.) with **HBcat** (0.9 equiv.) using complex **C1·OTf** at 40 ºC.

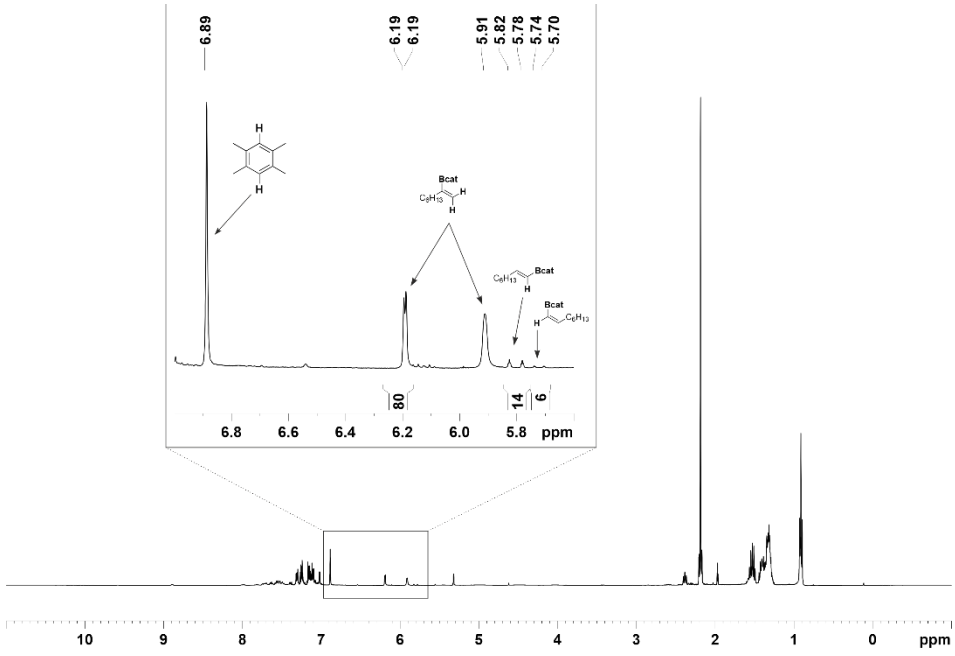

Figure 3.17. Catalytic hydroboration of **S1** (1.0 equiv.) with **HBcat** (0.9 equiv.) using complex **C1·OTf** at 0 ºC.

3.4.5 Conversions and yields at different reaction times

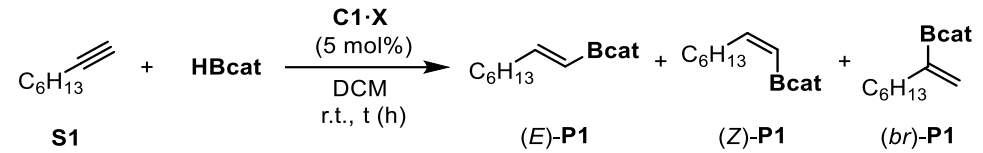

S1 (1.0 equiv.) (0.9 equiv.) (*E*)-P1 (*Z*)-P1 (*br*)-P1

Table 3.10. Conversions and yields for the hydroboration reaction using **C1·OTf** and **C1·BArF** at different reaction times.[a]

Entry	C1·OTf			C1·BArF		
	t (h)	Conv. (%)	HB Yield (%)[b]	t (h)	Conv. (%)	HB Yield (%)[b]
1	0	0	0	0	0	0
2	0.3	49.1	49.1	0.4	49.0	4.2
3	0.4	69.2	57.3	1.5	65.3	20.1
4	0.6	72.5	61.8	3.0	77.7	38.6
5	1.2	85.1	85.1	5.3	80.9	44.3
6	4.3	93.1	93.1	24.0	89.6	75.4
7	6.5	95.2	95.2			
8	24	99.9	99.9			

[a] Reactions were performed in deuterated dichloromethane (*ca.* 0.3 M) under N_2 atmosphere at room temperature. Conversions and yields were determined by ^1H NMR using 1,2,4,5-tetramethylbenzene as the internal standard. HBcat = catecholborane. [b] HB = Hydroboration.

3.4.6 Derivatization and isolation of Bdan borane products

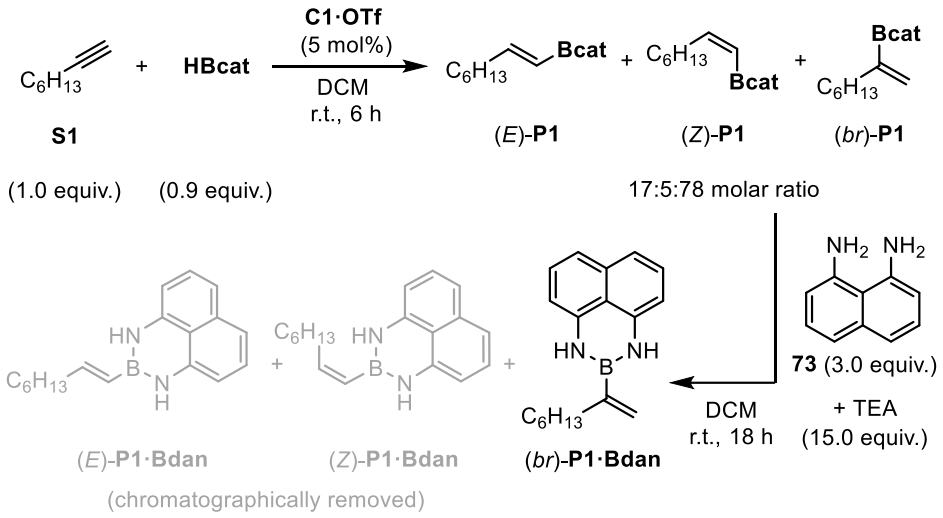

General procedure for derivatization[151] and isolation of borane products: The hydroboration reaction was performed following the general procedure indicated above (Section 3.4.4). In a separate vial, 129 mg of 1,8-diaminonaphthalene **73** (3.0 equiv.) was dissolved in TEA (15.0 equiv.) and 500 μL of DCM. The hydroboration reaction mixture was then added dropwise to the latter solution. The resulting reaction mixture was stirred for 18 h at room temperature and the solvent was removed under vacuum. Finally, the crude reaction mixture was purified by column chromatography using SiO_2 and a mixture of CyHex, DCM and TEA as eluent (100:0:0→78:20:2, CyHex:DCM:TEA).

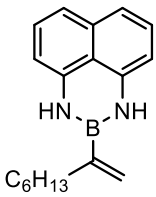
(*br*)-**P1·Bdan**

(*br*)-**P1·Bdan**: (*br*)-**P1·Bdan** was obtained as a colorless oil (14.6 mg, 25% yield). **^{1}H NMR** (400 MHz, $CDCl_3$) δ: 7.12 (t, *J* = 8.2 Hz, 2 H), 7.03 (dd, *J* = 8.2, 0.8 Hz, 2 H), 6.35 (dd, *J* = 7.3, 0.9 Hz, 2 H), 5.74 (br s, 2 H), 5.52 (s, 2 H), 2.22 (t, *J* = 7.4 Hz, 2 H), 1.51 – 1.44 (m, 2 H), 1.39 – 1.28 (m, 6 H), 0.91 (t, *J* = 7.0 Hz, 3 H) ppm. **^{13}C{^{1}H} NMR**

[151] Adapted from Yuan, K.; Wang, S. *Org. Lett.* **2017**, *19*, 1462-1465.

(100 MHz, $CDCl_3$) δ:[152] 141.1, 136.4, 127.6, 123.1, 119.8, 117.6, 105.8, 35.6, 31.8, 29.4, 29.1, 26.9, 22.7, 14.1 ppm. **$^{11}B\{^1H\}$ NMR** (128 MHz, $CDCl_3$) δ: 28.4 ppm. Spectroscopic NMR data were consistent with those previously reported.[126d]

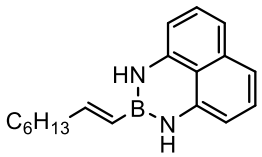

(*E*)-**P1·Bdan**

(*E*)-**P1·Bdan**: (*E*)-**P1·Bdan** was provided as a colorless oil (2.3 mg, 4 % Yield). **^1H NMR** (400 MHz, $CDCl_3$) δ: 7.10 (t, *J* = 8.0 Hz, 2 H), 6.99 (d, *J* = 8.1 Hz, 2 H), 6.37 (dt, *J* = 18.1, 6.4 Hz, 1 H), 6.31 (d, *J* = 7.4 Hz, 2 H), 5.69 (br s, 2 H), 5.55 (d, *J* = 18.3 Hz, 1 H), 2.20 (m, 2 H), 1.51 – 1.43 (m, 2 H), 1.39 – 1.30 (m, 6 H), 0.90 (t, *J* = 7.0 Hz, 3 H) ppm. **$^{13}C\{^1H\}$ NMR** (100 MHz, $CDCl_3$) δ:[152] 148.3, 141.4, 136.5, 127.7, 117.5, 105.7, 36.0, 31.9, 29.0, 28.8, 22.8, 14.3 ppm. **$^{11}B\{^1H\}$ NMR** (128 MHz, $CDCl_3$) δ: 27.5 ppm. Spectroscopic NMR data were consistent with those previously reported.[153]

[152] The signal of the carbon bonded to the boron atom was not observed due to quadrupolar relaxation.

[153] Nishikawa, D.; Hirano, K.; Miura, M. *J. Am. Chem. Soc.* **2015**, *137*, 15620-15623.

3.4.7 One-pot hydroboration/*Csp*²–*Csp*² coupling process

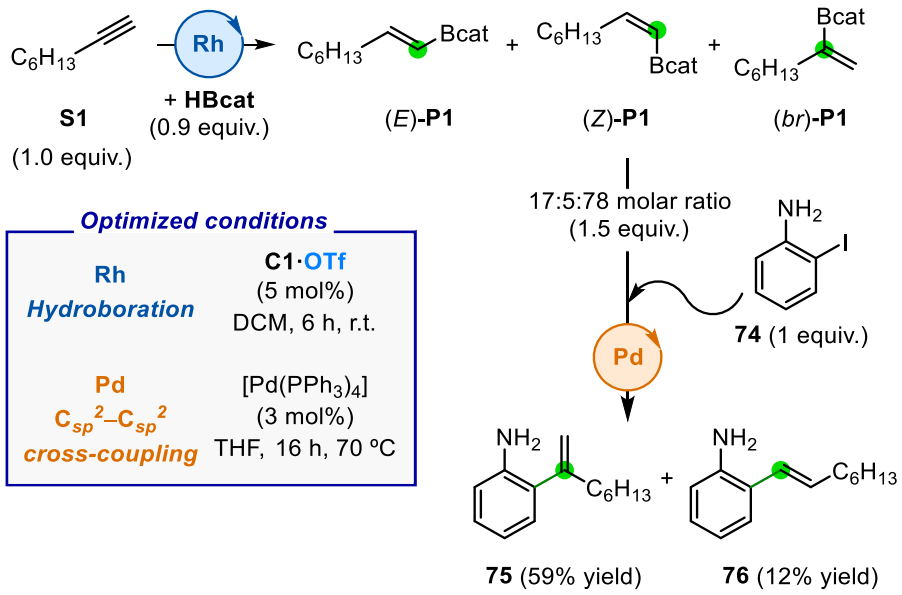

One-pot process for the hydroboration and C–C coupling. *Hydroboration*: 157.0 mg (5 mol%) of **C1·OTf** and 10.0 mL of dichloromethane (0.3 M) were placed under N_2 in a 25 mL Schlenk flask provided with a stirrer. Then, 439.0 µL, (3.0 mmol, 1.0 equiv.) of 1-octyne **S1** and 295.0 µL (2.7 mmol, 0.9 equiv.) of catecholborane **HBcat** were added. The reaction mixture was stirred at room temperature for 6 h. The resulting dark red solution was partially evaporated and mixed with 3 mL of *n*-pentane, leading to the appearance of a red precipitate, which was removed. Volatiles were evaporated under vacuum to yield 549 mg of a mixture of (*br*)-**P1**, (*E*)-**P1** and (*Z*)-**P1** as a brown oil. This mixture of alkenyl boronates was directly used in the next step. *C-C coupling*:[154] a pressure tube provided with a stirrer was charged under N_2 with 52.8 mg (3 mol%) of tetrakis(triphenylphosphine)palladium, 184.0 mg (4.5 mmol, 3.0 equiv.) of powdered sodium hydroxide, 337.0 mg (1.5 mmol, 1.0 equiv.) of 2-iodoaniline **74**, the hydroboration mixture previously prepared (2.3 mmol of alkenyl boronates, 1.5 equiv.) and 4.6 mL of

[154] Adapted from Satoh, M.; Miyaura, N.; Suzuki, A. *Synthesis* **1987**, *1987*, 373-377.

tetrahydrofuran. This mixture was heated at reflux for 16 h and then cooled down to room temperature. The unreacted borane was decomposed by adding 1.3 mL of NaOH 3 M and 0.3 mL of 30% H_2O_2. The resulting mixture was extracted with toluene (2 x 80 mL). The organic phase was washed with saturated NaCl solution (140 mL) and dried over Na_2SO_4. The solvent was removed under vacuum and the residue was purified by flash chromatography using *n*-pentane as the eluent in order to isolate products **75** (1st fraction: 60 mg, >95% purity, 0.3 mmol; 2nd fraction: 242 mg, 89% purity, 1.06 mmol; 59% overall yield) and **76** (36 mg, 0.18 mmol, 12% yield) as viscous oils.

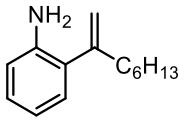

75

Product 75: **^{1}H NMR** (400 MHz, $CDCl_3$) δ: 7.06 (dd, *J* = 7.4, 1.6 Hz, 1 H), 6.98 (dd, *J* = 7.5, 1.6 Hz, 1 H), 6.74 – 6.68 (m, 2 H), 5.26 (m, 1 H), 5.04 (d, *J* = 2.3 Hz, 1 H), 3.78 (s, 2 H), 2.36 (t, *J* = 7.4 Hz, 2 H), 1.45 – 1.37 (m, 2 H), 1.33 – 1.25 (m, 6 H), 0.87 (t, *J* = 7.0 Hz, 3 H) ppm. **^{13}C{^{1}H} NMR** (100 MHz, $CDCl_3$) δ: 148.3, 143.3, 129.0, 128.7, 127.9, 118.2, 115.5, 114.4, 37.5, 31.8, 29.2, 22.8, 14.2 ppm. **HRMS** (ESI) *m/z*: calcd. for $C_{14}H_{22}N$ $[M+H]^+$ 204.1752, found 204.1738.

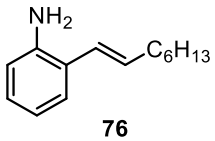

76

Product 76: **^{1}H NMR** (400 MHz, $CDCl_3$) δ: 7.22 (dd, *J* = 7.6, 1.4 Hz, 1 H), 7.06 (td, *J* = 7.7, 1.5 Hz, 1 H), 6.74 (d, *J* = 7.6 Hz, 1 H), 6.67 (dd, *J* = 8.0, 1.2 Hz 1 H), 6.39 (d, *J* = 15.8 Hz, 1 H), 6.07 (dt, *J* = 15.7, 7.0 Hz, 1 H), 3.70 (s, 2 H), 2.25 – 2.19 (m, 2 H), 1.50 – 1.43 (m, 2 H), 1.33 – 1.24 (m, 6 H), 0.87 (t, *J* = 6.9 Hz, 3 H) ppm. **^{13}C{^{1}H} NMR** (100 MHz, $CDCl_3$) δ: 143.4, 127.9, 127.5, 125.3, 124.6, 119.0, 115.9, 114.4, 33.6, 31.9, 29.6, 29.0, 22.8, 14.2 ppm. **HRMS** (ESI) *m/z*: calcd. for $C_{14}H_{22}N$ $[M+H]^+$ 204.1752, found 204.1744.

3.4.8 Spectroscopic analysis of the substrate scope

Catalytic hydroboration of S1 *with* HBcat *using complex* C1·OTf

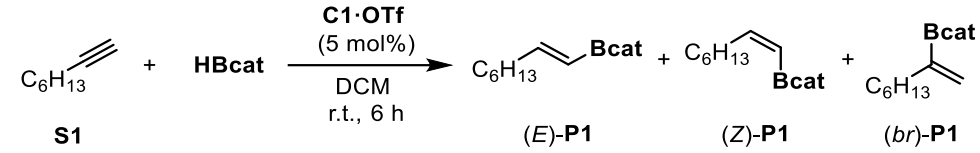

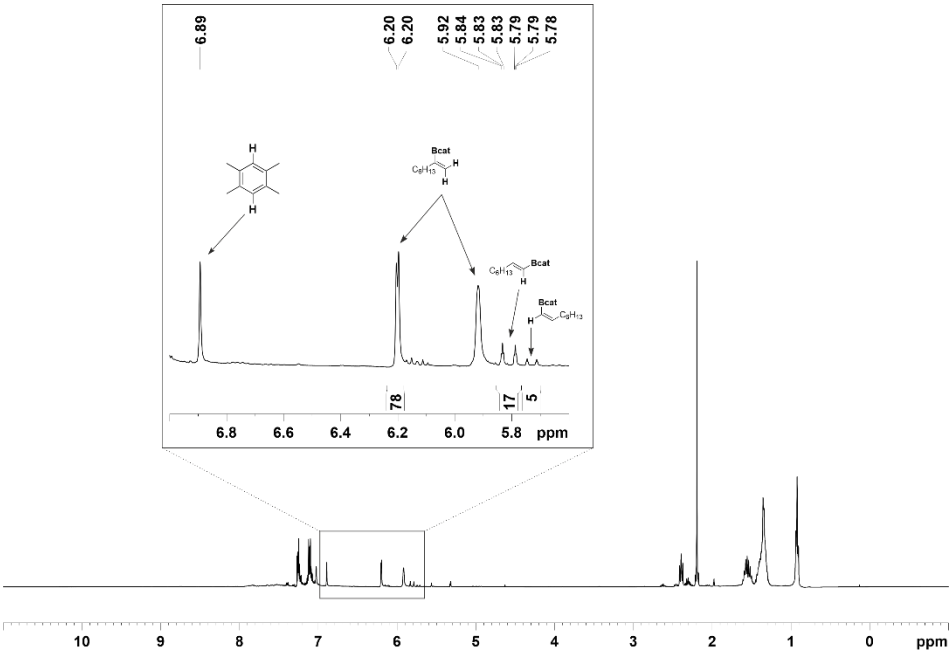

Figure 3.18. Reaction mixture ^{1}H NMR (400 MHz, CD_2Cl_2) of the catalytic hydroboration of **S1** and **HBcat** using complex **C1·OTf**.

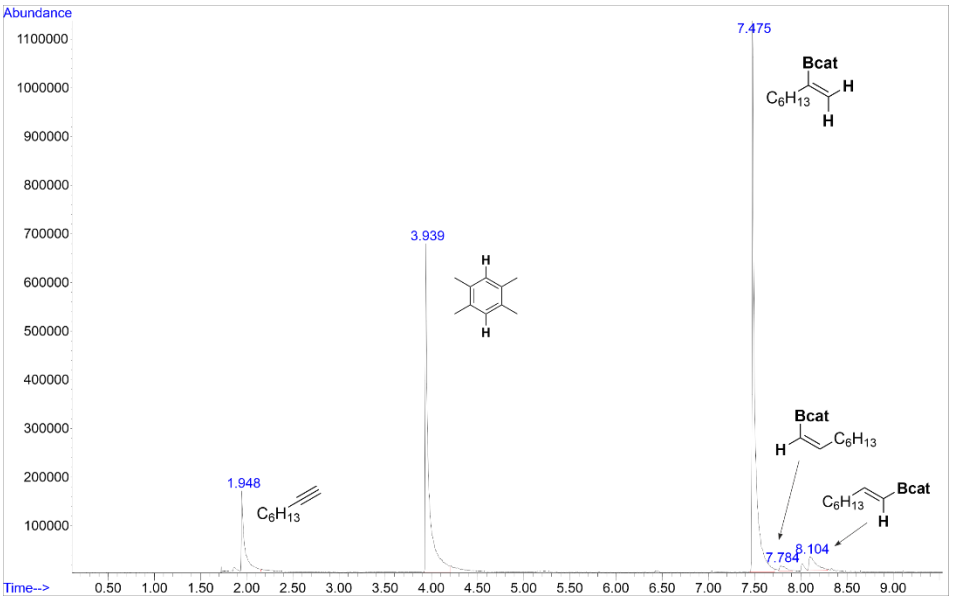

Figure 3.19. Reaction mixture GC-MS of the catalytic hydroboration of **S1** and **HBcat** using complex **C1·OTf**.

Spectroscopic characterization of (*E*)-**P1,** (*Z*)-**P1** and (*br*)-**P1** mixture:[155] **^{1}H NMR** (400 MHz, CD_2Cl_2) δ:[156] 7.27 – 7.24 (m, Bcat 6 H), 7.12 –.7.09 (m, Bcat 6 H), 6.19 (d, *J* = 3.1 Hz, (*br*)-**P1**, 1 H), 5.91 (s, (*br*)-**P1**, 1 H), 5.81 (dt, *J* = 18.0, 1.5 Hz, (*E*)-**P1**, 1 H), 5.72 (d, *J* = 13.6 Hz, (*Z*)-**P1**, 1 H), 2.39 (t, *J* = 7.7 Hz, (*br*)-**P1**, 2 H), 2.35 – 2.26 (m, (*E*)-**P1**, 2 H), 1.61 – 1.46 (m, CH_2 (*E*)-**P1**, (*Z*)-**P1** and (*br*)-**P1**), 1.45 – 1.26 (m, CH_2 (*E*)-**P1**, (*Z*)-**P1** and (*br*)-**P1**), 0.96 – 0.87 (m, CH_3 (*E*)-**P1**, (*Z*)-**P1** and (*br*)-**P1**) ppm. **GC-MS** *m/z*: calcd. for (*E*)-**P1** $[M]^+$ 230.2, found 230.2; calcd. for (*Z*)-**P1** $[M]^+$ 230.2, found 230.2; calcd. for (*br*)-**P1** $[M]^+$ 230.2, found 230.2.

[155] Products obtained from the hydroboration reaction have been characterized using ^{1}H NMR as a mixture of products (*E*)-**P1,** (*Z*)-**P1** and (*br*)-**P1.**

[156] For characterization of (*E*)-**P1,** (*Z*)-**P1** and (*br*)-**P1**, see reference 70.

***Catalytic hydroboration of* S2 *with* HBcat *using complex* C1·OTf**

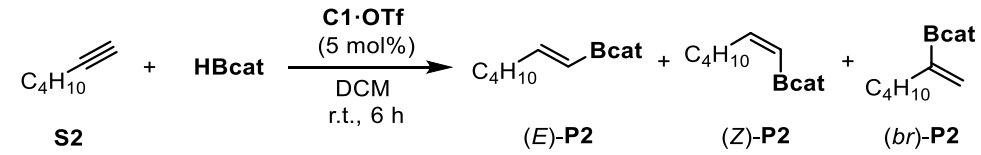

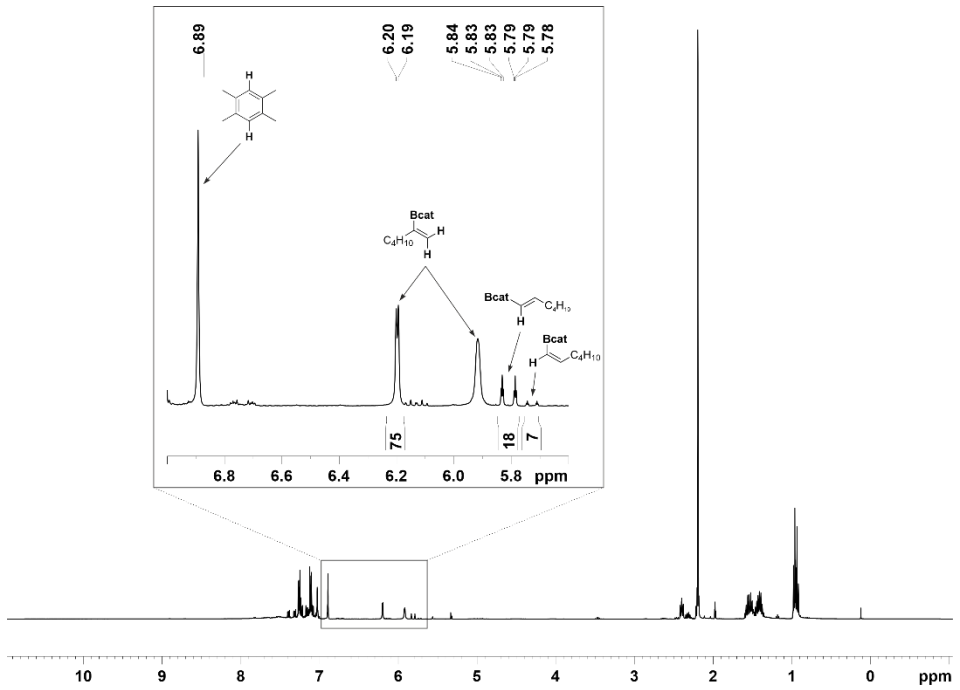

Figure 3.20. Reaction mixture ^{1}H NMR (400 MHz, CD_2Cl_2) of the catalytic hydroboration of **S2** and **HBcat** using complex **C1·OTf**.

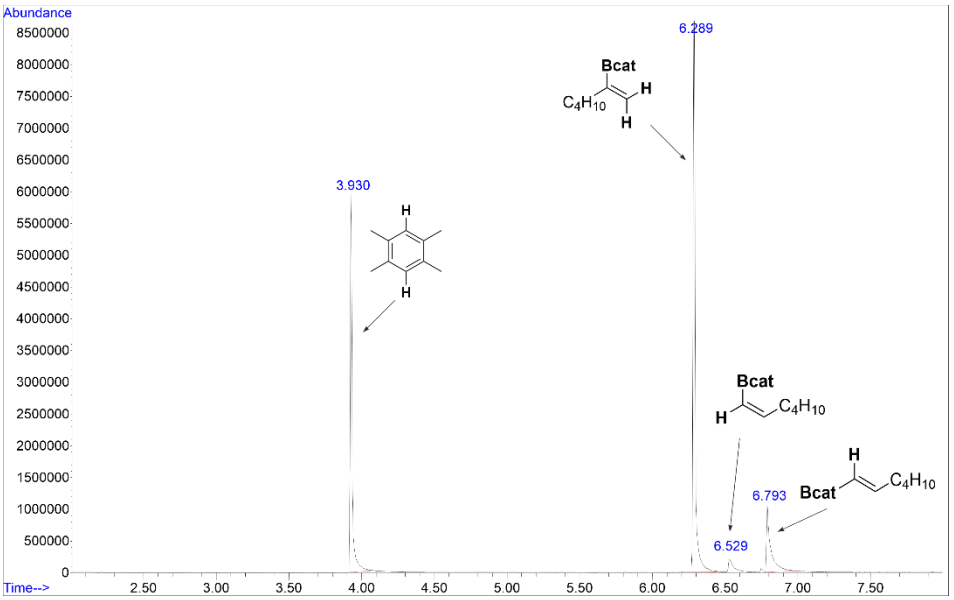

Figure 3.21. Reaction mixture GC-MS of the catalytic hydroboration of **S2** and **HBcat** using complex **C1·OTf**.

Spectroscopic characterization of (*E*)-**P2,** (*Z*)-**P2** and (*br*)-**P2** mixture:[155] **^{1}H NMR** (400 MHz, CD_2Cl_2) δ:[157] 7.28 – 7.20 (m, Bcat, 6 H), 7.14 – 7.06 (m, Bcat, 6 H), 6.19 (d, *J* = 3.0 Hz, (*br*)-**P2**, 1 H), 5.91 (s, (*br*)-**P2**, 1 H), 5.81 (dt, *J* = 18.0, 1.5 Hz, (*E*)-**P2**, 1 H), 5.72 (dt, *J* = 13.6, 1.5 Hz, (*Z*)-**P2**, 1 H), 2.40 (t, *J* = 7.6 Hz, (*br*)-**P2**, 2 H), 2.35 – 2.27 (m, (*E*)-**P2**, 2 H), 1.61 – 1.46 (m, CH_2 (*E*)-**P2**, (*Z*)-**P2** and (*br*)-**P2**), 1.46 – 1.34 (m, CH_2 (*E*)-**P2**, (*Z*)-**P2** and (*br*)-**P2**), 0.98 – 0.87 (m, CH_3 (*E*)-**P2**, (*Z*)-**P2** and (*br*)-**P2**) ppm. **GC-MS** *m/z*: calcd. for (*E*)-**P2** $[M]^+$ 202.1, found 202.1; calcd. for (*Z*)-**P2** $[M]^+$ 202.1, found 202.1; calcd. for (*br*)-**P2** $[M]^+$ 202.1, found 202.1.

[157] ^{1}H NMR signals of (*E*)-**P2,** (*Z*)-**P2** and (*br*)-**P2** have been asigned based on their homologous compounds (*E*)-**P1,** (*Z*)-**P1** and (*br*)-**P1**. (a) For characterization of (*E*)-**P2**, see reference 150; (b) For analogous Bpin (pinacholborane) compounds, see: Ganić, A.; Pfaltz, A. *Chem. – Eur. J.* **2012**, *18*, 6724-6728 for (*br*)-isomer.

***Catalytic hydroboration of* S3 *with* HBcat *using complex* C1·OTf**

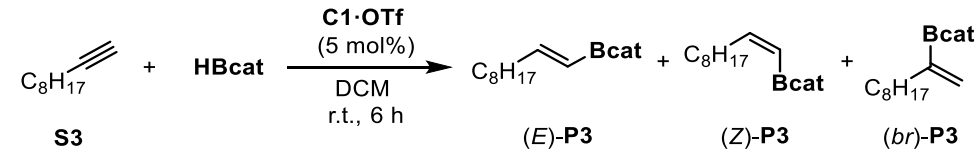

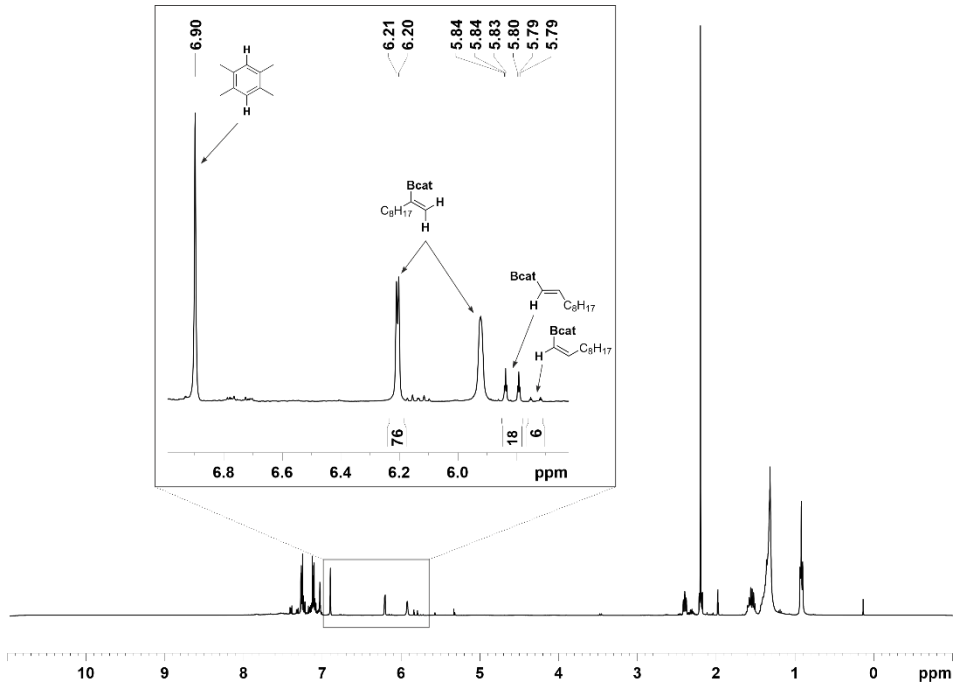

Figure 3.22. Reaction mixture ^{1}H NMR (400 MHz, CD_2Cl_2) of the catalytic hydroboration of **S3** and **HBcat** using complex **C1·OTf**.

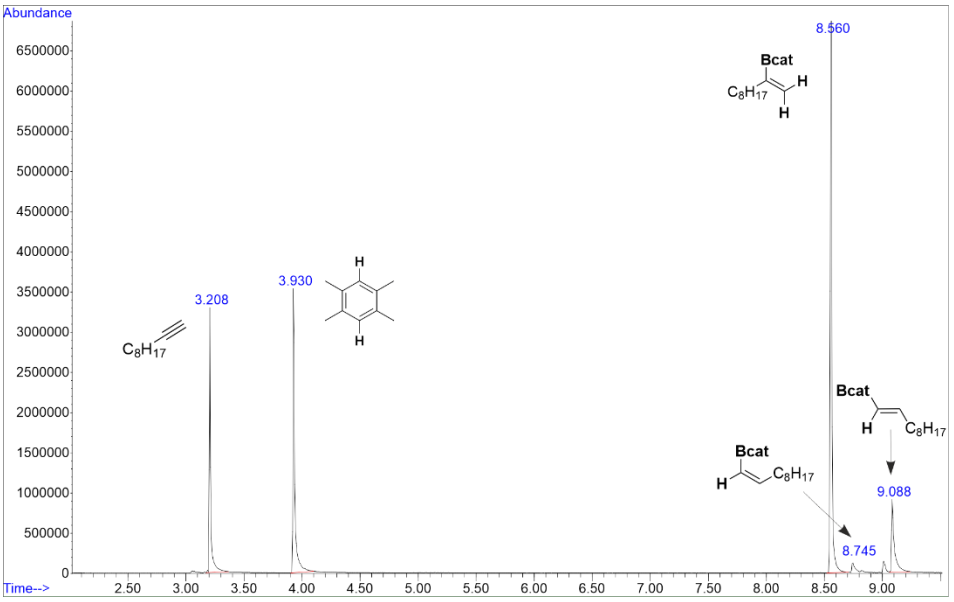

Figure 3.23. Reaction mixture GC-MS of the catalytic hydroboration of **S3** and **HBcat** using complex **C1·OTf**.

Spectroscopic characterization of (*E*)-**P3,** (*Z*)-**P3** and (*br*)-**P3** mixture:[155] **^{1}H NMR** (400 MHz, CD_2Cl_2) δ:[158] 7.28 – 7.21 (m, Bcat, 6 H), 7.14 – 7.07 (m, Bcat, 6 H), 6.20 (d, *J* = 2.9 Hz, (*br*)-**P3**, 1 H), 5.92 (s, (*br*)-**P3**, 1 H), 5.81 (dt, *J* = 18.1, 1.6 Hz, (*E*)-**P3**, 1 H), 5.73 (dt, *J* = 13.6, 1.5 Hz, (*Z*)-**P3**, 1 H), 2.40 (t, *J* = 7.5 Hz, (*br*)-**P3**, 2 H), 2.35 – 2.26 (m, (*E*)-**P3**, 2 H), 1.65 – 1.47 (m, CH_2 (*E*)-**P3**, (*Z*)-**P3** and (*br*)-**P3**), 1.46 – 1.25 (m, CH_2 (*E*)-**P3**, (*Z*)-**P3** and (*br*)-**P3**), 0.96 – 0.87 (m, CH_3 (*E*)-**P3**, (*Z*)-**P3** and (*br*)-**P3**) ppm. **GC-MS** *m/z*: calcd. for (*E*)-**P3** $[M]^+$ 258.2, found 258.1; calcd. for (*Z*)-**P3** $[M]^+$ 258.2, found 258.1; calcd. for (*br*)-**P3** $[M]^+$ 258.2, found 258.2.

[158] ^{1}H NMR signals of (*E*)-**P3,** (*Z*)-**P3** and (*br*)-**P3** have been asigned based on their homologous compounds (*E*)-**P1,** (*Z*)-**P1** and (*br*)-**P1**. (a) For characterization of (*Z*)-**P3**, see: Ohmura, T.; Yamamoto, Y.; Miyaura, N. *J. Am. Chem. Soc.* **2000**, *122*, 4990-4991; (b) For analogous Bpin (pinacholborane) compounds, see: Takagi, J.; Takahashi, K.; Ishiyama, T.; Miyaura, N. *J. Am. Chem. Soc.* **2002**, *124*, 8001-8006 for (*Z*)- and (*br*)-isomes; Lu, W.; Shen, Z. *Org. Lett.* **2019**, *21*, 142-146 for (*E*)-isomer.

***Catalytic hydroboration of* S4 *with* HBcat *using complex* C1·OTf**

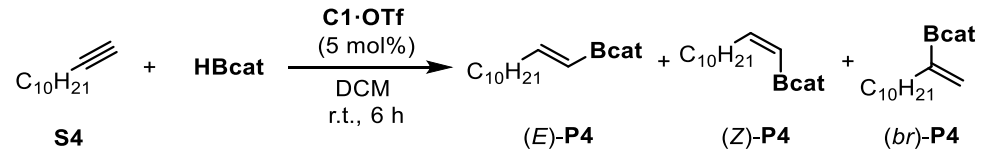

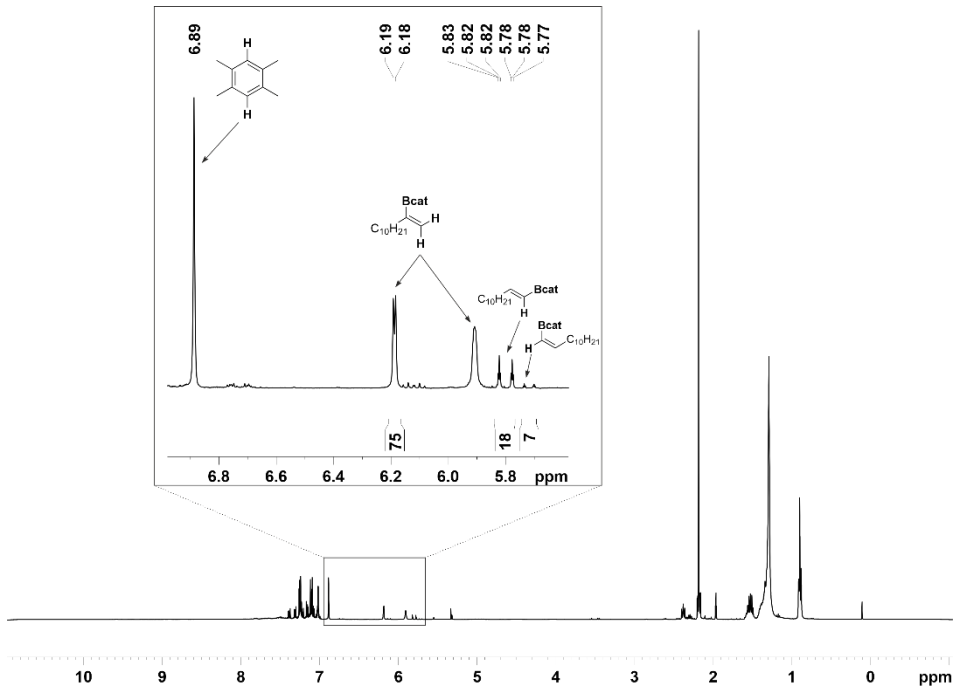

Figure 3.24. Reaction mixture ^{1}H NMR (400 MHz, CD_2Cl_2) of the catalytic hydroboration of **S4** and **HBcat** using complex **C1·OTf**.

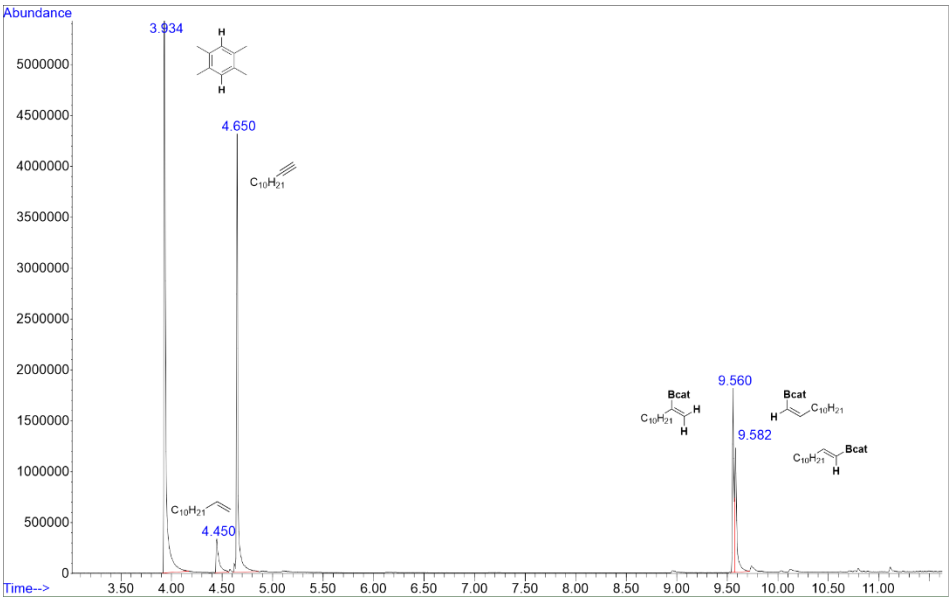

Figure 3.25. Reaction mixture GC-MS of the catalytic hydroboration of **S4** and **HBcat** using complex **C1·OTf**.

Spectroscopic characterization of (*E*)-**P4,** (*Z*)-**P4** and (*br*)-**P4** mixture:[155] **^{1}H NMR** (400 MHz, CD_2Cl_2) δ:[159] 7.28 – 7.21 (m, Bcat, 6 H), 7.14-7.07 (m, Bcat, 6 H), 6.19 (d, *J* = 2.9 Hz, (*br*)-**P4**, 1 H), 5.91 (s, (*br*)-**P4**, 1 H), 5.80 (dt, *J* = 18.0, 1.6 Hz, (*E*)-**P4**, 1 H), 5.71 (dt, *J* = 13.6, 1.5 Hz, (*Z*)-**P4**, 1 H), 2.38 (t, *J* = 7.7 Hz, (*br*)-**P4**, 2 H), 2.34 – 226 (m, (*E*)-**P4**, 2 H), 1.59 – 1.47 (m, CH_2 (*E*)-**P4**, (*Z*)-**P4** and (*br*)-**P4**), 1.44 – 1.23 (m, CH_2 (*E*)-**P4**, (*Z*)-**P4** and (*br*)-**P4**), 0.94 – 0.86 (m, CH_3 (*E*)-**P4**, (*Z*)-**P4** and (*br*)-**P4**) ppm. **GC-MS** *m/z*: calcd. for (*E*)-**P4** $[M]^+$ 286.2, found 286.1; calcd. for (*br*)-**P4** $[M]^+$ 286.2, found 286.1.

[159] ^{1}H NMR signals of (*E*)-**P4,** (*Z*)-**P4** and (*br*)-**P4** have been asigned based on their homologous compounds (*E*)-**P1,** (*Z*)-**P1** and (*br*)-**P1**.

***Catalytic hydroboration of* S5 *with* HBcat *using complex* C1·OTf**

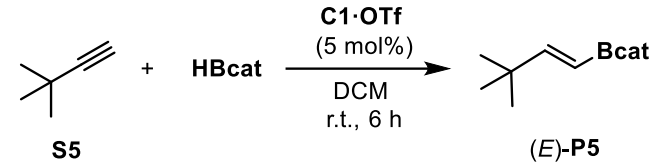

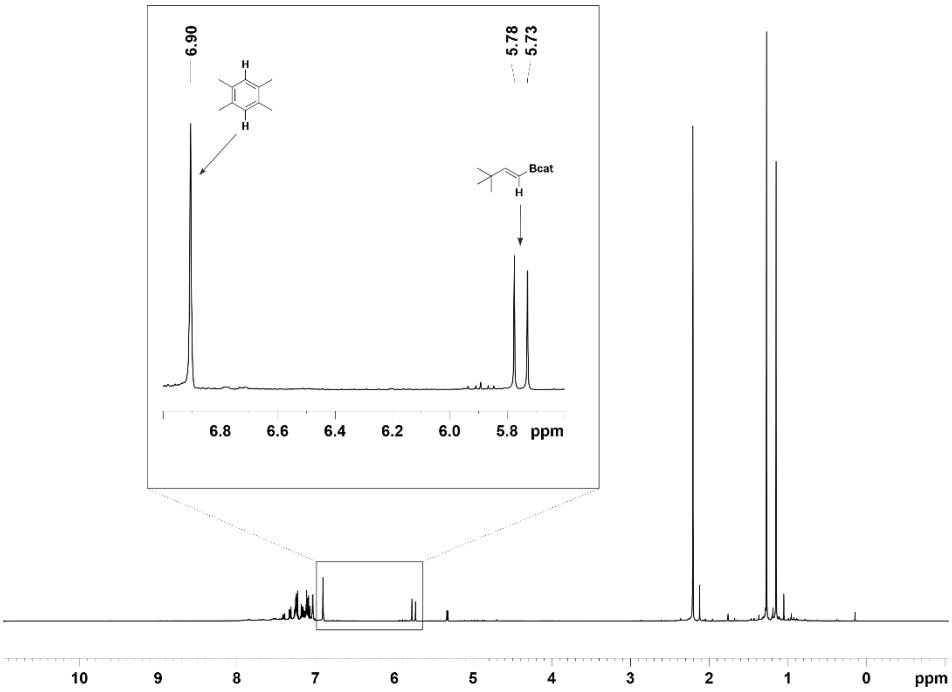

Figure 3.26. Reaction mixture ^{1}H NMR (400 MHz, CD_2Cl_2) of the catalytic hydroboration of **S5** and **HBcat** using complex **C1·OTf**.

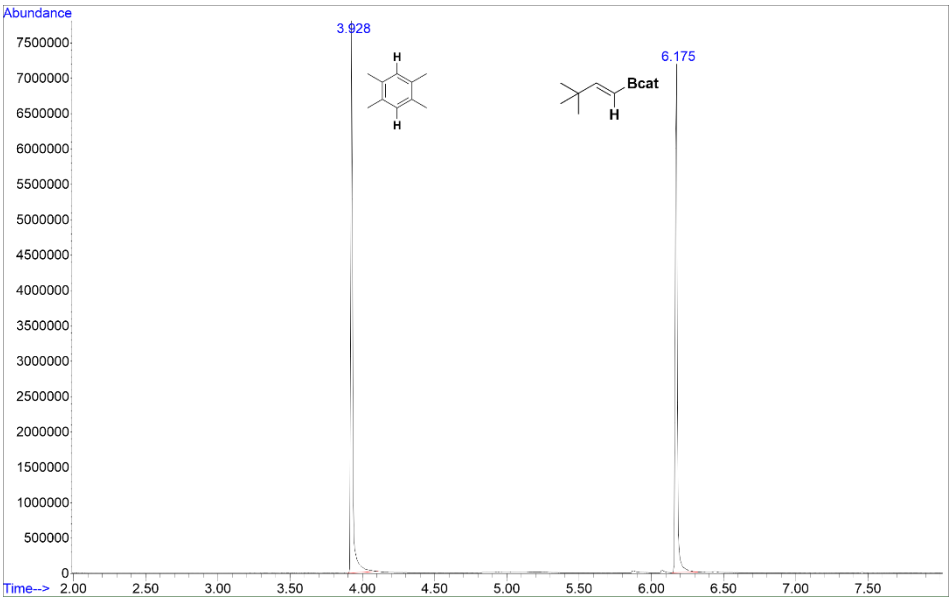

Figure 3.27. Reaction mixture GC-MS of the catalytic hydroboration of **S5** and **HBcat** using complex **C1·OTf**.

Spectroscopic characterization of (*E*)-**P5**: **^{1}H NMR** (400 MHz, CD_2Cl_2) δ:[160] 7.30 – 7.24 (m, Bcat, 2 H), 7.19 – 7.06 (m, Bcat, 2 H), 5.79 (d, *J* = 18.3 Hz, (*E*)-**P5**, 1 H), 1.18 (s, (*E*)-**P5**, 9 H) ppm. **GC-MS** *m/z*: calcd. for calcd. for (*E*)-**P5** $[M]^+$ 202.1, found 202.1.

[160] For characterization of (*E*)-**P5**, see reference 150.

***Catalytic hydroboration of* S6 *with* HBcat *using complex* C1·OTf**

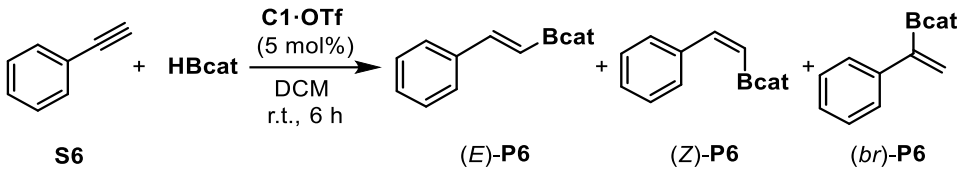

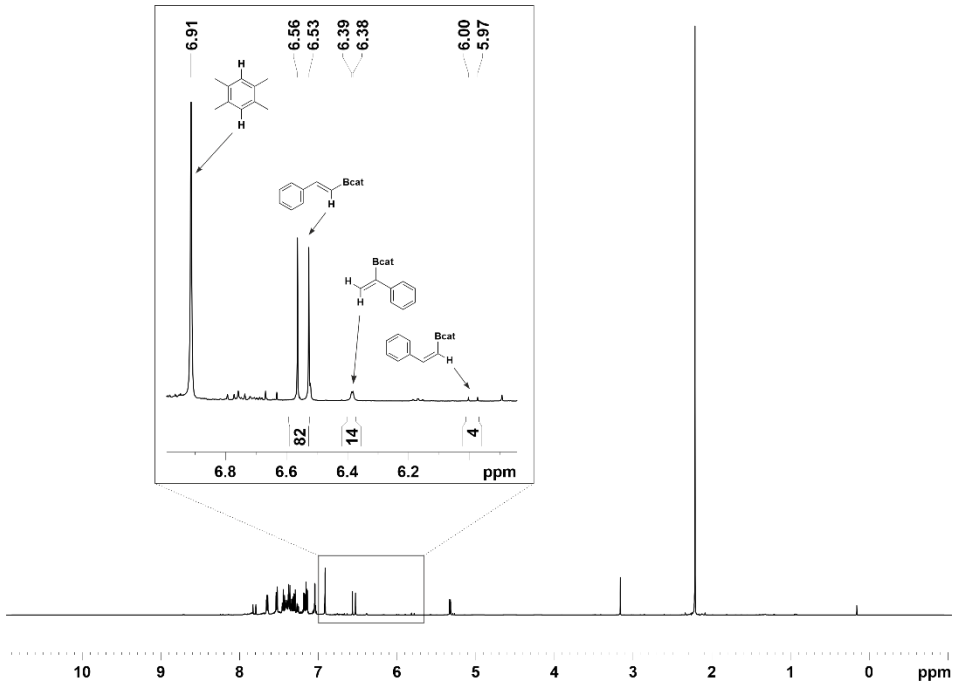

Figure 3.28. Reaction mixture ^{1}H NMR (400 MHz, CD_2Cl_2) of the catalytic hydroboration of **S6** and **HBcat** using complex **C1·OTf**.

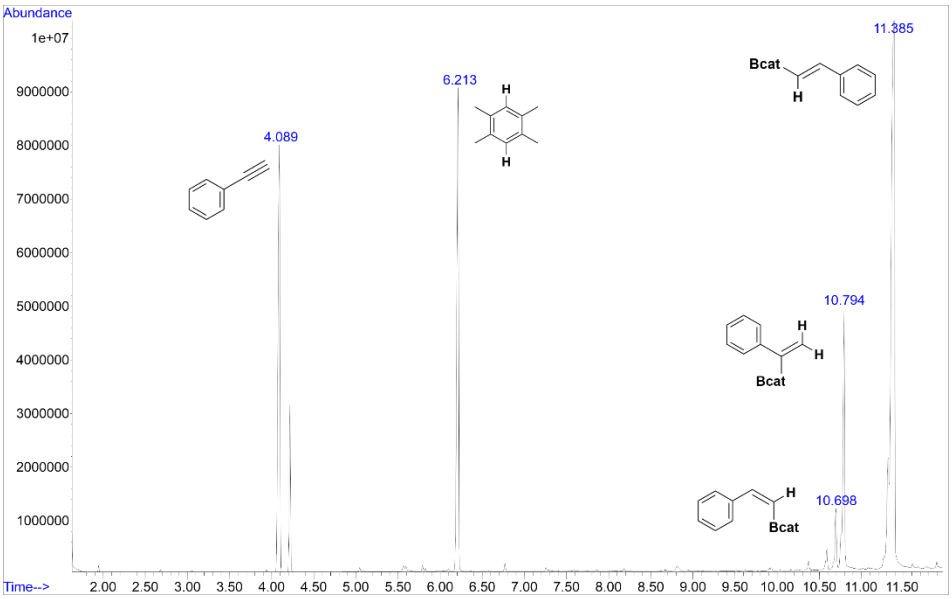

Figure 3.29. Reaction mixture GC-MS of the catalytic hydroboration of **S6** and **HBcat** using complex **C1·OTf**.

Spectroscopic characterization of (*E*)-**P6,** (*Z*)-**P6** and (*br*)-**P6** mixture:[155] **^{1}H NMR** (400 MHz, CD_2Cl_2) δ:[161] 7.80 (d, *J* = 18.4 Hz, (*E*)-**P6**, 1 H), 7.67 – 7.12 (m, Bcat, CH, (*E*)-**P6**, (*Z*)-**P6** and (*br*)-**P6**), 6.55 (d, *J* = 18.5 Hz, (*E*)-**P6**,1 H), 6.38 (d, *J* = 2.1 Hz, (*br*)-**P6**,1 H), 5.99 (d, *J* = 14.8 Hz, (Z)-**P6**,1 H) ppm. **GC-MS** *m/z*: calcd. for (*E*)-**P6** $[M]^+$ 222.1, found 222.1; calcd. for (*Z*)-**P6** $[M]^+$ 222.1, found 222.1; calcd. for (*br*)-**P6** $[M]^+$ 222.1, found 222.2.

[161] For characterization of (*E*)-**P6,** (*Z*)-**P6** and (*br*)-**P6**, see reference 70 and 150.

***Catalytic hydroboration of* S7 *with* HBcat *using complex* C1·OTf**

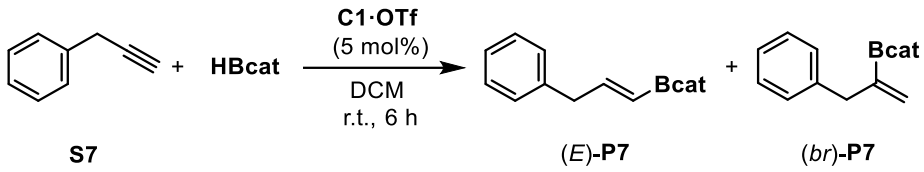

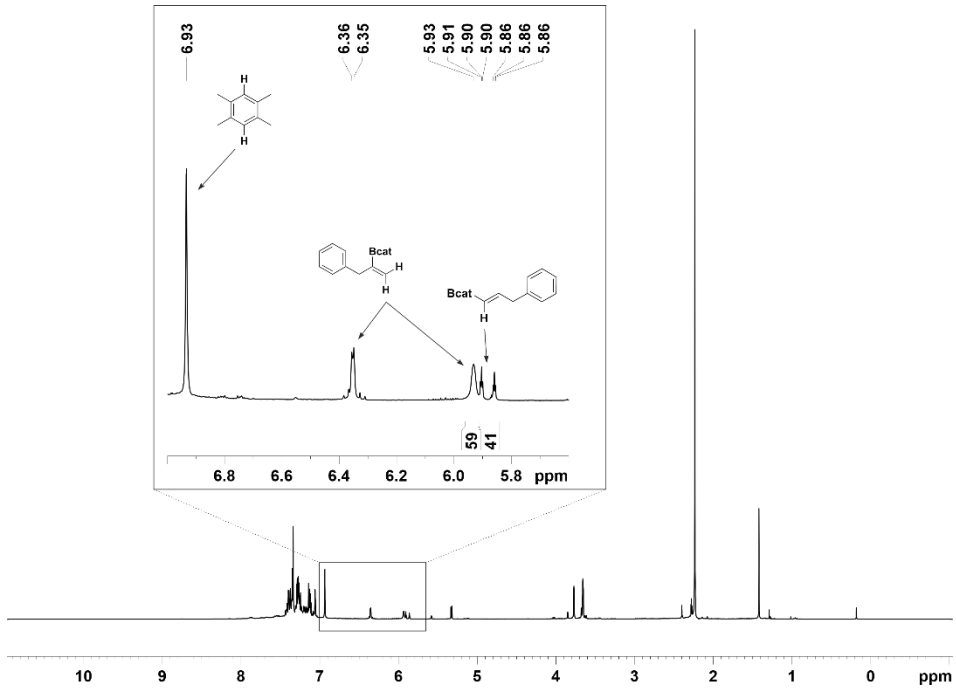

Figure 3.30. Reaction mixture ^{1}H NMR (400 MHz, CD_2Cl_2) of the catalytic hydroboration of **S7** and **HBcat** using complex **C1·OTf**.

Figure 3.31. Reaction mixture GC-MS of the catalytic hydroboration of **S7** and **HBcat** using complex **C1·OTf**.

Spectroscopic characterization of (*E*)-**P7** and (*br*)-**P7** mixture: **^{1}H NMR** (400 MHz, CD_2Cl_2) δ:[162] 7.46 – 7.07 (m, Bcat, CH, (*E*)-**P7**, and (*br*)-**P7**), 6.38 (d, *J* = 2.5 Hz, (*br*)-**P7**,1 H), 5.95 (s, (*br*)-**P7**,1 H) 5.90 (dt, *J* = 18.1, 1.7 Hz, (*E*)-**P7**,1 H), 3.80 (s, CH_2 (*br*)-**P7**,2 H) ppm. **GC-MS** *m/z*: calcd. for (*E*)-**P7** $[M]^+$ 236.1, found 236.1; calcd. for (*br*)-**P7** $[M]^+$ 236.1, found 236.1.

[162] For analogous Bpin (pinacholborane) compounds, see: (a) Armstrong, R. J.; Sandford, C.; García-Ruiz, C.; Aggarwal, V. K. *Chem. Commun.* **2017**, *53*, 4922-4925 for (*E*)-isomer; (b) Mao, L.; Bertermann, R.; Emmert, K.; Szabó, K. J.; Marder, T. B. *Org. Lett.* **2017**, *19*, 6586-6589 for (*br*)-isomer.

***Catalytic hydroboration of* S8 *with* HBcat *using complex* C1·OTf**

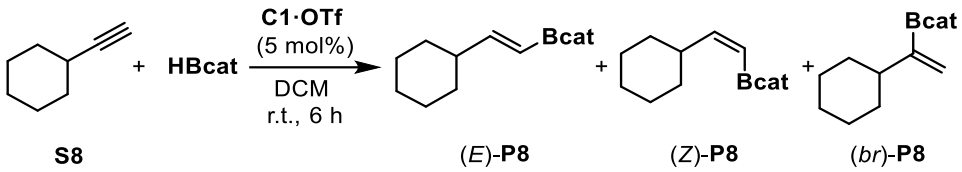

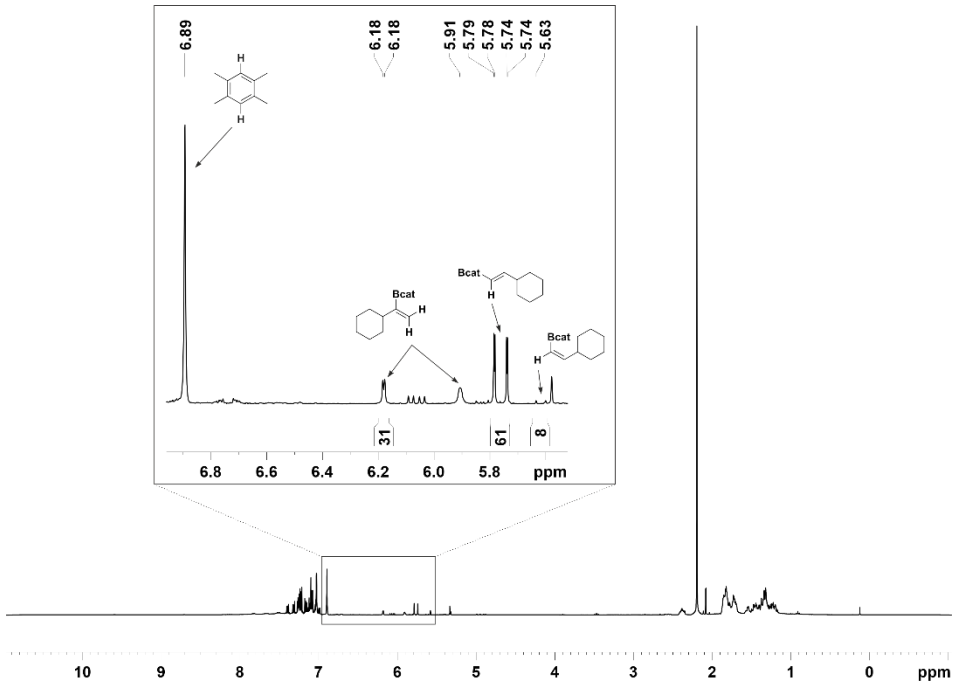

Figure 3.32. Reaction mixture ^{1}H NMR (400 MHz, CD_2Cl_2) of the catalytic hydroboration of **S8** and **HBcat** using complex **C1·OTf**.

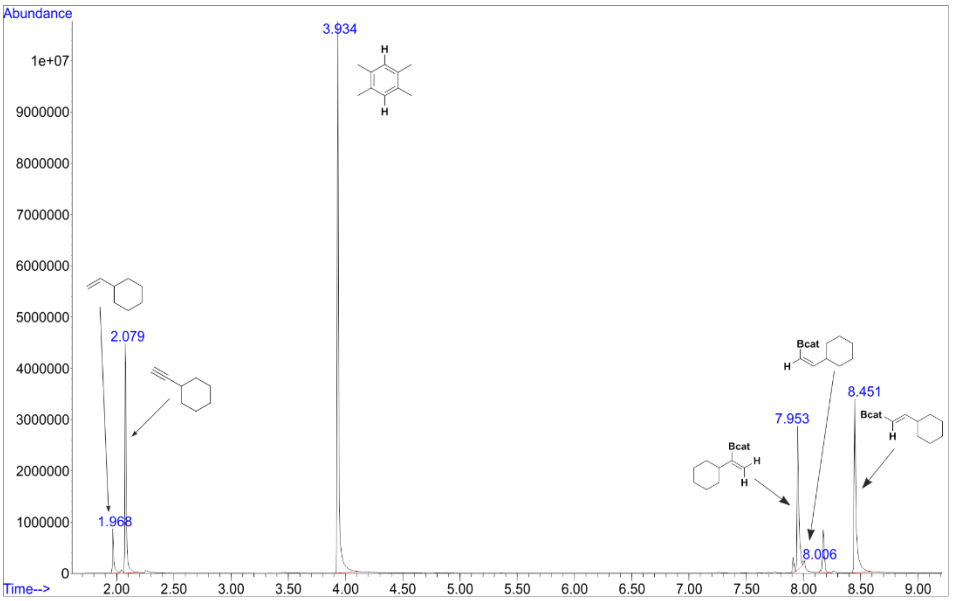

Figure 3.33. Reaction mixture GC-MS of the catalytic hydroboration of **S8** and **HBcat** using complex **C1·OTf**.

Spectroscopic characterization of (*E*)-**P8,** (*Z*)-**P8** and (*br*)-**P8** mixture: **^{1}H NMR** (400 MHz, CD_2Cl_2) δ:[163] 7.43 – 7.05 (m, Bcat, 12 H), 6.18 (d, *J* = 2.8 Hz, (*br*)-**P8**, 1 H), 5.90 (s, (*br*)-**P8**, 1 H), 5.76 (dd, *J* = 18.1, 1.7 Hz, (*E*)-**P8**, 1 H), 5.63 (d, *J* = 13.7 Hz, (*Z*)-**P8**, 1 H), 2.60 – 2.51 (m, (*br*)-**P8**, 2 H), 2.44 – 2.32 (m, (*E*)-**P8**, 2 H), 1.92 – 1.13 (m, CH_2 (*E*)-**P8**, (*Z*)-**P8** and (*br*)-**P8**) ppm. **GC-MS** *m/z*: calcd. for (*E*)-**P8** $[M]^+$ 228.1, found 228.1; calcd. for (*Z*)-**P8** $[M]^+$ 228.1, found 228.1; calcd. for (*br*)-**P8** $[M]^+$ 228.1, found 228.1.

[163] For characterization of (*E*)-**P8**, see reference 157a. For analogous Bpin (pinacholborane) compounds, see: (a) Obligacion, J. V.; Neely, J. M.; Yazdani, A. N.; Pappas, I.; Chirik, P. J. *J. Am. Chem. Soc.* **2015**, *137*, 5855-5858 for (*Z*)-isomer; (b) Coombs, J. R.; Zhang, L.; Morken, J. P. *Org. Lett.* **2015**, *17*, 1708-1711 for (*br*)-isomer.

***Catalytic hydroboration of* S9 *with* HBcat *using complex* C1·OTf**

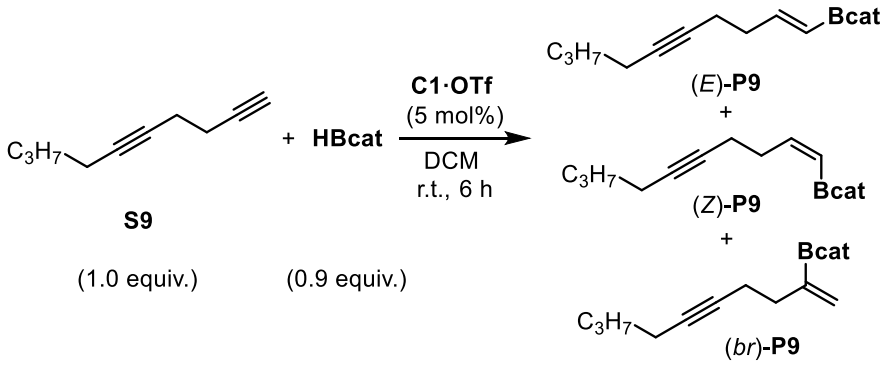

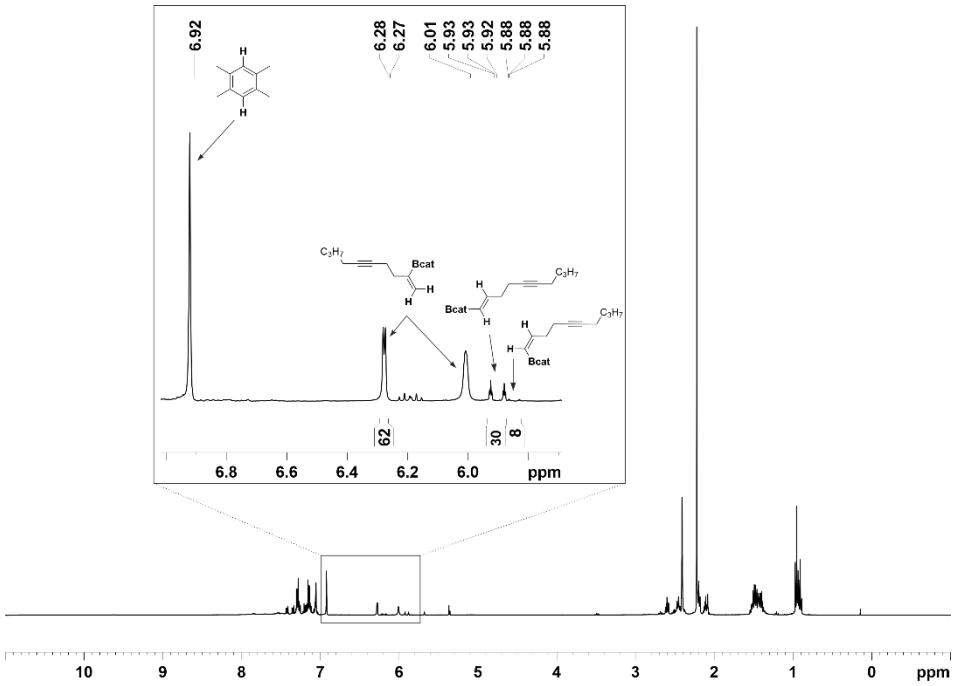

Figure 3.34. Reaction mixture ^{1}H NMR (400 MHz, CD_2Cl_2) of the catalytic hydroboration of **S9** and **HBcat** using complex **C1·OTf**.

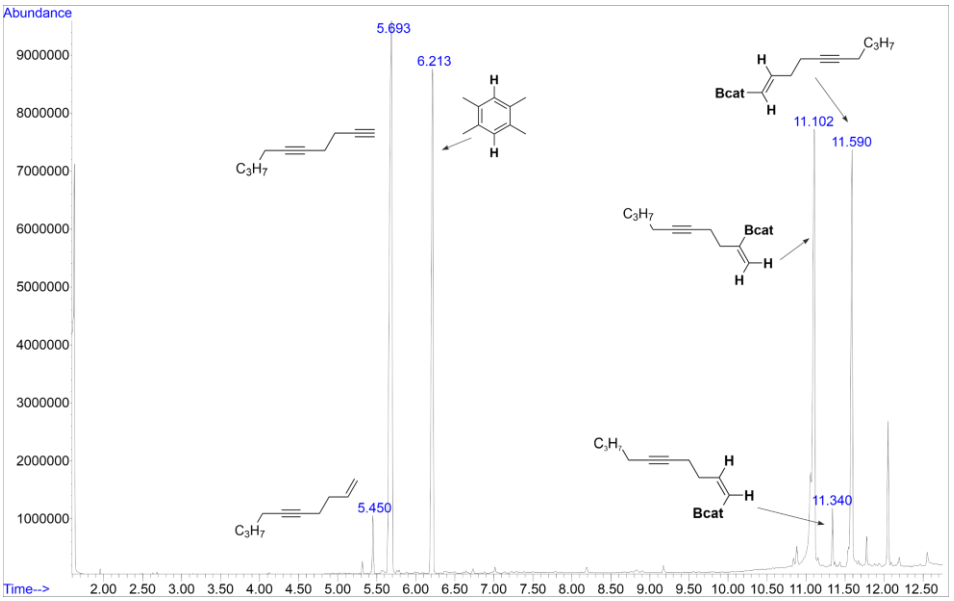

Figure 3.35. Reaction mixture GC-MS of the catalytic hydroboration of **S9** and **HBcat** using complex **C1·OTf**.

Spectroscopic characterization of (*E*)-**P9,** (*Z*)-**P9** and (*br*)-**P9** mixture: **^{1}H NMR** (400 MHz, CD_2Cl_2) δ:[164] 7.32 – 7.24 (m, Bcat, 6 H), 7.22 – 7.11 (m, Bcat, 6 H), 6.24 (d, *J* = 2.8 Hz, (*br*)-**P9**, 1 H), 5.97 (s, (*br*)-**P9**, 1 H), 5.87 (dt, *J* = 18.1, 1.5 Hz, (*E*)-**P9**, 1 H), 5.81 (dt, *J* = 13.7, 1.5 Hz, (*Z*)-**P9**, 1 H), 2.56 (t, *J* = 7.4 Hz, (*br*)-**P9**, 2 H), 2.51 – 2.31 (m, CH_2 (*E*)-**P9**, (*Z*)-**P9** and (*br*)-**P9**), 2.11 – 2.03 (m, CH_2 (*E*)-**P9**, (*Z*)-**P9** and (*br*)-**P9**), 1.52 – 1.30 (m, CH_2 (*E*)-**P9**, (*Z*)-**P9** and (*br*)-**P9**), 0.96 – 0.83 (m, CH_3 (*E*)-**P9**, (*Z*)-**P9** and (*br*)-**P9**) ppm. **GC-MS** *m/z*: calcd. for (*E*)-**P9** $[M-H]^+$ 281.2, found 281.1; calcd. for (*Z*)-**P9** $[M-H]^+$ 281.2, found 281.1; calcd. for (*br*)-**P9** $[M-H]^+$ 281.2, found 281.1.

[164] ^{1}H NMR signals of (*E*)-**P9,** (*Z*)-**P9** and (*br*)-**P9** have been asigned based on their analogous compounds (*E*)-**P1,** (*Z*)-**P1** and (*br*)-**P1**.

***Catalytic hydroboration of* S10 *with* HBcat *using complex* C1·OTf**

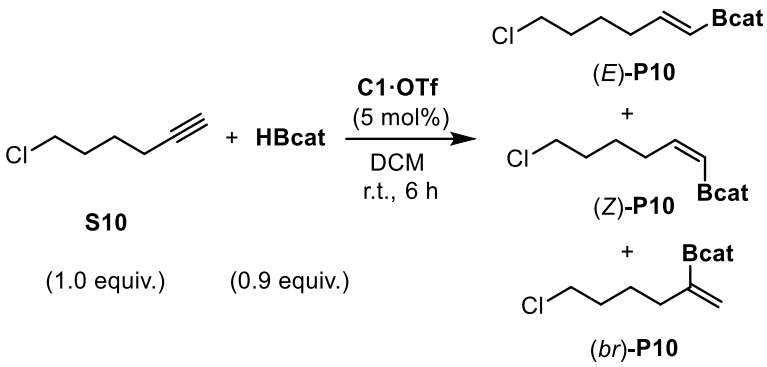

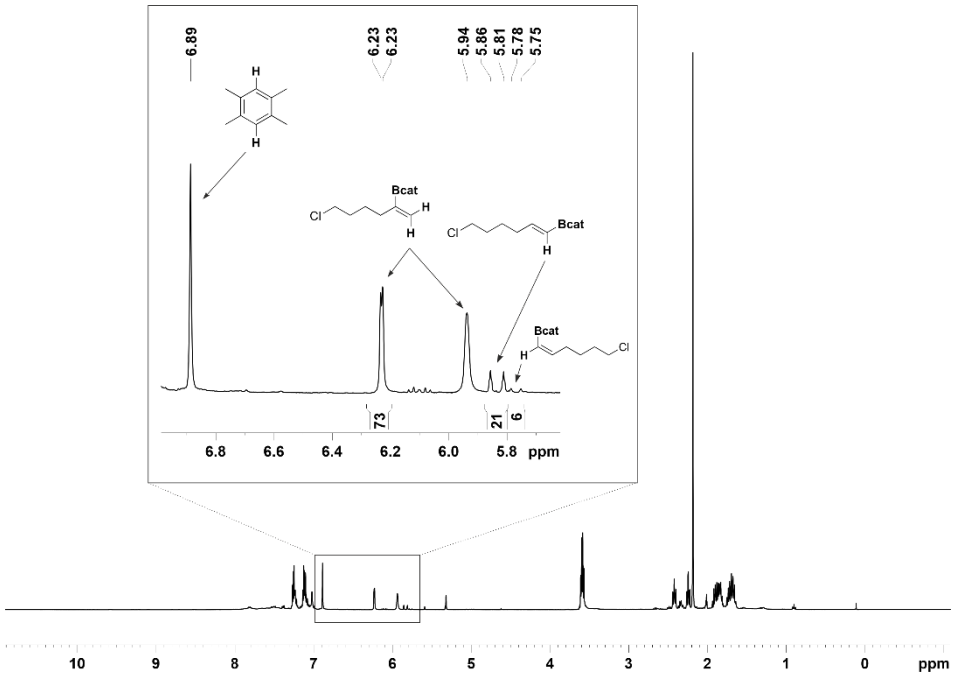

Figure 3.36. Reaction mixture ^{1}H NMR (400 MHz, CD_2Cl_2) of the catalytic hydroboration of **S10** and **HBcat** using complex **C1·OTf**.

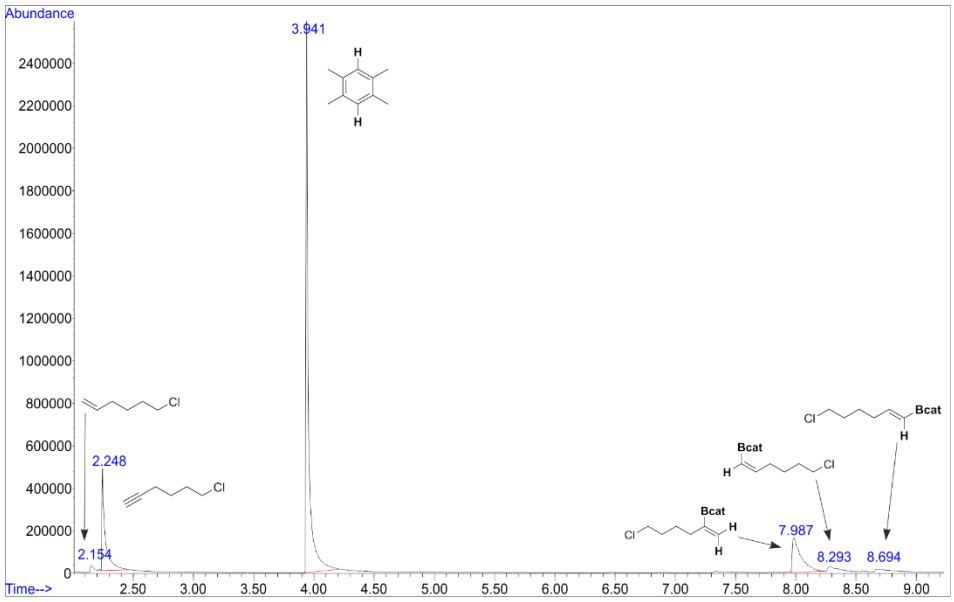

Figure 3.37. Reaction mixture GC-MS of the catalytic hydroboration of **S10** and **HBcat** using complex **C1·OTf**.

Spectroscopic characterization of (*E*)-**P10,** (*Z*)-**P10** and (*br*)-**P10** mixture:[155] **^{1}H NMR** (400 MHz, CD_2Cl_2) δ:[165] 7.30 – 7.19 (m, Bcat, 6 H), 7.17 – 7.05 (m, Bcat, 6 H), 6.23 (d, *J* = 2.8 Hz, (*br*)-**P10**, 1 H), 5.94 (s, (*br*)-**P10**, 1 H), 5.83 (d, *J* = 18.1 Hz, (*E*)-**P10**, 1 H), 5.76 (d, *J* = 13.6 Hz, (*Z*)-**P10**, 1 H), 3.63 – 3.53 (m, CH_2 (*E*)-**P10**, (*Z*)-**P10** and (*br*)-**P10**), 2.42 (t, *J* = 7.7 Hz, (*br*)-**P10**, 2 H), 2.38 – 2.29 (m, (*E*)-**2a**, 2 H), 1.95 – 1.79 (m, CH_2 (*E*)-**P10**, (*Z*)-**P10** and (*br*)-**P10**), 1.77 – 1.62 (m, CH_2 (*E*)-**P10**, (*Z*)-**P10** and (*br*)-**P10**) ppm. **GC-MS** *m/z*: calcd. for (*E*)-**P10** $[M]^+$ 236.1, found 236.0; calcd. for (*Z*)-**P10** $[M]^+$ 236.1, found 236.0; calcd. for (*br*)-**P10** $[M]^+$ 236.1, found 236.0.

[165] ^{1}H NMR signals of (*E*)-**P10,** (*Z*)-**P10** and (*br*)-**P10** have been asigned based on their analogous compounds (*E*)-**P1,** (*Z*)-**P1** and (*br*)-**P1**. (a) For characterization of the analogous (*E*)-2-(6-chloropent-1-en-1-yl)benzo[d][1,3,2]dioxaborole, see: reference 150. (b) For analogous Bpin (pinacholborane) compounds, see reference 157b for (*br*)-isomer.

***Catalytic hydroboration of* S11 *with* HBcat *using complex* C1·OTf**

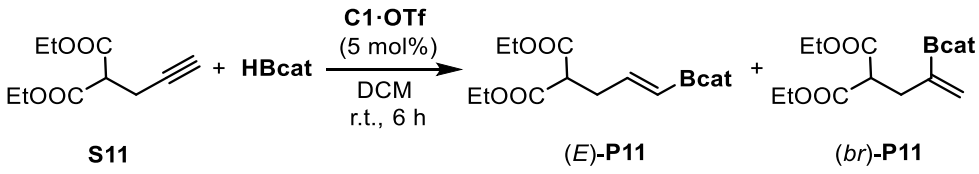

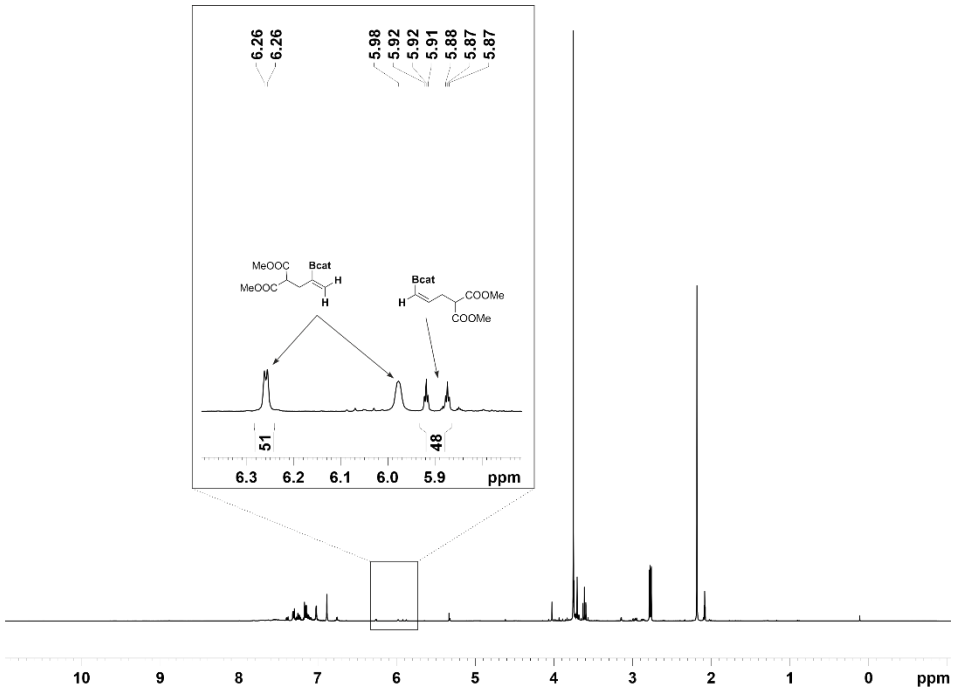

Figure 3.38. Reaction mixture ^{1}H NMR (400 MHz, CD_2Cl_2) of the catalytic hydroboration of **S11** and **HBcat** using complex **C1·OTf**.

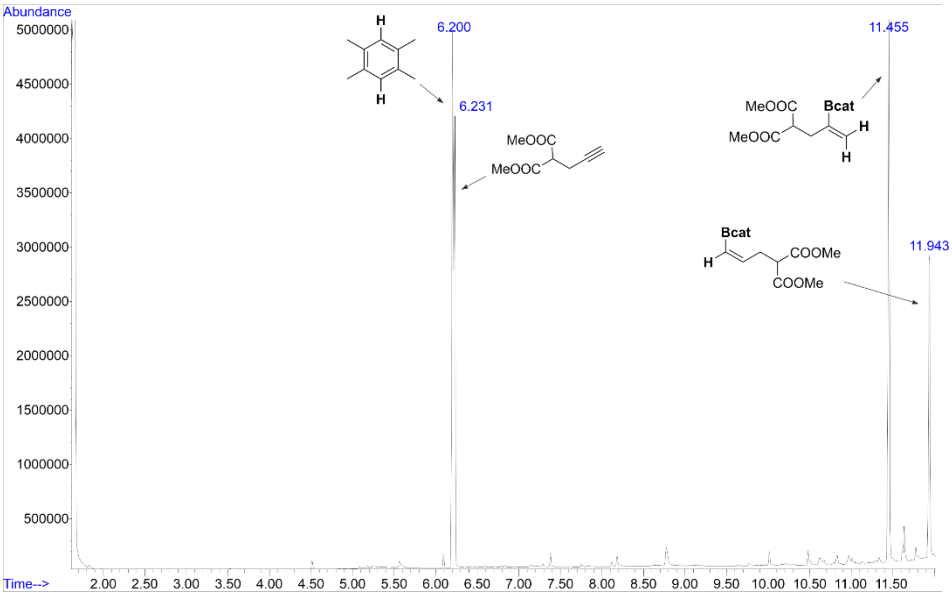

Figure 3.39. Reaction mixture GC-MS of the catalytic hydroboration of **S11** and **HBcat** using complex **C1·OTf**.

Spectroscopic characterization of (*E*)-**P11**, (*Z*)-**P11** and (*br*)-**P11** mixture:[155] **^{1}H NMR** (400 MHz, CD_2Cl_2) δ:[166] 7.40 – 7.08 (m, Bcat, 8 H), 6.26 (d, *J* = 2.6 Hz, (*br*)-**P11**, 1 H), 5.98 (s, (*br*)-**P11**, 1 H), 5.90 (dt, *J* = 18.1, 1.5 Hz, (*E*)-**P11**, 1 H) ppm. **GC-MS** *m/z*: calcd. for (*E*)-**P11** $[M]^+$ 290.1, found 290.1; calcd. for (*br*)-**P11** $[M]^+$ 290.1, found 290.1.

[166] ^{1}H NMR signals of (*E*)-**P11** and (*br*)-**P11** have been asigned based on their analogous compounds (*E*)-**P1** and (*br*)-**P1**.

3.4.9 Mechanistic rationale

General procedure for the NMR study of the hydroboration reaction: Under N_2 atmosphere, 30.0 mg (0.03 mmol, 1.0 equiv.) of the **C1·OTf** catalyst along with 600.0 µL of deuterated dichloromethane were placed into a 3 mL vial. Then, 4.3 µL, (0.03 mmol, 1.0 equiv.) of 1-octyne **S1** and 3.5 µL (0.03 mmol, 1.0 equiv.) of catecholborane **HBcat** were subsequently added. The reaction mixture was transferred to an NMR J-Young tube and analyzed by ^{1}H and $^{11}B\{^{1}H\}$ NMR.

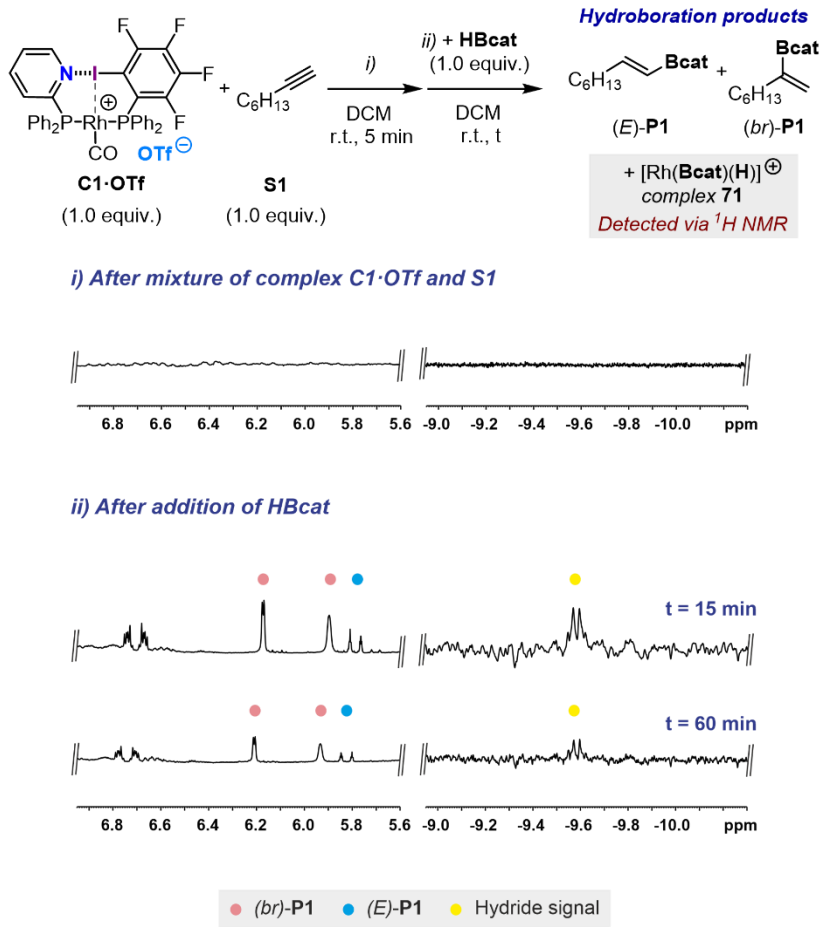

Figure 3.40. ^{1}H NMR study of hydroboration reaction using **C1·OTf** (1.0 equiv.) and **S1** (1.0 equiv.): (a) without **HBcat**; (b) at 15 min after **HBcat** (1.0 equiv.) addition; (c) at 60 min after **HBcat** addition.

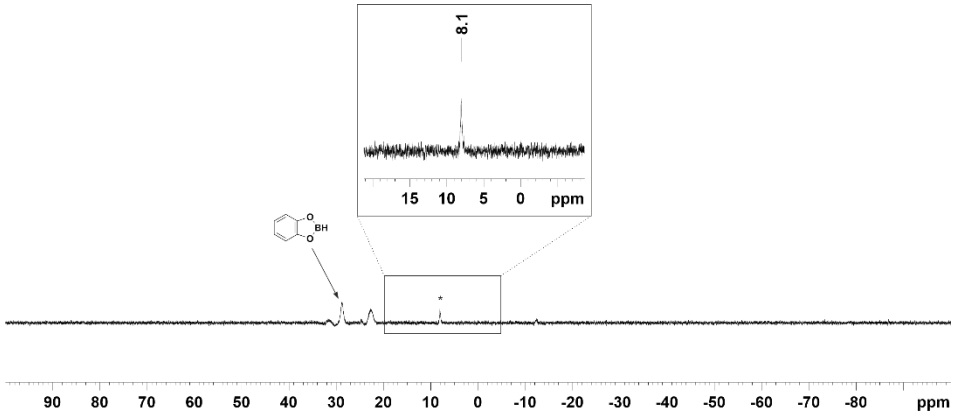

Figure 3.41. $^{11}B\{^{1}H\}$ NMR spectrum at 15 min after catecholborane **HBcat** addition.

3.4.10 Collection of NMR spectra

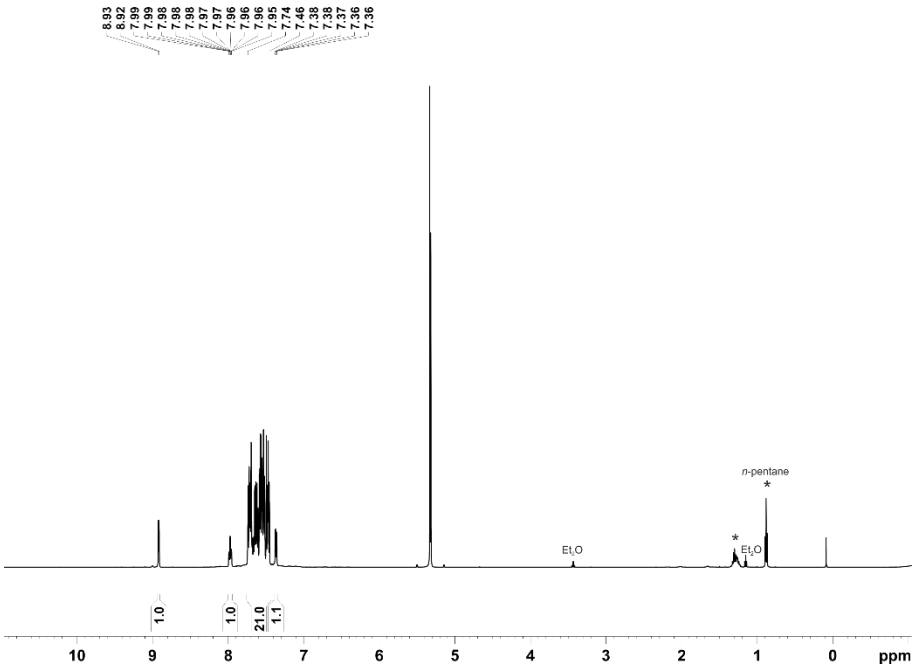

Figure 3.42. ^{1}H NMR (500 MHz, CD_2Cl_2) for complex **C1·OTf**.

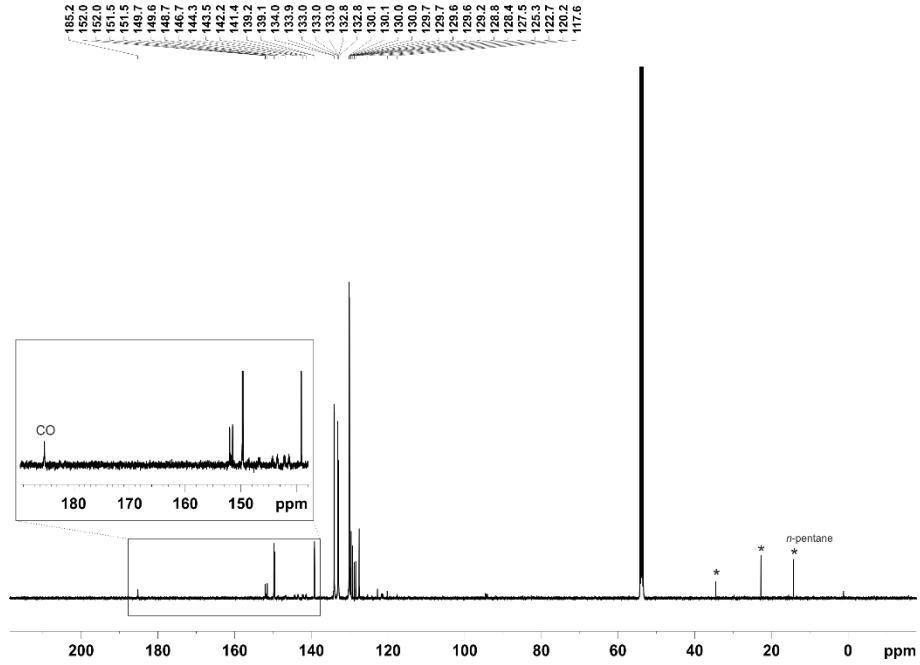

Figure 3.43. $^{13}C\{^{1}H\}$ NMR (126 MHz, CD_2Cl_2) for complex **C1·OTf.**

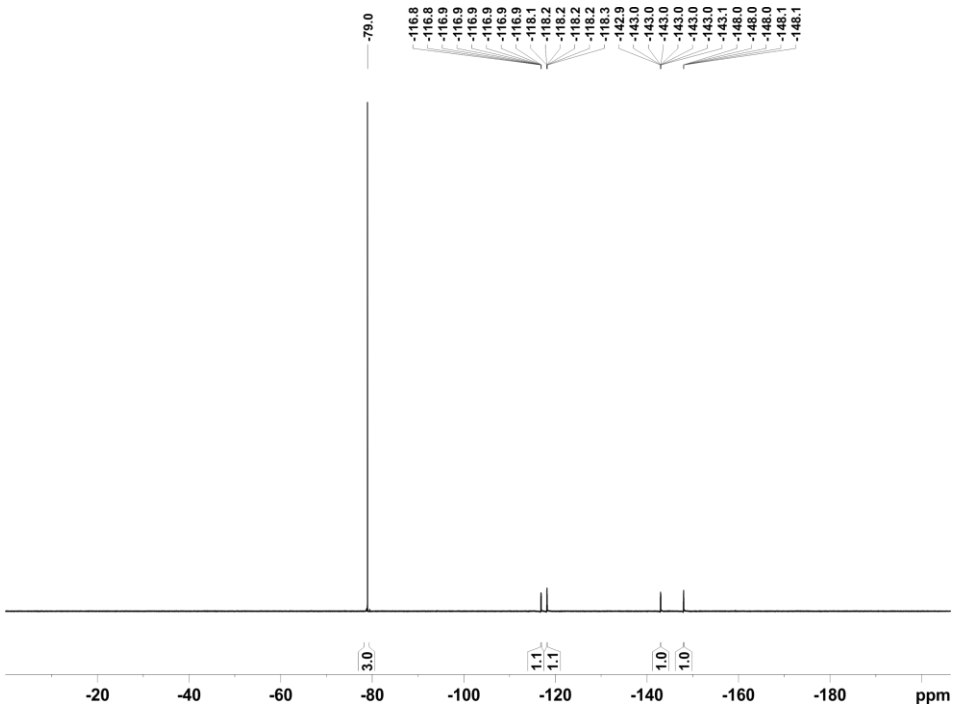

Figure 3.44. $^{19}F\{^{1}H\}$ NMR (471 MHz, CD_2Cl_2) for complex **C1·OTf**.

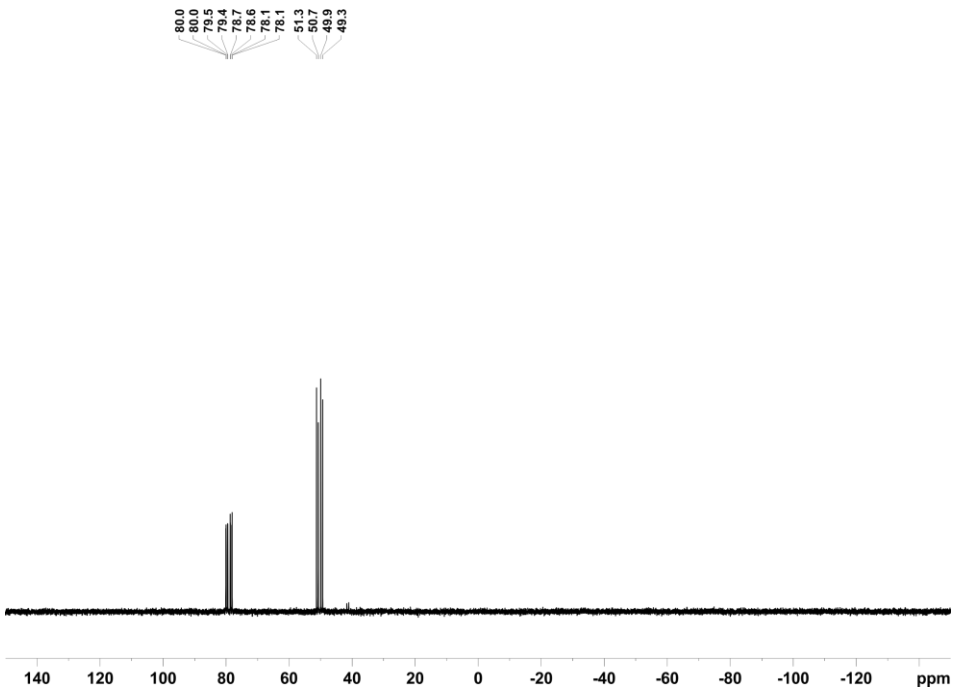

Figure 3.45. $^{31}P\{^{1}H\}$ NMR (203 MHz, CD_2Cl_2) for complex **C1·OTf**.

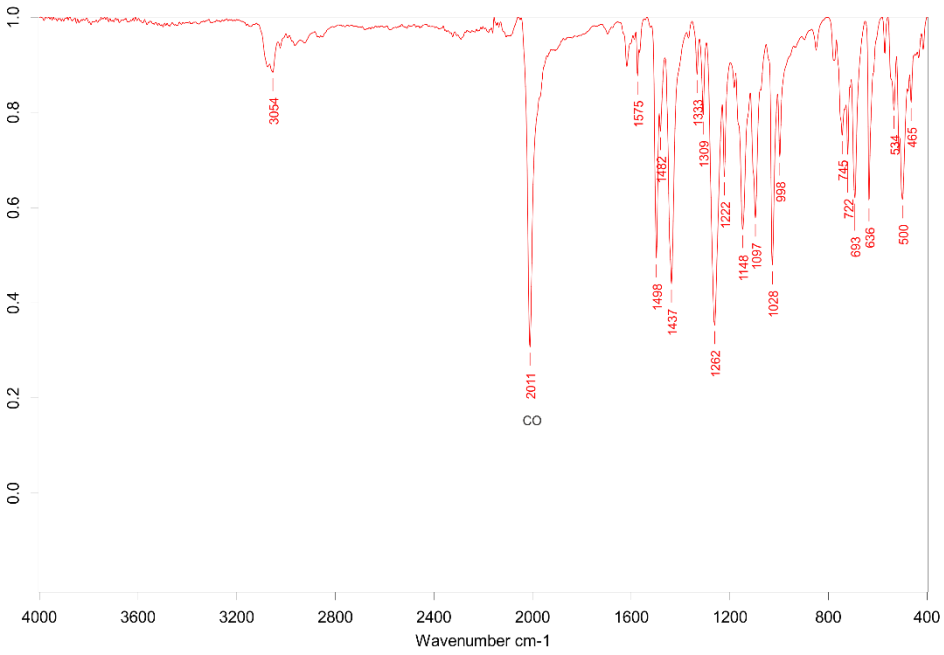

Figure 3.46. IR spectrum for complex **C1·OTf**.

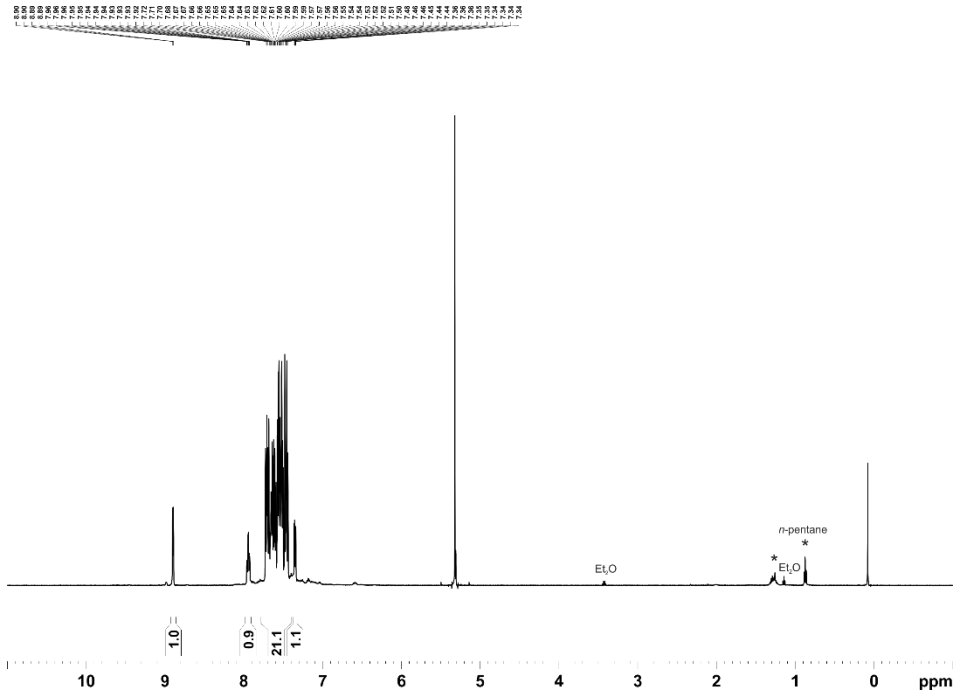

Figure 3.47. ^{1}H NMR (500 MHz, CD_2Cl_2) for complex **C1·NTf₂**.

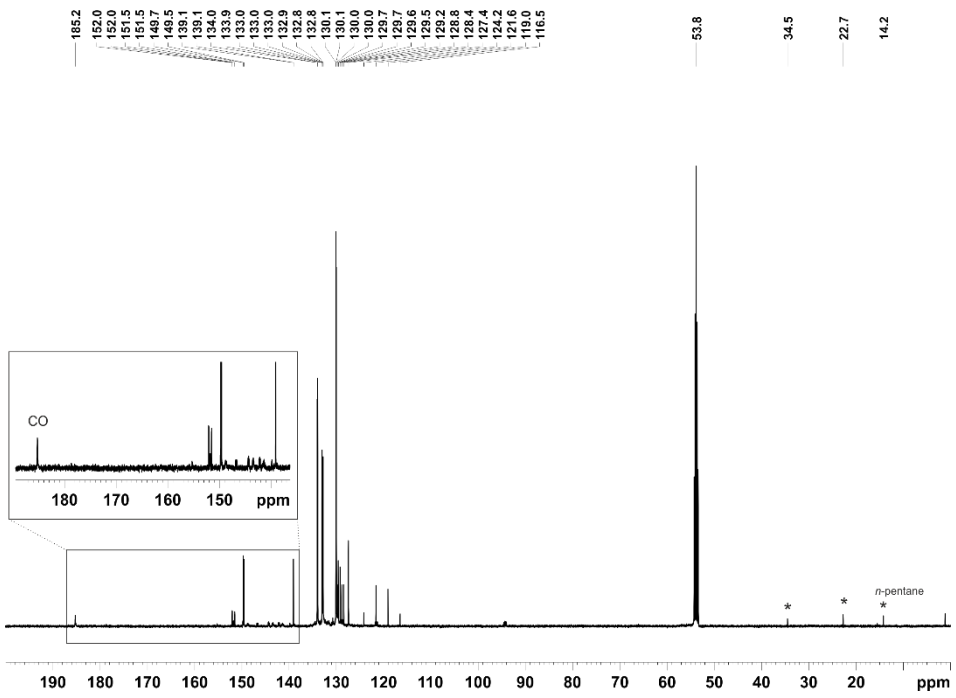

Figure 3.48. $^{13}C\{^{1}H\}$ NMR (126 MHz, CD_2Cl_2) for complex **C1·NTf₂**.

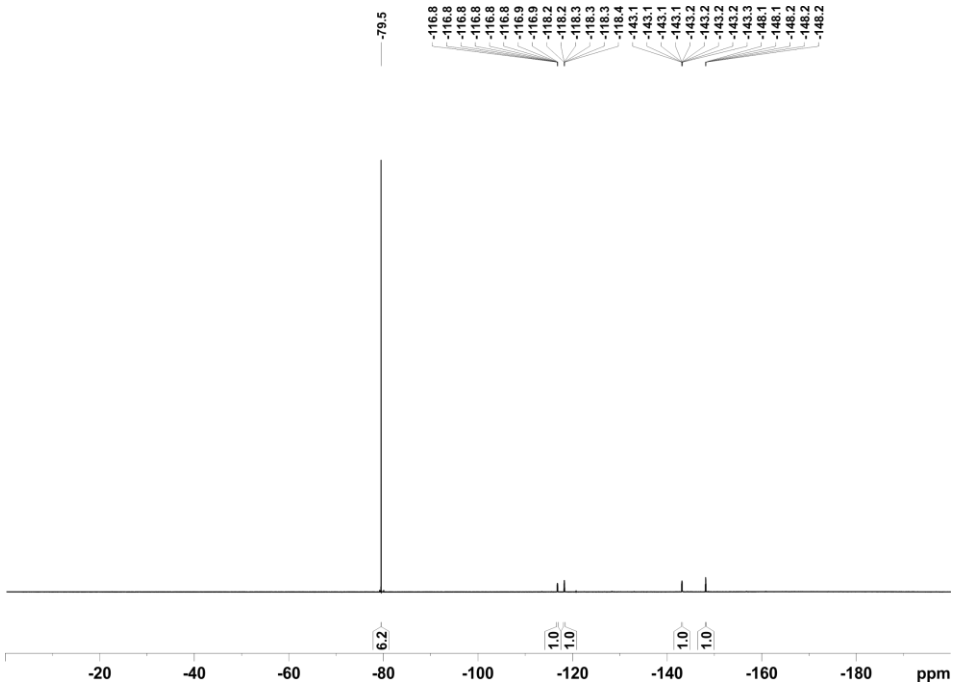

Figure 3.49. $^{19}F\{^{1}H\}$ NMR (471 MHz, CD_2Cl_2) for complex **C1·NTf₂**.

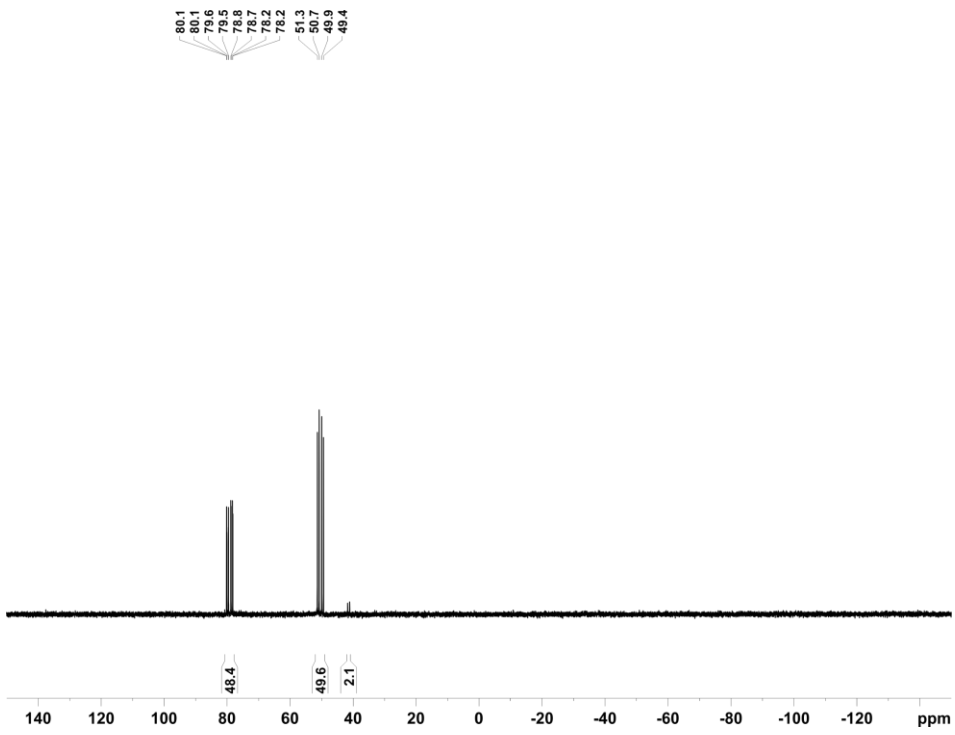

Figure 3.50. $^{31}P\{^{1}H\}$ IGD NMR (203 MHz, CD_2Cl_2) for complex **C1·NTf₂**.

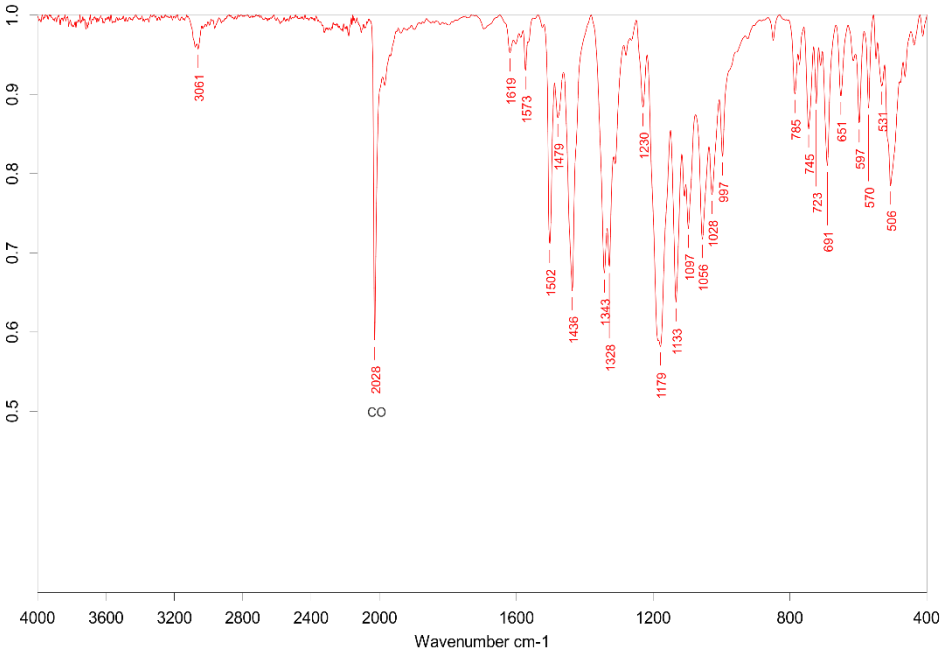

Figure 3.51. IR spectrum for complex **C1·NTf₂**.

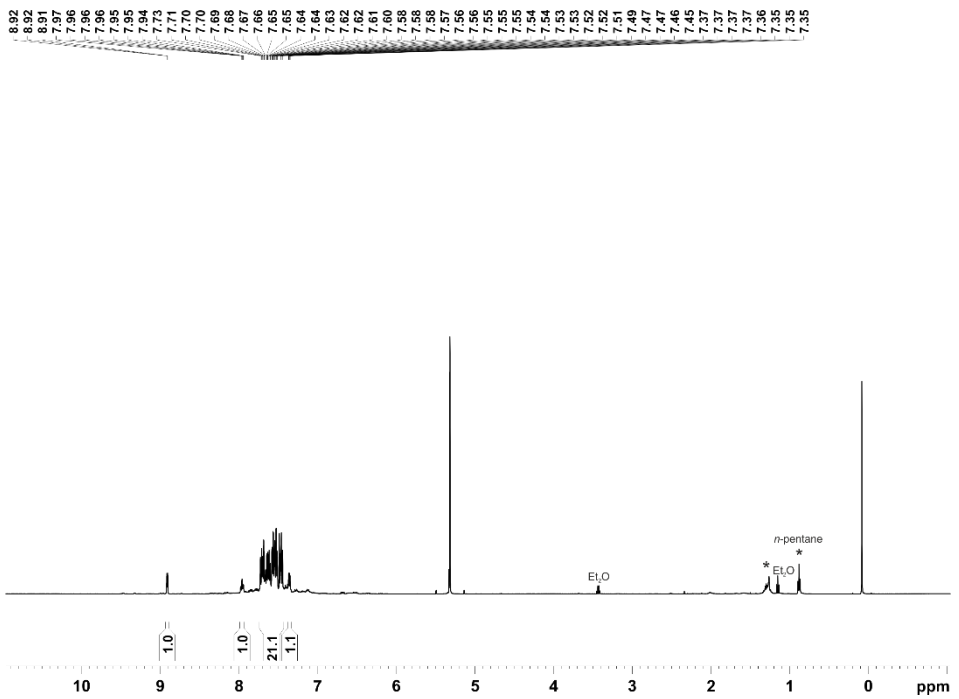

Figure 3.52. ^{1}H NMR (500 MHz, CD_2Cl_2) for complex **C1·BF4**.

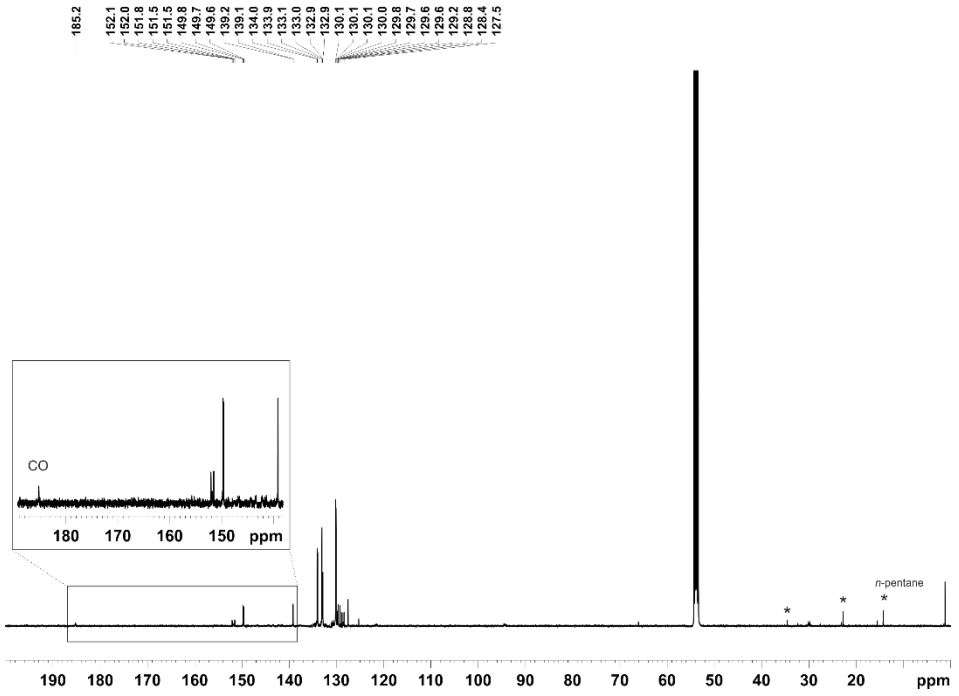

Figure 3.53. $^{13}C\{^{1}H\}$ NMR (126 MHz, CD_2Cl_2) for complex **C1·BF4**.

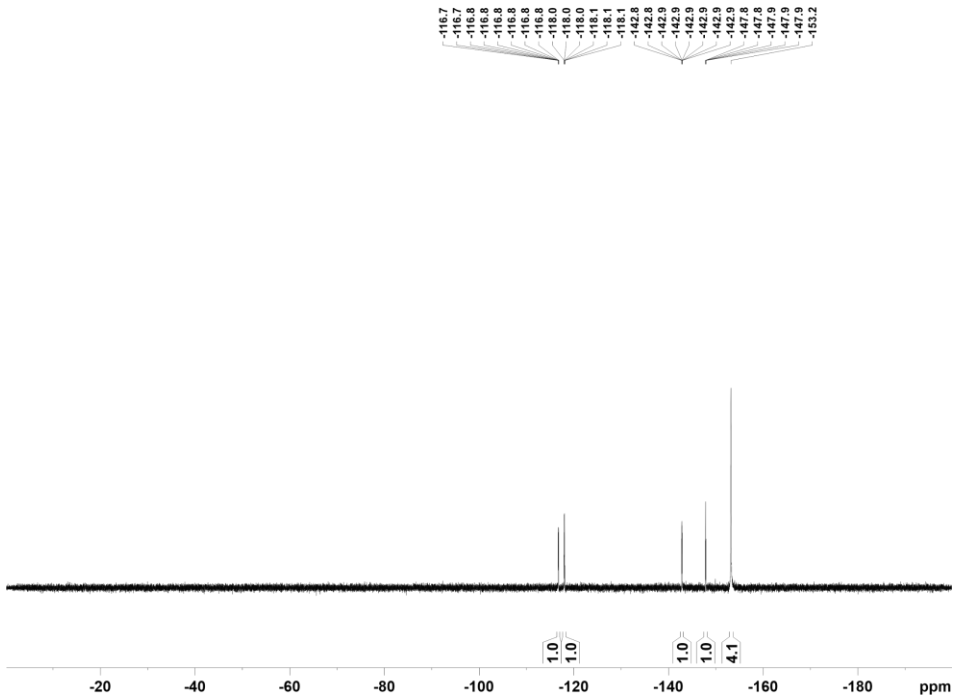

Figure 3.54. $^{19}F\{^{1}H\}$ NMR (471 MHz, CD_2Cl_2) for complex **C1·BF4**.

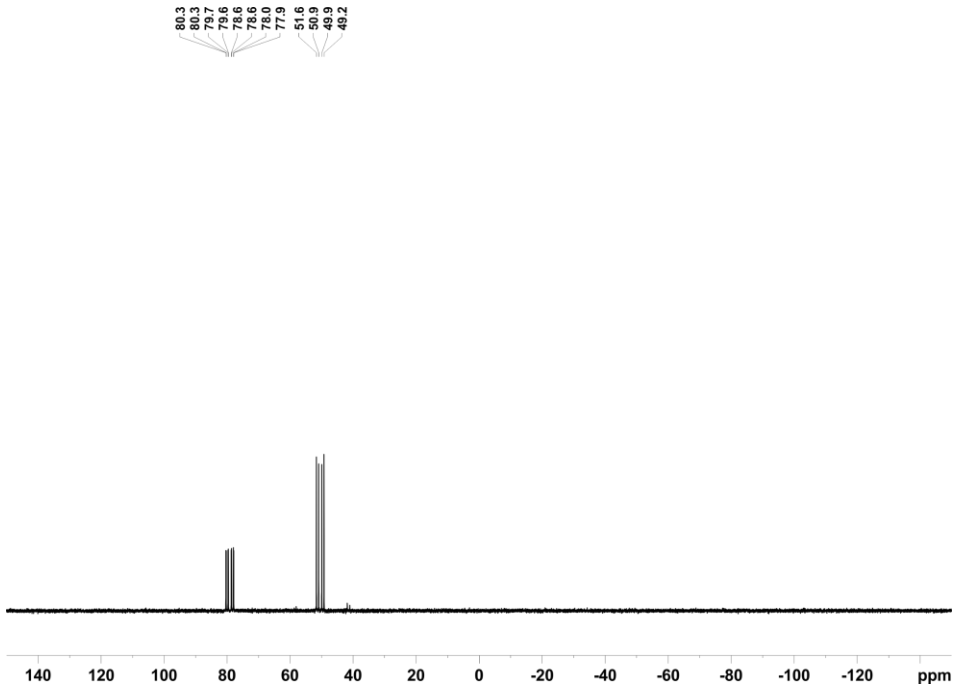

Figure 3.55. $^{31}P\{^{1}H\}$ NMR (202 MHz, CD_2Cl_2) for complex **C1·BF4**.

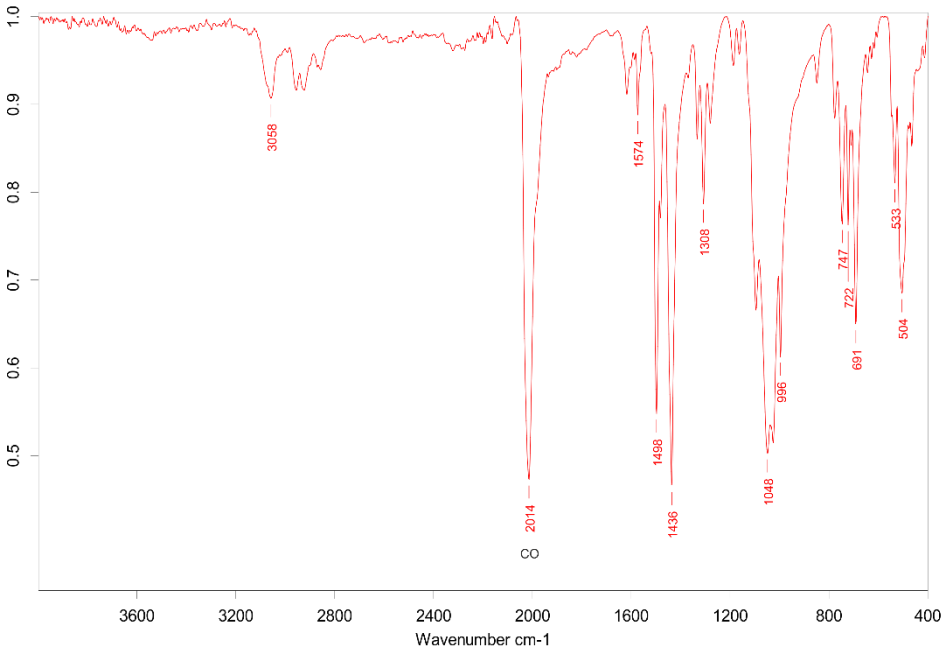

Figure 3.56. IR spectrum for complex **C1·BF$_4$.**

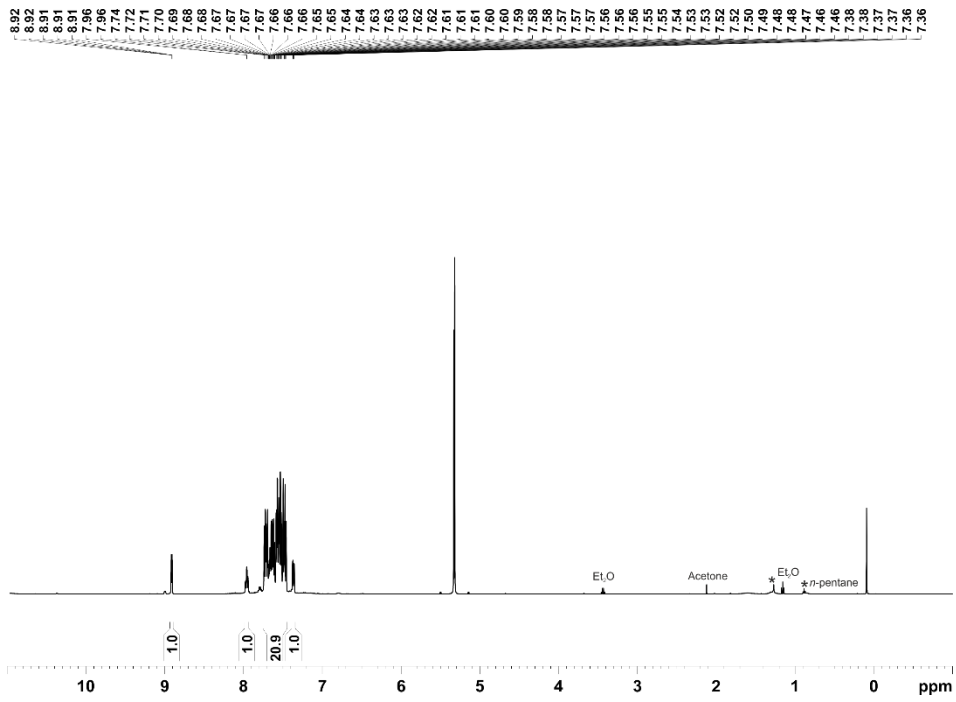

Figure 3.57. ^{1}H NMR (500 MHz, CD_2Cl_2) for complex **C1·PF$_6$.**

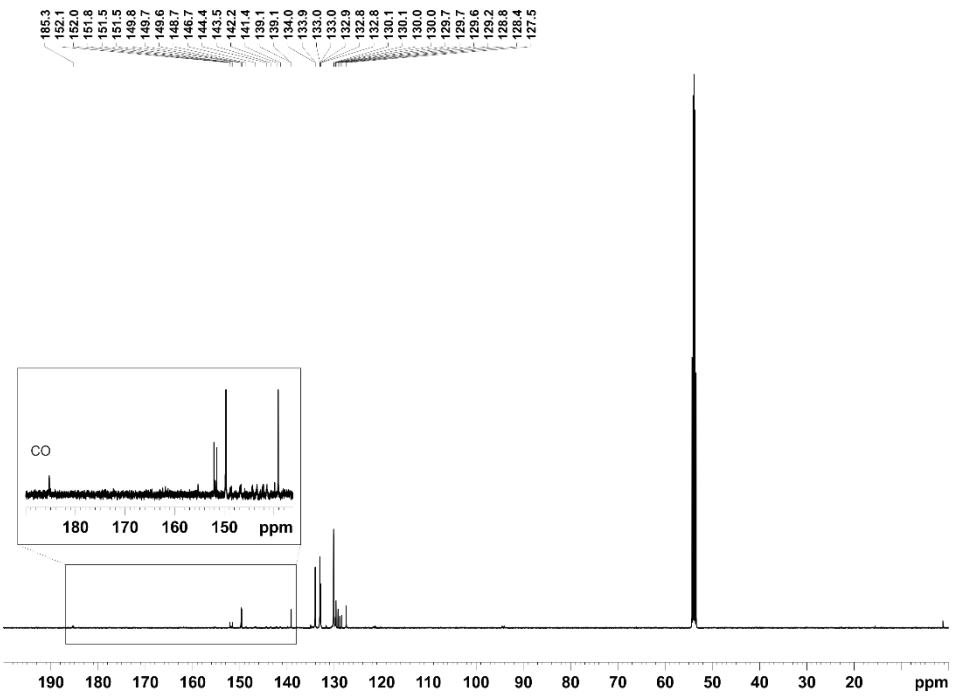

Figure 3.58. $^{13}C\{^{1}H\}$ NMR (126 MHz, CD_2Cl_2) for complex **C1·PF$_6$**.

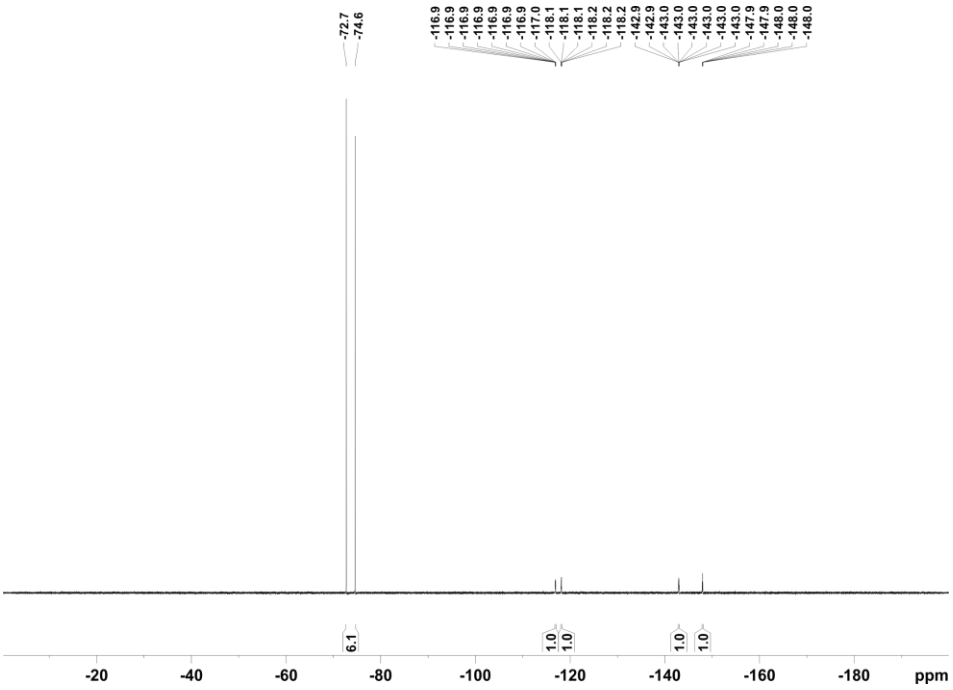

Figure 3.59. $^{19}F\{^{1}H\}$ NMR (471 MHz, CD_2Cl_2) for complex **C1·PF$_6$**.

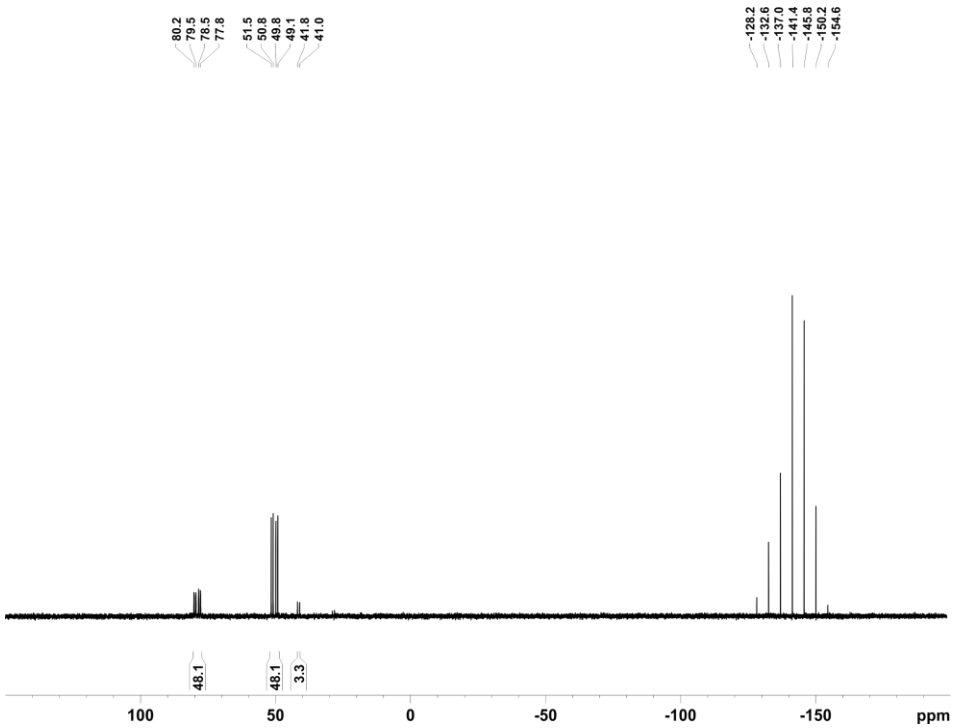

Figure 3.60. $^{31}P\{^{1}H\}$ IGD NMR (203 MHz, CD_2Cl_2) for complex **C1·PF$_6$**.

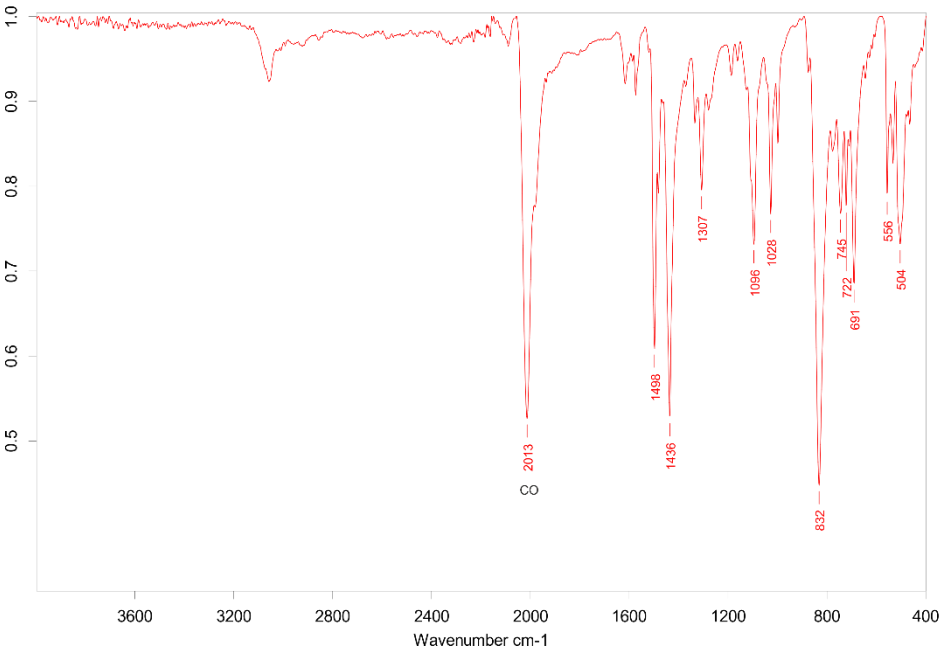

Figure 3.61. IR spectrum for complex **C1·PF$_6$**.

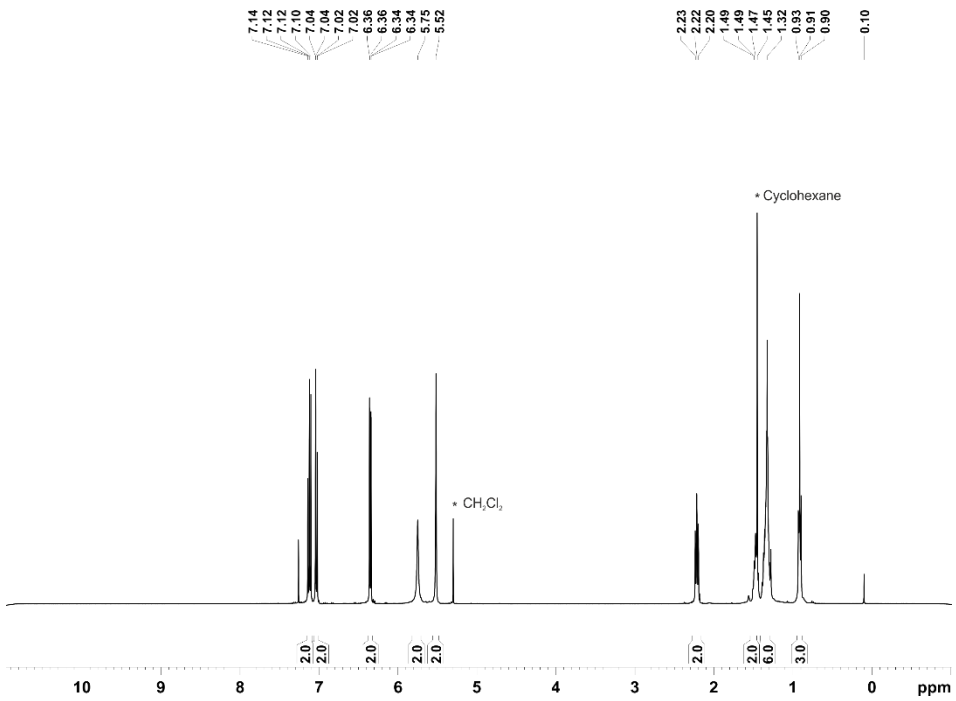

Figure 3.62. ^{1}H NMR (500 MHz, $CDCl_3$) for product (*br*)-**P1·Bdan.**

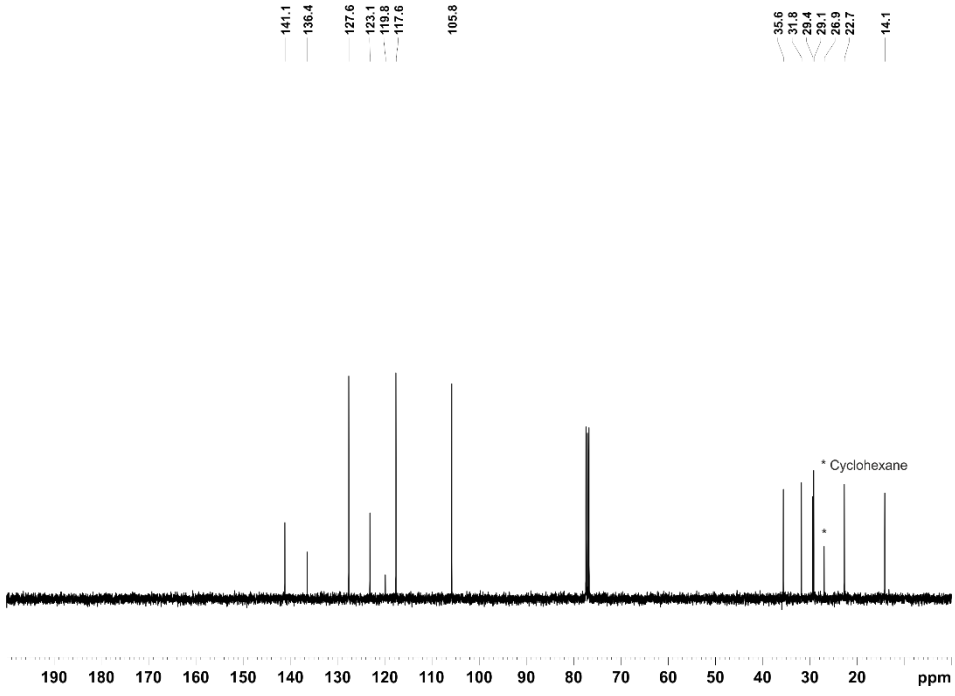

Figure 3.63. $^{13}C\{^{1}H\}$ NMR (126 MHz, $CDCl_3$) for product (*br*)-**P1·Bdan.**

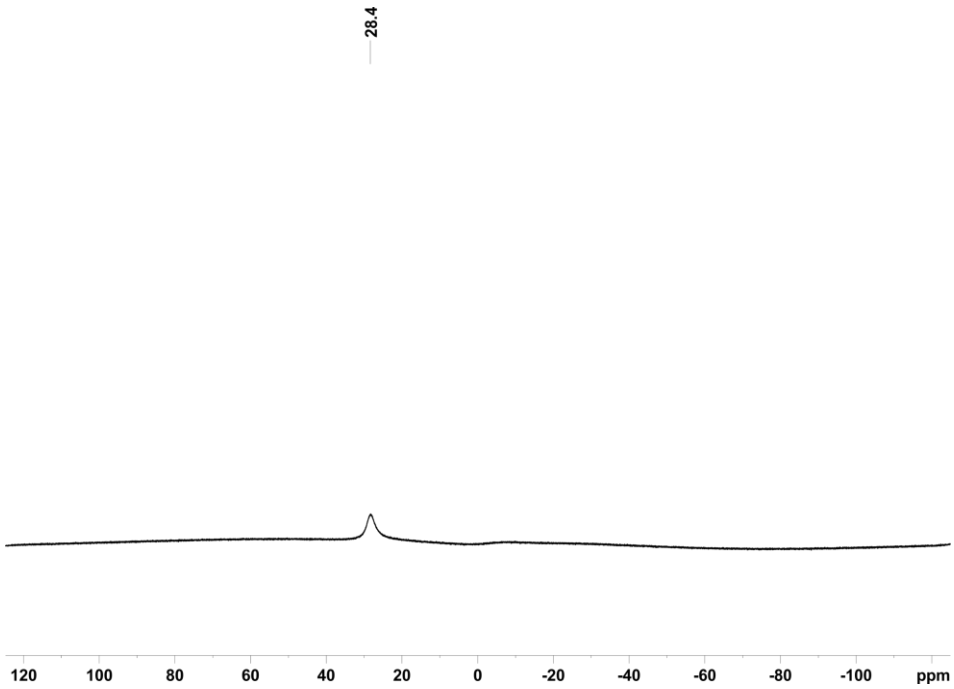

Figure 3.64. $^{11}B\{^{1}H\}$ NMR (160 MHz, $CDCl_3$) for product (*br*)-**P1·Bdan.**

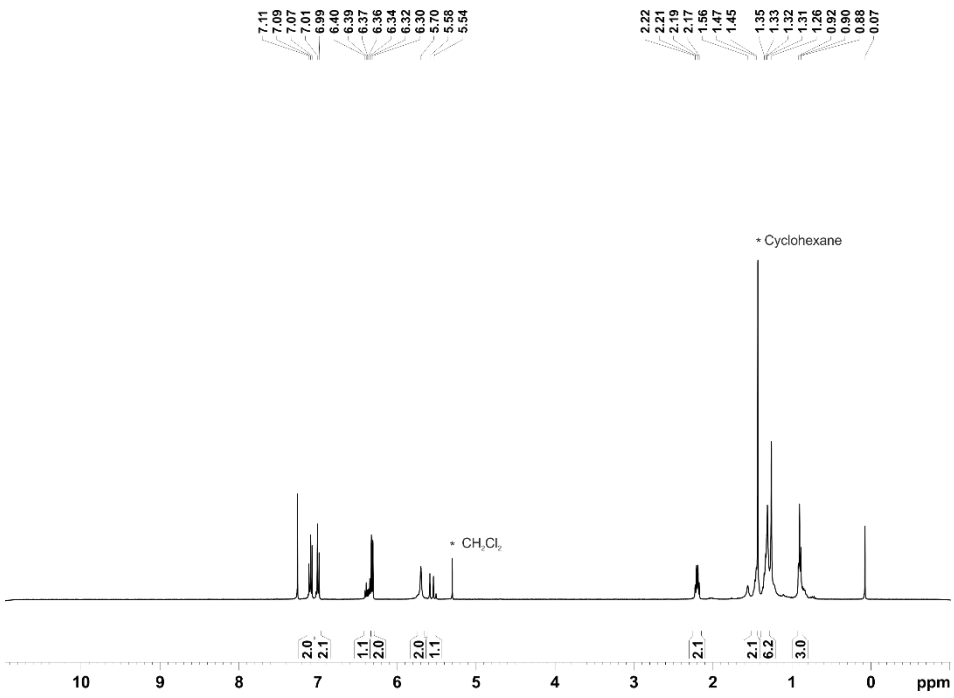

Figure 3.65. ^{1}H NMR (500 MHz, $CDCl_3$) for product (*E*)-**P1·Bdan.**

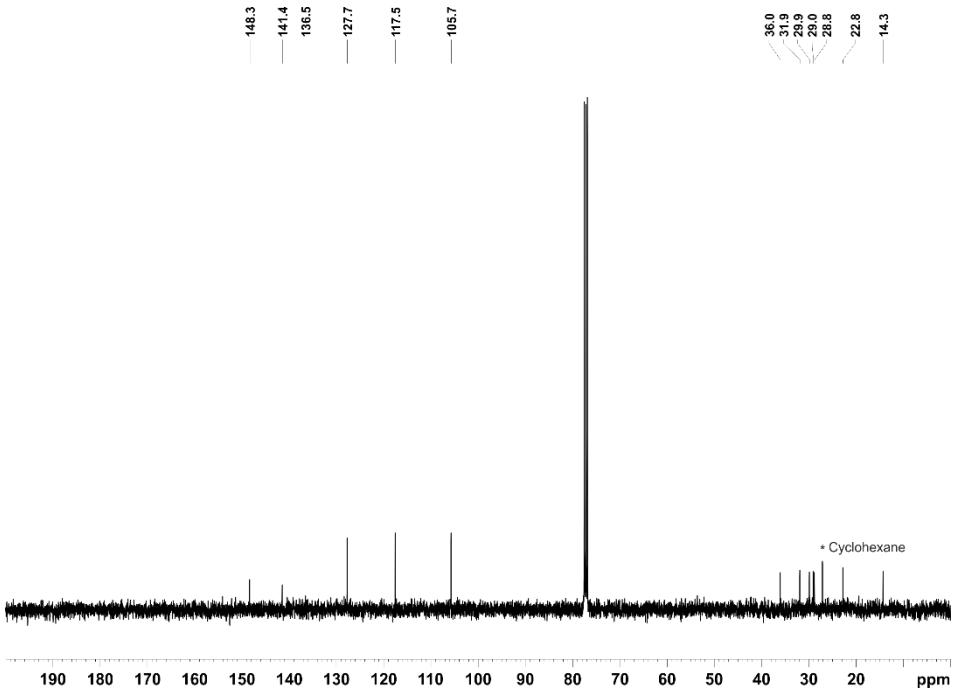

Figure 3.66. $^{13}C\{^{1}H\}$ NMR (126 MHz, $CDCl_3$) for product (*E*)-**P1·Bdan.**

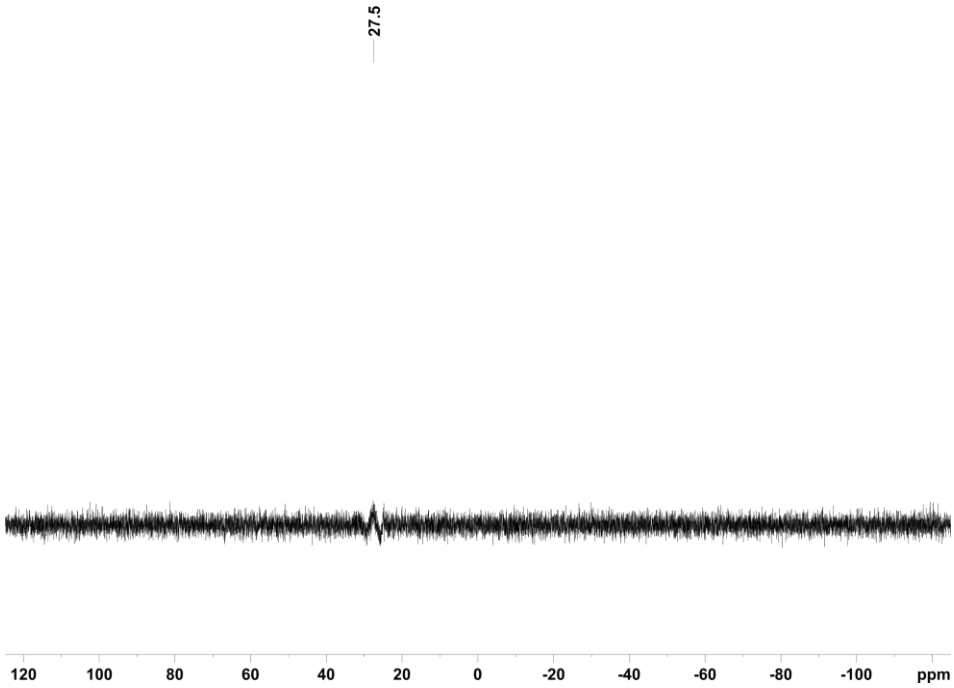

Figure 3.67. $^{11}B\{^{1}H\}$ NMR (160 MHz, $CDCl_3$) for product (*E*)-**P1·Bdan.**

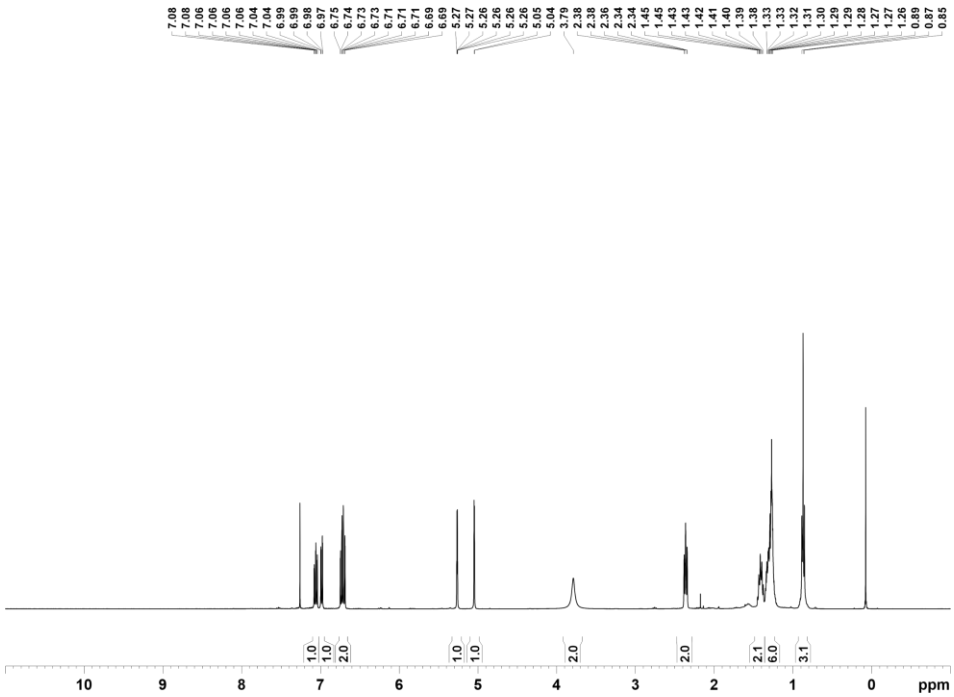

Figure 3.68. ^{1}H NMR (400 MHz, $CDCl_3$) for product **75**.

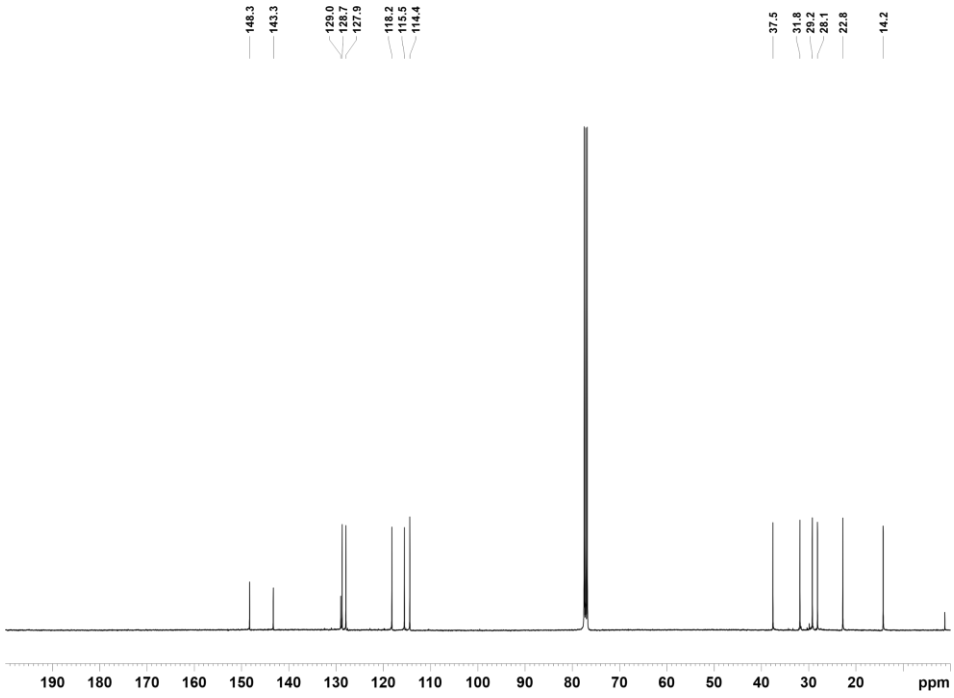

Figure 3.69. $^{13}C\{^{1}H\}$ NMR (100 MHz, $CDCl_3$) for product **75.**

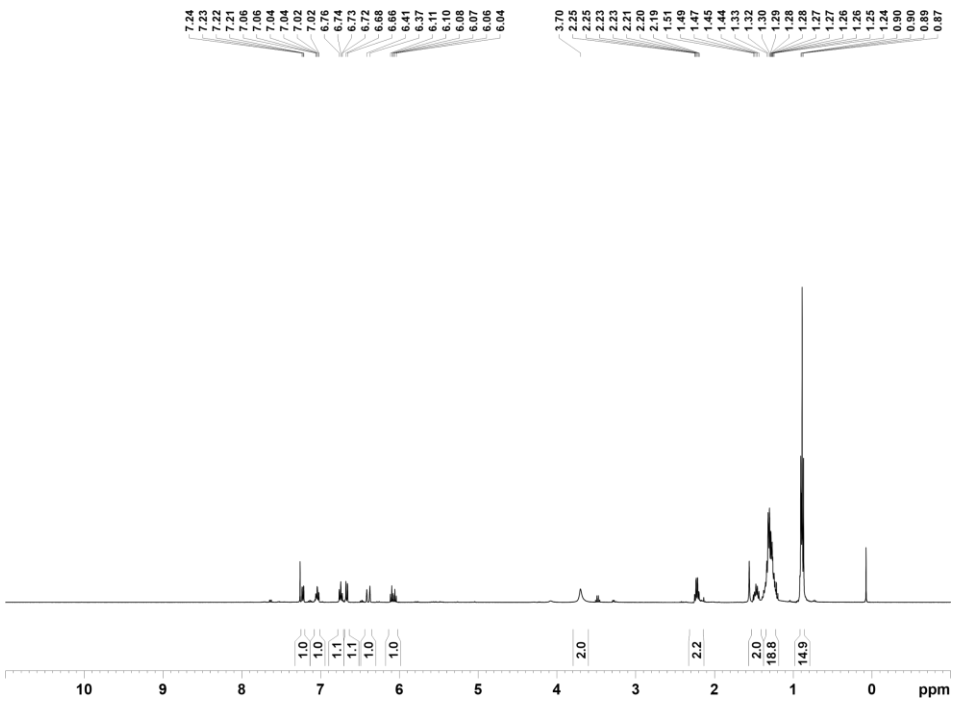

Figure 3.70. ^{1}H NMR (400 MHz, $CDCl_3$) for product **76**.

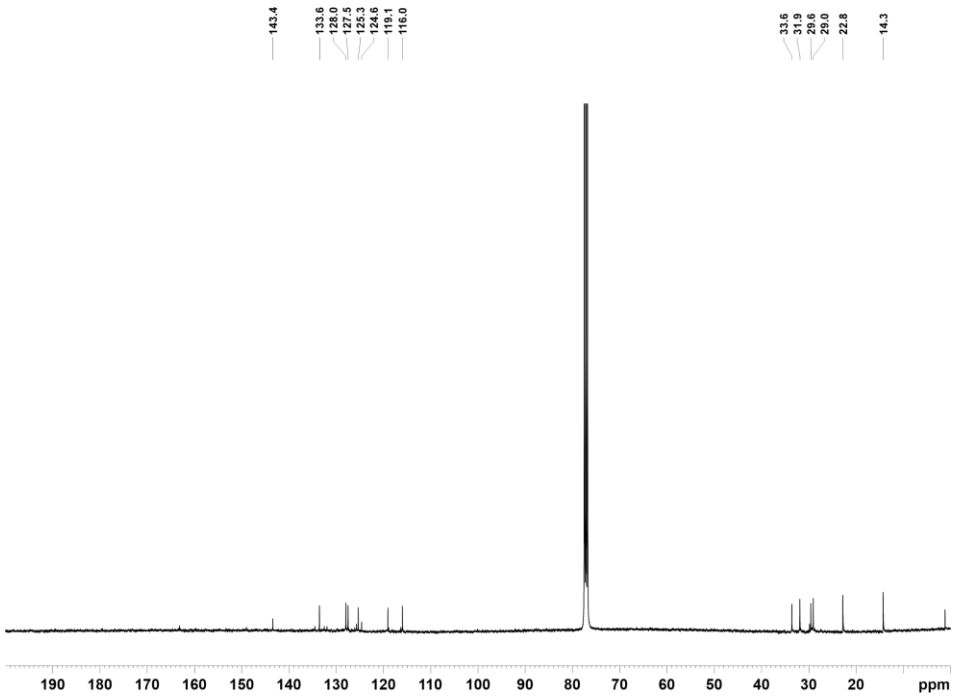

Figure 3.71. $^{13}C\{^{1}H\}$ NMR (100 MHz, $CDCl_3$) for product **76.**

CHAPTER IV:

CATALYTIC INTRAMOLECULAR [4+2] CYCLIZATIONS OF DIEN-γ-YNES ENABLED BY THE COOPERATIVE ACTION OF Rh/Ag DERIVATIVES

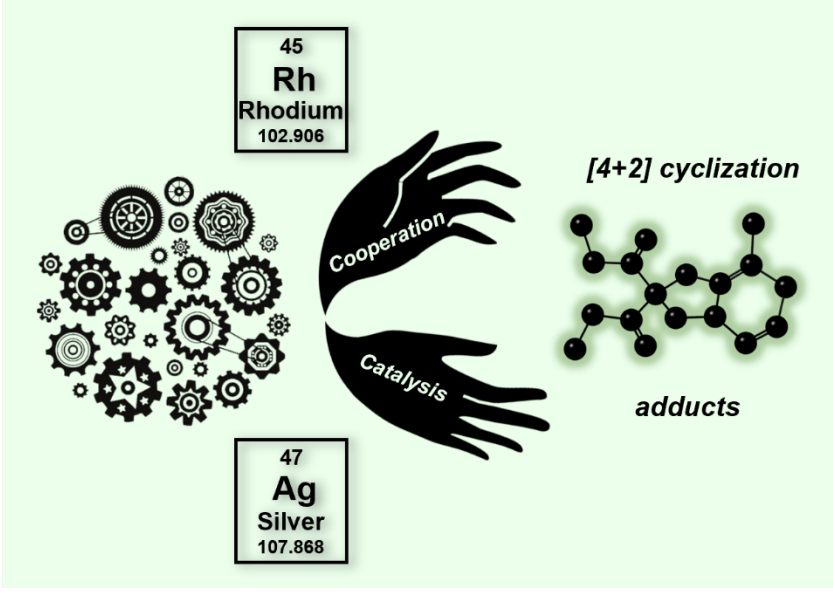

4.1 INTRODUCTION

The Diels-Alder reaction has been one of the most prominent transformations in organic synthesis given its versatility for constructing substituted six-membered rings in a highly (stereo)selective fashion.[167] Uncatalyzed Diels Alder reactions often require high thermal levels and are limited by restrictive stereoelectronic requirements. At first glance, metal-catalyzed [4+2] cycloadditions may seem a redundant synthetic methodology as the thermal counterpart (*i.e.*, the Diels Alder reaction) does exist. However, metal-catalyzed [4+2] cycloadditions offer important advantages since they often proceed at low temperatures and are not limited by the electronic requirements of the thermal Diels-Alder reactions.[168] The importance of intramolecular [4+2] cycloadditions relies on their ability and usefulness for constructing naturally occurring polycyclic rings.[167d,169] Amongst the myriad of conceivable intramolecular [4+2] cycloaddition reactions, those on trienes and/or dienynes deserve special mention due to the structural richness and biological interest of the final products.[170] Trienes and dienynes have been successfully cyclized by intramolecular [4+2] cycloadditions employing diverse transition

[167] For recent reviews on the Diels-Alder Reaction, see the following references and those cited therein: (a) Nicolaou, K. C.; Snyder, S. A.; Montagnon, T.; Vassilikogiannakis, G. *Angew. Chem., Int. Ed.* **2002**, *41*, 1668-1698; (b) Takao, K.; Munakata, R.; Tadano, K. *Chem. Rev.* **2005**, *105*, 4779-4807; (c) Gregoritza, M.; Brandl, F. P. *Eur. J. Pharm. Biopharm.* **2015**, *97*, 438-453; (d) Min, L.; Hu, Y.-J.; Fan, J.-H.; Zhang, W.; Li, C.-C. *Chem. Soc. Rev.* **2020**, *49*, 7015-7043; (e) Houk, K. N.; Liu, F.; Yang, Z.; Seeman, J. I. *Angew. Chem. Int. Ed.* **2021**, *60*, 12660-12681.

[168] Lewis acid catalysts have certainly proved to be the most effective in this chemistry (for recent reviews, see the following references and those cited therein: (a) Tiekink, E. H.; Vermeeren, P.; Bickelhaupt, F. M.; Hamlin, T. A. *Eur. J. Org. Chem.* **2021**, *2021*, 5275-5283; (b) Vermeeren, P.; Tiezza, M. D.; van Dongen, M.; Fernández, I.; Bickelhaupt, F. M.; Hamlin, T. A. *Chem. – Eur. J.* **2021**, *27*, 10610-10620; (c) Vermeersch, L.; De Proft, F.; Faulkner, V.; De Vleeschouwer, F. *Int. J. Mol. Sci.* **2023**, *24*, 4938-4963. However, the use of Lewis acids as catalysts is limited to activated dienophiles.

[169] For example, see: Quadrelli, P. *Modern Applications of Cycloaddition Chemistry*. Elsevier, 2019.

[170] (a) Qiao, C.; Zhang, W.; Han, J.-C.; Li, C.-C. *Org. Lett.* **2016**, *18*, 4932-4935; (b) Shibata, Y.; Tanaka, K. Rhodium(I)-Catalyzed [2+2+2] and [4+2] Cycloadditions. In *Rhodium Catalysis in Organic Synthesis*, 2019; pp 183-228; (c) Krishna, G.; Grudinin, D. G.; Nikitina, E. V.; Zubkov, F. I. *Synthesis* **2021**, *54*, 797-863; (d) Doerksen, R. S.; Hodík, T.; Hu, G.; Huynh, N. O.; Shuler, W. G.; Krische, M. J. *Chem. Rev.* **2021**, *121*, 4045-4083.

metal-based catalysts,[171] with numerous examples involving Rh(I)-based complexes.[172]

Since the seminal examples of intramolecular [4+2] cycloaddition of dienynes reported by Livinghouse *et al.*[173] other authors reported the successful use of Rh-phosphane complexes as catalysts in this transformation.[174] Rhodium(I)-catalyzed intramolecular [4+2] cycloadditions of dienynes were found to proceed with excellent chemo- and diastereo-selectivities with the diene containing more than one substituent and the C≡C bond being in an internal or terminal position of the substrate. Neutral rhodium(I) complexes of the type $[RhCl(PR_3)_3]$,[173a,175] $[RhCl(R_2P\text{-linker-}PR_2)]$[173b] or cationic rhodium(I)

[171] For Ni, see: (a) Wender, P. A.; Jenkins, T. E. *J. Am. Chem. Soc.* **1989**, *111*, 6432; (b) Wender, P. A.; Smith, T. E. *J. Org. Chem.* **1995**, *60*, 2962; (c) Wender, P. A.; Smith, T. E. *J. Org. Chem.* **1996**, *61*, 824; (d) Wender, P. A.; Smith, T. E. *Tetrahedron* **1998**, *54*, 1255-1275. For Ir, see: (e) Shibata, T.; Takasaku, K.; Takesue, Y.; Hirata, N.; Takagi, K. *Synlett* **2002**, 1681-1682. For Au see: (f) Kusama, H.; Karibe, Y.; Onizawa, Y.; Iwasawa, N. *Angew. Chem., Int. Ed.* **2010**, *49*, 4269; (g) Kim, S.-M.; Park, J.-H.; Chung, Y.-K. *Chem. Commun.* **2011**, *47*, 6719-6721. For Pd see: (h) Kumar, K.; Jolly, R. S. *Tetrahedron Lett.* **1998**, *39*, 3047-3048. For Co see: (i) Park, K. H.; Choi, S. Y.; Kim, S. Y.; Chung, Y. K. *Synlett* **2006**, 527-532; (j) Biletskyi, B.; Tenaglia, A.; Clavier, H. *Tetrahedron Lett.* **2018**, *59*, 103-107.

[172] For selected reviews, see: (a) Ojima, I.; Vu, A.; Bonafoux, D. Product Class 5: Organometallic Complexes of Rhodium. In *Science of Synthesis*, Vol. 1; 2002; pp 531-616; (b) Robinson, J. E. Rhodium(I)-Catalyzed [4+2] and [4+2+2] Carbocyclizations. In *Modern Rhodium-Catalyzed Organic Reactions*, 2005; pp 241-262; (c) Marinetti, A.; Jullien, H.; Voituriez, A. *Chem. Soc. Rev.* **2012**, *41*, 4884-4908.

[173] (a) Jolly, R. S.; Luedtke, G.; Sheehan, D.; Livinghouse, T. *J. Am. Chem. Soc.* **1990**, *112*, 4965; (b) McKinstry, L.; Livinghouse, T. *Tetrahedron* **1994**, *50*, 6145; (c) O'Mahony, D. J. R.; Belanger, D. B.; Livinghouse, T. *Synlett* **1998**, *1998*, 443-445.

[174] (a) Gilbertson, S. R.; Hoge, G. S. *Tetrahedron Lett.* **1998**, *39*, 2075-2078; (b) Wang, B.; Cao, P.; Zhang, X. *Tetrahedron Lett.* **2000**, *41*, 8041-8044; (c) Motoda, D.; Kinoshita, H.; Shinokubo, H.; Oshima, K. *Angew. Chem., Int. Ed.* **2004**, *43*, 1860-1862; (e) Yoo, W.-J.; Allen, A.; Villeneuve, K.; Tam, W. *Org. Lett.* **2005**, *7*, 5853-5856; (f) Saito, A.; Ono, T.; Hanzawa, Y. *J. Org. Chem.* **2006**, *71*, 6437-6443; (g) Saito, A.; Ono, T.; Takahashi, A.; Taguchi, T.; Hanzawa, Y. *Tetrahedron Lett.* **2006**, *47*, 891-895; (h) Shen, M.-H.; Liang, X.-C.; Li, C.; Wu, H.; Qu, H.-Y.; Wang, F.-M.; Xu, H.-D. *Tetrahedron Lett.* **2019**, *60*, 1025-1028.

[175] For example, see: O'Mahony, D. J. R.; Belanger, D. B.; Livinghouse, T. *Org. Biomol. Chem.* **2003**, *1*, 2038-2040.

derivatives such as [Rh (R_2P-linker-PR_2)]$^+$[174b,176] have been commonly used as catalysts.

A silver salt, usually $AgSbF_6$, is used in combination with the rhodium precursor and the ligand for preparing the cationic rhodium active catalysts. It has been suggested that silver is required as a halide scavenger to generate *in situ* catalytically active cationic Rh(I) complexes from the neutral rhodium precursors (for instance [{Rh(CO)$_2$(μ-Cl)}$_2$] or [{RhCl(cod)}$_2$]).[172-174] Thus, it is normally proposed in the literature that silver neither intervenes in the catalytic cycle nor has an influence in the reactivity beyond the generation of catalytically cationic Rh(I) complexes. To the best of our knowledge, few examples of [4+2] cycloadditions of dienynes catalyzed by cationic Rh(I) complexes, whose preparation does not involve silver salts, are reported in the literature,[176b,176d] with low cycloaddition yields being described. Electro-deficient cationic rhodium complexes do generally show higher catalytic activity and mediate the [4+2] cycloadditions under milder conditions than their neutral analogues.[173a,173b,175,176] Enantioselective versions of this reaction have also been investigated employing rhodium complexes derived from DIOP,[173b] (*S*,*S*)-Me,Me-DuPhos,[177] Et-DuPhos and enantiopure bicyclic dienes as chiral ligands.[178] *N*-heterocyclic carbenes (NHC) have also proven to be useful ligands for the rhodium-catalyzed intramolecular [4+2] cycloadditions of dienynes.[179]

---

[176] For some examples, see: (a) Matsuda, I.; Shibata, M.; Sato, S.; Izumi, Y. *Tetrahedron Lett.* **1987**, *28*, 3361-3362; (b) Heath, H.; Wolfe, B.; Livinghouse, T.; Bae, S. K. *Synthesis* **2001**, *2001*, 2341-2347; (d) Miyauchi, Y.; Noguchi, K.; Tanaka, K. *Org. Lett.* **2012**, *14*, 5856-5859.

[177] Gilbertson, S. R.; Hoge, G. S.; Genov, D. G. *J. Org. Chem.* **1998**, *63*, 10077-10080.

[178] (a) Aikawa, K.; Akutagawa, S.; Mikami, K. *J. Am. Chem. Soc.* **2006**, *128*, 12648-12649; (b) Shintani, R.; Sannohe, Y.; Tsuji, T.; Hayashi, T. *Angew. Chem., Int. Ed.* **2007**, *46*, 7277-7280.

[179] (a) Lee, S. I.; Park, S. Y.; Park, J. H.; Jung, I. G.; Choi, S. Y.; Chung, Y. K.; Lee, B. Y. *J. Org. Chem.* **2006**, *71*, 91-96; (b) Gómez, F. J.; Kamber, N. E.; Deschamps, N. M.; Cole, A. P.; Wender, P. A.; Waymouth, R. M. *Organometallics* **2007**, *26*, 4541-4545.

Supramolecular catalysis has been a rapidly expanding discipline in recent years. By combining classical concepts of catalysis and supramolecular chemistry, highly efficient and selective supramolecular catalysts have been tailored by carefully selecting the reversible interaction(s) to be used (*i.e.*, hydrogen bond, metal–ligand, electrostatic or diverse van der Waals interactions) with the ligands, substrates, additives, etc. of the catalytic event. Distinct applications have been accomplished,[2,6b,8,9c,10a-c,11a-c,12b,12c] mainly based on (*i*) the construction of bi- or multidentate catalyst libraries, (*ii*) building of polynuclear complexes, (*iii*) the alteration of the coordination spheres of a metal catalyst and (*iv*) the control of the substrate reactivity.

The design of artificial catalysts incorporating common tools in enzyme catalysis[2,6b,115a,180] (for instance, confinement of the substrates and the active site within a catalytic pocket, creation of a hydrophobic pocket in water, self-replication and allosteric properties, etc.) has also led to systems capable of competing with the catalytic proficiency of enzymes. Overall, supramolecular catalysis has allowed for the development of new catalytic pathways/reactions not achievable with classical covalent catalysts.

Within the numerous supramolecular interactions available, halogen bonding[43] is increasingly gaining importance in supramolecular catalysis

[180] (a) Leenders, S. H. A. M.; Gramage-Doria, R.; de Bruin, B.; Reek, J. N. H. *Chem. Soc. Rev.* **2015**, *44*, 433-448; (b) Bistri, O.; Reinaud, O. *Org. Biomol. Chem.* **2015**, *13*, 2849-2865; (c) Deraedt, C.; Astruc, D. *Coord. Chem. Rev.* **2016**, *324*, 106-122; (d) Kosikova, T.; Philp, D. *Chem. Soc. Rev.* **2017**, *46*, 7274-7305; (e) De Martino, M. T.; Abdelmohsen, L. K. E. A.; Rutjes, F. P. J. T.; van Hest, J. C. M. *Beilstein Journal of Organic Chemistry* **2018**, *14*, 716-733; (f) Lipshutz, B. H.; Ghorai, S.; Cortes-Clerget, M. *Chem. – Eur. J.* **2018**, *24*, 6672-6695; (g) Li, X.; Wu, J.; He, C.; Meng, Q.; Duan, C. *Small* **2019**, *15*, 1804770; (h) Fang, Y.; Powell, J. A.; Li, E.; Wang, Q.; Perry, Z.; Kirchon, A.; Yang, X.; Xiao, Z.; Zhu, C.; Zhang, L.; Huang, F.; Zhou, H.-C. *Chem. Soc. Rev.* **2019**, *48*, 4707-4730; (i) van Leeuwen, P. W. N. M.; Raynal, M. Supramolecular Catalysis in Water. In *Supramolecular Chemistry in Water*, 2019; pp 525-561; (j) Wang, K.; Jordan, J. H.; Hu, X.-Y.; Wang, L. *Angew. Chem. Int. Ed.* **2020**, *59*, 13712-13721; (k) Morimoto, M.; Bierschenk, S. M.; Xia, K. T.; Bergman, R. G.; Raymond, K. N.; Toste, F. D. *Nature Catalysis* **2020**, *3*, 969-984; (l) Saha, R.; Mondal, B.; Mukherjee, P. S. *Chem. Rev.* **2022**, *122*, 12244-12307; (m) Pan, T.; Wang, Y.; Xue, X.; Zhang, C. *Exploration* **2022**, *2*, 20210095; (n) Acosta-Calle, S.; Miller, A. J. M. *Acc. Chem. Res.* **2023**, *56*, 971-981.

due to its well-defined directionality, strength,[43] tolerance to changes in the polarity of the solvent[52] and highly successful applications in organocatalysis.[53,54] Our research group has pioneered the construction of halogen-bonded bisphosphane metal complexes from building blocks that contain both the complementary supramolecular motifs required for the assembly process, as well as the phosphino groups for catalysis.[70,71] Specifically, pyridyl- (**L1**) and iodotetrafluoroaryl-substituted (**L2**) phosphanes were assembled in the presence of a rhodium(I) precursor to form the halogen-bonded complex [Rh(CO)(κ³*I,P,P*-**L1·L2**)]BArF **C1·BArF** (Scheme 1.13). The efficacy of **C1·BArF** as catalyst was demonstrated in the hydroboration of terminal alkynes with maximized regioselectivities towards the non-conventional branched alkenylboronic acid derivatives (see Chapter III).

The interesting structural features of XBphos-Rh-BArF **C1·BArF** (*i.e.*, its κ³*I,P,P*-tridentate cationic nature, robustness and stability) prompted us to investigate its catalytic activity in [4+2] cycloadditions of dien-γ-ynes, with the aim of filling gaps in the existing catalytic tools for this chemistry.[181]

[181] Interestingly, metal-mediated [4+2] cycloadditions on dien-γ-ynes with a monosubstituted diene unit (*i.e.*, R-CH=CH-CH=CH_2 substrates) are unreported. Dien-γ-ynes **S12**-**S19**, whose [4+2] cycloaddition will be described in the discussion that follows, are known compounds in the literature with their [4+2] cycloadditions having not been studied. For the reported applications of **S12**-**S19**, see: (a) Schiller, R.; Pour, M.; Fáková, H.; Kuneš, J.; Císařová, I. *J. Org. Chem.* **2004**, *69*, 6761-6765; (b) Ni, Y.; Montgomery, J. *J. Am. Chem. Soc.* **2004**, *126*, 11162-11163; (c) Kimura, M.; Ezoe, A.; Mori, M.; Tamaru, Y. *J. Am. Chem. Soc.* **2005**, *127*, 201-209; (d) Wender, P. A.; Christy, J. P. *J. Am. Chem. Soc.* **2006**, *128*, 5354-5355; (e) López-Durán, R.; Martos-Redruejo, A.; Buñuel, E.; Pardo-Rodríguez, V.; Cárdenas, D. J. *Chem. Commun.* **2013**, *49*, 10691-10693.

4.2 RESULTS AND DISSCUSION

We reasoned that the **C1·BArF**'s cationic nature would make them it an ideal catalyst to be used in metal-catalyzed [4+2] cycloadditions without the need of using silver derivatives. Our studies began with the [4+2] intramolecular cyclization of substrate **S12** employing **C1·BArF** as catalyst and standard reaction conditions for this chemistry (Table 4.1). To our surprise, this initial experiment revealed that **C1·BArF** itself did not mediate the reaction, with *ca.* 20% of the starting material being degraded. However, the combined use of **C1·BArF** and AgBArF led to active catalytic systems at room temperature with formation of the target cycloaddition product **P12** (51% yield, mean value of multiple experiments; entry 2, Table 4.1).

Regrettably, the cycloaddition reaction employing the **C1·BArF**/AgBArF catalytic system suffered from a lack of reproducibility. After having carried out the synthesis of AgBArF[182] six times and performed the rhodium-catalyzed cycloaddition eleven times by using freshly prepared AgBArF, the conversion (mean value = 74%; standard deviation (σ) = 17%) and yield (mean value = 51%; standard deviation (σ) = 19%) values for **S12** and **P12**, respectively, were highly dispersed. We attributed the lack of reproducibility of the reaction to several drawbacks of AgBArF, such as the poor reproducibility of its synthesis, the lack of well-described protocols for quantifying the silver content, as well as the low stability of AgBArF salt over short and long periods of time.[182,183]

As counterions tend to have important effects in the outcome of [4+2] cycloadditions,[184] besides the difficulties encountered when using AgBArF,

[182] Hayashi, Y.; Rohde, J. J.; Corey, E. J. *J. Am. Chem. Soc.* **1996**, *118*, 5502-5503.

[183] It is well-established that AgBArF decomposes under vacuum, at room temperature and in the presence of light and traces of water, which makes its handling and use in catalysis difficult. For example, see: Golden, J. H.; Mutolo, P. F.; Lobkovsky, E. B.; DiSalvo, F. J. *Inorg. Chem.* **1994**, *33*, 5374-5375.

[184] For references on the effects of the counterions in [4+2] cycloadditions, see for example reference 173c and: Macchioni, A. *Chem. Rev.* **2005**, *105*, 2039-2073.

we used the combination of **C1·BArF** with diverse commercially available silver salts in order to maximize the yield of the reaction.

Table 4.1. Catalyst screening for [4+2] cycloadditions of **S12.**

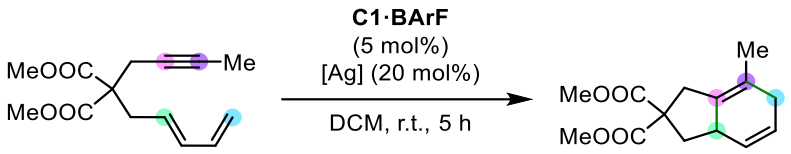

S12 (1.0 equiv.) **P12**

Entry	Rh catalyst	Ag salt	Conv. (%)	Yield (%)
1	**C1·BArF**	none	17	<1
2	**C1·BArF**	AgBArF	50 – >99	31 – 87
3	**C1·BArF**	$AgSbF_6$	>99	63
4	**C1·BArF**	$AgBF_4$	>99	61
5	**C1·BArF**	AgOMs	34	14
6	**C1·BArF**	$AgNO_3$	71	43
7	**C1·BArF**	AgOTf	>99	73
8	**C1·BArF**	AgOTf	>99	82
9[b]	-	AgOTf	25	<1

[a] Determined by ^1H NMR spectroscopy using 1,3,5-trimethoxybenzene as internal standard. [b] 5 mol% of AgOTf was used.

The aim of these experiments was also to determine whether the activity of the catalyst was an effect of the BArF anion of the catalyst or not. The use of diverse silver salts (*i.e.*, $AgSbF_6$, $AgBF_4$, AgOMs, $AgNO_3$ and AgOTf, entries 3-7, Table 4.1) led in all cases to active catalytic systems to a greater or lesser extent , with 5% of **C1·BArF** and 5% of AgOTf being the highest performing catalytic system (3 experiments, mean value = 82%; σ = 1%, entry 8, Table 4.1). In order to demonstrate the relevance of the silver salt in the catalyzed cycloaddition, AgOTf was tested in absence of our cationic

Rh(I) complex under the same reaction conditions. The use of AgOTf as catalyst did not mediate the cycloaddition either (Table 4.1, compare entries 1 and 9 for the results with **C1·BArF** or AgOTf, respectively). These results demonstrate that even employing a cationic Rh(I) complex derived from a bisphosphane ligand, the presence of silver is required for the cycloaddition to take place.

With the optimal conditions in hand, the structural diversity of the substrates was expanded to demonstrate the scope of application of this transformation (8 substrates, Scheme 4.1). Regrettably, dien-γ-ynes with a monosubstituted alkyne motif (**S14**)[185] and that bearing a substituent at the terminal carbon of the diene unit (**S19**) did not lead to the target [4+2] cycloadducts, with partial degradation of the starting material towards polymeric materials being observed. It should be noted that our catalytic system is only selective towards the cycloaddition of dien-γ-ynes, as triene **S13** was not transformed into the expected cycloadduct **P13** (Scheme 4.1).

Dien-γ-ynes containing a substituent in the triple bond and a monosubstituted diene unit led efficiently to the cycloaddition products with yield ranging from 66% to quantitative yield (see products **P12**, **P15**, **P16**, **P17** and **P18**, Scheme 4.1). As for the substituents at the alkyne motif, both alkyl and aryl groups are tolerated (*i.e.*, **S12**, **S16**, **S17** with alkyl substituents and **S15** and **S18** with phenyl groups).

[185] The lack of reactivity of terminal alkynes (*e.g.* **S14** in Scheme 4.1) could be attributed to the preferential C–H activation of the terminal triple bond by silver. See reference 188a and: Sivaguru, P.; Cao, S.; Babu, K. R.; Bi, X. *Acc. Chem. Res.* **2020**, *53*, 662-675.

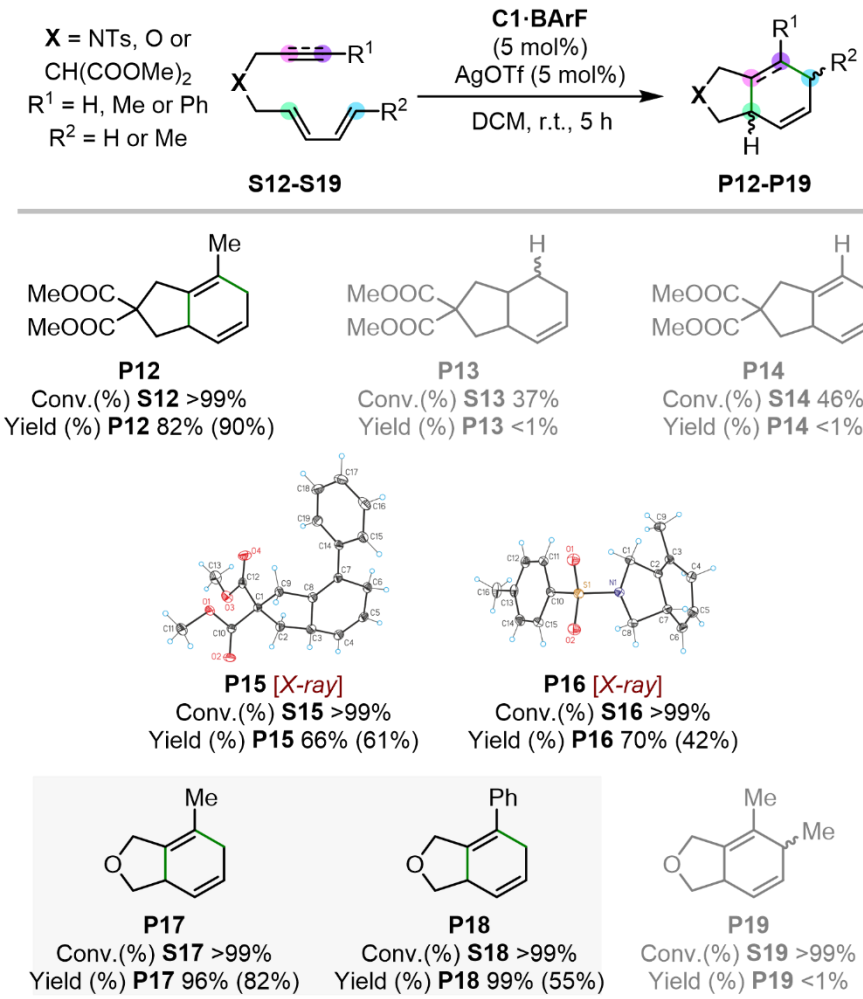

Scheme 4.1. C1·BArF/AgOTf-catalyzed [4+2] cycloaddition for an array of structurally diverse substrates.[186]

The **C1·BArF**/AgOTf catalytic system allows for *C*-, *O*- and *N*-groups in the chain connecting the diene and alkyne units, with the substrate **S18** containing an oxygen group between the two unsaturated groups providing the highest yield after the cycloaddition (product **P18**, Scheme 4.1). Cycloaddition products were properly characterized with standard spectroscopic techniques (see the section 4.4) and crystals suitable for

[186] Cycloaddition yields were calculated by ^{1}H NMR spectroscopy using 1,3,5-trimethoxybenzene as internal standard. Isolated yields in brackets.

X-Ray diffraction analysis were grown for **P15** and **P16**, which allowed for the unequivocal determination of their structure.

As previously mentioned, the role of the silver salts is reported to be restricted to the generation of active cationic Rh(I) complexes by abstraction of the chlorido ligand coordinated to the rhodium(I) center. We have clearly demonstrated that the presence of a silver salt was essential for the cycloaddition to take place, even though no chlorido ligands were directly bound to our rhodium-based catalytic system. This experimental observation pointed to a cooperative action between Rh(I) and Ag(I) centers in the cycloaddition reactions. Considering the nature of silver(I) derivatives and recent discoveries in their reactivity,[187] including that towards C-C unsaturated bonds,[188] a number of hypotheses for the role of silver in our chemistry were made. Moreover, to demonstrate the validity of our hypotheses, suitably designed experiments were conducted.

(i) Ag(I) as an intermediary in the cycloaddition.

Silver salts are known to promote cycloaddition reactions.[188] However, the reaction of **S12** in the only presence of AgOTf did not lead to the cycloadduct **P12** (see entry 9 in Table 4.1). In order to determine whether silver was involved in any of the multiple steps towards the final cycloaddition product or not, additional experiments were performed. In the event of the activation of the triple bond by Ag(I), the first cyclization reaction would lead to the cationic intermediate **77**, prone to be captured by a nucleophile such as MeOH, with compound **78** being formed. Interestingly, the reaction of **S12** in the presence of catalytic amounts of

[187] (a) Yao, L.; Yu, X.; Mo, C.; Wu, J. *Org. Biomol. Chem.* **2012**, *10*, 9447-9451; (b) Yang, S.; Rui, K.-H.; Tang, X.-Y.; Xu, Q.; Shi, M. *J. Am. Chem. Soc.* **2017**, *139*, 5957-5964.

[188] For more information on silver(I)-catalyzed reactions, see: (a) Szpilman, A. M. C., E. M. Cycloaddition Reactions. In *Silver in Organic Chemistry*, 2010; pp 43-82; (b) Koo, J.; Park, H.-S.; Shin, S. *Tetrahedron Lett.* **2013**, *54*, 834-839; (c) Fang, G.; Bi, X. *Chem. Soc. Rev.* **2015**, *44*, 8124-8173; (d) Li, M.; Wu, W.; Jiang, H. *ChemCatChem* **2020**, *12*, 5034-5050.

AgOTf or the **C1·BArF**/AgOTf catalytic system in MeOH did not lead to product **78**, ruling out this hypothesis (Scheme 4.2a).

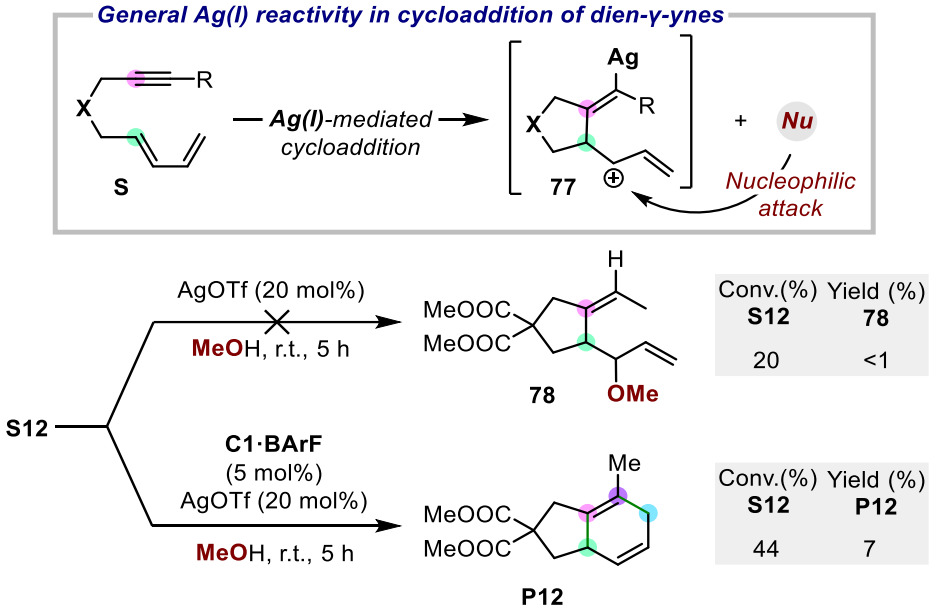

Scheme 4.2. Evaluation of silver(I) as mediator of the cycloaddition.

(ii) Ag(I)-phosphane species as active catalysts.

It has been found in literature that Ag(I)-phosphane complexes are catalytically active in a broad range of transformations, including cycloadditions.[188] Moreover, since silver species act as ligand abstractors (chloride or even phosphane ligands),[189] it could also be hypothesized that silver could abstract the phosphane ligands of **C1·BArF** with degradation of the Rh(I) derivative and formation of the corresponding Ag(I)-phosphane complexes, which could in turn promote the cycloaddition reaction. To rule this possibility out, NMR analysis of mixtures of **C1·BArF** in the presence of AgOTf showed no decomposition of the halogen bond-assembled complex (Scheme 4.3a) Besides, experiments combining Ag(I) and the monophosphanes present in

[189] Perez-Ortega, I.; Albeniz, A. C. *Dalton Trans.* **2023**, *52*, 1425-1432, Pérez-Ortega, I.; Albéniz, A. C. *Dalton Trans.* **2023**, *52*, 1425-1432.

C1·BArF (*i.e.*, **L1** and **L2**) were conducted under the standard reaction conditions (Scheme 4.3b) without the cycloadduct **P12** being formed. Consequently, the hypothesis of Ag(I)-phosphane complexes being the catalysts of the cycloadditions was also discarded.

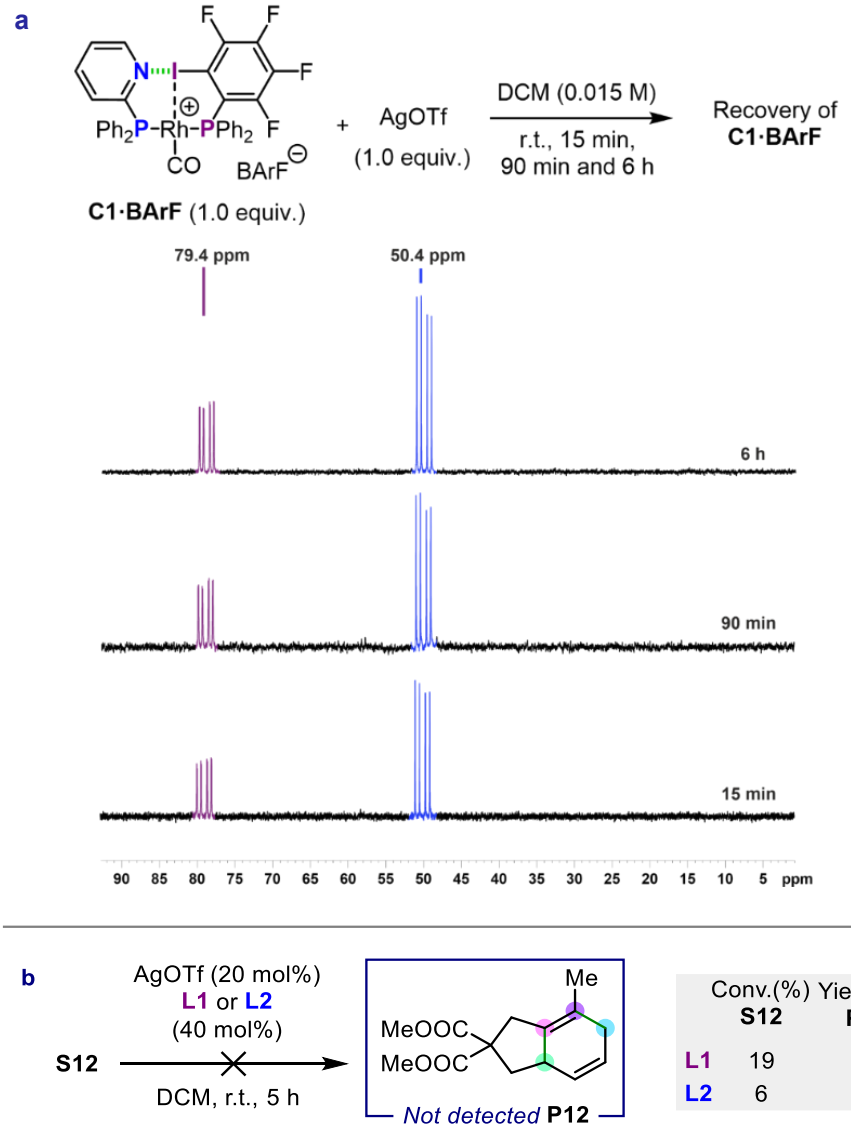

Scheme 4.3. (a) ^{31}P NMR analysis of the mixture of **C1·BArF** (1.0 equiv.) in the presence of AgOTf (1.0 equiv.); (b) Silver(I)-phosphane complexes as active catalytic systems in cycloaddition reactions.

(iii) Ag(I) as oxidizing agent.

It could also be hypothesized that silver acts as an oxidizing agent of rhodium with formation of Rh(III) species. Rh(III) complexes are known to be active in numerous cycloadditions.[190] However, after recording the NMR spectra of a 1:1 **C1·BArF** /AgOTf mixture, **C1·BArF** proved to be stable under the reaction conditions (6 h, Scheme 4.3), which ruled this hypothesis out.

(iv) Activation of the substrate by Ag(I).

We also hypothesized that silver(I) could act as Lewis acid towards the substrate and,[191] therefore, function as an activator of the substrates converting them into better electrophiles. Due to its d^{10} electronic configuration, silver favors interactions with C≡C alkynes, referred to as alkynophilicity.[188c,192] To study potential interactions between silver triflate and substrate **S12**,[192c-e] NMR coordination studies between these two reagents in a 1:1 molar ratio were performed. Interestingly, important downfield shifts in the protons of the groups bonded to the C≡C triple bond and of those on the diene unit in **S12** were observed when AgOTf was mixed with **S12** (see Scheme 4.4). These results indicate that silver is interacting with all the unsaturated C–C bonds in the substrate making them more electrophilic and prone to attract electron density from the metal center.

[190] For some examples, see: (a) Seoane, A.; Casanova, N.; Quiñones, N.; Mascareñas, J. L.; Gulías, M. *J. Am. Chem. Soc.* **2014**, *136*, 7607-7610; (b) Li, B.; Guo, C.; Shen, N.; Zhang, X.; Fan, X. *Org. Chem. Front.* **2020**, *7*, 3698-3704; (c) Yan, X.; Pi, C.; Cui, X.; Cui, X.; Wu, Y. *Org. Lett.* **2023**, *25*, 2953-2957.

[191] Muñoz, M. P. *Chem. Soc. Rev.* **2014**, *43*, 3164-3183.

[192] The affinity of silver towards unsaturated bonds has been well studied. For selected examples, see: (a) Winstein, S.; Lucas, H. J. *J. Am. Chem. Soc.* **1938**, *60*, 836. (b) Trueblood, K. N.; Lucas, H. J. *J. Am. Chem. Soc.* **1952**, *74*, 1338; (c) Gorin, D. J.; Toste, F. D. *Nature* **2007**, *446*, 395-403; (d) Dias, H. V. R.; Wu, J. *Eur. J. Inorg. Chem.* **2008**, 509-522 and references therein.

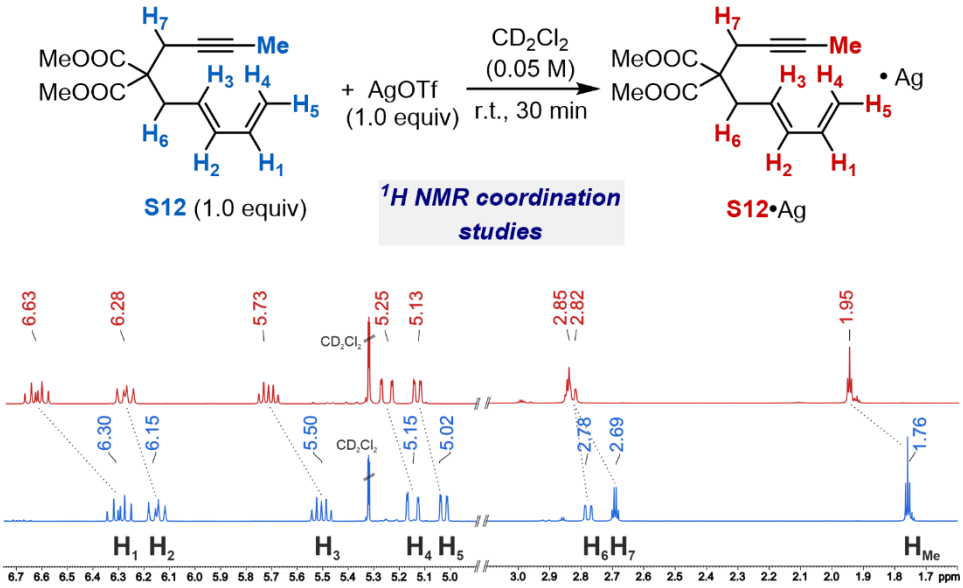

Scheme 4.4. Formation of **S12•Ag** adduct.

Based on the results previously mentioned and literature reports, we propose a reaction pathway leading to the [4+2] cycloadducts enabled by the cooperative action of Rh/Ag derivatives.[187,193] It is usually assumed that the rhodium-catalyzed cycloaddition reaction starts with the coordination of the dien-γ-yne and proceeds by oxidative cyclization, σ,π-allylic isomerization and reductive elimination processes.[170b,172b,178b] Low temperature NMR studies were performed with **S12** and **C1·BArF** and AgOTf in a 1:1:1 molar ratio (from 193 to 298 K) without any reaction intermediate (for instance the corresponding rhodacycle) being observed, while the corresponding cycloadduct was detected at temperatures above 283 K (Figure 4.1, see section 4.4 for more details). Thus, it can be

[193] For other examples of multimetallic catalytic processes, see: (a) Allen, A. E.; MacMillan, D. W. C. *Chem. Sci.* **2012**, *3*, 633-658. For recent examples of double activation catalysis, see: (b) Shi, Y.; Peterson, S. M.; Haberaecker, W. W.; Blum, S. A. *J. Am. Chem. Soc.* **2008**, *130*, 2168-2169; (c) Xu, H.; Zuend, S. J.; Woll, M. G.; Tao, Y.; Jacobsen, E. N. *Science* **2010**, *327*, 986-990; (d) Nakao, Y. Cooperative Double Activation Metal/Metal and Metal/Organic Catalysis Enabling Challenging Organic Reactions. In *Molecular Technology: Synthesis Innovation*, Vol. 4; 2019; pp 95-118.

concluded that cycloadditions catalyzed by **C1·BArF** and AgOTf are fast reactions with low energy barriers.

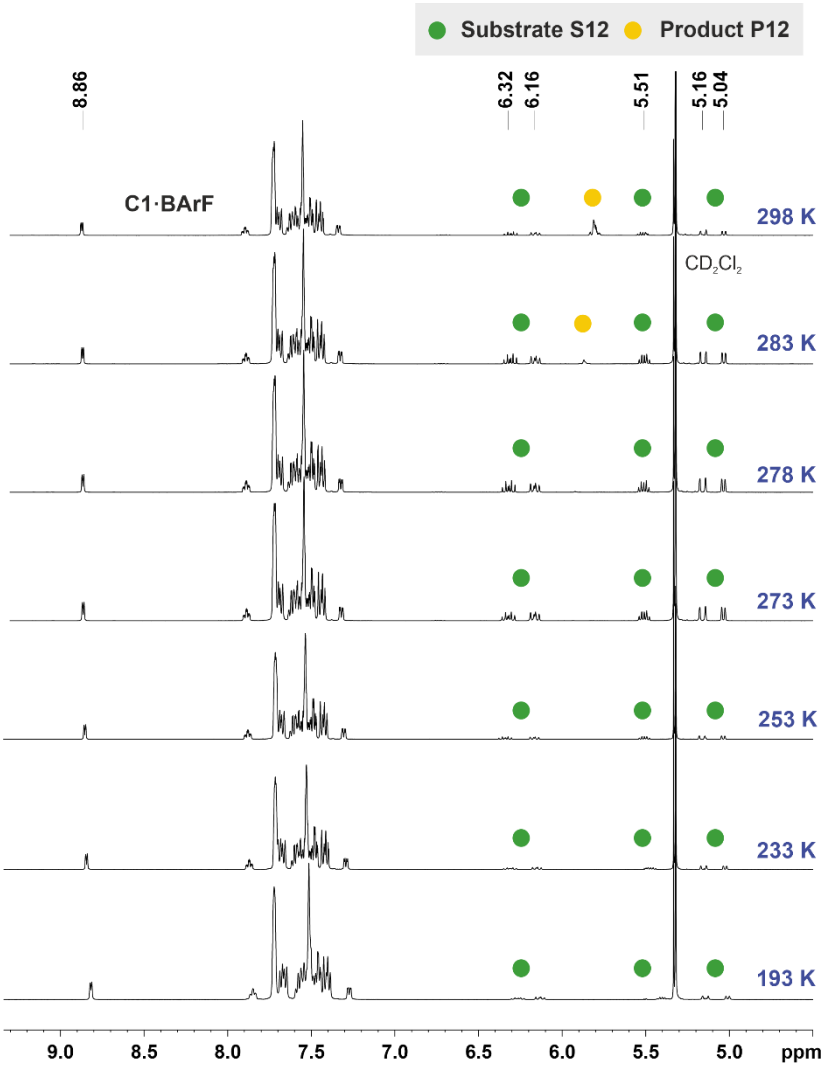

Figure 4.1. Low temperature ^{1}H NMR experiments of stoichiometric **C1·BArF**-mediated [4+2] cycloaddition of **S12.**

Thus, we propose that in combination with the commonly accepted catalytic cycle for rhodium-catalyzed [4+2] cycloadditions,[170b,172b,178b,194] dien-γ-ynes **S** form a 1:1 complex with the silver(I) salt, yielding

[194] Liao, W.; Yu, Z.-X. *J. Org. Chem.* **2014**, *79*, 11949-11960.

intermediate **S•Ag** (see Scheme 4.5). Rhodium-mediated oxidative cyclization would afford intermediate **I**. The rhodium center supplies two out of the six electrons involved in the oxidative cyclization process. This step might be favored by the interaction of the Ag(I) center with the substrate's unsaturated C–C bonds, as the **S•Ag** complex is more prone to attract electron density from the rhodium center. Complexation of silver with the substrate might take place simultaneously with a rapid transmetalation process to the rhodium center, as reported in the literature in related processes.[187b] Alkynes generally undergo oxidative cyclization more easily than do alkenes[172b] due to additional coordination of the alkyne moiety to the rhodium center in the corresponding transition state.[194] For this reason, we assumed that, the alkyne and the alkene group three bonds away are the unsaturated C–C bonds involved in the oxidative cyclization step, which is supposed to be irreversible.[194]

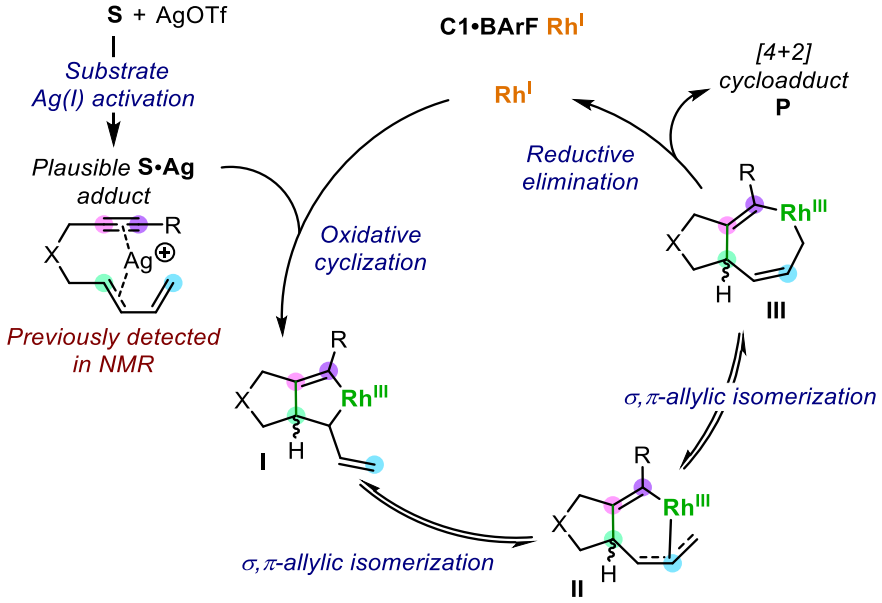

Scheme 4.5. Proposed reaction pathway for intramolecular [4+2] cycloadditions of dien-γ-ynes.

The reaction pathway might proceed further by σ,π-allylic isomerization followed by reductive elimination steps from intermediate **III** affording

the final cycloaddition product **P**.[178b] Computational studies on the rhodium(I) [4+2] cyclization of a benchmark dien-γ-yne in the absence of silver revealed that the reaction pathway indicated in Scheme 4.5 was the most energetically favored.[194]

4.3 CONCLUSIONS

In summary, we have developed an efficient intramolecular [4+2] cycloaddition of dien-γ-ynes mediated by the rhodium(I) complex derived from **C1·BArF** in combination with a silver(I) salt. Under optimized catalytic reactions conditions, the cooperative action of the Rh/Ag derivatives efficiently leads to the corresponding [4+2] cycloadducts (yields ranging from 66% to 99%) with high selectivity. The synthetic protocol features simple operation and good functional group tolerance and represents a good example of the cooperative action of two metals in catalysis.

Studies aimed at determining the role of rhodium(I) and Ag(I) derivatives were performed and revealed that both metallic derivatives are required for the reaction to take place. Concretely, whilst rhodium is responsible for the cycloaddition process, silver activates the dien-γ-ynes by increasing their electrophilicity due to coordination of Ag(I) to the unsaturated C–C bonds. The role of silver(I) derivatives used for generating the rhodium(I) catalysts developed by other research groups should be revisited in order to determine whether silver(I) derivatives have the mere role of abstracting chlorido ligands from rhodium complexes or are also necessary for activating the dien-γ-ynes towards [4+2] cycloadditions in analogous manner to that herein demonstrated.

4.4 EXPERIMENTAL SECTION

4.4.1 General considerations

All syntheses were carried out using chemicals as purchased from commercial sources unless otherwise stated. Air- and moisture-sensitive manipulations or reactions were performed under inert atmosphere, either in a glove box or with standard Schlenk techniques. Glassware was dried *in vacuo* before use with a hot air gun. All solvents were dried by using a solvent purification system (SPS). Silica gel 60 (230–400 mesh) was used for column chromatography. NMR spectra were recorded in 400 MHz or 500 MHz spectrometers in $CDCl_3$ or CD_2Cl_2 unless otherwise cited. ^{1}H and $^{13}C\{^{1}H\}$ NMR chemical shifts are quoted in ppm relative to residual solvent peaks. $^{19}F\{^{1}H\}$ NMR chemical shifts are quoted in ppm relative to $CFCl_3$ in $CDCl_3$. $^{31}P\{^{1}H\}$ NMR chemical shifts are quoted in ppm relative to 85% phosphoric acid in water. HRMS spectra were recorded using ESI ionization method in positive mode. GC-MS analyses were performed using EI as ionization method. GC analyses were performed with a flame ionization detector. IR spectra were recorded using Attenuated Total Reflection (ATR) technique unless otherwise cited. Ligands **L1** is commercially available and was used as received. (2-iodo-3,4,5,6-tetrafluorobenzene)diphenylphosphane ligand **L2** and XBphos-Rh **C1·BArF** were prepared according to previous literature reports.[70]

4.4.2 General structural comments on X-Ray crystals

Crystals suitable for X-Ray measurement for compounds **P15** and **P16** were obtained by slow diffusion of *n*-pentane into concentrated solutions of Et_2O. The measured crystals were prepared under inert conditions immersed in perfluoropolyether as protecting oil for manipulation.

Crystal structure determination of **P15** and **P16** was carried out using an Appex DUO Kappa 4-axis goniometer equipped with an Appex 2 4K CCD area detector, a Microfocus Source E025 IuS using MoK_α radiation (0.71073 Å), Quazar MX multilayer Optics as monochromator and an Oxford Cryosystems low temperature device Cryostream 700 plus (T = −173 °C). Full-sphere data collection was used with ω and φ scans. *Programs used:* Data collection APPEX-2,[100] data reduction Bruker Saint[101] V/60A and absorption correction SADABS.[102]

Structure solution and refinement: Crystal structure solution was achieved using the computer program SHELXT.[103] Visualization was performed with the program SHELXle.[104] Missing atoms were subsequently located from difference Fourier synthesis and added to the atom list. Least-squares refinement on F^2 using all measured intensities was carried out using the program SHELXL 2015.[105] All non-hydrogen atoms were refined including anisotropic displacement parameters.

Table 4.2. Crystal data and structural parameters for complex **P15.**

Compound	**P15**
Formula	$C_{19}H_{20}O_4$
Formula weight (total)	312.35
Crystal size (mm^3)	0.4 x 0.3 x 0.02
Temp (K)	100(2)
Crystal system	Triclinic
Space group	P-1
A (Å)	7.3448(4)
B (Å)	10.2147(6)
C (Å)	11.2849(6)
α (deg)	77.3161(18)
β (deg)	88.990(3)
γ (deg)	84.549(3)
V ($Å^3$)	796.89(8)
Z	2
ρ (Mg/m^3)	1.302
μ (mm^{-1})	0.091
θ range (°)	1.916 to 32.107
Reflec. collected	11327
Independent reflections	5139[R(int) = 0.0250]
Absorpt. correct.	Multi-scan
Trans. max/min	0.74/0.70
Data/restraints/parameters	5139/ 0/ 210
R1/wR2 [I>2σ(I)]	0.0541/0.1311
R1/wR2 [all data]	0.0764/0.1435
Goodness-of-fit (F^2)	1.035
Peak/hole ($e/Å^3$)	0.747/-0.317

Table 4.3. Crystal data and structural parameters for complex **P16.**

Compound	**P16**
Formula	$C_{16}H_{19}NO_2S$
Formula weight (total)	289.38
Crystal size (mm^3)	0.5 x 0.4 x 0.1
Temp (K)	100(2)
Crystal system	Monoclinic
Space group	P $2_1/c$
A (Å)	13.8211(5)
B (Å)	7.9161(3)
C (Å)	13.5898(5)
α (deg)	90
β (deg)	102.8982(9)
γ (deg)	90
V ($Å^3$)	1449.33
Z	4
ρ (Mg/m^3)	1.326
μ (mm^{-1})	0.224
θ range (°)	2.985 to 32.639
Reflec. collected	23328
Independent reflections	5174[R(int) = 0.0245]
Absorpt. correct.	Multi-scan
Trans. max/min	0.74/0.66
Data/restraints/parameters	5174/ 0/ 183
R1/wR2 [I>2σ(I)]	0.0330/0.0901
R1/wR2 [all data]	0.0375/0.0936
Goodness-of-fit (F^2)	1.085
Peak/hole ($e/Å^3$)	0.494/-0.357

4.4.3 Synthesis of dienyne substrates

All substrates **S12-S19** are well-known in literature and were synthesized following already reported methodologies and synthetic procedures previously adapted by our group.[111] Spectroscopic data of the pure substrates **S12-S19** are described in this section.

(*E*)-2-(but-2-yn-1-yl)-2-(penta-2,4-dien-1-yl)malonate **S12** was obtained as a colorless oil.

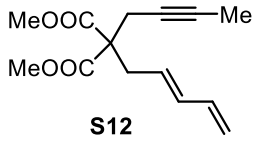

S12

S12: **^{1}H NMR** (400 MHz, $CDCl_3$) δ: 6.22 (dt, *J* = 17.1 Hz, *J* = 10.2 Hz, 1 H), 6.07 (dd, *J* = 14.9 Hz, *J* = 10.6 Hz, 1 H), 5.44 (m, 1 H), 5.08 (d, *J* = 16.9 Hz, 1 H), 4.96 (d, *J* = 10.1 Hz, 1 H), 3.67 (s, 6 H), 2.75 (d, *J* = 7.7 Hz, 2 H), 2.67 (m, 2 H), 1.70 (br s, 3 H) ppm. **^{13}C{^{1}H} NMR** (101 MHz, $CDCl_3$) δ: 170.5, 136.7, 135.4, 127.6, 116.7, 79.1, 73.3, 57.5, 52.7, 35.6, 23.3, 3.5 ppm. ^{1}H NMR and ^{13}C{^{1}H} NMR data in agreement with those previously reported.[181e]

(*E*)-2-allyl-2-(penta-2,4-dien-1-yl)malonate **S13** was obtained as a colorless oil.

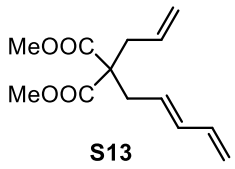

S13

S13: **^{1}H NMR** (400 MHz, $CDCl_3$) δ: 6.27 (dt, *J* = 16.9 Hz, *J* = 10.3 Hz, 1 H), 6.06 (dd, *J* = 14.9 Hz, *J* = 10.6 Hz, 1 H), 5.6 – 5.57 (m, 1 H), 5.52 – 5.44 (m, 1 H), 5.13 – 5.05 (m, 3 H), 4.99 (d, *J* = 10.1 Hz, 1 H), 3.68 (s, 6 H), 2.64 (d, *J* = 7.6 Hz, 2 H), 2.61 (d, *J* = 7.3 Hz, 2 H) ppm. **^{13}C{^{1}H} NMR** (101 MHz, $CDCl_3$) δ: 171.2, 136.7, 135.2, 132.4, 127.8, 119.3, 116.6, 57.9, 52.5, 37.2, 36.0 ppm. ^{1}H NMR and ^{13}C{^{1}H} NMR data in agreement with those previously reported.[181d]

(*E*)-2-(penta-2,4-dien-1-yl)-2-(prop-2-yn-1-yl)malonate **S14** was obtained as a colorless oil.

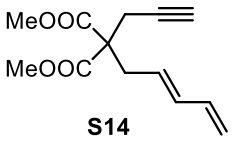

S14

S14: **^{1}H NMR** (400 MHz, $CDCl_3$) δ: 6.29 (dt, *J* = 17.0 Hz, *J* = 10.2 Hz, 1 H), 6.16 (dd, *J* = 14.8 Hz, *J* = 10.4 Hz, 1 H), 5.51 – 5.44 (m, 1 H), 5.15 (d, *J* = 17.8 Hz, 2 H), 5.04 (d, *J* = 10.2, 2 H), 3.74 (s, 6 H), 2.84 (d, *J* = 7.8 Hz, 2 H), 2.79 (d, *J* = 2.6 Hz, 2 H), 2.03 (t, *J* = 2.7 Hz, 1 H) ppm. **^{13}C{^{1}H} NMR** (101 MHz, $CDCl_3$) δ: 170.3, 136.6, 135.8, 127.2, 117.0, 78.9, 71.7, 57.2, 53.0, 35.6, 23.0 ppm. ^{1}H NMR and ^{13}C{^{1}H} NMR data in agreement with those previously reported.[181e]

(*E*)-2-(penta-2,4-dien-1-yl)-2-(3-phenylprop-2-yn-1-yl)malonate **S15** was obtained as a yellowish oil.

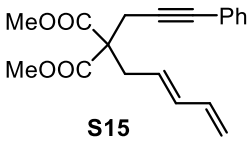

S15

S15: **^{1}H NMR** (400 MHz, $CDCl_3$) δ: 7.39 – 7.36 (m, 2 H), 7.30 – 7.27 (m, 3 H), 6.30 (dt, *J* = 16.8 Hz, *J* = 10.2 Hz, 1 H), 6.18 (dd, *J* = 15.0 Hz, *J* = 10.4 Hz, 1 H), 5.57 – 5.51 (m, 1 H), 5.15 (d, *J* = 17.8 Hz, 1 H), 5.04 (d, *J* = 10.2 Hz, 1 H), 3.76 (s, 6 H), 3.01 (s, 2 H), 2.89 (d, *J* = 7.7 Hz, 2 H) ppm. **^{13}C{^{1}H} NMR** (101 MHz, $CDCl_3$) δ: 170.4, 136.7, 135.8, 131.8, 128.4, 128.2, 127.4, 123.3, 116.9, 84.4, 83.9, 57.7, 52.9, 35.9, 24.0 ppm. ^{1}H NMR and ^{13}C{^{1}H} NMR data in agreement with those previously reported.[181e]

(*E*)-*N*-(but-2-yn-1-yl)-N-(penta-2,4-dien-1-yl)-*p*-toluenesulfonamide **S16** was obtained as a white solid.

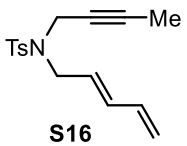

S16

S16: **^{1}H NMR** (500 MHz, $CDCl_3$) δ: 7.73 (d, *J* = 8.2 Hz, 2 H), 7.29 (d, *J* = 8.3 Hz, 2 H), 6.31 (dt, *J* = 17.1 Hz, *J* = 10.3 Hz, 1 H), 6.20 (dd, *J* = 14.9 Hz, *J* = 10.7 Hz, 1 H), 5.57 (dt, *J* = 14.3 Hz, *J* = 7.3 Hz, 1 H), 5.20 (d, *J* = 16.5 Hz, 1 H), 5.10 (d, *J* = 9.9 Hz, 1 H), 4.01 – 3.99 (m, 2 H), 3.82 (d, *J* = 7.0 Hz, 2 H), 2.42 (s, 3 H), 1.55 (t, *J* = 2.1 Hz, 3 H) ppm. **^{13}C{^{1}H} NMR** (126 MHz, $CDCl_3$) δ: 143.4, 136.4, 136.0, 135.3, 129.4, 128.0, 127.5, 118.2, 81.7, 71.8, 48.1, 36.5, 21.6, 3.4 ppm. ^{1}H NMR and ^{13}C{^{1}H} NMR data were in agreement with those previously reported.[181e]

(*E*)-5-(but-2-yn-1-yloxy)penta-1,3-diene **S17** was obtained as a colorless oil.

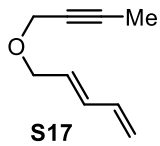

S17: **^{1}H NMR** (400 MHz, $CDCl_3$) δ: 6.39 – 6.23 (m, 2 H), 5.77 (dt, *J* = 14.7 Hz, *J* = 6.2 Hz, 1 H), 5.22 (d, *J* = 16.5 Hz, 1 H), 5.10 (d, *J* = 10.0 Hz, 1 H), 4.10 – 4.06 (m, 2 H), 1.85 (t, *J* = 2.2 Hz, 1 H) ppm. **^{13}C{^{1}H} NMR** (101 MHz, $CDCl_3$) δ: 136.3, 133.7, 129.4, 117.7, 82.5, 75.1, 69.6, 57.7, 3.6 ppm. ^{1}H NMR and ^{13}C{^{1}H} NMR data in agreement with those previously reported.[181c]

(*E*)-(3-(penta-2,4-dien-1-yloxy)prop-1-yn-1-yl)benzene **S18** was obtained as a yellow oil.

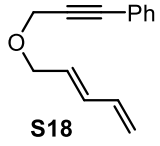

S18: **^{1}H NMR** (400 MHz, $CDCl_3$) δ: 7.47 – 7.44 (m, 2 H), 7.33 – 7.29 (m, 3 H), 6.42 – 6.28 (m, 2 H), 5.82 (dt, *J* = 14.2 Hz, *J* = 6.3 Hz, 1 H), 5.24 (d, *J* = 16.7 Hz, 1 H), 5.13 (dd, *J* = 9.9 Hz, 1 H), 4.38 (s, 2 H), 4.18 (d, *J* = 6.2 Hz, 2 H) ppm. **^{13}C{^{1}H} NMR** (101 MHz, $CDCl_3$) δ: 136.4, 134.2, 131.9, 129.4, 128.6, 128.4, 122.8, 118.1, 86.5, 85.2, 69.9, 58.0 ppm. ^{1}H NMR and ^{13}C{^{1}H} NMR data in agreement with those previously reported.[181c]

(*E*)-5-(but-2-yn-1-yloxy)penta-1,3-diene **S19** was obtained as a colorless oil.

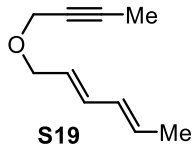

S19: **^{1}H NMR** (300 MHz, $CDCl_3$) δ: 6.21 (d, , *J* = 15.2 Hz, 1 H), 6.05 (d, *J* = 15.0 Hz, 1 H), 5.75 – 5.56 (m, 2 H), 4.07 (q, *J* = 2.3 Hz, 2 H), 4.04 (d, *J* = 6.4 Hz, 2 H), 1.85 (t, *J* = 2.3 Hz, 3 H), 1.75 (d, *J* = 6.7 Hz, 3 H) ppm. **^{13}C{^{1}H} NMR** (75 MHz, $CDCl_3$) δ: 133.8, 130.8, 130.2, 126.0, 82.4, 75.2, 69.9, 57.5, 18.1, 3.6 ppm. ^{1}H NMR and ^{13}C{^{1}H} NMR data in agreement with those previously reported.[181b]

4.4.4 General procedure for AgBArF synthesis

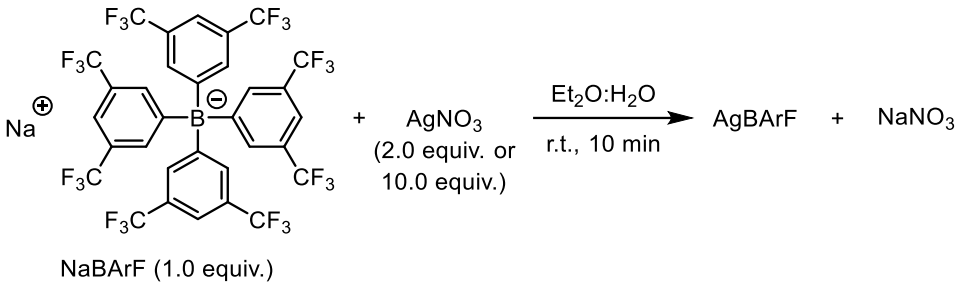

AgBArF was synthesized following already reported methodologies.[182,183] General procedure for the AgBArF synthesis: An Et_2O solution (20.0 mL) of NaBArF (500 mg, 0.6 mmol, 1.0 equiv.) was vigorously shaken for 10 min with an aqueous solution (10.0 mL) of $AgNO_3$ (194 mg, 1.2 mmol, 2.0 equiv.) in a separatory funnel wrapped with aluminum foil. After the reaction, the Et_2O phase was separated, and the volatiles were removed under vacuum until a clear oil was observed, which was further concentrated. The resulting white/beige solid (610 mg, quantitative yield) was dissolved in 0.6 mL of dry DCM (0.1 M). Then, with the aim of removing the water from the synthesis, this solution was dried overnight in the glovebox's freezer by using molecular sieves 4 Å. After filtering the molecular sieves out, DCM was evaporated. The resulting residue was redissolved in Et_2O.[195] For the characterization of the obtained AgBArF, Et_2O was evaporated. Spectroscopic data were in agreement with those reported in literature. [182,183]

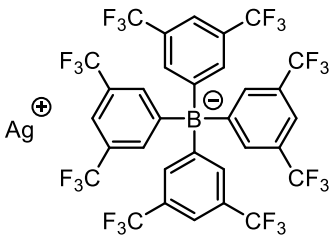

^{1}H NMR (500 MHz, THF-d8) δ: 7.79 – 7.76 (m, 8 H), 7.56 (br s, 4 H) ppm.

[195] AgBArF must be storaged as Et_2O containing compound. See references 182 and 183.

4.4.5 General procedure for the Rh-catalyzed cyclization reaction

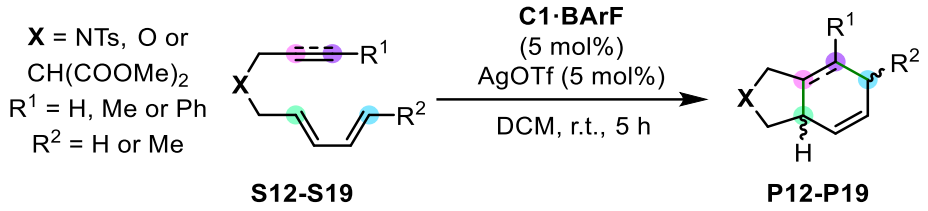

General procedure for the cyclization reaction: Under N_2 atmosphere, the rhodium(I) catalyst (5 mol%), the silver(I) salt (20 or 5 mol%) along with dry DCM (0,1 M) as solvent were added to a 10 mL screw cap vial provided with a stirrer. Then, after stirring the yellow mixture for 1 min, 1.0 equiv. of dienyne substrates **S12-S19** was subsequently added. The mixture was stirred at room temperature for 5 hours. Afterwards, the reaction mixture was passed through a silica pad, and the volatiles were removed under vacuum. A known amount of 1,3,5-trimethoxybencene (Sigma-Aldrich TraceCERT®) as internal standard was added to the reaction mixture, which was analyzed *via* ^{1}H NMR. Cyclization products were isolated by standard column chromatography using *n*-pentane:Et_2O mixtures as eluent.

4.4.6 Characterization of the cyclization products

All products have been previously isolated and fully characterized by our group. ^{1}H NMR and ^{13}C{^{1}H} NMR data corresponding to cyclization products were in agreement with those previously reported by our group.[111]

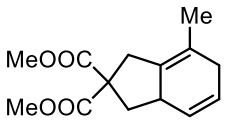

P12

Product **P12** was obtained from substrate **S12**. For the preparation of **P12**: 3.5 mg (5 mol%) of **C1·BArF**, 0.5 mg (5 mol%) of AgOTf and 10.0 mg (0.05 mmol, 1,0 equiv.) of **S12**. **P12** was achieved as a colorless oil (9.9 mg, 90% yield).**^{1}H NMR** (400 MHz, $CDCl_3$) δ: 5.78 – 5.69 (m, 2 H), 3.73 (s, 3 H), 3.70 (s, 3 H), 3.03 – 2.80 (m, 3 H), 2.69 – 2.57 (m, 2 H), 2.51 – 2.39 (m, 1 H), 1.75 (t, *J* = 12.6 Hz, 1 H), 1.63 (s, 3 H) ppm. **^{13}C{^{1}H}**

NMR (101 MHz, $CDCl_3$) δ: 173.0, 172.6, 131.1, 126.8, 125.7, 122.7, 57.8, 52.9, 52.8, 40.1 39.7, 36.1, 32.7, 18.9 ppm.

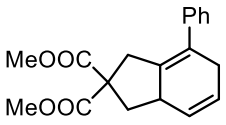

P15

Product **P15** was obtained from substrate **S15**. For the preparation of **P15**: 6.0 mg (5 mol%) of **C1·BArF**, 0.9 mg (5 mol%) of AgOTf and 21.1 mg (0.07 mmol, 1.0 equiv.) of **S15**. **P15** was achieved as a colorless oil (13.0 mg, 60% yield).**^{1}H NMR** (400 MHz, $CDCl_3$) δ: 7.38 – 7.20 (m, 6 H), 5.91 – 5.81 (m, 2 H), 3.76 (s, 3 H), 3.65 (s, 3 H), 3.20 – 2.83 (m, 5 H), 2.68 (dd, *J* = 12.6 Hz, *J* = 7.1 Hz, 1 H), 1.89 (t, *J* = 12.5 Hz, 1 H) ppm. **^{13}C{^{1}H} NMR** (101 MHz, $CDCl_3$) δ: 173.0, 172.4, 141.6, 134.5, 128.3, 128.0, 126.9, 126.5, 125.7, 57.7, 53.0, 52.8, 40.4, 39.8, 37.4, 32.3 ppm.

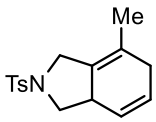

P16

Product **P16** was obtained from substrate **S16**. For the preparation of **P16**: 10.0 mg (5 mol%) of **C1·BArF**, 1.5 mg (5 mol%) of AgOTf and 33.1 mg (0.1 mmol, 1,0 equiv.) of **S16**. **P16** was achieved as a colorless oil (26.1 mg, 42% yield).**^{1}H NMR** (400 MHz, $CDCl_3$) δ: 7.72 (d, *J* = 8.3 Hz, 2 H), 7.31 (d, *J* = 8.1 Hz, 2 H), 5.79 – 5.74 (m, 1 H), 5.66 (d *J* =.9.9 Hz, 1 H), 3.97 (dm, *J* = 13.5 Hz, 1 H), 3.84 – 3.77 (m, 2 H), 3.06 – 2.95 (m, 1 H), 2.67 – 2.55 (m, 2 H), 2.49 – 2.36 (m, 4 H), 1.58 (s, 3 H) ppm. **^{13}C{^{1}H} NMR** (101 MHz, $CDCl_3$) δ: 143.5, 133.9, 129.8, 128.0, 127.8, 127.0, 124.3, 123.6, 52.8, 49.2, 39.1, 32.4, 21.7, 19.1 ppm.

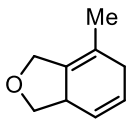

P17

Product **P17** was obtained from substrate **S17**. For the preparation of **P17**: 6.7 mg (5 mol%) of **C1·BArF**, 1.0 mg (5 mol%) of AgOTf and 15.4 mg (0.08 mmol, 1,0 equiv.) of **S17**. **P17** was achieved as a colorless oil (8.5 mg, 82% yield).**^{1}H NMR** (400 MHz, $CDCl_3$) δ: 5.87 – 5.81 (m, 1 H), 5.76 (dm, *J* = 9.8 Hz, 1 H), 4.42 – 4.32 (m, 2 H), 4.16 (t, *J* = 7.5 Hz, 1 H), 3.21 (dd, *J* = 11.3 Hz, *J* = 7.2 Hz, 1 H), 3.12 – 3.01 (m, 1 H), 2.77 – 2.68 (m, 1 H), 2.55 – 2.46 (m, 1 H), 1.64 (s, 3 H) ppm. **^{13}C{^{1}H} NMR** (101 MHz, $CDCl_3$) δ: 131.3, 127.1, 123.4, 121.9, 72.1, 68.1, 40.3, 32.7, 19.2 ppm.

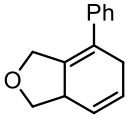

P18

Product **P18** was obtained from substrate **S18**. For the preparation of **P18**: 7.7 mg (5 mol%) of **C1·BArF**, 1.1 mg (5 mol%) of AgOTf and 28.2 mg (0.09 mmol, 1,0 equiv.) of **S18**. **P18** was achieved as a colorless oil (8.5 mg, 48% yield).**^{1}H NMR** (400 MHz, $CDCl_3$) δ: 7.38 – 7.20 (m, 5 H), 6.02 – 5.96 (m, 1 H), 5.84 (dm, *J* = 9.9 Hz, 1 H), 4.63 (dm, *J* = 13.1 Hz, 1 H), 4.26 – 4.20 (m, 2 H), 3.38 – 3.17 (m, 3 H), 3.05 – 2.92 (m, 1 H) ppm. **^{13}C{^{1}H} NMR** (101 MHz, $CDCl_3$) δ: 140.9, 134.9, 128.6, 127.7, 127.5, 127.5, 127.3, 123.4, 71.8, 69.2, 41.3, 31.7 ppm.

4.4.7 Experiments involving silver(I) salt

AgOTf salt as catalyst

General procedure: Under N_2 atmosphere, 2.1 mg of AgOTf (0.01 mmol, 20 mol%) along with 0.6 mL of degassed and dry MeOH (0,1 M) as solvent were added to a 10 mL screw cap vial provided with a stirrer. Then, after stirring the mixture for 1 min, 10.1 mg (0.04 mmol, 1.0 equiv.) of dienyne substrates **S12** was subsequently added. The mixture was stirred at room temperature for 5 hours. Afterwards, the reaction mixture was passed through a silica pad, and the volatiles were removed under vacuum. A known amount of 1,3,5-trimethoxybencene (Sigma-Aldrich TraceCERT®) as internal standard was added to the reaction mixture, which was analyzed *via* ^{1}H NMR.

AgOTf/phosphane species as catalysts

General procedure: Under N_2 atmosphere, 2.7 mg (0.01 mmol, 20 mol%) of AgOTf and 5.6 mg (0.02 mmol, 40 mol%) of **L1** or 9.6 mg (0.02 mmol, 40 mol%) of **L2** along with 0.6 mL of dry DCM (0,1 M) as solvent were added to a 10 mL screw cap vial provided with a stirrer. Then, after stirring the mixture for 1 min, 13.0 mg (0.05 mmol, 1.0 equiv.) of dienyne substrates **S12** was subsequently added. The mixture was stirred at room temperature for 5 hours. Afterwards, the reaction mixture was passed

through a silica pad, and the volatiles were removed under vacuum. A known amount of 1,3,5-trimethoxybencene (Sigma-Aldrich TraceCERT®) as internal standard was added to the reaction mixture, which was analyzed *via* ^{1}H NMR.

Competition experiment

General procedure: Under N_2 atmosphere, 6.3 mg (0.004 mmol, 5 mol%) of **C1·BArF**, 3.7 mg of AgOTf (0.01 mmol, 20 mol%) along with 0.6 mL of degassed and dry MeOH (0,1 M) as solvent were added to a 10 mL screw cap vial provided with a stirrer. Then, after stirring the mixture for 1 min, 17.9 mg (0.07 mmol, 1.0 equiv.) of dienyne substrates **S12** was subsequently added. The mixture was stirred at room temperature for 5 hours. Afterwards, the reaction mixture was passed through a silica pad, and the volatiles were removed under vacuum. A known amount of 1,3,5-trimethoxybencene (Sigma-Aldrich TraceCERT®) as internal standard was added to the reaction mixture, which was analyzed *via* ^{1}H NMR.

4.4.8 NMR spectroscopic experiments

NMR analysis of stoichiometric C1·BArF*/AgOTf mixtures*

General procedure for the NMR study: Under N_2 atmosphere, 13.1 mg (0.01 mmol, 1.0 equiv.) of **C1·BArF** complex and 1.9 mg (0.01 mmol, 1.0 equiv.) of AgOTf along with 600.0 μL of deuterated DCM were placed into a 3 mL vial. The reaction mixture was stirred for 15 min, 90 min or 6 hours, transferred to an NMR tube and finally analyzed by ^{1}H and ^{31}P{^{1}H} NMR.

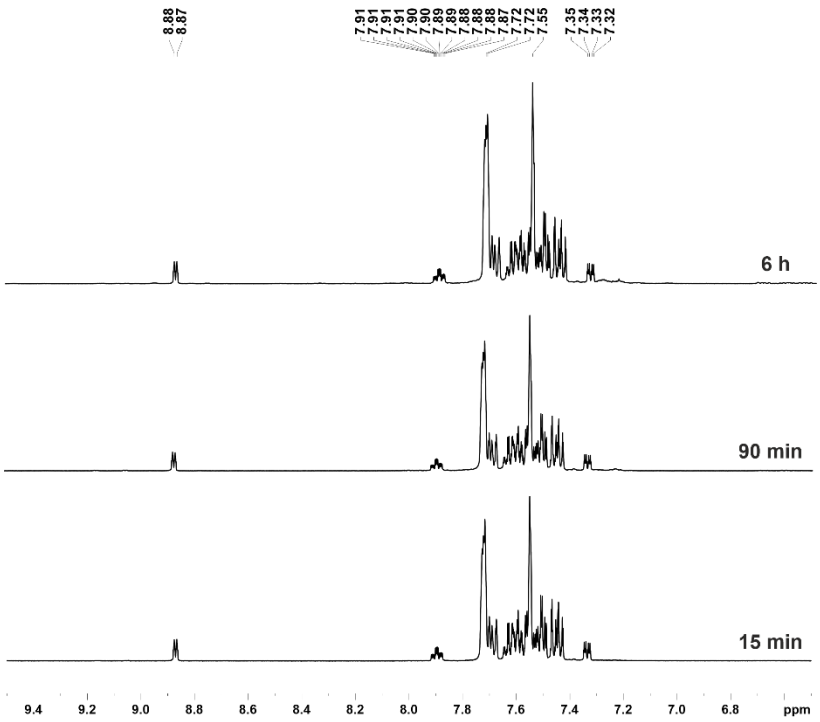

Figure 4.2. ^{1}H NMR analysis of the mixture of **C1·BArF** (1.0 equiv.) in the presence of AgOTf (1.0 equiv.).

Variable temperature NMR investigation of stoichiometric reaction

General procedure for the NMR study: Under N_2 atmosphere, 18.5 mg (0.01 mmol, 1.0 equiv.) of **C1·BArF** complex and 2.7 mg (0.01 mmol, 1.0 equiv.) of AgOTf along with 600.0 μL of deuterated DCM were placed into a 10.0 mL Schlenk. The reaction mixture was cooled to −90 °C by using a previously prepared acetone bath. Then, 2.6 mg (0.01 mmol, 1.0 equiv.) of dienyne substrate **S12** was added at this temperature. The resulting yellow mixture was rapidly transferred to an NMR J-Young tube, which was in an acetone bath at −90 °C, and then analyzed by ^{1}H, ^{31}P{^{1}H} and ^{19}F{^{1}H} NMR.

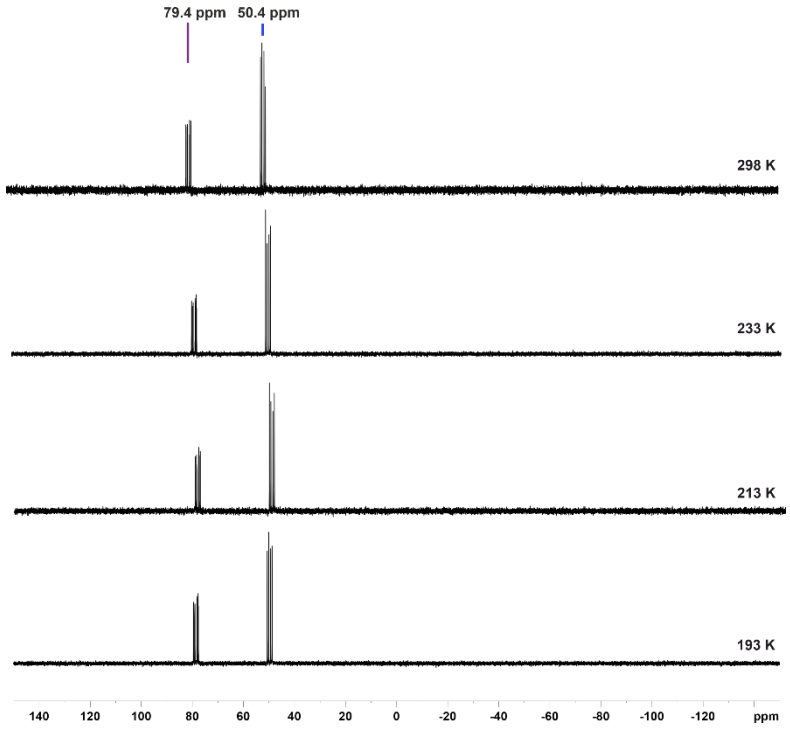

Figure 4.3. Low temperature ^{31}P NMR experiments of stoichiometric [4+2] cycloaddition od **S12.**

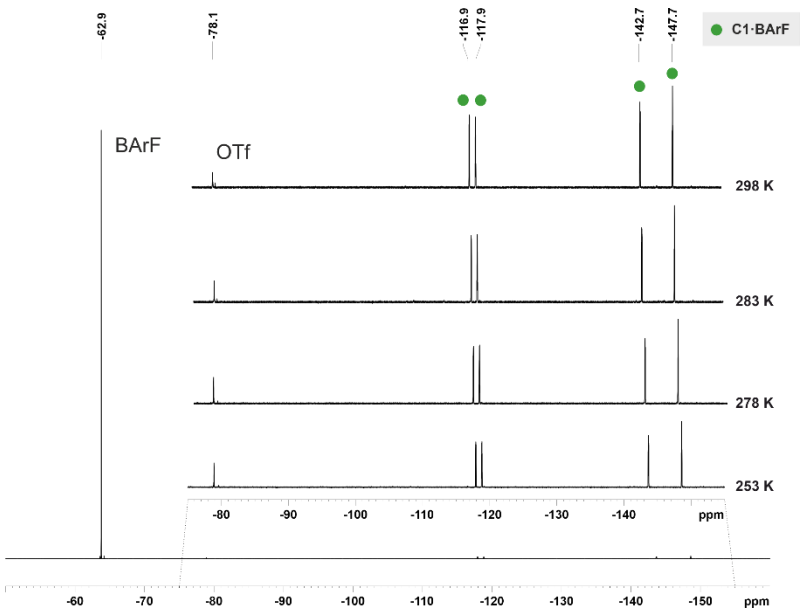

Figure 4.4. Low temperature ^{19}F NMR experiments of stoichiometric [4+2] cycloaddition od **S12.**

NMR studies of Ag:substrate adduct formation

General procedure: Under N_2 atmosphere, 10.4 mg (0.04 mmol, 1.0 equiv.) of AgOTf along with 500.0 μL of deuterated DCM were placed into a 3.0 mL vial. Then, after stirring the mixture for 1 min, 10.0 mg (0.04 mmol, 1.0 equiv.) of dienyne substrates **S12** was subsequently added. The reaction mixture was stirred for 5 h, transferred to an NMR tube and finally analyzed by ^{1}H NMR.

4.4.9 Collection of NMR spectra

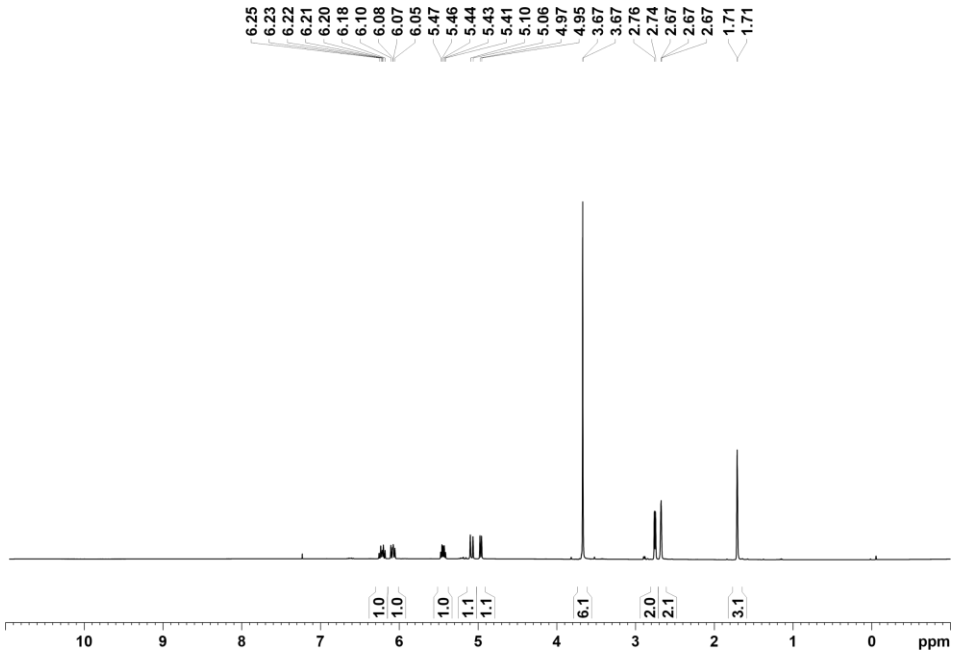

Figure 4.5. ^{1}H NMR (400 MHz, $CDCl_3$) for substrate **S12**.

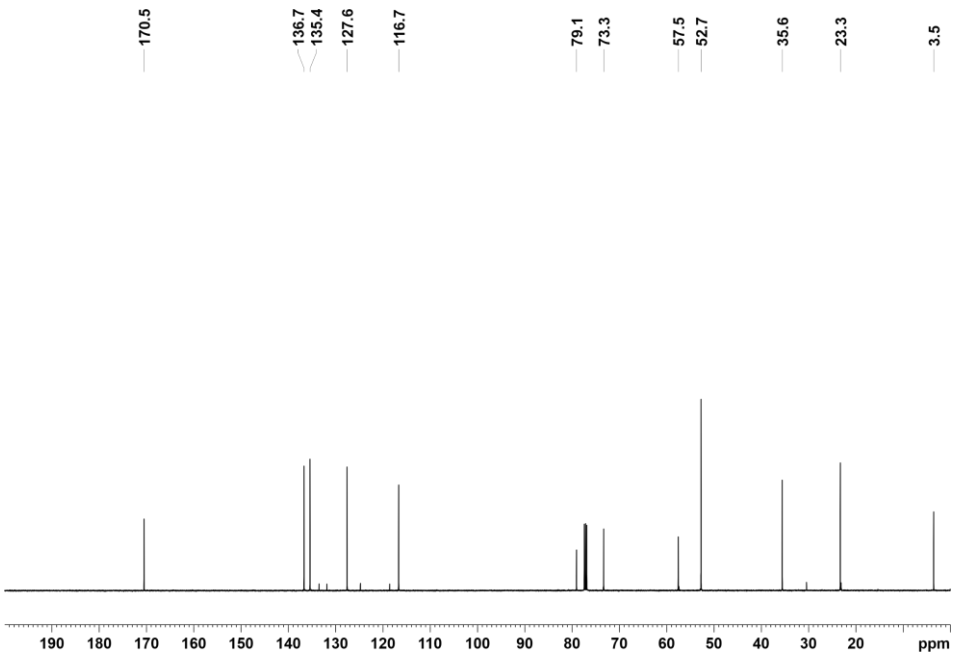

Figure 4.6. $^{13}C\{^{1}H\}$ NMR (101 MHz, $CDCl_3$) for substrate **S12.**

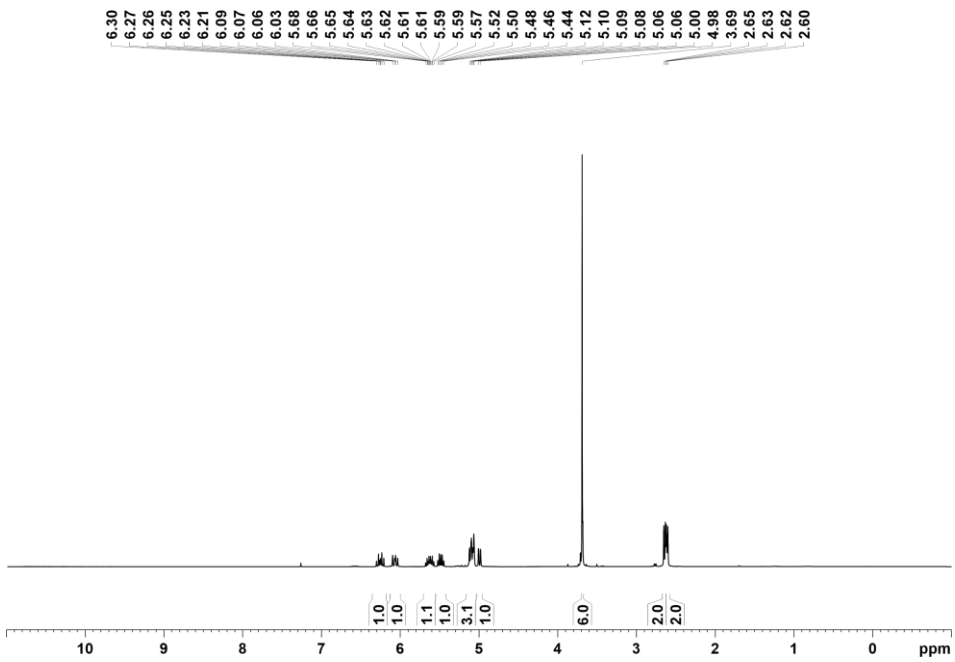

Figure 4.7. ^{1}H NMR (400 MHz, $CDCl_3$) for substrate **S13**.

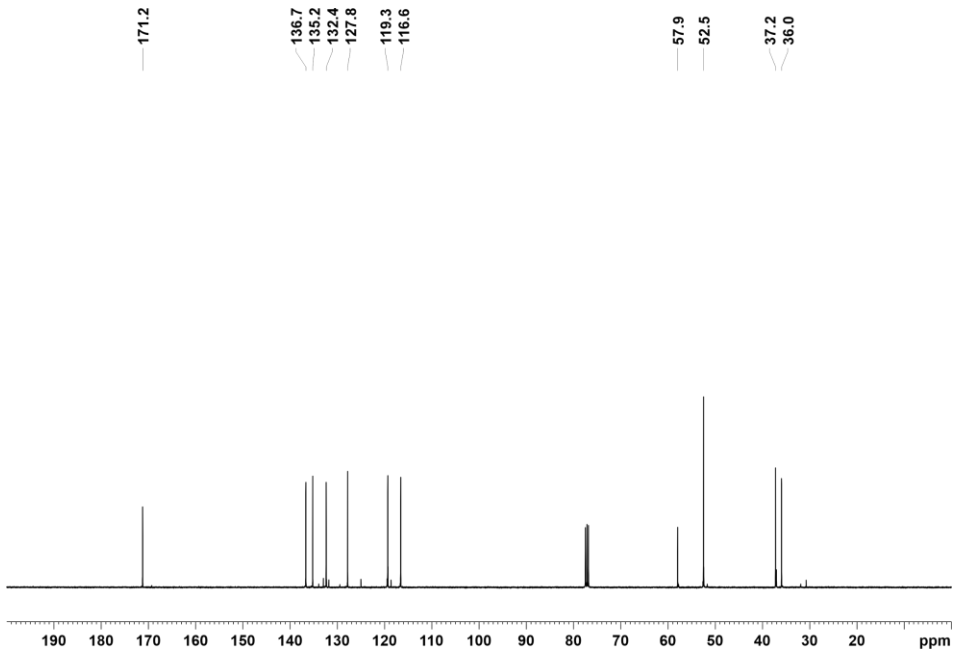

Figure 4.8. $^{13}C\{^{1}H\}$ NMR (101 MHz, $CDCl_3$) for substrate **S13.**

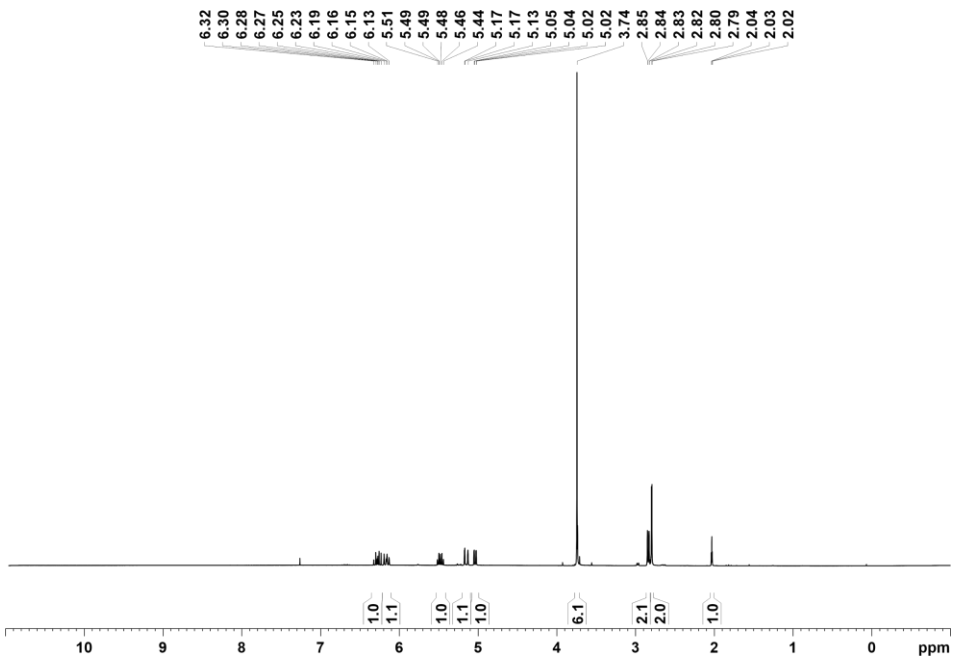

Figure 4.9. ^{1}H NMR (400 MHz, $CDCl_3$) for substrate **S14**.

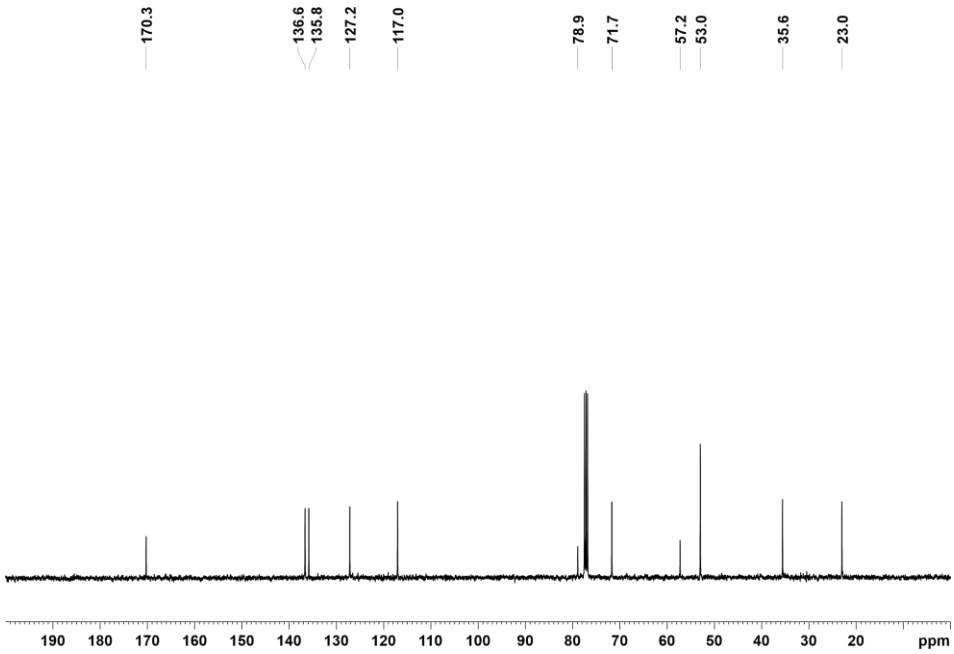

Figure 4.10. $^{13}C\{^{1}H\}$ NMR (101 MHz, $CDCl_3$) for substrate **S14.**

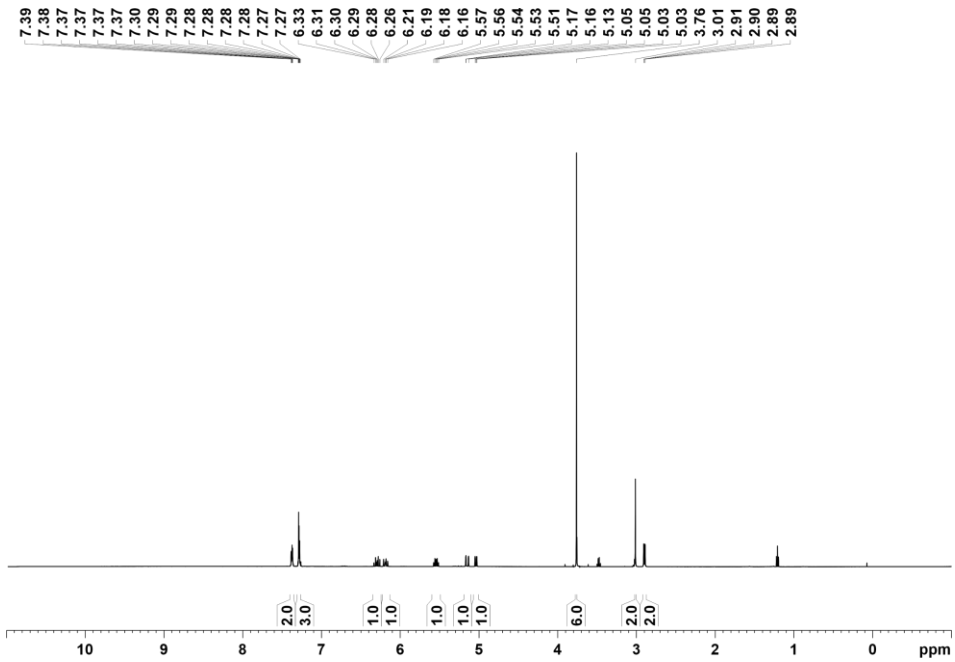

Figure 4.11. ^{1}H NMR (400 MHz, $CDCl_3$) for substrate **S15.**

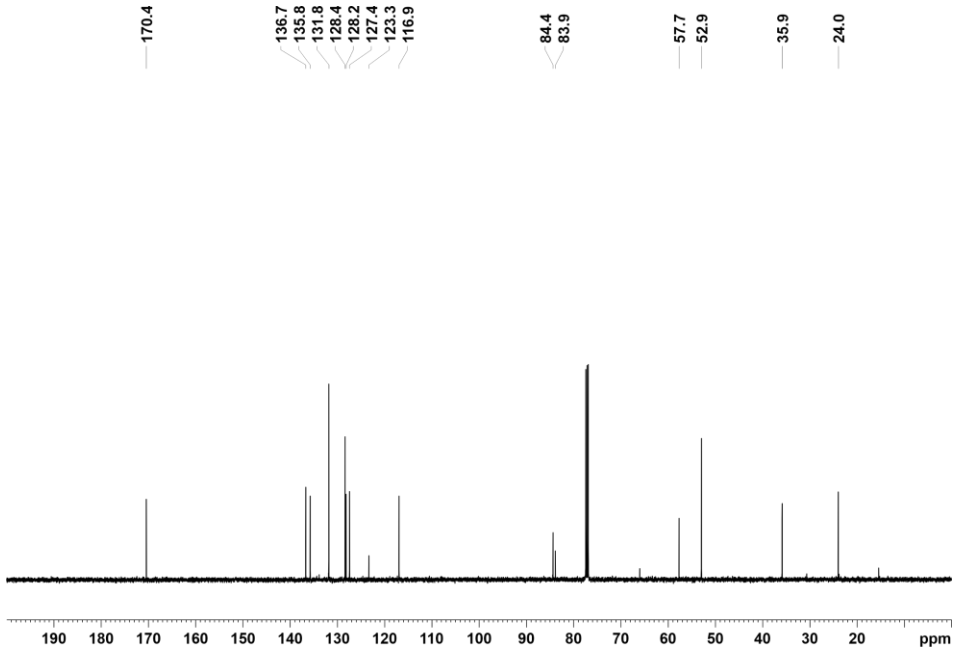

Figure 4.12. $^{13}C\{^{1}H\}$ NMR (101 MHz, $CDCl_3$) for substrate **S15.**

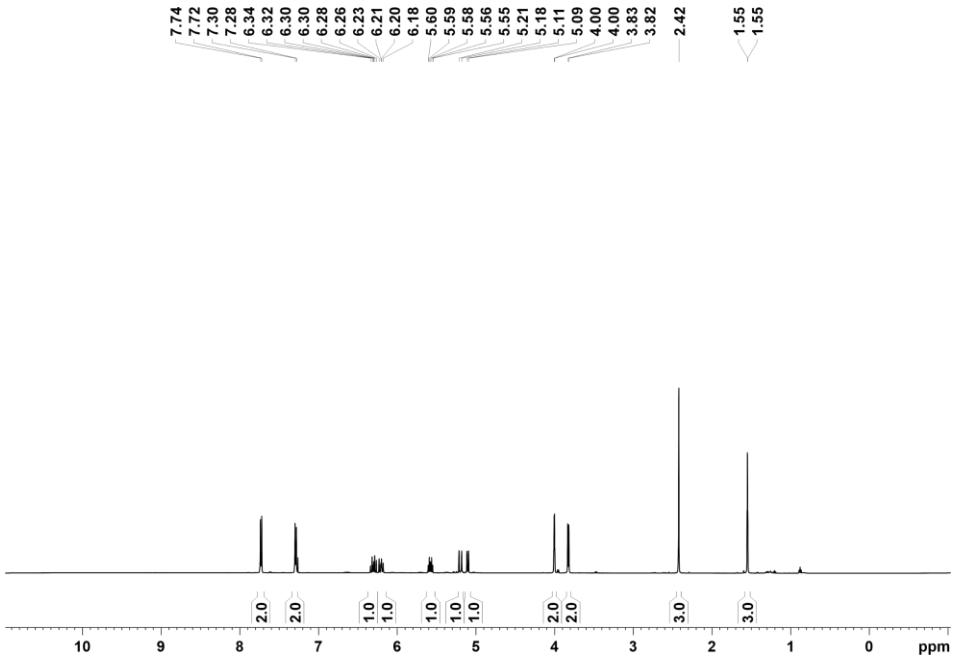

Figure 4.13. ^{1}H NMR (500 MHz, $CDCl_3$) for substrate **S16.**

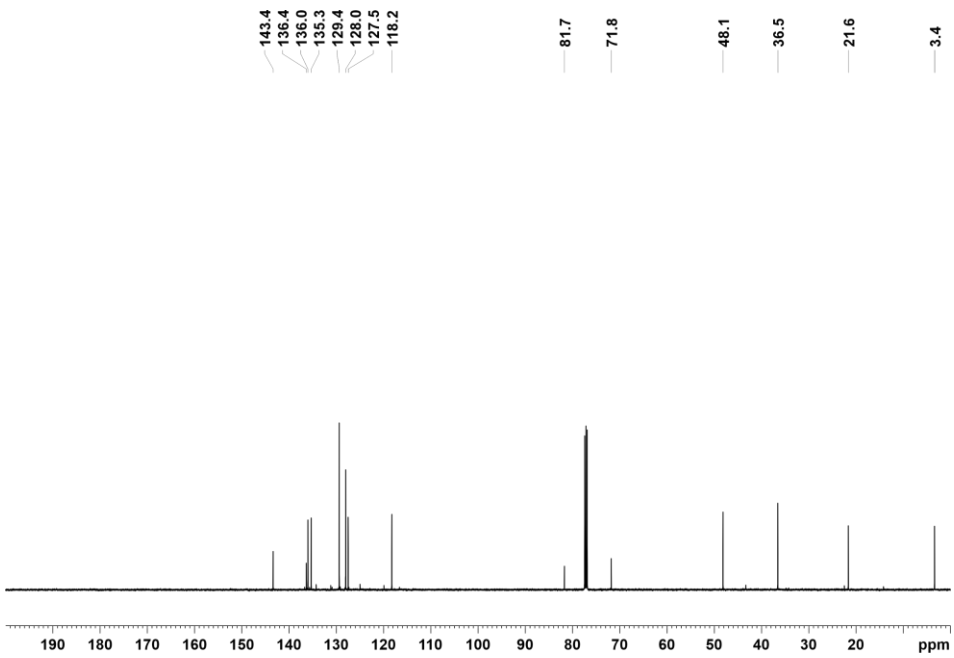

Figure 4.14. $^{13}C\{^{1}H\}$ NMR (126 MHz, $CDCl_3$) for substrate **S16.**

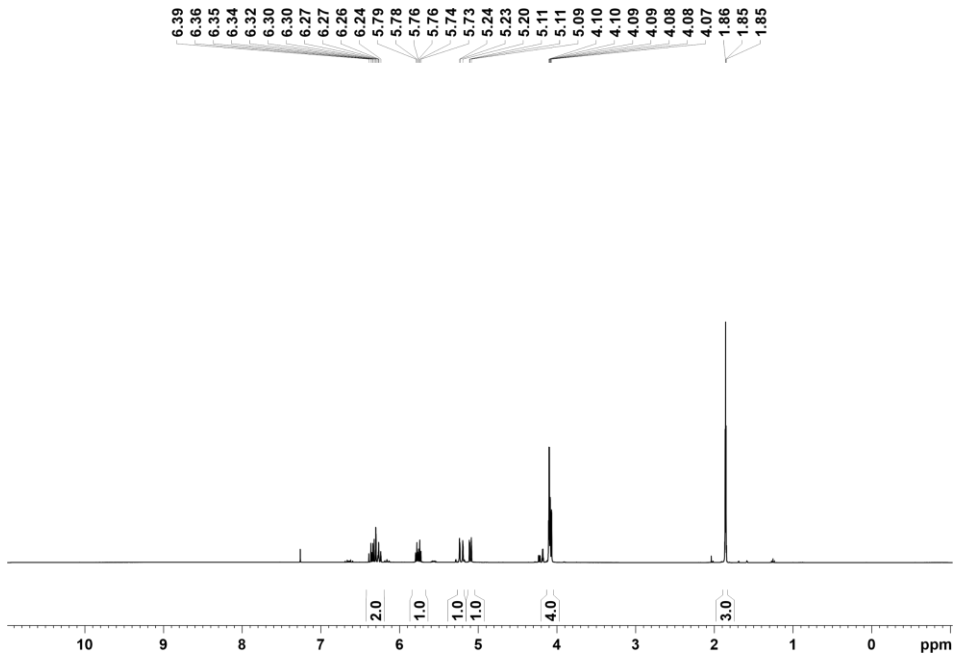

Figure 4.15. ^{1}H NMR (400 MHz, $CDCl_3$) for substrate **S17.**

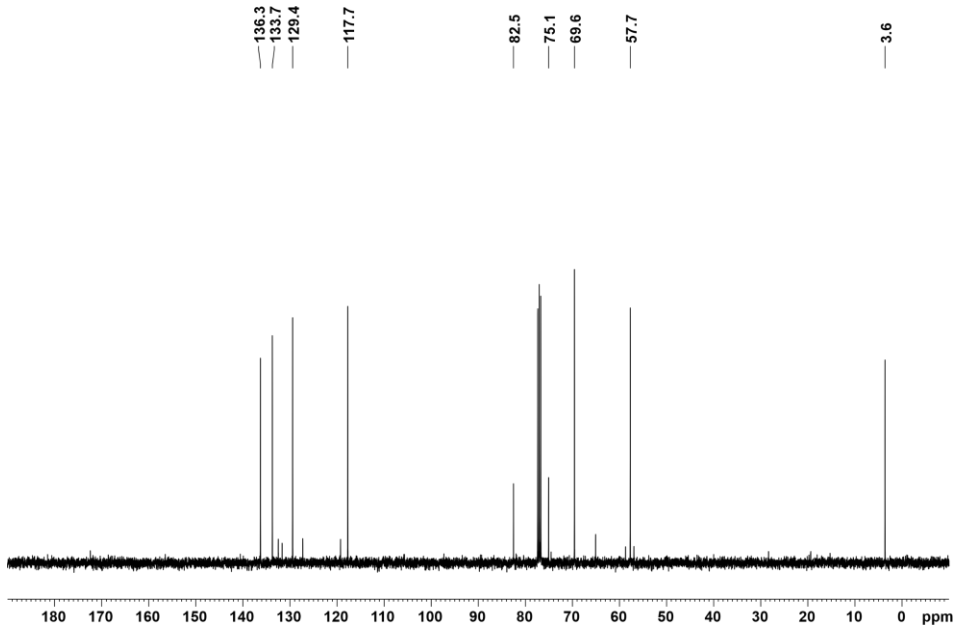

Figure 4.16. $^{13}C\{^{1}H\}$ NMR (101 MHz, $CDCl_3$) for substrate **S17.**

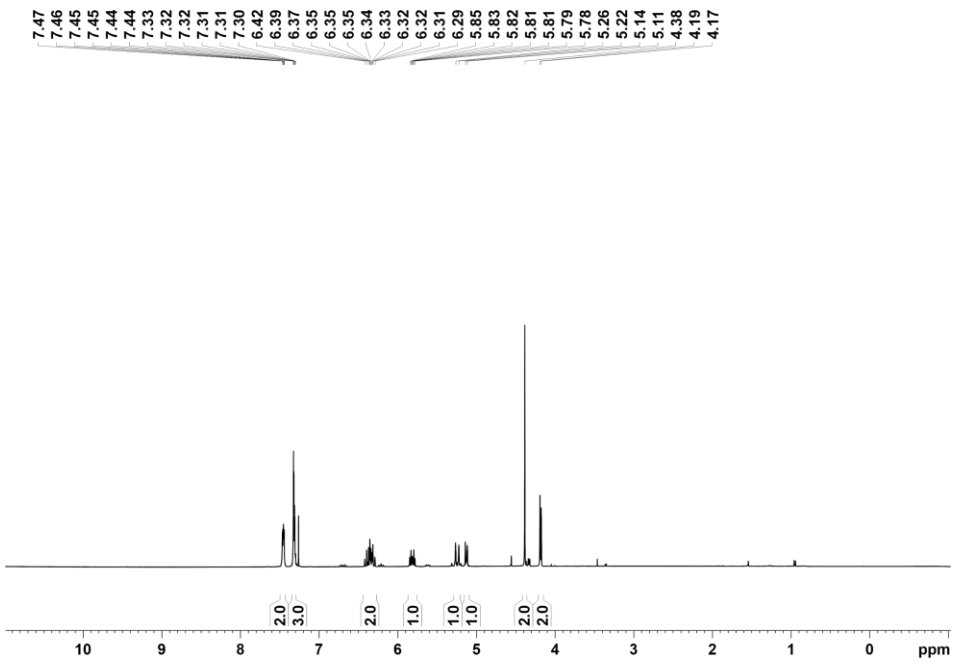

Figure 4.17. ^{1}H NMR (400 MHz, $CDCl_3$) for substrate **S18.**

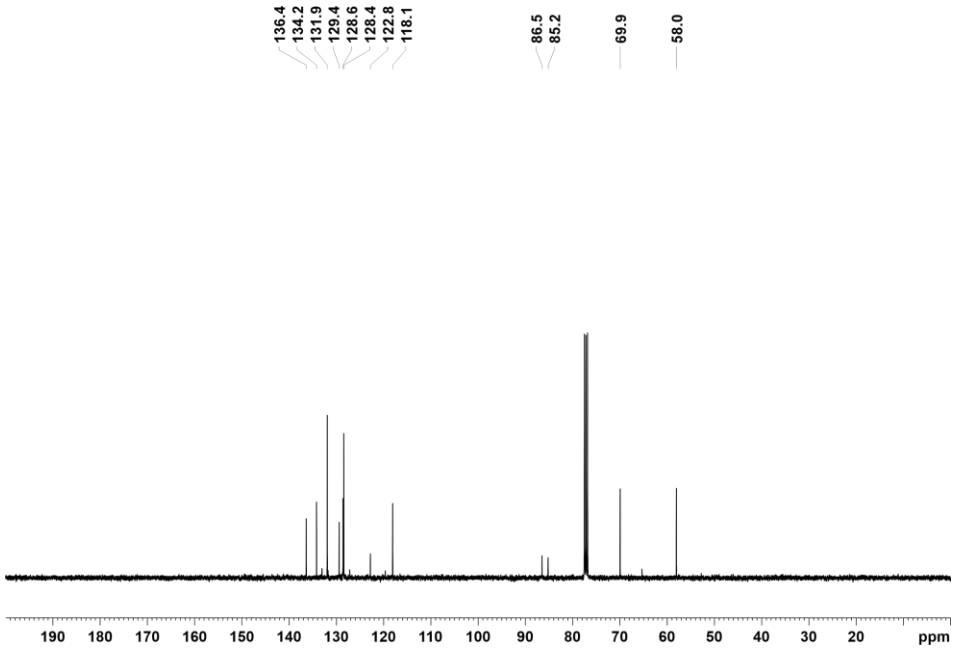

Figure 4.18. $^{13}C\{^{1}H\}$ NMR (101 MHz, $CDCl_3$) for substrate **S18.**

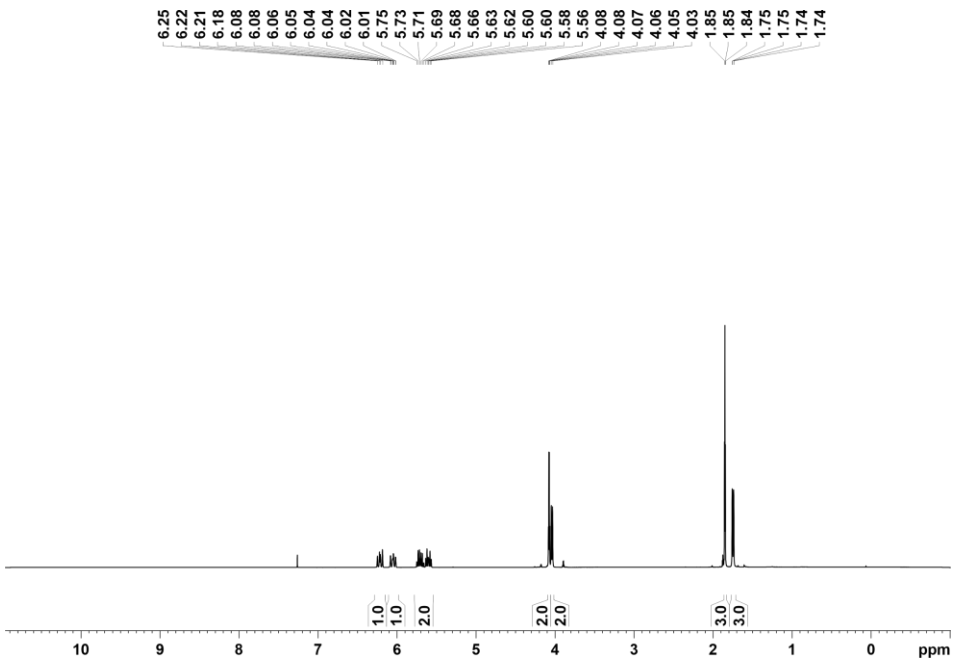

Figure 4.19. ^{1}H NMR (300 MHz, $CDCl_3$) for substrate **S19.**

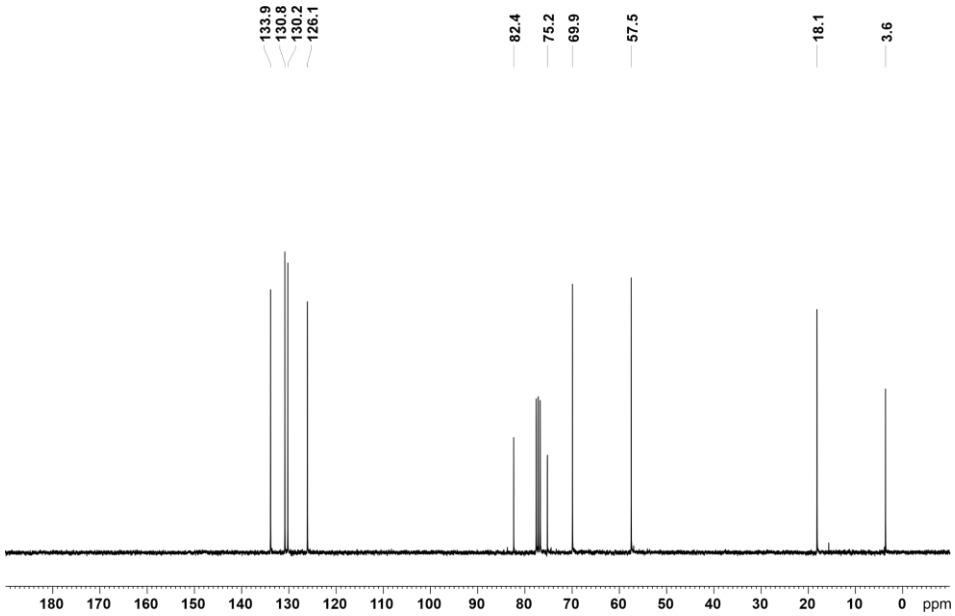

Figure 4.20. $^{13}C\{^{1}H\}$ NMR (75 MHz, $CDCl_3$) for substrate **S19.**

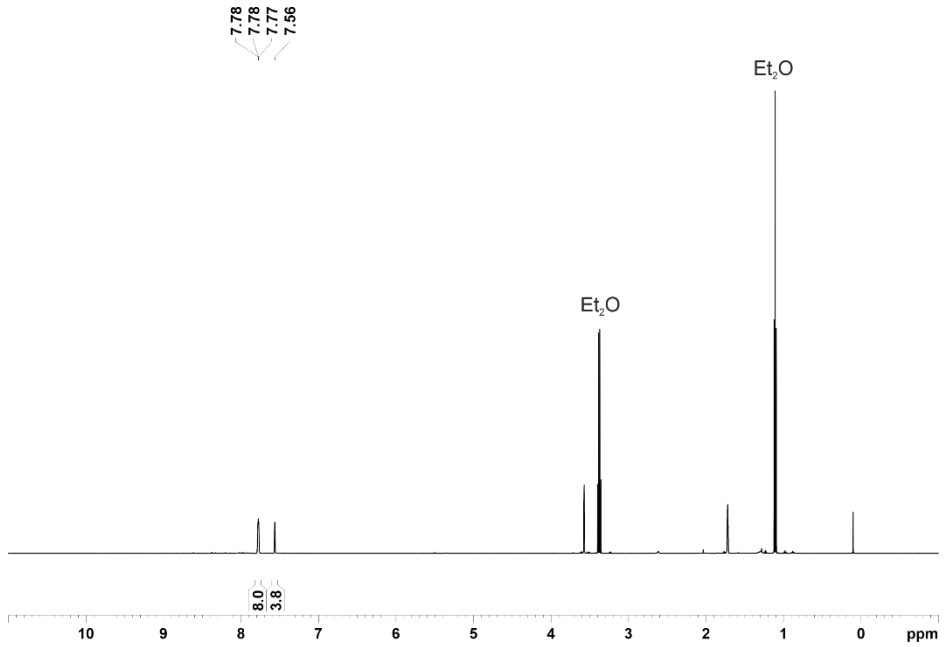

Figure 4.21. ^{1}H NMR (500 MHz, THF-d_8) for product AgBArF**.**

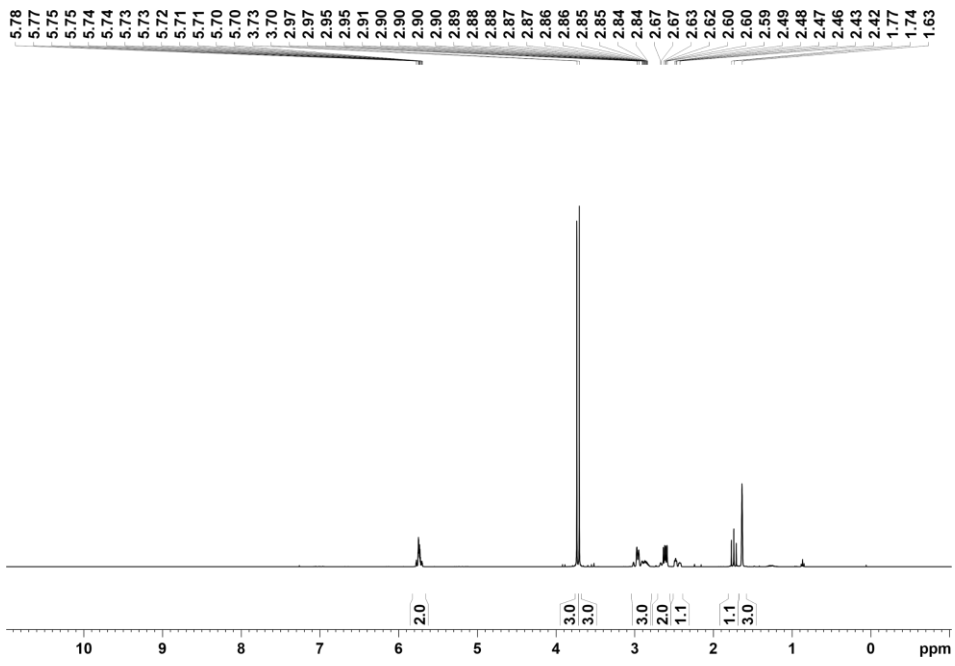

Figure 4.22. ^{1}H NMR (400 MHz, $CDCl_3$) for product **P12.**

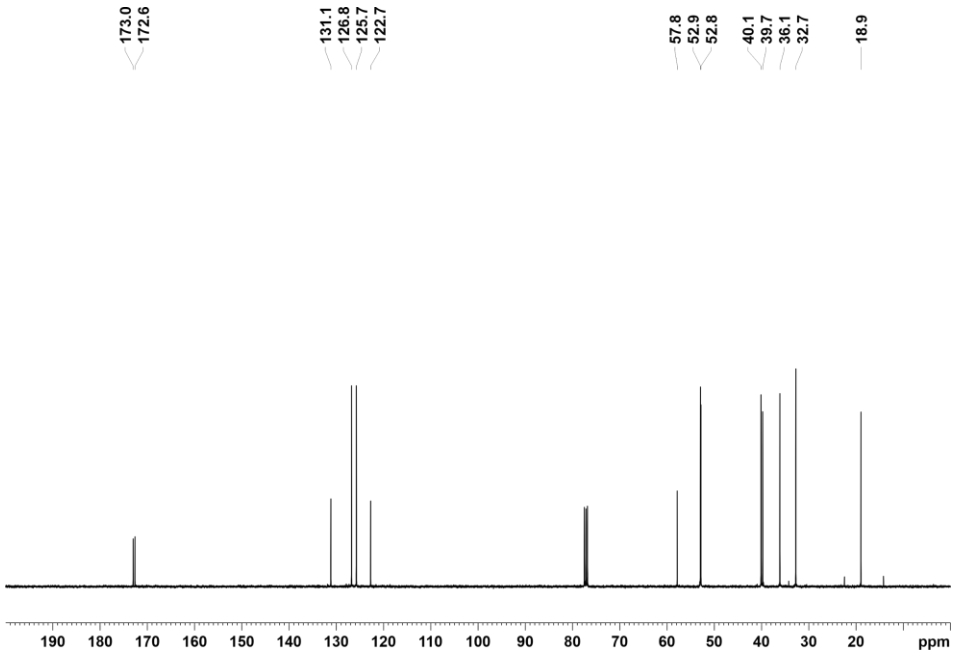

Figure 4.23. $^{13}C\{^{1}H\}$ NMR (101 MHz, $CDCl_3$) for product **P12.**

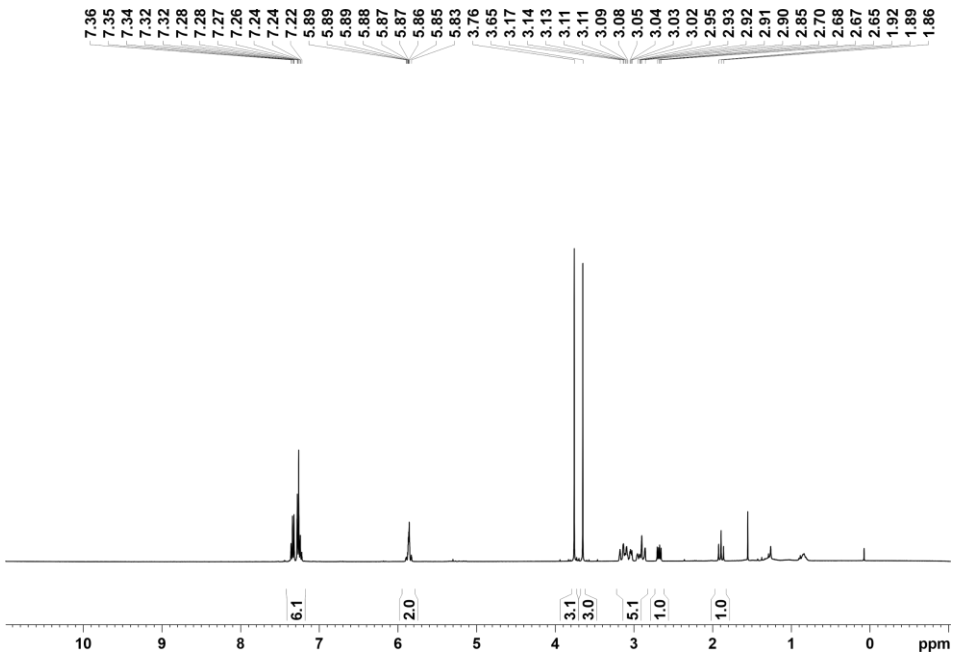

Figure 4.24. ^{1}H NMR (400 MHz, $CDCl_3$) for product **P15.**

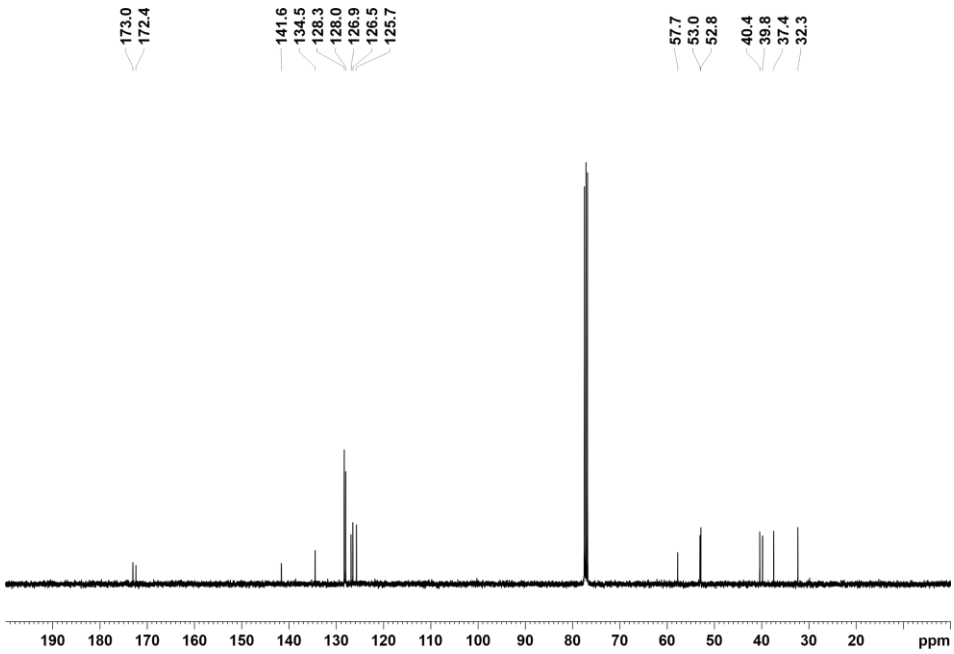

Figure 4.25. $^{13}C\{^{1}H\}$ NMR (101 MHz, $CDCl_3$) for product **P15.**

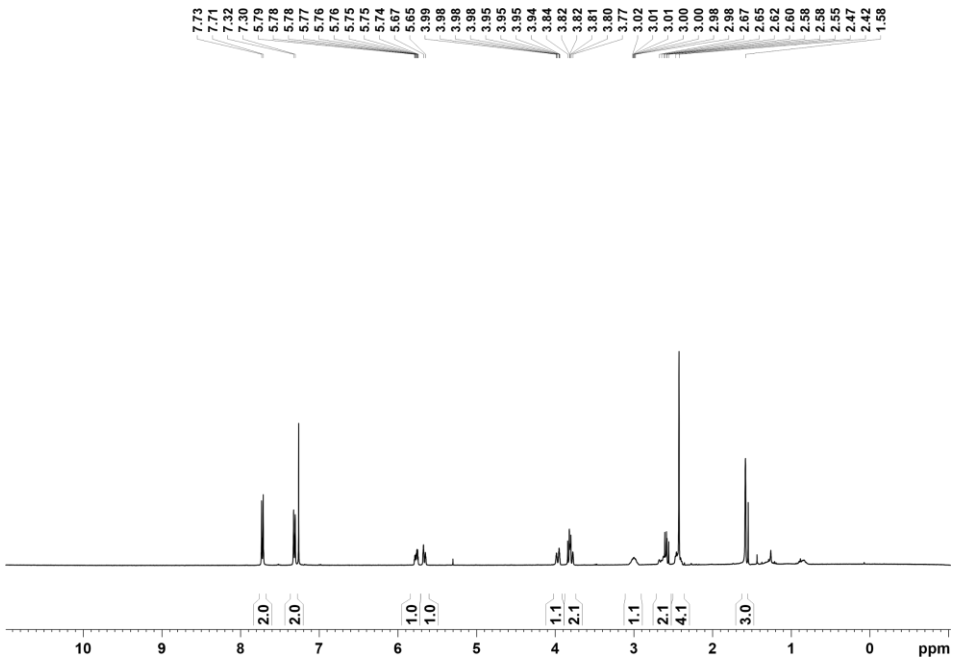

Figure 4.26. ^{1}H NMR (400 MHz, $CDCl_3$) for product **P16.**

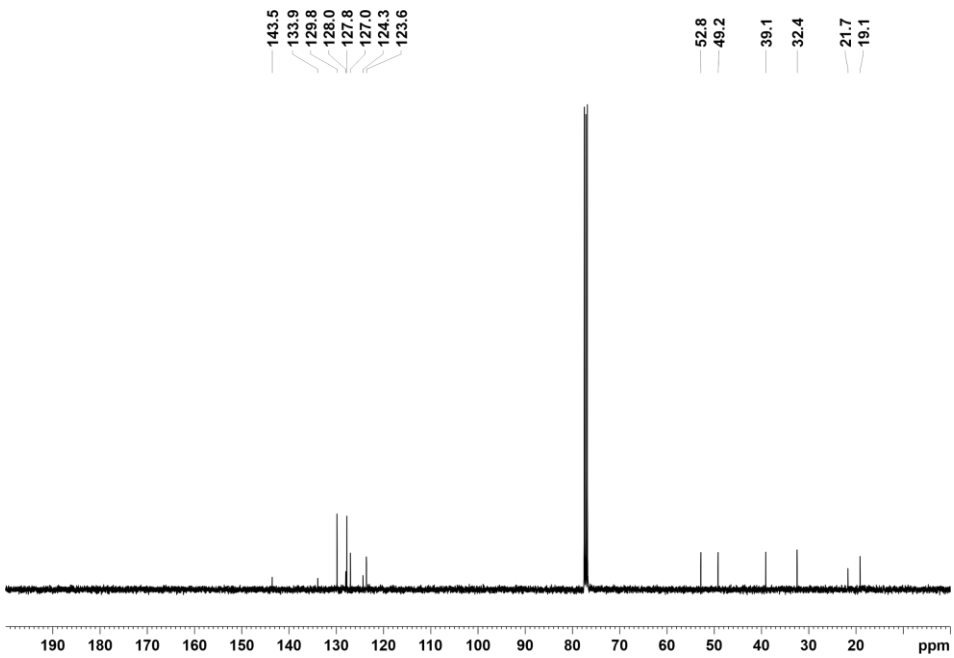

Figure 4.27. $^{13}C\{^{1}H\}$ NMR (101 MHz, $CDCl_3$) for product **P16.**

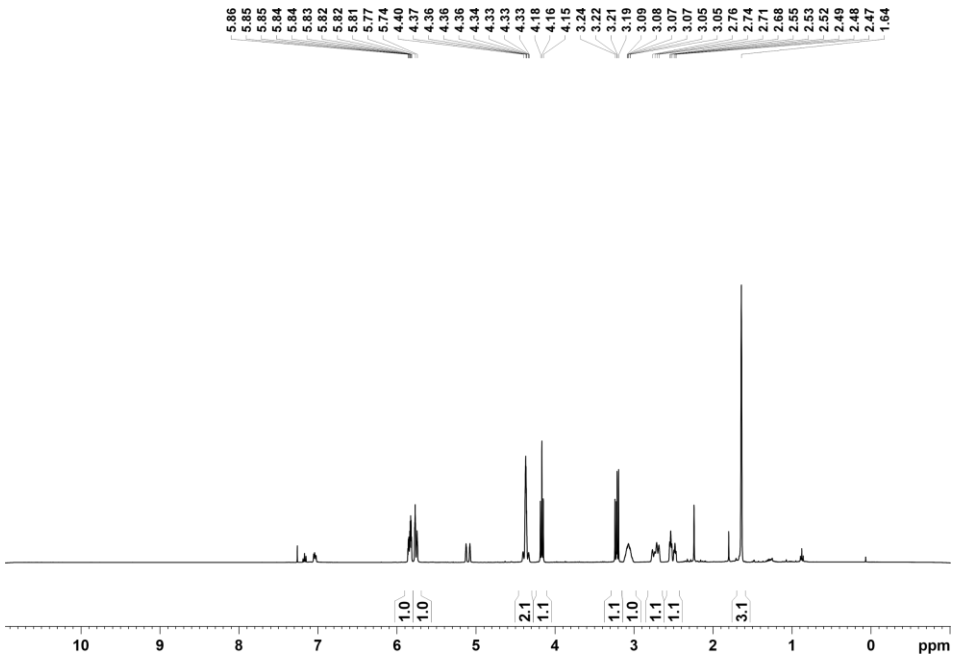

Figure 4.28. ^{1}H NMR (400 MHz, $CDCl_3$) for product **P17.**

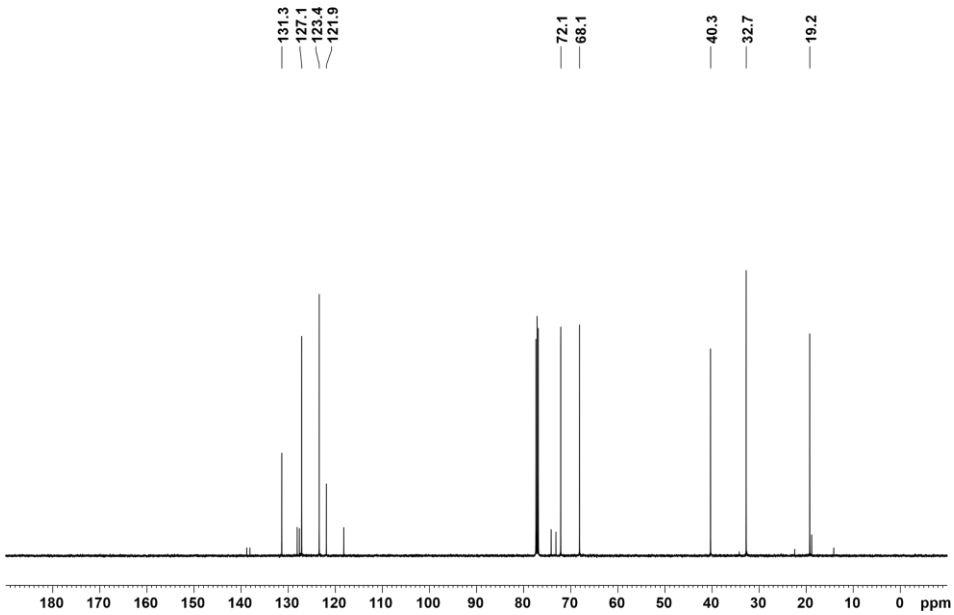

Figure 4.29. $^{13}C\{^{1}H\}$ NMR (101 MHz, $CDCl_3$) for product **P17.**

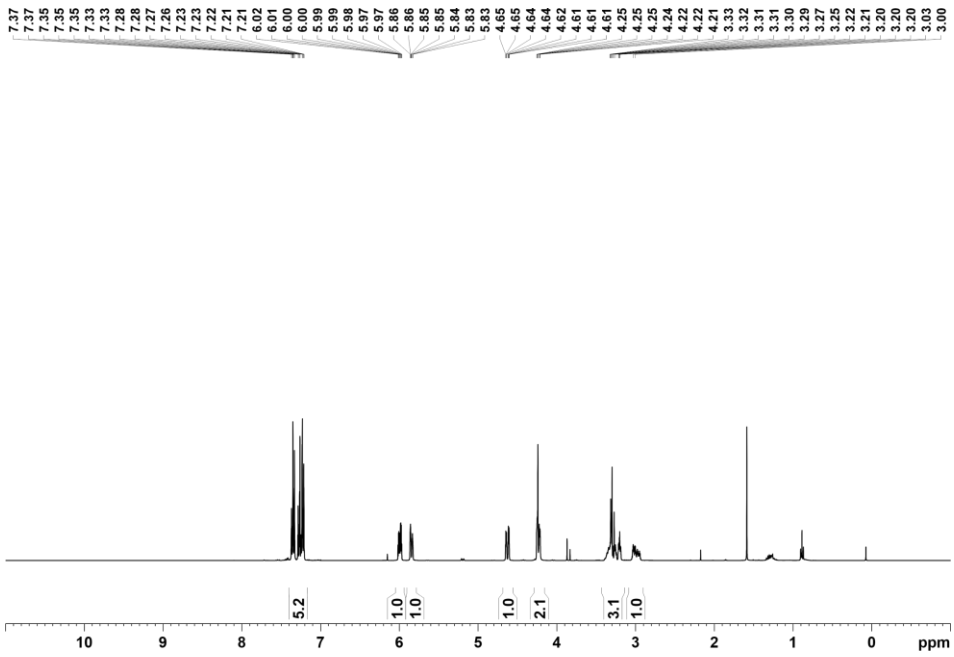

Figure 4.30. ^{1}H NMR (400 MHz, $CDCl_3$) for product **P18.**

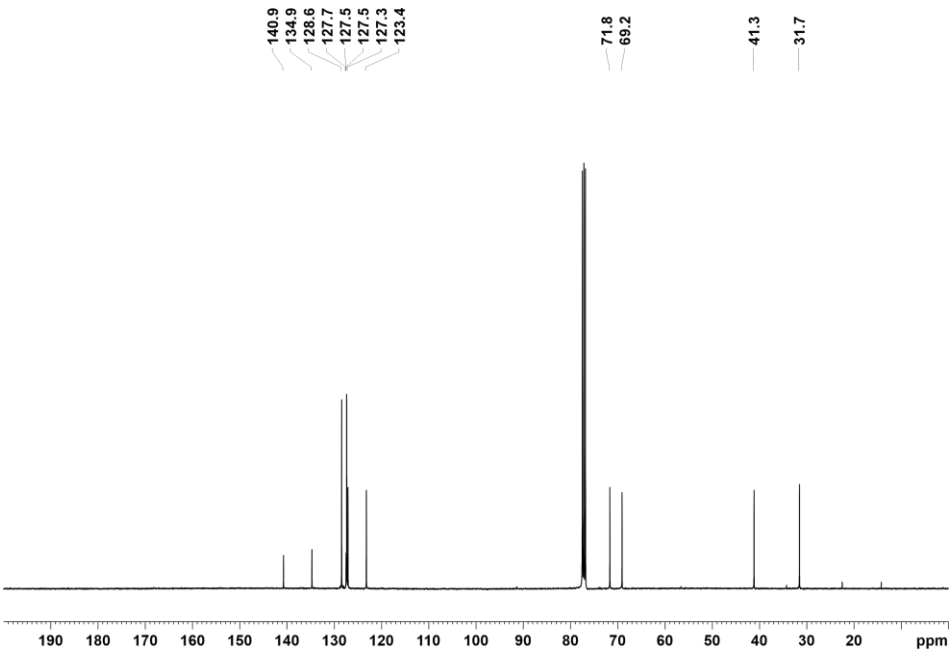

Figure 4.31. $^{13}C\{^{1}H\}$ NMR (101 MHz, $CDCl_3$) for product **P18.**

CHAPTER V:

TOWARDS NEW HALOGEN BOND-ASSEMBLED Ir(I) CATALYSTS AND THEIR APPLICATION IN DOUBLE HYDROALKOXYLATION REACTIONS

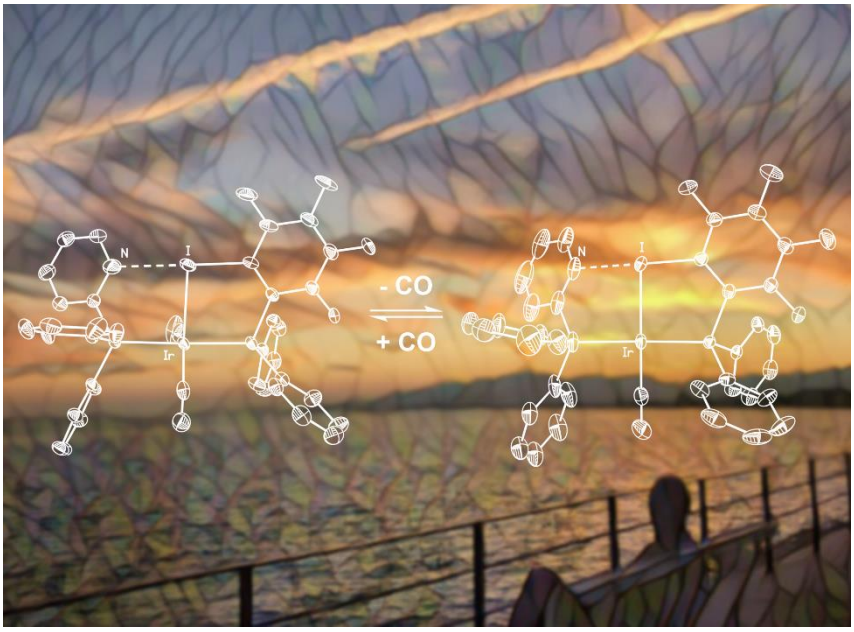

5.1 INTRODUCTION

Transition metal-based complexes have played and still play a significant role in many organic transformations, since they are able to catalyze pivotal reactions in organic synthesis in a chemo-, regio, and/or stereo-selective manner.[5,113,114] In spite of the fact that metal-based reaction intermediates (involved in the catalytic cycles) containing third-row transition metals are frequently less reactive than those from metals belonging to the first- and second-row, the development of catalytic methodologies involving iridium as catalytic metal has undergone a major growth in the last decades.[196] Moreover, it is well-established that some of the most important catalytic reactions, such as (asymmetric) hydrogenation[19,197] allylic substitution,[198] or C–H functionalization[199] such as borylation reaction,[200] among others, are catalyzed by iridium-based complexes, which demonstrates the importance that iridium has gained in catalysis.

[196] (a) Takeuchi, R. *Synlett* **2002**, *2002*, 1954-1965; (b) Takeuchi, R.; Kezuka, S. *Synthesis* **2006**, *2006*, 3349-3366; (c) Oro, L. A.; Claver, C. *Iridium Complexes in Organic Synthesis*. John Wiley & Sons, 2008; (d) Suzuki, T. *Chem. Rev.* **2011**, *111*, 1825-1845; (e) Andersson, P. G. *Iridium Catalysis*. Vol. 34; Springer, 2011.

[197] For general information, see: (a) Källström, K.; Munslow, I.; Andersson, P. G. *Chem. – Eur. J.* **2006**, *12*, 3194-3200; (b) Margalef, J.; Pàmies, O.; Diéguez, M. Iridium-Catalyzed Asymmetric Hydrogenation. In *Iridium Catalysts for Organic Reactions*, 2021; pp 153-205. For some examples, see: (c) Núñez-Rico, J. L.; Fernández-Pérez, H.; Benet-Buchholz, J.; Vidal-Ferran, A. *Organometallics* **2010**, *29*, 6627-6631; (d) Núñez-Rico, J. L.; Vidal-Ferran, A. *Org. Lett.* **2013**, *15*, 2066-2069; (e) Núñez-Rico, J. L.; Fernández-Pérez, H.; Vidal-Ferran, A. *Green Chem.* **2014**, *16*, 1153-1157; (f) Balakrishna, B.; Bauzá, A.; Frontera, A.; Vidal-Ferran, A. *Chem. – Eur. J.* **2016**, *22*, 10607-10613.

[198] (a) Hartwig, J. F.; Pouy, M. J. Iridium-Catalyzed Allylic Substitution. In *Iridium Catalysis*, 2011; pp 169-208; (b) Liu, W.-B.; Xia, J.-B.; You, S.-L. Iridium-Catalyzed Asymmetric Allylic Substitutions. In *Transition Metal Catalyzed Enantioselective Allylic Substitution in Organic Synthesis*, 2012; pp 155-207; (c) Tosatti, P.; Nelson, A.; Marsden, S. P. *Org. Biomol. Chem.* **2012**, *10*, 3147-3163; (d) Cheng, Q.; Tu, H.-F.; Zheng, C.; Qu, J.-P.; Helmchen, G.; You, S.-L. *Chem. Rev.* **2019**, *119*, 1855-1969.

[199] (a) Woźniak, Ł.; Tan, J.-F.; Nguyen, Q.-H.; Madron du Vigné, A.; Smal, V.; Cao, Y.-X.; Cramer, N. *Chem. Rev.* **2020**, *120*, 10516-10543; (b) Nishimura, T. *Chem. Rec.* **2021**, *21*, 3532-3545.

[200] (a) Xu, L.; Wang, G.; Zhang, S.; Wang, H.; Wang, L.; Liu, L.; Jiao, J.; Li, P. *Tetrahedron* **2017**, *73*, 7123-7157; (b) Fernández, E. Iridium-Catalyzed Undirected Homogeneous C–H Borylation Reaction. In *Iridium Catalysts for Organic Reactions*, 2021; pp 207-225.

In general, the use of efficient catalysts, in terms of activity and selectivity, requires a rational design and efficient preparation of ligands suitable for the desired reactivities. Ligand synthesis, which consists of multiple synthetic steps of variable complexity, can occasionally constitute an important drawback in the construction of libraries of structurally diverse ligands. As an interesting alternative to the classical approach involving covalent synthesis, supramolecular chemistry has emerged as an efficient tool for the construction of complex ligand skeletons *via* self-assembly of complementary building blocks.[2b,8,9c,10] Numerous examples involving non-covalent interactions (hydrogen bonding,[10,25b,28-37] metal-ligand,[25,26] ionic[38,39] and π-π interactions[40]) for the preparation of supramolecular catalytic systems have been already reported and described in detail in Chapter I.

To the best of our knowledge, the use of halogen bonding interactions for constructing the backbone of a metal catalysts remained unexplored until our research group[70] reported the first example on the use of this supramolecular interaction as a tool to assemble complementary building blocks in the presence of a rhodium-based metal precursor (Scheme 1.13). The lack of examples related to this area of research and the importance and wide applicability of iridium chemistry prompted us to expand the diversity of XBphos complexes to metals different to rhodium as metal center, as for instance the analogous iridium(I) derivatives.

As previously mentioned, iridium is a versatile transition metal capable of performing a wide range of relevant organic transformations in a selective manner. Among the broad spectrum of iridium-catalyzed reactions,[196] hydroelementation of unsaturated C–C bonds[201] represents one of the most interesting and utilized transformations in organic

[201] (a) Alonso, F.; Beletskaya, I. P.; Yus, M. *Chem. Rev.* **2004**, *104*, 3079-3160; (b) Wathier, M.; Love, J. A. *Eur. J. Inorg. Chem.* **2016**, *2016*, 2391-2402.

synthesis due to the relevance of the products obtained at the synthetic and pharmacological level.

Particularly, hydroalkoxylation of alkynes is an efficient and straightforward method for the formation of a broad range of *O*-containing heterocycles (*e.g.*, *O*-containing spiro-type compounds)[201a,202] depending on the inter- or intramolecular mode of the reaction. In addition, many organic structures available with this chemistry are known to possess biological activity (Figure 5.1).[203]

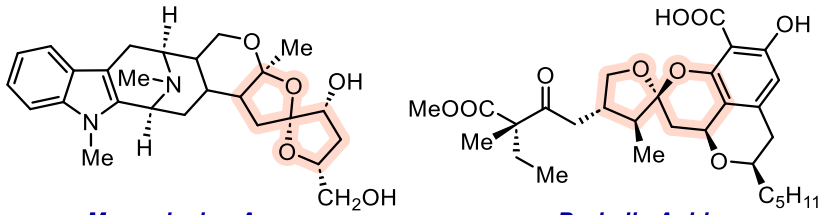

Figure 5.1. Examples of biologically active *O*-containing spiro molecules.

Numerous examples of catalysts for hydroalkoxylation reactions based on palladium or platinum[204] have been reported. Gabriele and co-workers[204d] described the palladium-catalyzed intramolecular hydroalkoxylation of readily available 2-alkynylbenzyl alcohols **79** with the aim of forming (*Z*)-1-alkylidene-1,3-dihydroisobenzofurans **80** and

[202] (a) Genin, E.; Antoniotti, S.; Michelet, V.; Genêt, J.-P. *Angew. Chem. Int. Ed.* **2005**, *44*, 4949-4953; (b) Smith, M. B. *March's Advanced Organic Chemistry: Reactions, Mechanisms, and Structure*. John Wiley & Sons, 2020; (c) Nanda, S. K.; Mallik, R. *Chem. – Eur. J.* **2021**, *27*, 15571-15604.

[203] For some relevant examples, see: (a) Kam, T.-S.; Choo, Y.-M.; Komiyama, K. *Tetrahedron* **2004**, *60*, 3957-3966; (b) Ghosh, A. K.; Leshchenko, S.; Noetzel, M. *J. Org. Chem.* **2004**, *69*, 7822-7829; (c) Stierle, A. A.; Stierle, D. B.; Kelly, K. *J. Org. Chem.* **2006**, *71*, 5357-5360; (d) Vaillancourt, V.; Pratt, N. E.; Perron, F.; Albizati, K. F. The Total Synthesis of Spiroketal-Containing Natural Products. In *The Total Synthesis of Natural Products*, Vol. 8; 2007; pp 533-691; (e) Xu, Z.; Li, Y.; Xiang, Q.; Pei, Z.; Liu, X.; Lu, B.; Chen, L.; Wang, G.; Pang, J.; Lin, Y. *J. Med. Chem.* **2010**, *53*, 4642-4653.

[204] For some examples, see: (a) Utimoto, K. *Pure Appl. Chem.* **1983**, *55*, 1845-1852; (b) Kataoka, Y.; Matsumoto, O.; Tani, K. *Organometallics* **1996**, *15*, 5246-5249; (c) Kadota, I.; Lutete, L. M.; Shibuya, A.; Yamamoto, Y. *Tetrahedron Lett.* **2001**, *42*, 6207-6210; (d) Gabriele, B.; Salerno, G.; Fazio, A.; Pittelli, R. *Tetrahedron* **2003**, *59*, 6251-6259; (e) Hartman, J. W.; Sperry, L. *Tetrahedron Lett.* **2004**, *45*, 3787-3788; (f) Das, A.; Buzzetti, L.; Puriņš, M.; Waser, J. *ACS Catal.* **2022**, *12*, 7565-7570.

1*H*-isochromenes **81** as products in a straightforward manner (Scheme 5.1). The authors observed that, depending on the substitution pattern of the starting material (2-alkenyl benzyl alcohol **79**), as well as on the reaction conditions, one cyclization mode was favored over the other (*i.e.*, 5-*exo-dig* or 6-*endo-dig*) giving rise to two different products: furane containing derivatives **80** or isochromenes **81**. The authors observed that the selectivity of the reaction depended on the solvent used, with isochromenes **81** being the most abundant products when using dioxane as solvent.

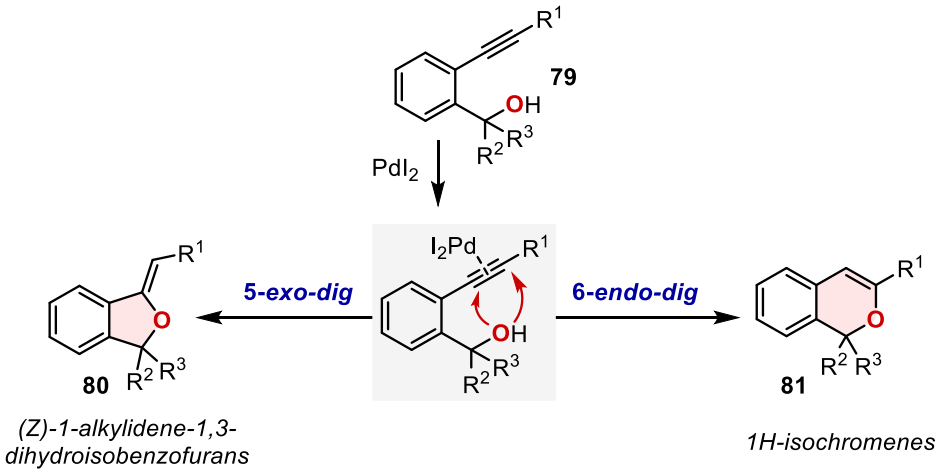

Scheme 5.1. Palladium-catalyzed intramolecular hydroalkoxylation od 2-alkynylbenzyl alcohols **79**.

The preparation of an array of *O*-containing heterocycles *via* ruthenium-based[201a,205] vinylidene complexes has been also explored. In addition, a vast number of research activities on this topic has focused on the use of gold-based complexes in inter- and intramolecular hydroalkoxylations, leading to a broad array of *O*-containing

[205] For selected examples, see: (a) Kücükbay, H.; Cetinkaya, B.; Guesmi, S.; Dixneuf, P. H. *Organometallics* **1996**, *15*, 2434-2439; (b) Trost, B. M.; Rhee, Y. H. *J. Am. Chem. Soc.* **2002**, *124*, 2528-2533; (c) Iio, K.; Sachimori, S.; Watanabe, T.; Fuwa, H. *Org. Lett.* **2018**, *20*, 7851-7855; (d) Nishimura, K.; Hanzawa, R.; Sugai, T.; Fuwa, H. *J. Org. Chem.* **2021**, *86*, 6674-6697.

derivatives.[202c,206] Along these lines, the group of Plé[207] recently reported an elegant and robust methodology for the synthesis of spirocyclic *O*-containing (and *N*-containing) derivatives *via* intramolecular hydroalkoxylation of alkynes with tertiary alcohols **82** (Scheme 5.2). Several spirocycles with an oxazinone ring **83** could be obtained in good to excellent yields under microwave irradiation by using a low catalyst loading and short reaction times.

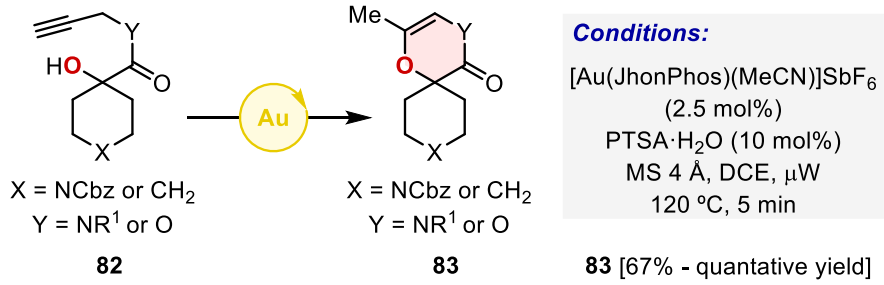

Scheme 5.2. Gold-catalyzed hydroalkoxylation reaction.

Group 9 transition metals were also found to be catalytically active in hydroalkoxylation reactions. Concretely, the use of rhodium- and iridium-complexes in the above-mentioned transformation has been reported in the literature.[208] In 2007, the group of Steinborn described the intermolecular addition of methanol to a variety of internal alkynes catalyzed by the 18-crown-6 ether adduct of sodium hexachloroiridate $[(18C6{\cdot}Na)_2][Ir(Cl)_6]$ **84** (18C6 stands for the abbreviation of the crown

[206] For some examples, see: (a) Teles, J. H.; Brode, S.; Chabanas, M. *Angew. Chem. Int. Ed.* **1998**, *37*, 1415-1418; (b) Antoniotti, S.; Genin, E.; Michelet, V.; Genêt, J.-P. *J. Am. Chem. Soc.* **2005**, *127*, 9976-9977; (c) Goodwin, J. A.; Aponick, A. *Chem. Commun.* **2015**, *51*, 8730-8741.

[207] Soklou, K. E.; Marzag, H.; Bouillon, J.-P.; Marchivie, M.; Routier, S.; Plé, K. *Org. Lett.* **2020**, *22*, 5973-5977.

[208] For selected examples, see: (a) Elgafi, S.; Field, L. D.; Messerle, B. A. *J. Organomet. Chem.* **2000**, *607*, 97-104; (b) Masui, D.; Kochi, T.; Tang, Z.; Ishii, Y.; Mizobe, Y.; Hidai, M. *J. Organomet. Chem.* **2001**, *620*, 69-79; (c) Trost, B. M.; Rhee, Y. H. *J. Am. Chem. Soc.* **2003**, *125*, 7482-7483; (d) Genin, E.; Antoniotti, S.; Michelet, V.; Genêt, J.-P. *Angew. Chem. Int. Ed.* **2005**, *44*, 4949-4953; (e) Messerle, B. A.; Vuong, K. Q. *Pure Appl. Chem.* **2006**, *78*, 385-390; (f) Konkol, M.; Schmidt, H.; Steinborn, D. *J. Mol. Catal. A: Chem.* **2007**, *261*, 301-305; (g) Messerle, B. A.; Vuong, K. Q. *Organometallics* **2007**, *26*, 3031-3040; (h) Dang, Y.; Qu, S.; Wang, Z.-X.; Wang, X. *Organometallics* **2013**, *32*, 2804-2813.

ether fragment).[208f] In the same year, Messerle and co-workers[208g] reported an efficient method based on rhodium- and iridium-catalyzed consecutive inter- and intramolecular double hydroalkoxylations for the preparation of a structurally diverse set of *O,O*-ketals (Scheme 5.3). Mechanistic studies using low temperature NMR spectroscopy and deuteration analysis were also carried out for the iridium-based complex **87** with the aim of clarifying whether the intramolecular addition proceeded through activation of the alkyne moiety or of the O–H bond. These investigations pointed to a π-coordination of the alkyne moiety to the iridium center as a first step of the catalytic cycle followed by a sequential inter- and intramolecular addition of two different OH groups leading to the formation of the final *O,O*-ketal derivatives.

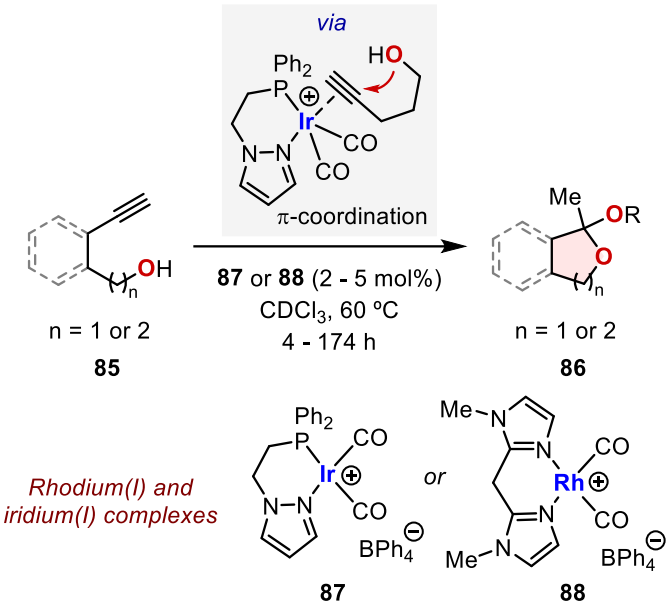

Scheme 5.3. Rhodium(I)- and iridium(I)-catalyzed double hydroalkoxylation reaction of alkynol derivatives.

The lack of examples in which halogen bond has been explored as a suitable tool for the construction of bidentate ligand skeletons (only reported for rhodium complexes), together with the well-established catalytic activity of iridium(I)-based complexes in the preparation of

relevant *O,O*-ketal-containing compounds *via* hydroalkoxylation reactions, prompted us to evaluate Ir(I) complexes analogous to XBphos-Rh as catalysts for the consecutive inter- and intramolecular double hydroalkoxylation of alkynyl alcohols.

5.2 RESULTS AND DISCUSSION

Synthesis and characterization of halogen-bonded Ir(I) complexes

With the aim of expanding the structural diversity of the XBphos metal complexes, we directed research efforts to the preparation of halogen-bonded complexes containing other metals than rhodium. We turned our attention to the preparation of the iridium analogue of complex XBphos-Rh **C1** and tackled its preparation following a similar strategy to that employed for **C1** (see Scheme 1.13).

Initially, we took advantage of the synthetic protocol developed by Roberto *et al*[209] to prepare *in situ* the dimeric iridium complex [{Ir(CO)$_2$(μ-Cl)}$_2$] from the commercially available cycloocta-1,5-diene iridium(I) precursor [{Ir(μ-Cl)(cod)}$_2$] (Scheme 5.4).

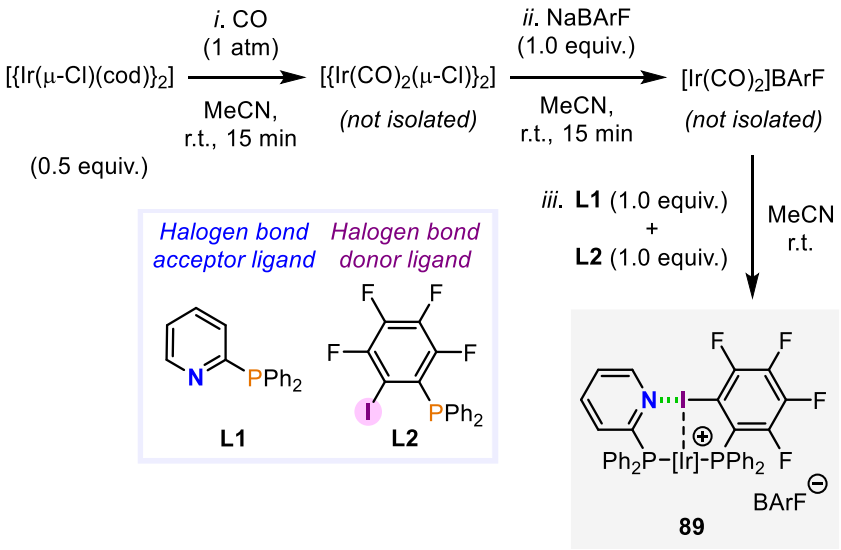

Scheme 5.4. Synthesis of iridium(I) halogen-bonded complexes **89**.

Dicarbonyl iridium(I) complex [{Ir(CO)$_2$(μ-Cl)}$_2$] was straightforwardly prepared by bubbling CO gas at atmospheric pressure (CO balloon) for

[209] Roberto, D.; Cariati, E.; Psaro, R.; Ugo, R. *Organometallics* **1994**, *13*, 4227-4231.

15 minutes into a solution of [{Ir(μ-Cl)(cod)}$_2$] in acetonitrile, MeCN, (Scheme 5.4). The resulting iridium-based complex was not isolated and allowed to react with equimolar amounts of the corresponding halide scavenger (*i.e.*, NaBArF) to form a putative [Ir(CO)$_2$]BArF intermediate, which was not isolated. Subsequently, the iridium-based intermediate [Ir(CO)$_2$]BArF was allowed to react with an equimolar mixture of our phosphane ligands **L1** and **L2**, which contains complementary halogen bonding motifs, at room temperature in acetonitrile. A crystalline material was obtained (for more details, see section 5.4).

^{31}P{^{1}H} NMR analysis of the crystalline material revealed the formation of two different iridium-phosphane complexes. The multiplicity of the signals of the major iridium complex were in agreement with the expected halogen bond-assembled iridium structure **89** (Scheme 5.4). Signals with higher intensity appeared in ^{31}P{^{1}H} NMR spectrum as two doublets with a large phosphorus-phosphorus coupling constant ($^2J_{P-P}$ = 240 Hz, see Figure 5.2) pointing to a halogen bond-assembled *trans*-spanning bisphosphane coordinated to the iridium(I) center.

On the other hand, the phosphino group bonded to the fluorine-substituted fragment in **L2** was not further split by virtue of its coupling with the active ^{19}F nucleus placed three bonds away as previously observed for the rhodium analogue **C1**. Coupling with the ^{19}F nucleus could be only observed as a broadening of the corresponding phosphorus signal (see line widths at half height: 22 Hz for those signals that correspond to the ligand **L2** vs. 14 Hz in the case of pyridyl-based ligand **L1**, see Figure 5.2).

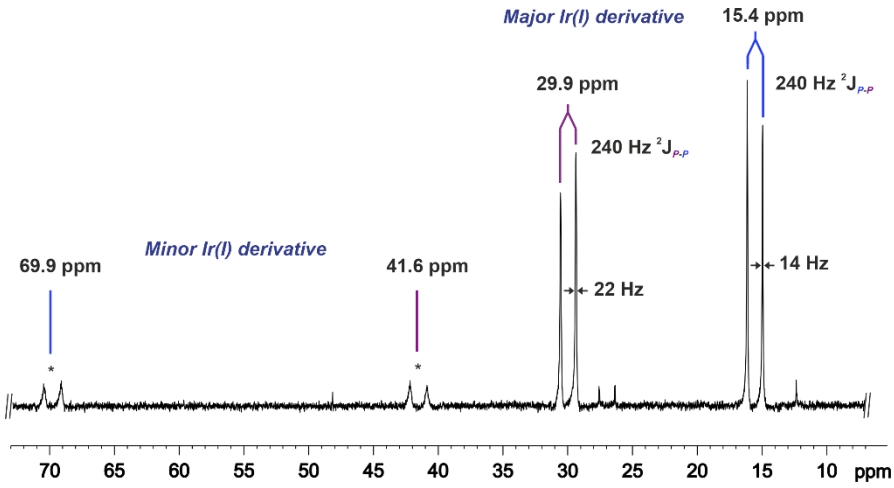

Figure 5.2. ^{31}P NMR spectrum of iridium-phosphane complexes **89**.

Regarding the number of carbonyl ligands coordinated to the iridium center, we expected the coordination of one CO molecule as observed for the rhodium analogue **C1**, since 4-coordinated square planar geometries are predominantly favored for both rhodium(I) and iridium(I) complexes (although 5-coordinated geometries can be also found in some examples).[210] However, two different bands of equal intensity attributable to CO groups at 2028 and 1991 cm^{-1} were observed in the solid state IR spectrum (Table 5.1), indicating the formation of the dicarbonyl iridium complex [Ir(CO)$_2$(κ^3*I,P,P*-**L1**·**L2**)]BArF **C9** as major compound.

Table 5.1. IR spectroscopic data of dicarbonyl iridium(I) complexes **C9** and **C1**.

	C9	**C1**[a]
$\tilde{\upsilon}_{CO}$ (cm^{-1})	2028, 1991	2036

[a] Previously reported by our group. Ref. 70.

[210] (a) Cobalt, Rhodium and Iridium. In *Chemistry of the Elements*, 1997; pp 1113-1143; (b) Crabtree, R. H. *The Organometallic Chemistry of the Transition Metals*. John Wiley & Sons, 2009.

NMR studies in solution, concretely $^{31}P\{^{1}H\}$–$^{31}P\{^{1}H\}$ NMR exchange spectroscopy experiments (*i.e.*, EXSY),[211] revealed that both **L1** and **L2** phosphino groups in the complex [Ir(CO)$_2$(κ^3*I,P,P*-**L1**·**L2**)]BArF **C9** were exchanging in the NMR time scale with the same ligands present in the second most abundant component of the reaction mixture (Figure 5.3). Though we did not have yet at this point a structure of the complex, results from EXSY analysis indicated that the most abundant and second most abundant iridium species were in equilibrium in solution through equilibria involving ligand coordination.

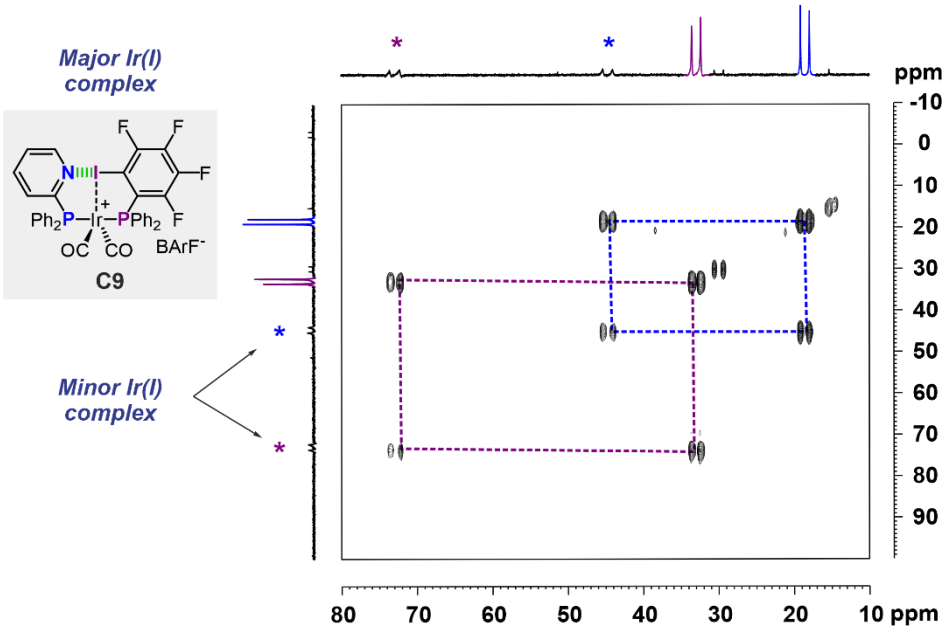

Figure 5.3. $^{31}P\{^{1}H\}$–$^{31}P\{^{1}H\}$ NMR EXSY spectrum.

Fortunately, it was discovered that washing protocols allowed the isolation of the second most abundant iridium complex in the original mixture in moderate purity (*ca.* 80%; quantified *via* $^{31}P\{^{1}H\}$ IGD NMR spectroscopy[211]). The $^{31}P\{^{1}H\}$ IGD NMR spectrum showed a doublet of doublets for the signal at higher chemical shift (δ = 69.9 ppm) and a doublet for the one at lower chemical shift (δ = 41.6 ppm). The large

[211] Berger, S.; Braun, S. *200 and More NMR Experiments*. Wiley-VCH, 2004.

coupling constant was attributed to the coupling between the two inequivalent phosphorus nuclei through two bonds ($^2J_{P-P}$ = 265 Hz) and the smaller one was assigned to the coupling between the phosphorus group and the fluorine atom placed three bonds away ($^3J_{P-F}$ = 14 Hz) for ligand **L2**. Even though NMR characterization demonstrated the expected *trans*-coordination mode of both halogen bond ligands to the iridium center, other spectroscopic techniques were utilized for confirming the structure of the iridium-based structure. ESI-MS analysis pointed to the monocarbonyl complex [Ir(CO)(κ³*I,P,P*-**L1·L2**)]BArF **C10**, and only one intense CO band in the IR spectrum (2026 cm^{-1}) was observed.[212] Thus, spectroscopic data were pointing to the monocarbonyl iridium complex [Ir(CO)(κ³*I,P,P*-**L1·L2**)]BArF **C10**.

High-quality single crystals of both [$Ir(CO)_2$(κ³*I,P,P*-**L1·L2**)]BArF **C9** and [Ir(CO)(κ³*I,P,P*-**L1·L2**)]BArF **C10** complexes were obtained. **C9** was obtained as the most abundant compound in the crystalline material as bright yellow crystals. Taking advantage of the differences in the solubility of the two most abundant iridium complexes in cold toluene, high quality single crystals corresponding to the second most abundant complex **C10** could also be isolated from the mother liquors and analyzed by X-Ray diffraction. Thus, X-Ray analysis allowed us to unequivocally establish the structure of both iridium complexes. The crystal structure of the most abundant complex **C9** obtained from the mixture **89** (Scheme 5.4) had a pentacoordinate geometry with the formula [$Ir(CO)_2$(κ³*I,P,P*-**L1·L2**)]BArF (see Figure 5.4). Relevant X-Ray parameters have been summarized in Table 5.2.

[212] As the isolated material still contains around 10% of [$Ir(CO)_2$(κ³*I,P,P*-**L1·L2**)]BArF **C7**, the less intense CO band observed at 1991 cm^{-1} was attributed to this impurity.

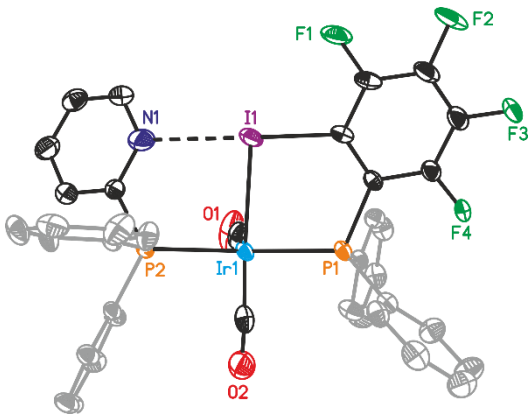

Figure 5.4. Crystal structure of dicarbonyl iridium complex **C9**. BArF anion and hydrogen atoms have been omitted for the sake of clarity. Color scheme: C: black or grey, P: orange, Ir: blue, N: violet, I: purple, O: red, F: green.

Table 5.2. Relevant halogen bond parameters of complexes **C9** and **C1**.

	C9	**C1**[a]
N···I (Å)	2.922(5)	2.757(8)
N···X–C (º)	151.8(2)	169.4(5)
M–I (Å)[b]	2.7412(6)	2.5535(7)
P–M–P (º)[b]	178.34	176.86

[a] **C1** data were obtained from the X-Ray structure reported by our group (Ref. 70) and have been included here to aid comparison. [b] M refers to the corresponding metal center: rhodium or iridium.

X-Ray analysis confirmed the presence of the halogen bonding interaction, showing that nitrogen and iodine atoms were aligned with a N···I distance of 2.922(5) Å and with a N···I–C bond angle of 151.8(2)° (Table 5.2). The N···I distance in complex [Ir(CO)$_2$(κ^3*I,P,P*-**L1**·**L2**)]BArF **C9** appeared to be longer than that in the rhodium analogue XBphos-Rh **C1** (2.922(5) Å for **C9** compared to 2.757(8) Å for **C1**, Table 5.2). Besides, the N···I–C angle (151.8(2)º) deviates from the ideal value (*i.e.*, 180º) in a greater extent than does XBphos-Rh **C1** with a N···I–C value of 169.4(5)º.

The important deviation from the ideal geometrical parameters for the iridium complex arises probably from the observed trigonal bipyramidal geometry for the iridium center in **C9** instead of the square planar one in XBphos-Rh **C1**. It is interesting to note that iodine appeared to be coordinated to the iridium center (Ir–I distance = 2.741 Å, Table 5.2) also forming a tridentate κ³*I,P,P*-type halogen-bonded ligand.

The structure of the second most abundant iridium-based complex **C10** was also confirmed by using X-Ray analysis. As it can be observed in Figure 5.5, complex **C10** presents a square planar geometry like its rhodium analogue **C1** with the formula [Ir(CO)(κ³*I,P,P*-**L1·L2**)]BArF.

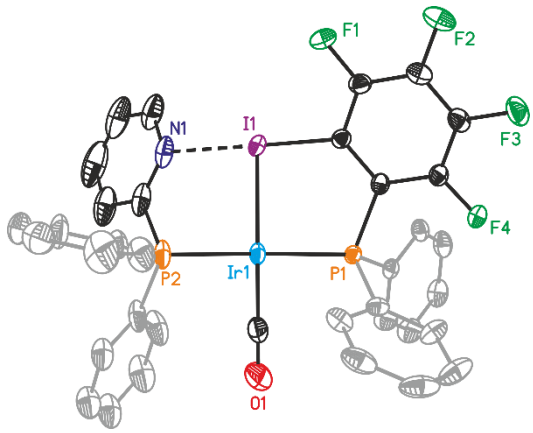

Figure 5.5. Crystal structure of monocarbonyl iridium complex **C10**. BArF anion and hydrogen atoms have been omitted for the sake of clarity. Color scheme: C: black or grey, P: orange, Ir: blue, N: violet, I: purple, O: red, F: green.

Table 5.3. Relevant halogen bond parameters of complex **C10**.

	C10
N···I (Å)	2.752(4)
N···X–C (º)	168.5(1)
Ir–I (Å)	2.6007(5)
P–Ir–P (º)	176.52(4)

The iodine and nitrogen atoms are aligned with a N···I distance of 2.752(4) Å and with a N···I–C bond angle of 168.5(1)º (Table 5.3). In this case, both structural parameters are very close to those reported by our research team for XBphos-Rh **C1**. X-Ray analysis also confirmed that the iodine atom in [Ir(CO)(κ³*I,P,P*-**L1·L2**)]BArF **C10** is coordinated to the iridium center (Ir–I distance = 2.6007(5) Å). Besides, a *trans*-spanning bisphosphane coordination to the iridium center (P–Ir–P angle of 176.52(4)º) was also demonstrated by using X-Ray analysis.

Since a selective synthesis of each of the two complexes was not possible, and it was not feasible to selectively isolate in a pure way neither complex [Ir(CO)$_2$(κ³*I,P,P*-**L1·L2**)]BArF **C9** nor [Ir(CO)(κ³*I,P,P*-**L1·L2**)]BArF **C10** by crystallization techniques or washing protocols, we devised an alternative route for selectively synthesizing each iridium complex.

Based on the work reported by Khrustalev *et al.,*[213] we envisaged that the selective oxidation of one carbonyl ligand in **C9** by using stoichiometric amounts of trimethylamine *N*-oxide (TMAO) as oxidizing agent (Scheme 5.5), followed by suitable purification techniques, could be an excellent alternative for the preparation of monocarbonyl complex [Ir(CO)(κ³*I,P,P*-**L1·L2**)]BArF **C10**. However, after several attempts to isolate the monocarbonyl complex [Ir(CO)(κ³*I,P,P*-**L1·L2**)]BArF **C10** following the aforementioned synthetic route, complex mixtures of numerous iridium-phosphane complexes were obtained. Consequently, the strategy was abandoned.

[213] Varshavsky, Y. S.; Galding, M. R.; Cherkasova, T. G.; Smirnov, S. N.; Khrustalev, V. N. *J. Organomet. Chem.* **2007**, *692*, 5788-5794.

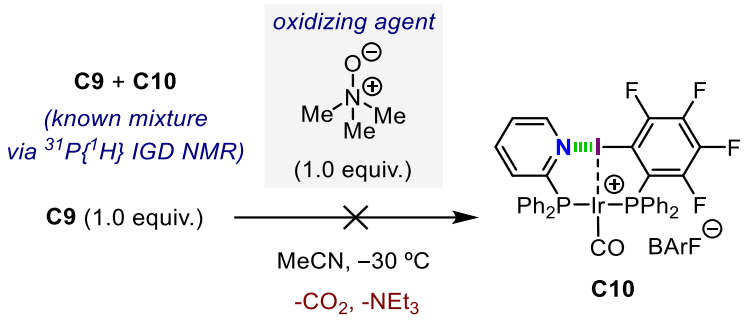

Scheme 5.5. Selective synthesis of monocarbonyl complex **C10** *via* selective oxidation of carbonyl groups.

Since the formation of the dicarbonyl [Ir(CO)$_2$(κ^3*I,P,P*-**L1**·**L2**)]BArF **C9** complex was favored over **C10**, we turned our attention to a new synthetic route in order to isolate exclusively this iridium complex. (Scheme 5.6).

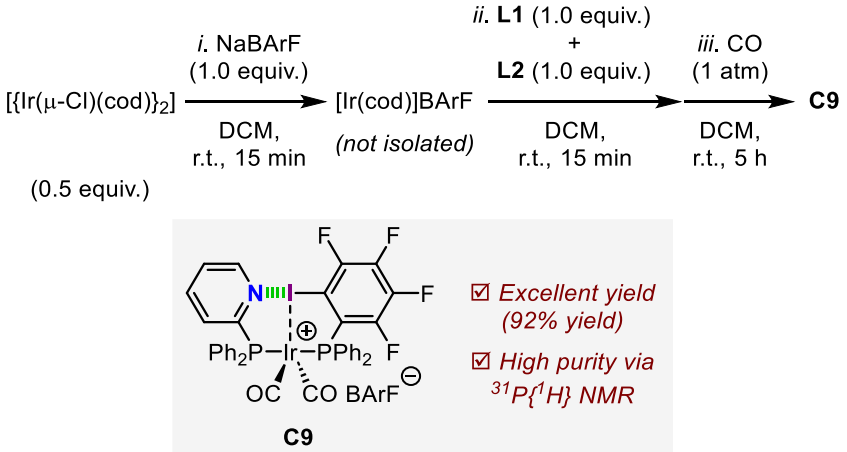

Scheme 5.6. Optimized preparation of [Ir(CO)$_2$(κ^3*I,P,P*-**L1**·**L2**)]BArF **C9** complex.

We envisaged that the *in situ* formation of intermediate [Ir(cod)]BArF, which is known to be quite stable and ideal starting material in the preparation of iridium complexes, could be achieved from [{Ir(μ-Cl)(cod)}$_2$] and NaBArF as halide scavenger. After the addition of an equimolecular mixture of **L1** and **L2** to [Ir(cod)]BArF, the N$_2$ atmosphere of the reaction was changed to a CO atmosphere by using a balloon. Stirring

continued for 5 hours. We hypothesized that CO would slowly dissolve in the reaction mixture, displace the cod ligand and coordinate to the iridium(I) metal center. Finally, after following this strategy, *n*-pentane was layered onto the solution of the reaction mixture in dichloromethane. A crystalline material was subsequently isolated (for more details, see section 5.4). Spectroscopic data for the resulting crystalline material were in agreement with those previously obtained for [Ir(CO)$_2$(κ^3*I,P,P*-**L1**·**L2**)]BArF **C9** complex.

Catalytic double hydroalkoxylation of alkynyl alcohols

The interesting structural characteristics of our [Ir(CO)$_2$(κ^3*I,P,P*-**L1**·**L2**)]BArF **C9** complex, combined with the activity that this type of iridium-based complexes present in hydroalkoxylation reactions, prompted us to investigate its catalytic features with the aim of complementing the already existing hydroalkoxylation catalytic tools. We envisaged that the halogen bond-assembled iridium(I) complex **C9** could be a potential catalyst in hydroalkoxylation reactions of alkynyl alcohols.

Initially, pent-4-yn-1-ol **S20**, a linear alkynyl alcohol, was selected as model substrate to evaluate the catalytic performance of complex **C9** in this chemistry. Besides, these initial reactivity studies also aimed at optimizing the reaction conditions. The efficiency of our iridium-based complex **C9** was preliminary tested under already reported conditions using chloroform as solvent at 30 and 40 °C (see entry 1 and 2). The preliminary results showed the formation of the *O,O*-ketal product **P20a**, pointing to a consecutive double intra- and intermolecular hydroalkoxylation reaction. Our model substrate **S20** reacted in an intramolecular manner leading to the 5-*exo-dig* cyclization product 2-methylenetetrahydrofuran, which evolved by subsequent incorporation of a second molecule of **S20** to the *O,O*-ketal product **P20a**. High conversions were calculated by ^{1}H NMR at both temperatures (see entries 1 and 2, Table 5.4). However, complex reaction mixtures were observed

with the yield towards the expected product **P20a** being rather low (only 22% and 41% of product **P20a** at 30 and 40 °C, respectively, see entries 1 and 2, Table 5.4). In addition, 5-methyl-2,3-dihydrofuran **90** was also detected by ^{1}H NMR. This compound was formed by C=C bond isomerization in the cyclization product 2-methylenetetrahydrofuran.

Table 5.4. Optimization of iridium-catalyzed double hydroalkoxylation of pent-4-yn-1-ol using complex **C9** as catalyst.[a]

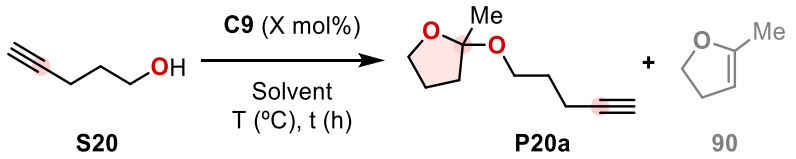

Entry	**C9** (mol%)	**Solvent**	**T** (ºC)	**t** (h)	Conv. (%)	Yield **P20a** (%)	Yield **90** (%)
1	2	$CHCl_3$	30	24	95	22	2
2	2	$CHCl_3$	40	24	93	41	6
3	2	DCE	30	24	86	45	10
4	2	DCE	60	24	92	10	2
5	2	DCM	30	24	89	88	<1
6	1	DCM	30	24	60	58	<1
7	5	DCM	30	24	87	82	<1
8	2	DCM	30	12	49	23	<1
9	2	DCM	30	48	81	70	<1

[a] Reactions were performed under an N_2 atmosphere. Conversions and yields were determined by ^{1}H NMR using 1,2,4,5-tetramethylbenzene as the internal standard.

Similar results were obtained with DCE as solvent, which was selected as the solvent of choice with the aim of testing higher reaction temperatures. The same trend was found after 24 h. Low yields towards

product **P20a** were observed (45% and 10% of **P20a** at 30 and 60 °C, respectively, see entry 3 and 4, Table 5.4).

Afterwards, we moved towards the use of DCM as solvent. Interestingly, the use of such solvent at 30 °C led to the best results in terms of yield of the product **P20a** (89% of conversion and 88% of yield, entry 5, Table 5.4). When the catalyst loading was reduced to 1 mol%, moderate conversion and yield were observed (60% of conversion and 58% of yield, entry 6, Table 5.4). However, increasing the catalyst loading to 5 mol% did not bring any advantage (compare entries 5 and 7, Table 5.4).

Concerning the reaction times, it is well-known that in the presence of cationic Rh(I) and Ir(I) complexes long reaction times are needed for this type of linear alkynyl alcohol substrates to cyclize (even more than 60 hours in the case of pent-4-yn-1-ol **S20** at 60 °C).[208e,209g] Employing our halogen-bonded iridium(I) complex **C9** as catalyst, a good conversion was observed after 24 h. The reaction mixture was also analyzed after 12 h (entry 8, Table 5.4) and lower conversion and yield were observed, demonstrating that longer reaction times were needed under our catalytic conditions. On the other hand, the conversion of the substrate was not altered after 48 h of reaction, but a slight decrease in the reaction yield was observed (compare entries 5 and 9, Table 5.4).

When the catalytic hydroalkoxylation reaction was carried out in the presence of a small excess of an external *O*-nucleophile (*i.e.*, methanol), the *O,O*-ketal resulting from the incorporation of methanol (*i.e.*, **P20b**) to the five-membered reaction intermediate was formed (Scheme 5.7).

It was found that, in the presence of our halogen bond-assembled iridium(I) complex **C9**, the *O,O*-ketal **P20b** was detected as the most abundant product in the ^{1}H NMR spectrum when a small excess of methanol (1.2 equiv., entry 1, Table 5.5) was added to the reaction mixture. Also, small quantities of product **P20a** were detected in the reaction mixture.

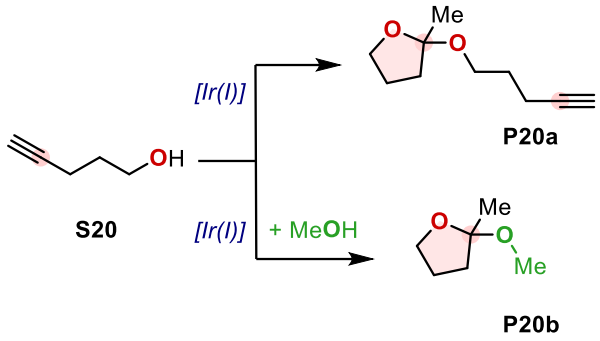

Scheme 5.7. Iridium(I)-catalyzed consecutive double intra- and intermolecular hydroalkoxylation in the absence or presence of methanol.

Table 5.5. Influence of the amount of the secondary alcohol on the outcome of the hydroalkoxylation reaction.[a]

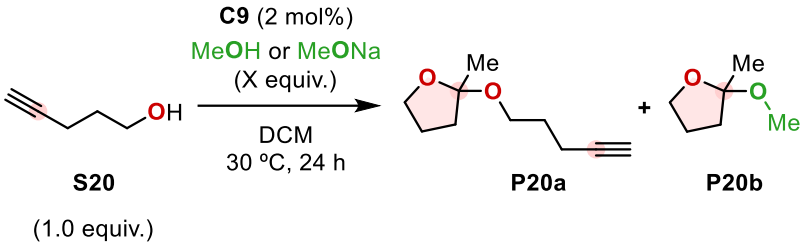

Entry	**MeOH** or **MeONa** (equiv.)	Conv. (%)	Yield **P20a** (%)	Yield **P20b** (%)
1	MeOH; 1.2	70	16	49
2	NaOMe; 1.2	<1	<1	<1
3	MeOH; 0.5	79	43	17
4	MeOH; 0.25	70	61	8
5	MeOH; 5.0	95	<1	68

[a] Reactions were performed under an N_2 atmosphere. Conversion and yield were determined by ^1H NMR using 1,2,4,5-tetramethylbenzene as the internal standard.

To aid comparison, sodium methoxide (as an alternative to methanol with a higher nucleophilicity) was also utilized (entry 2, Table 5.5). However, the use of sodium methoxide was found to be detrimental since the starting pent-4-yn-1-ol **S20** remained unaltered. As expected, when the amount of methanol was decreased, higher yields of product **P20a** were obtained (43% and 61% yield of **P20a**, compare entries 3 and 4, Table 5.5). On the other hand, addition of a large excess of methanol (5.0 equiv., entry 5, Table 5.5) led to excellent conversion of pent-4-yn-1-ol **S20** under the optimized conditions and gave rise to the *O,O*-ketal product **P20b** in a highly selective manner.

With the aim of further optimizing our iridium-catalyzed reaction, we envisaged that the use of basic or acidic additives could favor the reaction. Some common organic bases were tested under our optimized conditions (Scheme 5.8).

Unfortunately, the presence of organic bases such as DBU, DIPEA or TEA in the reaction mixture was detrimental to the course of the reaction, with starting material **S20** being recovered after 24 h according to ^{1}H NMR analysis. Other, less nucleophilic, bases were also tested. The use of 2,4,6-trimethylpyridine or 2,6-di-*tert*-butylpyridine led to moderate conversions and yields (37% conversion for 2,4,6-trimethylpyridine and 51% for 2,6-di-*tert*-butylpyridine, see Scheme 5.8). Nevertheless, none of the organic bases tested led to better results than those previously obtained under standard conditions. No conversion of the initial pent-4-yn-1-ol **S20** was detected after the addition of inorganic bases (*i.e.*, Cs_2CO_3 or K_3PO_4) or Lewis acids (*i.e.*, CuCl or $AlCl_3$) to the reaction mixture. The use of weak organic acids such as benzoic acid did not affect the catalytic performance of the iridium complex **C9**, with the same conversion and yield being obtained in the presence or absence or benzoic acid (compare Scheme 5.8 with entry 5 in Table 5.4).

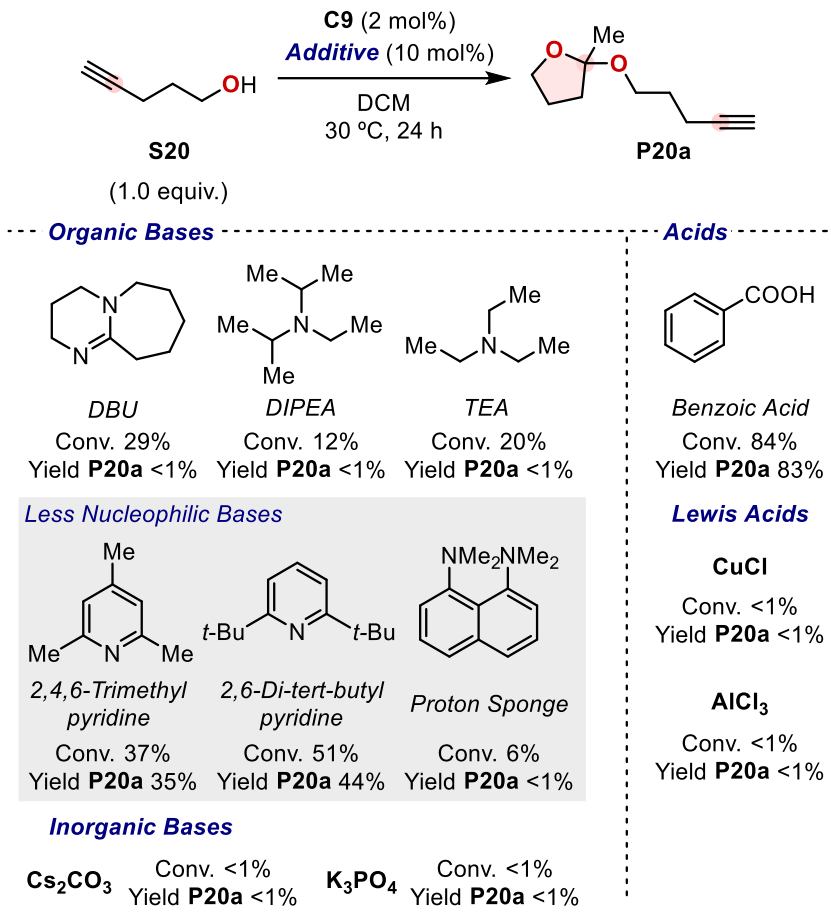

Scheme 5.8. Screening of different bases and acids under optimized conditions.

With the optimized conditions in hand, we turned our attention to extending the scope of the reaction. Initially, we decided to study the influence of the secondary alcohol in the formation of *O,O*-ketals under our reaction conditions (Scheme 5.9). Aliphatic alcohols such as ethanol led to the formation of the expected *O,O*-ketal product **P20c** in good yield. However, a more sterically hindered alcohol derivative such as isopropanol led to the formation of a mixture of both **P20a** and **P20d**, being derivative **P20a** predominantly achieved as major product. These results are in contrast to those obtained by using ethanol. On the other hand, the use of aromatic alcohols such as phenol did not lead to the expected product according to ^{1}H NMR analysis (Scheme 5.9).

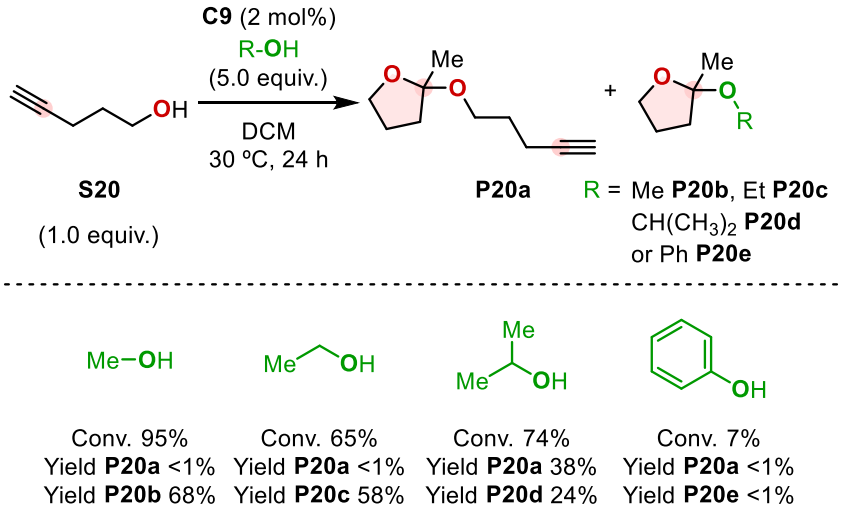

Scheme 5.9. Influence of the secondary alcohol.

Afterwards, an array of structurally diverse alkynyl alcohols were tested in the presence of catalytic amounts of our halogen bond-assembled complex [Ir(CO)$_2$(κ^3*I,P,P*-**L1**·**L2**)]BArF **C9** with or without MeOH as secondary *O*-nucleophile (Scheme 5.10). Compared to pent-4-yn-1-ol **S20**, the internal analogue pent-3-yn-1-ol **S21** led to the 5-*endo-dig* cyclization product, which further evolved to product **P20a** in moderate yield. Surprisingly, in this case, the presence of MeOH seemed to be detrimental for the reaction since the starting material remained unaltered.

In view of the fact that of our halogen bond-assembled iridium(I) complex **C9** was active in the formation of *O,O*-ketals starting from linear alkynyl alcohol **S20**, we directed our efforts to the study of homologous linear alkynyl alcohols with the aim of preparing *O*-containing 4-, 6- or 7-membered rings. Unfortunately, no conversion was observed in these cases and the starting materials remained unaltered according to ^{1}H NMR analysis.

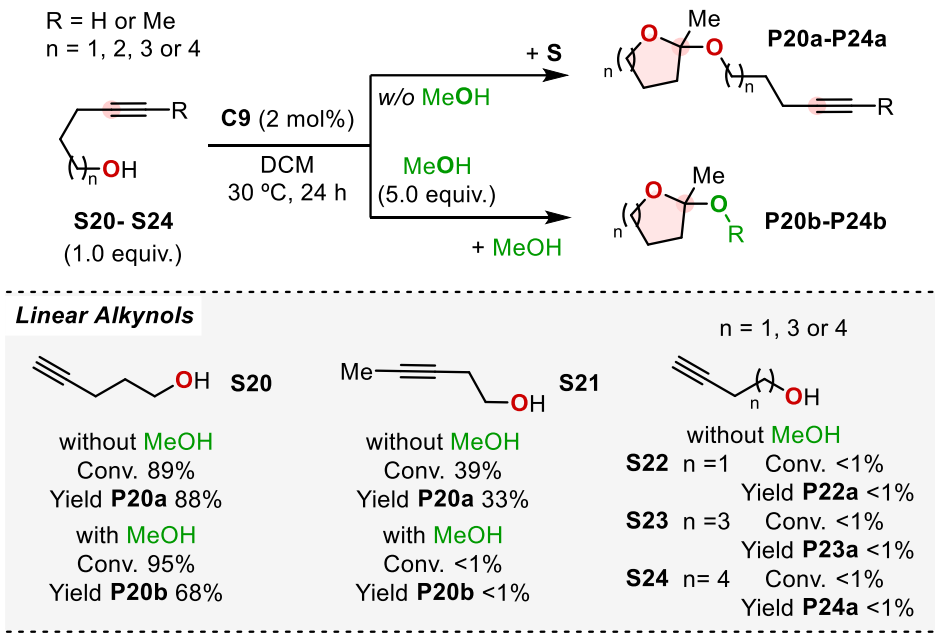

Scheme 5.10. Expansion of the scope of linear alkyl substrates in double intra- and intermolecular hydroalkoxylation reactions.

The lack of reactivity of substrates **S22**, **S23** and **S24** might be attributed to the unfavored cyclization processes leading to four, six or seven-membered rings, respectively (Scheme 5.10). In general, 4-membered rings should be easily formed in terms of entropic factors due to the close proximity of the two reacting groups in the starting material. However, for these ring systems, enthalpic factors are rather important since they are directly related to the strain energy of the transition state and the final product, which could exceed the entropic factors.[214] Therefore, the lack of reactivity of **S22** might be correlated to strain factors. In general, the formation of five membered rings is a highly favored pathway[215] due to the cooperative combination of positive enthalpic and entropic factors. For 6- to 11-membered rings, the unfavorable enthalpic

[214] (a) Illuminati, G.; Mandolini, L. *Acc. Chem. Res.* **1981**, *14*, 95-102; (b) Galli, C.; Mandolini, L. *Eur. J. Org. Chem.* **2000**, *2000*, 3117-3125.

[215] (a) Stirling, C. J. *Angew. Chem. Int. Ed.* **1968**, *7*, 648-&; (b) Illuminati, G.; Mandolini, L.; Masci, B. *J. Am. Chem. Soc.* **1975**, *97*, 4960-4966; (c) Casadei, M. A.; Galli, C.; Mandolini, L. *J. Am. Chem. Soc.* **1984**, *106*, 1051-1056.

contribution, together with the resulting entropy loss due to the ring closure, generally lead to lower reactivities towards the ring closure process.[214b,] These arguments could justify why substrates **S23** and **S24** didn't exhibit reactivity in the hydroalkoxylation reactions.

Considering the relevance of bicyclic *O*-containing compounds in organic synthesis and biological chemistry,[201,202] we studied the hydroalkoxylation of substrates leading to the formation of bicyclic *O,O*-ketals. Racemic mixtures of both diastereomeric 2-(prop-2-ynyl)cyclohexanol products *rac-cis*-**S25** and *rac-trans*-**S25** were studied as substrates under our optimized conditions.

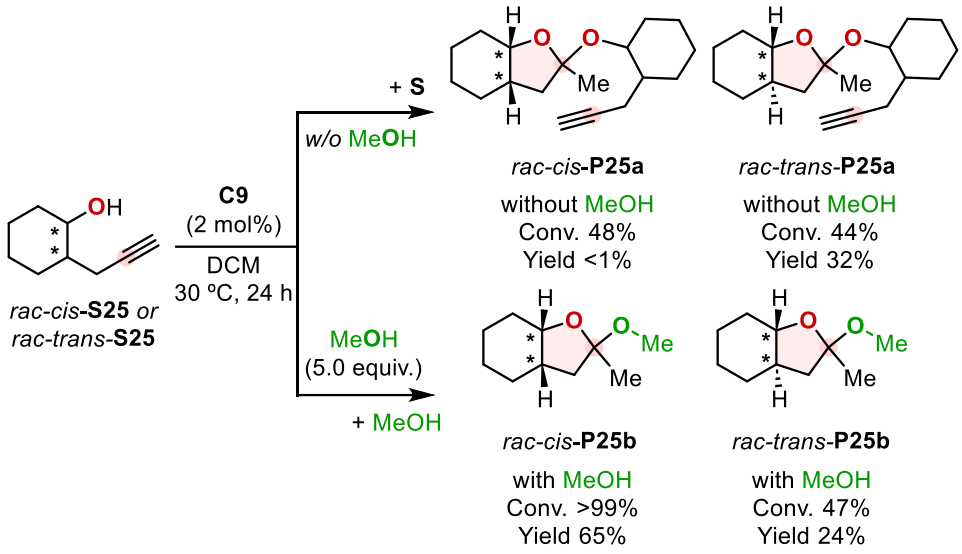

Scheme 5.11. Expansion of the scope of the reaction to bicyclic products in double intra- and intermolecular hydroalkoxylation reactions.

Whilst the cyclization product *rac-cis*-**P25a** derived from *rac-cis*-**S25** was not detected in the reaction mixture, an excellent yield of *rac-cis*-**P25b** was obtained when adding a large excess of MeOH (65% yield, Scheme 5.11). On the contrary, the cyclization of *rac-trans*-**S25** took place both in the absence or presence of methanol, although in low yields,

leading to two interesting *O*-containing derivatives: *rac-trans*-**P25a** and *rac-trans*-**P25b**.

Subsequently, we turned our attention to the hydroalkoxylation of precursors of spirocyclic compounds. The iridium-catalyzed cyclization of (1-(prop-2-yn-1-yl)cyclohexyl)methanol **S26** gave rise to spirocyclic products **P26a** and **P26b** in good and excellent yields (87% and 96% yield, respectively, Scheme 5.12).

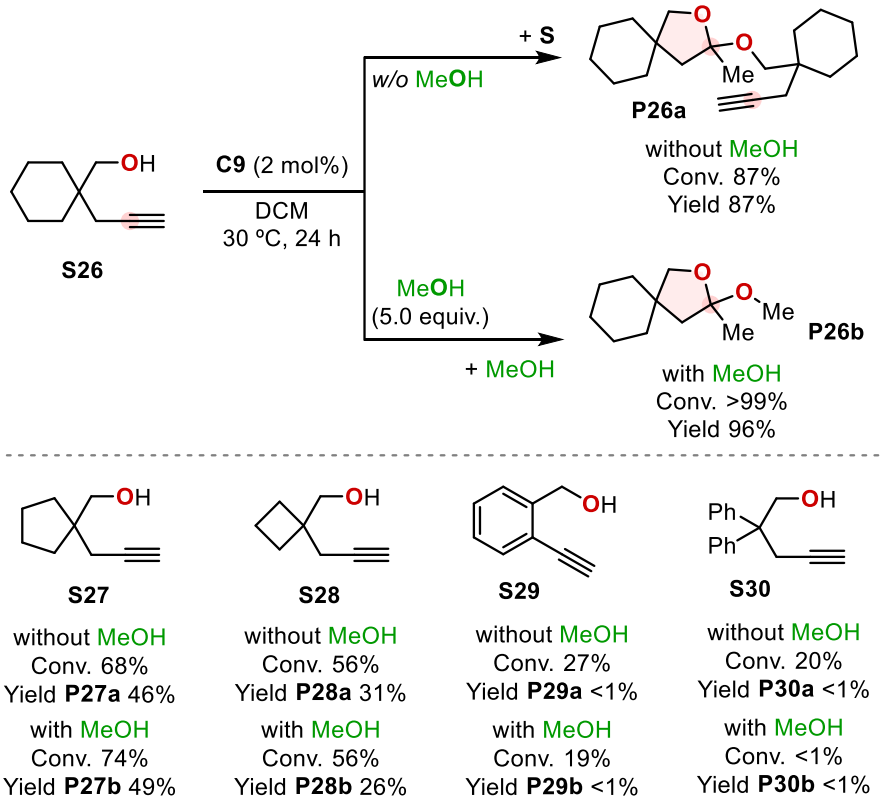

Scheme 5.12. Expansion of the scope of the reaction to bicyclic and spirocyclic products in intra- and intermolecular hydroalkoxylation reactions.

In addition, compounds (1-(prop-2-yn-1-yl)cyclopentyl)methanol **S27** and (1-(prop-2-yn-1-yl)cyclobutyl)methanol **S28** were also converted into the corresponding *O*-containing derivatives employing halogen-bonded iridium complex **C9** as catalyst (from 26% to 49% of calculated yield,

Scheme 5.12). In contrast, the substrates (2-ethynylphenyl)methanol **S29** and 2,2-diphenylpent-4-yn-1-ol **S30** were not cyclized with our synthetic methodology.

Mechanistic investigations

We also performed research activities aiming at gaining mechanistic insights into the hydroalkoxylation reactions catalyzed by **C9**.

An initial interaction between the substrate and the iridium(I)-based catalyst is required for the reaction to take place. In order to generate an empty vacancy available for the coordination of the substrate, one CO ligand has to dissociate (Scheme 5.13).

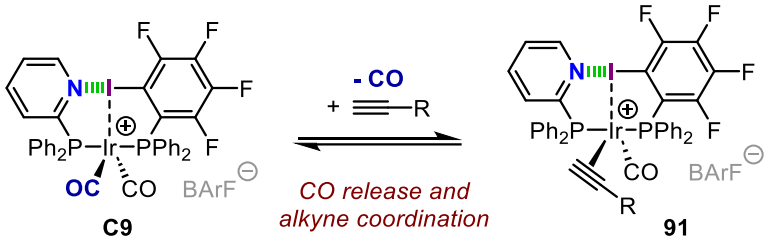

Scheme 5.13. CO release and substrate coordination step.

In order to demonstrate the influence of CO in the ability of the substrate to coordinate or dissociate to the iridium center, the hydroalkoxylation reaction was performed under CO atmosphere by using a CO balloon (Scheme 5.14).

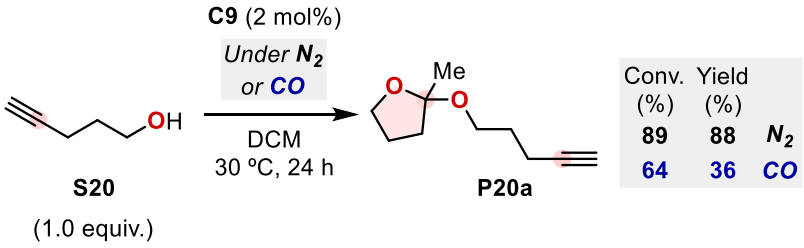

Scheme 5.14. Hydroalkoxylation of **S20** under N_2 and CO atmosphere.

Product **P20a** was obtained in lower yields when the reaction was performed under CO atmosphere than under standard conditions (36% yield under CO compared to 88% yield under N_2 atmosphere, Scheme 5.14). These results point to an important influence of the CO ligand on the catalytic reaction.

Moreover, we further studied the reaction in the presence or absence of CO by using NMR spectroscopy. The starting complex [Ir(CO)$_2$(κ^3*I,P,P*-**L1·L2**)]BArF **C9** was detected in the reaction mixture by $^{31}P\{^1H\}$ and ^1H NMR analysis after 24 hours when the reaction was carried out under CO atmosphere, whereas it was not detected after 12 hours when the reaction was carried out under nitrogen (see Figure 5.6). This observation indicates a less effective coordination of substrate **S20** to the iridium center due to the CO saturation. $^{31}P\{^1H\}$ and ^1H NMR analysis of the reaction mixture (both under N_2 or CO atmosphere) showed the formation of a new phosphane-iridium complex (*i.e.,* signals marked in green, Figure 5.6).

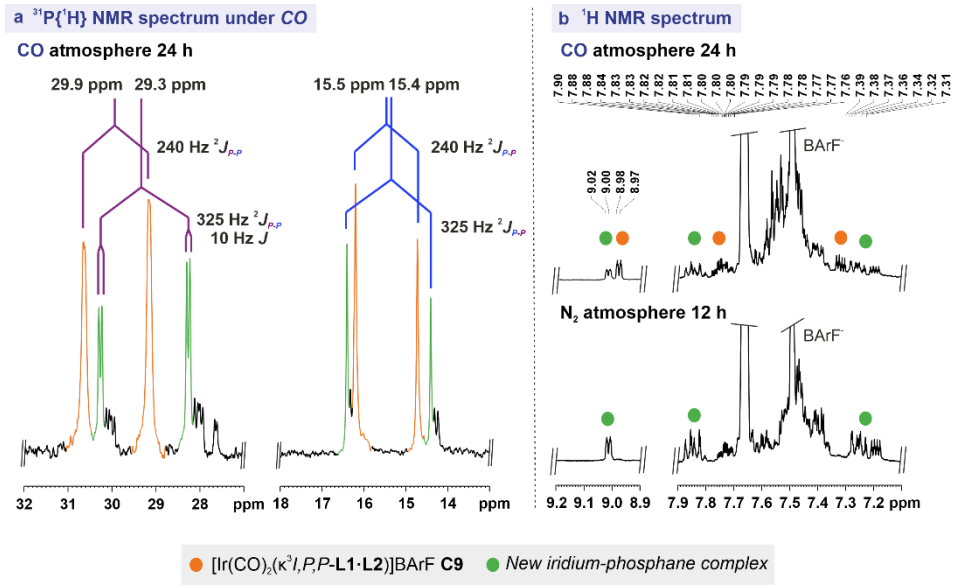

Figure 5.6. (a) $^{31}P\{^1H\}$ NMR under CO after 24 h; (b) ^1H NMR under CO after 24 h and under N_2 after 12 hours.

According to literature precedents,[208g] two mechanistic scenarios can be proposed for hydroalkoxylation reactions of alkynyl-based compounds catalyzed by iridium(I) catalysts. These mechanistic scenarios are related to the activation mode of the alkynyl alcohol: (*i*) the metal center activates the –OH group leading to the formation of intermediate **92** (Scheme 5.15Scheme 5.15. Mechanistic scenarios for the iridium-mediated intramolecular hydroalkoxylation.); and (*ii*) the alkyne moiety coordinates to the metal center with the resulting complex evolving to the final cyclic structures. In this case, after the electrophilic activation of the terminal alkyne (*i.e.*, π-coordination of the alkyne), an iridium vinylidene complex **94** could be formed.[216] However, the formation of the six-membered metal-vinylidene intermediate was excluded since the corresponding cyclization products were not detected (Scheme 5.15).[216]

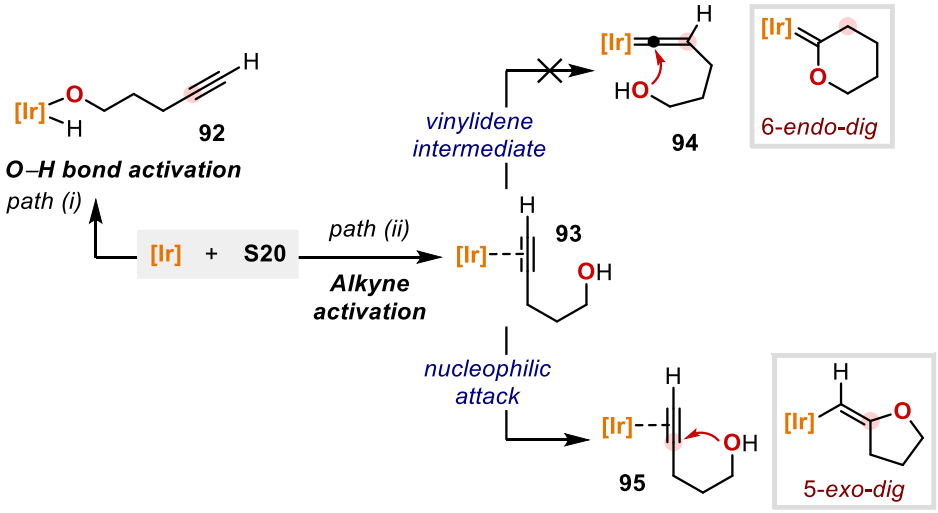

Scheme 5.15. Mechanistic scenarios for the iridium-mediated intramolecular hydroalkoxylation.

On the contrary, *exo*-cyclization products constituted the main products obtained when using our iridium-based complex **C9**. Consequently, the

[216] (a) Trost, B. M.; McClory, A. *Chem. – Asian J.* **2008**, *3*, 164-194; (b) Roh, S. W.; Choi, K.; Lee, C. *Chem. Rev.* **2019**, *119*, 4293-4356.

metal activation of the alkyne followed by *O*-nucleophilic attack constitutes a plausible reaction pathway.

With the aim of elucidating the first steps of our iridium(I)-catalyzed hydroalkoxylation reactions (*i.e.*, whether O-H bond activation or C≡C coordination followed by *O*-nucleophilic attack was taking place), mechanistic experiments based on spectroscopic analysis were carried out. Our model substrate **S20** and pent-1-yne **96** (analogous carbon framework but lacking the –OH group) were separately allowed to react in a stoichiometric way with the catalyst [Ir(CO)$_2$(κ^3*I,P,P*-**L1·L2**)]BArF **C9** at room temperature. The resulting reaction mixtures were analyzed by NMR.

In the case of alkynyl alcohol substrate **S20**, ^{31}P{^{1}H} and ^{1}H NMR[217] experiments revealed the formation of a new organometallic iridium complex after one hour of reaction (green signals, Figure 5.7a). Interestingly, a signal in the ^{1}H NMR spectrum was detected at –13.60 ppm (Figure 5.7a). This signal correlates with a hydrido ligand directly bonded to the iridium metal center. The existence of this Ir–H bond pointed at first sight to the activation of the –OH group of the alkynyl alcohol **S20**.

An identical stoichiometric experiment was performed with pent-1-yne **96**, which did not contain an –OH group. Surprisingly, NMR spectroscopic data showed the formation of a very similar iridium-phosphane complex when using pent-1-yne **96** as substrate. Almost identical chemical shifts of the pyridine moiety were found in ^{1}H NMR (multiplets ranging from 7.20 to 9.10 ppm) as well as the presence of a hydride signal at –13.61 ppm (Figure 5.7b).

[217] Unfortunately, relevant carbon atoms belonging to **S20** and **96** could not be analyzed *via* ^{13}C{^{1}H} NMR since the signals of *sp*-carbons coupled to several NMR active nuclei (^{31}P and ^{19}F) had very low intensity in the ^{13}C{^{1}H} NMR spectrum.

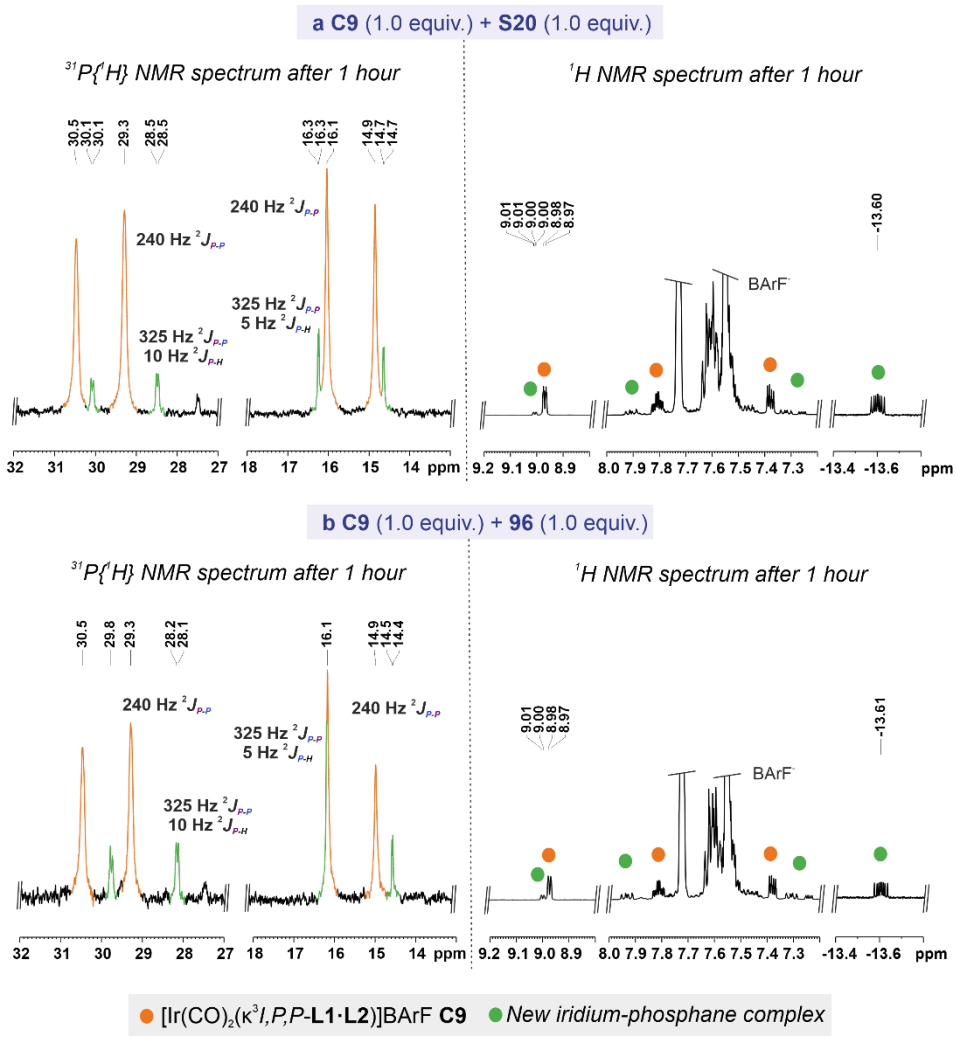

Figure 5.7. (a) $^{31}P\{^{1}H\}$ and ^{1}H NMR spectra obtained after mixing complex **C9** (1.0 equiv.) and substrate **S20** (1.0 equiv.) for 1 h; (b) $^{31}P\{^{1}H\}$ and ^{1}H NMR spectra obtained after mixing complex **C9** (1.0 equiv.) and substrate **96** (1.0 equiv.) for 1 h.

The similarities of the NMR spectral data for iridium complexes derived from **S20** and **96** suggested the formation of iridium-based intermediates with similar electronic nature and structure. Thus, we hypothesized that the above-mentioned iridium species might potentially come from the C–H activation of the alkyne moiety, therefore excluding the -OH activation as the first step of the reaction pathway, forming a plausible structure, which was closely related to those shown in Scheme 5.16. It is

interesting to note that, to the best of our knowledge, this mechanistic possibility has not been described and considered in the literature up to now.

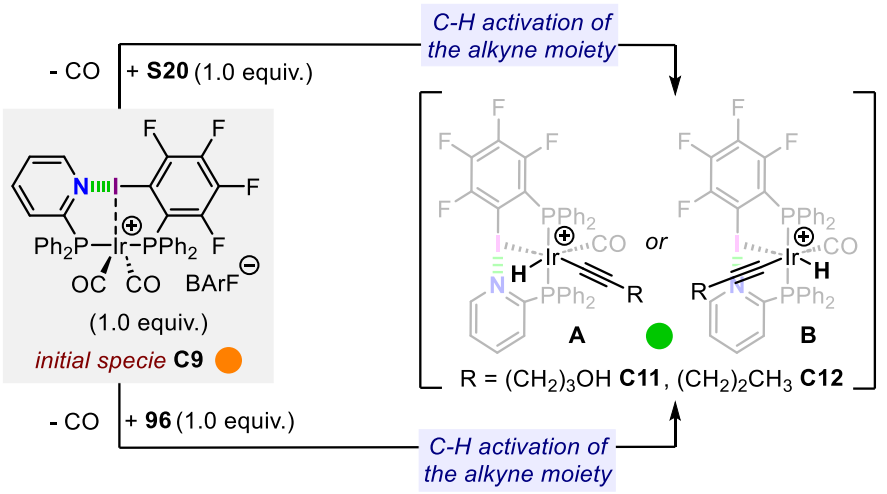

Scheme 5.16. Stoichiometric experiments by using the selected model substrate **S20** and pent-1-yne **96**.

Relevant spectroscopic data extracted from stoichiometric NMR experiments are summarized in Table 5.6. Regarding the proposed structure of intermediates **C11** and **C12**, the signals observed at upfield ^{1}H NMR regions pointed to the formation of monohydride iridium(III) intermediates after the C–H activation step (Scheme 5.16). Moreover, considering the chemical shift found for these hydride ligands (–13.60 ppm for **S20** and –13.61 ppm for **96,** Table 5.6), we hypothesized that these hydrido ligands are bonded in a *trans*-position to the CO or iodo groups in structures **A** and **B**, respectively.[218]

Both inequivalent phosphorus atoms in complex **C11** and **C12** were observed as doublets of doublets. The larger phosphorus-phosphorus coupling constant ($^{2}J_{P\text{-}P}$ = 325 Hz for both substrates, **S20** and **96**, Table

[218] For some examples of characteristic ^{1}H NMR shifts of hydrides in penta- and hexacoordinated iridium complexes, see: Werner, H.; Höhn, A.; Dziallas, M. *Angew. Chem. Int. Ed. Eng.* **1986**, *25*, 1090-1092.

5.6) is attributed to a *trans*-coordination fashion between both complementary ligands **L1** and **L2** as expected for our halogen bond-assembled iridium complexes.

Table 5.6. Relevant ^{1}H, $^{31}P\{^{1}H\}$ $^{19}F\{^{1}H\}$ NMR spectral data of complex **C9** and intermediates **C11** and **C12**.

		^{1}H NMR		$^{31}P\{^{1}H\}$ NMR		$^{19}F\{^{1}H\}$ NMR
		Chemical shift, δ (ppm)				
		o-H pyridine **L1**	Hydride signal	δ (ppm)	^{2}J (Hz)	δ (ppm)
L1		8.68	-	−0.9	-	-
C9	**L1**	8.97	-	15.4	(*P-P*) 240	−110.4 −114.4 −142.6 −147.2
	L2			29.9	(*P-P*) 240	
C11	**L1**	9.00	−13.60	15.2	(*P-P*) 325 (P-H) 5	−112.7 −114.6 −142.3 −147.2
	L2			29.0	(*P-P*) 325 (*P-H*) 10	
C12	**L1**	9.01	−13.61	15.5	(*P-P*) 325 (*P-H*) 5	−112.5 −114.5 −142.1 −147.0
	L2			29.3	(*P-P*) 325 (*P-H*) 10	

Additionally, the considerable change in the magnitude of the observed phosphorus-phosphorus coupling constant compared to the one measured for the initial [Ir(CO)$_2$(κ^3*I,P,P*-**L1**·**L2**)]BArF **C9** complex might come from the important variation in the geometry of the organometallic iridium complex. This observation is in agreement with the geometrical

modification of the iridium intermediate after the C–H activation process of the corresponding substrate (**S20** or **96,** Scheme 5.16), which becomes a six-coordinated octahedral complex.

Furthermore, it was observed in **C11** and **C12** that both phosphino groups belonging to **L1** and **L2** were further split due to its coupling with the hydrido ligand placed two bonds away and the fluor atom placed three bonds away in the case of **L2**. Small phosphorus-hydride coupling constants were found ($^2J_{P\text{-}H}$ = 10 Hz for **L2** and $^2J_{P\text{-}H}$ = 5 Hz for **L1**, Table 5.6), pointing to a *cis*-coordination mode of both phosphane ligands to the hydrido ligand (structures **C11** and **C12** in Scheme 5.16).

Regarding the existence of the non-covalent interaction and the bidentate coordination mode of our halogen bond-assembled ligands during the course of the catalytic reaction, all the spectroscopic data obtained point to the existence of the halogen bonding interaction between **L1** and **L2**. Chemical shifts corresponding to the proton placed in *ortho*-position to the nitrogen atom of the pyridine moiety were consistent with those observed for the initial halogen bond-assembled [Ir(CO)$_2$(κ^3*I,P,P*-**L1·L2**)]BArF **C9** complex (8.97 ppm for **C9** compared to 9.00 and 9.01 ppm for intermediates **C11** and **C12**, respectively, Table 5.6). These ^{1}H NMR chemical shifts (compared to the one observed for the free ligand **L1**: 8.68 ppm, Table 5.6) were found to be characteristic of the linear N···I halogen-bonded structure, contrary to those signals found when the nitrogen atom of the pyridine moiety is not involved in the formation of the halogen bond.

Additionally, chemical shifts observed in the ^{19}F{^{1}H} NMR spectra, were in agreement with those observed for the halogen-bonded structure present in the complex [Ir(CO)$_2$(κ^3*I,P,P*-**L1·L2**)]BArF **C9**. Therefore, all these spectroscopic evidence point to the existence of the N···I halogen bonding interaction and confirms the structure of the proposed intermediates **C11** and **C12** (Scheme 5.16).

Hence, a proposed mechanism based on the previously mentioned spectroscopic investigations for the consecutive double intra- and intermolecular hydroalkoxylation of alkynyl alcohols catalyzed by our complex [Ir(CO)$_2$(κ^3*I,P,P*-**L1**·**L2**)]BArF **C9** is shown in Figure 5.8. As demonstrated before, the reaction starts with a C–H activation process, leading to the formation of two iridium(III) intermediates depending on the relative position of the hydrido and alkynyl ligands (Scheme 5.16). In the discussion that follows, the catalytic cycle involving intermediate **C11A** (*i.e.*, hydride ligand located in a *trans*-position to the CO ligand) is the only one depicted in Figure 5.8. An analogous reaction manifold involving complex **C11B** should also be kept in mind.

Assuming that the hydrido-iridium intermediate **C11A** detected in NMR constitutes an active on-cycle intermediate, we propose that after CO release and subsequent alkyne coordination, the complex **IV** is formed. C–H activation of the terminal alkyne moiety takes then place leading to complex **C11A**. After the intramolecular nucleophilic attack of the *O*-nucleophile to the C≡C bond and subsequent rearrangement, the formation of vinyl iridium(III) intermediate **VA** takes place. It has been proposed in the literature that an isomerization process occurs and leads to the formation of the intermediate **VA'**. According to literature precedents for analogous chemistry,[208g] both complexes **VA** and **VA'** may undergo an intermolecular addition of a hydroxy-containing molecule (*e.g.*, substrate **S20** or MeOH). Finally, the desired *O,O*-ketal product **P20** is formed from both intermediates **VIA** or **VIA'** after a reductive elimination process. The iridium(I) complex **IV** is regenerated after coordination of a new **S20** molecule. An analogous catalytic cycle can be postulated with the hydrido-iridium intermediate **C11B** constituting an alternative on-cycle intermediate. We do not have at present any evidence of which reaction manifold is the preferred one, *i.e.* that involving **C11A** or **C11B**.

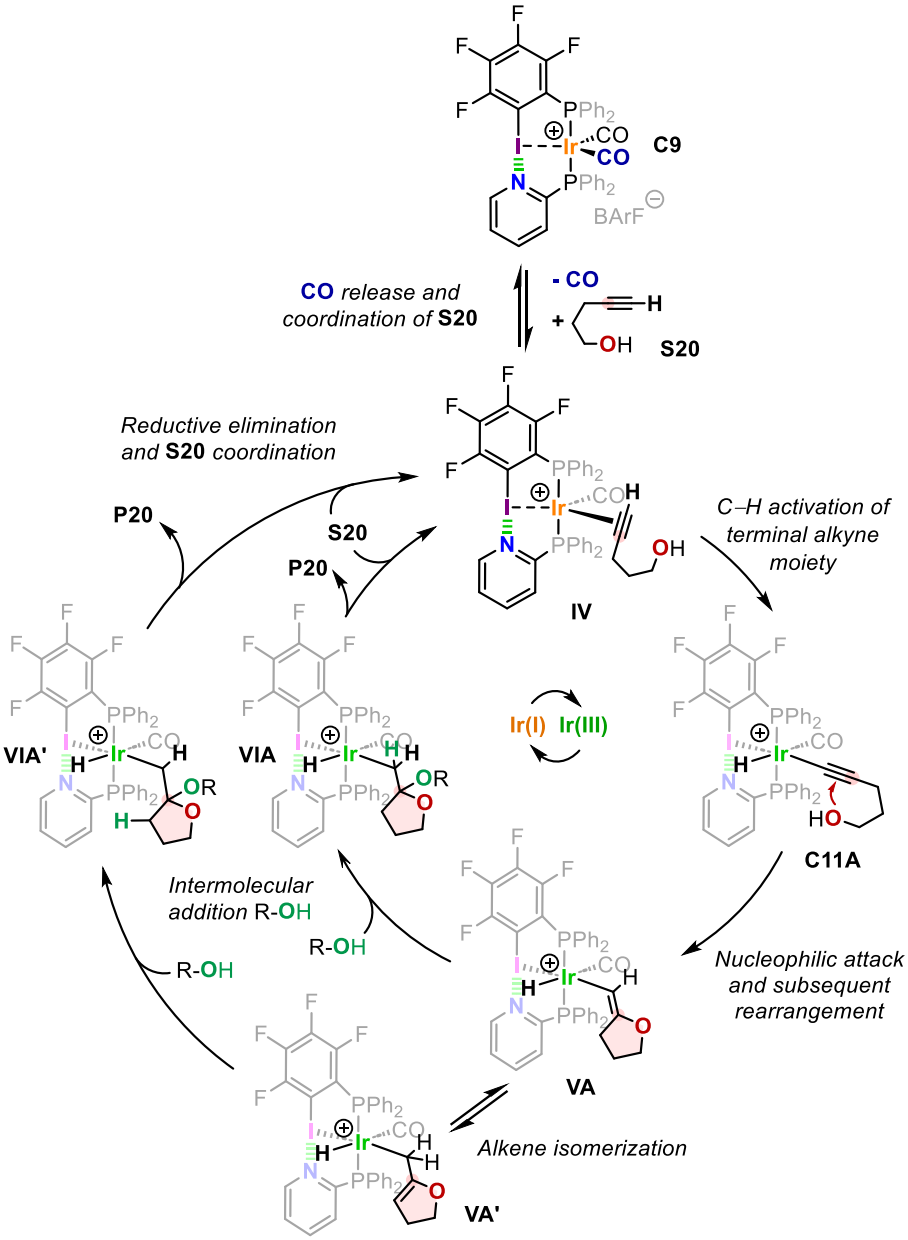

Figure 5.8. Proposed mechanism for consecutive double intra- and intermolecular hydroalkoxylation reaction of **S20** catalyzed by our Ir(I) complex **C9**. BArF counterion was removed for the sake of clarity.

5.3 CONCLUSIONS

In summary, two closely related halogen-bonded iridium complexes [Ir(CO)$_2$(κ^3*I,P,P*-**L1·L2**)]BArF **C9** and [Ir(CO)(κ^3*I,P,P*-**L1·L2**)]BArF **C10** have been successfully prepared and fully characterized in solution and in the solid state. NMR spectroscopic analysis revealed an equilibrium between **C9** and **C10**, involving exchange of one CO molecule taking place in solution. Crystals suitable for X-Ray analysis allowed for the unequivocal elucidation of the structure of both iridium(I) complexes: a trigonal bipyramidal complex in case of **C9** and a square planar complex in the monocarbonyl derivative **C10**.

Our halogen bond-assembled complex [Ir(CO)$_2$(κ^3*I,P,P*-**L1·L2**)]BArF **C9** has been efficiently applied in consecutive double intra- and intermolecular hydroalkoxylation of alkynyl alcohols for the synthesis of *O,O*-ketal products. An array of structural diverse alkynol substrates have been tested under our optimized conditions by using **C9** as catalyst. Best results in terms of conversion and reaction yield have been achieved when using linear alkynyl alcohol **S20** and cyclic substrate **S26**, which led to the formation of *O*-containing spirocyclic compounds.

Additionally, mechanistic experiments have been carried out with the aim of clarifying the hydroalkoxylation reaction pathway with complex [Ir(CO)$_2$(κ^3*I,P,P*-**L1·L2**)]BArF **C9** as catalyst. A C–H activation of the terminal triple bond has been proposed as the first step of the catalytic cycle according to the observed spectroscopic evidence. These also strongly supported the existence of the halogen bonding interaction during the course of the catalytic cycle, pointing to a bidentate nature of our halogen bond-assembled ligand after the C–H activation of alkynyl alcohol substrates.

5.4 EXPERIMENTAL SECTION

5.4.1 General considerations

All syntheses were carried out using chemicals as purchased from commercial sources unless otherwise stated. Air- and moisture-sensitive manipulations or reactions were performed under inert atmosphere, either in a glove box or with standard Schlenk techniques. Glassware was dried *in vacuo* before use with a hot air gun. All solvents were dried by using a solvent purification system (SPS). Silica gel 60 (230–400 mesh) was used for column chromatography. NMR spectra were recorded in 400 MHz or 500 MHz spectrometers in $CDCl_3$ or CD_2Cl_2 unless otherwise cited. ^{1}H and $^{13}C\{^{1}H\}$ NMR chemical shifts are quoted in ppm relative to residual solvent peaks. $^{19}F\{^{1}H\}$ NMR chemical shifts are quoted in ppm relative to $CFCl_3$ in $CDCl_3$. $^{31}P\{^{1}H\}$ NMR chemical shifts are quoted in ppm relative to 85% phosphoric acid in water. HRMS spectra were recorded using ESI ionization method in positive mode. IR spectra were recorded using Attenuated Total Reflection (ATR) technique unless otherwise cited. Ligand **L1** is commercially available and was used as received. (2-iodo-3,4,5,6-tetrafluorobenzene)diphenylphosphine ligand **L2** was prepared according to previous literature reports.[70]

5.4.2 General structural comments on X-Ray crystals

Crystals suitable for X-Ray analysis of complexes **C9** and **C10** were obtained by slow diffusion of *n*-pentane into concentrated solutions of dichloromethane at −25 ºC under inert atmosphere. The measured crystals were prepared under inert conditions immersed in perfluoropolyether as protecting oil for manipulation.

Crystal structure determination of **C9** and **C10** was carried out using an Appex DUO Kappa 4-axis goniometer equipped with an Appex 2 4K CCD area detector, a Microfocus Source E025 IuS using MoK_α radiation (0.71073 Å), Quazar MX multilayer Optics as monochromator and an Oxford Cryosystems low temperature device Cryostream 700 plus (T-= -173 ˚C). Full-sphere data collection was used with ω and φ scans. *Programs used:* Data collection APPEX-2,[100] data reduction Bruker Saint[101] V/60A and absorption correction SADABS.[102]

Structure solution and refinement: Crystal structure solution was achieved using the computer program SHELXT.[103] Visualization was performed with the program SHELXle.[104] Missing atoms were subsequently located from difference Fourier synthesis and added to the atom list. Least-squares refinement on F^2 using all measured intensities was carried out using the program SHELXL 2015.[105] All non-hydrogen atoms were refined including anisotropic displacement parameters.

Comments to the structure **C9**: The asymmetric unit contains one molecule of the metal complex, one BArF anion and a dichloromethane molecule. In the coordination complex, the aromatic ring with the iodine atom is disordered in two orientations with an approximate ratio of 60:40. In the BArF anion some of the CF_3-groups are disordered in two orientations. The structure contains heavy iridium atoms which typically show residual electron densities in its surroundings. Only an empirical absorption correction was possible for this dataset. No significant

improvement could be observed by using spherical harmonics for strong absorbers. The structure was also checked for possible missing disorder or solvents and no errors could be detected. It was considered that the appearing residual densities are not affecting significantly the quality of the structure thus it is publishable.

Comments to **C10**: The asymmetric unit contains one molecule of the metal complex, one BArF anion and a half dichloromethane molecule. In the metal complex, the iodine atom, the fluorinated aromatic ring and the nitrogen atom of the pyridine ring are disordered in two orientations with a ratio of 86:14. In the BArF anion some of the CF_3 groups are disordered in two orientations. The 0.5 dichloromethane molecules are disordered in two locations with a ratio of 0.25:25. The high electron densities are most probably due to the presence of the heavy atoms: iridium and iodine, and the observed disorder related to the iodine atom. The iodine atom and part of the main molecule are disordered in a minimum of two orientations with a ratio 86:14.

Table 5.7. Crystal data and structural parameters for complex **C9.**

Compound	**C9**
Formula	$C_{70}H_{38}BCl_2F_{28}IIrNO_2P_2$
Formula weight (total)	1915.78
Crystal size (mm^3)	0.20 x 0.20 x 0.04
Temp (K)	100(2)
Crystal system	triclinic
Space group	P_{-1}
A (Å)	13.2538(8)
B (Å)	16.1267(10)
C (Å)	18.2722(11)
α (deg)	69.4999(16)
β (deg)	75.3530(18)
γ (deg)	89.7419(17)
V ($Å^3$)	3524.0(4)
Z	2
ρ (Mg/m^3)	1.805
μ (mm^{-1})	2.573
θ range (°)	31.649
Reflec. collected	66930
Independent reflections	23299[R(int) = 0.0387]
Absorpt. correct.	Multi-scan
Trans. min/max	0.545/0.904
Parameters	1130
R1/wR2 [I>2σ(I)]	0.0479/0.1158
R1/wR2 [all data]	0.0646/0.1257
Goodness-of-fit (F^2)	1.026
Peak/hole ($e/Å^3$)	4.021/–2.379

Table 5.8. Crystal data and structural parameters for complex **C10.**

Compound	**C10**
Formula	$C_{68.50}H_{37}BClF_{28}IIrNOP_2$
Formula weight (total)	1849.29
Crystal size (mm^3)	0.30 x 0.25 x 0.10
Temp (K)	100(2)
Crystal system	triclinic
Space group	P_{-1}
A (Å)	13.0171(11)
B (Å)	15.9408(14)
C (Å)	18.3558(16)
α (deg)	77.654(2)
β (deg)	73.813(2)
γ (deg)	88.4128(19)
V ($Å^3$)	3571.2(5)
Z	2
ρ (Mg/m^3)	1.720
μ (mm^{-1})	2.500
θ range (°)	33.783
Reflec. collected	52907
Independent reflections	26880[R(int) = 0.0456]
Absorpt. correct.	Multi-scan
Trans. min/max	0.579/0.788
Parameters	1212
R1/wR2 [I>2σ(I)]	0.0529/0.1466
R1/wR2 [all data]	0.0618/0.1539
Goodness-of-fit (F^2)	1.029
Peak/hole ($e/Å^3$)	4.475/–3.490

5.4.3 Synthesis of iridium(I) complexes C9 and C10

Initial synthesis of C9 *and* C10

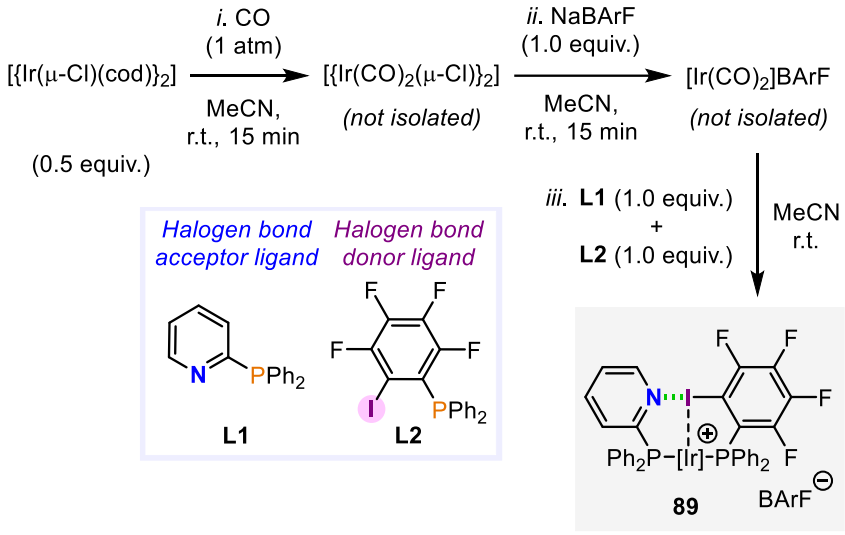

General procedure for **C9** and **C10**: [{Ir(μ-Cl)(cod)}$_2$] (30.2 mg, 0.05 mmol, 0.5 equiv.) was introduced into a flame-dried Schlenk flask and 6.0 mL (0.01 M) of dried and deoxygenated acetonitrile were added. Then, CO was bubbled into this solution at atmospheric pressure (balloon) and at room temperature for 15 minutes. A change in the color from bright yellow to off-yellow was observed. After 15 minutes under CO atmosphere, a solution of NaBArF (82.6 mg, 0.1 mmol, 1.0 equiv.) in 1.0 mL of acetonitrile was added to the previous solution. The resulting mixture was stirred for 15 minutes. Then, a solution of 2-pyridyldiphenylphosphine **L1** (24.6 mg, 0.1 mmol, 1.0 equiv.) and 2-iodo-3,4,5,6-tetrafluorobenzene diphenylphosphane **L2** (42.3 mg, 0.1 mmol, 1.0 equiv.) in 1.0 mL of acetonitrile was added dropwise to the previous mixture. A change in color from off-yellow to dark green and finally to bright yellow was observed, in addition to the formation of a fine precipitate (presumably sodium chloride) in the reaction mixture. The resulting suspension was filtered by using a nylon filter. The filtrate was concentrated *in vacuo*, and the resulting orange oil was treated with cold *n*-pentane (2.0 mL) obtaining an

orange solid. Solvents were removed and the resulting material was purified by recrystallization: slow diffusion of *n*-pentane (five-fold excess, 0.5 mL) into a concentrated solution of the orange solid in DCM (0.1 mL). The solution was allowed to stand at room temperature overnight, and the resulting crystals were filtered and washed with cold *n*-pentane (4 x 3.0 mL). Finally, these crystals were dried under vacuum to afford [Ir(CO)$_2$(κ^3*I,P,P*-**L1·L2**)]BArF **C9** (127 mg, 78% purity, 0.19 mmol, 26% yield). The resulting crystalline mixture was washed with cold toluene (4 x 2.0 mL) and dried *in vacuo*. Subsequently, complex [Ir(CO)(κ^3*I,P,P*-**L1·L2**)]BArF **C10** (5.42 mg, 83% purity, 3·10^{-3} mmol, 6% yield) was isolated as a bright yellow solid.

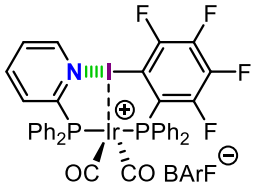

C9

^{1}H NMR (500 MHz, CD_2Cl_2) δ: 8.96 (s, 1 H), 7.93 – 7.33 (m, 35 H). **^{13}C{^{1}H} NMR** (126 MHz, CD_2Cl_2) δ:[219] 175.5 (C_{CO}), 161.7 (q, *J* = 49.7 Hz, C_{BArF}), 150.1 (d, *J* = 18.4 Hz), 138.2 (C_{Py}), 134.8 (C_{BArF}), 133.6 (d, *J* = 11.3 Hz, C_{Ph}), 133.0 (C_{Ph}), 132.7 (C_{Ph}), 129.7 – 129.3 (m), 128.8 (qm, *J* = 31.6 Hz, C_{BArF}), 124.5 (q, *J* = 271.9 Hz, C_{BArF}), 117.4 (m, C_{BArF}) ppm. **^{19}F{^{1}H} NMR** (471 MHz, CD_2Cl_2) δ: –62.9 (s, 24 F), –110.4 (br s, 1 F), –114.4 (s, 1 F), –142.6 (s, 1 F), –147.2 (t, *J* = 19.7 Hz, 1 F) ppm. **^{31}P{^{1}H} IGD NMR** (202 MHz, CD_2Cl_2) δ: 29.9 (d $^2J_{P-P}$ = 240 Hz), 15.4 (d, $^2J_{P-P}$ = 240 Hz) ppm. **IR** (neat): 2028, 1991, 1501, 1439, 1353, 1274, 1120, 1030, 886, 681, 510 cm^{-1}. **HRMS** (ESI$^+$): *m/z* calcd. for $C_{36}H_{24}F_4INOP_2Ir^+$ [M–CO–BArF]$^+$ 941.9914, found: 941.9881.

[219] A heavily overlapped $^{13}C\{^1H\}$ NMR spectrum was observed due to multiple couplings of the carbons with other NMR active heteronuclei present in the molecule. Carbons were assigned as it follows: C_{CO} (carbonyl carbon), C_{BArF} (BArF anion carbons), C_{Ph} (phenyl ring carbons) and C_{Py} (pyridyl ring carbons).

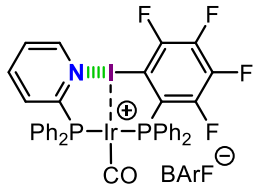

C10

^{1}H NMR (500 MHz, CD_2Cl_2) δ: 8.89 (s, 1 H), 7.90 – 7.38 (m, 35 H). **^{13}C{^{1}H} NMR** (126 MHz, CD_2Cl_2) δ:[219] 170.9 (C_{CO}), 161.8 (q, J = 49.7 Hz, C_{BArF}), 148.8 (d, J = 17.7 Hz), 138.7 (C_{Py}), 134.8 (C_{BArF}), 133.7 (d, J = 12.1 Hz, C_{Ph}), 133.1 – 132.5 (m, C_{Ph}), 131.0 (d, J = 11.7 Hz, C_{Ph}), 129.6 (d, J = 11.5 Hz), 128.8 (qm, J = 31.3 Hz, C_{BArF}), 127.3, 124.5 (q, J = 271.6 Hz, C_{BArF}), 117.4 (m, C_{BArF}) ppm. **^{19}F{^{1}H} NMR** (363 MHz, CD_2Cl_2) δ: –62.9 (s, 24 F), –117.2 (m, 1 F), –117.8 (m, 1 F), –142.3 (m, 1 F), –147.1 (m, 1 F) ppm. **^{31}P{^{1}H} IGD NMR** (202 MHz, CD_2Cl_2) δ: 69.9 (dd, $^{2}J_{P-P}$ = 265, Hz, $^{3}J_{P-F}$ = 14 Hz), 41.6 (d, $^{2}J_{P-P}$ = 265 Hz) ppm. **IR** (neat): 2026, 1501, 1440, 1353, 1274, 1155, 1121,681, 509 cm^{-1}. **HRMS** (ESI^{+}): m/z calcd. for $C_{36}H_{24}F_4INOP_2Ir^{+}$ [M–BArF]$^{+}$ 941.9914, found: 941.9896.

Selective synthesis of complex C9

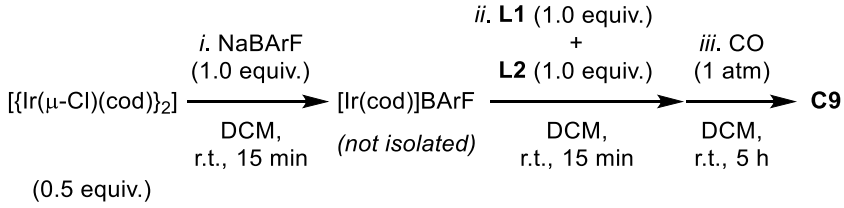

General procedure for **C9**: Under N_2 atmosphere to a flame-dried Schlenk flask were added 36.8 mg of [{Ir(μ-Cl)(cod)}$_2$] (0.06 mmol, 0.5 equiv.) along with 5.0 mL of dry DCM. A solution of NaBArF (102.0 mg, 0.1 mmol, 1.0 equiv.) in 2.5 mL of DCM was added to the complex solution, observing a change from an initial orange to a dark red color followed by the formation of a precipitate (supposedly NaCl). After 15 minutes, a solution of 2-pyridyldiphenylphosphine **L1** (28.8 mg, 0.1 mmol, 1.0 equiv.) and 2-iodo-3,4,5,6-tetrafluorobenzene diphenylphosphane **L2** (53.1 mg, 0.1 mmol, 1.0 equiv.) in 2.5 mL of DCM was dropwise added to the mixture. Then, the N_2 atmosphere was exchanged to a CO atmosphere (1 atm., by using a balloon). Stirring was continued for 5 h under CO

atmosphere, and after this time a bright yellow solution was finally observed. The resulting mixture was filtered by using a nylon filter, and the yellow mixture was directly allowed to crystallize by using a DCM/*n*-pentane (1:3) mixture at –20 ºC overnight. Finally, the liquid phase was removed, and the bright yellow crystalline solid was washed with *n*-pentane (3 x 2.0 mL) yielding a fine yellow solid (92% yield).

5.4.4 General procedure for the Ir(I)-catalyzed hydroalkoxylation

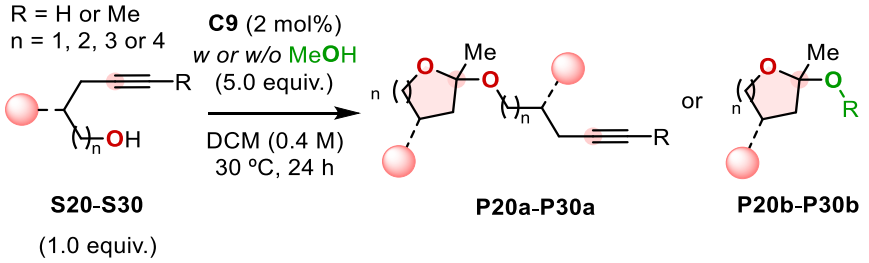

General procedure for iridium-catalyzed hydroalkoxylation reaction: Under N_2 atmosphere, alkynyl alcohol substrate (0.3 mmol, 1.0 equiv.) and dry methanol (5.0 equiv.) were added to a solution of [Ir(CO)$_2$(κ^3*I,P,P*-**L1**·**L2**)]BArF **C9** (2 mol%) in dry DCM (0.4 M). The reaction mixture was stirred for 24 h at 30 ºC. Afterwards, a known amount of 1,2,4,5-tetramethyl-benzene (Sigma-Aldrich TraceCERT®) (0.05 equiv.) was added as internal standard, and the reaction mixture was analyzed *via* ^{1}H NMR. The most relevant products were isolated *via* standard column chromatographic method by using *n*-pentane:Et$_2$O mixtures (100:0→95:5) as eluent.[220]

[220] Isolation of compounds which were obtained in low yields was not possible. Besides, acyclic *O,O*-ketals presented an inherent instability under acidic conditions. They are also non-stable in the presence of water. For more information, see: (a) Matsutani, H.; Ichikawa, S.; Yaruva, J.; Kusumoto, T.; Hiyama, T. *J. Am. Chem. Soc.* **1997**, *119*, 4541-4542; (b) von Angerer, S.; Warriner, S. L. Product Class 6: Acyclic and Semicyclic *O/O* Acetals. In *Category 4, Compounds with Two Carbon Heteroatom Bonds*, Vol. 29; 2007; (c) Williams, D. B. G.; Cullen, A.; Fourie, A.; Henning, H.; Lawton, M.; Mommsen, W.; Nangu, P.; Parker, J.; Renison, A. *Green Chem.* **2010**, *12*, 1919-1921.

5.4.5 Synthesis of alkynyl alcohol starting materials

Linear alkynyl alcohols pent-4-yn-1-ol **S20**, pent-3-yn-1-ol **S21**, but-3-yn-1-ol **S22**, hex-5-yn-1-ol **S23** and hept-6-yn-1-ol **S24** were all commercially available compounds and they were used as received.

Synthesis of 2-(prop-2-ynyl)cyclohexan-1-ol substrates S25

Racemic mixtures of both diastereomeric 2-(prop-2-ynyl)cyclohexanol products *rac-cis*-**S25** and *rac-trans*-**S25** are well known in literature. Both compounds have been prepared following reported methodologies.[221]

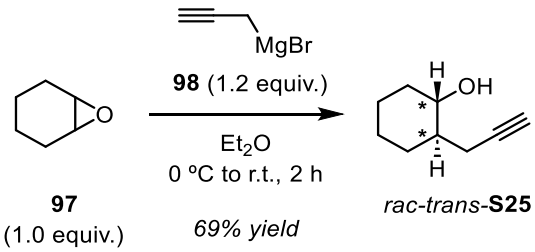

Under nitrogen atmosphere, a solution of freshly prepared propargylmagnesium bromide **98** (13.0 mmol, 1.2 equiv.) in dry Et_2O (10.0 mL) was added dropwise *via* cannula to a dry Et_2O solution (10 mL) of **97** (10.8 mmol, 1.0 equiv.) over 30 min at 0 °C. After the propargyl magnesium bromide addition was complete, the mixture was allowed to stir for 1 hour at room temperature, until TLC analysis showed that the starting material was completely consumed. The reaction mixture was diluted with saturated aqueous NH_4Cl and extracted by EtOAc (2 x 20.0 mL). The combined organic phases were washed with water, brine and dried by using Na_2SO_4. The eluent was concentrated *in vacuo* to give the crude product, which was purified by standard column chromatography using CyHex:EtOAc 90:10 mixture as eluent. *rac-trans*-**S25** was obtained

[221] For the synthesis of (*1R,2S*) 2-(prop-2-ynyl)cyclohexan-1-ol, **S26**, see: Man, Z.; Dai, H.; Shi, Y.; Yang, D.; Li, C.-Y. *Org. Lett.* **2016**, *18*, 4962-4965. For the Mitsunobu reaction, see: Fu, J.; Shang, H.; Wang, Z.; Chang, L.; Shao, W.; Yang, Z.; Tang, Y. *Angew. Chem.* **2013**, *125*, 4292-4296.

as a colorless oil (1.0 g, 69% yield). Spectroscopic data were in agreement with those previously reported in literature.[222]

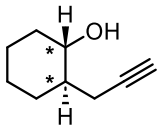

*rac-trans-**S25***

2-(Prop-2-ynyl)cyclohexan-1-ol *rac-trans-***S25**: **^{1}H NMR** (400 MHz, $CDCl_3$) δ: 3.41 – 3.35 (m, 1 H), 2.48 – 2.42 (m, 1 H), 2.35 – 2.28 (m, 1 H), 1.99 – 1.92 (m, 2 H), 1.89 – 1.82 (m, 1 H), 1.78 – 1.63 (m, 2 H), 1.49 – 1.38 (m, 1 H), 1.34 – 1.10 (m, 4 H) ppm. **^{13}C{^{1}H} NMR** (101 MHz, $CDCl_3$) δ: 83.1, 73.7, 69.8, 44.1, 35.7, 30.4, 25.5, 25.0, 21.9 ppm.

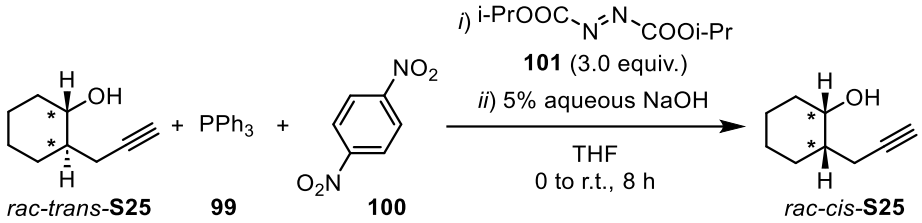

To a mixture of alkynyl alcohol *rac-trans-***S25** (350 mg, 2.5 mmol, 1.0 equiv.), triphenylphosphine **99** (2.4 g, 8.9 mmol, 3.5 equiv.) and 4-nitrobenzoic acid **100** (1.3 g, 7.6 mmol, 3.0 equiv.) in anhydrous THF (30.0 mL), diisopropylazodicarboxylate **101** (1.5 g, 7.6 mmol, 3.0 equiv.) was added dropwise at 0 °C. The reaction mixture was allowed to warm up to ambient temperature and stirred for 8 h. Afterwards, the reaction mixture was cooled to 0 °C and 1 N HCl (17.0 mL) was added. The resulting solution was extracted twice with Et_2O (3 x 20 mL), and the combined organic layers were washed with brine (30 mL), dried over Na_2SO_4 and concentrated under vacuum. The residue was purified by flash chromatography using CyHex:EtOAc (80:20) mixture as eluent, and the pure ester was used in the next step.

The previously isolated ester compound (687 mg, 2.4 mmol) was dissolved in tetrahydrofuran (30 mL) and the solution was cooled to 0 °C.

[222] a) Pale, P.; Chuche, J. *Eur. J. Org. Chem.* **2000**, *2000*, 1019-1025; b) Patil, N. T.; Kavthe, R. D.; Raut, V. S.; Reddy, V. V. N. *J. Org. Chem.* **2009**, *74*, 6315-6318.

5% aqueous NaOH (28.0 mL) was added, and the reaction mixture was stirred at ambient temperature for 12 h. The reaction mixture was extracted with Et_2O (3 x 50.0 mL). The combined organic phases were washed with water (100 mL), 1 N HCl (100 mL) and brine (100 mL), dried over Na_2SO_4 and concentrated *in vacuo*. Purification by flash column chromatography using CyHex:EtOAc mixtures (100:0→80:20) led to the isolation of *rac-cis*-**S25** as a colorless oil (66% overall yield). Spectroscopic data were in agreement with those reported in literature.[223]

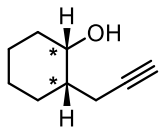

rac-cis-**S25**

2-(Prop-2-ynyl)cyclohexan-1-ol *rac-cis*-**S25: ^{1}H NMR** (400 MHz, $CDCl_3$) δ: 4.05 (br s, 1 H), 2.33 – 2.23 (m, 1 H), 2.19 – 2.13 (m, 1 H), 1.97 (t, *J* = 2.6 Hz, 1 H), 1.82 – 1.1.74 (m, 1 H), 1.60 – 1.40 (m, 5 H), 1.31 – 1.23 (m, 1 H) ppm. **^{13}C{^{1}H} NMR** (101 MHz, $CDCl_3$) δ: 83.4, 69.2, 68.4, 40.8, 33.0, 26.2, 25.0, 21.5, 20.0 ppm.

[223] Luo, F. T.; Schreuder, I.; Wang, R. T. *J. Org. Chem.* **1992**, *57*, 2213-2215.

Synthesis of (1-(prop-2-yn-1-yl)cycloalkyl)methanol substrates S26, S27 *and* S28

(1-(Prop-2-yn-1-yl)cycloalkyl)methanol substrates **S26**, **S27** and **S28** are all known compounds and were synthesized following already reported methodologies.[224] All the spectroscopic data were in agreement with the reported compounds.

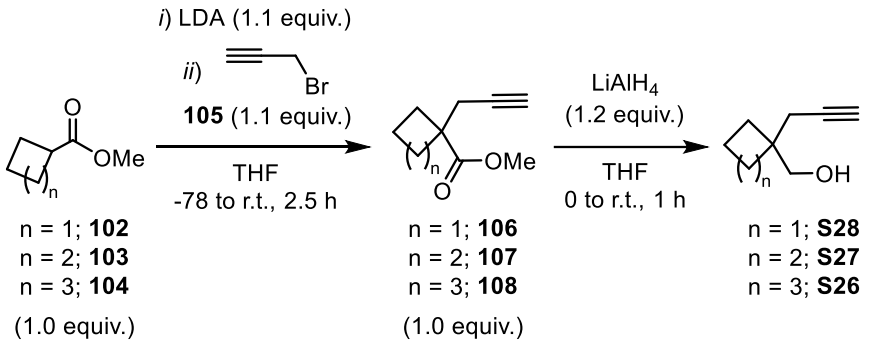

General procedure: *n*-Butyllithium (1.6 M in hexanes,1.1 equiv.) at −78 °C was added dropwise with stirring to diisopropylamine (1.1 equiv.). Then, THF (0.8 M) was added to dissolve all the solids generated. Methyl cycloalkanecarboxylate **102**, **103** or **104** (1.0 equiv.) was added to this LDA solution over 30 min. After 1 h, propargyl bromide **105** (80% in toluene, 1.1 equiv.) was added dropwise to the reaction mixture. The resulting solution was kept at −78 °C for 1 h and warmed to room temperature over 1 h. The reaction was quenched with saturated aqueous NH_4Cl and extracted three times with EtOAc. The organic phase washed with 2 M aqueous HCl, saturated aqueous $NaHCO_3$ and brine; dried over Na_2SO_4 and concentrated *in vacuo* to afford pure methyl 1-(prop-2-ynyl)cycloalkanecarboxylate **106**, **107** and **108** (quantitative yields) as orange oils, which were directly utilized in the next step. All the spectroscopic data were in agreement with the reported compounds.

[224] Chen, Y.; Lee, C. *J. Am. Chem. Soc.* **2006**, *128*, 15598-15599.

By using a spatula, $LiAlH_4$ (1.06 g, 27.8 mmol, 1.2 equiv.) was portionwise added to a solution of **106**, **107** or **108** (1.0 equiv.) in THF (0.4 M) at 0 °C. After stirring for 30 min, the reaction mixture was quenched with saturated aqueous NH_4Cl, treated with 2 M aqueous HCl to dissolve the aluminum salts, and extracted three times with EtOAc. The combined organic layers were washed with saturated aqueous $NaHCO_3$ and brine; dried over Na_2SO_4 and concentrated *in vacuo*. Products **S26**, **S27** and **S28** were obtained in a pure way as orange oils.

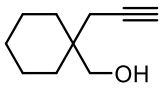

S26

(1-(prop-2-yn-1-yl)cyclohexyl)methanol, **S26**: **^{1}H NMR** (400 MHz, $CDCl_3$) δ: 3.54 (s, 2 H), 2.25 (d, *J* = 2.5 Hz, 2 H), 1.99 (t, *J* = 2.6 Hz, 1 H), 1.70 (br s, 1 H), 1.4 – 1.33 (m, 11 H) ppm. **^{13}C{^{1}H} NMR** (101 MHz, $CDCl_3$) δ: 82.0, 70.4, 68.5, 37.6, 31.8, 26.1, 25.1, 21.5 ppm. ^{1}H NMR and ^{13}C{^{1}H} NMR data were in agreement with those previously reported.[224]

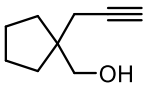

S27

(1-(prop-2-yn-1-yl)cyclopentyl)methanol, **S27**: **^{1}H NMR** (400 MHz, $CDCl_3$) δ: 3.53 (s, 2 H), 2.29 (d, *J* = 2.6 Hz, 2 H), 1.95 (t, *J* = 2.6 Hz, 1 H), 1.68 – 1.58 (m, 5 H), 1.52 – 1.49 (m, 4 H) ppm. **^{13}C{^{1}H} NMR** (101 MHz, $CDCl_3$) δ: 82.0, 68.3, 67.9, 46.2, 33.3, 25.8, 24.3 ppm. ^{1}H NMR and ^{13}C{^{1}H} NMR data were in agreement with those previously reported.[222b]

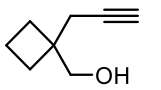

S28

(1-(prop-2-yn-1-yl)cyclobutyl)methanol, **S28**: **^{1}H NMR** (400 MHz, $CDCl_3$) δ: 3.66 (s, 2 H), 2.40 (d, *J* = 2.6 Hz, 2 H), 1.97 (t, *J* = 2.7 Hz, 1 H), 1.91 – 1.84 (m, 6 H), 1.61 (br s, 1 H) ppm. **^{13}C{^{1}H} NMR** (101 MHz, $CDCl_3$) δ: 82.2, 69.7, 68.4, 42.3, 27.7, 26.6, 15.0 ppm. ^{1}H NMR and ^{13}C{^{1}H} NMR data were in agreement with those previously reported.[225]

[225] Han, Z.-Y.; Guo, R.; Wang, P.-S.; Chen, D.-F.; Xiao, H.; Gong, L.-Z. *Tetrahedron Lett.* **2011**, *52*, 5963-5967.

Synthesis of (2-ethynylphenyl)methanol S29

Compound (2-ethynylphenyl)methanol **S29** has been previously reported in literature. **S29** and has been synthesized following known methodologies.

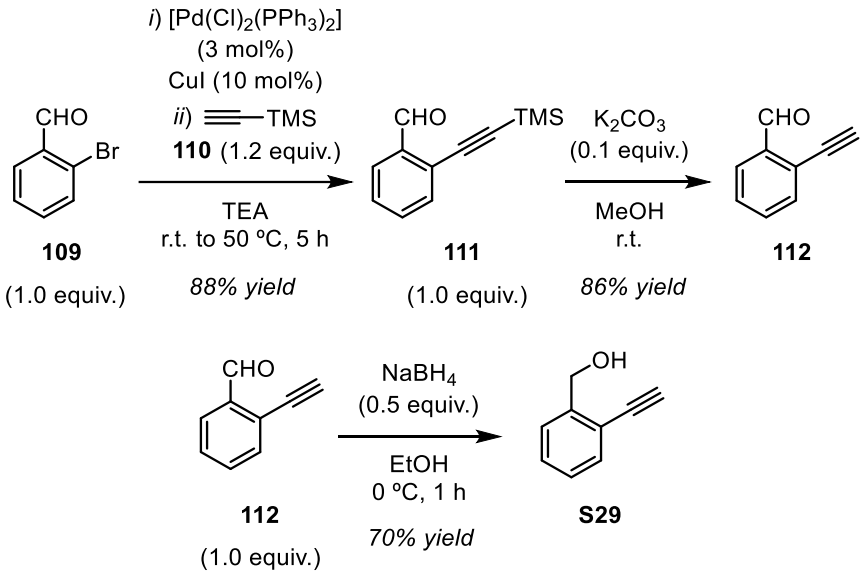

2-Bromobenzaldehyde **109** (1.0 g, 5.6 mmol, 1.0 equiv.) was added to a TEA solution (6.0 mL, 1 M) of $[Pd(Cl)_2 (PPh_3)_2]$ (118 mg, 0.2 mmol, 3 mol%) and CuI (107 mg, 0.6 mmol, 10 mol%) and stirred for 10 min. Then, trimethylsilylacetylene **110** (662 mg, 6.7 mmol, 1.2 equiv.) was added dropwise over 10 min. The resulting suspension was allowed to stir for 4 h at 50℃. After completion of the reaction, the mixture was filtered through a short celite pad and concentrated under vacuum. The residue was eluted through a silica pad using EtOAc as eluent to finally afford product **111** (995 mg, 88% yield) as a pale brown oil. Spectroscopic data were in agreement with those previously reported.[221]

To 2-((trimethylsilyl)ethynyl)benzaldehyde **111** (995 mg, 4.9 mmol, 1.0 equiv.), 5.0 mL of MeOH and K_2CO_3 (79.0 mg, 0.6 mmol, 0.1 equiv.) were added and stirred at room temperature until TLC analysis showed that **111** was completely consumed. The resulting mixture was filtered

through a short pad of silica and the volatiles were removed under vacuum. The product **112** (550 mg, 86% yield) was isolated in high purity and was directly used in the next step. Spectroscopic data were in agreement with those previously reported.[226]

$NaBH_4$ (82.8 mg, 2.1 mmol, 0.5 equiv.) was added portionwise to a solution of **112** (547 mg, 4.2 mmol, 1.0 equiv.) in anhydrous EtOH (7.0 mL, 0.6 M) at 0 °C under nitrogen atmosphere. The reaction mixture was stirred at 0 °C for 1 h before it was warmed to room temperature. The reaction mixture was concentrated, diluted with 5.0 mL of water, and extracted with Et_2O (3 × 10.0 mL). The combined organic phase was washed with brine, dried over Na_2SO_4 and concentrated *in vacuo*. Finally, the crude was purified by standard column chromatography using CyHex:EtOAc (80:20) mixture as eluent to give the product **S29** (390 mg, 70% yield) as a white solid. Spectroscopic data were in agreement with those previously reported in literature.[226]

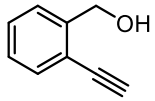

S29

(2-ethynylphenyl)methanol, **S29**: **^{1}H NMR** (400 MHz, $CDCl_3$) δ: 7.51 (d, *J* = 7.8 Hz, 1 H), 7.45 (d, *J* = 7.5 Hz, 1 H), 7.38 (t, *J* = 7.5 Hz, 1 H), 7.26 (t, *J* = 7.6 Hz, 1 H), 4.84 (d, *J* = 5.9 Hz, 2 H), 3.33 (s, 1 H), 2.06 (t, *J* = 6.0 Hz, 1 H) ppm. **^{13}C{^{1}H} NMR** (101 MHz, $CDCl_3$) δ: 143.3, 133.0, 129.4, 127.6, 127.4, 120.3, 82.1, 81.4, 63.9 ppm.

[226] Wang, X.; Silverman, R. B. *J. Org. Chem.* **1998**, *63*, 7357-7363.

Synthesis of 2,2-diphenylpent-4-yn-1-ol S30

Compound 2,2-diphenylpent-4-yn-1-ol **S30** has been previously reported in literature. **S30** has been synthesized following known methodologies.[227]

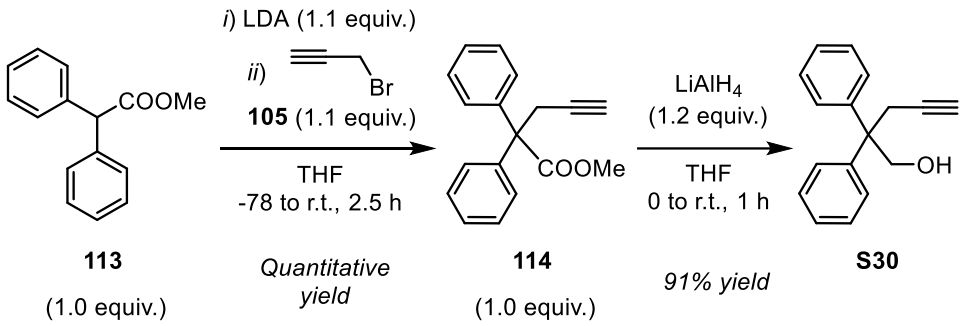

n-Butyllithium (1.6 M in hexanes ,3.0 mL, 4.8 mmol, 1.1 equiv.) was added to diisopropylamine (0.7 mL, 4.8 mmol, 1.1 equiv.) at −78 °C with stirring. Then, THF (5.0 mL, 0.9 M) was added to dissolve all the solids generated. A THF solution (15.0 mL) of methyl diphenylcarboxylate **113** (1.0 g, 4.4 mmol, 1.0 equiv.) was slowly added to the LDA solution and further stirred for 1.5 h at the same temperature. Afterwards, propargyl bromide **105** (0.4 mL, 4.6 mmol, 1.1 equiv.) was added. The reaction mixture was then allowed to warm to room temperature and further stirred for 15 h. The resulting solution was then quenched with aqueous NH_4Cl (10 mL), extracted with EtOAc (3 x 15 mL), and the organic phase was washed with water, brine and finally dried over anhydrous Na_2SO_4. Solvent was then removed under reduced pressure. Product **114** was obtained in quantitative yield in high purity and was directly used in the next step. Spectroscopic data were in agreement with those previously reported in literature.

By using a spatula, $LiAlH_4$ (229 mg, 5.8 mmol, 1.2 equiv.) was portionwise added to a solution of **114** (1.3 g, 4.9 mmol, 1.0 equiv.) in THF

[227] (a) Nakamura, I.; Chan, C. S.; Araki, T.; Terada, M.; Yamamoto, Y. *Adv. Synth. Catal.* **2009**, *351*, 1089-1100; (b) , .

(10.0 mL, 0.5 M) at 0 °C. After stirring for 30 min, the reaction mixture was quenched with saturated aqueous NH_4Cl (10 mL), treated with 2 M aqueous HCl (5 mL) to dissolve the aluminum salts, and extracted with EtOAc (3 x 20 mL). The combined organic layers were washed with saturated aqueous $NaHCO_3$ and brine; dried over Na_2SO_4 and concentrated *in vacuo*. Product **S30** was obtained in a pure way (1.1 g, 91% yield). Spectroscopic data were in agreement with those previously reported in literature.[228]

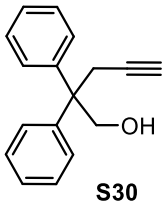

S30

2,2-diphenylpent-4-yn-1-ol, **S30**: **^{1}H NMR** (400 MHz, $CDCl_3$) δ: 7.35 – 7.20 (m, 10 H), 4.31 (d, *J* = 5.9 Hz, 2 H), 3.10 (d, *J* = 2.7 Hz, 2 H), 1.95 (t, *J* = 2.7 Hz, 1 H), 1.45 (br t, *J* = 6.1 Hz, 1 H) ppm. **^{13}C{^{1}H} NMR** (101 MHz, $CDCl_3$) δ: 144.5, 128.4, 128.1, 126.9, 81.5, 71.7, 68.5, 51.7, 27.6 ppm.

5.4.6 Characterization of relevant products

O,O-ketals obtained by using pent-4-yn-1-ol **S20** and pent-3-yn-1-ol **S21** as starting material are well known in literature.[208a,208g,229]

Products **P26a** and **P26b** obtained from (1-(prop-2-yn-1-yl)cyclohexyl)methanol **S26** have been directly isolated from the reaction mixture by using standard chromatographic techniques employing *n*-pentane:Et_2O mixtures (100:0→95:5) as eluent.

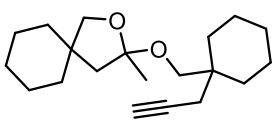

P26a

Product **P26a**: **P26a** was obtained as a colorless oil. **^{1}H NMR** (400 MHz, $CDCl_3$) δ: 3.65 (d, *J* = 8.4 Hz, 1 H), 3.58 (d, *J* = 8.4 Hz, 1 H), 3.35 (d, *J* = 8.9 Hz, 1 H), 3.21 (d, *J* = 8.9 Hz,

[228] (a) Aponick, A.; Li, C.-Y.; Palmes, J. A. *Org. Lett.* **2009**, *11*, 121-124; (b) Minkler, S. R. K.; Isley, N. A.; Lippincott, D. J.; Krause, N.; Lipshutz, B. H. *Org. Lett.* **2014**, *16*, 724-726.

[229] Gabriele, B.; Salerno, G.; De Pascali, F.; Costa, M.; Chiusoli, G. P. *J. Organomet. Chem.* **2000**, *593-594*, 409-415.

1 H) 2.22 (br s, 2 H), 1.93 (t, *J* = 2.6 Hz, 1 H), 1.88 (d, *J* = 13.0 Hz, 1 H), 1.62 (d, *J* = 13.0 Hz, 1 H) 1.54 – 1.32 (m, 23 H) ppm. **^{13}C{^{1}H} NMR** (101 MHz, $CDCl_3$) δ: 107.9, 82.6, 78.0, 69.9, 64.9, 43.5, 38.2, 36.8, 36.5, 32.5, 32.4, 26.4, 26.1, 26.0, 24.3, 23.8, 22.8, 21.8, 21.7 ppm. **HRMS** (ESI$^+$): *m*/*z* calcd. for $C_{20}H_{32}O_2Na^+$ $[M+Na]^+$ 327.2318, found: 327.2298.

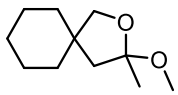

P26b

Product **P26b**: **P26b** was obtained as a colorless oil. **^{1}H NMR** (400 MHz, $CDCl_3$) δ: 3.67 (d, *J* = 8.4 Hz, 1 H), 3.54 (d, *J* = 8.4 Hz, 1 H), 3.19 (s, 3 H), 1.86 (d, *J* = 13.1 Hz, 1 H), 1.67 (d, *J* = 13.0 Hz, 1 H) 1.52 – 1.35 (m, 13 H) ppm. **^{13}C{^{1}H} NMR** (101 MHz, $CDCl_3$) δ: 107.0, 76.7, 50.1, 47.2, 42.5, 36.6, 35.5, 24.8, 23.1, 22.5, 21.2 ppm. **HRMS** (ESI$^+$): *m*/*z* calcd. for $C_{10}H_{17}O^+$ $[M-OMe]^+$ 153.1279, found: 153.1271.

5.4.7 Mechanistic experiments

Spectroscopic investigation under catalytic conditions

Under CO atmosphere after 24 h

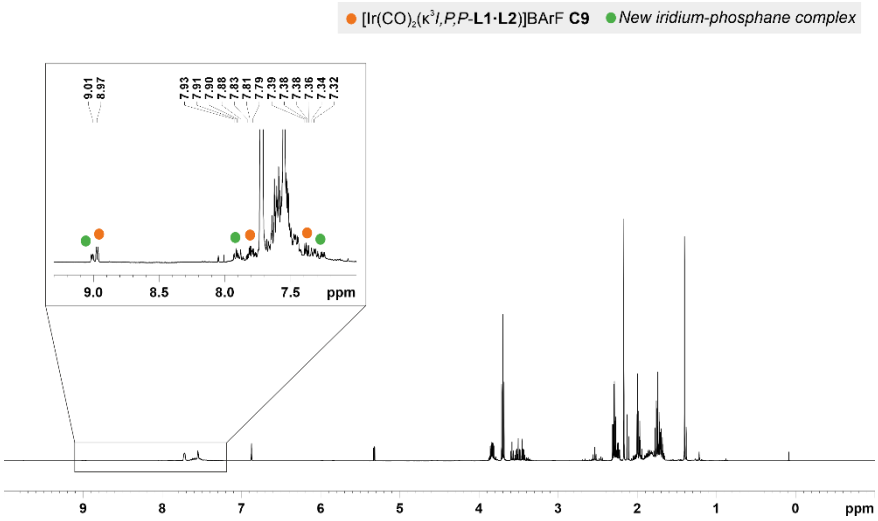

Figure 5.9. ^{1}H NMR (400 MHz, CD_2Cl_2) of catalytic hydroalkoxylation reaction of **S20** under CO using complex **C9**.

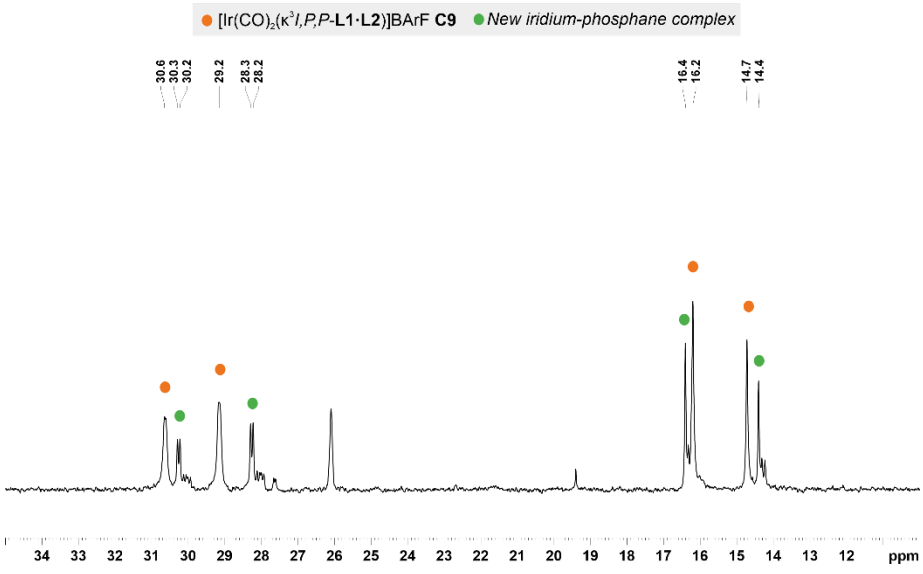

Figure 5.10. $^{31}P\{^{1}H\}$ NMR (162 MHz, CD_2Cl_2) of catalytic hydroalkoxylation reaction of **S20** under CO using complex **C9**.

Under N_2 atmosphere after 12 h

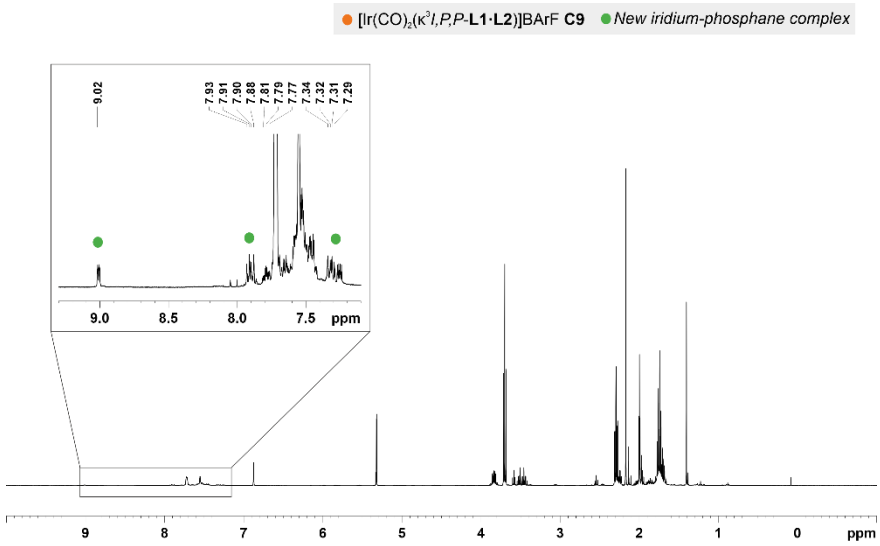

Figure 5.11. ^{1}H NMR (400 MHz, CD_2Cl_2) of catalytic hydroalkoxylation reaction of **S20** under N_2 using complex **C9**.

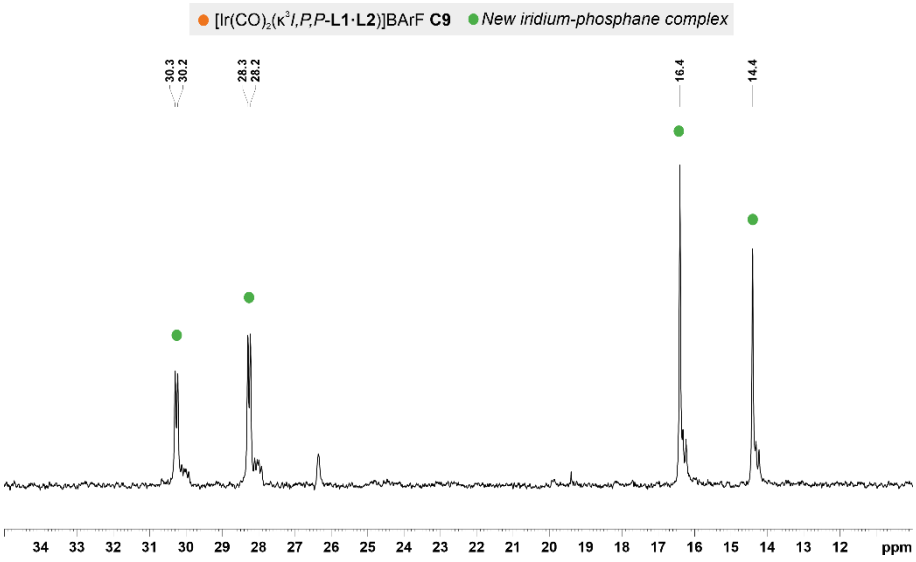

Figure 5.12. $^{31}P\{^{1}H\}$ NMR (162 MHz, CD_2Cl_2) of catalytic hydroalkoxylation reaction of **S20** under CO using complex **C9**.

Spectroscopic investigation under stoichiometric conditions

General procedure for the stoichiometric experiments: Under N_2 atmosphere, substrate **S20** or **96** (1.0 equiv.) was added to a solution of our halogen bond-assembled iridium(I) complex **C9** (1.0 equiv., 0.01 mmol) in dry deuterated DCM (0.65 mL). The reaction mixture was stirred for 1 h at room temperature. Afterwards, the reaction mixture was analyzed by NMR spectroscopy.

Using pent-4-yn-1-ol **S20**

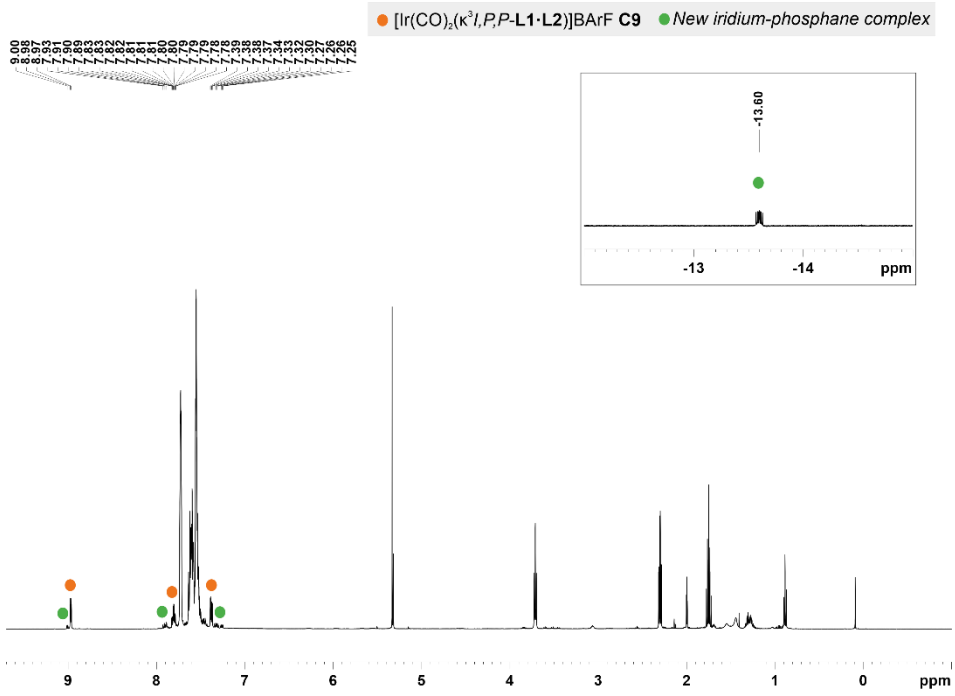

Figure 5.13. ^{1}H NMR (500 MHz, CD_2Cl_2) of pent-4-yn-1-ol **S20** and **C9**.

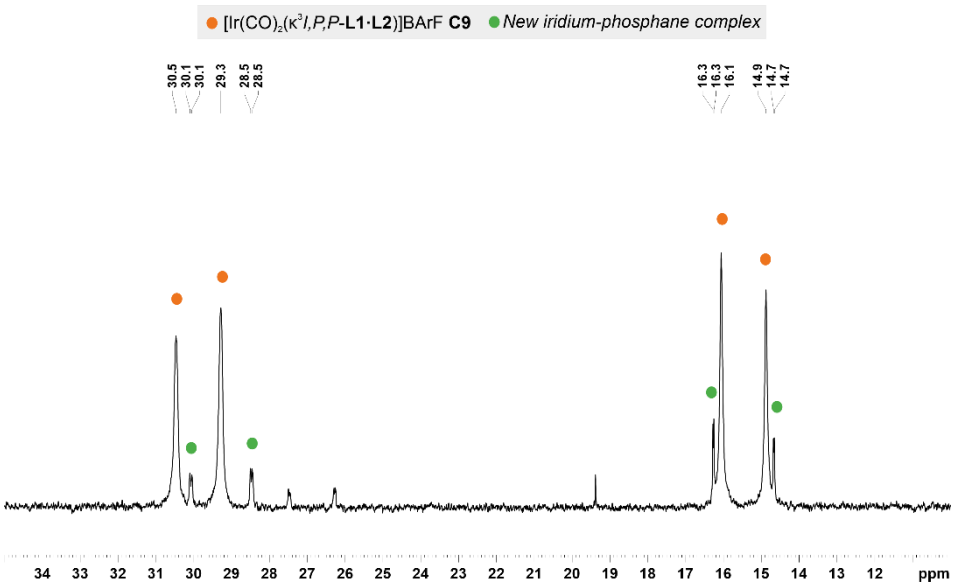

Figure 5.14. $^{31}P\{^{1}H\}$ NMR (162 MHz, CD_2Cl_2) of pent-4-yn-1-ol **S20** and **C9**.

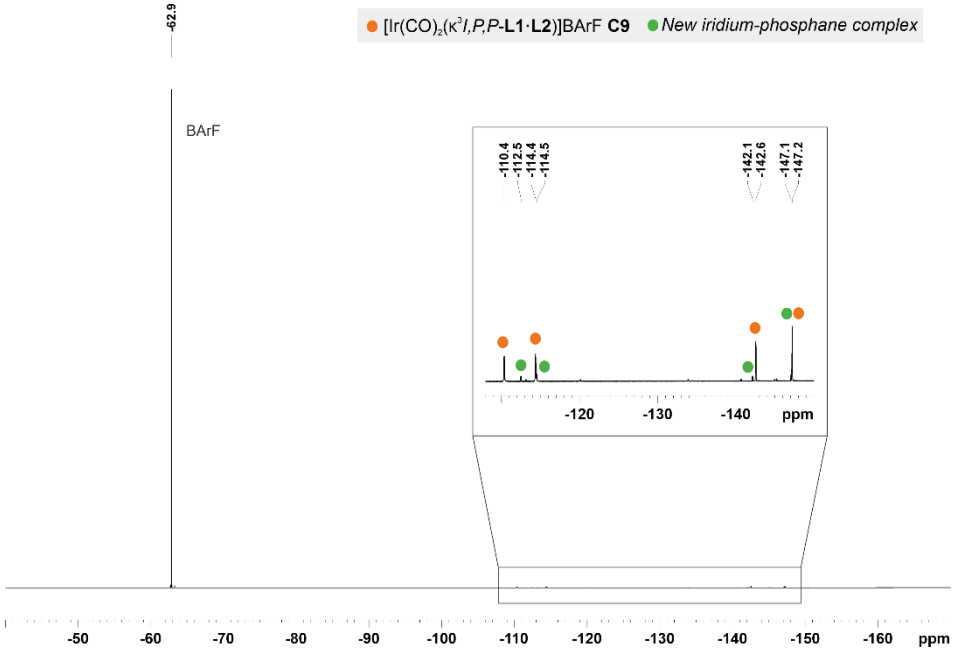

Figure 5.15. ^{19}F NMR (471 MHz, CD_2Cl_2) of pent-4-yn-1-ol **S20** and **C9**.

Using pent-1-yne **96**

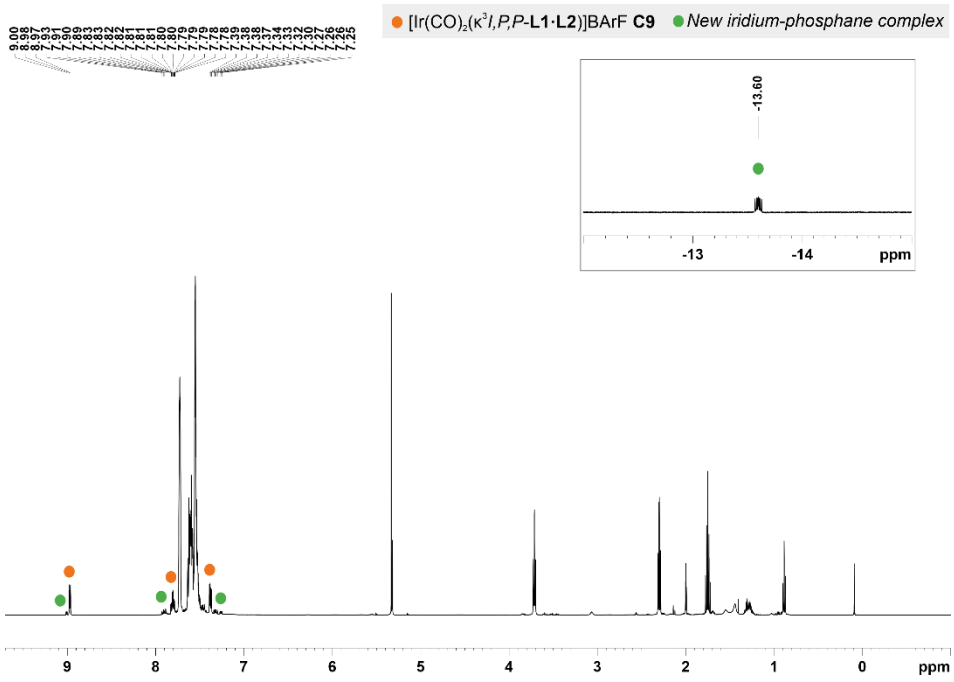

Figure 5.16. ^{1}H NMR (500 MHz, CD_2Cl_2) of pent-1-yne **96** and **C9**.

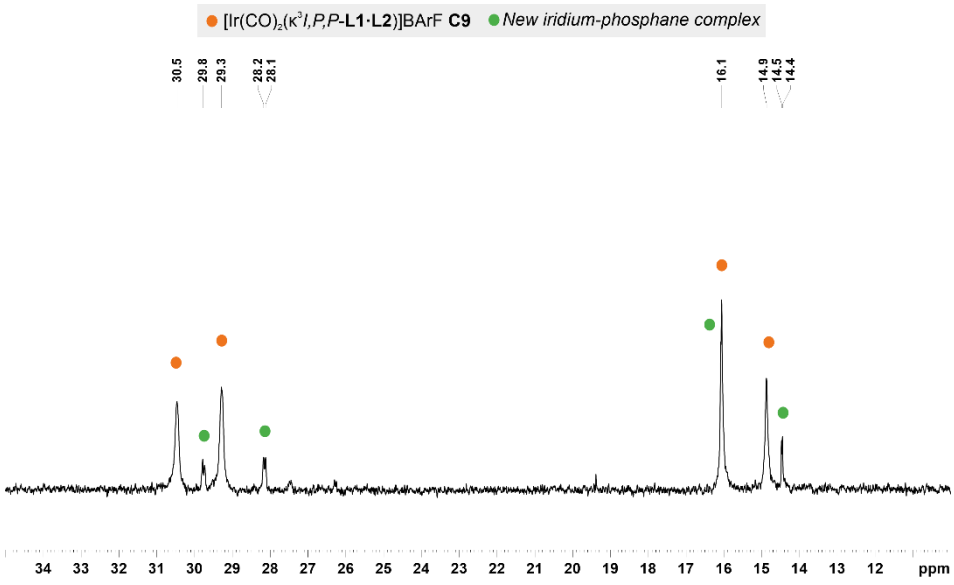

Figure 5.17. $^{31}P\{^{1}H\}$ NMR (162 MHz, CD_2Cl_2) of pent-1-yne **96** and **C9**.

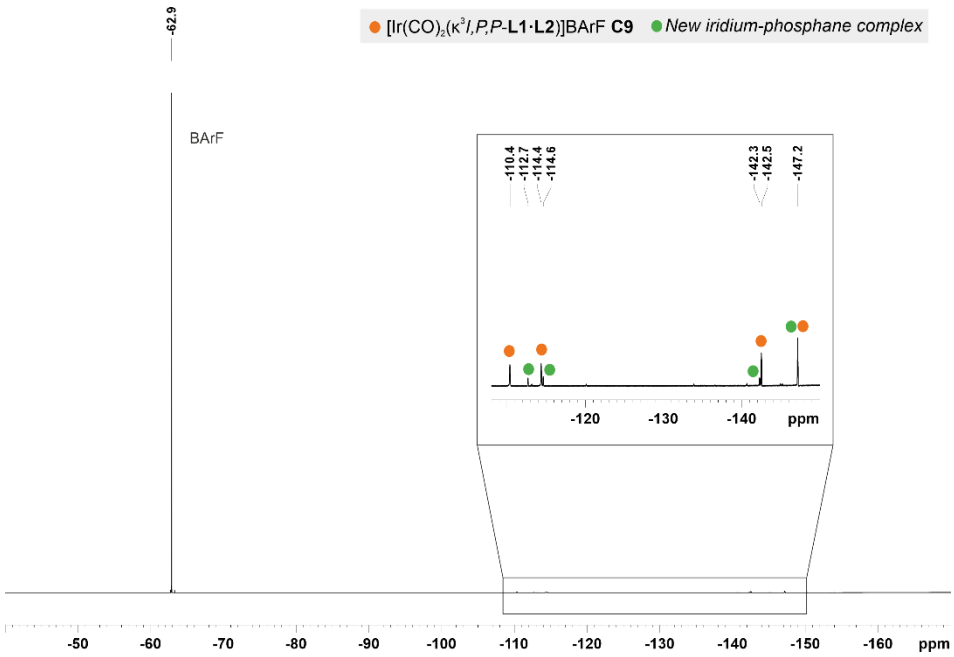

Figure 5.18. ^{19}F NMR (471 MHz, CD_2Cl_2) of pent-1-yne **96** and **C9**.

5.4.8 Collection of NMR spectra

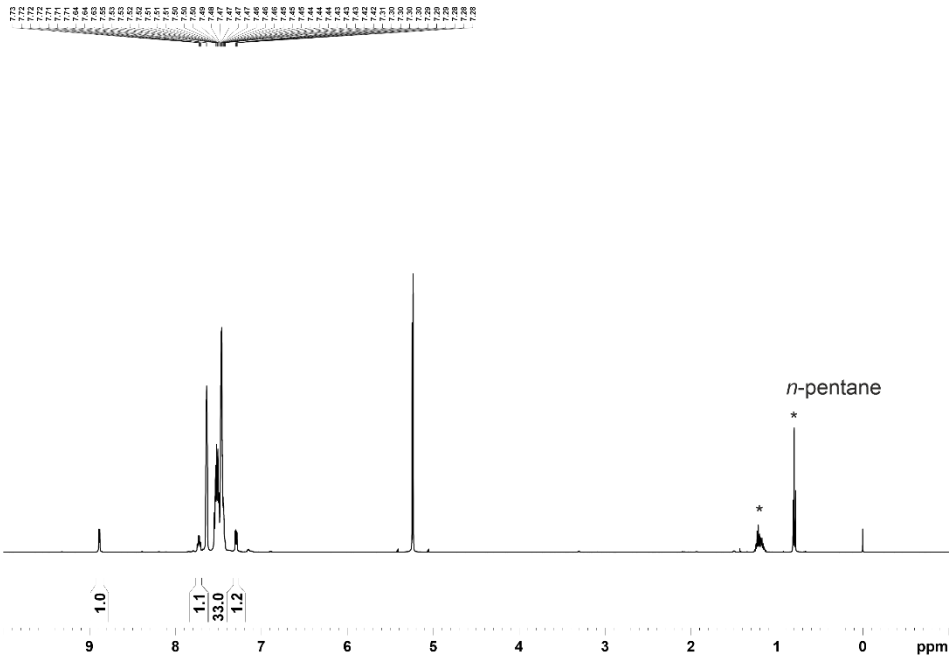

Figure 5.19. ^{1}H NMR (500 MHz, CD_2Cl_2) for complex **C9.**

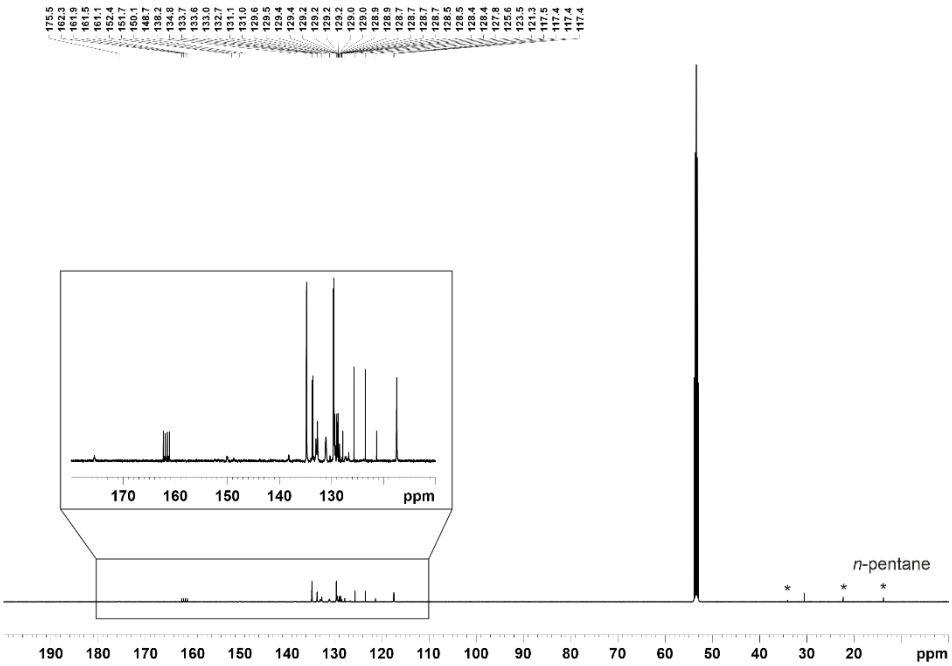

Figure 5.20. $^{13}C\{^{1}H\}$ NMR (126 MHz, CD_2Cl_2) for complex **C9**.

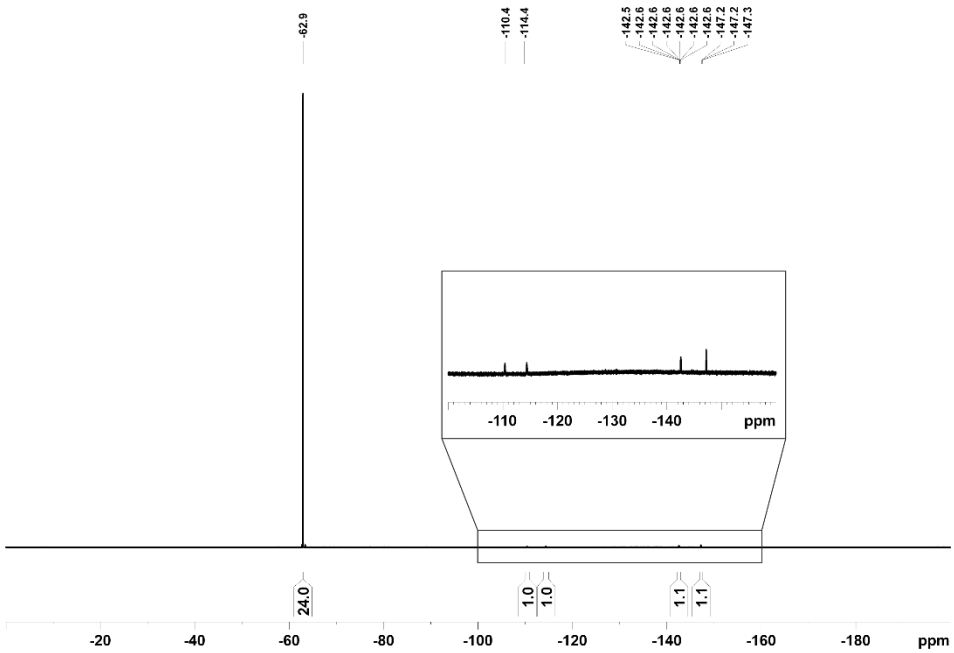

Figure 5.21. $^{19}F\{^{1}H\}$ NMR (471 MHz, CD_2Cl_2) for complex **C9**.

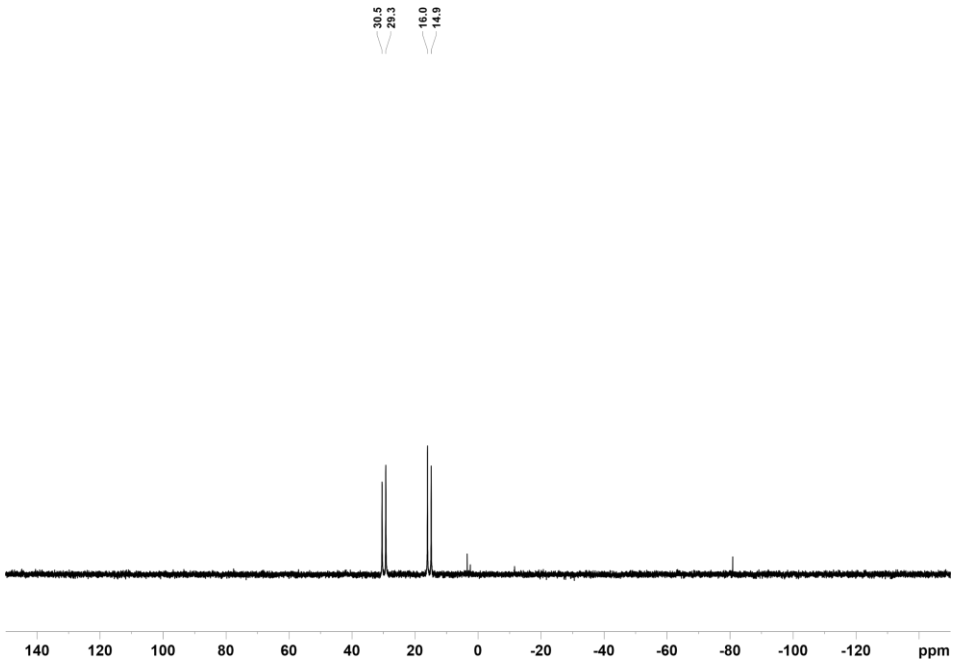

Figure 5.22. $^{31}P\{^{1}H\}$ NMR (203 MHz, CD_2Cl_2) for complex **C9**.

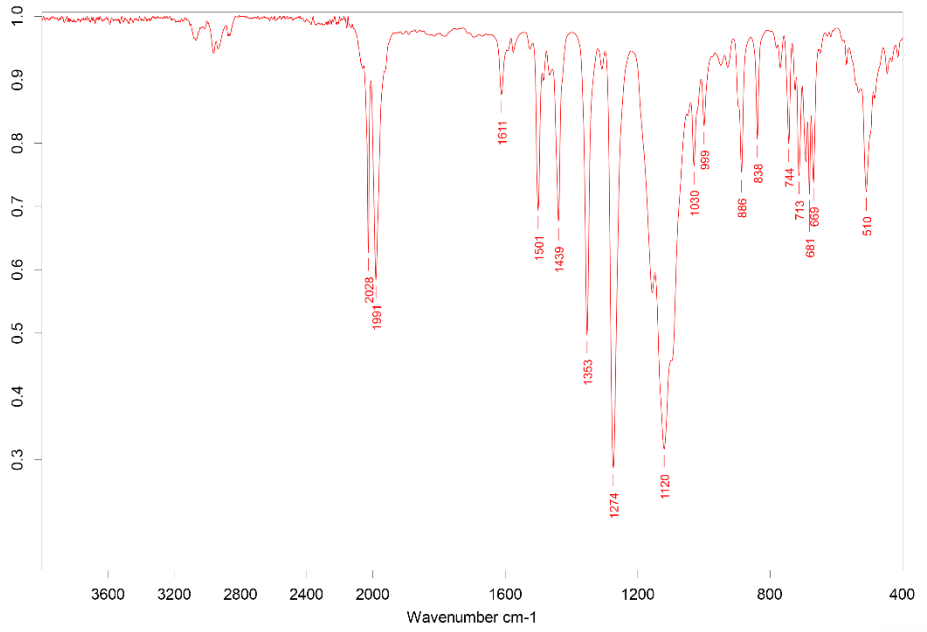

Figure 5.23. IR spectrum for complex **C9**.

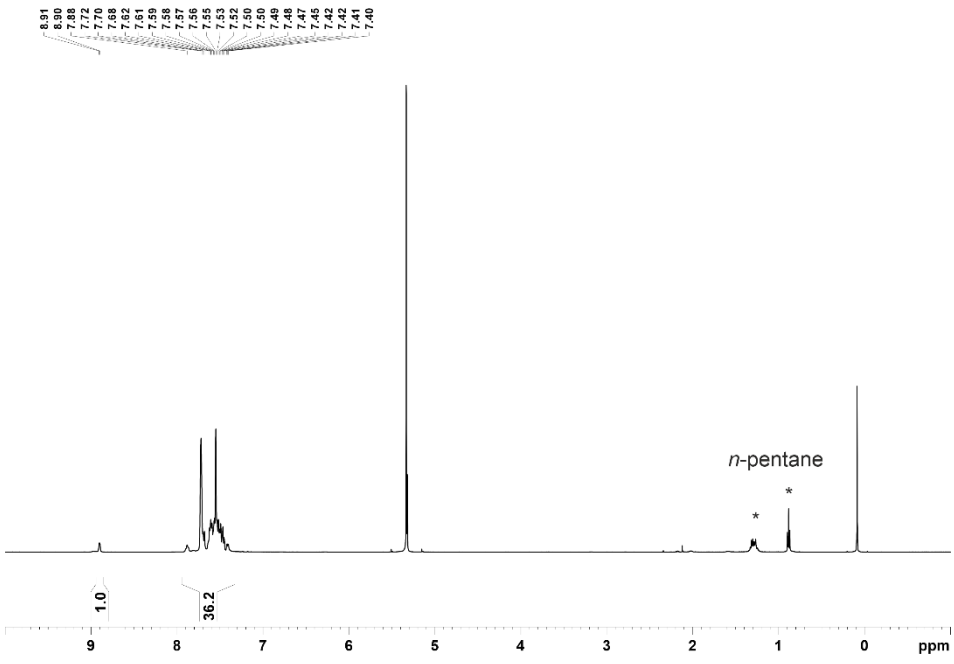

Figure 5.24. ^{1}H NMR (500 MHz, CD_2Cl_2) for complex **C10**.

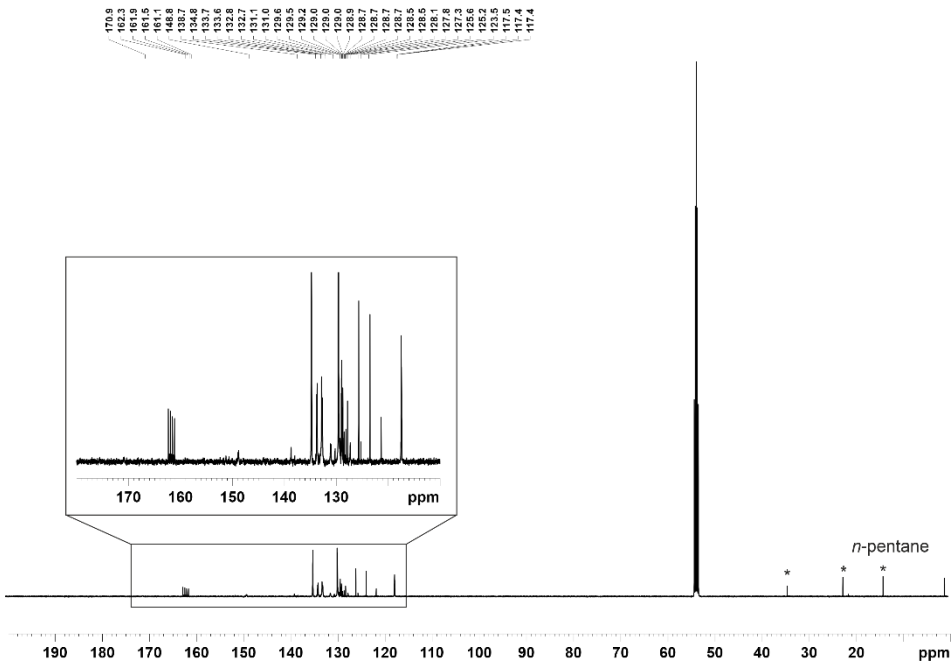

Figure 5.25. $^{13}C\{^{1}H\}$ NMR (126 MHz, CD_2Cl_2) for complex **C10**.

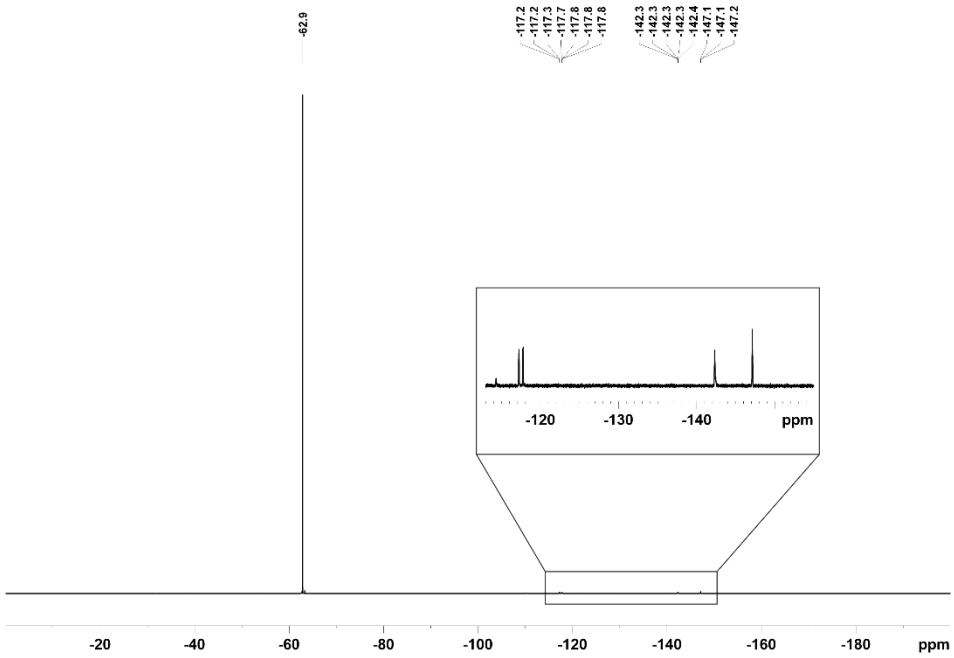

Figure 5.26. $^{19}F\{^{1}H\}$ NMR (471 MHz, CD_2Cl_2) for complex **C10.**

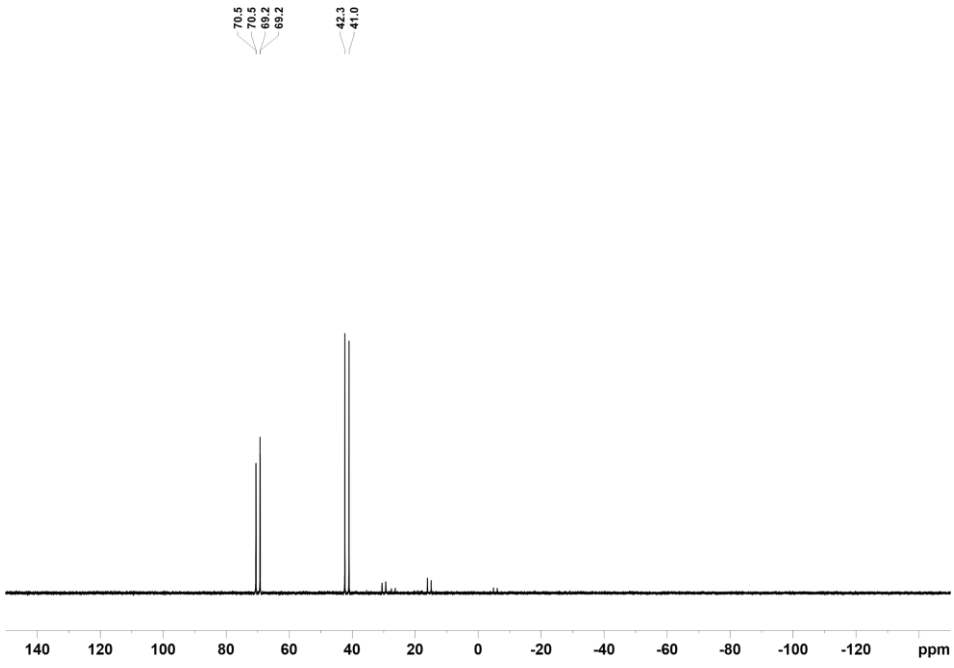

Figure 5.27. $^{31}P\{^{1}H\}$ IGD NMR (203 MHz, CD_2Cl_2) for complex **C10**.

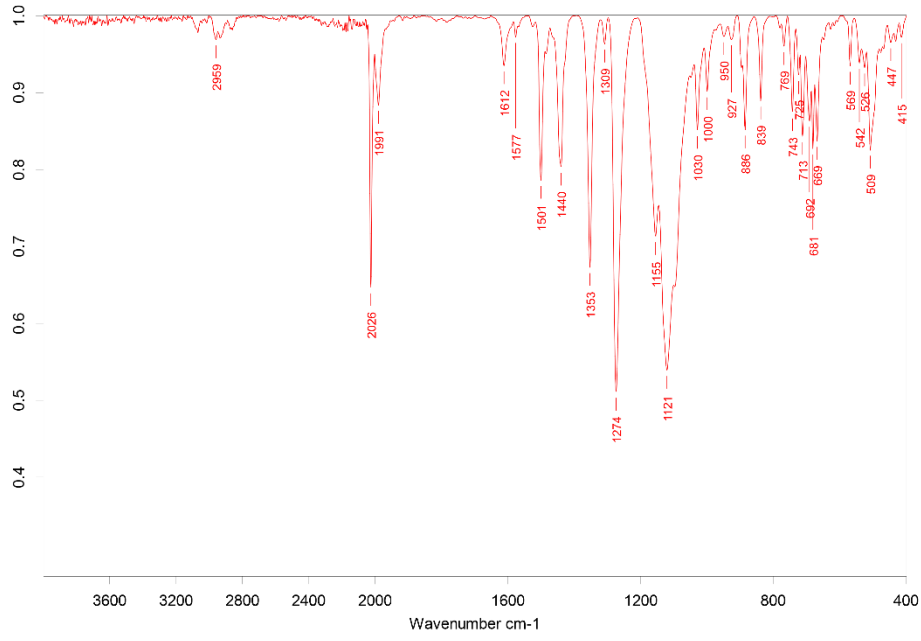

Figure 5.28. IR spectrum for complex **C10**.

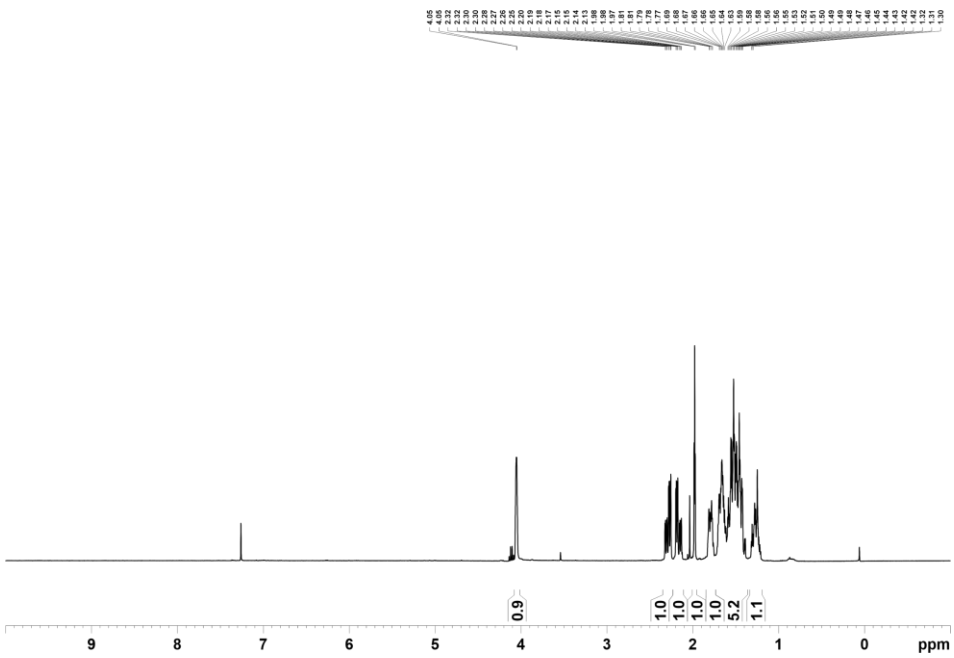

Figure 5.29. ^{1}H NMR (400 MHz, $CDCl_3$) for compound *rac-cis*-**S25**.

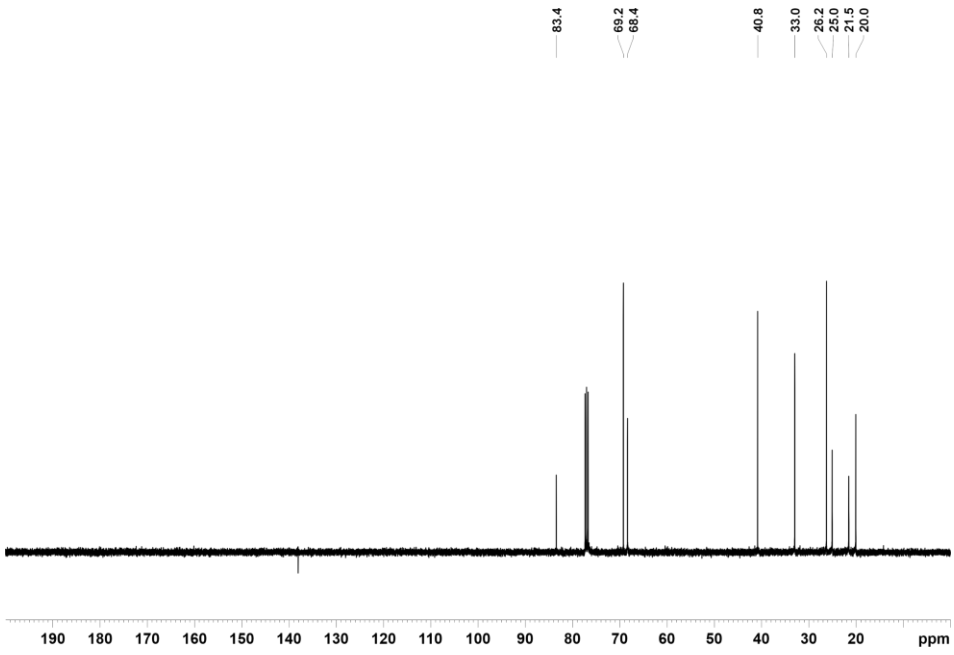

Figure 5.30. $^{13}C\{^{1}H\}$ NMR (101 MHz, $CDCl_3$) for compound *rac-cis*-**S25**.

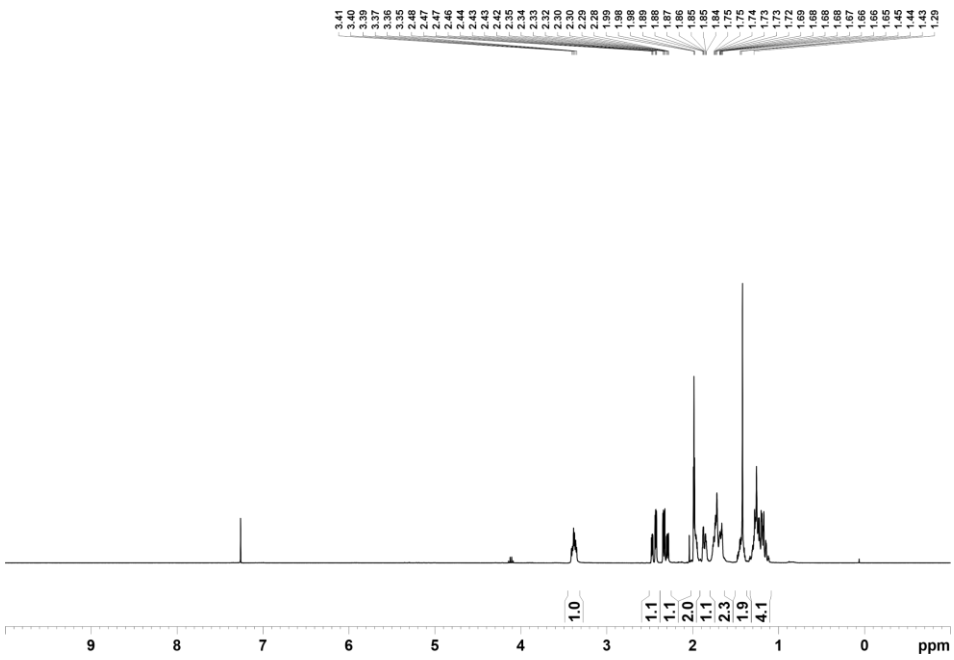

Figure 5.31. ^{1}H NMR (400 MHz, $CDCl_3$) for compound *rac-trans*-**S25**.

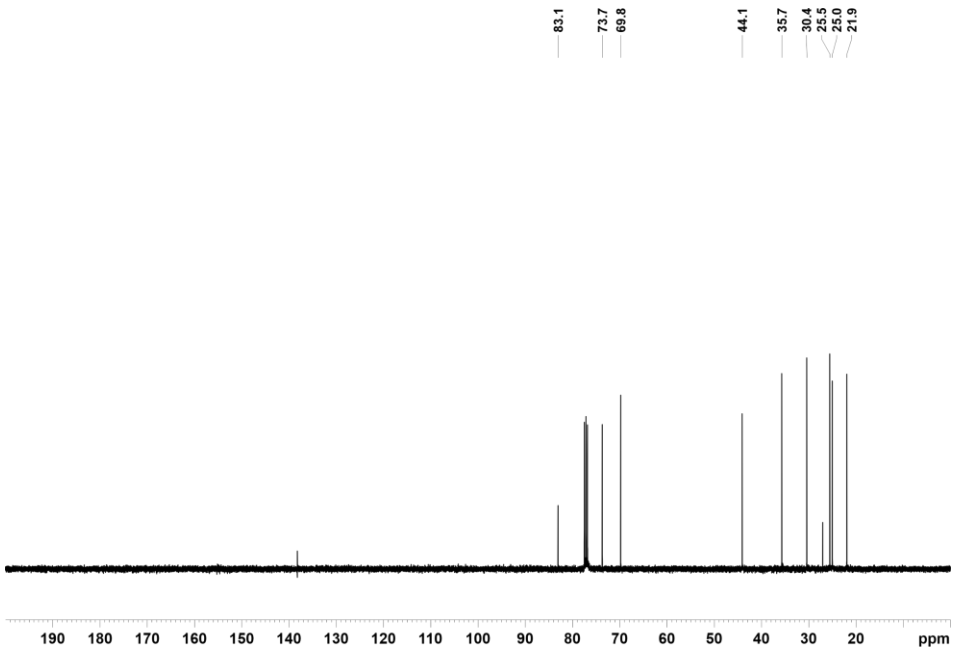

Figure 5.32. $^{13}C\{^{1}H\}$ NMR (101 MHz, $CDCl_3$) for compound *rac-trans*-**S25**.

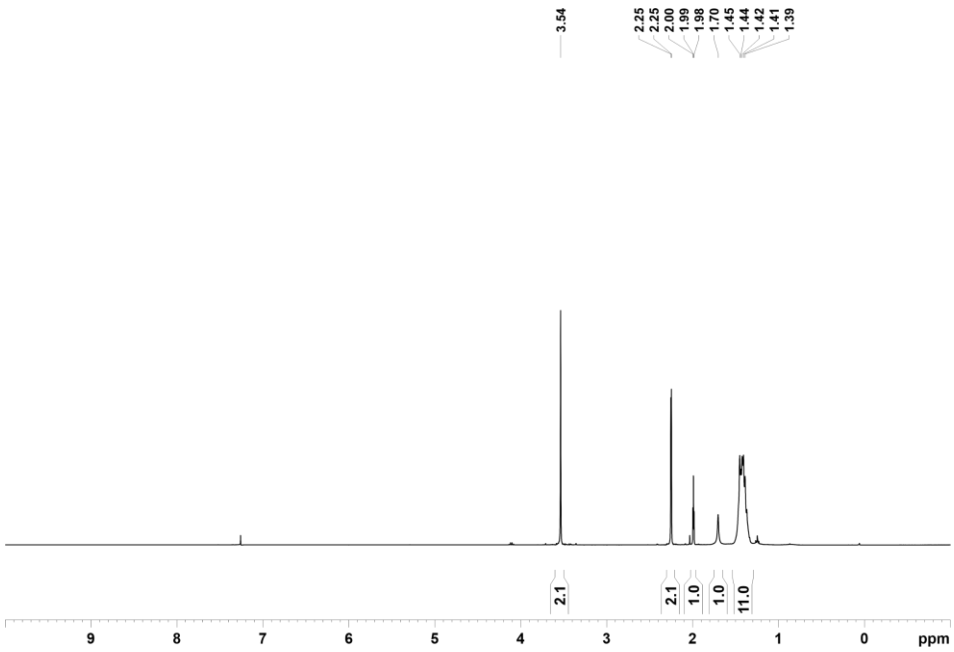

Figure 5.33. ^{1}H NMR (400 MHz, $CDCl_3$) for compound **S26**.

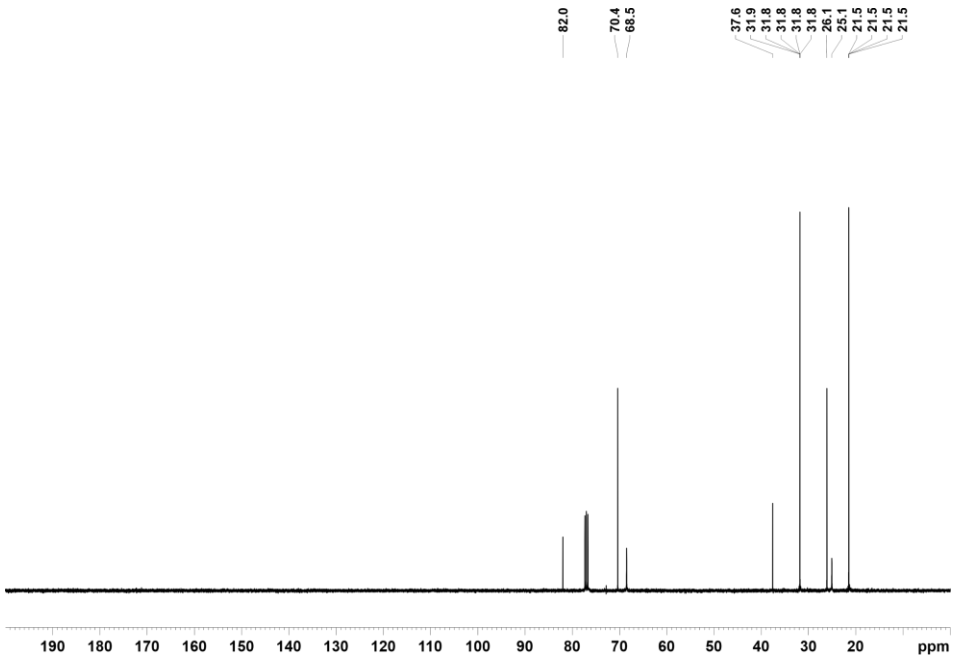

Figure 5.34. $^{13}C\{^{1}H\}$ NMR (101 MHz, $CDCl_3$) for compound **S26**.

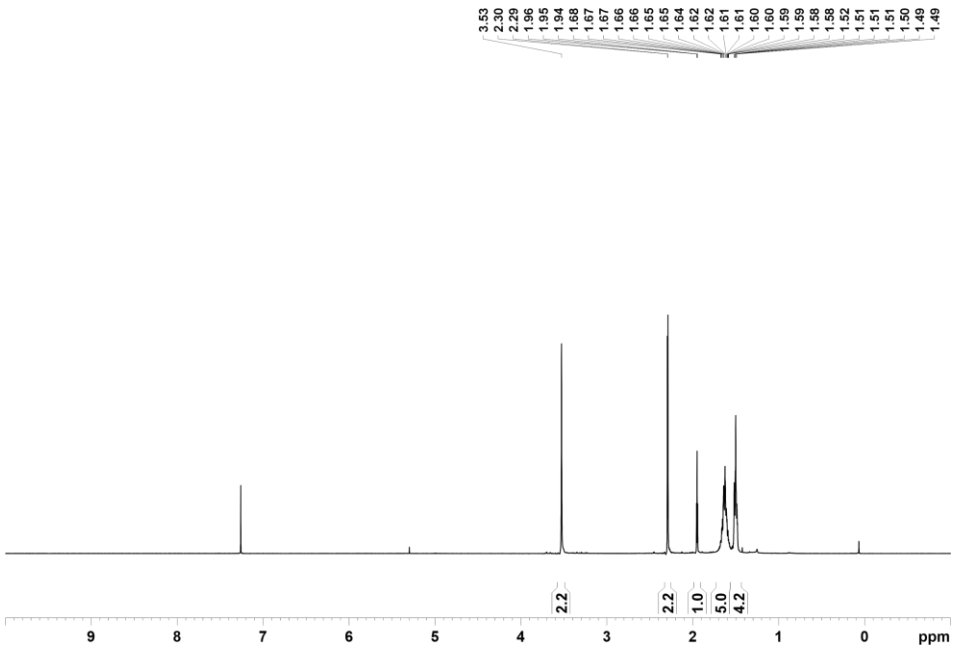

Figure 5.35. ^{1}H NMR (400 MHz, $CDCl_3$) for compound **S27**.

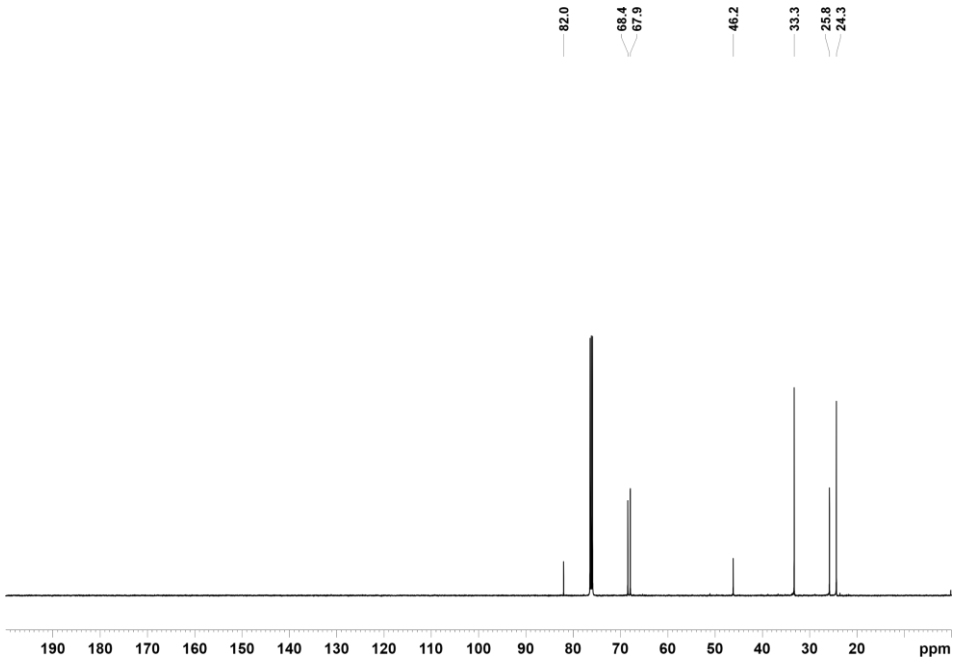

Figure 5.36. $^{13}C\{^{1}H\}$ NMR (101 MHz, $CDCl_3$) for compound **S27**.

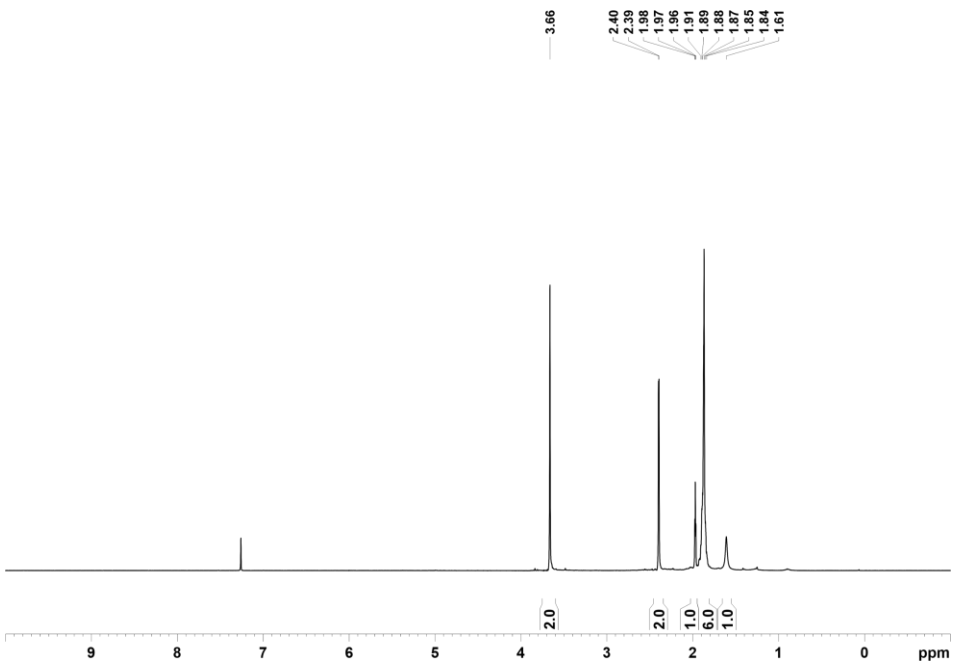

Figure 5.37. ^{1}H NMR (400 MHz, $CDCl_3$) for compound **S28**.

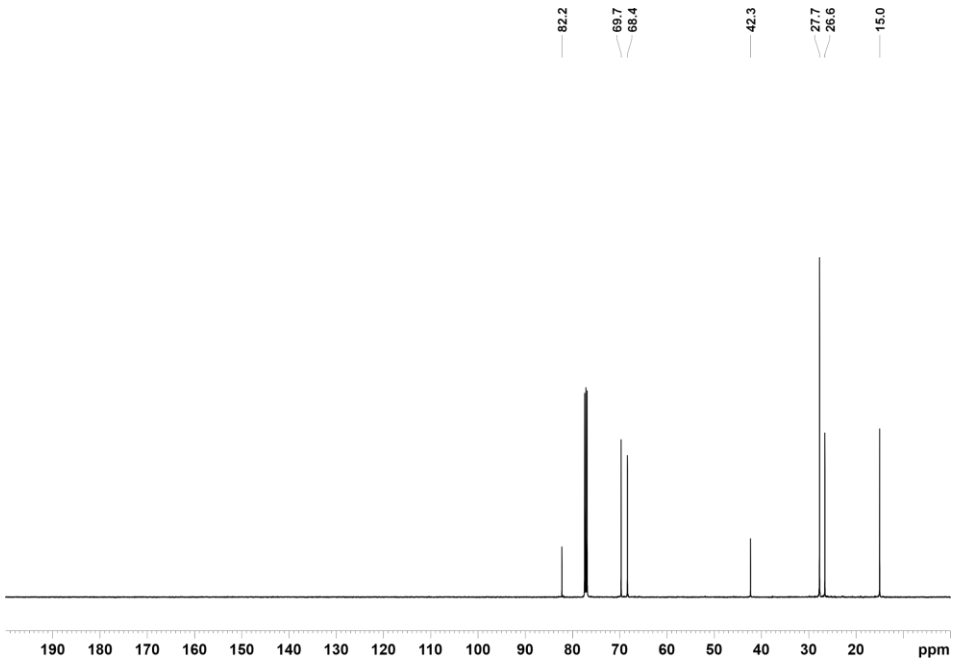

Figure 5.38. $^{13}C\{^{1}H\}$ NMR (101 MHz, $CDCl_3$) for compound **S28**.

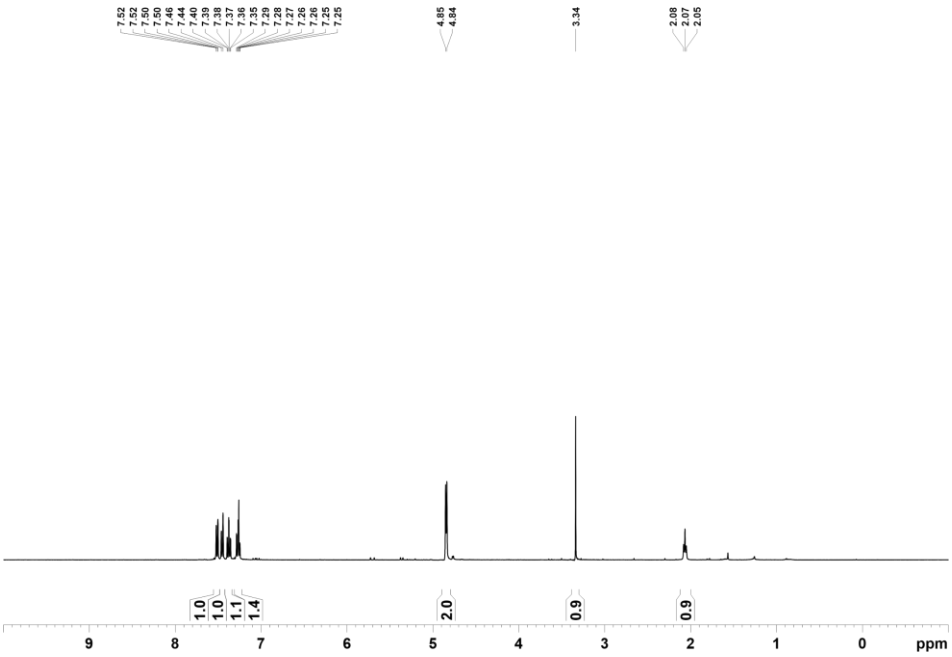

Figure 5.39. ^{1}H NMR (400 MHz, $CDCl_3$) for compound **S29**.

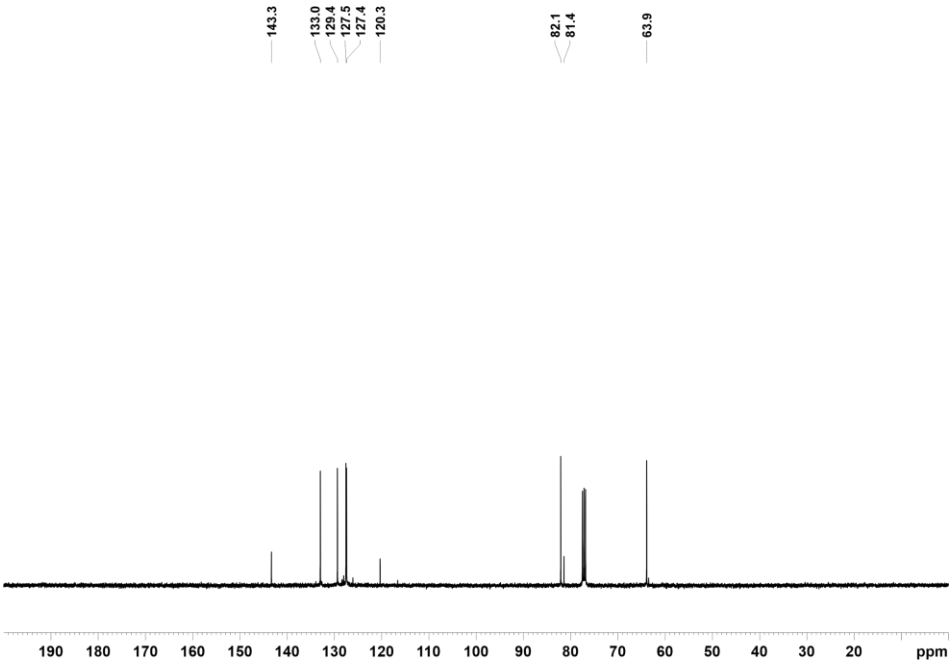

Figure 5.40. $^{13}C\{^{1}H\}$ NMR (101 MHz, $CDCl_3$) for compound **S29**.

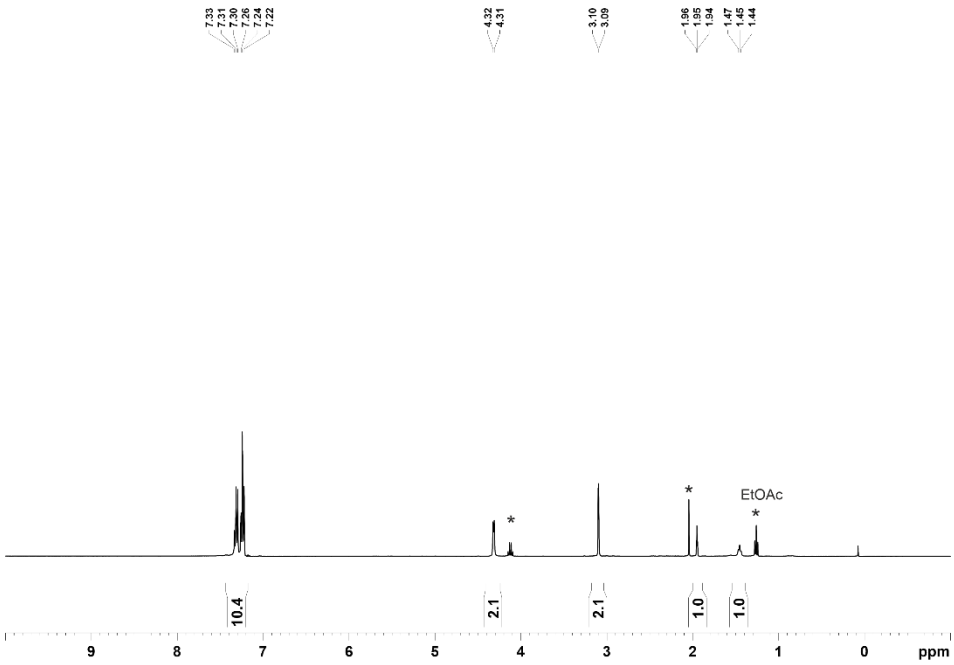

Figure 5.41. ^{1}H NMR (400 MHz, $CDCl_3$) for compound **S30**.

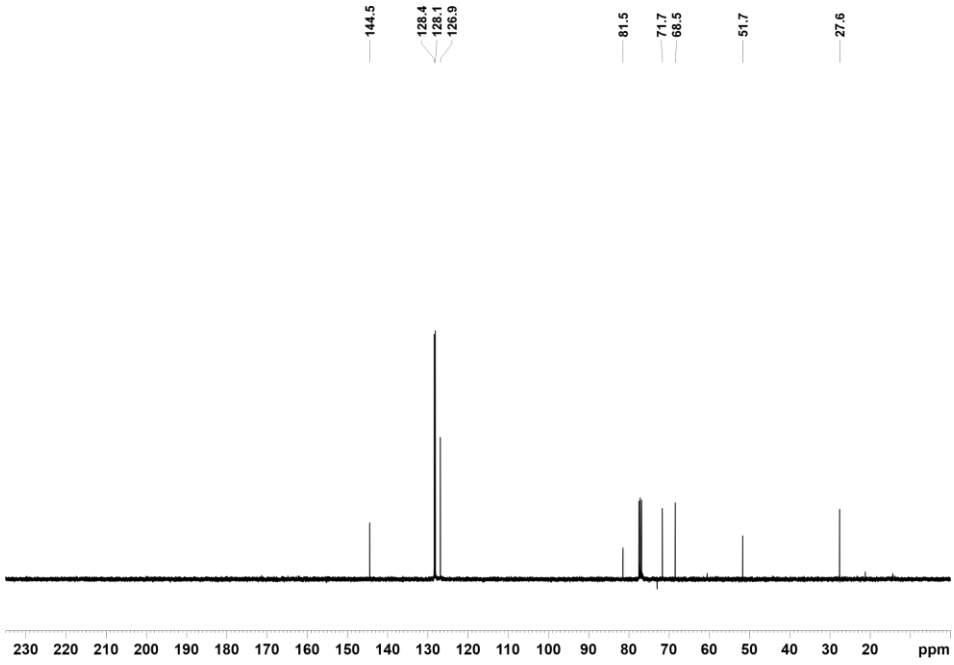

Figure 5.42. $^{13}C\{^{1}H\}$ NMR (101 MHz, $CDCl_3$) for compound **S30**.

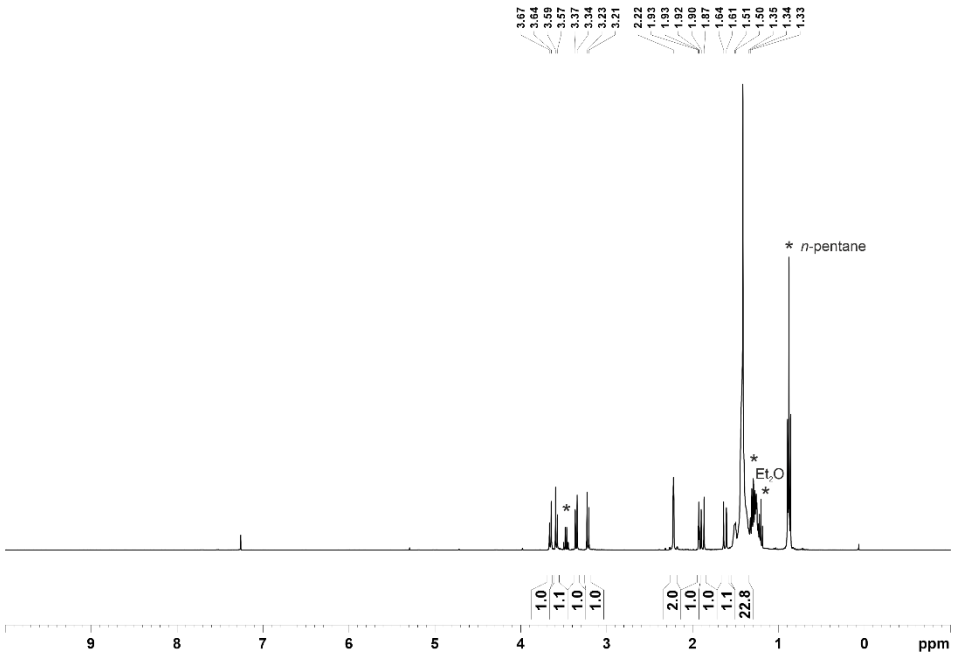

Figure 5.43. ^{1}H NMR (400 MHz, $CDCl_3$) for product **P26a**.

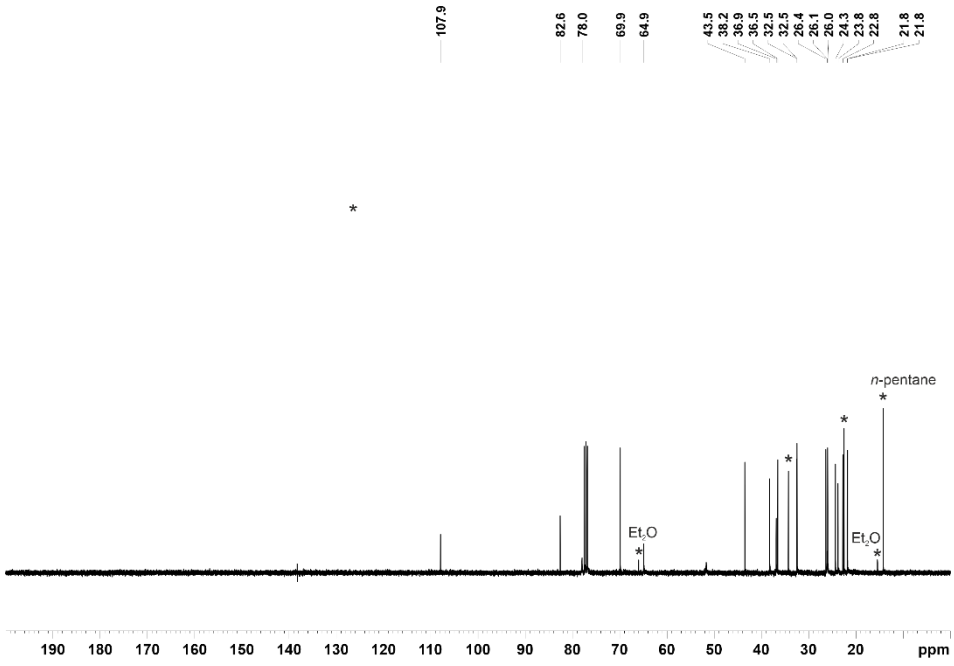

Figure 5.44. $^{13}C\{^{1}H\}$ NMR (101 MHz, $CDCl_3$) for product **P26a**.

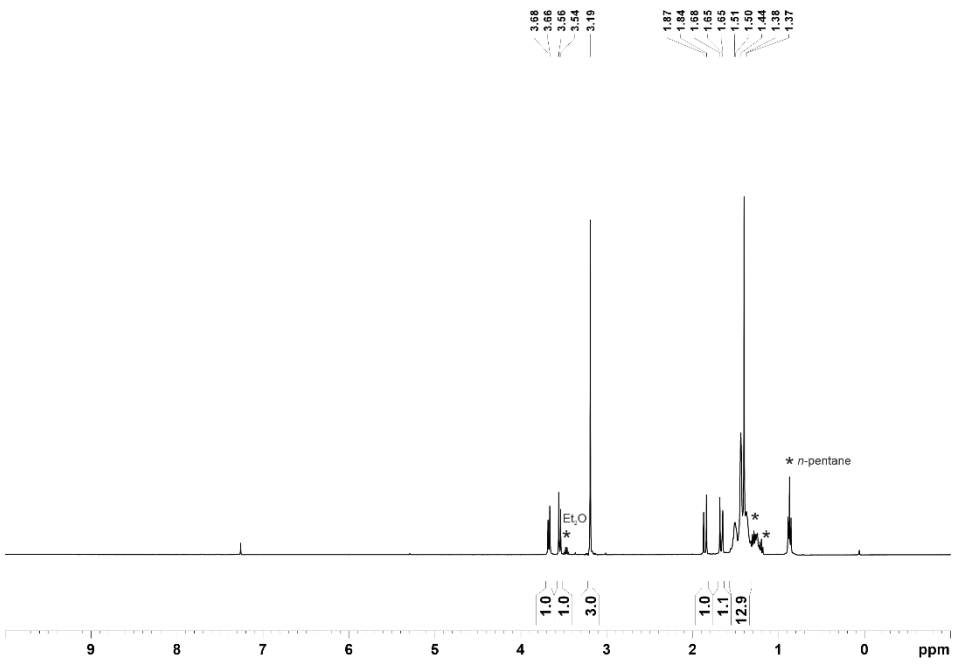

Figure 5.45. ^{1}H NMR (400 MHz, $CDCl_3$) for product **P26b**.

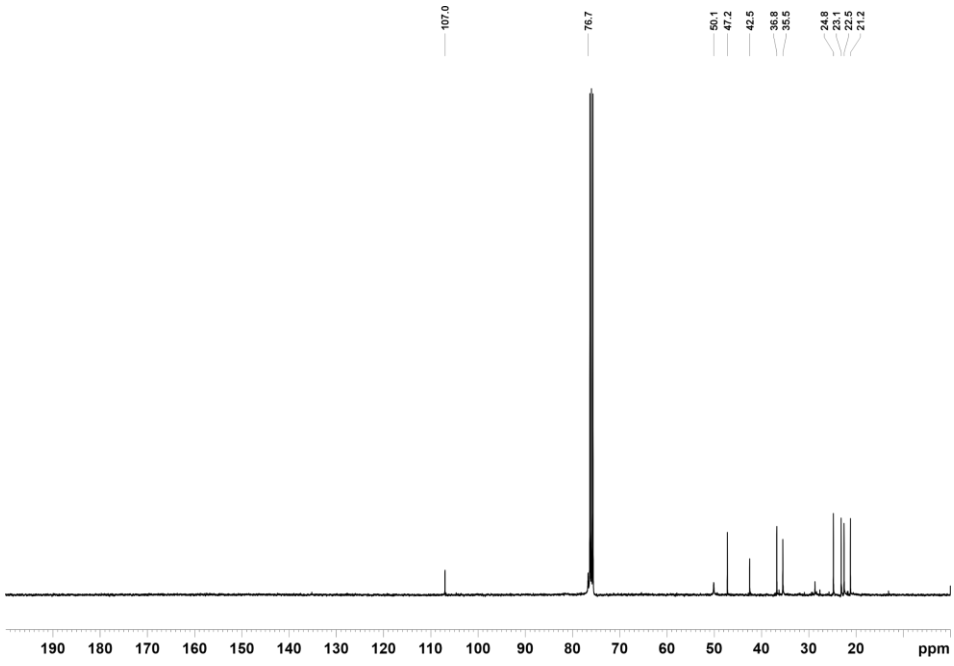

Figure 5.46. $^{13}C\{^{1}H\}$ NMR (101 MHz, $CDCl_3$) for product **P26.**

CHAPTER VI:

GENERAL CONCLUSIONS

6.1 GENERAL CONCLUSIONS

Chapter II*: Expanding the structural diversity of halogen bond donors and acceptors as building blocks towards halogen bond-assembled rhodium(I) complexes*.

The results explained in this chapter illustrate the effects that modifications on the halogen bond acceptor and donor ligands cause on the structure of the final rhodium(I) complexes. Structurally diverse halogen bond acceptor and donor ligands have been designed, synthesized, and subsequently tested in the preparation of halogen bond-assembled rhodium(I) complexes. The final complexes have been fully characterized by spectroscopic techniques in solution and in the solid state. An extensive study of the NMR spectral data obtained for rhodium(I) complexes has allowed for the rationalization of the outcome of the complexation processes and halogen bond formation.

First, it has been demonstrated that halogen bond acceptors containing a phosphaamidine moiety efficiently led to halogen bond-assembled complexes in combination with (2-iodo-3,4,5,6-tetrafluorobenzene)phosphane-based halogen bond donor **L2**. Two new complexes have been synthesized and fully characterized (**C2** and **C3**), being structurally and electronically analogous to the seminal halogen-bonded rhodium complex prepared by the group (*i.e.* XBphos-Rh **C1**). Second and last, substitution of the iodo group in (2-iodo-3,4,5,6-tetrafluorobenzene)phosphane-based halogen bond donor **L2** led to changes in the Rh−P complexation processes. For instance, a κ^2*P,N*-type coordination mode of the pyridine containing ligand **L1** was observed in the final complexes when fluorine was chosen as the halogen bond donor group (complexes derived from **L5**). The substitution of the iodo group in the halogen bond donor by a bromo substituent (**L6**) led to the new complex **C5**, whose structure in the solid state incorporated the expected halogen bond-assembled bisphosphane moiety. However, ^{31}P NMR

analysis in solution showed the formation of the new complex [Rh(CO)(κ²*N*,*P*-**L1**)(κ*P*-**L6**)]BArF **C6** by destruction of the halogen bond and coordination of the halogen bond acceptor **L1** to the rhodium center in a κ²*P*,*N*-fashion. The use of an alternative halogen bond acceptor with enhanced basicity at the nitrogen atom did not revert this behavior and the final complex **C8** did not involve halogen bonding interaction.

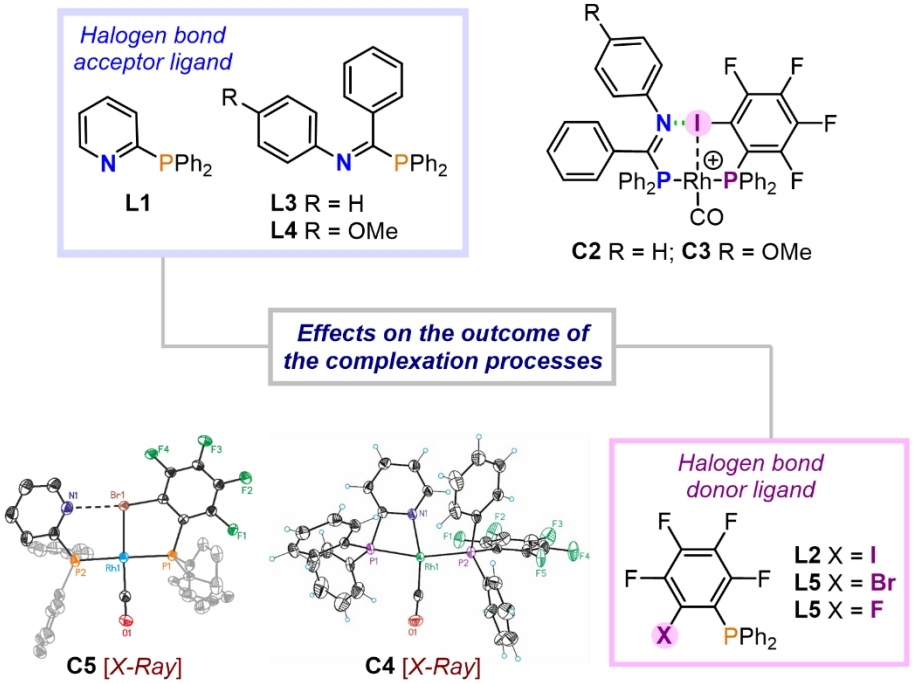

Chapter III: *Counterion variation: a useful lever for maximizing the regioselectivity in the hydroboration of terminal alkynes.*

In this chapter a series of XBphos-Rh **C1** analogues incorporating diverse counterions were successfully synthesized and characterized. With the aim of maximizing the regioselectivity of the hydroboration of alkynes towards the branched alkenyl boronates by variation of the counterion, octy-1-ne **S1** was used as the benchmark substrate and catecholborane **HBcat** as the borane source.

We demonstrated that the stronger the coordination ability of the counterion, the higher the activity and selectivity towards hydroboration products were. The use of (sub)stoichiometric amounts of catecholborane **HBcat** was proven to be beneficial for the preparation of the branched hydroboration products with the highest yields being obtained under these conditions. An array of structurally diverse alkynes was subjected to hydroboration conditions employing XBphos-Rh-OTf **C1·OTf** as the catalyst. Our study concluded that linear and inactivated alkyl-substituted alkynes led to the highest levels of chemo- and regio-selectivity in the hydroboration reaction.

The practicality of our synthetic method was demonstrated by developing a one-pot hydroboration/Csp^2–Csp^2 coupling process. We demonstrated that the coordination ability of the counterion can be correlated with the electronic richness of the metal center and the activity of the XBphos-Rh-X **C1·X** catalyst in hydroborations: OTf > NTf_2 > BArF > BF_4 ≈ PF_6. As for the mechanistic rationale of the reaction, NMR studies demonstrated that the hydroboration process starts with the oxidative addition of **HBcat** to the rhodium(I) center. The reaction further proceeds with the coordination of the alkyne followed by hydride migration/C–B reductive elimination reaction pathway **A,** or boryl migration/C–H reductive elimination reaction pathway **B,** to give product (*br*)-**P** after a reductive elimination step.

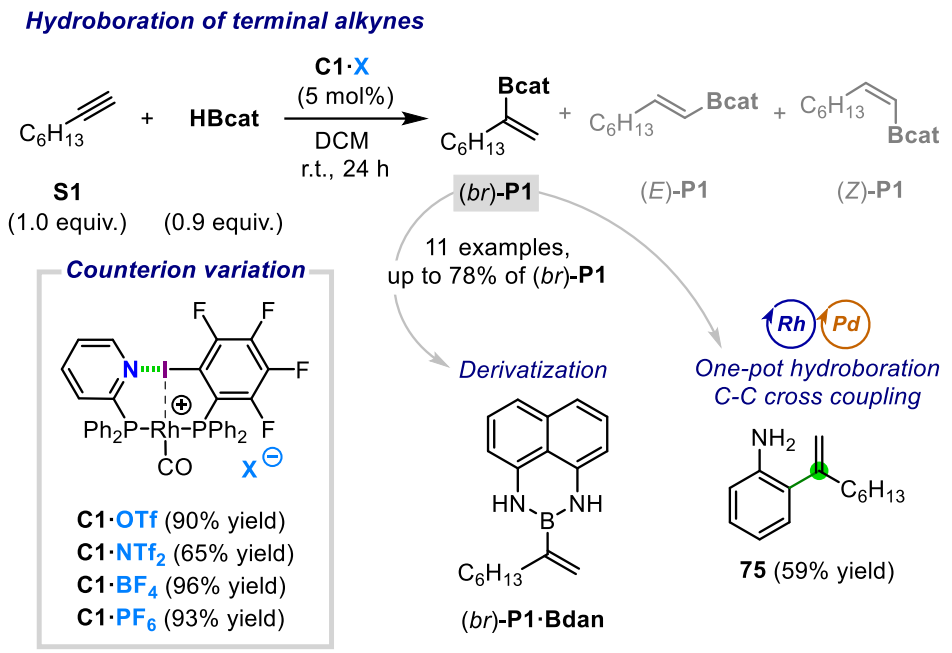

Chapter IV: *Catalytic intramolecular [4+2] cyclization of dien-γ-ynes enabled by the cooperative action of Rh/Ag derivatives.*

In this chapter an efficient intramolecular [4+2] cycloaddition of dien-γ-ynes mediated by the rhodium(I) complex derived from a halogen-bonded bisphosphane **C1·BArF** in combination with a silver(I) salt have been developed. Under optimized catalytic reaction conditions, the cooperative action of the Rh/Ag derivatives efficiently led to the corresponding [4+2] cycloadducts (yields ranging from 66% to 99%) with high selectivity. The synthetic protocol features simple operation and good functional group tolerance and represents a good example of the cooperative action of two metals in catalysis.

Studies aimed at determining the role of rhodium(I) and Ag(I) derivatives were performed and revealed that both metallic derivatives are required for the reaction to take place. Concretely, whilst rhodium is responsible for the cycloaddition process, silver activates the dien-γ-ynes

by increasing their electrophilicity due to coordination of Ag(I) to the unsaturated C–C bonds. The role of silver(I) derivatives used for generating the rhodium(I) catalysts developed by other research groups should be revisited in order to determine whether silver(I) derivatives have the mere role of abstracting chlorido ligands from rhodium complexes or are also necessary for activating the dien-γ-ynes towards [4+2] cycloadditions in analogous manner to that herein demonstrated.

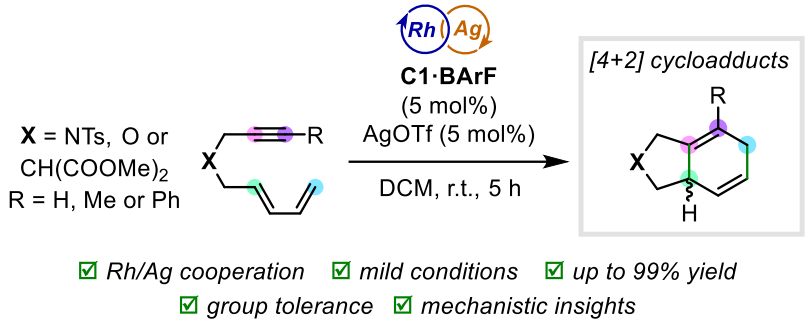

Chapter V: *Toward new halogen bond-assembled Ir(I) catalysts and their application in double hydroalkoxylation reactions.*

In this chapter two closely related halogen-bonded iridium complexes [Ir(CO)$_2$(κ^3*I,P,P*-**L1·L2**)]BArF **C9** and [Ir(CO)(κ^3*I,P,P*-**L1·L2**)]BArF **C10** have been successfully prepared and fully characterized in solution and in the solid state. NMR spectroscopic analysis revealed an equilibrium between **C9** and **C10**, involving exchange of one CO molecule taking place in solution. Crystals suitable for X-Ray analysis allowed for the unequivocal elucidation of the structure of both iridium(I) complexes: a trigonal bipyramidal complex in case of **C9** and a square planar complex in the monocarbonyl derivative **C10**.

Our halogen bond-assembled complex [Ir(CO)$_2$(κ^3*I,P,P*-**L1·L2**)]BArF **C9** has been efficiently applied in consecutive double intra- and intermolecular hydroalkoxylation of alkynyl alcohols for the synthesis of *O,O*-ketal products. An array of structural diverse alkynol substrates have

been tested under our optimized conditions by using **C9** as catalyst. Best results in terms of conversion and reaction yield have been achieved when using linear alkynyl alcohol **S20** and cyclic substrate **S26**, which led to the formation of *O*-containing spirocyclic compounds.

Additionally, mechanistic experiments have been carried out with the aim of clarifying the hydroalkoxylation reaction pathway with complex [Ir(CO)$_2$(κ^3*I,P,P*-**L1·L2**)]BArF **C9** as catalyst. A C–H activation of the terminal triple bond has been proposed as the first step of the catalytic cycle according to the observed spectroscopic evidence. These also strongly supported the existence of the halogen bonding interaction during the course of the catalytic cycle, pointing to a bidentate nature of our halogen bond-assembled ligand after the C–H activation of alkynyl alcohol substrates.